



Provided by the author(s) and University of Galway in accordance with publisher policies. Please cite the published version when available.

Title	A theoretical and kinetic modelling study of free radical addition reactions to unsaturated C2, C3 and C5 hydrocarbons
Author(s)	Sun, Yanjin
Publication Date	2021-02-02
Publisher	NUI Galway
Item record	<a href="http://hdl.handle.net/10379/16528">http://hdl.handle.net/10379/16528</a>

Downloaded 2024-04-26T20:01:51Z

Some rights reserved. For more information, please see the item record link above.



**A theoretical and kinetic modelling study of free radical addition reactions to unsaturated C<sub>2</sub>, C<sub>3</sub> and C<sub>5</sub> hydrocarbons**

Yanjin Sun

(M.Sc, B. Eng.)

Submitted in fulfillment of the requirements for the  
degree of

Doctor of Philosophy

School of Chemistry

National University of Ireland, Galway



Supervisor: Prof. Henry J. Curran

Head of School: Dr. Patrick O'Leary

Submitted November 2020



## Abstract

Radical addition to the double bond of an olefin is an important reaction class in combustion mechanism development. Addition reactions of free radicals to small alkenes ( $C_2 - C_3$ ) have been studied here at high levels of theory. To develop detailed pyrolysis and oxidation mechanisms of larger alkenes, a series of theoretical studies have been carried out for  $\dot{H}$  atom addition reactions to  $C_4 - C_5$  alkenes at the Combustion Chemistry Centre ( $C^3$ ) at NUI Galway. As a further step of this systematic project, addition reactions of  $\dot{H}$  atoms to dienes have been studied at similar levels of theory.

From the perspective of  $\dot{H}$  atom addition to 1,3-pentadiene, an ab initio and transition state theory (TST) study has been carried out for the reactions on the  $\dot{C}_5H_9$  potential energy surface (PES) in *this thesis*, with the calculations of thermochemistry, high-pressure limiting and pressure-dependent rate constants. A chemical kinetic model describing reactions related to the  $\dot{C}_5H_9$  PES was developed with thermochemistry and rate constants for  $\dot{H}$  atom addition reactions, H-atom abstraction reactions by  $\dot{H}$  atoms and other radicals (e.g.  $\dot{C}H_3$ ,  $\dot{O}H$ ), and unimolecular decomposition reactions of related species. This model was then incorporated into AramcoMech3.0 to simulate experimental species concentration profiles available in the literature. The pressure-dependent rate constants calculated were compared to the literature results, with a difference of 40% in the partition function calculations at 300 K observed between this work and the literature data. This is due to the use of different density functional theory (DFT) methods for the hindered rotor treatment.

To validate the uncertainties of rate constants that stem from the use of different electronic structure methods for the hindered-rotor treatment, the rotations of rotors that are newly formed from radical additions to  $C_2/C_3$  unsaturated hydrocarbons were calculated using twelve DFT methods. For rotors formed by  $\dot{R} + C_2$  alkenes/alkynes, the DFT results were also compared with DLPNO-CCSD(T)/CBS results. The uncertainties in the hindrance potential, rotational constant and partition function calculations stemmed from the use of different DFT methods for the internal rotor treatment and were discussed for the rotors formed by these radical addition reactions.

# Declaration

This is to certify that:

1. This thesis consists of my original work towards the degree of Doctor of Philosophy except where indicated appropriately.
2. All other literature material used has been appropriately cited.

## Acknowledgements

First and foremost, I would like to express my sincerest gratitude to my supervisor Prof. Henry Curran for providing me not only the precious opportunity to study at the Combustion Chemistry Centre, but also for a lot great opportunities and experiences to study outside of Ireland. I also want to thank you for your support and encouragement during my PhD which gave me more confidence to finish the PhD study. Thank you!

Great thanks to Prof. Chongwen Zhou for introducing me to the world of theoretical calculations, your patient guidance always helped me in solving problems during my study. I also would like to say thanks to your family who gave me so much help and support in my daily life. Thank you to my friend and mentor Dr. Kieran Somers, who taught me both the theoretical knowledge and a careful and responsible attitude towards work. I am so grateful to you for always giving me generous help to overcome the most difficult problems of the papers and guiding me to explore the interesting aspects of the work. Thank you! Thank you also to Dr. Stephen Klippenstein for your generous guidance in theoretical calculations, and also your kind support throughout my visit at Argonne National Laboratory.

A big thank you to all of the past and present members and visitors of C<sup>3</sup> group—Yingjia, Ultan, Manik, Amrit, Snehasish, Zhaohong, Mohammadreza, Patrick, Ahmed, Shashank, Vaibhav, and Morad, thank you all for accompanying me on this journey! Thank you to Shijun, Yang, Nitin, Gavin, Haitao, Yingtao, Sergio for being such good friends to me. Quande and Jinhu, thank you for your support and help both in study and life, you are the best roommates ever! Jennifer, I am so lucky to start my PhD study together with you and you are always so warm and friendly to me, hope we can be best friends forever. Special thanks to Colin for being our Chicago tour guide and it was such a great memory.

Thank you to all the friends that I met in Galway, Alice and Jingjing, I am so grateful to have you as roommates—you made my life more interesting and enjoyable! Thanks to everyone in the School of Chemistry for always being so friendly to me and making great efforts to help me with my research.

Finally, thank you to my family and my best friend Qian! 亲爱的爸爸妈妈, 毛妹毛弟, 谢谢你们一直以来对我无条件的理解和支持! 毛毛, 这几年工作照顾家里, 辛苦了! 谢谢姚倩同学对我的陪伴和开导! 这张学位证有你们的一半, 永远爱你们!

聪明在于学习，

天才在于积累。

——华罗庚

Cleverness lies in diligence,

genius lies in accumulation.

——Hua Luogeng



## Traceable Achievements

### Peer-Reviewed Papers

1. **Y. Sun**, C-W. Zhou, K.P. Somers, H.J. Curran, An ab Initio/transition state theory study of the reactions of  $\dot{C}_5H_9$  species of relevance to 1,3-pentadiene. Part I: Potential energy surfaces, thermochemistry and high-pressure Limiting rate constants, *Journal of Physical Chemistry A* 123(22) (2019) 9019–9052.
2. **Y. Sun**, C-W. Zhou, K.P. Somers, H.J. Curran, An Ab Initio/Transition State Theory Study of the Reactions of  $\dot{C}_5H_9$  Species of Relevance to 1,3-Pentadiene, Part II: Pressure Dependent Rate Constants and Implications for Combustion Modelling, *Journal of Physical Chemistry A* 124 (23) (2020) 4605–4631.
3. **Y. Sun**, K.P. Somers, Q-D Wang, H.J. Curran, Hindered Rotor Benchmarks for the Transition States of Free Radical Additions to Unsaturated Hydrocarbons, *Physical Chemistry Chemical Physics* 22 (2020) 27241–27254.
4. Q-D Wang, **Y. Sun**, H. J. Curran, Comparative Chemical Kinetic Analysis and Skeletal Mechanism Generation for Syngas Combustion with NO<sub>x</sub> Chemistry, *Energy and Fuels* 34(1) (2020) 949–964.
5. Q-D Wang, **Y. Sun**, M-M Sun, J-H Liang, Chemical Kinetics of Hydrogen Atom Abstraction from Propargyl Sites by Hydrogen and Hydroxy Radicals, *International Journal of Molecular Sciences* 20(13) (2019) 3227.

## Conference Proceedings

1. Y. Sun, C-W Zhou, K. P. Somers, H. J. Curran, “An Ab-initio and Kinetic Study of the Reactions of  $\dot{C}_5H_9$  species of Relevance to 1,3-Pentadiene”, KAUST Research Conference: Future of Fuel, Jeddah, Saudi Arabia, 4–7<sup>th</sup> March, 2019.
2. Y. Sun, K. P. Somers, H. J. Curran, “Influence of 1-D Hindered Rotor Model on High-pressure Limit Rate Constant Arising from Electronic Structure Method Selection for Vinyl + Ethylene and Vinyl + Propene Reactions”, 37<sup>th</sup> International Symposium on Combustion, Dublin, 29<sup>th</sup> July–3<sup>rd</sup> August, 2018.
3. Y. Sun, C-W Zhou, H. J. Curran, “An Ab Initio and Kinetic Study of the Reaction of  $\dot{H}$  atoms with 1,3-Pentadiene”, Proceedings of the 3<sup>rd</sup> General meeting and workshop on SECs in Industry of SMARTCATs Action, Czech Academy of Sciences, Prague, Czech Republic, 25–27<sup>th</sup> October, 2017.
4. Y. Sun, C-W Zhou, H. J. Curran, “An Ab Initio and Kinetic Study of the Reaction of 1, 3-Pentadiene +  $\dot{H}$ ”, Proceedings of the European Combustion Meeting, University of Zagreb, Croatia, 18–21<sup>st</sup> April, 2017.

## Oral Presentations:

1. “Combustion Chemistry: Ab Initio and Kinetic Study of the Reaction of H atoms with 1,3-Pentadiene”, Chemistry Research Day, NCBES Building, 9<sup>th</sup> January, 2019.

## Research Visits:

### 2.1 Affiliation: Argonne National Laboratory

Location: Chicago, USA

Host(s): Dr. Stephen Klippenstein

Duration: 4 weeks; 6<sup>th</sup> April – 4<sup>th</sup> May, 2019

# Chapters

1. Introduction.....	1
1.1 Background.....	1
1.2 Quantum chemistry .....	4
1.3 Chemical kinetics and thermodynamics.....	11
1.4 Quantum and kinetic calculation software .....	14
1.5 Chemical kinetic modelling.....	25
1.6 Goals and Overview of This Thesis .....	28
References .....	29
2. An Ab Initio/Transition State Theory Study of the Reactions of $\dot{C}_5H_9$ Species of Relevance to 1,3-Pentadiene, Part I: Potential Energy Surfaces, Thermochemistry and High-pressure Limiting Rate Constants .....	37
3. An Ab Initio/Transition State Theory Study of the Reactions of $\dot{C}_5H_9$ Species of Relevance to 1,3-Pentadiene, Part II: Pressure Dependent Rate Constants and Implications for Combustion Modelling .....	111
4. Hindered Rotor Benchmarks for the Transition States of Free Radical Additions to Unsaturated Hydrocarbons .....	165
5. Comparative chemical kinetic analysis and skeletal mechanism generation for syngas combustion with $NO_x$ chemistry.....	199
6. Chemical Kinetics of Hydrogen Atom Abstraction from Propargyl Sites by Hydrogen and Hydroxy Radicals.....	237
7. Conclusions.....	261
Appendix A.....	265
Appendix B.....	273
Appendix C.....	279



# List of Figures

1.1	The main functions and detailed commands of the InSyLyCO code [40] .....	15
1.2	Density of states for internal rotation of the transition state 1,4- $\dot{C}_4H_7$ calculated at different levels of theory, with 6-311++G(d,p) basis set used for these five method .....	21
1.3	Hinder-rotor partition function calculated using Fourier series expansion fitted from hindrance potentials, with 6-311++G(d,p) basis set used for these five methods .....	22
1.4	General schematic mechanism for fuel oxidation [25, 104] .....	27
2.1	Different configurations of 1,3-pentadiene .....	46
2.2	Schematic for numbering the ring-structured $C_5$ species .....	46
2.3	Schematic for different types of linear $\dot{C}_5H_9$ radicals .....	47
2.4	Schematic for endo- and exo-cycloaddition reactions of alkenyl radicals.....	48
2.5	The mean difference graph for enthalpy of formation at 298 K.....	51
2.6	The mean difference graph for entropy at 298 K.....	52
2.7	The mean difference graph for heat capacity at 298 K.....	52
2.8	PES for H-atom abstraction from 1,3-pentadiene by $\dot{H}$ atoms .....	59
2.9	Rate constants for H-atom abstraction from 1,3-pentadiene. (b) rate constant comparisons between H-atom abstraction from 1,3-pentadiene and propene, (c) rate constant comparisons between H-atom abstraction reaction from 1,3-pentadiene and 1,3-butadiene.....	61
2.10	Potential energy surface for the entrance channels. (b) High-pressure limiting rate constants of the entrance channels for $\dot{H}$ atom addition to 1,3-pentadiene.....	62
2.11	High-pressure limiting rate constant comparison between H-atom abstraction and $\dot{H}$ atom addition reactions from/to 1,3-pentadiene.....	63
2.12	High-pressure limiting and pressure-dependent rate constant comparisons for $\dot{H}$ atoms addition to 1,3-pentadiene, 1,3-butadiene, propene and 1-butene.....	65

2.13	Evans-Polanyi correlation for $\dot{\text{H}}$ atom addition to linear dienes and alkynes.....	67
2.14	Complete $\dot{\text{C}}_5\text{H}_9$ potential energy surface for $\dot{\text{H}}$ atom addition reaction of 1,3-pentadiene.....	69
2.15	Potential energy surface for the isomerization and decomposition reactions of 2,4- $\dot{\text{C}}_5\text{H}_9$ radicals. (b) Comparison of the high-pressure limiting rate constants for subsequent reactions of 2,4- $\dot{\text{C}}_5\text{H}_9$ (W1).....	75
2.16	Potential energy surface for the isomerization and decomposition reactions of 2,5- $\dot{\text{C}}_5\text{H}_9$ radicals. (b) Comparison of the high-pressure limiting rate constants for subsequent reactions of 2,5- $\dot{\text{C}}_5\text{H}_9$ (W2).....	76
2.17	Potential energy surface for the isomerization and decomposition reactions of 1,3- $\dot{\text{C}}_5\text{H}_9$ radical. (b) Comparison of the high-pressure limiting rate constants for subsequent reactions of 1,3- $\dot{\text{C}}_5\text{H}_9$ (W4).....	78
2.18	Potential energy surface for the isomerization and decomposition reactions of 1,4- $\dot{\text{C}}_5\text{H}_9$ radical. (b) Comparison of the high-pressure limiting rate constants for subsequent reactions of 1,4- $\dot{\text{C}}_5\text{H}_9$ (W3).....	79
2.19	PES for the formation and subsequent reactions of W14 ( $\text{kcal mol}^{-1}$ ). (b) Comparison of the high-pressure limiting rate constants for subsequent reactions of 3-methyl-1-buten-4-yl (W14).....	81
2.20	2.20 (a) High-pressure limiting rate constants for the subsequent reactions of 1,4- $\dot{\text{C}}_5\text{H}_9$ . (b) High-pressure limiting rate constants for the subsequent reactions of 3-methyl-1-buten-4-yl (W14).....	82
2.21	PES for the isomerization and decomposition reactions of 2,2- $\dot{\text{C}}_5\text{H}_9$ radical. (b) Comparison of the high-pressure limiting rate constants for subsequent reactions of 2,2- $\dot{\text{C}}_5\text{H}_9$ (W7).....	83
2.22	PES for the isomerization and decomposition reactions of 2,3- $\dot{\text{C}}_5\text{H}_9$ radical. (b) Comparison of the high-pressure limiting rate constants for subsequent reactions of 2,3- $\dot{\text{C}}_5\text{H}_9$ (W8).....	84
2.23	PES for the isomerization and decomposition reactions of 1,2- $\dot{\text{C}}_5\text{H}_9$ radical. (b) Comparison of the high-pressure limiting rate constants for subsequent reactions	

of 1,2- $\dot{C}_5H_9$ (W11).....	86
2.24 PES for the isomerization and decomposition reactions of 1,1- $\dot{C}_5H_9$ radical. (b) Comparison of the high-pressure limiting rate constants for subsequent reactions of 1,1- $\dot{C}_5H_9$ .....	87
2.25 PES for the isomerization and decomposition reactions of 1,5- $\dot{C}_5H_9$ radical. (b) Comparison of the high-pressure limiting rate constants for subsequent reactions of 1,5- $\dot{C}_5H_9$ radicals.....	88
2.26 PES for the formation and subsequent reactions of W5, W13 and W20. (b) PES for the formation and subsequent reactions of W6, W9 and W21.....	90
2.27 PES for the formation and subsequent reactions of four-membered ring $\dot{C}_5H_9$ radicals.....	90
2.28 Evans-Polanyi relationships for the exo- and endo-cycloaddition reactions. (b) High-pressure limiting rate constant comparisons for cyclisation reactions forming cyclic $\dot{C}_5H_9$ radicals.....	91
2.29 Evans-Polanyi relationships at 0 K for the isomerisation reactions of cyclic $\dot{C}_5H_9$ radicals.....	93
2.30 Evans-Polanyi relationships for C–C and C–H bond breaking reactions of cyclic $\dot{C}_5H_9$ radicals.....	95
2.31 Evans-Polanyi relationships for the 1,2- to 1,5-H shift isomerization reactions of linear $\dot{C}_5H_9$ radicals.....	97
2.32 Evans-Polanyi relationships for the C–H and C–C bond breaking reactions at 0 K, (b) High-pressure limiting rate constant comparisons for the C–H and C–C bond breaking reactions of $\dot{C}_5H_9$ radicals.....	99
2.33 The important reaction channels for $\dot{H}$ atom addition to 1,3-butadiene and 1,3-pentadiene with the energies for all species are relative to their corresponding reactants on two potential energy surfaces.....	102
2.34 High-pressure limiting rate constant comparisons for important reaction pathways of 1,3-butadiene + $\dot{H}$ [8] and 1,3-pentadiene + $\dot{H}$ .....	103
3.1 Flux analysis at 20% fuel consumption for 0.0001% 1,3- $C_5H_8$ , 0.01% $\dot{H}$ in $N_2$ , $p = 1$ atm, $T = 1400$ K.....	123

3.2	Flux analysis at 20% fuel consumption for 0.0001% 1,3-C <sub>5</sub> H <sub>8</sub> , 0.01% $\dot{\text{H}}$ in N <sub>2</sub> , $p = 1$ atm, $T = 1800$ K.....	124
3.3	Simplified $\dot{\text{C}}_5\text{H}_9$ PES with ZPVE corrected restricted energies relative to 1,3-pentadiene + $\dot{\text{H}}$ .....	126
3.4	(a) The pressure-dependent rate constants and high-pressure limiting rate constants for 1,3-pentadiene + $\dot{\text{H}} \rightarrow$ all products as a function of temperature. (b) The pressure-dependent and high-pressure limiting rate constants for 1,3-pentadiene + $\dot{\text{H}} \rightarrow$ thermodynamically stabilized wells and bimolecular products at 0.01, 0.1, 1, 10, and 100 atm.....	129
3.5	(a) The branching ratios for important products from $\dot{\text{H}}$ addition to 1,3-pentadiene at 1 atm. (b) The branching ratios for 2,4- $\dot{\text{C}}_5\text{H}_9$ radical (W1) and 1,3-butadiene + $\dot{\text{C}}\text{H}_3$ (P14) produced from $\dot{\text{H}}$ addition to 1,3-pentadiene at 0.01, 0.1, 1, 10, and 100 atm.....	130
3.6	The total rate constant comparisons between the H-atom abstraction reactions by $\dot{\text{H}}$ atoms and $\dot{\text{H}}$ atom addition reactions from/to 1,3-pentadiene.....	131
3.7	(a) The branching ratios for important products generated by $\dot{\text{H}}$ atom addition to 1,4-pentadiene at 1 atm. (b) The branching ratios for 1,4- $\dot{\text{C}}_5\text{H}_9$ radical (W3), 1,3-butadiene + $\dot{\text{C}}\text{H}_3$ (P14), $\dot{\text{C}}_2\text{H}_3 + \text{C}_3\text{H}_6$ (P12), and $\text{C}_2\text{H}_4 + \dot{\text{C}}_3\text{H}_5\text{-a}$ (P15) produced from $\dot{\text{H}}$ atom addition to 1,4-pentadiene at 1, 10, and 100 atm.....	132
3.8	(a) Rate constant comparisons for H-atom abstraction reactions of 1,4-pentadiene by $\dot{\text{H}}$ atoms. (b) The total rate constant comparisons between the H-atom abstraction reactions by $\dot{\text{H}}$ atoms and $\dot{\text{H}}$ atom addition reactions from/to 1,4-pentadiene.....	133
3.9	(a) The branching ratios for important products from $\dot{\text{H}}$ atom addition to cyC <sub>5</sub> H <sub>8</sub> at 1 atm, (b) the branching ratios for cy $\dot{\text{C}}_5\text{H}_9$ radical (W15) and $\text{C}_2\text{H}_4 + \dot{\text{C}}_3\text{H}_5\text{-a}$ (P15) produced from $\dot{\text{H}}$ atom addition to cyC <sub>5</sub> H <sub>8</sub> at 0.01, 0.1, 1, 10, and 100 atm.....	134
3.10	(a) Rate constant comparisons for H-atom abstraction reactions of cyC <sub>5</sub> H <sub>8</sub> by $\dot{\text{H}}$ atoms from this work and literature [15]. (b) The total rate constant comparisons between the H-atom abstraction reactions by $\dot{\text{H}}$ atoms and $\dot{\text{H}}$ atom addition	

reactions from/to $\text{cyC}_5\text{H}_8$ .....	135
3.11 (a) The branching ratios for important products from allyl addition to ethylene at 1 atm. (b) the branching ratios for $1,5\text{-}\dot{\text{C}}_5\text{H}_9$ (W10) and $1,4\text{-C}_5\text{H}_8 + \dot{\text{H}}$ (P22) produced from allyl addition to ethylene at 0.01, 1.0 and 100 atm.....	136
3.12 The total rate constant comparisons between the H-atom abstraction reactions and addition reactions of allyl radical with ethylene.....	136
3.13 (a) The branching ratios for important products from vinyl addition to propene at 1 atm. (b) The branching ratios for $1,4\text{-}\dot{\text{C}}_5\text{H}_9$ (W3), $1,3\text{-C}_5\text{H}_8 + \dot{\text{H}}$ , $1,3\text{-C}_4\text{H}_6 + \dot{\text{C}}\text{H}_3$ (P14) and $1,4\text{-C}_5\text{H}_8 + \dot{\text{H}}$ (P22) produced from vinyl addition to propene at 0.01, 0.1, 1, 10 and 100 atm.....	137
3.14 The total rate constant comparisons between the H-atom abstraction reactions and addition reactions of vinyl radical and propene.....	138
3.15 Comparison of the experimental and calculated rate constants for vinyl + alkenes (ethylene, propene and butene isomers) at 0.13 atm.....	140
3.16 (a) The comparisons of pressure-dependent rate constants and high-pressure limiting rate constants for $1,3\text{-}\dot{\text{C}}_5\text{H}_9 \rightarrow$ all products as a function of temperature. (b) The branching ratios for main products from decomposition of $1,3\text{-}\dot{\text{C}}_5\text{H}_9$ radical at 0.01, 0.1, 1, 10 and 100 atm.....	142
3.17 Rate constant comparisons for the $\beta$ -scission reaction of $1,3\text{-}\dot{\text{C}}_5\text{H}_9$ radical forming $1,3\text{-C}_4\text{H}_6 + \dot{\text{C}}\text{H}_3$ .....	143
3.18 (a) The comparisons of pressure-dependent rate constants and high-pressure limiting rate constants for $1,4\text{-}\dot{\text{C}}_5\text{H}_9 \rightarrow$ all products as a function of temperature. (b) The branching ratios for main products from decomposition of $1,4\text{-}\dot{\text{C}}_5\text{H}_9$ radical at 0.01, 0.1, 1, 10 and 100 atm.....	144
3.19 (a) The comparisons of pressure-dependent rate constants and high-pressure limiting rate constants for $1,5\text{-}\dot{\text{C}}_5\text{H}_9 \rightarrow$ all products as a function of temperature. (b) The branching ratios for main products from decomposition of $1,5\text{-}\dot{\text{C}}_5\text{H}_9$ radical at 0.01, 0.1, 1, 10 and 100 atm.....	145
3.20 High-pressure limiting rate constants for $\beta$ -scission reaction of $1,5\text{-}\dot{\text{C}}_5\text{H}_9$ radical to allyl + ethylene.....	146

3.21 (a)	The comparisons of pressure-dependent rate constants and high-pressure limiting rate constants for $\text{cy}\dot{\text{C}}_5\text{H}_9 \rightarrow$ all products as a function of temperature.	
(b)	The branching ratios for main products from decomposition of $\text{cy}\dot{\text{C}}_5\text{H}_9$ radical at 0.01, 0.1, 1, 10 and 100 atm.....	147
3.22	Rate constants for (a) C–H $\beta$ -scission reaction of $\text{cy}\dot{\text{C}}_5\text{H}_9$ radicals forming $\text{cyC}_5\text{H}_8 + \dot{\text{H}}$ . (b) C–C $\beta$ -scission reaction of $\text{cy}\dot{\text{C}}_5\text{H}_9$ radicals forming $1,5\text{-}\dot{\text{C}}_5\text{H}_9$ .....	149
3.23	The branching ratios of $\text{cy}\dot{\text{C}}_5\text{H}_9$ radicals comparing with high-pressure limiting rate constants in the literature.....	151
3.24 (a)	The comparisons of pressure-dependent rate constants and high-pressure limiting rate constants for $2,4\text{-}\dot{\text{C}}_5\text{H}_9 \rightarrow$ all products as a function of temperature.	
(b)	The branching ratios for main products from decomposition of $2,4\text{-}\dot{\text{C}}_5\text{H}_9$ radical at 0.01, 0.1, 1, 10 and 100 atm.....	151
3.25 (a)	The comparisons of pressure-dependent rate constants and high-pressure limiting rate constants for $2,5\text{-}\dot{\text{C}}_5\text{H}_9 \rightarrow$ all products as a function of temperature.	
(b)	The branching ratios for main products from decomposition of $2,5\text{-}\dot{\text{C}}_5\text{H}_9$ radical at 0.01, 0.1, 1, 10 and 100 atm.....	153
3.26	Experimental [12] and modelled concentration profiles for products generated from $\dot{\text{H}}$ atoms addition to cyclopentane at temperatures over 950–1116 K and pressures of 2.3–3.4 bar.....	155
3.27	Experimental [16] and simulated concentration profiles for reactants used in experimental studies for $\dot{\text{H}}$ atom addition to cyclopentene at temperatures over 997–1167 K and pressures at 2.6–3.7 bar.....	156
3.28	Experimental [16] and simulated concentration profiles for products generated from $\dot{\text{H}}$ atom addition to cyclopentene at temperatures over 997–1167 K and pressures at 2.6–3.7 bar.....	158
4.1	Hindrance potentials for the rotor formed by $\dot{\text{C}}\text{H}_3$ radical addition to $\text{C}_2\text{H}_2$ calculated using twelve DFT methods.....	178
4.2 (a)	The deviations of bond lengths for the newly formed rotors in the TSs of $\dot{\text{C}}\text{H}_3$ , $\dot{\text{C}}_2\text{H}_3$ , $\dot{\text{C}}_2\text{H}_5$ , $\text{CH}_3\dot{\text{O}}$ radical additions to $\text{C}_2\text{H}_2$ , calculated at DFT and	

	CCSD(T)-F12/cc-pVDZ-F12 levels of theory. (b) The dihedrals of the newly formed rotors in the TS of $\dot{C}_2H_3$ radical addition to $C_2H_2$ , calculated at DFT and CCSD(T)-F12/cc-pVDZ-F12 levels of theory.....	181
4.3	(a) The hindrance potential energy deviations plot with $[E_{HR}(DFT) - E_{HR}(DFT^{mean})]$ on the $y$ -axis and $[E_{HR}(DFT) + E_{HR}(DFT^{mean})] \times 0.5$ on the $x$ -axis, of which $E_{HR}(DFT^{mean})$ is averaging over 32 rotors for each DFT method. (b) The hindrance potential energy deviations plot with $[E_{HR}(DFT) - E_{HR}(DFT^{mean})_r]$ on the $y$ -axis and $[E_{HR}(DFT) + E_{HR}(DFT^{mean})_r] \times 0.5$ on the $x$ -axis, of which $E_{HR}(DFT^{mean})_r$ is averaging over 12 DFT methods for each rotor.....	184
4.4	The linear correlation of mean hindered barriers and the maximum energy deviations of twelve DFT methods for rotors formed by $\dot{C}H_3/\dot{C}_2H_3/\dot{C}_2H_5/CH_3\dot{O} + C_2H_2/C_2H_4/C_3H_4-a/C_3H_4-p/C_3H_6$ .....	185
4.5	Hindrance potentials for internal rotors formed by $\dot{C}H_3, \dot{C}_2H_3, \dot{C}_2H_5, CH_3\dot{O}$ radical additions to $C_2H_2$ calculated at CCSD(T) and DLPNO-CCSD(T) level of theories with the use of different basis sets.....	186
4.6	Hindrance potentials for internal rotors formed by $\dot{C}H_3, \dot{C}_2H_3, \dot{C}_2H_5, CH_3\dot{O}$ additions to $C_2H_4$ calculated at CCSD(T) and DLPNO-CCSD(T) level of theories with the use of different basis sets.....	187
4.7	(a) The hindrance potential energies calculated using twelve DFT methods for the rotor formed by $\dot{C}_2H_3$ radical addition to $C_2H_2$ . (b) The hindrance potential energies calculated at DLPNO-CCSD(T)/CBS level of theory based on optimized geometries calculated using twelve DFT methods for the rotor formed by $\dot{C}_2H_3$ radical addition to $C_2H_2$ .....	188
4.8	The relative potential energy deviations $\Delta E_{HR}^{relative}(DLPNO - DFT)$ for each DFT method in comparison with the benchmarking DLPNO-CCSD(T)/CBS energies for rotors formed by $\dot{C}_2H_3$ radical additions to $C_2H_2$ .....	189
4.9	The maximum deviations between DFT and DLPNO-CCSD(T)/CBS potential energies for rotors formed by $\dot{C}H_3/\dot{C}_2H_3/\dot{C}_2H_5/CH_3\dot{O}$ radical additions to $C_2H_2/C_2H_4$ .....	191

4.10	The percentage deviations between DFT and the corresponding mean energies for rotors formed by $\dot{\text{C}}\text{H}_3/\dot{\text{C}}_2\text{H}_3/\dot{\text{C}}_2\text{H}_5/\text{CH}_3\dot{\text{O}}$ radical additions to $\text{C}_2\text{H}_2/\text{C}_2\text{H}_4$ at 300 K.....	192
4.11	The maximum percentage differences of $Q_{\text{HR}}$ ( $T = 300$ K) between DFT and DLPNO-CCSD(T)/CBS results.....	193
5.1	Element flux analysis of N during ignition delay time simulation of syngas/air mixture at initial temperature of 1200 K with equivalence ratio ( $\varphi$ ) of 1.0 and pressure of 20 atm.....	208
5.2	Element flux analysis of N during ignition delay time simulation of $\text{NH}_3$ /air mixture at initial temperature of 1500 K with equivalence ratio ( $\varphi$ ) of 1.0 and pressure of 20 atm.....	210
5.3	Sensitivity analysis of auto-ignition for $\text{H}_2/\text{N}_2\text{O}/\text{Ar}$ mixture (0.01/0.0016/0.9784) by using the five detailed mechanisms at pressure of 20 atm and temperatures of 950 K and 1500 K.....	213
5.4	Sensitivity analysis of auto-ignition for $\text{H}_2/\text{NO}_2/\text{Ar}$ mixture (0.01/0.0016/0.9784) by using the five detailed mechanisms at pressure of 20 atm and temperatures of 950 K and 1500 K.....	215
5.5	Reaction rate constants for reaction $\dot{\text{H}} + \text{NO}_2 = \dot{\text{O}}\text{H} + \dot{\text{N}}\text{O}$ as a function of temperature.....	217
5.6	Reaction rate constants used for reaction $\text{HONO} + \dot{\text{O}}\text{H} = \text{H}_2\text{O} + \text{NO}_2$ as a function of temperature.....	218
5.7	Reaction rate constants for reaction $\text{HNO} + \text{O}_2 = \dot{\text{N}}\text{O} + \text{H}\dot{\text{O}}_2$ as a function of temperature.....	220
5.8	Ignition delay times from shock tube experiments [41] in comparison to model predictions for 0.0133 $\text{H}_2$ /0.0067 $\text{O}_2$ /0.0001 $\text{NO}_2$ /0.9799 $\text{Ar}$ mixtures (mole fraction) at different pressures.....	224
5.9	Ignition delay times from shock tube experiments in comparison to model predictions for 0.01 $\text{H}_2$ /0.01 $\text{O}_2$ /0.0032 $\text{N}_2\text{O}$ /0.9768 $\text{Ar}$ mixtures (mole fraction) at different pressures [40].....	225
5.10	Ignition delay times from shock tube experiments [66] in comparison to model	

predictions for 0.01143NH <sub>3</sub> /0.00857O <sub>2</sub> /0.98Ar mixtures (mole fraction) at different pressures.....	226
5.11 Sensitivity analysis for the auto-ignition of a NH <sub>3</sub> /O <sub>2</sub> /Ar mixture using the updated detailed mechanisms at a pressure of 20 atm and at a temperature of 1500 K.....	227
5.12 $\dot{\text{N}}\text{O}$ and NO <sub>2</sub> species profiles as a function of temperature from experiment and modeling results. Symbols represent experimental measurements [68].....	228
5.13 ROP analysis for NO species during JSR simulations for 0.01 H <sub>2</sub> /0.05 O <sub>2</sub> /0.93975 N <sub>2</sub> /0.00025 NO mixture with residence time of 0.24 s at 30 atm and 850 K.....	229
5.14 Laminar flame speed comparisons between experimental data and mechanism predictions for H <sub>2</sub> /N <sub>2</sub> O mixture diluted by 60% Ar at 1.0 atm and 300 K.....	229
6.1 Optimized geometries (in Å and degrees) of TSs for the abstraction reactions by $\dot{\text{H}}$ atom at M06-2X/cc-pVTZ level.....	240
6.2 Optimized geometries (in Å and degrees) of TSs for the studied abstraction reactions by $\dot{\text{O}}\text{H}$ radical at M06-2X/cc-pVTZ level.....	241
6.3 Relative potential energies of the internal rotation of H atom in $\dot{\text{O}}\text{H}$ radical along the reaction center for (a) 1-butyne, (b) 4-penten-1-yne, and (c) 3-phenyl-1-propyne, respectively .....	243
6.4 Mulliken charge distributions of the TSs for 1-butyne, 4-penten-1-yne, and 3-phenyl-1-propyne with $\dot{\text{O}}\text{H}$ , respectively.....	244
6.5 Computed BDEs for C–H bond in acetylene and propyne. (a) W1BD method, (b) CCSD(T)/CBS method, (c) Recommended value from Luo [6].....	245
6.6 Computed rate constants for the H-atom abstraction reaction of propyne with $\dot{\text{H}}$ at the propargyl site.....	250
6.7 Computed rate constants for the H-atom abstraction reaction of propyne with $\dot{\text{O}}\text{H}$ at the propargyl site.....	250
6.8 Computed rate constants for the abstraction reactions with $\dot{\text{H}}$ at the propargyl site.....	251
6.9 Computed rate constants for the abstraction reactions with $\dot{\text{O}}\text{H}$ at propargyl	

site.....	252
B.1 (a) PES for unimolecular decomposition of 1,3-pentadiene. (b) High-pressure limiting rate constant comparison for 1,3-pentadiene dissociation reactions.....	274
B.2 PES for H-atom abstraction reactions from 1,4-pentadiene by $\dot{\text{H}}$ atoms.....	275
B.3 (a) PES for H-atom abstraction reactions from cyclopentene by $\dot{\text{H}}$ atoms. (b) High-pressure limiting rate constant comparison for H-atom abstraction reactions from cyclopentene by $\dot{\text{H}}$ atoms.....	276
B.4 (a) PES for H-atom abstraction reactions from propene by vinyl radicals. (b) High-pressure limiting rate constant comparison for H-atom abstraction reactions from propene by vinyl radicals.....	277
B.5 (a) High-pressure limiting rate constant comparison for $\beta$ -scission reactions of 1,3- $\dot{\text{C}}_5\text{H}_9$ radicals. (b) High-pressure limiting rate constant comparison for $\beta$ -scission reactions of 1,4- $\dot{\text{C}}_5\text{H}_9$ radicals.....	278
C.1 Rotational constants for the newly formed methyl rotors of $\dot{\text{C}}\text{H}_3$ radical additions to $\text{C}_2\text{H}_2/\text{C}_2\text{H}_4/\text{C}_3\text{H}_4\text{-a}/\text{C}_3\text{H}_4\text{-p}/\text{C}_3\text{H}_6$ calculated using twelve DFT methods.....	286
C.2 Rotational constants for rotors formed by $\dot{\text{C}}_2\text{H}_3$ radical additions to $\text{C}_2\text{H}_2/\text{C}_2\text{H}_4/\text{C}_3\text{H}_4\text{-a}/\text{C}_3\text{H}_4\text{-p}/\text{C}_3\text{H}_6$ calculated using twelve DFT methods.....	287
C.3 Rotational constants for rotors formed by $\dot{\text{C}}_2\text{H}_5$ radical additions to $\text{C}_2\text{H}_2/\text{C}_2\text{H}_4/\text{C}_3\text{H}_4\text{-a}/\text{C}_3\text{H}_4\text{-p}/\text{C}_3\text{H}_6$ calculated using twelve DFT methods.....	288
C.4 Rotational constants for rotors formed by $\text{CH}_3\dot{\text{O}}$ radical additions to $\text{C}_2\text{H}_2/\text{C}_2\text{H}_4/\text{C}_3\text{H}_4\text{-a}/\text{C}_3\text{H}_4\text{-p}/\text{C}_3\text{H}_6$ calculated using twelve DFT methods.....	289
C.5 Hindrance potentials for the newly formed methyl rotors of $\dot{\text{C}}\text{H}_3$ radical additions to $\text{C}_2\text{H}_2/\text{C}_2\text{H}_4/\text{C}_3\text{H}_4\text{-a}/\text{C}_3\text{H}_4\text{-p}/\text{C}_3\text{H}_6$ calculated using twelve DFT methods.....	290
C.6 Hindrance potentials for the newly formed methyl rotors of $\dot{\text{C}}_2\text{H}_3$ radical additions to $\text{C}_2\text{H}_2/\text{C}_2\text{H}_4/\text{C}_3\text{H}_4\text{-a}/\text{C}_3\text{H}_4\text{-p}/\text{C}_3\text{H}_6$ calculated using twelve DFT methods.....	291
C.7 Hindrance potentials for the newly formed methyl rotors of $\dot{\text{C}}_2\text{H}_5$ radical	

additions to C <sub>2</sub> H <sub>2</sub> /C <sub>2</sub> H <sub>4</sub> /C <sub>3</sub> H <sub>4</sub> -a/C <sub>3</sub> H <sub>4</sub> -p/C <sub>3</sub> H <sub>6</sub> calculated using twelve DFT methods.....	292
C.8 Hindrance potentials for the newly formed methyl rotors of CH <sub>3</sub> Ö radical additions to C <sub>2</sub> H <sub>2</sub> /C <sub>2</sub> H <sub>4</sub> /C <sub>3</sub> H <sub>4</sub> -a/C <sub>3</sub> H <sub>4</sub> -p/C <sub>3</sub> H <sub>6</sub> calculated using twelve DFT methods.....	293
C.9 The relative potential energy differences calculated using DFT and DLPNO-CCSD(T)/CBS methods for rotors formed by ĊH <sub>3</sub> /Ċ <sub>2</sub> H <sub>3</sub> /Ċ <sub>2</sub> H <sub>5</sub> /CH <sub>3</sub> Ö radical additions to C <sub>2</sub> H <sub>2</sub> and C <sub>2</sub> H <sub>4</sub> , and potential energy differences are relative to the lowest energy difference of each hindrance potential.....	294
C.10 The percentage deviations between DFT and the corresponding mean energies for rotors formed by ĊH <sub>3</sub> /Ċ <sub>2</sub> H <sub>3</sub> /Ċ <sub>2</sub> H <sub>5</sub> /CH <sub>3</sub> Ö radical additions to C <sub>2</sub> H <sub>2</sub> /C <sub>2</sub> H <sub>4</sub> at 500 K, 1000 K and 2000 K.....	295



# List of Tables

1.1	Computational costs for rate constant calculations using different grid and cutoff parameters in MESS input files for 2,4- $\dot{C}_5H_9$ radical decomposition at 1 atm .....	24
2.1	Available reactions on $\dot{C}_5H_9$ PES in the literature .....	40
2.2	The category of H-shift isomerization reactions for linear $\dot{C}_5H_9$ radicals .....	48
2.3	Thermochemistry comparison of 54 species on $\dot{C}_5H_9$ PES with literature data .....	53
2.4	Thermochemistry comparisons of 54 species on $\dot{C}_5H_9$ PES with literature data .....	55
2.5	The barrier heights for H-atom abstraction reaction of propene, 1,3-butadiene and 1,3-pentadiene by $\dot{H}$ atoms to generate different products and molecular hydrogen .....	61
2.6	The reaction enthalpies and barrier heights at 0 K for $\dot{H}$ atom addition to different alkynes and dienes .....	68
2.7	Structures and relative energies (0 K, ZPE corrected, kcal mol <sup>-1</sup> ) for all the species on the $\dot{C}_5H_9$ PES .....	70
2.8	Barrier heights (0 K, ZPE corrected, kcal mol <sup>-1</sup> ) of the transition states on the $\dot{C}_5H_9$ PES .....	72
2.9	Calculated heats of reactions and energy heights (kcal mol <sup>-1</sup> ) at 0 K for the cycloaddition reactions .....	92
2.10	Calculated heats of reactions and barrier heights (kcal mol <sup>-1</sup> ) at 0 K for the isomerisation reactions of cyclic $\dot{C}_5H_9$ radicals .....	94
2.11	Calculated heats of reactions and barrier heights (kcal mol <sup>-1</sup> ) at 0 K for the $\beta$ -scission reactions of cyclic $\dot{C}_5H_9$ radicals .....	95
2.12	Calculated heats of reactions and activation energies for the H-shift reactions .....	98
2.13	Calculated heats of reaction and barrier heights for the $\beta$ -scission reactions at 0 K .....	100

3.1	Summary of the theoretical and experimental literature studies relevant to $\dot{C}_5H_9$ species .....	114
3.2	Zero-point vibrational energy corrected electronic energies (kcal mol <sup>-1</sup> ) relative to 1,3-pentadiene + $\dot{H}$ .....	127
3.3	Comparison of the partition function ratios between this work and literature for vinyl + propene $\rightarrow$ 1,4- $\dot{C}_5H_9$ .....	141
4.1	Summary of the most widely used literature studies relevant to different radical ( $\dot{C}H_3$ , $\dot{C}_2H_3$ , $\dot{C}_2H_5$ , $CH_3\dot{O}$ ) additions to C <sub>2</sub> -C <sub>3</sub> alkenes, alkynes and dienes .....	169
4.2	The geometries of the TSs formed by 32 radical additions to different unsaturated hydrocarbons with the axis of the target hindered rotors marked with dashed lines .....	171
4.3	The optimized geometries and dihedrals of D(C <sub>2</sub> -C <sub>1</sub> -C <sub>6</sub> -C <sub>5</sub> ) for the TSs of $\dot{C}_2H_3$ radical addition to C <sub>2</sub> H <sub>2</sub> , calculated at two DFT and CCSD(T)-F12/cc-pVDZ-F12 levels of theory .....	182
5.1	Species related to the syngas/NO <sub>x</sub> combustion reaction system in the selected detailed mechanisms and the derived skeletal mechanism .....	206
5.2	Thermodynamic properties of selected important N-containing species in the reaction mechanisms .....	207
5.3	Updated reactions and the corresponding reaction rate coefficients .....	220
6.1	The computed reaction barriers using different methods for H-atom abstraction reactions of propyne and 1-butyne by $\dot{H}$ and $\dot{O}H$ radicals .....	246
6.2	Reaction barriers and enthalpies for different alkynes reacting with H atoms at M08-HX/cc-pVTZ level .....	248
6.3	Potential energies for the studied alkynes with $\dot{O}H$ at M08-HX/cc-pVTZ level .....	248
6.4	Fitted Arrhenius coefficients of the studied reactions in $k(T) = AT^n \exp(-E_a/RT)$ .....	253
A.1	<i>T</i> <sub>1</sub> diagnostic values for all the species excluding TSs on the $\dot{C}_5H_9$ PES .....	265
A.2	Open-shell <i>T</i> <sub>1</sub> diagnostic values for all TSs on the $\dot{C}_5H_9$ PES .....	268
A.3	The reaction enthalpies at 298 K and barrier heights for $\dot{H}$ atom addition to	

different alkynes and dienes .....	271
C.1 The bond lengths of the newly formed rotors for the TSs of $\dot{\text{C}}\text{H}_3$ , $\dot{\text{C}}_2\text{H}_3$ , $\dot{\text{C}}_2\text{H}_5$ , $\text{CH}_3\dot{\text{O}}$ radical additions to $\text{C}_2\text{H}_2$ .....	280
C.2 The dihedrals of the newly formed rotors for the TSs of $\dot{\text{C}}\text{H}_3$ , $\dot{\text{C}}_2\text{H}_3$ , $\dot{\text{C}}_2\text{H}_5$ , $\text{CH}_3\dot{\text{O}}$ radical additions to $\text{C}_2\text{H}_2$ .....	281
C.3 $T_1$ diagnostic values of the CCSD(T)/cc-pVQZ calculations .....	282
C.4 Maximum differences of the hindered barriers calculated using twelve DFT methods for the newly formed internal rotors in target reactions .....	283
C.5 Maximum differences of rotational constants calculated using twelve DFT methods for the newly formed internal rotors in target reactions .....	284
C.6 Maximum percentage errors of $Q_{\text{HR}}$ as a function of temperature calculated using twelve DFT methods for the newly formed internal rotors in target reactions .....	285
C.7 Maximum deviations of hindrance potential energies between DFT and DLPNO-CCSD(T) methods for rotors formed through $\dot{\text{C}}\text{H}_3/\dot{\text{C}}_2\text{H}_3/\dot{\text{C}}_2\text{H}_5/\text{CH}_3\dot{\text{O}}$ radical additions to $\text{C}_2\text{H}_2/\text{C}_2\text{H}_4$ .....	296
C.8 Maximum deviations of $Q_{\text{HR}}$ between DFT and DLPNO-CCSD(T) methods for rotors formed through $\dot{\text{C}}\text{H}_3/\dot{\text{C}}_2\text{H}_3/\dot{\text{C}}_2\text{H}_5/\text{CH}_3\dot{\text{O}}$ radical additions to $\text{C}_2\text{H}_2/\text{C}_2\text{H}_4$ .....	297



# Chapter 1

## General Introduction

### 1. Background

Currently, global energy demand, which is escalating due to the continuous increase in world population and rise in living standards, is largely met by fossil fuels [1, 2]. Based on the statistical data published by Eurostat database [3] in 2018, the biggest share in final energy consumption in Europe was transport (30.5%), of which primary energy consumption derived mostly from fossil fuels (at least 36.7%), followed by natural gas (21.4%), with electricity consumption amounting to 23.0%. Although the use of fossil fuels as energy suppliers has many disadvantages, such as limited reserves, non-homogeneous distribution of these reserves, and pollutant gas emissions, fuels will continue to be the most significant source of energy for the foreseeable future. To improve the combustion efficiency of fuels and reduce associated emissions, it is vital to understand the underlying chemistry of the combustion processes controlling fuel oxidation, which is considered as the connection between engine performance and fuel structure [4].

Commercial transportation fuels such as gasoline, diesel, aviation kerosene, etc. are complex mixtures of hundreds to thousands of hydrocarbons (including linear and branched paraffins, naphthenes, olefins and aromatics) and oxygenated chemical species [5-7]. In spite of the limited quantities of olefins (alkenes) in gasoline, they have a notable effect on its oxidative stability and autoignition characteristics [8]. In addition, olefins are important and common intermediates formed during the pyrolysis and oxidation of large alkanes, cycloalkanes and alcohols in practical fuels, which highlights their importance in combustion chemistry.

Detailed kinetic mechanisms describing the pyrolysis and oxidation of hydrocarbon fuels are nowadays widely used in the design of internal combustion engines to meet increasingly stringent environmental and energy efficiency standards. A survey of the 2015

volume of Combustion and Flame finds studies implementing kinetics models for biofuels, gasoline, diesel, and jet fuel surrogates and blends, large alkanes, aromatics, naphthenes, foundational fuels, pollutants, energetic materials, and fire inhibitors [9].

Combustion mechanisms for fuels generally consist of thousands of reactions with their associated rate coefficients, and the thermodynamic and transport properties for each species involved in these reactions. There are hundreds to thousands of chemical species involved in the pyrolysis and oxidation of fuels, with many key intermediates having very short lifetimes, which increases the difficulty of experiments in capturing and measuring these radicals either qualitatively or quantitatively. Many, if not most, of these properties have never been studied with direct experiments under any conditions, let alone at the temperatures and pressures relevant to practical combustion and pyrolysis devices [10]. Consequently, the use of quantum chemistry for the calculation of rate constants has become a key tool for mechanism development [11-14], which is accomplished through the continuing advances in theoretical methodologies and computational capabilities.

Alkanes are the simplest type of hydrocarbon, so knowledge of the combustion of these compounds is essential to the fundamental understanding of the combustion of all hydrocarbon and oxygenated fuels [15]. The oxidation chemistry of alkanes at low and high temperatures has been widely studied, with comprehensive mechanisms developed and reviewed in the literature [15-19]. The reactions of alkyl radicals are central to the chemistry of alkanes, with the thermochemistry of alkyl radicals and the kinetic properties of their related reactions being relatively well established [15, 20-24]. To accurately understand the chemistry of alkane oxidation, mechanisms describing the oxidation of other fuels such as olefins (alkenes, dienes, etc.) are also needed. For instance, alkenes are produced in the low-temperature oxidation of alkanes, particularly via the sequence  $\text{R}\dot{\text{O}}_2 \leftrightarrow \text{olefin} + \text{H}\dot{\text{O}}_2$  [25]. Thus, the oxidation mechanisms of alkanes, alkenes and dienes are all inter-linked.

Based on the theoretical and experimental studies of alkene consumption including propene [26, 27], 1-butene [12], iso-butene [28], 1- and 2-pentene [29], including both pyrolysis and oxidation, detailed kinetic models were developed and validated against experimental results. On the basis of these previous work on alkenes, it is found that the reaction kinetics of H atom addition to the C=C double bond plays a significant role in fuel

consumption kinetics and influences the predictions of high-temperature ignition delay times (IDTs), product species concentrations, and flame speed measurements [30]. Moreover, C<sub>3</sub>–C<sub>4</sub> dienes (allene and 1,3-butadiene) are important intermediates in the formation of soot and poly-aromatic hydrocarbons (PAH) through the proposed “C<sub>2</sub> + C<sub>4</sub>” benzene formation and propargyl radical combination pathways [31]. Therefore, an accurate knowledge of diene oxidation chemistry is essential to the further development of models describing PAH and soot formation [11].

The chemistries of alkenes and dienes are inter-linked. The  $\dot{C}_5H_9$  radicals can be formed via  $\dot{H}$  atom addition to 1,3-pentadiene and also by H-atom abstraction reactions from 1- and 2-pentene. Hence, dienes and their related alkenyl radicals are important intermediates in the pyrolysis and oxidation of higher-order hydrocarbons, with their oxidation kinetics important in the hierarchical development of kinetic mechanisms describing hydrocarbon combustion.

$\dot{H}$  atom addition to 1,3-butadiene and its related reactions on the  $\dot{C}_4H_7$  PES was studied by Li et al. [30] using two different series of ab initio electronic structure methods. The thermochemistry and pressure-dependent rate constants calculated were used by Zhou et al. [11] to develop a kinetic model describing 1,3-butadiene pyrolysis and oxidation. Power et al. [29] calculated the chemistry of  $\dot{H}$  atoms reacting with 1- and 2-pentene at a similar level of theory to the current work. Based on our understanding of 1,3-butadiene chemistry,  $\dot{H}$  atom addition to 1,3-pentadiene and its related reactions on the  $\dot{C}_5H_9$  PES is studied theoretically in *this thesis* to help improve our knowledge of detailed C<sub>5</sub> combustion chemistry.

The thermochemistry and rate constants (high-pressure limiting and pressure-dependent) calculated are compared with available literature data and implemented in AramcoMech3.0 [11] to simulate concentration profiles in shock tube experiments. Due to the complexity of the  $\dot{C}_5H_9$  PES (which involves 63 species and 88 transition states), the study of 1,3-pentadiene +  $\dot{H}$  is divided and published in two parts. The first part presents the comprehensive  $\dot{C}_5H_9$  PES, thermochemistry for C<sub>5</sub> species and high-pressure limiting rate constants for related reactions. The second presents the construction of a kinetic model consisting of pressure-dependent rate constants, which are used to simulate the experimental species concentration profiles for  $\dot{H}$  atom addition reactions to cyclopentane and cyclopentene.

The one-dimensional (1-D) hindered-rotor approximation is most widely used in the quantum mechanical treatment of low frequency vibrational modes, and the PES for the rotation is usually scanned using electronic structure methods. Through the partition function comparisons of the  $\dot{\text{C}}_2\text{H}_3 + \text{C}_3\text{H}_6$  reaction between our  $\dot{\text{C}}_5\text{H}_9$  work and the literature, it was found that the electronic structure methods used for internal rotation scans can induce uncertainties of up to 40% in calculated rate constants. To investigate the uncertainties in rate constants for  $\dot{\text{H}}$  atom addition reactions of  $\text{C}_2 - \text{C}_3$  unsaturated hydrocarbons induced from the use of different electronic structure methods, twelve prevalent DFT methods (four functions with three basis sets, B3LYP [32], M06-2X [33],  $\omega$ B97X-D [34], and B2PLYP-D3 [35] functionals with 6-31+G(d,p), 6-311++G(d,p) [36] and cc-pVTZ [37] basis sets) are adopted in *this thesis* for internal rotor treatment of the newly formed rotors in the transition states (TSs). The hindrance potentials, rotational constants and partition functions of these newly formed rotors calculated using these twelve DFT methods are compared and validated against the high-level DLPNO-CCSD(T)/cc-pVTZ results.

The remaining sub-sections of this Chapter will outline the methodologies and programs used in *this thesis* to explore the chemistry of  $\dot{\text{H}}$  atom addition reactions to  $\text{C}_2 - \text{C}_3$  unsaturated hydrocarbons and  $\text{C}_5$  dienes.

## 2. Quantum chemistry

Quantum chemistry applies quantum mechanics to problems in chemistry, with its influence being evident in all branches of chemistry [38]. Levine published a book [38] in 2000 (the 5<sup>th</sup> edition) to introduce quantum chemistry to graduate students and help them to understand modern methods of electronic structure calculations. For physical chemists, quantum mechanics is generally used to (1) theoretically calculate molecular properties; (2) calculate properties of TSs in chemical reactions, which are used for rate constant calculations; (3) calculate thermodynamic properties (e.g. enthalpy, entropy and heat capacity) of gases with the aid of statistical mechanics; (4) interpret molecular spectra, thereby allowing experimental determination of molecular properties (e.g. bond lengths, bond angles, dipole moments, barriers to internal rotation, and energy differences between conformational isomers); (5) understand intermolecular forces; (6) describe bonding in solids.

Ab initio means ‘from the beginning’ in Latin and hence ab initio calculations involve the solution of the Schrödinger Equation, which is the fundamental equation of quantum mechanics. The Schrödinger equation is a linear partial differential equation that describes the wave function or state function of a quantum-mechanical system [39]. The time-independent Schrödinger equation or the Schrödinger wave equation for a single particle of mass  $m$  moving in one-dimensional (in Cartesian coordinates) is given as:

$$\left[ -\frac{\hbar^2}{2m} \nabla^2 + V(x,y,z) \right] \psi(x,y,z) = E\psi(x,y,z) \quad (1)$$

Where  $\hbar$  is Planck’s constant in J s radian<sup>-1</sup>.  $\psi$  describes the state of the system in quantum mechanics as a product of spatial terms and is known as the wavefunction or the state function.  $V$  is the potential energy function and  $E$  is the energy of the system. For these cases, the probability density does not change with time and hence, these states are called stationary states [38]. The Laplace operator is defined as  $\nabla^2 = \frac{\partial^2}{\partial x^2} + \frac{\partial^2}{\partial y^2} + \frac{\partial^2}{\partial z^2}$  for cartesian systems.

Knowing the state, we cannot say that an electron is distributed over a large region of space as a wave is distributed. We can only predict the probabilities of various possible results. It is the probability patterns, namely wave functions, used to describe an electron’s motion that behaves like a wave and satisfies a wave equation [38].

For complex molecules, the time-independent form of the Schrödinger equation is similar to Eq. 1, but includes coordinates for every atom. The Hamiltonian operator  $\hat{H}$  for complex molecules can be expressed as:

$$\hat{H} = -\frac{\hbar^2}{2} \sum_{\alpha=1}^N \frac{1}{m_{\alpha}} \nabla_{\alpha}^2 - \frac{\hbar^2}{2m_e} \sum_{i=1}^n \nabla_i^2 + \sum_{\alpha=1}^{N-1} \sum_{\alpha>\beta}^N \frac{Z_{\alpha}Z_{\beta}e^2}{4\pi\epsilon_0 r_{\alpha\beta}} - \sum_{\alpha=1}^N \sum_{i=1}^n \frac{Z_{\alpha}e^2}{4\pi\epsilon_0 r_{\alpha i}} + \sum_{i=1}^{n-1} \sum_{j=i+1}^n \frac{e^2}{4\pi\epsilon_0 r_{ij}} \quad (2)$$

where the first term represents the operator for the kinetic energy of the nuclei; the second term represents the operator for the kinetic energy of the electrons; the third term represents the repulsion potential energy between the nuclei,  $r_{\alpha\beta}$  is the distance between nuclei  $\alpha$  and  $\beta$  named after atomic numbers  $Z_{\alpha}$  and  $Z_{\beta}$ , respectively; the fourth term represents the attraction potential between the nuclei and the electrons, with  $r_{i\alpha}$  being the distance between the nucleus  $\alpha$  and the electron  $i$ ; the fifth term represents the inter-electronic repulsion potential, with  $r_{ij}$  being the distance between electrons  $i$  and  $j$ . This Hamiltonian is incomplete because it omits

spin-orbit and other interactions, but the omitted terms are small unless the atomic number of the atoms is very high [38].

The time-independent Schrödinger equation for complex molecules is difficult to solve, therefore, the Born-Oppenheimer (BO) approximation is used [38]. Since electrons are much lighter and move much faster than nuclei, the position of the nuclei can be fixed and the position of the electrons can be defined relative to them. To solve these sets of equations for molecules, the first step is to fix the nuclear coordinates, then solve the electronic Schrödinger equation, and finally repeat the procedure for various nuclear coordinates. For each nuclear coordinate, a different set of energy levels are obtained, which are used for further analysis as described in the following Sections.

To study elementary gas-phase combustion reactions, ab initio and DFT methods are considered the current gold standard due to the accuracy they provide in the computation of molecular geometries, vibrational frequencies, and electronic energies [40]. In *this Section*, an overview of the DFT and ab initio methods applied for quantum calculations will be illustrated, with a detailed description of functionals and basis sets provided.

## 2.1 Geometry optimization and frequency calculations

The theoretical calculation of an elementary reaction usually starts with geometry optimization which determines the equilibrium geometry of the minima on a PES. For each minimum and TS, an initial guess of the geometry is first provided, thereafter the energy is computed iteratively until the optimization reaches convergence, or the geometry is adjusted and the energy is re-computed. The converged geometry of a stationary point can provide us not only the structural properties of a molecule, but also with its rotational constants, which can be used in the subsequent thermodynamic and kinetic calculations.

The vibrational frequencies of a minimum on the PES are usually calculated following a previous geometry optimization using the same method. The vibrational frequencies correspond to the usual bending, stretching and/or rocking motions. In comparison to the wells (reactants, products, complexes or intermediates) on the PES, TSs lose a further real degree of freedom due to their motion along the reaction co-ordinate, which corresponds to the transition from reactants to products and is normally presented as a negative (imaginary)

frequency [41]. An animation of a “real” imaginary frequency illustrated using the Chemcraft software [42] should connect the reactants and products via the optimized TS geometry. The vibrational wavenumbers are subsequently used in thermodynamic and kinetic calculations.

Four prevalent density functionals (B3LYP, M06-2X,  $\omega$ B97X-D and B2PLYP-D3) with four widely used basis sets (two Pople basis sets, 6-31+G(d,p) and 6-311++G(d,p), and two Dunning basis sets cc-pVTZ and aug-cc-pVTZ) have been used in the optimization and frequency calculations. Among the ever increasing number of DFT methods, the hybrid functional B3LYP has emerged as a good compromise between computational cost, coverage, and accuracy of results [43]. Therefore, the B3LYP functional coupled with a 6-31+G(d,p) basis set was used for initial optimizations, which was then supplemented with other DFT methods for further geometry optimizations.

The B3LYP exchange-correlation functional is constructed with the Becke three-parameter hybrid functionals [44], the Lee-Yang-Parr (LYP) expression for non-local correlation [45], and the VWN functional for local correlation [46]. The parameters determining the weight of each individual functional are typically specified by fitting a functional’s predictions to experimental or accurately calculated thermochemical data [47].

The M06-2X functional [33], namely a hybrid meta-GGA exchange-correlation functional, is a high non-locality functional with double the amount of nonlocal exchange (2X), and it is parameterized only for non-metals [33]. This functional is recommended for applications involving main-group thermochemistry, kinetics, non-covalent interactions, and excited states.

The  $\omega$ B97X-D functional is a long-range corrected hybrid DFT-D functional, which includes 100% long-range exact exchange, a small fraction (about 22%) of short-range exact exchange, a modified B97 exchange density functional for short-range interaction, the B97 correlation density functional [48], and empirical dispersion corrections. This functional can yield satisfactory accuracy for thermochemistry, kinetics, and non-covalent interactions [34].

The B2PLYP-D3 functional is one of double-hybrid functionals which combine exact Hartree-Fock (HF) [49] exchange with an MP2-like correlation to a DFT calculation, which has the same computational cost as the MP2 method compared to the lower cost of other DFT methods. The B2PLYP functional developed by Grimme et al. contains the Becke 1988 (B88)

exchange [50], the LYP correlation [45] and a second-order perturbation treatment (PT2) correlation based on a hybrid-GGA part [51]. B2PLYP is nowadays a widely recognized functional, which, in combination with an empirical London-dispersion term (e.g. with “-D3” appended to the functional name) [35], has resulted in it being very accurate and robust for several ground and excited-state studies [35, 52-54].

The choice of basis set is of considerable importance in quantum calculations, as this influences accuracy and computational cost. Pople basis sets are commonly used as a compromise between accuracy and computational cost [55]. The 6-311++G(d,p) basis set is one of the basis sets used for optimization calculations, with “6” representing the number of primitive Gaussian functions used to describe core and valence orbitals, and “311” indicating that the valence orbitals are composed of three basis functions each, the first one composed of a linear combination of three primitive Gaussian functions, the other composed of a linear combination of one primitive Gaussian function. The “++” and “d,p” represent diffuse and polarization functions on heavy atoms and hydrogen, respectively.

One of the most widely used basis sets was developed by Dunning and co-workers [37, 56], which is cc-pVXZ where  $X = D, T, Q, 5, 6, \dots$  (D = double, T = triple, etc.) for first- and second-row atoms. The “cc-p” stands for “correlation-consistent polarized” and the “V” indicates they are valence-only basis sets. Moreover, larger shells of polarization functions (e.g. double-zeta, triple-zeta) are included successively. When the “aug-” prefix is used with the cc-pVXZ basis sets, one diffuse function of each function type in use for a given atom is added [56, 57]. The Dunning basis sets are the current state-of-the-art for correlated or post-HF calculations.

## 2.2 Intrinsic reaction coordinate

Frequency analysis is usually employed to verify the nature of a stationary point with the presence of a single imaginary frequency indicating a transition-state structure. When it is unclear from the animation of the imaginary frequency whether the TS found connects the reactants and the target products, the theoretical treatment of chemical reactions invariably requires some sort of reaction path following the calculation [58]. The intrinsic reaction coordinate (IRC) [58], also called the minimum energy path (MEP) or reaction path analysis,

is defined as the steepest descent path in mass-weighted Cartesian coordinates that connects the TS to reactants and products on the potential. Checkpoint files (.chk) were normally specified in the input files of optimization calculations in *this thesis*. Once the TS structure was obtained, the checkpoint file from the successful TS search was used as an input for the IRC calculation, where previously calculated force constants were required.

### 2.3 Internal rotation

It has been understood for decades that errors are introduced by applying the harmonic oscillator (HO) approximation to low frequency vibrational modes [59]. A common approach for the treatment of hindered rotors is to assume uncoupled rotation and treat internal rotors with an effective one-dimensional Hamiltonian [60]. One of the most successful methods for treating internal rotation is the 1-D hindered rotor (1-D HR) model [61-63]. According to this model, each single bond between carbon atoms is treated as an axis of rotation between two counter-rotating tops. The potential energy surface for the rotation is determined by starting at a transition-state structure and then progressively rotating the top over  $360^\circ$ , which can be reduced to  $120^\circ$  for methyl rotors.

In *this thesis*, each internal rotation is treated via (1) removing the contribution of low-frequency vibrations that were hindered/free rotors and (2) including the associated contribution of each internal rotation and used for following thermodynamic and kinetic calculations. Four prevalent DFT functionals including B3LYP, M06-2X,  $\omega$ B97X-D and B2PLYP-D3 with three basis sets (6-31+G(d,p), 6-311++G(d,p), and cc-pVTZ) are used for relaxed potential energy surface scans, where the barriers and minima on the hindrance potentials are determined for these internal rotors. The dihedral angle of interest is increased by  $10^\circ$  each time, keeping the dihedral angle fixed at each step but allowing all other geometric variables to be optimized. The potential energy (single-point energy) and the rotational constant are computed at each increment and the hindrance potential as a function of angle is thus generated.

### 2.4 Single point energy

The accuracy of the dynamical description of a chemical reaction depends on the quality

of the information related to the PES [64]. Unfortunately, the complete construction of the PES is even today limited to small molecular systems, and it becomes prohibitive as the number of degrees of freedom rises. A commonly used approach to avoid this high cost is optimizing the geometries of stationary points at one level of calculation (level  $Y$ ) and then carrying out single point energy (SPE) calculations based on the optimized geometries at a higher level (level  $X$ ). For properties of stable species, a single-point energy calculated using level  $X$  at a geometry optimized with level  $Y$  is denoted  $X//Y$  [65]. This method is basically limited to conventional transition state theory and tunneling calculations that neglect reaction-path curvature and corner cutting [66]. The electronic energy of a molecule in a vacuum at 0 K, the wave function and other requested properties are calculated through the SPE calculation at a single fixed geometry.

The composite CCSD(T)[67]/CBS is an approach where accurate extrapolation to the complete basis set limit (CBS) is made at a lower level (e.g. MP2 with cc-pVTZ and cc-pVQZ), and higher-order terms are calculated using coupled clusters with singles, doubles, and perturbative triples polarization functions (e.g. CCSD(T) with cc-pVDZ or cc-pVTZ), in a basis set as large as possible [68, 69]. Due to its advantages and widespread use, this method is known as the “gold standard” in quantum chemistry and has been the method of choice for over 20 years to obtain accurate bond energies and molecular properties [70]. Its computational cost formally scales as the seventh power of the size of the system and can be prohibitive for large molecules. With the use of supercomputers provided by the Irish Centre for High-End Computing (ICHEC), we were able to carry out SPE calculations at the CCSD(T)/CBS level for up to  $C_5$  systems.

In our “Hindered Rotor Benchmarks for the Transition States of Free Radical Additions to Unsaturated Hydrocarbons” project (abbreviated as the “HR Benchmark” project hereinafter), the CCSD(T)-F12/cc-pVTZ-F12 method and the domain-based local pair natural orbital coupled cluster method (DLPNO-CCSD(T)) [71] with cc-pVTZ, cc-pVQZ, def2-TZVPP, def2-QZVPP [72, 73] basis sets were also used for SPE calculations, in order to benchmark the hindrance potential energies calculated using DFT methods for internal rotors. The DLPNO-CCSD(T) method is based on the combination of the concepts of pair natural orbitals (PNOs) and projected atomic orbitals (PAOs). Each PNO is expanded in a set of

PAOs that in turn belong to a given electron pair specific domain [71]. The idea of domain based estimation of the correlation energy was initially proposed by Pulay and co-workers [74, 75], thereafter it was further developed and popularized by Neese (who developed the ORCA software) [76] and co-workers [71, 77].

The Karlsruhe basis sets (def2-TZVPP and def2-QZVPP in *this thesis*) proposed by Ahlrichs and co-workers [72, 73], constitute balanced and economical basis sets of graded quality from partially polarized double zeta to heavily polarized quadruple zeta for all elements up to radon (Rn,  $Z = 86$ ) [78]. These basis sets are also called the def2 basis sets since they are developed as a second generation of default basis sets for the popular TURBOMOLE program [79]. For the def2-TZVPP basis set, “TZV” denotes valence triple zeta, and “PP” denotes heavily polarized.

Once the optimized geometries, frequencies, hindrance potentials and single-point energies are computed for the reactant(s), transition state and product(s) of a chemical reaction, all the information required to compute the thermodynamic and kinetic quantities is available.

### **3. Chemical kinetics and thermodynamics**

#### **3.1 Pressure-dependent rate constants**

The rate coefficients for many reactions (e.g., abstraction reactions, addition reactions with a low energy exit channel, and addition reactions for large molecules) are effectively independent of pressure [10]. In the high-pressure limit, thermal equilibration is complete via numerous collisions of the molecules and the distribution of excited molecules is simply a Boltzmann distribution. The high-pressure limiting rate constant is independent of pressure and reduces to a Boltzmann average of the micro-canonical dissociation rates. The fall-off from the high-pressure limit is particularly severe for small molecules at higher temperatures and lower pressures.

In the low-pressure limit, every molecule that gets excited above the dissociation threshold ultimately dissociates, and the rate of dissociation is determined by the rate of collisional activation. This rate is linearly dependent on the number of collisions and thus the

pressure [9]. Deviations from the low-pressure limit are also observed when the reaction proceeds over deep wells, and particularly at lower temperatures and higher pressures.

At intermediate pressures, higher energy states are depleted by reaction and collisions are not sufficiently rapid to maintain a Boltzmann distribution. The pressure dependence for the rate coefficient stems from a complicated competition between the dissociation process and the thermal equilibration via collisional excitation/de-excitation. The distribution of reacting energy states, and thus the thermal rate constant, depends on the rate of collisions between the bath gas and the excited molecule [10]. The master equation calculations incorporated in MESS proceed by first constructing the global relaxation matrix which describes both chemical transformations and collisional energy relaxation, then finding the eigenstates of the relaxation matrix, and finally extracting from those the full set of phenomenological chemical rate coefficients [80].

### 3.2 Rate constant expression

A tunneling corrected transition state theory expression [10] for temperature-dependent rate constants for pressure-independent reactions is generally written as:

$$k^{\text{TST}}(T) = \kappa \frac{k_{\text{B}}T}{h} \frac{Q^{\ddagger}(T)}{Q_{\text{react}}(T)} \exp\left(-\frac{\Delta E^{\ddagger}}{k_{\text{B}}T}\right) \quad (1)$$

where  $\kappa$  is a correction factor to account for tunneling and non-classical reflection,  $k_{\text{B}}$  and  $h$  are the Boltzmann and Planck constants, respectively. The Boltzmann factor accounts for the probability of having sufficient energy ( $\Delta E^{\ddagger}$ ) to cross the barrier.  $Q_{\text{react}}$  and  $Q^{\ddagger}$  are the partition functions for the reactants and the TS, respectively. These quantities can be calculated directly from ab initio electronic structure theory described in *this thesis* in Section 2.1 – 2.4. We have adopted reasonably high levels of theory to carry out quantum calculations and obtain reliable quantities aiming to improve the accuracy of the partition function determinations.

The relationship between the reaction rate constant and temperature was experimentally elucidated by Svante Arrhenius in 1889 [81] based on earlier work by Van't Hoff in 1884 [82]. Arrhenius deduced that a plot of  $\ln(k)$  vs  $1/T$  showed a linear dependence of the former on the latter. The correlation ultimately was improved to a modified Arrhenius equation, which is

shown as follows:

$$k = AT^n \exp(-Ea/RT) \quad (2)$$

where  $A$  is the pre-exponential factor,  $n$  is an additional factor added to account for curvature in the rate constant as a function of temperature,  $R$  is the gas constant and  $Ea$  is the energy barrier that the reactants must surmount in order to react. These three parameters are termed the Arrhenius parameters for reactions and are fundamental to chemical kinetic modelling. This equation offers a succinct way to represent a rate constant over a wide temperature range, and subsequently  $A$ ,  $n$  and  $Ea$  are widely adopted as variables which one uses as input in popular kinetic modelling codes (e.g. Chemkin-Pro suite) [83]. Although the Arrhenius equation can adequately describe the temperature-dependence of the rate constant of many chemical reactions, it is still regarded as an empirical correlation [40].

### 3.3 Thermodynamics and chemical equilibria

A variety of sources, including high-level ab initio studies, experimental studies, online databases, and review studies have been used to update the thermochemistry. Thermodynamics and kinetics both play central roles in developing a detailed chemical combustion model. They are inextricably linked by formulas internally used in the simulation of any chemical reaction. The fundamental thermodynamic properties of interest in kinetic model development are the enthalpy, entropy and heat capacity as a function of temperature, which are used during the modelling simulations to determine species thermodynamic properties, thermal transport properties, and reaction equilibrium constants.

The 0 K formation enthalpies are used as input quantities in MESS, along with vibrational frequencies, rotational constants, and hindrance potentials, to calculate temperature-dependent partition functions of each species, with the resulting partition functions used to calculate temperature-dependent thermochemical properties. These thermochemical properties are fitted to NASA polynomial format and implemented in chemical models for modelling simulations.

The enthalpies of formation at 0 K for all species were calculated based on atomization approaches in *this thesis*, using a combination of compound methods (CBS-APNO [84], G3

[85], and G4 [86]) based on the geometry optimized at different DFT levels of theory. These compound methods consist of a pre-defined routine of cost-effective calculations, which are intended to achieve high accuracy by approximating one high-level computation [40]. Simmie and Somers [87, 88] showed that this approach can reproduce values reported in the ATcT database [89] to within approximately 1 kcal mol<sup>-1</sup>, which has been proven by comparison of the results with literature data.

In Chemkin-Pro, the thermochemical properties for each species in the chemical system (in NASA polynomial format) must be provided at first to define the chemistry of reactions. For reversible reactions, the reverse rate constants are related to the forward rate constants through the equilibrium constants. The thermochemistry properties are used to calculate equilibrium constants and reverse-rate coefficients for a reaction. Equilibrium constants are directly related to the net Gibb's free energy of the reaction, as determined by the thermochemistry properties of the species involved in the reaction. Thermochemistry can also be used to derive the forward rate constants of a reaction, when the forward rate constants are unknown, but sensible rate constants for the reverse of this reaction can be inferred based on an analogy with a similar well-known chemical reaction or from literature studies.

## **4. Quantum and kinetic calculation software**

### **4.1 Gaussian supplemented with preprocessing and postprocessing codes**

All calculations were carried out using the supercomputer, Kay and Fionn, run by ICHEC. Most calculations were performed using the Gaussian 09 [90] and Gaussian 16 software package [91], with input files generated and output files post-processed by the Instant System for Lysing Computational Output (InSyLyCO) code developed by Somers [40] and my own small codes. The application Chemcraft was used to generate the input geometries, and also visualize the output structures and frequencies. Gaussian jobs on Kay were run via shared memory on a single compute node with 40 processes and 120 GB memory specified in the Gaussian input files.

The main functions of InSyLyCO code are shown in Fig. 1.1, which can be divided into two aspects—generating input files for different calculation types and post-processing the output files (extracting the results of interest for the following quantum calculations or for the



efficient way is directly building the initial guess geometry through Chemcraft program based on optimized geometries of reactants and used as the input for the following optimization calculations.

The “GenXYZInp” (“perl Insylyco.pl” should be typed before any option command and is neglected hereinafter for concision) command is executed to extract the cartesian coordinates obtained from the previous step and generate input files for Gaussian calculations. The methods, keywords, and other parameters used for calculations are specified in the “AutoQC.inp” file which should be edited before executing this command.

The following step is “GenCalcDict” operation which searches for all the Gaussian input files in target directory (shown in “Bin information”), and generate a list of these input files which includes the methods, type of calculations and so on. With this list, the “AutoGauss” command can be executed to generate batch files to run Gaussian jobs on ICHEC. The “ReDoCon” and “ReDoUnCon” option can be used with “AutoGauss” to regenerate batch files for converged and/or un-converged jobs.

After running Gaussian jobs on ICHEC, the “GetQCOut” command is executed to generate a list of the output files (.log files for Gaussian). Then the “PreProQC” command is able to preprocess the output files via extracting useful information, such as calculation types, methods, termination conditions, error messages and so on. The “LogViz” command allows us to visualize output files one by one using Chemcraft to double-check whether the results are accurate. The “PostProQC” command with different options (“OPT”, “SPE”, “HR\_SCAN”, etc.) can extract geometries and/or energies according to calculation types which can be used for following calculations or result discussions.

In our “HR Benchmark” project, there were over 12,000 jobs calculated and analyzed. To extract geometries and energies accurately and efficiently, some python codes were written following the basic thought of InSyLyCO. The main body of one of the python codes is shown below as an example, which consists of different functions defined in separate files.

```

#####
#           DLPNO-CCSD(T) INPUT GENERATION CODE           #
#####

import os
import os.path
import glob
from pathlib import Path, PureWindowsPath, PurePosixPath
import pathlib
import shutil

# IMPORT USER DEFINED FUNCTIONS
from logfile_searching import LogFileSearching
from ScanReading_6 import ScanReading
from Sgeom_searching import SgeomSearching
from Input_making_3 import InputMaking
from orca_input_searching import ORCAInputSearching
from QZ_TZ import QZ_Copy_to_TZ
from TZ_Rename import TZFileRename
from Batch_generator_qz import BatchGenerator_QZ
from Batch_generator_tz import BatchGenerator_TZ

# ENTER INPUT INFORMATION
ts_name = input('Enter TS name: ')
conf_name = input('Enter conformer name: ')

# SET MAIN PATH
mpath = os.path.join('C:\AbInitio\HRBenchmark\TS', ts_name, conf_name, 'HR_SCAN\SPE')

# RUN FUNCTIONS
LogFileSearching(ts_name, conf_name)
ScanReading(ts_name, conf_name)
SgeomSearching(ts_name, conf_name)
InputMaking(ts_name, conf_name)
ORCAInputSearching(ts_name, conf_name)

# CLEAN CACHE FILES, LIKE SGEOM FILES
os.chdir(str(mpath))
for dirpath, dirnames, filenames in os.walk('.'):
    for filename in filenames:
        if filename.endswith('-sgeom.txt'):
            sgeom_path = os.path.join(dirpath, filename)
            print(sgeom_path)
            os.remove(str(sgeom_path))
        if filename.endswith('zmatrix.txt'):
            zmatrix_path = os.path.join(dirpath, filename)
            print(zmatrix_path)

```

```

        os.remove(str(zmatrix_path))
    if filename.startswith('orca_input_files') :
        orcainp_path = os.path.join(dirpath, filename)
        print(orcainp_path)
        os.remove(str(orcainp_path))

QZ_Copy_to_TZ(ts_name, conf_name)
# REPLACE THE METHOD AND DIR TO TZ
TZFileRename(ts_name, conf_name)
ORCAInputSearching(ts_name, conf_name)

# CLEAN CACHE FILES
os.remove('orca_input_files.txt')
os.remove('orca_input_files_qz.txt')
os.remove('orca_input_files_tz.txt')
os.remove('QZ_directories.txt')

BatchGenerator_QZ(ts_name, conf_name)
BatchGenerator_TZ(ts_name, conf_name)

# CLEAN CACHE FILES
for dirpath, dirnames, filenames in os.walk('.') :
    for filename in filenames:
        if filename.endswith('.txt') :
            txt_path = os.path.join(dirpath, filename)
            print(txt_path)
            os.remove(str(txt_path))

# CREATE ZIP FILE FOR SPE FOLDER
upper_mpath = str(Path(mpath).parents[0])
os.chdir(upper_mpath)
shutil.make_archive('SPE', 'zip', mpath)

#####
#                               END OF CODE                               #
#####

```

This code aims at extracting optimized geometries of each points along the scanned hindrance potentials calculated at twelve DFT levels of theory for each TS, and generating compatible Gaussian input files for the following SPE calculations at DLPNO-CCSD(T)/cc-pVXZ ( $X = T, Q$ ) levels of theory. The basic thought of this code can be explained as follows:

- (1) Modules and user-defined functions are imported at the beginning of the code. The first function “LogFileSearching” searches for scan output files calculated using different DFT methods for a specific TS and generates a list of these output files.
- (2) The “ScanReading” function reads in the information of each scan file, locates the keywords “Z-Matrix orientation:”, “Stationary point found” and/or “Optimization stopped” and saves the line number of these keywords.
- (3) The “SgeomSearching” function extracts and saves the optimized cartesian coordinate of each stationary point based on the line numbers.
- (4) The “InputMaking” function creates compatible ORCA input files (.inp) with previously obtained geometries and methods, keywords, other parameters required by the code during the execution. The input files are created for the DLPNO-CCSD(T)/cc-pVQZ level of theory at first. Temporary files are cleaned when necessary to keep the target directory clean and tidy.
- (5) Input files for DLPNO-CCSD(T)/cc-pVQZ calculations are copied to a folder (e.g. “\TS\TS1\CONF1\HR\_SCAN\SPE\B2PLYPD3\_6-31+GDP\DLPNO\_CCSDT\_CCPVTZ”) newly created via the “QZ\_Copy\_to\_TZ” function.
- (6) The “TZFileRename” function searches for input files in the TZ folder and rename the basis set from “cc-pVQZ” to “cc-pVTZ”.
- (7) The “ORCAInputSearching” function searches for ORCA input files both in TZ and QZ folders and generates a list.
- (8) “BatchGenerator” functions generate batch files for ORCA input files which allow us to run ORCA jobs on ICHEC. Finally, all of the input and batch files are zipped into one file and uploaded to ICHEC.

## 4.2 ORCA software

ORCA is a general-purpose quantum chemistry program package that features virtually all modern electronic structure methods (DFT, many-body perturbation and coupled cluster theories, and multi-reference and semi-empirical methods) [71, 76]. The DLPNO-CCSD(T)

and the CCSD(T)-F12 calculations in *this thesis* were carried out using the ORCA 4.2 software [76] installed on Kay, which were run on a single compute node with 120 GB memory specified in the input files. In ORCA, there are default keywords available for SPE calculations to control the accuracy of this method. These keywords select predefined sensible sets of thresholds, such as “TightPNO” and “TightSCF” keywords, which are used in the input files to request tight DLPNO thresholds and tight SCF convergence during the calculations. Further tightening the  $T_{\text{CutPNO}}$  threshold could result in more accurate results in principle, but the computational cost often approaches that of canonical CCSD(T).

For CCSD(T)-F12 optimizations, the quasi-Newton like hessian mode following algorithm [92] implemented in ORCA are used for TS searching [76]. This algorithm maximizes the energy with respect to one (usually the lowest) eigenmode and minimized the energy with respect to the remaining  $3N-7$  [93] eigenmodes of the Hessian. Depending on the initial guess of the TS geometry optimized using the DFT methods in this work, the HF method was used to provide analytic first derivatives and second derivative matrices (Hessian). With this Hessian, the TS eigenvector with its negative eigenvalue and also the exact force constants for all other eigenmodes (which should have positive force constants) were calculated. Starting from the initial guess structure, the algorithm for TS optimization had to climb uphill with respect to the TS mode (which is listed in the last column of the “Redundant Internal Coordinate” list in the optimization output file). The TS mode numbers reflected their magnitudes in the TS eigenvector. Thus, at this point we could check whether our TS optimization followed the right mode.

### 4.3 MultiWell program suite

The MultiWell computer program suite [94] is designed for chemical kinetics calculations that involve complex coupled unimolecular reaction systems, which consist of multiple stable species, multiple reaction channels interconnecting them, and multiple dissociation channels from each stable species.[95, 96] The program suite consists of twelve software tools and three of them (DenSum, Thermo, LAMM) have been used during my PhD studies.

The DenSum code performs exact counts for sums and densities of states via the

Stein-Rabinovitch extension [97] of the Beyer-Swinehart algorithm [98]. This code is the best choice for separable degrees of freedom, such as vibrational modes and symmetrical or unsymmetrical hindered rotational modes [94]. The densities and sums of states for internal rotation of the TS formed by vinyl radical addition to ethylene were calculated using DenSum and shown in Fig. 1.2 as an example. The energy grain size used in this work was  $5 \text{ cm}^{-1}$ , the number of array elements used in the first portion of the double array was 1500, the total number of array elements to be employed was 2000 and the maximum energy was  $5 \times 10^4 \text{ cm}^{-1}$ . The fluctuations in the states were captured at low energies for each method and the density of states became continuous at energy larger than  $1000 \text{ cm}^{-1}$ .

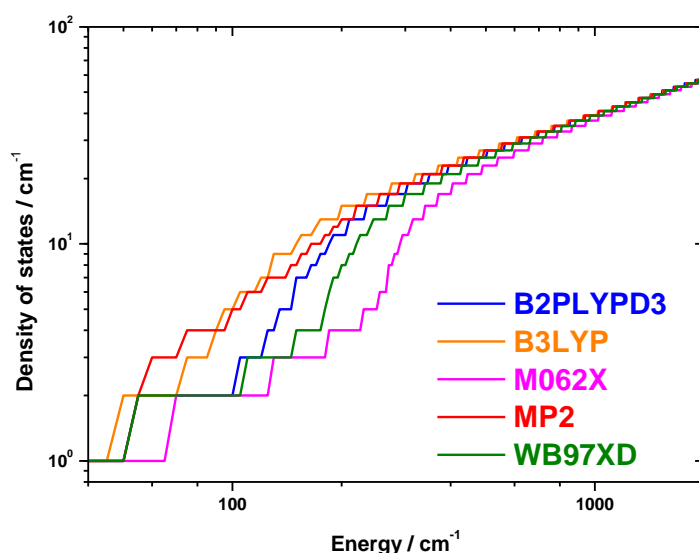


**Fig. 1.2** Density of states for internal rotation of the transition state 1,4-Ċ<sub>4</sub>H<sub>7</sub> calculated at different levels of theory, with 6-311++G(d,p) basis set used for these five methods.

The Thermo code calculates the entropy, heat capacity, and  $H(T) - H(0)$  for individual species, based on vibrational frequencies, moments of inertia, internal rotation barriers, and electronic state properties. When provided with parameters for reactants and the TSs, it uses canonical transition state theory (CTST) to calculate rate constants and partition functions (including tunneling corrections based on the 1-D unsymmetrical Eckart barrier). For instance, the hinder-rotor partition function ( $Q_{\text{HR}}$ ) corresponding to the internal rotation of the TS formed by vinyl radical addition to propene was calculated using Thermo and shown in Fig.

1.3. The differences of partition functions corresponding to this internal rotor were within 1.6 times at 500 K and decreased to about 1.1 times at 2000 K. The influence of hinder-rotor treatment on partition function calculation decreased as temperature increases.

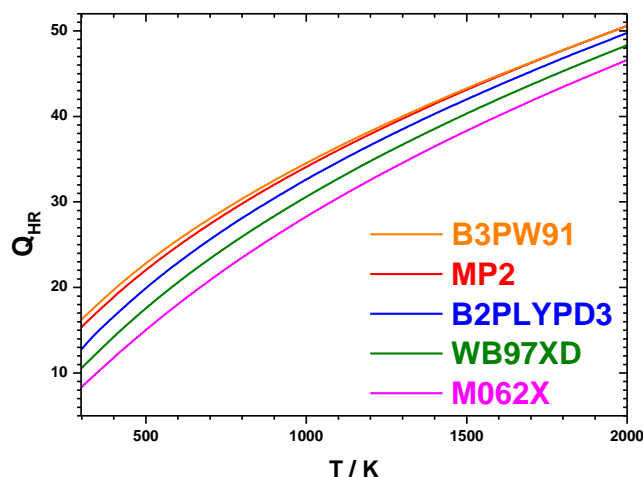


**Fig. 1.3** Hinder-rotor partition function calculated using Fourier series expansion fitted from hindrance potentials, with 6-311++G(d,p) basis set used for these five methods.

The LAMM code uses Cartesian coordinates along the hindrance potential (obtained from scan calculations) to compute the effective mass for hindered internal rotations. This code computes the torsion rotational constants  $B(\chi)$  and the hindrance potential energies  $V(\chi)$ , based on the output file from the scan calculations. The output from LAMM is used as part of the input data file needed to compute sums and densities of states (DenSum) and partition functions (Thermo).

#### 4.4 MESS: master equation system solver

MESS [80, 99] is a master equation solver used to calculate temperature- and pressure-dependent rate coefficients and thermodynamic properties for bimolecular-to-complex and internal isomerization reactions via the solution of the one-dimensional master equation. The exponential-down model of collisional energy transfer (CET) is used to model collisional energy relaxation in RRKM computations, which assumes a multiple exponential form for the transition probability as a function of energy difference between initial and final energies. The collision frequency used in the master equation

simulation is estimated using the Lennard-Jones (L-J) potentials for each buffer gas. The low-frequency torsional modes are treated as 1-D hindered rotors whose hindrance potentials and rotational constants as a function of dihedral are used to calculate the energy levels for the rotation by solving a 1-D Schrödinger equation, and then the partition functions as a function of temperature are calculated. The asymmetrical Eckart barrier model provides a one-dimensional tunneling correction to the number of states for barriers.

Moreover, there are some global keywords in the MESS input file which can influence the calculation of rate constants as shown in Table 1.1. In preparation for the MESS calculations of a specific system, different values for energy grid parameters and cut-off parameters have been tested to carefully confirm the global keywords used in our rate constant calculations.

The  $\dot{\text{H}}$  atom addition to 1,3-pentadiene system was selected to test the influence of these parameters, and the calculated rate constants for 2,4- $\dot{\text{C}}_5\text{H}_9$  radical decomposition at 1 atm in the temperature range 300–2000 K were taken as an example to quantify the differences. The target parameters were energy grid parameters including “Energy StepOverTemperature” (ESOT), “ExcessEnergyOverTemperature” (EEOT), “ModelEnergyLimit” (MEL), and cutoff parameters “ChemicalEigenvalueMax” (CEM). The base values of these parameters (ESOT = 0.2, EEOT = 40, MEL = 400 kcal mol<sup>-1</sup>, CEM = -0.1) were selected based on those used in the literature and/or MESS input templates for a similar system. The computational costs in relation to the use of these parameters are listed in Table 1.1.

**Table 1.1** Computational costs for rate constant calculations using different grid and cutoff parameters in MESS input files for 2,4- $\dot{\text{C}}_5\text{H}_9$  radical decomposition at 1 atm.

	EnergyStep OverTemperature	ExcessEnergy OverTemperature	Model EnergyLimit	Chemical EigenvalueMax	CPUtime [hrs]
1	0.2	30	400	<b>1.0</b>	0.5
2	0.2	30	400	<b>0.2</b>	0.5
3	0.2	30	400	<b>0.1</b>	0.5
4	0.2	30	<b>400</b>	<b>-0.1</b>	0.5
5	0.2	30	<b>300</b>	-0.1	0.5
6	0.2	30	<b>500</b>	-0.1	0.5
7 <sup>a</sup>	0.2	<b>40</b>	400	-0.1	0.7
8	0.2	<b>60</b>	400	-0.1	1.5
9	0.2	<b>80</b>	400	-0.1	2.6
10	<b>0.15</b>	30	400	-0.1	1.2
11	<b>0.1</b>	30	400	-0.1	3.9

<sup>a</sup> The base values for these four parameters.

The “EnergyStepOverTemperature” parameter stands for the ratio of the energy grain size to the temperature. The computational costs increase as the value of ESOT decreases from 0.2 to 0.1, while the rate constants for 2,4- $\dot{\text{C}}_5\text{H}_9$  radical decomposition show a minor difference within 1.0%. Hence, the base value for ESOT should be small enough with reasonable computational cost for our  $\text{C}_5$  system.

The “ExcessEnergyOverTemperature” parameter represents the ratio of the highest energy in the global relaxation matrix to the temperature, which is counted from the highest barrier in the model. To validate whether the initial value of EEOT is large enough for our system, the value of EEOT has been varied from 30 to 80. As EEOT increases, the computational costs increase and the rate constants become converged with EEOT over 40 (our base value).

The “ModelEnergyLimit” parameter stands for the highest energy that will ever be used in the partition function evaluations. Typically a value of 400 kcal mol<sup>-1</sup> for MEL is appropriate, which is proved by our rate constant comparisons. The change of MEL based on the initial values has no obvious influence on the computational costs.

The value of the “ChemicalEigenvalueMax” parameter is used to separate chemically significant modes from others (e.g. the internal energy relaxation eigenvalues).[100] When

the CEM is negative, the ratio of successive eigenvalues is explored from the top down, until the ratio lies below the threshold. The change of CEM from  $-0.1$  to  $1.0$  doesn't show an obvious influence on both the computational costs and the rate constants.

Through the parameter analysis, the base values selected for these global parameters used in our rate constant calculations were proven to be reasonable. We have also selected rational levels of theory for quantum calculations based on our experience in quantum chemistry and literature studies. The temperature- and pressure-dependent rate constants calculated using RRKM theory with Master Equation analysis were fitted to the modified Arrhenius expression as a function of temperature.

## **5. Chemical kinetic modelling**

### **5.1 Shock tube**

The chemical kinetics of fuel oxidation processes can be experimentally probed in well-defined, laboratory-scale reactors, including shock tubes, rapid compression machines, flow reactors, and flames. Shock tubes quickly compress a test mixture from near room temperatures and pressures to highly elevated conditions, which can be maintained after the compression process for a period of chemical interest.

Recent advances in shock tube design include the use of tailoring and driver inserts to achieve near-constant temperature/pressure and longer test times, and the use of laser-absorption measurements to quantify fuel concentration and test gas temperature [101]. Speciation profiles of the reactant and products can provide a temporal record of their concentration during the progress of the combustion process. These time-histories also provide strong constraints on reaction pathways and rate constants of detailed reaction mechanisms used to model the chemistry of these processes.

A shock tube study of  $\dot{H}$  atom addition to cyclopentene was performed by Manion and Awan [102, 103] with the concentration profiles provided for the reactants and products. Species were quantitated using gas chromatography with flame ionization and mass spectrometric detection (GC/FID/MS) in their experiment. The experimental concentration profiles have been used to validate the reliability of our model.

## 5.2 Rate of production analysis

A rate of production analysis (ROP) is a useful tool to explore reaction pathways and quickly identify the dominant reaction paths in the reacting-flow simulations. A ROP analysis determines the contribution of each reaction to the net production or destruction rates of a species. This analysis is particularly useful for ideal reactors, such as 0-D and plug-flow systems. The reactor model in the Chemkin-Pro suite computes normalized values of the reaction contributions to the species production and destruction rates. The ROP analysis has been used for our  $\dot{H}$  atom addition to 1,3-pentadiene system to identify the dominant reaction pathways at different temperatures and pressures, with the resulting dominant pathways being very helpful in simplifying complicated potential energy surfaces for large systems.

## 5.3 Hierarchy of mechanisms

Recently, a brief but interesting introduction of the history of chemical kinetic modeling with some emphasis on the development of chemical kinetic mechanisms describing fuel oxidation was published by Curran [25]. Curran presented the general schematic mechanism for fuel oxidation as shown in Fig. 1.4. The major classes of elementary reactions considered in most of the mechanisms include 25 reaction classes, which were described in detail in Curran's work [104], with nine reaction classes involved in high-temperature chemistry and 16 reaction classes involved in low-temperature chemistry. The reaction class number has been extended to 31 by Bugler et al. [15] through an evaluation of recent quantum-chemically derived rate coefficients from the literature pertinent to important low-temperature oxidation reaction classes.

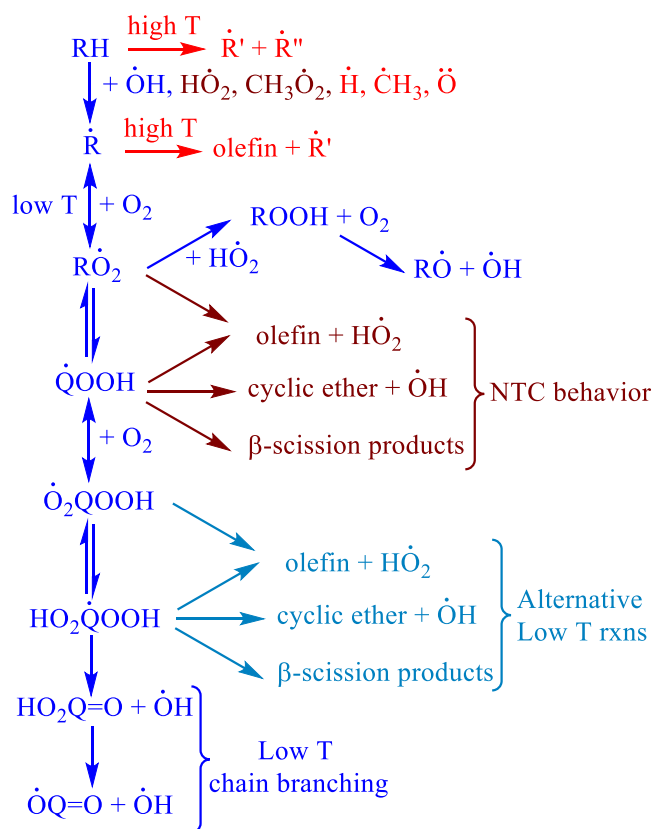


**Fig. 1.4** General schematic mechanism for fuel oxidation [25, 104].

A detailed chemical kinetic mechanism consists of dozens to hundreds of elementary chemical reactions with associated rate constants, and thermodynamic, transport properties for each species. Typically, the development of a chemical kinetic model requires modelers to adopt the best measured and/or calculated rate constant and thermochemistry for target reactions from the literature. The performance of a mechanism is generally compared to experimental results and, in practice, some optimizations of the mechanism may be needed via adjusting the rate constants to fit a wide range of experimental targets.

Based on the experience in earlier mechanism developments, the oxidation of any fuel at high temperatures depends largely on  $C_0$ – $C_4$  chemistry. It is now commonly accepted that it is possible to manually or automatically generate mechanisms by first generating a core  $C_0$ – $C_4$  mechanism and then building the chemistry for larger components upon this. The Combustion Chemistry Centre ( $C^3$ ) continues to work on detailed mechanism development and our previous kinetic mechanism AramcoMech3.0 [11], which mainly focuses on  $C_0$ – $C_4$  kinetics, has been widely recognized and used in the community. An updated version of the

detailed chemical mechanism, namely NUIGMech1.0 [105] has been published recently with the C<sub>0</sub>–C<sub>7</sub> chemistry being comprehensively validated.

## 6. Goals and Overview of This Thesis

There were two major goals in this study. One was to construct detailed chemical kinetic mechanisms to numerically describe the pyrolysis and oxidation of C<sub>5</sub> dienes in fundamental laboratory reactors, and thus fill the void in the literature with respect to the combustion chemistry of these compounds. In order to meet this goal, we have carried out quantum calculations at reasonably high levels of theory, implemented the quantum results into a kinetic model and simulated the species profiles of the reactant and products under experimental conditions.

Another goal was to validate the influence of different electronic structure methods used for internal hindered rotor treatments in the TSs formed by radical addition to unsaturated hydrocarbons, which, to our knowledge, has not been fully discussed in the literature. The high-level benchmarking calculations were also employed for these rotors, and reliable DFT methods were recommended for the internal rotor treatment for different reaction types considering both accuracy and computational cost.

The supplementary information presented as figures and tables is provided in the appendix of *this thesis*. The developed kinetic models, MESS output files and other additional materials can be downloaded through the DOI link provided at the first page of each paper (Chapter 2–6).

## References

- [1] L. Stougie, N. Giustozzi, H. van der Kooi, A. Stoppato, Environmental, economic and exergetic sustainability assessment of power generation from fossil and renewable energy sources, *International Journal of Energy Research* 42 (2018) 2916-2926.
- [2] C. Acar, I. Dincer, The potential role of hydrogen as a sustainable transportation fuel to combat global warming, *International Journal of Hydrogen Energy* 45 (2020) 3396-3406.
- [3] P. Gentiloni, M.M. Kotzeva, G. Gueye, Eurostat database, 2018.
- [4] F.L. Dryer, Chemical kinetic and combustion characteristics of transportation fuels, *Proceedings of the Combustion Institute* 35 (2015) 117-144.
- [5] Y. Li, A. Alfazazi, B. Mohan, E. Alexandros Tingas, J. Badra, H.G. Im, S. Mani Sarathy, Development of a reduced four-component (toluene/n-heptane/iso-octane/ethanol) gasoline surrogate model, *Fuel* 247 (2019) 164-178.
- [6] B.-w. Mei, W. Li, S.-y. Ma, H.-y. Wang, H.-q. Pan, F. Qi, Y.-y. Li, Investigation on 1-heptene/air laminar flame propagation under elevated pressures, *Chinese Journal of Chemical Physics* 32 (2019) 99-106.
- [7] M. Mehl, H.J. Curran, W.J. Pitz, C.K. Westbrook, Chemical kinetic modeling of component mixtures relevant to gasoline, Lawrence Livermore National Lab.(LLNL), Livermore, CA (United States), 2009.
- [8] S.M. Sarathy, A. Farooq, G.T. Kalghatgi, Recent progress in gasoline surrogate fuels, *Progress in Energy and Combustion Science* 65 (2018) 67-108.
- [9] S.J. Klippenstein, From theoretical reaction dynamics to chemical modeling of combustion, *Proceedings of the Combustion Institute* 36 (2017) 77-111.
- [10] S.J. Klippenstein, C. Cavallotti, Chapter 2 - Ab initio kinetics for pyrolysis and combustion systems, in: T. Faravelli, F. Manenti, E. Ranzi (Eds.), *Computer Aided Chemical Engineering*, Elsevier (2019) 115-167.
- [11] C.-W. Zhou, Y. Li, U. Burke, C. Banyon, K.P. Somers, S. Ding, S. Khan, J.W. Hargis, T. Sikes, O. Mathieu, E.L. Petersen, M. AlAbbad, A. Farooq, Y. Pan, Y. Zhang, Z. Huang, J. Lopez, Z. Loparo, S.S. Vasu, H.J. Curran, An experimental and chemical kinetic modeling study of 1,3-butadiene combustion: Ignition delay time and laminar flame speed measurements, *Combustion and Flame* 197 (2018) 423-438.
- [12] Y. Li, C.-W. Zhou, H.J. Curran, An extensive experimental and modeling study of 1-butene oxidation, *Combustion and Flame* 181 (2017) 198-213.
- [13] J. Bugler, A. Rodriguez, O. Herbinet, F. Battin-Leclerc, C. Togbé, G. Dayma, P. Dagaut, H.J. Curran, An experimental and modelling study of n-pentane oxidation in two jet-stirred reactors: The importance of pressure-dependent kinetics and new reaction pathways, *Proceedings of the Combustion Institute* 36 (2017) 441-448.
- [14] J. Bugler, B. Marks, O. Mathieu, R. Archuleta, A. Camou, C. Grégoire, K.A. Heufer, E.L. Petersen, H.J. Curran, An ignition delay time and chemical kinetic modeling study of the pentane isomers, *Combustion and Flame* 163 (2016) 138-156.
- [15] J. Bugler, K.P. Somers, E.J. Silke, H.J. Curran, Revisiting the Kinetics and Thermodynamics of the Low-Temperature Oxidation Pathways of Alkanes: A Case Study of the Three Pentane Isomers, *The Journal of Physical Chemistry A* 119 (2015) 7510-7527.
- [16] J. Zádor, C.A. Taatjes, R.X. Fernandes, Kinetics of elementary reactions in

low-temperature autoignition chemistry, *Progress in Energy and Combustion Science* 37 (2011) 371-421.

[17] F. Battin-Leclerc, Detailed chemical kinetic models for the low-temperature combustion of hydrocarbons with application to gasoline and diesel fuel surrogates, *Progress in Energy and Combustion Science* 34 (2008) 440-498.

[18] L. Cai, H. Pitsch, S.Y. Mohamed, V. Raman, J. Bugler, H. Curran, S.M. Sarathy, Optimized reaction mechanism rate rules for ignition of normal alkanes, *Combustion and Flame* 173 (2016) 468-482.

[19] H.J. Curran, Rate constant estimation for C<sub>1</sub> to C<sub>4</sub> alkyl and alkoxy radical decomposition, *International Journal of Chemical Kinetics* 38 (2006) 250-275.

[20] J. Badra, A. Farooq, Site-specific reaction rate constant measurements for various secondary and tertiary H-abstraction by OH radicals, *Combustion and Flame* 162 (2015) 2034-2044.

[21] J. Badra, E.F. Nasir, A. Farooq, Site-Specific Rate Constant Measurements for Primary and Secondary H- and D-Abstraction by OH Radicals: Propane and n-Butane, *The Journal of Physical Chemistry A* 118 (2014) 4652-4660.

[22] R. Sivaramakrishnan, J.V. Michael, B. Ruscic, High-temperature rate constants for H/D+ C<sub>2</sub>H<sub>6</sub> and C<sub>3</sub>H<sub>8</sub>, *International Journal of Chemical Kinetics* 44 (2012) 194-205.

[23] K. Zhang, C. Banyon, C. Togbé, P. Dagaut, J. Bugler, H.J. Curran, An experimental and kinetic modeling study of n-hexane oxidation, *Combustion and Flame* 162 (2015) 4194-4207.

[24] K. Zhang, C. Banyon, J. Bugler, H.J. Curran, A. Rodriguez, O. Herbinet, F. Battin-Leclerc, C. B'Chir, K.A. Heufer, An updated experimental and kinetic modeling study of n-heptane oxidation, *Combustion and Flame* 172 (2016) 116-135.

[25] H.J. Curran, Developing detailed chemical kinetic mechanisms for fuel combustion, *Proceedings of the Combustion Institute* 37 (2019) 57-81.

[26] S.M. Burke, W. Metcalfe, O. Herbinet, F. Battin-Leclerc, F.M. Haas, J. Santner, F.L. Dryer, H.J. Curran, An experimental and modeling study of propene oxidation. Part 1: Speciation measurements in jet-stirred and flow reactors, *Combustion and Flame* 161 (2014) 2765-2784.

[27] S.M. Burke, U. Burke, R. Mc Donagh, O. Mathieu, I. Osorio, C. Keesee, A. Morones, E.L. Petersen, W. Wang, T.A. DeVerter, M.A. Oehlschlaeger, B. Rhodes, R.K. Hanson, D.F. Davidson, B.W. Weber, C.-J. Sung, J. Santner, Y. Ju, F.M. Haas, F.L. Dryer, E.N. Volkov, E.J.K. Nilsson, A.A. Konnov, M. Alrefae, F. Khaled, A. Farooq, P. Dirrenberger, P.-A. Glaude, F. Battin-Leclerc, H.J. Curran, An experimental and modeling study of propene oxidation. Part 2: Ignition delay time and flame speed measurements, *Combustion and Flame* 162 (2015) 296-314.

[28] C.-W. Zhou, Y. Li, E. O'Connor, K.P. Somers, S. Thion, C. Keesee, O. Mathieu, E.L. Petersen, T.A. DeVerter, M.A. Oehlschlaeger, G. Kukkadapu, C.-J. Sung, M. Alrefae, F. Khaled, A. Farooq, P. Dirrenberger, P.-A. Glaude, F. Battin-Leclerc, J. Santner, Y. Ju, T. Held, F.M. Haas, F.L. Dryer, H.J. Curran, A comprehensive experimental and modeling study of isobutene oxidation, *Combustion and Flame* 167 (2016) 353-379.

[29] J. Power, K.P. Somers, C.-W. Zhou, S. Peukert, H.J. Curran, Theoretical, Experimental, and Modeling Study of the Reaction of Hydrogen Atoms with 1- and 2-Pentene, *The Journal of Physical Chemistry A* 123 (2019) 8506-8526.

- [30] Y. Li, S.J. Klippenstein, C.-W. Zhou, H.J. Curran, Theoretical Kinetics Analysis for H Atom Addition to 1,3-Butadiene and Related Reactions on the  $\dot{C}_4H_7$  Potential Energy Surface, *The Journal of Physical Chemistry A* 121 (2017) 7433-7445.
- [31] S.S. Nagaraja, J. Power, G. Kukkadapu, S. Dong, S.W. Wagnon, W.J. Pitz, H.J. Curran, A single pulse shock tube study of pentene isomer pyrolysis, *Proceedings of the Combustion Institute*, (2020).
- [32] A.D. Becke, A new mixing of Hartree–Fock and local density-functional theories, *The Journal of chemical physics* 98 (1993) 1372-1377.
- [33] Y. Zhao, D.G. Truhlar, The M06 suite of density functionals for main group thermochemistry, thermochemical kinetics, noncovalent interactions, excited states, and transition elements: two new functionals and systematic testing of four M06-class functionals and 12 other functionals, *Theoretical Chemistry Accounts* 120 (2008) 215-241.
- [34] J.-D. Chai, M. Head-Gordon, Long-range corrected hybrid density functionals with damped atom–atom dispersion corrections, *Physical Chemistry Chemical Physics* 10 (2008) 6615-6620.
- [35] S. Grimme, J. Antony, S. Ehrlich, H. Krieg, A consistent and accurate ab initio parametrization of density functional dispersion correction (DFT-D) for the 94 elements H-Pu, *The Journal of chemical physics* 132 (2010) 154104.
- [36] R. Ditchfield, W.J. Hehre, J.A. Pople, Self-Consistent Molecular-Orbital Methods. IX. An Extended Gaussian-Type Basis for Molecular-Orbital Studies of Organic Molecules, *The Journal of Chemical Physics* 54 (1971) 724-728.
- [37] T.H. Dunning Jr, Gaussian basis sets for use in correlated molecular calculations. I. The atoms boron through neon and hydrogen, *The Journal of chemical physics* 90 (1989) 1007-1023.
- [38] I.N. Levine, *Quantum chemistry*, Fifth ed., Prentice-Hall, Inc. Upper Saddle River, New Jersey 07458, United States of America, 2000.
- [39] D.J. Griffiths, D.F. Schroeter, *Introduction to quantum mechanics*, Cambridge University Press, 2018.
- [40] K.P. Somers, *On the Pyrolysis and Combustion of Furans: Quantum Chemical, Statistical Rate Theory, and Chemical Kinetic Modelling Studies*, School of Chemistry, National University of Ireland, Galway, National University of Ireland, Galway, 2014.
- [41] E.G. Lewars, *Computational Chemistry Introduction to the Theory and Applications of Molecular and Quantum Mechanics*, 2 ed., Springer Netherlands, 2003.
- [42] Chemcraft - graphical software for visualization of quantum chemistry computations. <https://www.chemcraftprog.com>.
- [43] J. Tirado-Rives, W.L. Jorgensen, Performance of B3LYP Density Functional Methods for a Large Set of Organic Molecules, *Journal of Chemical Theory and Computation* 4 (2008) 297-306.
- [44] A.D. Becke, Density-functional thermochemistry. III. The role of exact exchange, *The Journal of Chemical Physics* 98 (1993) 5648-5652.
- [45] C. Lee, W. Yang, R.G. Parr, Development of the Colle-Salvetti correlation-energy formula into a functional of the electron density, *Physical review B* 37 (1988) 785.
- [46] S.H. Vosko, L. Wilk, M. Nusair, Accurate spin-dependent electron liquid correlation energies for local spin density calculations: a critical analysis, *Canadian Journal of physics* 58

(1980) 1200-1211.

- [47] J.P. Perdew, M. Ernzerhof, K. Burke, Rationale for mixing exact exchange with density functional approximations, *The Journal of chemical physics* 105 (1996) 9982-9985.
- [48] A.D. Becke, Density-functional thermochemistry. V. Systematic optimization of exchange-correlation functionals, *The Journal of chemical physics* 107 (1997) 8554-8560.
- [49] J.C. Slater, A simplification of the Hartree-Fock method, *Physical review* 81 (1951) 385.
- [50] A.D. Becke, Density-functional exchange-energy approximation with correct asymptotic behavior, *Physical review A* 38 (1988) 3098.
- [51] S. Grimme, Semiempirical hybrid density functional with perturbative second-order correlation, *The Journal of chemical physics* 124 (2006) 034108.
- [52] L. Goerigk, S. Grimme, Efficient and Accurate Double-Hybrid-Meta-GGA Density Functionals Evaluation with the Extended GMTKN30 Database for General Main Group Thermochemistry, Kinetics, and Noncovalent Interactions, *Journal of chemical theory and computation* 7 (2011) 291-309.
- [53] S. Grimme, F. Neese, Double-hybrid density functional theory for excited electronic states of molecules, *The Journal of chemical physics* 127 (2007) 154116.
- [54] M. Korth, S. Grimme, "Mindless" DFT benchmarking, *Journal of chemical theory and computation* 5 (2009) 993-1003.
- [55] M.W.D. Hanson-Heine, Uncontracted core Pople basis sets in vibrational frequency calculations, *International Journal of Quantum Chemistry* 118 (2018) e25761.
- [56] D.E. Woon, T.H. Dunning, Gaussian basis sets for use in correlated molecular calculations. III. The atoms aluminum through argon, *The Journal of Chemical Physics* 98 (1993) 1358-1371.
- [57] R.A. Kendall, T.H. Dunning Jr, R.J. Harrison, Electron affinities of the first-row atoms revisited. Systematic basis sets and wave functions, *The Journal of chemical physics* 96 (1992) 6796-6806.
- [58] H.P. Hratchian, H.B. Schlegel, Using Hessian updating to increase the efficiency of a Hessian based predictor-corrector reaction path following method, *Journal of chemical theory and computation* 1 (2005) 61-69.
- [59] K.S. Pitzer, W.D. Gwinn, Energy levels and thermodynamic functions for molecules with internal rotation I. Rigid frame with attached tops, *The Journal of Chemical Physics* 10 (1942) 428-440.
- [60] J. Pfaendtner, X. Yu, L.J. Broadbelt, The 1-D hindered rotor approximation, *Theoretical Chemistry Accounts* 118 (2007) 881.
- [61] J.P.A. Heuts, R.G. Gilbert, L. Radom, Determination of arrhenius parameters for propagation in free-radical polymerizations: An assessment of ab initio procedures, *The Journal of Physical Chemistry* 100 (1996) 18997-19006.
- [62] V. Van Speybroeck, P. Vansteenkiste, D. Van Neck, M. Waroquier, Why does the uncoupled hindered rotor model work well for the thermodynamics of n-alkanes?, *Chemical physics letters* 402 (2005) 479-484.
- [63] V. Van Speybroeck, D. Van Neck, M. Waroquier, S. Wauters, M. Saeys, G.B. Marin, Ab initio study of radical addition reactions: Addition of a primary ethylbenzene radical to ethene (I), *The Journal of Physical Chemistry A* 104 (2000) 10939-10950.
- [64] J. Espinosa-Garcia, J.C. Corchado, Reliability of the Single-Point Calculation Technique

at Characteristic Points of the Potential Energy Surface, *The Journal of Physical Chemistry* 99 (1995) 8613-8616.

[65] K.B. Wiberg, *Ab Initio Molecular Orbital Theory*, *Journal of Computational Chemistry* 7 (1986) 379-379.

[66] B.J. Lynch, D.G. Truhlar, What are the best affordable multi-coefficient strategies for calculating transition state geometries and barrier heights?, *The Journal of Physical Chemistry A* 106 (2002) 842-846.

[67] K. Raghavachari, G.W. Trucks, J.A. Pople, M. Head-Gordon, A fifth-order perturbation comparison of electron correlation theories, *Chemical Physics Letters* 157 (1989) 479-483.

[68] J. Řezáč, P. Hobza, Describing Noncovalent Interactions beyond the Common Approximations: How Accurate Is the “Gold Standard,” CCSD(T) at the Complete Basis Set Limit?, *Journal of Chemical Theory and Computation* 9 (2013) 2151-2155.

[69] S. Tsuzuki, K. Honda, T. Uchimaru, M. Mikami, K. Tanabe, Origin of attraction and directionality of the  $\pi/\pi$  interaction: model chemistry calculations of benzene dimer interaction, *Journal of the American Chemical Society* 124 (2002) 104-112.

[70] R.O. Ramabhadran, K. Raghavachari, Extrapolation to the gold-standard in quantum chemistry: Computationally efficient and accurate CCSD (T) energies for large molecules using an automated thermochemical hierarchy, *Journal of chemical theory and computation* 9 (2013) 3986-3994.

[71] C. Riplinger, F. Neese, An efficient and near linear scaling pair natural orbital based local coupled cluster method, *The Journal of chemical physics* 138 (2013) 034106.

[72] F. Weigend, F. Furche, R. Ahlrichs, Gaussian basis sets of quadruple zeta valence quality for atoms H–Kr, *The Journal of chemical physics* 119 (2003) 12753-12762.

[73] F. Weigend, R. Ahlrichs, Balanced basis sets of split valence, triple zeta valence and quadruple zeta valence quality for H to Rn: Design and assessment of accuracy, *Physical Chemistry Chemical Physics* 7 (2005) 3297-3305.

[74] P. Pulay, Localizability of dynamic electron correlation, *Chemical physics letters* 100 (1983) 151-154.

[75] S. Sæbø, P. Pulay, Local configuration interaction: An efficient approach for larger molecules, *Chemical physics letters* 113 (1985) 13-18.

[76] F. Neese, Software update: the ORCA program system, version 4.0, *Wiley Interdisciplinary Reviews: Computational Molecular Science* 8 (2018) e1327.

[77] Y. Guo, C. Riplinger, U. Becker, D.G. Liakos, Y. Minenkov, L. Cavallo, F. Neese, Communication: An improved linear scaling perturbative triples correction for the domain based local pair-natural orbital based singles and doubles coupled cluster method [DLPNO-CCSD (T)], *The Journal of Chemical Physics* 148 (2018) 011101.

[78] J. Zheng, X. Xu, D.G. Truhlar, Minimally augmented Karlsruhe basis sets, *Theoretical Chemistry Accounts* 128 (2011) 295-305.

[79] R. Ahlrichs, F. Furche, C. Hättig, W. Klopper, M. Sierka, F. Weigend, *Turbomole—program package for ab initio electronic structure calculations*, Institut für Physikalische Chemie und Elektrochemie, Lehrstuhl für Theoretische Chemie, Universität Karlsruhe, Kaiserstr, 2010.

[80] Y. Georgievskii, S.J. Klippenstein, MESS.2016.3.23, 2016, <https://tcg.cse.anl.gov/papr/codes/mess.html>.

- [81] S. Arrhenius, On the reaction rate of the inversion of non-refined sugar upon souring, *Zeitschrift für Physikalische Chemie* (1889) 226-248.
- [82] J.H. Van't Hoff, *Etudes de dynamique chimique*, Muller, 1884.
- [83] ANSYS CHEMKIN-PRO 15131, *Reaction Design*: San Diego, 2013, <https://www.ansys.com/products/fluids/ansys-chemkin-pro>.
- [84] J.W. Ochterski, G.A. Petersson, J.A. Montgomery Jr, A complete basis set model chemistry. V. Extensions to six or more heavy atoms, *The Journal of chemical physics* 104 (1996) 2598-2619.
- [85] L.A. Curtiss, K. Raghavachari, P.C. Redfern, V. Rassolov, J.A. Pople, Gaussian-3 (G3) theory for molecules containing first and second-row atoms, *The Journal of chemical physics* 109 (1998) 7764-7776.
- [86] L.A. Curtiss, P.C. Redfern, K. Raghavachari, Gaussian-4 theory, *The Journal of chemical physics* 126 (2007) 084108.
- [87] J.M. Simmie, K.P. Somers, Benchmarking compound methods (CBS-QB3, CBS-APNO, G3, G4, W1BD) against the active thermochemical tables: a litmus test for cost-effective molecular formation enthalpies, *The Journal of Physical Chemistry A* 119 (2015) 7235-7246.
- [88] K.P. Somers, J.M. Simmie, Benchmarking compound methods (CBS-QB3, CBS-APNO, G3, G4, W1BD) against the active thermochemical tables: formation enthalpies of radicals, *The Journal of Physical Chemistry A* 119 (2015) 8922-8933.
- [89] B. Ruscic, D.H. Bross, *Active Thermochemical Tables (ATcT) values based on ver. 1.122d of the Thermochemical Network*, Argonne National Laboratory; available at [ATcT.anl.gov](http://ATcT.anl.gov), 2018.
- [90] M.J. Frisch, G.W. Trucks, H.B. Schlegel, G.E. Scuseria, M.A. Robb, J.R. Cheeseman, G. Scalmani, V. Barone, G.A. Petersson, H. Nakatsuji, X. Li, M. Caricato, A.V. Marenich, J. Bloino, B.G. Janesko, R. Gomperts, B. Mennucci, H.P. Hratchian, J.V. Ortiz, A.F. Izmaylov, J.L. Sonnenberg, Williams, F. Ding, F. Lipparini, F. Egidi, J. Goings, B. Peng, A. Petrone, T. Henderson, D. Ranasinghe, V.G. Zakrzewski, J. Gao, N. Rega, G. Zheng, W. Liang, M. Hada, M. Ehara, K. Toyota, R. Fukuda, J. Hasegawa, M. Ishida, T. Nakajima, Y. Honda, O. Kitao, H. Nakai, T. Vreven, K. Throssell, J.A. Montgomery Jr., J.E. Peralta, F. Ogliaro, M.J. Bearpark, J.J. Heyd, E.N. Brothers, K.N. Kudin, V.N. Staroverov, T.A. Keith, R. Kobayashi, J. Normand, K. Raghavachari, A.P. Rendell, J.C. Burant, S.S. Iyengar, J. Tomasi, M. Cossi, J.M. Millam, M. Klene, C. Adamo, R. Cammi, J.W. Ochterski, R.L. Martin, K. Morokuma, O. Farkas, J.B. Foresman, D.J. Fox, *Gaussian 09 Revision A.02*, Wallingford, CT, 2016.
- [91] M.J. Frisch, G.W. Trucks, H.B. Schlegel, G.E. Scuseria, M.A. Robb, J.R. Cheeseman, G. Scalmani, V. Barone, G.A. Petersson, H. Nakatsuji, X. Li, M. Caricato, A.V. Marenich, J. Bloino, B.G. Janesko, R. Gomperts, B. Mennucci, H.P. Hratchian, J.V. Ortiz, A.F. Izmaylov, J.L. Sonnenberg, Williams, F. Ding, F. Lipparini, F. Egidi, J. Goings, B. Peng, A. Petrone, T. Henderson, D. Ranasinghe, V.G. Zakrzewski, J. Gao, N. Rega, G. Zheng, W. Liang, M. Hada, M. Ehara, K. Toyota, R. Fukuda, J. Hasegawa, M. Ishida, T. Nakajima, Y. Honda, O. Kitao, H. Nakai, T. Vreven, K. Throssell, J.A. Montgomery Jr., J.E. Peralta, F. Ogliaro, M.J. Bearpark, J.J. Heyd, E.N. Brothers, K.N. Kudin, V.N. Staroverov, T.A. Keith, R. Kobayashi, J. Normand, K. Raghavachari, A.P. Rendell, J.C. Burant, S.S. Iyengar, J. Tomasi, M. Cossi, J.M. Millam, M. Klene, C. Adamo, R. Cammi, J.W. Ochterski, R.L. Martin, K. Morokuma, O. Farkas, J.B. Foresman, D.J. Fox, *Gaussian 16 Rev. C.01*, Wallingford, CT, 2016.

- [92] B. Hess, C. Kutzner, D. Van Der Spoel, E. Lindahl, GROMACS 4: algorithms for highly efficient, load-balanced, and scalable molecular simulation, *Journal of chemical theory and computation* 4 (2008) 435-447.
- [93] M. Bühl, C. Reimann, D.A. Pantazis, T. Bredow, F. Neese, Geometries of third-row transition-metal complexes from density-functional theory, *Journal of chemical theory and computation* 4 (2008) 1449-1459.
- [94] J.R. Barker, T.L. Nguyen, J.F. Stanton, C. Aieta, M. Ceotto, F. Gabas, T.J.D. Kumar, C.G.L. Li, L.L. Lohr, A. Maranzana, N.F. Ortiz, J.M. Preses, J.M. Simmie, J.A. Sonk, P.J. Stimac, MultiWell-2017 Software Suite, J. R. Barker, University of Michigan, Ann Arbor, Michigan, USA, 2017.
- [95] J.R. Barker, Multiple-Well, multiple-path unimolecular reaction systems. I. MultiWell computer program suite, *International Journal of Chemical Kinetics* 33 (2001) 232-245.
- [96] J.R. Barker, Energy transfer in master equation simulations: A new approach, *International Journal of Chemical Kinetics* 41 (2009) 748-763.
- [97] S.E. Stein, B.S. Rabinovitch, Accurate evaluation of internal energy level sums and densities including anharmonic oscillators and hindered rotors, *The Journal of Chemical Physics* 58 (1973) 2438-2445.
- [98] T. Beyer, D.F. Swinehart, Algorithm 448: number of multiply-restricted partitions, *Communications of the ACM* 16 (1973) 379.
- [99] Y. Georgievskii, J.A. Miller, M.P. Burke, S.J. Klippenstein, Reformulation and solution of the master equation for multiple-well chemical reactions, *The Journal of Physical Chemistry A* 117 (2013) 12146-12154.
- [100] J.A. Miller, S.J. Klippenstein, Determining phenomenological rate coefficients from a time-dependent, multiple-well master equation: "species reduction" at high temperatures, *Physical Chemistry Chemical Physics* 15 (2013) 4744-4753.
- [101] S. Wang, D.F. Davidson, R.K. Hanson, Shock tube techniques for kinetic target data to improve reaction models, *Computer Aided Chemical Engineering*, Elsevier 2019, pp. 169-202.
- [102] I.A. Awan, D.R. Burgess Jr, W. Tsang, J.A. Manion, Shock tube study of the decomposition of cyclopentyl radicals, *Proceedings of the Combustion Institute* 33 (2011) 341-349.
- [103] J.A. Manion, I.A. Awan, A shock tube study of H atom addition to cyclopentene, *International Journal of Chemical Kinetics* 50 (2018) 225-242.
- [104] H.J. Curran, P. Gaffuri, W.J. Pitz, C.K. Westbrook, A comprehensive modeling study of iso-octane oxidation, *Combustion and flame* 129 (2002) 253-280.
- [105] M. Baigmohammadi, V. Patel, S. Nagaraja, A.K. Ramalingam, S. Martinez, S. Panigrahy, A.A.E.S. Mohamed, K.P. Somers, U. Burke, K.A. Heufer, A. Pekalski, H.J. Curran, A Comprehensive Experimental and Simulation Study of the Ignition Delay Time Characteristics of Binary Blended Methane, Ethane, and Ethylene Over a Wide Range of Temperature, Pressure, Equivalence ratio, and Dilution, *Energy & Fuels*, 34(7) (2020) 8808-8823.



## Chapter 2

# **An Ab Initio/Transition State Theory Study of the Reactions of $\dot{C}_5H_9$ Species of Relevance to 1,3-Pentadiene, Part I: Potential Energy Surfaces, Thermochemistry and High-pressure Limiting Rate Constants**

Published in: Journal of Physical Chemistry A 123(22) (2019) 9019–9052.

DOI: <https://doi.org/10.1021/acs.jpca.9b06628>

### **Authors and Contributions**

(1) Yanjin Sun

National University of Ireland, Galway

Contribution: Ab initio calculations and manuscript preparation.

(2) Chong-Wen Zhou

School of Energy and Power Engineering, Beihang University

Contribution: Supervised ab initio calculations and reviewed the manuscript.

(3) Kieran P. Somers

National University of Ireland, Galway

Contribution: Supervised ab initio calculations and reviewed the manuscript.

(4) Henry J. Curran

National University of Ireland, Galway

Contribution: Project Management and manuscript review.

## Abstract

In this study, the reactions of  $\dot{\text{C}}_5\text{H}_9$  radicals are theoretically investigated, with a particular emphasis on hydrogen atom addition reactions to 1,3-pentadiene ( $\text{C}_5\text{H}_8$ ) to form  $\dot{\text{C}}_5\text{H}_9$  radicals, although the subsequent isomerization and decomposition reactions of the  $\dot{\text{C}}_5\text{H}_9$  radicals are also of direct relevance to the radicals formed from the pyrolysis and oxidation of species including pentene and cyclopentane. Moreover, H-atom abstraction reactions by hydrogen atoms from 1,3-pentadiene are also investigated.

The geometries and frequencies of 63 potential energy surface (PES) minima and 88 transition states are optimized at the  $\omega\text{B97X-D/aug-cc-pVTZ}$  level of theory. Spin-unrestricted open-shell single point energies for all the species are calculated at the CCSD(T)/aug-cc-pVTZ level of theory with basis set corrections from MP2/aug-cc-pVXZ (where  $X = \text{T}$  and  $\text{Q}$ ). A 1-dimensional hindered rotor treatment is employed for torsional modes, with the M06-2X/6-311++G(D,P) method used to compute the potential energy as a function of dihedrals angle. The high-pressure limiting rate constants and the thermochemical properties for  $\text{C}_5$  species are calculated using the Master Equation System Solver (MESS) with conventional transition state theory and comparisons are made with existing available literature data.

A hydrogen atom can add to the terminal carbon atom of 1,3-pentadiene to form the 2,4- $\dot{\text{C}}_5\text{H}_9$  radical and/or the internal carbon atoms to form 2,5- $\dot{\text{C}}_5\text{H}_9$ , 1,4- $\dot{\text{C}}_5\text{H}_9$  and 1,3- $\dot{\text{C}}_5\text{H}_9$  radicals. Among the four entrance channels for  $\dot{\text{H}}$  atom addition reactions, the formation of 2,4- $\dot{\text{C}}_5\text{H}_9$  and 1,3- $\dot{\text{C}}_5\text{H}_9$  radicals are more exothermic in comparison to the other  $\dot{\text{C}}_5\text{H}_9$  isomers (2,5- $\dot{\text{C}}_5\text{H}_9$ , 1,4- $\dot{\text{C}}_5\text{H}_9$ ) due to the resonantly stabilized allylic structure. Consequently, the formation of the former are generally dominant in terms of barrier heights.  $\dot{\text{H}}$  atom addition reactions to 1,3-pentadiene are compared to available  $\text{C}_3$ – $\text{C}_5$  alkenes and dienes, with external addition calculated to be kinetically favoured over internal addition. However, the correlation between heats of formation and energy barriers for  $\dot{\text{H}}$  atom addition to 1,2-dienes is different than that for 1,3- and 1,4-dienes. Hydrogen atom addition and abstraction rate constants are also compared for 1,3-pentadiene, with addition found to be dominant.

The subsequent unimolecular reactions on the  $\dot{\text{C}}_5\text{H}_9$  PES are found to be highly complex with reactions taking place on a multiple-well multiple-channel PES. For clarity, the reaction mechanism and kinetics of each  $\dot{\text{C}}_5\text{H}_9$  radical are discussed individually in terms of the computed enthalpy of the reaction and activation, the transition state structure/reaction class, and also in terms of the combustion species for which the reactions are of potential

importance. The reactions on the  $\dot{C}_3H_9$  PES are divided into three reaction classes (H-shift isomerization, cycloaddition and  $\beta$ -scission reactions), the reactivity-structure-based estimation rules for energy barriers are derived for these three reaction classes and compared to literature results for alkyl radicals.

## 1. Introduction

Petroleum fuels are used worldwide to produce energy for electricity and transportation. Diesel, petrol and natural gas contain both saturated and unsaturated hydrocarbons, with the unsaturated hydrocarbon portion being a much smaller fraction. Despite their relatively small amount (typically approximately 10% in gasoline [1]), unsaturated hydrocarbons have a significant influence on the flame speed of fuels. For fuels which have the same carbon number, the more unsaturated the molecule, the higher is the flame speed [2]. Acyclic 1,3-dienes represent the simplest conjugated system and they are involved in both thermal and photochemical synthetically useful reactions [3]. The propargyl ( $\dot{C}_3H_3$ ) radical, which is considered to be one of the most important benzene precursors, is found in remarkably high concentrations in 1,3-pentadiene flames [4]. Moreover, 1,3-dienes are also important intermediates in the pyrolysis and oxidation of higher-order hydrocarbons, and their combustion kinetics are important to the hierarchical development of kinetic mechanisms for hydrocarbon combustion.

Alkenes are primary products of the combustion of alkanes and in turn, dienes are important products of the combustion of alkenes. In the case of 1-butene oxidation in a jet-stirred reactor, 1,3-butadiene was measured in significant concentrations [5]. The sensitivity analyses of the oxidation of 1-pentene in a rapid compression machine have shown the importance of the formation of dienes involving the abstraction of a hydrogen atom next to the allylic radical centre by reacting with  $O_2$  [6]. In order to understand the combustion chemistry of alkenes, more studies of dienes are needed. However, there have been few kinetic studies of dienes larger than  $C_4$ , while the presence of two double bonds in diene molecules increases the system's chemical complexity.

Based on previous studies of butadiene oxidation [7, 8],  $\dot{H}$  atom addition reactions were found to be very important in the accurate prediction of both ignition delay times at high-temperatures ( $> 1000$  K) and flame speeds. For instance,  $\dot{H}$  atom addition to the terminal carbon atom of 1,3-butadiene inhibits reactivity resulting in the consumption of  $\dot{H}$  atoms, forming resonantly stabilized 1,3- $\dot{C}_4H_7$  radicals. However,  $\dot{H}$  atom addition to the internal carbon atom of 1,3-butadiene promotes reactivity by ultimately generating reactive

vinyl radicals and ethylene. At temperatures below 1200 K, the oxidation reactions of alkenes are initiated by H-atom abstraction reactions by oxygen molecules to produce alkyl and hydroperoxyl radicals [9]. Considering the importance of hydrogen atom addition and H-atom abstraction reactions by small radicals, the reactions between hydrogen atoms and 1,3-pentadiene are studied in this paper. For 1,3-pentadiene, there are four linear isomers (1,2-, 1,3-, 1,4- and 2,3-pentadiene) which are included on the  $C_5H_8 + \dot{H}$  potential energy surface (PES), so their related reactions are also considered in this paper.

Hydrogen atom addition to  $C_5H_8$  produces  $\dot{C}_5H_9$  alkenyl radicals, which can also be generated through H-atom abstraction reactions of 1-pentene and 2-pentene. The resonantly stabilized radicals such as  $\dot{C}_5H_9$ , their addition reactions on the double bonds, and cyclization processes are of great importance in the understanding of the first aromatic ring and the successive growth of polycyclic aromatic hydrocarbons (PAH) [10]. To the authors' knowledge there has been no direct study of the reactions of  $\dot{H}$  atoms with 1,3-pentadiene, but some of the reactions on the associated  $\dot{C}_5H_9$  PES have been reported in the literature and are listed in Table 2.1. The energies of species on the  $\dot{C}_5H_9$  PES were computed using composite methods [11-14] (e.g. G3 [15], CBS/QB3 [16]) or estimated from thermodynamic properties in the literature [17, 18] as discussed below.

**Table 2.1** Available reactions on  $\dot{C}_5H_9$  PES in the literature.

Reactions	Experimental measurements	Theoretical calculations
Propene + vinyl $\rightleftharpoons$ products	[11]	[11]
Allyl + ethylene $\rightleftharpoons$ products		[13], [14], [24]
1,3- $\dot{C}_5H_9 \rightleftharpoons$ 1,3-butadiene + methyl and other products		[17], [21]
1,4- $\dot{C}_5H_9 \rightleftharpoons$ 3-methyl-buten-4-yl and other products		[17], [25]
1,5- $\dot{C}_5H_9 \rightleftharpoons$ allyl + ethylene and other products	[18], [29]	[17], [24]
Cyclopentyl $\rightleftharpoons$ 1,5- $\dot{C}_5H_9$ and other products	[29]	[12], [24]

Goldsmith et al. [11] studied the reaction of vinyl radicals with propene over the temperature range 300 – 700 K at three pressures (15, 25 and 100 Torr (0.13 atm)) in a flow reactor. Vinyl radicals were generated via laser photolysis of vinyl iodide at 266 nm and they used direct absorption to monitor the reaction of vinyl + propene. They also studied 15 species and 48 transition states on the  $\dot{C}_5H_9$  PES at the G3 level of theory. The PES for each hindered rotor was calculated at the B3PW91 [19]/6-31+G(d,p) [20, 21] level of theory. The

$\dot{C}_5H_9$  radical was initially formed by vinyl radical addition to propene and the subsequent isomerization, ring-formation and decomposition reactions were also studied. RRKM/ME simulations were performed using Variflex [22] on a simplified PES to predict pressure-dependent rate constants and branching fractions for the major channels. Their calculations suggested that at high temperatures the dominant products were 1,3-butadiene + methyl radical, ethylene + allyl radical, and 1,3-pentadiene +  $\dot{H}$  atom.

Wang et al. [13, 14] studied allyl radical addition to ethylene because it is the simplest resonantly stabilized radical addition reaction. They also studied reactions on  $\dot{C}_5H_9$  PES, including 20 stationary species and 24 transition states and generated a simplified PES based on CBS-QB3 derived enthalpies. The optimized geometries, frequencies and electronic energies for all the species were calculated using the CBS-QB3 composite method. Pressure- and temperature-dependent rate constants for the multi-well and multi-channel PES were calculated based on a steady-state analysis using Quantum-Rice-Ramsperger-Kassel (QRRK) theory [23]. The high-pressure limiting rate constants for reactions on the simplified PES were calculated in two ways; (i) from CBS-QB3 calculations and (ii) estimated based on rate rules. Matheu et al. [24] developed an automated method to compute pressure-dependent rate constants during automated mechanism generation. They demonstrated their method on a series of pressure-dependent reaction through cycloalkyl radical intermediates; similar conclusions to those of Wang et al. were reached, in that, for the allyl + ethylene reaction, the formation of 1,5- $\dot{C}_5H_9$  radicals was the dominant channel over almost the entire temperature range.

Tsang [17] studied the decomposition of 1-pentenyl radicals, including 1-penten-3-yl (1,3- $\dot{C}_5H_9$ ), 1-penten-4-yl (1,4- $\dot{C}_5H_9$ ), 1-penten-5-yl (1,5- $\dot{C}_5H_9$ ) based on related data in the literature. The high-pressure limiting rate constants were estimated based on detailed balance. The energy transfer effects and the pressure-dependence of the rate constants were determined through the solution of the master equation. A  $\dot{C}_5H_9$  PES containing five wells was generated. Tsang proposed that the important unsaturated products were 1,3-pentadiene, the pentadienes, and allyl and vinyl radicals. Based on literature studies, Kerr and Parsonage [21] estimated the rate constants of 1,3-butadiene + methyl  $\rightleftharpoons$  1,3- $\dot{C}_5H_9$  radical over the temperature range 353 – 453 K at a pressure of 4 bar. Carter and Tardy [25] studied the homoallylic isomerization of 1,4- $\dot{C}_5H_9$  through experiments and 1,3-butadiene was identified using vapor-phase chromatography (VPC) combined with the retention times of known samples. The 1,4- $\dot{C}_5H_9$  radicals were formed by  $\dot{H}$  atom addition to 1,4-pentadiene. The mechanism which they generated included a very fast ring-formation reaction from 1,4- $\dot{C}_5H_9$

to form 2-methyl-cyclopropylmethyl and the subsequent  $\beta$ -scission reaction to produce large quantities of 3-methyl-1-buten-4-yl radical. This channel was supposed to be the most favored channel to form methyl + 1,3-butadiene for 1,4-pentadiene +  $\dot{\text{H}}$  and was also included in Goldsmith et al.'s study [11]. It was proposed that the  $\text{C}_3$  and  $\text{C}_4$  products resulting from the decomposition of 1,4-pentadiene +  $\dot{\text{H}}$  were primarily propene and 1,3-butadiene, with the  $\text{C}_3$  yield being about 20% that of 1,3-butadiene.

In existing combustion mechanisms (e.g. the LLNL Gasoline Surrogate Mechanism [26], KAUST Cyclopentane Oxidation Mechanism [27, 28]), the  $\dot{\text{C}}_5\text{H}_9$  radicals are usually represented by linear isomers. Moreover, the isomerization and ring-closing/opening reactions of these linear  $\dot{\text{C}}_5\text{H}_9$  radicals received less attention in contrast with  $\beta$ -scission reactions. Furthermore, the ring-structured  $\dot{\text{C}}_5\text{H}_9$  radicals have very limited studies excluding cyclopentyl radical. Thus, detailed calculations concerning ring-structured  $\dot{\text{C}}_5\text{H}_9$  radicals should be considered since their precursors, the cycloalkanes, are important components of common liquid fuels.

Tsang and Walker [18] studied the pyrolysis of 1,7-octadiene in a single-pulse shock tube over the temperature range 1040 – 1200 K and at pressures of 2-7 atm, the products are allyl + 1,5- $\dot{\text{C}}_5\text{H}_9$  or propene + 1,4-pentadiene. Decomposition of 1,5- $\dot{\text{C}}_5\text{H}_9$  was also studied and they proposed that most 1,5- $\dot{\text{C}}_5\text{H}_9$  radicals decomposed to form allyl and ethylene. The rate constant for 1,5- $\dot{\text{C}}_5\text{H}_9 \rightleftharpoons$  ethylene + allyl radical was measured to be about 20 times larger than that for 1,5- $\dot{\text{C}}_5\text{H}_9 \rightleftharpoons$  cyclopentene +  $\dot{\text{H}}$  at 1080 K and 2.5 atm.

Gierczak et al. [29] studied mutual isomerization of cyclopentyl and 1,5- $\dot{\text{C}}_5\text{H}_9$  radicals which are generated through the photolysis of hydrogen sulphide in the presence of either cyclopentene or 1,4-pentadiene. The experimental condition was at room temperature, and at pressures of 0.01 – 0.4 atm with the mixtures having  $\text{H}_2\text{S}$ /hydrocarbon ratios of 40/60. For the cyclopentene/ $\text{H}_2\text{S}$  mixture, the yields for ethylene and 1-pentene as a function of the total pressure were provided. Ethylene was formed through  $\beta$ -scission reactions of 1,5- $\dot{\text{C}}_5\text{H}_9$  and 1-pentene was formed in reactions of 1,5- $\dot{\text{C}}_5\text{H}_9$  with  $\text{H}_2\text{S}$ . The ratio of the yields for ethylene (unimolecular decomposition of 1,5- $\dot{\text{C}}_5\text{H}_9$ ) and 1-pentene (1,5- $\dot{\text{C}}_5\text{H}_9$  reacting with a hydrogen atom) was found to decrease with increasing pressure; the reaction of 1,5- $\dot{\text{C}}_5\text{H}_9$  with  $\dot{\text{H}}$  atoms was about seven times faster than the unimolecular decomposition reaction. Similarly, the yields for ethylene and cyclopentane as a function of the total pressure were provided for 1,4-pentadiene- $\text{H}_2\text{S}$  mixture. Cyclopentane was formed in reactions of cyclopentyl radicals with  $\text{H}_2\text{S}$ . The ratio of the yields for ethylene and cyclopentane showed that the  $\beta$ -scission reaction of 1,5- $\dot{\text{C}}_5\text{H}_9$  to form allyl + ethylene was over 12 times faster than the cycloaddition

reaction to form cyclopentyl radical at pressures below 0.5 atm and at room temperature.

Sirjean et al. [12] studied the thermal decomposition of cyclic alkyl radicals including cyclopentyl and methylcyclobutyl isomers. Quantum chemical calculations were performed at the CBS-QB3 level of theory and isodesmic reactions were used to calculate enthalpies of formation. In addition, high-pressure limiting, and pressure-dependent rate constants at 1 atm were calculated and fitted to Arrhenius expressions. For the ring-opening reactions, results showed that the energy barrier of the endo-ring-opening is higher compared to that for the exo-ring-opening one. For all cycloalkyl radicals considered, C–H bond breaking exhibited higher activation energies than C–C bond breaking excluding that for the cyclopentyl radical for which the ring-opening and  $\dot{\text{H}}$ -loss reactions were competitive.

In searching the literature data we found that there is no direct study of the thermal and chemically activated reactions of 1,3-pentadiene +  $\dot{\text{H}}$  and the  $\dot{\text{C}}_5\text{H}_9$  PES has not been systematically studied using quantum chemistry calculations. In the current paper, we studied the reactions on the  $\dot{\text{C}}_5\text{H}_9$  PES including  $\dot{\text{H}}$  atom addition to the four distinct unsaturated carbon atoms on 1,3-pentadiene which form four  $\dot{\text{C}}_5\text{H}_9$  isomers and the decomposition, isomerization, ring-closing/ring-opening reactions of these  $\dot{\text{C}}_5\text{H}_9$  radicals. In addition, the H-atom abstraction reactions of 1,3-pentadiene by  $\dot{\text{H}}$  atoms forming  $\dot{\text{C}}_5\text{H}_7$  radicals and  $\text{H}_2$ , and the unimolecular decomposition reactions of 1,3-pentadiene are also investigated. A chemical kinetic mechanism is developed combining the calculated thermochemical properties and high-pressure limiting rate constants to describe the chemistry of 1,3-pentadiene +  $\dot{\text{H}}$ . Homogeneous batch reactor simulations are carried out for a dilute 1,3-pentadiene/ $\dot{\text{H}}/\text{N}_2$  mixture to explore the important pathways on the  $\dot{\text{C}}_5\text{H}_9$  PES. Due to the complicated nature of the complete PES, a simplified PES is generated in part II of this study (Chapter 3), the pressure-dependent rate constants are calculated using the master equation code MESS [30, 31] and are compared with literature data.

## 2. Theoretical methods

The  $\omega\text{B97X-D}$  functional [32] with the aug-cc-pVTZ basis set [33] has been used to optimise geometries and compute vibrational frequencies for all of the stationary points using Gaussian 09 [34] and Gaussian 16 [35]. The  $\omega\text{B97X-D}$  functional yields satisfactory accuracy for thermochemistry, kinetics, and non-covalent interactions [32], thus no scale factor is employed to our computed zero-point energies and vibrational frequencies. Transition states were identified as species having a single imaginary frequency, with intrinsic reaction co-ordinate (IRC) calculations employed to verify the reactants/products for each transition

state. The M06-2X/6-311++G(d,p) level of theory [36] has been used in the intrinsic reaction coordinate (IRC) calculations [37]. The M06-2X/6-311++G(d,p) method has also been used to carry out relaxed potential energy surface scans of C–C bonds for each stationary point using a step size of 10 degrees. The energies as a function of dihedral angle were used as input for a 1-dimensional hindered rotor treatment of low-frequency vibrational modes. To obtain accurate energies for each species, single-point energies (SPEs) for minima and transition states are calculated using the CCSD(T) method [38] with the aug-cc-pVXZ basis set. A basis set correction is calculated from MP2/aug-cc-pVXZ calculations (where  $X = T, Q$ ) [39, 40]. The expression is as follows:

$$E_{\text{SPE}} = E_{\text{CCSD(T)/aug-cc-pVTZ}} + (E_{\text{MP2/aug-cc-pVQZ}} - E_{\text{MP2/aug-cc-pVTZ}}) \quad (1)$$

The multi-reference character in the wave function is indicated by the  $T_1$  diagnostic [41], the extent of the multi-reference character in a given species is diagnosed by inspecting the amplitudes from single excitations in the CCSD(T) calculations [42]. The  $T_1$  diagnostic values using the open-shell  $T_1$  formalism of Lee and co-workers [41, 43] are listed in Table A.1–A.2. Lee and Taylor suggested that  $T_1$  diagnostic values of less than  $\sim 0.02$  for closed-shell species were well described by single reference methods. However, Jayatilaka and Lee [43] proposed that  $T_1$  diagnostic values for open-shell species could be larger than those of closed-shell systems, where  $T_1$  values larger than  $\sim 0.02$  were typically suspect. In this study, the  $T_1$  diagnostic values for the 21 wells are within  $0.0153 \pm 0.008$ , with the maximum value being 0.026. For products, the  $T_1$  diagnostic values of stable molecules and radicals are within  $0.010 \pm 0.004$  and  $0.031 \pm 0.018$ , respectively, with the maximum  $T_1$  diagnostic value for radicals found to be 0.044. The  $T_1$  diagnostic values of vinylic and allylic radicals range from 0.028 – 0.044, and the  $T_1$  diagnostic values for allylic radicals (e.g.  $\text{C}=\text{CC}=\dot{\text{C}}\text{C}$ , 5-pentadienyl) are found to be smaller than those for vinylic radicals (e.g.  $\text{C}=\text{CC}=\dot{\text{C}}\text{C}$ , 4-pentadienyl). The relationship between the  $T_1$  diagnostic value and the degree of saturation, proximity to unsaturated bonds, was also observed in the work of Goldsmith et al. [44]. For the TSs in this paper the  $T_1$  diagnostic value is within  $0.027 \pm 0.015$  with a maximum value of 0.042. A  $T_1$  value of  $\leq 0.045$  has been found in unrestricted CCSD(T) calculations as a threshold for the suitability of this single-reference method [42, 45, 46]. Aiming to reduce spin contamination in the correlated wave function for SPEs, the ROCCSD(T) method is used in the SPE calculations for 31 important TSs which will be discussed in more detail in Chapter 3. The  $T_1$  diagnostic values for these restricted CCSD(T) calculations are within  $0.020 \pm 0.010$  with a maximum value of 0.032. Thus, the  $T_1$

diagnostics suggest the stable molecules and wells in this study do not show significant multi-reference character and the single-reference  $T_1$  formalisms are reliable. The vinylic and allylic radical products and TSs have larger  $T_1$  diagnostic values and multi-reference methods are recommended if the application requires tighter uncertainty for these species. However, the single-reference based method used in this study should be acceptable considering the trade-offs between computational cost and accuracy for the complex  $\dot{C}_5H_9$  PES.

The enthalpies of formation at 0 K for all species are calculated based on atomization approaches, using CBS-APNO, G3, G4 composite methods based on the geometry optimized at  $\omega$ B97X-D/aug-cc-pVTZ level of theory. Simmie and Somers [47, 48] showed that this approach reproduced values reported in the ATcT to within  $\sim 1$  kcal mol<sup>-1</sup>, and a comparison of our current results with literature data show a similar deviation. The 0 K formation enthalpies, vibrational frequencies, rotational constants, and 1-D internal rotational potentials are used as input for the MESS code to calculate temperature-dependent partition functions of each species, with the resulting partition functions used to calculate temperature-dependent thermochemical properties; enthalpies, entropies and heat capacities via calls to the ThermP code [49, 50] and converted to NASA polynomial format through PAC99 [49-51].

The high-pressure limiting rate constants are calculated using the (Predictive Automated Phenomenological Rates) PAPR code, the central code is (Master Equation System Solver) MESS which implements the one-dimensional Master Equation calculation for an arbitrary number of wells and products [30]. The low-frequency torsional modes are treated as one-dimensional hindered rotors, the global rotation and the internal rotations are decoupled and each internal rotation is described in one-dimension, ignoring the coupling between adjacent torsional modes [52]. The hindrance potentials as a function of dihedral angle are calculated at the M06-2X/6-311++G(d,p) level of theory. The quantum mechanical tunneling corrections are included for all transition states using an unsymmetrical Eckart barrier model [53]. The calculated high-pressure limiting rate constants are fitted to the modified Arrhenius expression as a function of temperature.

## 2.1 Lowest energy configuration of 1,3-pentadiene

1,3-pentadiene has four configurations depending on the orientation of the  $C_1-C_2-C_3-C_4$  and  $C_2-C_3-C_4-C_5$  dihedral angles as shown in Fig. 2.1. Based on our CCSD(T)/CBS// $\omega$ B97X-D/aug-cc-pVTZ computed energies, we find the trans-trans configuration is the most stable conformer, which is used as the basis for subsequent exploration of the PES. For wells which have different conformations, the energy for each

conformer is calculated and the energy and geometry of the most stable conformer is used for rate constant calculation for all the wells.

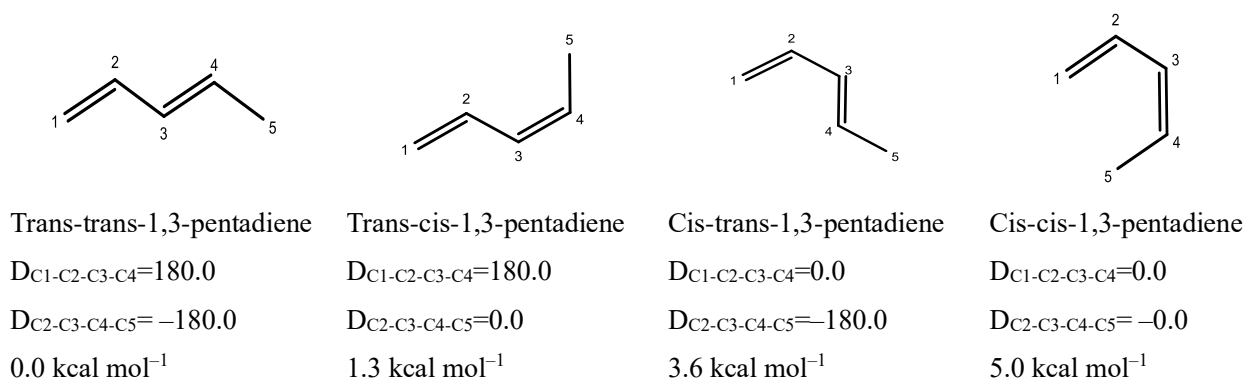


**Fig. 2.1** Different configurations of 1,3-pentadiene.

## 2.2 Naming scheme for species and reactions on $\dot{C}_5H_9$ PES

In this study, the  $C_5$  species are divided into four types, (1) linear dienes and alkynes, (2) cyclic alkenes, (3) linear alkenyl radicals and (4) cyclic alkyl radicals. The linear  $C_5$  species (the first and the third type) are named in terms of the location of the C–C double/triple bonds and/or radical positions. For linear stable species (e.g. 1,3- $C_5H_8$ ), the prefix numbers refer to the double or triple bond positions. For linear alkenyl radicals (e.g. 2,4- $\dot{C}_5H_9$ ), the first number refers to the position of the double bond and the second represents the radical site as shown in Fig. 2.2. For ring-structured  $C_5H_8$  species with a double bond on the ring (e.g. 3-methylcyclobutene), the numbering starts at the location of the C–C double bond on the ring and the prefix numbers represent the attached position of the substituents. For ring-structured  $C_5H_8$  species with a double bond on the substituents (e.g. 1-methylidene-2-methyl-cyclopropane), the numbering starts at the substituted ring atom and the prefix numbers represent the position of the substituents. The “-ylidene” suffix is used to indicate the attachment of a  $=CH_2$  or a  $-\dot{C}H_2$  group to the ring. Similarly, for cyclic alkyl radicals (e.g. 1,3-dimethyl-2-cyclopropyl), the numbering starts at a substituted ring atom and the prefix numbers represent the position of the substituent and radical position, respectively.

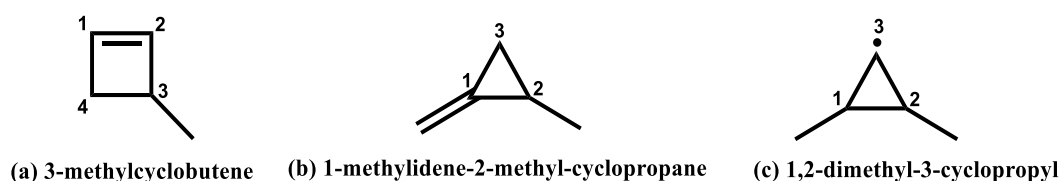


**Fig. 2.2** Schematic for numbering the ring-structured  $C_5$  species.

Three reaction classes, H-shift isomerization reactions, ring-closing/opening reactions and  $\beta$ -scission reactions, are included in the following discussions. The isomerization reactions are discussed in the following order: 1,2-H shift, 1,3-H shift, ..., 4,5-H shift, which is shown in Table 2.2 in greater detail. Thereafter, the ring-closing/opening reactions are discussed based on the ring sizes of the TSs combining with a sub-category including endo- or exo-cyclization. The  $\beta$ -scission reactions are simply divided into C–C and C–H bond breaking, with C–C bond breaking further divided into the formation of  $C_3 + C_2$  species and/or  $C_4 + C_1$  species.

The linear alkenyl radicals can be divided into six types (primary, primary-allylic, primary-vinylic; secondary, secondary-allylic, and secondary-vinylic) depending on the location of the radical site relative to the double bond. The structures of different linear  $\dot{C}_5H_9$  radicals and the corresponding radical types (with abbreviations) are illustrated in Fig. 2.3. Based on the radical types, the H-shift isomerization reactions fall into 18 subclasses (e.g., a primary-vinylic radical forming a secondary-vinylic radical via an H-shift isomerization reaction, which is abbreviated to  $1^\circ v-2^\circ v$ ) shown in Table 2.2. The barrier heights are averaged for reaction subclasses that are composed of more than one reaction, and these H-shift reactions are listed in Table 2.2 in the order of their barrier height. The reaction classes and barrier heights corresponding to the detailed reactions are listed in Table 2.12. The 1,3- $\dot{C}_5H_9$  radical in Table 2.2 is assigned as a primary allylic ( $1^\circ a$ ) to distinguish it from another secondary-allylic radical (2,4- $\dot{C}_5H_9$ ,  $2^\circ a$ ).

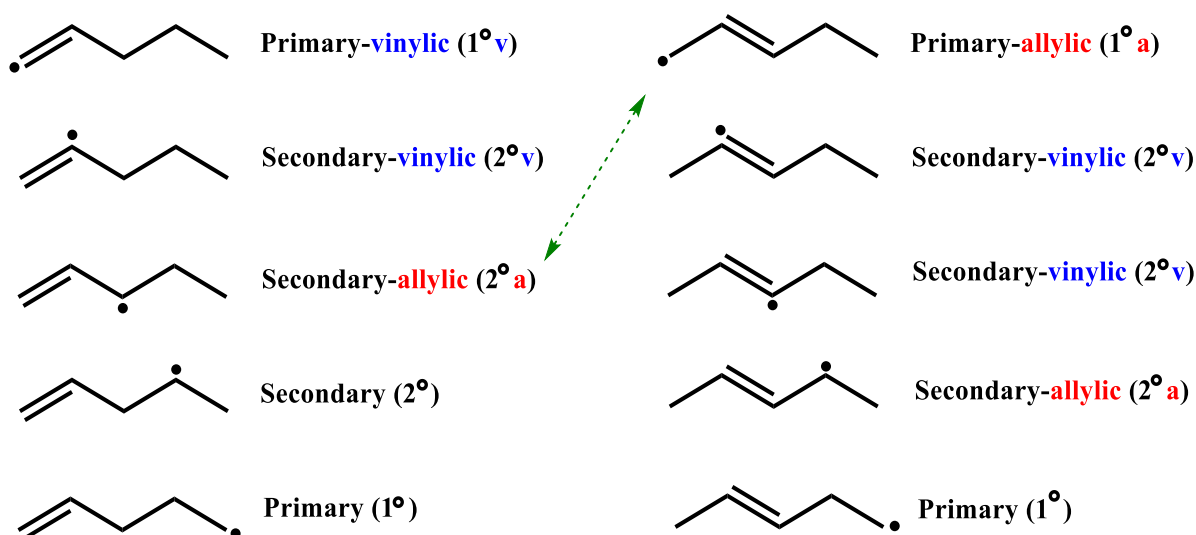


**Fig. 2.3** Schematic for different types of linear  $\dot{C}_5H_9$  radicals. The green arrow indicates the  $2^\circ a$  radical is equivalent to  $1^\circ a$  radical.

**Table 2.2** The category of H-shift isomerization reactions for linear  $\dot{C}_5H_9$  radicals. (kcal mol<sup>-1</sup>)

	Ring size	Reaction type	Reactant type	Product type	Averaged barrier height	
					Forward	Reverse
1	6	1°v→1°	primary-vinylic	primary	10.9	21.6
2	5	1°v→2°	primary-vinylic	secondary	15.9	29.3
3	6	1°→1°a	primary	primary-allylic	18.1	31.3
4	5	2°v→1°	secondary-vinylic	primary	20.4	27.3
5	3	1°→2°a	primary	secondary-allylic	33.4	49.3
6	3	2°→1°a	secondary	primary-allylic	34.2	47.3
7	4	1°→1°a	primary	primary-allylic	35.2	51.0
8	5	1°a→2°a	primary-allylic	secondary-allylic	36.0	38.7
9	4	1°v→1°a	primary-vinylic	primary-allylic	37.9	64.4
10	4	2°v→2°	secondary-vinylic	secondary	38.0	48.2
11	3	1°→2°	primary	secondary	38.5	41.2
12	4	2°v→2°a	secondary-vinylic	secondary-allylic	38.9	62.1
13	4	2°v→1°	secondary-vinylic	primary	39.2	46.7
14	4	2°v→1°a	secondary-vinylic	primary-allylic	41.2	61.9
15	3	2°v→2°a	secondary-vinylic	secondary-allylic	41.5	64.9
16	3	2°v→1°a	secondary-vinylic	primary-allylic	42.8	64.2
17	3	1°v→2°v	primary-vinylic	secondary-vinylic	43.2	47.4
18	3	2°v→2°v	secondary-vinylic	secondary-vinylic	47.5	47.7

The cycloaddition reactions of alkenyl radicals can be divided into endo- and/or exo-cycloadditions depending on the location of the radical site relative to the ring of the product. The addition to the far vinylic carbon leading to a cycloalkyl radical (radical site on the ring) is referred to as an endo-cycloaddition. The addition to the near vinylic carbon leading to a cycloalkyl-carbinyl radical (radical site on the substituent) is referred to as an exo-cycloaddition [14]. For instance, 1,4- $\dot{C}_5H_9$  radicals can undergo endo-cycloaddition to form methyl-3-cyclobutyl and/or exo-addition to form 1-methylidene-cyclopropylmethyl as shown in Fig. 2.4.

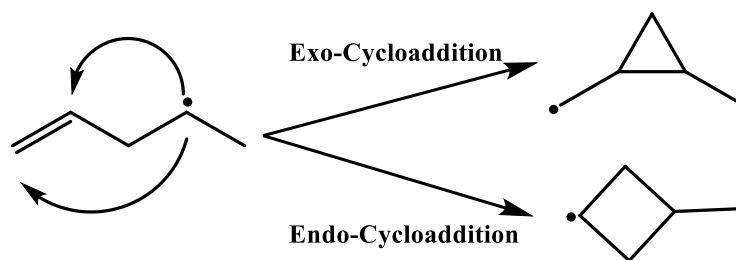


**Fig. 2.4** Schematic for endo- and exo-cycloaddition reactions of alkenyl radicals.

### 3. Results and discussion

#### 3.1 Thermochemistry calculations

The thermochemistry of the C<sub>5</sub> species investigated, including comparisons with literature data, are presented in Tables 2.3 and 2.4. A Bland-Altman plot [54] is used to illustrate the agreement between this study and literature data from the Active Thermochemical Tables (ATcT) [55, 56], the Third Millennium Ideal Gas and Condensed Phase Thermochemical Database for Combustion [57] (abbreviated as Burcat’s database in this paper), the NIST Chemistry Webbook [58], and other theoretical calculations [12, 44, 59]. The Bland-Altman plot has been used by Simmie and Sheahan [60] to validate the reliability of their calculated formation enthalpies against the ATcT. The ATcT provide reliable, accurate, and internally consistent thermochemistry by utilizing the thermochemical network (TN) approach [61]. However, most of the C<sub>5</sub> species on  $\dot{C}_5H_9$  PES are not provided in the ATcT. Burcat [57] and Ruscic applied the G3B3 [62, 63] method to more than 1300 species and calculated the thermochemistry properties with updates from ATcT. For the C<sub>5</sub> species, the uncertainty for enthalpies of formation at 298 K are recommended to within 0.8 – 1.9 kcal mol<sup>-1</sup> in Burcat’s database [57]. There are also various literature data collected from the NIST database [58] included in the comparison.

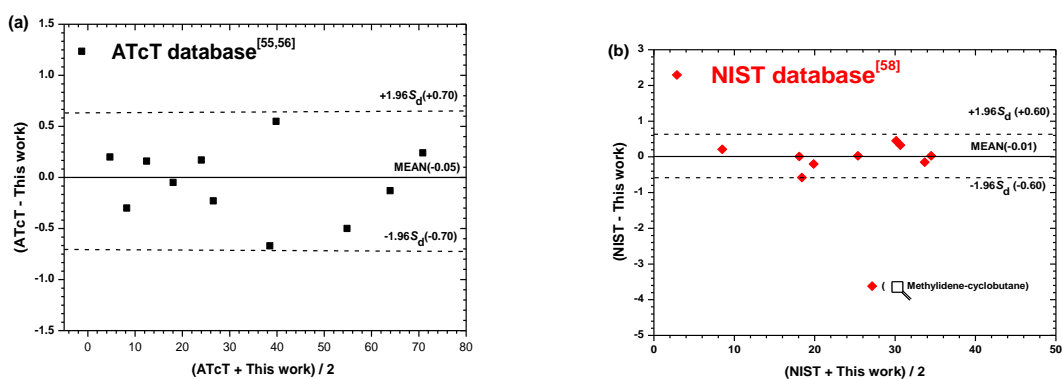
Differences between literature enthalpies of formation values and those calculated in this study are shown in Fig. 2.5. For each literature source, the x-axis is the average of the literature value and the result calculated in this paper; the y-axis is the difference between the literature value and the calculated result. The accepted convention for expressing uncertainties of thermochemical quantities, followed by virtually all thermochemical tabulations, is to provide earnest estimates of 95% confidence intervals [64]. The associated 95% limits of agreement are about twice (1.96) those of the sample standard deviation [60] where the standard deviation is given by:

$$\sigma = \sqrt{\frac{\sum(d_i - \bar{d})^2}{n-1}} \quad (2)$$

In eq. 2,  $d_i$  is defined as the deviation between a specific literature source and the calculated value for one species;  $\bar{d}$  is the average of  $d_i$ ;  $n$  is the number of species possessing literature data. The mean deviation  $\bar{d}$  is shown in solid line on the Bland-Altman plot; the 95% limits of agreement, given by the expression:  $(\bar{d} \pm 1.96\sigma)$ , are shown in dash lines.

Since most of the C<sub>5</sub>H<sub>8</sub> and  $\dot{C}_5H_9$  species are not included in the ATcT database, the thermochemical properties of nine C<sub>2</sub>–C<sub>4</sub> molecules have also been calculated and compared with the ATcT values to determine the uncertainty of the method used in this paper. As shown

in Fig. 2.5(a), deviations in enthalpy of formation values from this study and the ATcT are within  $-0.05 \pm 0.70$  kcal mol<sup>-1</sup> with 95% confidence limits. The maximum deviation is  $-0.67$  kcal mol<sup>-1</sup>. For existing data collated from the NIST database, there is one outlier (methylidene-cyclobutane) [65], which we neglect because the original experimental data is for methyl-cyclobutane and has been used for methylidene-cyclobutane by mistake. The revised NIST dataset agrees with our calculated results within  $+0.01 \pm 0.60$  kcal mol<sup>-1</sup> with a maximum deviation of  $-0.58$  kcal mol<sup>-1</sup>. The calculated enthalpies are also compared with Burcat's database with the maximum difference being 1.42 kcal mol<sup>-1</sup>. The  $\Delta_f H^\circ(298.15$  K) of cyclobutene in Burcat's database is from version 1.110 of the ATcT and is 0.73 kcal mol<sup>-1</sup> smaller than  $\Delta_f H^\circ(298.15$  K) in the latest version 1.122d. Since the  $\Delta_f H^\circ(298.15$  K) from the latest version 1.122d of the ATcT has already been discussed in Fig. 2.5(a), Burcat's value for cyclobutene is neglected in our comparison. The revised Burcat database agrees with our calculations within  $+0.42 \pm 1.15$  kcal mol<sup>-1</sup>. Since the minimum uncertainty for  $\Delta_f H^\circ(0$  K) calculated from the CBS-QB3/G3/G4 combination method is 1.0 kcal mol<sup>-1</sup> in this study; and the uncertainty of Burcat's database for C<sub>5</sub> species is up to 1.91 kcal mol<sup>-1</sup>. Thus the deviation between this study and Burcat's database for  $\Delta_f H^\circ(298.15$  K) is acceptable. Sirjean et al. [12] used isodesmic reactions to calculate the enthalpies of formation and proposed the uncertainty for their calculations as being within 0.9 kcal mol<sup>-1</sup>. Awan et al. [59] studied the thermochemical properties of 1,5- $\dot{C}_5H_9$  and cyclopentyl based on structural properties calculated at the G3MP2B3 level of theory. In either case, they have made slight adjustments to the low-frequency vibrations to fit their experimental shock tube data. They proposed the thermochemical values derived from the G3MP2B3 calculations had uncertainty typically within 1.4 kcal mol<sup>-1</sup>. The deviations in comparison to Sirjean and Awan's calculations are within  $+0.55 \pm 1.01$  kcal mol<sup>-1</sup> which agree well with the uncertainty proposed in their papers.



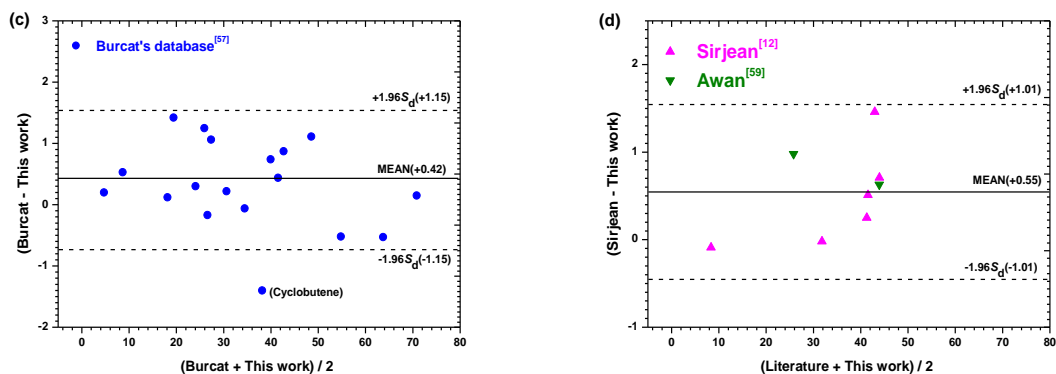


**Fig. 2.5** The mean difference graph for enthalpy of formation at 298 K. (Units: kcal mol<sup>-1</sup>).

The calculated entropies at 298 K are compared with the NIST and Burcat databases, Fig. 2.6. The deviations between this study and NIST are within  $0.37 \pm 1.38$  cal K<sup>-1</sup> mol<sup>-1</sup>, and the maximum deviation is 1.43 cal K<sup>-1</sup> mol<sup>-1</sup>. The difference plot for the 298.15 K entropy shows most of the results are within 2 cal K<sup>-1</sup> mol<sup>-1</sup> deviation with Burcat's database excluding 1,3-butadiene (P14) and 1,3-pentadien-5-yl (P33), for which differences of 3.71 and 3.88 cal mol<sup>-1</sup> K<sup>-1</sup> are observed. Goldsmith and co-workers calculated thermochemical properties of C<sub>0</sub>–C<sub>4</sub> molecules using the RQCISD(T)/cc-pV $\infty$ QZ//B3LYP/6-311++G(d,p) method. The ab initio calculated entropy for 1,3-butadiene at 298.15 K is 0.6 cal K<sup>-1</sup> mol<sup>-1</sup> smaller than this study and the difference is within the uncertainty of 1.3 cal mol<sup>-1</sup> K<sup>-1</sup> proposed in their paper. Thus the  $S^\circ$  (298.15 K) of 1,3-butadiene in Burcat's database is not included in the comparison. For 1,3-pentadien-5-yl radical (C=CC=C or C=CC=CC), the C–C bond rotational barrier ( $\sim 13$  kcal mol<sup>-1</sup>) for CH<sub>2</sub>=CH– group is used in Burcat's database to calculate  $S^\circ$  (298.15 K) for 1,3-pentadien-5-yl radical by analogy to allyl hydroperoxide (C=CCOOH) [66]. However, the electrons are actually delocalized on five carbons of the radical and no internal rotation is considered in this study due to the allylic structure. This internal rotor contribution is possibly the major reason for the 3.88 cal K<sup>-1</sup> mol<sup>-1</sup> difference between this study and the value presented in Burcat's database. This value is also neglected in consideration of the error in internal rotor treatment of the 1,3-pentadien-5-yl radical. The revised Burcat's database agrees with our calculated  $S^\circ$  (298.15 K) within  $-0.10 \pm 1.54$  cal K<sup>-1</sup> mol<sup>-1</sup>, with a maximum deviation of  $-1.86$  cal K<sup>-1</sup> mol<sup>-1</sup>.

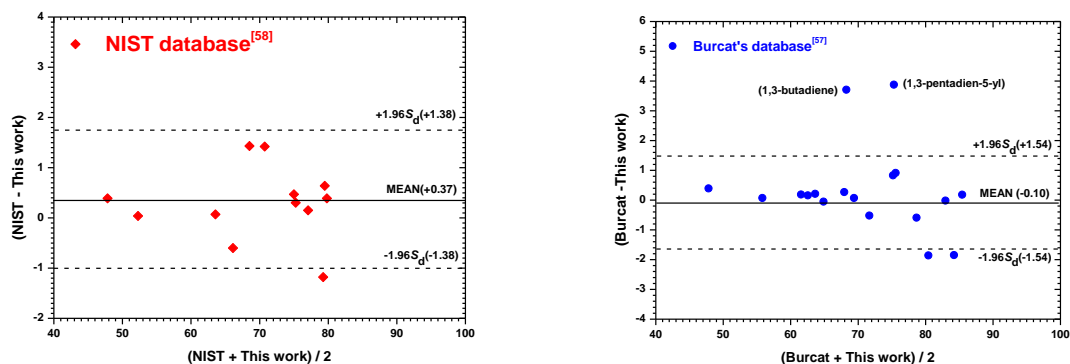


**Fig. 2.6** The mean difference graph for entropy at 298 K. (Units:  $\text{cal K}^{-1} \text{mol}^{-1}$ ).

The heat capacities at 300 K calculated in this paper (Fig. 2.7) agree very well with the NIST database, with differences within  $0.15 \pm 0.57 \text{ cal K}^{-1} \text{mol}^{-1}$ ; the largest difference is  $0.62 \text{ cal K}^{-1} \text{mol}^{-1}$  for cyclopentene. The calculated result also agrees with Burcat's database within  $0.15 \pm 0.57 \text{ cal K}^{-1} \text{mol}^{-1}$ . Thus, it is shown that the differences between this study and the available literature data for enthalpy, entropy at 298.15 K and heat capacity at 300 K are within  $1.5 \text{ kcal mol}^{-1}$ ,  $2.0$  and  $1.5 \text{ cal K}^{-1} \text{mol}^{-1}$ , respectively. Since the existing thermochemistry data for  $\text{C}_5$  species are limited in comparison to small molecules, the calculated thermochemistry values in this study can be complementary for thermochemistry studies.

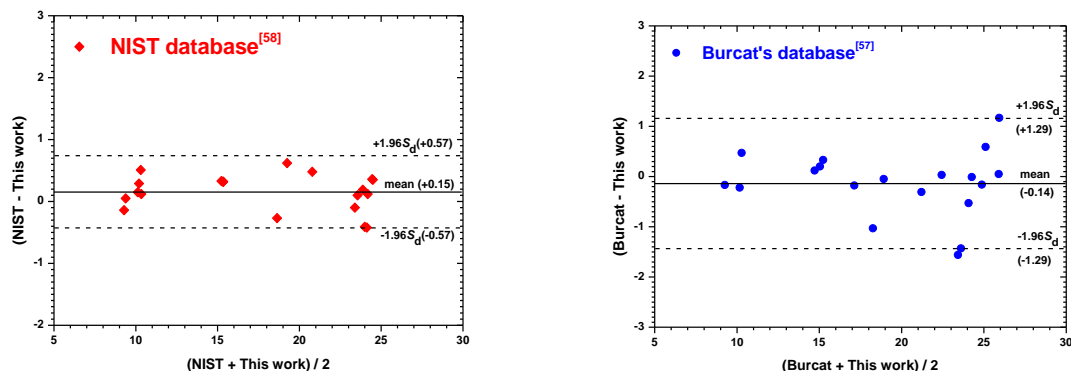


**Fig. 2.7** The mean difference graph for heat capacity at 298 K. (Units:  $\text{cal K}^{-1} \text{mol}^{-1}$ ).

**Table 2.3** Thermochemistry comparison of 54 species on  $\dot{C}_5H_9$  PES between literature data and present work calculated using CCSD(T)/CBS// $\omega$ B97X-D/aug-cc-pVTZ method.

Label	Species	$\Delta H_{f,298}^\ominus$ [kcal mol <sup>-1</sup> ]		$S_{298}^\ominus$ [cal K <sup>-1</sup> mol <sup>-1</sup> ]	
		This study	Ref.	This study	Ref.
R	Trans-1,3-pentadiene	18.7	20.1±1.9 <sup>b</sup> , 18.1±0.2 <sup>c</sup>	75.1	76.0 <sup>b</sup> , 75.4 <sup>c</sup>
	Cis-1,3-pentadiene	20.0	19.8±0.2 <sup>c</sup>	77.0	77.2 <sup>c</sup>
W1	2,4- $\dot{C}_5H_9$	24.1		79.2	
W2	2,5- $\dot{C}_5H_9$	41.3	41.7 <sup>b</sup> , 41.8 <sup>d</sup>	85.3	85.5 <sup>b</sup> , 84.5 <sup>d</sup>
W3	1,4- $\dot{C}_5H_9$	41.2	41.4 <sup>d</sup>	87.8	85.8 <sup>d</sup>
W4	1,3- $\dot{C}_5H_9$	26.8	27.9±1.9 <sup>b</sup>	83.0	82.9 <sup>b</sup>
W5	1,2-dimethyl-3-cyclopropyl	55.8		76.4	
W6	Sec-ethyl-cyclopropanyl	44.7		82.6	
W7	2,2- $\dot{C}_5H_9$	48.1		84.7	
W8	2,3- $\dot{C}_5H_9$	48.2		84.1	
W9	Ethyl-2-cyclopropyl	57.0		80.3	
W10	1,5- $\dot{C}_5H_9$	43.6	44.3 <sup>d</sup> , 44.2 <sup>e</sup>	86.3	86.1 <sup>d</sup> , 84.2 <sup>e</sup>
W11	1,2- $\dot{C}_5H_9$	49.8		85.1	
W12	1,1- $\dot{C}_5H_9$	54.0		84.7	
W13	1-methylidene-cyclopropylmethyl	44.1		78.9	
W14	3-methyl-1-buten-4-yl	42.2	43.1 <sup>b</sup> , 43.7 <sup>d</sup>	85.2	83.3 <sup>b</sup> , 85.0 <sup>d</sup>
W15	Cyclopentyl	25.3	26.6 <sup>b</sup> , 26.3 <sup>e</sup>	71.9	71.4 <sup>b</sup> , 73.4 <sup>e</sup>
W16	Methyl-2-cyclobutyl	46.6		78.2	
W17	Methyl-3-cyclobutyl	46.3		77.0	
W18	Methyl-1-cyclobutyl	44.1		76.9	
W19	Methylidene-cyclobutyl	46.0		74.4	
W20	1,2-dimethyl-1-cyclopropyl	52.5		80.0	
W21	1-ethyl-cyclopropyl	54.4		82.3	
P1	Ethylene	12.4	12.5 <sup>a</sup>	52.3	52.3±0.4 <sup>c</sup>
	1-propenyl	64.0	63.9±0.2 <sup>a</sup> , 63.5 <sup>b</sup>	64.9	64.8 <sup>b</sup>
P3	1,3-dimethyl-cyclopropene	49.9		78.2	
P4	2,3-pentadiene	31.8	31.8±0.2 <sup>c</sup>	79.8	78.7 <sup>c</sup>
P5	2-pentyne	30.5	30.7±0.8 <sup>b</sup> ,	81.4	79.5 <sup>b</sup>
			30.8±0.5 <sup>c</sup>		
P8	Ethenyl-cyclopropane	29.9	30.4 <sup>c</sup> , 31.4±0.3 <sup>c</sup>	75.8	
P9	Ethylidene-cyclopropane	38.3		74.3	
P11	1,2-pentadiene	33.8	33.6±0.16 <sup>c</sup>	79.6	80.0 <sup>c</sup>
P12	Vinyl	70.7	71.0 <sup>a</sup> , 70.9 <sup>b</sup>	55.8	55.9 <sup>b</sup>
	Propene	4.6	4.8±0.1 <sup>a</sup> , 4.8 <sup>b</sup>	63.5	63.7 <sup>b</sup> , 63.6±0.9 <sup>c</sup>
P13	1-methylidene-2-methyl-cyclopropane	38.7		75.0	
P14	1,3-butadiene	26.7	26.4±0.1 <sup>a</sup> , 26.5 <sup>b</sup>	66.4	70.1 <sup>b</sup> , 65.8±1.3 <sup>c</sup>
P15	Allyl	39.6	40.1±0.1 <sup>a</sup> , 40.3 <sup>b</sup>	61.4	61.6 <sup>b</sup>
P17	1-ethyl-cyclopropene	52.3		78.5	
P18	3-ethyl-cyclopropene	55.5		79.0	
P20	1-pentyne	34.5	34.4±0.8 <sup>b</sup> ,	79.0	78.4 <sup>b</sup>
			34.5±0.5 <sup>c</sup>		
P21	Acetylene	55.1	54.6 <sup>a</sup> , 54.5 <sup>b</sup>	47.6	48.0 <sup>b</sup> , 48.0 <sup>c</sup>
	1-propyl	23.9	24.1±0.2 <sup>a</sup> , 24.2 <sup>b</sup>	69.4	69.4 <sup>b</sup>
P22	1,4-pentadiene	25.4	25.4±0.3 <sup>c</sup>	79.2	79.8 <sup>c</sup>
P23	Cyclopentene	8.4	8.1 <sup>a</sup> , 8.9 <sup>b</sup> , 8.6 <sup>c</sup> ,	67.8	68.1 <sup>b</sup> , 69.2 <sup>c</sup>
			8.3 <sup>d</sup>		
P24	3-methylcyclobutene	31.3		72.6	
P25	1-methylcyclobutene	28.4		72.4	

P26	Isoprene	18.1	18.0 <sup>a</sup> , 18.2 <sup>b</sup> , 18.1 <sup>c</sup>	74.8	75.6 <sup>b</sup> , 75.2 <sup>c</sup>
P27	Cyclobutene	38.9	38.2 <sup>a</sup> , 37.5 <sup>b</sup>	62.5	62.6 <sup>b</sup>
P28	Methylenecyclobutane	29.0	25.3 <sup>c</sup>	70.0	71.4±0.2 <sup>c</sup>
P29	Trans-1,3-pentadien-1-yl	78.5		77.2	
	Cis-1,3-pentadien-1-yl	79.2		77.6	
P30	1,3-pentadien-2-yl	67.3		78.2	
P31	1,3-pentadien-3-yl	68.1		78.3	
P32	1,3-pentadien-4-yl	75.4		78.1	
P33	1,3-pentadien-5-yl	48.0	49.1±1.9 <sup>b</sup>	73.4	77.3 <sup>b</sup>

<sup>a</sup> Active Thermochemical Tables (Branco Ruscic Argonne National Lab.) [55].

<sup>b</sup> Third Millennium Ideal Gas and Condensed Phase Thermochemical Database for Combustion (Burcat) [57].

<sup>c</sup> NIST Chemistry Webbook [58].

<sup>d</sup> Calculated values from Sirjean et al. [12] using CBS/QB3 and isodesmic reaction method.

<sup>e</sup> Calculated values from Awan et al. [59] at G3MP2B3 level of theory.

**Table 2.4** Thermochemistry comparisons of 54 species on  $\dot{C}_5H_9$  PES between literature data and present work calculated using CCSD(T)/CBS// $\omega$ B97X-D/aug-cc-pVTZ method.

Label	Species	$C_p(T)$ [cal K <sup>-1</sup> mol <sup>-1</sup> ]													
		This study							Literature						
		300	400	500	600	800	1000	1500	300	400	500	600	800	1000	1500
R	Trans-1,3-pentadiene	24.2	31.4	36.0	40.7	47.3	52.3	60.1	23.8 <sup>c</sup> 22.6 <sup>b</sup>	29.9	35.4	40.0	47.3	52.7	61.0
	Cis-1,3-pentadiene	23.4	29.7	35.3	40.0	46.6	51.8	59.8	23.3 <sup>c</sup>	29.5	35.0	39.8	47.2	52.6	61.0
W1	2,4- $\dot{C}_5H_9$	24.4	30.3	36.0	41.1	49.0	55.0	64.3							
W2	2,5- $\dot{C}_5H_9$	25.4	31.0	36.5	41.3	48.7	54.5	63.5	26.5 <sup>b</sup> 25.9 <sup>d</sup>	31.6	37.0	41.7	49.2	54.9	63.8
W3	1,4- $\dot{C}_5H_9$	24.2	30.0	35.6	40.6	48.3	54.2	63.4	24.2 <sup>d</sup>	30.2	35.9	40.8	48.7	54.6	63.7
W4	1,3- $\dot{C}_5H_9$	24.8	31.1	36.9	42.1	49.7	55.6	64.7	25.4 <sup>b</sup>						
W5	1,2-dimethyl-3-cyclopropyl	24.0	30.2	36.1	41.3	49.2	55.1	64.3							
W6	sec-ethyl-cyclopropanyl	23.2	29.7	35.9	41.3	49.2	55.1	64.3							
W7	2,2- $\dot{C}_5H_9$	25.6	30.9	36.2	41.0	48.6	54.4	63.5							
W8	2,3- $\dot{C}_5H_9$	25.2	30.7	36.0	40.9	48.5	54.3	63.5							
W9	2-ethyl-cyclopropyl	24.4	31.1	37.2	42.5	50.1	55.8	64.7							
W10	1,5- $\dot{C}_5H_9$	25.0	31.1	36.8	41.8	49.2	54.8	63.7	24.8 <sup>d</sup>	31.2	37.0	41.8	49.4	55.0	63.9
W11	1,2- $\dot{C}_5H_9$	25.1	31.1	36.7	41.6	49.1	54.8	63.7							
W12	1,1- $\dot{C}_5H_9$	25.4	31.3	36.9	41.7	49.2	54.9	63.8							
W13	1-methylidene-cyclopropylmethyl	25.3	31.9	37.7	42.7	50.1	55.7	64.6							
W14	3-methyl-1-buten-4-yl	25.9	31.9	37.4	42.2	49.4	54.9	63.7	25.9 <sup>b</sup> 25.3 <sup>d</sup>	31.9	37.7	42.5	49.8	55.3	64.0
W15	Cyclopentyl	21.4	28.6	35.5	41.5	50.1	56.5	66.1	21.1 <sup>b</sup> 22.1 <sup>e</sup>	29.8	36.6	42.3	51.0	57.2	66.7
W16	Methyl-2-cyclobutyl	23.4	30.2	36.6	42.2	50.2	56.3	65.5							
W17	Methyl-3-cyclobutyl	23.3	30.3	36.7	42.3	50.4	56.4	65.6							
W18	Methyl-1-cyclobutyl	21.8	28.6	35.1	40.9	49.4	55.7	65.3							
W19	Methylidene-cyclobutyl	22.5	29.5	36.0	41.6	49.8	55.9	65.2							
W20	1,2-dimethyl-1-cyclopropyl	23.8	30.0	35.9	41.2	49.1	55.1	64.3							
W21	1-ethyl-cyclopropyl	23.9	30.3	36.3	41.6	49.4	55.3	64.5							

P1	Ethylene	10.1	12.3	14.5	16.5	19.6	22.1	25.9	10.3 <sup>c</sup>	12.7	14.9	16.8	19.9	22.4	26.1
									10.2±0.7 <sup>c</sup>	12.5±0.9	14.7±1.0	16.7±1.1	19.8±1.1	22.2±1.1	26.1±0.8
	1-propenyl	14.9	18.0	21.0	23.6	27.5	30.6	35.5	15.1 <sup>b</sup>						
P2	Methyl	9.4	10.1	10.8	11.5	12.8	13.9	16.1	9.2 <sup>c</sup>	10.0	10.7	11.5	12.8	14.0	16.2
									9.4±0.2 <sup>c</sup>	10.1±0.3	10.9±0.4	11.6±0.4	12.9±0.5	14.0±0.5	16.2±0.5
									9.2 <sup>b</sup>						
P3	1,3-dimethyl-cyclopropene	23.1	28.6	33.8	38.5	45.6	51.1	59.5							
P4	2,3-pentadiene	23.8	29.0	34.0	38.5	45.5	50.9	59.4	24.0 <sup>c</sup>	29.5	34.5	39.0	46.1	51.6	60.0
P5	2-pentyne	24.3	29.7	34.8	39.3	46.4	51.8	60.3	23.8 <sup>b</sup>						
									23.9 <sup>c</sup>	29.6	34.8	39.3	46.5	51.9	60.2
P8	Ethenyl -cyclopropane	22.8	28.8	34.5	39.4	46.6	52.0	60.4							
P9	Ethylidene-cyclopropane	22.3	28.4	34.1	39.1	46.4	51.9	60.4							
P11	1,2-pentadiene	24.1	29.6	34.7	39.2	46.1	51.4	59.6	24.24 <sup>c</sup>	30.3	35.7	40.3	47.6	52.8	61.2
P12	Vinyl	10.3	12.1	13.7	15.1	17.2	18.9	21.7	10.4±0.6 <sup>c</sup>	12.3±0.7	13.9±0.7	15.2±0.7	17.4±0.8	19±0.7	21.8±0.6
									10.1 <sup>b</sup>						
	Propene	15.1	18.6	22.1	25.3	30.1	33.9	39.9	15.4±1 <sup>c</sup>	19.1±1.4	22.6±1.5	25.6±1.6	30.5±1.7	34.2±1.6	40.2±1.2
									15.4 <sup>b</sup>						
P13	1-methylidene-2-methyl-cyclopropane	22.7	28.9	34.6	39.5	46.7	52.1	60.5							
P14	1,3-butadiene	18.8	23.9	28.4	32.0	36.8	40.4	46.1	18.5±1.9 <sup>c</sup>	24±2.3	28.7±2.2	32.4±1.9	37.6±1.5	41.1±1.3	46.6±1
									17.7 <sup>b</sup>						
P15	Allyl	14.7	18.4	21.7	24.5	28.5	31.6	36.5	14.8 <sup>b</sup>						
									14.9±1.2 <sup>f</sup>	18.7±1.4	22.0±1.5	24.6±1.5	28.7±1.4	31.8±1.3	36.6±1.0
P17	1-ethyl-cyclopropene	22.8	28.5	33.9	38.7	45.8	51.2	59.6							
P18	3-ethyl-cyclopropene	23.0	29.0	34.5	39.2	46.2	51.5	59.8							
P20	1-pentyne	24.3	30.0	35.2	39.7	46.4	51.6	59.7	24.3 <sup>b</sup>						
									24.6 <sup>c</sup>	30.9	36.3	40.8	47.9	53.2	61.3
P21	Acetylene	10.1	11.6	12.7	13.6	14.8	15.9	17.7	10.6 <sup>c</sup>	12.0	13.1	13.9	15.2	16.2	18.2
									10.5 <sup>b</sup>						
	1-propyl	17.2	21.1	24.9	28.2	33.4	37.5	44.0	17.0 <sup>b</sup>						
P22	1,4-pentadiene	23.5	29.1	34.3	38.9	45.9	51.2	59.5	23.6 <sup>c</sup>	30.1	35.8	40.7	48.2	53.6	62.0
P23	Cyclopentene	18.9	25.8	32.4	38.1	46.2	52.2	61.1	18.9 <sup>b</sup>						
									19.6 <sup>c</sup>	26.8	33.2	38.6	46.7	52.6	61.3
									19.4 <sup>d</sup>	26.7	33.1	38.5	46.7	52.6	61.5
P24	3-methylcyclobutene	21.0	27.6	33.7	39.0	46.6	52.2	60.6							
P25	1-methylcyclobutene	21.0	27.2	33.1	38.3	45.9	51.7	60.4							

P26	Isoprene	24.3	31.0	36.7	41.4	47.7	52.6	60.1	22.9 <sup>b</sup>						
									24.7 <sup>c</sup>	31.0	36.4	40.9	47.9	53.2	61.2
P27	Cyclobutene	15.2	20.4	25.3	29.6	35.5	39.9	46.4	15.4 <sup>b</sup>						
									15.5 <sup>c</sup>	21.1	26.0	30.0	36.1	40.4	46.9
									15.5 <sup>d</sup>	21.0	25.9	29.9	35.9	40.2	46.7
P28	Methylidenecyclobutane	20.6	27.3	33.6	39.0	46.8	52.6	61.3	21.0 <sup>c</sup>	28.3	34.7	39.9	47.9	53.6	
P29	Trans-1,3-pentadien-1-yl	24.5	30.1	34.9	38.8	44.6	48.9	55.7							
	Cis-1,3-pentadien-1-yl	24.5	30.1	34.9	38.8	44.4	48.7	55.6							
P30	1,3-pentadien-2-yl	23.7	28.9	33.7	37.8	44.0	48.7	56.1							
P31	1,3-pentadien-3-yl	23.5	28.7	33.5	37.6	43.9	48.6	56.0							
P32	1,3-pentadien-4-yl	23.9	29.4	34.3	38.4	44.3	48.7	55.6							
P33	1,3-pentadien-5-yl	22.4	28.4	33.7	38.2	44.7	49.5	56.9	22.5 <sup>b</sup>						

<sup>b</sup> Third Millennium Ideal Gas and Condensed Phase Thermochemical Database for Combustion (Burcat) [57].

<sup>c</sup> NIST Chemistry Webbook [58].

<sup>d</sup> Calculated values from Sirjean et al. [12] using CBS/QB3 and isodesmic reaction method.

<sup>e</sup> Calculated values from Al Rashidi et al. [27, 28] at CCSD(T)-F12a/cc-pVTZ-F12//M06-2X/6-311++G(d,p) level of theory.

<sup>f</sup> Calculated values from Goldsmith et al. [44] at RQCISD(T)/cc-PV $\infty$ QZ//B3LYP/6-311++G(d,p) level of theory

## 3.2 Reactions of $\dot{\text{H}}$ with 1,3-pentadiene

### 3.2.1 H-atom abstraction reaction from 1,3-pentadiene by hydrogen atoms

H-atom abstraction from the five carbon atoms on 1,3-pentadiene can produce five different  $\dot{\text{C}}_5\text{H}_7$  isomers, with the associated PES shown in Fig. 2.8. The zero-point energy corrected electronic energies on this  $\dot{\text{C}}_5\text{H}_7$  PES are relative to the reactants (1,3-pentadiene +  $\dot{\text{H}}$ ). The relative energy trend for  $\dot{\text{C}}_5\text{H}_7$  isomers is in the order 1,3-pentadien-5-yl < 1,3-pentadien-2-yl < 1,3-pentadien-4-yl < 1,3-pentadien-3-yl < 1,3-pentadien-1-yl. The 1,3-pentadien-5-yl radical has two equivalent structures which are  $\text{C}=\text{CC}=\dot{\text{C}}$  and  $\text{C}=\dot{\text{C}}\text{C}=\text{C}$ , the third carbon atom in the latter structure is a doubly allylic carbon atom which can also be formed via H-atom abstraction from the third carbon atom ( $\text{C}=\text{CCC}=\text{C}$ ) on 1,4-pentadiene. Agapito et al. [67] proposed that the stabilization energy of 1,3-pentadien-5-yl is higher than that of allyl radicals and the spin density in the carbon atom is lower, which indicate a higher electron delocalization. Due to the nature of its structure, 1,3-pentadien-5-yl's energy is over  $26.5 \text{ kcal mol}^{-1}$  lower than the other four  $\dot{\text{C}}_5\text{H}_7$  radicals. For secondary vinylic radicals, the relative energies of 1,3-pentadien-4-yl and 1,3-pentadien-2-yl radicals are approximately  $1.1 \text{ kcal mol}^{-1}$  lower than that of 1,3-pentadien-3-yl. The relative energy of the primary vinylic 1,3-pentadien-1-yl radical is at least  $2.6 \text{ kcal mol}^{-1}$  higher than those for the secondary vinylic radicals.

H-atom abstraction from the terminal carbon atom ( $\text{C}=\text{CC}=\text{CC}$ ) of 1,3-pentadiene is over  $19.4 \text{ kcal mol}^{-1}$  more exothermic than for the other four abstraction channels and has the lowest energy barrier of  $7.7 \text{ kcal mol}^{-1}$ . Hence, 1,3-pentadien-5-yl is expected to be the most important product for H-atom abstraction from 1,3-pentadiene, and is also likely to be the dominant product for H-atom abstraction from 1,4-pentadiene due to its resonantly stabilized structure.

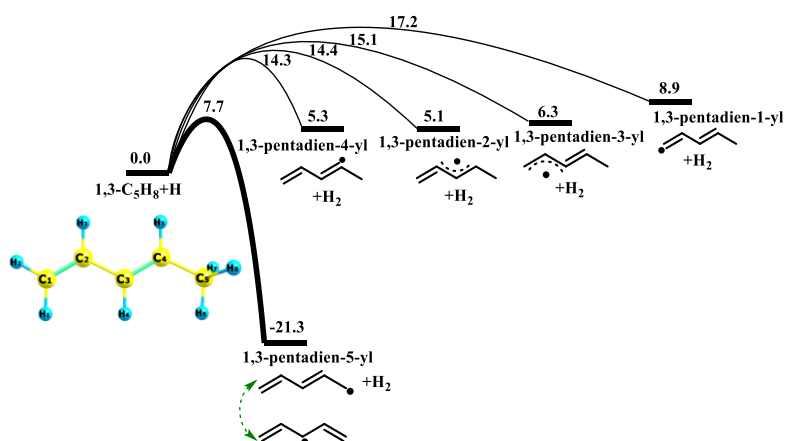


**Fig. 2.8** PES for H-atom abstraction from 1,3-pentadiene by  $\dot{\text{H}}$  atoms ( $\text{kcal mol}^{-1}$ ).

### 3.2.1.1 Rate constant comparison for H-atom abstraction reaction of 1,3-pentadiene

Rate constants for H-atom abstraction reactions from 1,3-pentadiene are shown in Fig. 2.9(a).  $\dot{\text{H}}$  atoms that abstract hydrogen atoms attached to the fifth carbon atom forming 1,3-pentadien-5-yl and a hydrogen molecule have a much higher rate constant than those for the other four channels. It is over four orders of magnitude higher at low temperature (300 K) and is approximately a factor of four higher at high temperature (2000 K). In addition, the  $k_{\infty}$  for formation of 1,3-pentadien-2-yl, 1,3-pentadien-3-yl, and 1,3-pentadien-4-yl radicals are similar over the entire temperature range, which are over an order of magnitude larger than the formation of 1,3-pentadien-1-yl at low temperature and the difference decreases to it being within 40% faster at 2000 K.

The energy barriers and  $k_{\infty}$  for H-atom abstraction reactions of 1,3-pentadiene are compared with those for propene [68]. Miller and Klippenstein [68] calculated the rate constants for H-atom abstraction reactions from propene by  $\dot{\text{H}}$  atoms at the rQCISD(T)/CBS//MP2/6-311++G(d,p) level of theory. Table 2.5 shows that the barrier heights for abstraction by  $\dot{\text{H}}$  atoms from the primary (C=CC) and secondary (C=CC) vinylic sites on propene are similar to those for 1,3-pentadiene with the differences being within 0.2  $\text{kcal mol}^{-1}$  of one another. However, the barrier height for H-atom abstraction from the allylic site on propene (C=CC) in Miller's work is 1.2  $\text{kcal mol}^{-1}$  higher than that on 1,3-pentadiene (C=CC=CC). In order to validate the reliability of our energy barriers, we have calculated rate constants for H-atom abstraction reactions from propene forming allylic radicals at the same level of theory as used in this study. The calculated energy barrier is 7.7  $\text{kcal mol}^{-1}$  which is 1.2  $\text{kcal mol}^{-1}$  lower than Miller's result and similar to that for the formation of 1,3-pentadien-5-yl radicals. Thus, the results of this work imply that the energy barriers for

H-atom abstraction reactions from propene and 1,3-pentadiene by  $\dot{\text{H}}$  atoms are similar.

Fig. 2.9(b) shows the  $k_{\infty}$  for the formation of 1-, 2-propenyl are similar to those for the corresponding reaction of 1,3-pentadiene at low temperatures, which is consistent with the energy barrier comparison results. However, the  $k_{\infty}(1,3\text{-C}_5\text{H}_8 + \dot{\text{H}} \rightleftharpoons 1,3\text{-pentadien-5-yl} + \text{H}_2)$  is four times slower than  $k_{\infty}(\text{C}_3\text{H}_6 + \dot{\text{H}} \rightleftharpoons \text{allyl} + \text{H}_2)$  from Miller's work at 300 K, becoming 20% faster than  $k_{\infty}(\text{C}_3\text{H}_6 + \dot{\text{H}} \rightleftharpoons \text{allyl} + \text{H}_2)$  at 2000 K. It is worth noting that the fitting temperature range of their rate constants was not provided in the paper, hence the rate constant comparison at low temperatures may be meaningless. The  $k_{\infty}(\text{C}_3\text{H}_6 + \dot{\text{H}} \rightleftharpoons \text{allyl} + \text{H}_2)$  calculated in this study are compared with  $k_{\infty}(1,3\text{-C}_5\text{H}_8 + \dot{\text{H}} \rightleftharpoons 1,3\text{-pentadien-5-yl} + \text{H}_2)$  and the latter are 50 – 80% faster than the former in the temperature range 300 – 2000 K. This is consistent with the conclusion of Agapito et al. [67] that 1,3-pentadien-5-yl radical has a higher electron delocalization than allyl radical and its formation is more exothermic, resulting in the formation of 1,3-pentadien-5-yl radicals being more thermodynamically preferred compared to allyl radicals. With the rate constants calculated at the same level of theory in this study, the  $k_{\infty}(\text{C}_3\text{H}_6 + \dot{\text{H}} \rightleftharpoons \text{allyl} + \text{H}_2)$  are found to be within a factor of two of those for the corresponding abstraction reactions from the same sites on 1,3-pentadiene.

The  $k_{\infty}$  for the H-atom abstraction reaction from 1,3-pentadiene is also compared with that for 1,3-butadiene [8], which is shown in Fig. 2.9(c). Li and co-workers calculated the energy barriers and rate constants for H-atom abstraction reactions of 1,3-butadiene by  $\dot{\text{H}}$  atoms at the CCSD(T)/CBS//M06-2X/6-311++G(d,p) level of theory with vibrational frequencies scaled by 0.983. The barrier heights for H-atom abstraction reactions of 1,3-butadiene are similar to those from the primary (C=CC=CC) and secondary (C=CC=CC) vinylic sites of 1,3-pentadiene with differences being within 0.3 kcal mol<sup>-1</sup>. The  $k_{\infty}$  for H-atom abstraction from the primary vinylic sites of 1,3-pentadiene are two to five times slower than those for the corresponding reaction channels from 1,3-butadiene over the temperature range 300 – 2000 K, while the difference of rate constants for H-atom abstraction from the secondary vinylic sites varies within 2 – 3 times over the same temperature range. The external symmetry number for 1,3-butadiene is two compared with one for 1,3-pentadiene, so the symmetry of their structures contributes twice as much to the rate constant deviation. If the influence of symmetry factor is considered, the rate constants for H-atom abstraction from the primary and secondary vinylic sites of 1,3-pentadiene are similar to those from 1,3-butadiene. Since the  $k_{\infty}$  for H-atom abstraction reactions of 1,3-butadiene and 1,3-pentadiene have a clear trend, the calculated results can also be used to predict and

validate the rate constants for H-atom abstraction reactions from larger 1,3-dienes.

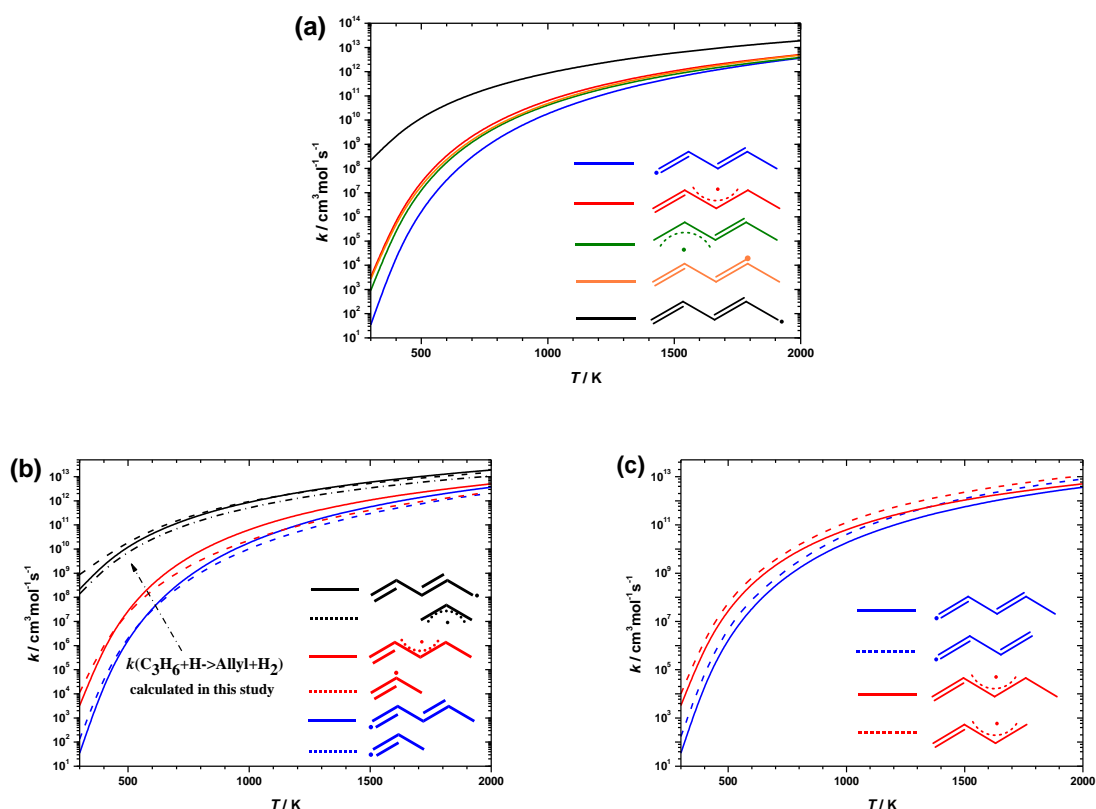


**Fig. 2.9** (a) Rate constants for H-atom abstraction from 1,3-pentadiene, (b) rate constant comparisons between H-atom abstraction from 1,3-pentadiene and propene, (c) rate constant comparisons between H-atom abstraction from 1,3-pentadiene and 1,3-butadiene.

**Table 2.5** The barrier heights for H-atom abstraction reaction of propene, 1,3-butadiene and 1,3-pentadiene by  $\dot{\text{H}}$  atoms to generate different products. ( $\text{kcal mol}^{-1}$ )

Label	Reactant	Product	Barrier height
1	1,3-C <sub>5</sub> H <sub>8</sub>	1,3-pentadien-1-yl	17.2
2	1,3-C <sub>5</sub> H <sub>8</sub>	1,3-pentadien-2-yl	14.4
3	1,3-C <sub>5</sub> H <sub>8</sub>	1,3-pentadien-3-yl	15.1
4	1,3-C <sub>5</sub> H <sub>8</sub>	1,3-pentadien-4-yl	14.3
5	1,3-C <sub>5</sub> H <sub>8</sub>	1,3-pentadien-5-yl	7.7
6	C <sub>3</sub> H <sub>6</sub>	1-propenyl	17.0 <sup>a</sup>
7	C <sub>3</sub> H <sub>6</sub>	2-propenyl	14.2 <sup>a</sup>
8	C <sub>3</sub> H <sub>6</sub>	Allyl	8.9 <sup>a</sup> , 7.7
9	1,3-C <sub>4</sub> H <sub>6</sub>	1,3-butadien-1-yl	16.9 <sup>b</sup>
10	1,3-C <sub>4</sub> H <sub>6</sub>	1,3-butadien-2-yl	14.6 <sup>b</sup>

<sup>a</sup> Calculated values from Miller and Klippenstein [68] at the rQCISD(T)/CBS//MP2/6-311++G(d,p) level of theory.

<sup>b</sup> Calculated values from Li et al. [8] at the CCSD(T)/CBS//M06-2X/6-311++G(d,p) level of theory.

### 3.2.2 $\dot{\text{H}}$ atom addition reactions to 1,3-pentadiene

There are four entrance channels for  $\dot{\text{H}}$  atom addition to 1,3-pentadiene forming four different  $\dot{\text{C}}_5\text{H}_9$  radicals (W1–W4), Fig. 2.10(a). The relative energies for the four  $\dot{\text{C}}_5\text{H}_9$  radicals are  $-44.5$  ( $2,4\text{-}\dot{\text{C}}_5\text{H}_9$ ),  $-28.4$  ( $2,5\text{-}\dot{\text{C}}_5\text{H}_9$ ),  $-28.7$  ( $1,4\text{-}\dot{\text{C}}_5\text{H}_9$ ) and  $-41.8$  ( $1,3\text{-}\dot{\text{C}}_5\text{H}_9$ ) kcal mol $^{-1}$  formed by addition at C<sub>1</sub>, C<sub>2</sub>, C<sub>3</sub> and C<sub>4</sub> respectively, with the addition reactions forming resonantly stabilized radicals being more dominant than those forming primary (1°) and secondary (2°) alkenyl radicals. In line with the reaction enthalpies, the barriers leading to the formation of resonantly stabilized radicals (W1, W4) are 2 – 3 kcal mol $^{-1}$  lower than those for the formation of the 1° and 2° alkenyl radicals ( $2,5\text{-}\dot{\text{C}}_5\text{H}_9$ ,  $1,4\text{-}\dot{\text{C}}_5\text{H}_9$ ). In turn, the high-pressure limiting rate constants of the four entrance channels follow clear trends depending on the reaction enthalpy, and reaction barrier, with high-pressure limiting product branching ratios shown in Fig. 2.10(b). The formation of the resonantly stabilized radicals account for approximately 90% of the branching ratio up to 2000 K, with the pathways forming 1° and 2° alkenyl radicals accounting for < 10% over the same temperature range.

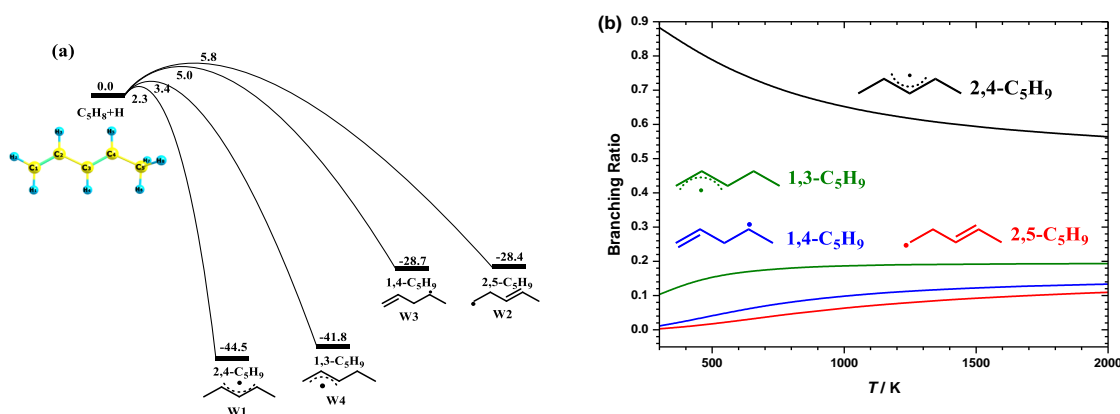


**Fig. 2.10** (a) Potential energy surface for the entrance channels (kcal mol $^{-1}$ ), (b) High-pressure limiting rate constants of the entrance channels for  $\dot{\text{H}}$  atom addition to 1,3-pentadiene.

### 3.2.3 High-pressure limiting rate constant comparison between H-atom abstraction and $\dot{\text{H}}$ atom addition reactions from/to 1,3-pentadiene

The high-pressure limiting rate constants for  $\dot{\text{H}}$  atom addition to 1,3-pentadiene are compared with the dominant channel for H-atom abstraction reactions from 1,3-pentadiene, with the result shown in Fig. 2.11. At low temperatures,  $\dot{\text{H}}$  atom addition reactions are over two orders of magnitude faster than abstraction reactions. However, the difference decreases as the temperature increases with the smallest difference being 60% faster at 2000 K. Hence,

H-atom abstraction from the allylic hydrogen atom in 1,3-pentadiene needs to be considered at high temperatures and can be competitive with  $\dot{\text{H}}$  atom addition reactions.

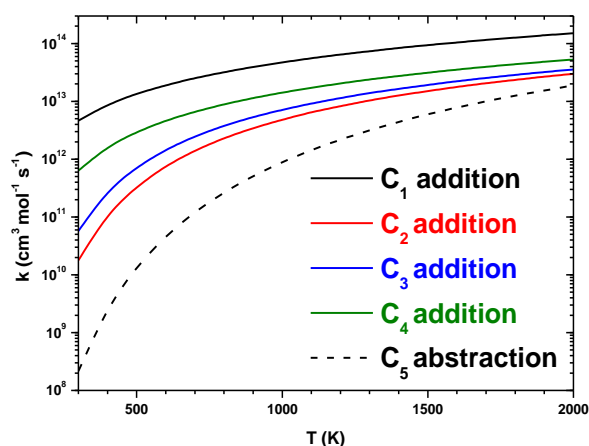


**Fig. 2.11** High-pressure limiting rate constant comparison between H-atom abstraction and  $\dot{\text{H}}$  atom addition reactions from/to 1,3-pentadiene.

### 3.2.4 $\dot{\text{H}}$ atom addition rate constant comparisons with 1-alkenes and 1,3-dienes

There have been a number of experimental investigations of the kinetics of  $\text{C}_3\text{H}_6 + \dot{\text{H}}$  [69-72],  $1\text{-C}_4\text{H}_8 + \dot{\text{H}}$  [70, 73-75], and  $1,3\text{-C}_4\text{H}_6 + \dot{\text{H}}$  [73, 76-78]. 1,3-butadiene is the simplest conjugated 1,3-diene and has two entrance channels for the  $\dot{\text{H}}$  atom addition reaction. Li et al. [8] studied  $\dot{\text{H}}$  atom addition to 1,3-butadiene at the ROCCSD(T)/CBS//M06-2X/6-311++G(d,p) level of theory. The  $k(1,3\text{-C}_3\text{H}_8 + \dot{\text{H}})$  calculated in this work is compared with the calculated and the experimental rate constants for  $\dot{\text{H}}$  atom addition to  $\text{C}_3\text{-C}_4$  1-alkenes [69-75] and 1,3-butadiene [73, 76-78] in the literature, Fig. 2.12. These experimental data are limited to room temperature and low pressures, except for Nametkin's experiments [77] at 1070–1120 K for  $1,3\text{-C}_4\text{H}_6 + \dot{\text{H}}$  and Manion's experiments [75] at 880–1120 K. Manion et al. [75] carried out the single-pulse shock tube experiments for  $1\text{-C}_4\text{H}_8 + \dot{\text{H}}$  at 880–1120 K and 145–245 kPa and derived the high-pressure limiting rate constants for  $1\text{-C}_4\text{H}_8 + \dot{\text{H}}$  considering both their experimental results and the then available literature data. Since most of the experimental data are not product specific, and the terminal addition reactions are dominant at low temperatures, the experimental results are compared with the calculated high-pressure limiting rate constants for the terminal addition of  $\dot{\text{H}}$  atoms to different 1-alkenes and 1,3-dienes. For pressure-dependent rate constants, the rate constants for terminal addition show significant fall-off at high temperatures and the chemically activated reactions start to play an important role. Hence, the pressure-dependent

$k_{\infty}(\text{C}_4\text{H}_6 + \dot{\text{H}} \rightarrow \text{all products})$  and  $k_{\infty}(\text{C}_3\text{H}_6 + \dot{\text{H}} \rightarrow \text{all products})$  are plotted and compared with the experimental data, Fig. 2.12.

The rate constants for  $\dot{\text{H}}$  atoms addition to 1,3-pentadiene and the other important channels on  $\dot{\text{C}}_5\text{H}_9$  PES are calculated with both unrestricted SPE and restricted SPE energies which will be discussed in more detail in Chapter 3 of this study. Considering the complexity of the  $\dot{\text{C}}_5\text{H}_9$  PES and the expensive computational cost of restricted SPE calculations, the unrestricted SPE calculation is used for the full PES and the restricted SPE calculation is only used for important reactions. Through the application of the restricted SPE calculation to the terminal addition TS, the  $T_1$  diagnostic value is reduced from 0.038 to 0.015 as shown in Table A.2. The energy barrier calculated from the restricted SPE is 1.2 kcal mol<sup>-1</sup> lower than that calculated from the unrestricted SPE, resulting in a 7.3 times difference at 300 K and a 1.4 times difference at 2000 K. Fig. 2.12 shows that  $k_{\infty}(1,3\text{-C}_5\text{H}_8 + \dot{\text{H}})$  is similar to  $k_{\infty}(1,3\text{-C}_4\text{H}_6 + \dot{\text{H}})$  at low temperatures (< 500 K) where the high-pressure limiting and the pressure-dependent rate constants for 1,3-C<sub>4</sub>H<sub>6</sub> +  $\dot{\text{H}}$  show good agreement with the experimental data. The same trend is also found for  $\dot{\text{H}}$  atom additions to 1-alkenes, in that the rate constants are similar for terminal addition at low temperatures. Through the trend comparison with terminal addition of  $\dot{\text{H}}$  atoms to 1-alkenes, the  $k_{\infty}(1,3\text{-C}_5\text{H}_8 + \dot{\text{H}})$  generated using restricted SPE calculations proves to be in good agreement with both the experimental and theoretical calculation results for 1,3-C<sub>4</sub>H<sub>6</sub> +  $\dot{\text{H}}$ . In addition, the  $k_{\infty}(1,3\text{-C}_5\text{H}_8 + \dot{\text{H}})$  produced using unrestricted SPE calculations is within a factor of two of the  $k_{\infty}(1,3\text{-C}_5\text{H}_8 + \dot{\text{H}})$  generated using restricted SPE calculations at temperatures above 800 K, which suggests the reasonable reliability of the unrestricted energy calculation at intermediate and high temperatures used in this work.

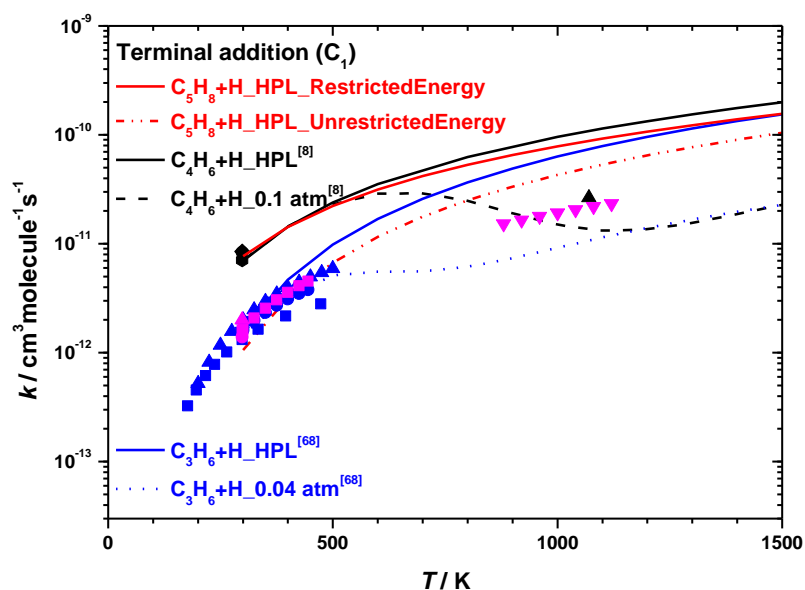


**Fig. 2.12** High-pressure limiting and pressure-dependent rate constant comparisons for  $\dot{\text{H}}$  atoms addition to 1,3-pentadiene, 1,3-butadiene, propene and 1-butene. The theoretical calculation results for 1,3- $\text{C}_4\text{H}_6 + \dot{\text{H}}$  and  $\text{C}_3\text{H}_6 + \dot{\text{H}}$  are from Li et al. [8] and Miller et al. [68], respectively. Different symbols represent experimental data in the literature.  $\text{C}_3\text{H}_6 + \dot{\text{H}}$  experiments: ■ Kurylo et al. at 0.07 atm [69]; ● Harris et al. at 0.07 atm [70]; ▲ Watanabe et al. at 0.66 atm [71]; ▼ Clarke et al. at 33.7–65.0 atm [72]. 1- $\text{C}_4\text{H}_8 + \dot{\text{H}}$  experiments: ■ Harris et al. at 0.07 atm [70]; ● Oka et al. at 0.07 atm [73]; ▲ Ishikawa et al. at 0.3–1.6 atm [74]; ▼ Experimentally derived high-pressure limiting rate constants from Manion et al. [75]. 1,3- $\text{C}_4\text{H}_6 + \dot{\text{H}}$  experiments: ● Daby et al. at 0.0016 atm [76]; ▲ Nametkin et al. at 0.13 atm [77]; ◆ Ishikawa et al. at 0.66 atm [78]; ◆ Oka et al. at 0.13 atm [73].

### 3.2.5 Evans-Polanyi correlation for H atom addition to $\text{C}_3$ – $\text{C}_5$ dienes and $\text{C}_2$ – $\text{C}_5$ alkynes

The reactions of 1,3-pentadiene with  $\dot{\text{H}}$  atoms are generally consistent with our understanding of the addition reactions of hydrogen atoms with lower molecular weight alkyne and diene species which can undergo both internal and external addition reactions, forming primary, secondary, allylic and/or vinylic alkenyl radicals. Fig. 2.13 compares the barrier heights versus reaction enthalpies at 0 K for the reactions of hydrogen atoms with acetylene [79], allene [80], propyne [68, 80, 81], butyne and butadiene isomers, pentyne and pentadiene isomers from this study. On the  $\dot{\text{C}}_5\text{H}_9$  PES, there are 5 linear  $\text{C}_5\text{H}_8$  isomers (1,2-, 1,4-, and 2,3-pentadiene, 1-, 2-pentyne) excluding 1,3-pentadiene. The barrier heights and reaction enthalpies for these  $\dot{\text{H}}$  atom addition reactions are listed in Table 2.6.

For C<sub>2</sub> – C<sub>5</sub> alkynes and C<sub>3</sub> – C<sub>5</sub> dienes, the barrier height for external addition is consistently lower than internal addition to the same species. The C<sub>3</sub>–C<sub>5</sub> dienes are observed to have different correlations of barrier heights and reaction enthalpies and can be divided into three groups. (1) The first group includes 1,3-dienes and the following trends emerge: external and internal hydrogen atom addition to 1,3-butadiene has slightly higher barrier heights (< 0.3 kcal mol<sup>-1</sup>) compared to the corresponding additions to 1,3-pentadiene. The Evans-Polanyi correlation for  $\dot{H}$  atom addition to linear 1,3-dienes is fitted to:  $E_{0K} = 0.18(\pm 0.02) \times \Delta_r H_{0K} + 10.84 (\pm 0.76 \text{ kcal mol}^{-1})$ , with an  $R^2$  of 0.94. (2) The correlation for 1,2- and 2,3-dienes are more complicated and the product types formed through  $\dot{H}$  atom addition reactions need to be considered. Hydrogen atom addition to the internal carbon atom (e.g. C=C=C, connected to two carbon atoms by double bonds) of 1,2- and 2,3-dienes forming allylic alkenyl radical appears to follow a different trend compared to the formation of vinylic alkenyl radicals. The Evans-Polanyi correlation for  $\dot{H}$  atom addition to linear 1,2- and 2,3-dienes forming allylic alkenyl radical is fitted as:  $E_{0K} = 0.24 (\pm 0.06) \times \Delta_r H_{0K} + 18.07 (\pm 3.41 \text{ kcal mol}^{-1})$ , with an  $R^2$  of 0.84. (3) Hydrogen atoms can also add to the internal and/or external carbon atoms of 1,2- and 2,3-dienes to form 1° and/or 2° vinylic alkenyl radicals. It is worth noting that  $\dot{H}$  atom addition reactions to alkynes and 1,4-dienes tend to have similar rate constants. Thus  $\dot{H}$  atoms addition to 1,2- and 2,3-dienes forming vinylic alkenyl radicals, 1,4-dienes and alkynes are put together as a third group. The Evans-Polanyi correlation for the third group is weaker than 1,3-dienes, with  $E_{0K} = 0.40 (\pm 0.07) \times \Delta_r H_{0K} + 17.55 (\pm 2.35 \text{ kcal mol}^{-1})$  and  $R^2 = 0.66$ . The Evans-Polanyi correlations between  $E_{0K}$  and  $\Delta_r H_{298K}$  for these three groups are also fitted and are listed as Table A.3, which might be useful when only  $\Delta_r H_{298K}$  values are available for reactions of interest in the literature.

It is clear from this analysis that: (1) the correlation between barrier heights and reaction enthalpies for 1,3-dienes are stronger than the other two group species; (2) The internal addition of hydrogen atoms to 1,2- and 2,3-dienes forming allylic alkenyl radicals are more exothermic and have higher barrier heights than the corresponding external addition forming vinylic alkenyl radicals; (3) 1,2-/1,3-dienes +  $\dot{H} \rightleftharpoons$  vinylic alkenyl radicals, 1,4-dienes +  $\dot{H} \rightleftharpoons$  alkenyl radicals and alkynes +  $\dot{H} \rightleftharpoons$  vinylic alkenyl radicals have similar correlated barrier heights and reaction enthalpies, the correlation ( $R^2 = 0.66$ ) is smaller in comparison with 1,3-dienes but is still acceptable when considering the number of reaction types included in the third group.

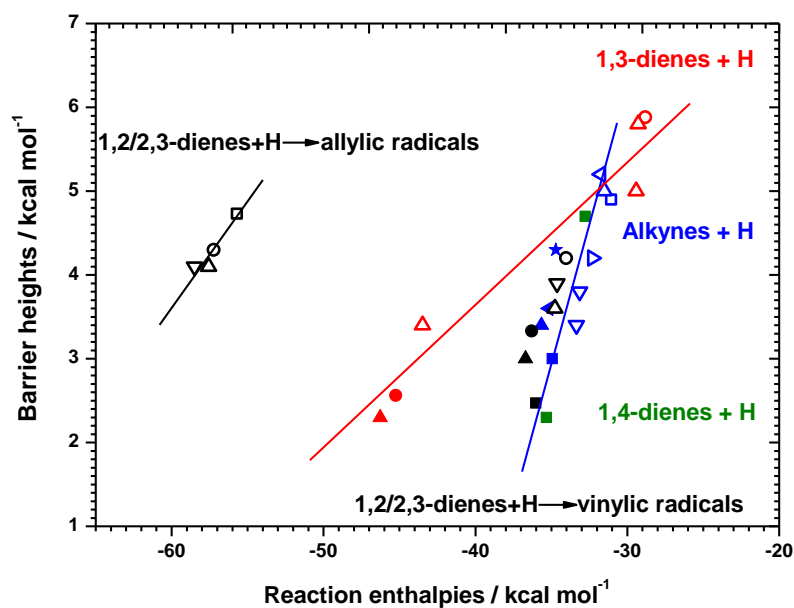


**Fig. 2.13** Evans-Polanyi correlation for  $\dot{\text{H}}$  atom addition to linear dienes and alkynes. Solid symbols represent external addition reactions of  $\dot{\text{H}}$  atom and open symbols represent internal addition. Different colours stand for different reaction types that are further divided into various symbols to represent different reactants. (1) 1,3-dienes, ● 1,3-butadiene [8]; ▲ 1,3-pentadiene. (2) 1,2- and 2,3-dienes, ■ allene (1,2-C<sub>3</sub>H<sub>4</sub>) [80]; ● 1,2-butadiene [8]; ▲ 1,2-pentadiene; ▼ 2,3-pentadiene. (3) 1,4-dienes, ▲ 1,4-pentadiene. (4) Alkynes, ★ C<sub>2</sub>H<sub>2</sub> [79], ◆ propyne (1-C<sub>3</sub>H<sub>4</sub>) [80], ◀ 1-butyne [8], ▶ 2-butyne [8], ▲ 1-pentyne, ▼ 2-pentyne.

**Table 2.6** The reaction enthalpies and barrier heights at 0 K for  $\dot{\text{H}}$  atom addition to different alkynes and dienes.

Label	Reactant	Addition position	Product	Product type	$\Delta_r H_{0\text{K}}$	$E_{0\text{K}}$
<b>1,2-dienes</b>						
1	1,2-C <sub>3</sub> H <sub>4</sub>	External	1,2- $\dot{\text{C}}_3\text{H}_5$	2°v	-36.0	2.5[80]
2	1,2-C <sub>3</sub> H <sub>4</sub>	Internal	1,3- $\dot{\text{C}}_3\text{H}_5$	1°a	-55.7	4.7[80]
3	1,2-C <sub>4</sub> H <sub>6</sub>	External	2,2- $\dot{\text{C}}_4\text{H}_7$	2°v	-36.3	3.3[8]
4	1,2-C <sub>4</sub> H <sub>6</sub>	Internal	1,2- $\dot{\text{C}}_4\text{H}_7$	2°v	-34.0	4.2[8]
5	1,2-C <sub>4</sub> H <sub>6</sub>	Internal	1,3- $\dot{\text{C}}_4\text{H}_7$	1°a	-57.2	4.3[8]
6	1,2-C <sub>5</sub> H <sub>8</sub>	External	2,2- $\dot{\text{C}}_5\text{H}_9$	2°v	-36.7	3.0
7	1,2-C <sub>5</sub> H <sub>8</sub>	Internal	1,2- $\dot{\text{C}}_5\text{H}_9$	2°v	-34.8	3.6
8	1,2-C <sub>5</sub> H <sub>8</sub>	Internal	1,3- $\dot{\text{C}}_5\text{H}_9$	1°a	-57.6	4.1
<b>2,3-dienes</b>						
9	2,3-C <sub>5</sub> H <sub>8</sub>	Internal	2,3- $\dot{\text{C}}_5\text{H}_9$	2°v	-34.6	3.9
10	2,3-C <sub>5</sub> H <sub>8</sub>	Internal	2,4- $\dot{\text{C}}_5\text{H}_9$	2°a	-58.5	4.1
<b>1,3-dienes</b>						
11	1,3-C <sub>4</sub> H <sub>6</sub>	External	1,3- $\dot{\text{C}}_4\text{H}_7$	1°a	-45.2	2.6[8]
12	1,3-C <sub>4</sub> H <sub>6</sub>	Internal	1,4- $\dot{\text{C}}_4\text{H}_7$	1°	-28.8	5.9[8]
13	1,3-C <sub>5</sub> H <sub>8</sub>	External	2,4- $\dot{\text{C}}_5\text{H}_9$	2°a	-46.3	2.3
14	1,3-C <sub>5</sub> H <sub>8</sub>	Internal	1,3- $\dot{\text{C}}_5\text{H}_9$	1°a	-43.5	3.4
15	1,3-C <sub>5</sub> H <sub>8</sub>	Internal	1,4- $\dot{\text{C}}_5\text{H}_9$	2°	-29.4	5.0
16	1,3-C <sub>5</sub> H <sub>8</sub>	Internal	2,5- $\dot{\text{C}}_5\text{H}_9$	1°	-29.3	5.8
<b>1,4-dienes</b>						
17	1,4-C <sub>5</sub> H <sub>8</sub>	External	1,4- $\dot{\text{C}}_5\text{H}_9$	2°	-35.3	2.3
18	1,4-C <sub>5</sub> H <sub>8</sub>	Internal	1,5- $\dot{\text{C}}_5\text{H}_9$	1°	-32.8	4.7
<b>Alkynes</b>						
19	C <sub>2</sub> H <sub>2</sub>	External	$\dot{\text{C}}_2\text{H}_3$	1°v	-34.7	4.3[79]
20	1-C <sub>3</sub> H <sub>4</sub>	External	$\dot{\text{C}}_3\text{H}_5\text{-s}$	2°v	-34.9	3.0[80]
21	1-C <sub>3</sub> H <sub>4</sub>	Internal	$\dot{\text{C}}_3\text{H}_5\text{-p}$	1°v	-31.1	4.9[80]
22	1-C <sub>4</sub> H <sub>6</sub>	External	1,2- $\dot{\text{C}}_4\text{H}_7$	2°v	-35.2	3.6[8]
23	1-C <sub>4</sub> H <sub>6</sub>	Internal	1,1- $\dot{\text{C}}_4\text{H}_7$	1°v	-31.7	5.2[8]
24	2-C <sub>4</sub> H <sub>6</sub>	Internal	2,2- $\dot{\text{C}}_4\text{H}_7$	2°v	-32.3	4.2[8]
25	1-C <sub>5</sub> H <sub>8</sub>	External	1,2- $\dot{\text{C}}_5\text{H}_9$	2°v	-35.7	3.4
26	1-C <sub>5</sub> H <sub>8</sub>	Internal	1,1- $\dot{\text{C}}_5\text{H}_9$	1°v	-31.5	5.0
27	2-C <sub>5</sub> H <sub>8</sub>	Internal	2,3- $\dot{\text{C}}_5\text{H}_9$	2°v	-33.1	3.8
28	2-C <sub>5</sub> H <sub>8</sub>	Internal	2,2- $\dot{\text{C}}_5\text{H}_9$	2°v	-33.4	3.4

### 3.3 Potential energy surface for $\dot{\text{H}}$ atom addition reactions to 1,3-pentadiene

The  $\dot{\text{C}}_5\text{H}_9$  PES consists of 63 species and 88 transition states that can be divided into isomerization,  $\beta$ -scission, ring-opening and ring-closing reaction types. The structures and zero-point energy corrected energies at 0 K for all minima are shown in Table 2.7, and the corresponding transition states (TS) energies relative to the reactants are shown in Table 2.8, together with literature values where they exist. Due to the complexity of the  $\dot{\text{C}}_5\text{H}_9$  PES, the complete  $\dot{\text{C}}_5\text{H}_9$  PES is illustrated in two parts (a) the formation of 2,4- $\dot{\text{C}}_5\text{H}_9$  radical (W1), 2,5- $\dot{\text{C}}_5\text{H}_9$  radical (W2) and their subsequent reactions. (b) the formation of 1,4- $\dot{\text{C}}_5\text{H}_9$  radical (W3), 1,3- $\dot{\text{C}}_5\text{H}_9$  radical (W4) and their subsequent reactions. In Fig. 2.14, the  $\dot{\text{H}}$  atom addition reactions to 1,3-pentadiene are shown as black lines, and the isomerization, ring-opening/closing and  $\beta$ -scission reactions are shown as blue, green and red lines,



**Table 2.7** Structures and relative energies (0 K, ZPE corrected, kcal mol<sup>-1</sup>) for all the species on the  $\dot{\text{C}}_5\text{H}_9$  PES.

Label	Species	Structure	This study	Literature
R	1,3-pentadiene+ $\dot{\text{H}}$		0.0	
W1	2,4- $\dot{\text{C}}_5\text{H}_9$		-44.5	-46.6 <sup>b</sup>
W2	2,5- $\dot{\text{C}}_5\text{H}_9$		-28.4	-28.4 <sup>b</sup>
W3	1,4- $\dot{\text{C}}_5\text{H}_9$		-28.7	-27.5 <sup>a</sup> , -29.0 <sup>b</sup>
W4	1,3- $\dot{\text{C}}_5\text{H}_9$		-41.8	-42.3 <sup>a</sup> , -43.7 <sup>b</sup>
W5	1,2-dimethyl-3-cyclopropyl		-13.6	-12.8 <sup>a</sup>
W6	Sec-ethyl-cyclopropanyl		-24.5	-25.7 <sup>b</sup>
W7	2,2- $\dot{\text{C}}_5\text{H}_9$		-21.3	-22.4 <sup>b</sup>
W8	2,3- $\dot{\text{C}}_5\text{H}_9$		-21.1	
W9	Ethyl-2-cyclopropyl		-12.5	
W10	1,5- $\dot{\text{C}}_5\text{H}_9$		-26.0	-25.5 <sup>a</sup> , -26.3 <sup>b</sup>
W11	1,2- $\dot{\text{C}}_5\text{H}_9$		-19.5	-19.0 <sup>a</sup> , -20.6 <sup>b</sup>
W12	1,1- $\dot{\text{C}}_5\text{H}_9$		-15.3	-15.9 <sup>a</sup> , -16.9 <sup>b</sup>
W13	1-methylidene-cyclopropylmethyl		-24.5	-24.1 <sup>a</sup> , -25.9 <sup>b</sup>
W14	3-methyl-1-buten-4-yl		-27.7	-25.6 <sup>a</sup>
W15	Cyclopentyl		-43.6	-44.9 <sup>b</sup>
W16	Methyl-2-cyclobutyl		-23.0	
W17	Methyl-3-cyclobutyl		-23.3	
W18	Methyl-1-cyclobutyl		-25.3	
W19	Methylidene-cyclobutyl		-23.0	
W20	1,2-dimethyl-1-cyclopropyl		-16.8	
W21	Ethyl-1-cyclopropyl		-15.1	
P1	Ethylene + 1-propenyl		6.3	
P2	3-methyl-cyclopropene methyl	$\text{CH}_3 +$	23.8	
P3	1,3-dimethyl-cyclopropene + $\dot{\text{H}}$	$\dot{\text{H}} +$	31.2	
P4	2,3-pentadiene + $\dot{\text{H}}$	$\dot{\text{H}} +$	13.1	
P5	2-pentyne + $\dot{\text{H}}$	$\dot{\text{H}} +$	11.5	
P6	Propyne + ethyl		1.9	2.5 <sup>b</sup>

P7	Butyne + methyl	$\text{CH}_3 + \text{C}\equiv\text{C}-\text{CH}_2\text{CH}_3$	3.1	
P8	Ethenyl-cyclopropane + $\dot{\text{H}}$	$\dot{\text{H}} + \text{Cyclopropane}-\text{CH}=\text{CH}_2$	11.3	
P9	Ethylidene-cyclopropane + $\dot{\text{H}}$	$\dot{\text{H}} + \text{Cyclopropane}-\text{C}(\text{CH}_3)=\text{CH}_2$	19.9	
P10	Methyl + 1,2-butadiene	$\text{CH}_3 + \text{C}=\text{C}=\text{CH}-\text{CH}_3$	2.1	
P11	1,2-pentadiene + $\dot{\text{H}}$	$\dot{\text{H}} + \text{C}=\text{C}=\text{CH}-\text{CH}_2-\text{CH}_3$	14.9	14.9 <sup>a</sup>
P12	Vinyl + propene	$\text{CH}_2=\text{CH} + \text{CH}_2=\text{CH}-\text{CH}_3$	5.1	4.8 <sup>a</sup> , 4.7 <sup>b</sup>
P13	1-methylidene-2-methyl-cyclopropane + $\dot{\text{H}}$	$\dot{\text{H}} + \text{Cyclopropane}-\text{C}(\text{CH}_3)=\text{CH}_2$	20.5	20.9 <sup>a</sup>
P14	1,3-butadiene + methyl	$\text{CH}_3 + \text{CH}_2=\text{CH}-\text{CH}=\text{CH}_2$	-9.8	-10.3 <sup>a</sup> , -9.1 <sup>b</sup>
P15	Ethylene + allyl	$\text{CH}_2=\text{CH}_2 + \text{CH}_2=\text{CH}-\dot{\text{C}}\text{H}_2$	-17.5	-18.4 <sup>a</sup> , -18.7 <sup>b</sup>
P16	Allene + ethyl	$\text{C}=\text{C}=\text{C} + \text{CH}_2-\text{CH}_3$	2.8	2.9 <sup>a</sup> , 3.2 <sup>b</sup>
P17	1-ethyl-cyclopropene + $\dot{\text{H}}$	$\dot{\text{H}} + \text{Cyclopropene}-\text{CH}_2\text{CH}_3$	33.4	
P18	3-ethyl-cyclopropene + $\dot{\text{H}}$	$\dot{\text{H}} + \text{Cyclopropene}-\text{CH}_2\text{CH}_2\text{CH}_3$	36.4	
P19	Cyclopropene + ethyl	$\text{Cyclopropene} + \text{CH}_2-\text{CH}_3$	25.4	
P20	1-pentyne + $\dot{\text{H}}$	$\dot{\text{H}} + \text{C}\equiv\text{C}-\text{CH}_2-\text{CH}_2-\text{CH}_3$	15.5	16.0 <sup>a</sup>
P21	Acetylene + 1-propyl	$\text{C}\equiv\text{C} + \text{CH}_2-\text{CH}_2-\text{CH}_3$	8.1	8.2 <sup>a</sup> , 9.2 <sup>b</sup>
P22	1,4-pentadiene + $\dot{\text{H}}$	$\dot{\text{H}} + \text{CH}_2=\text{CH}-\text{CH}_2-\text{CH}=\text{CH}_2$	6.5	6.8 <sup>a</sup> , 7.1 <sup>b</sup>
P23	Cyclopentene + $\dot{\text{H}}$	$\dot{\text{H}} + \text{Cyclopentene}$	-9.8	-10.4 <sup>b</sup>
P24	3-methylcyclobutene + $\dot{\text{H}}$	$\dot{\text{H}} + \text{Cyclobutene}-\text{CH}_2\text{CH}_3$	12.8	
P25	1-methylcyclobutene + $\dot{\text{H}}$	$\dot{\text{H}} + \text{Cyclobutene}-\text{CH}_2\text{CH}_3$	9.9	
P26	Isoprene + $\dot{\text{H}}$	$\dot{\text{H}} + \text{CH}_2=\text{C}(\text{CH}_3)-\text{CH}=\text{CH}_2$	-0.4	
P27	Cyclobutene + methyl	$\text{Cyclobutene} + \text{CH}_3$	2.3	
P28	Methylenecyclobutane + $\dot{\text{H}}$	$\dot{\text{H}} + \text{Cyclobutane}-\text{C}(\text{CH}_3)=\text{CH}_2$	10.8	10.4 <sup>b</sup>
P29	1,3-pentadien-1-yl + $\text{H}_2$	$\dot{\text{C}}\text{H}_2-\text{CH}=\text{CH}-\text{CH}_2-\text{CH}_2-\text{CH}_3 + \text{H}_2$	8.9	
P30	1,3-pentadien-2-yl + $\text{H}_2$	$\text{CH}_2=\dot{\text{C}}\text{H}-\text{CH}=\text{CH}-\text{CH}_2-\text{CH}_3 + \text{H}_2$	5.2	
P31	1,3-pentadien-3-yl + $\text{H}_2$	$\text{CH}_2=\text{CH}-\dot{\text{C}}\text{H}-\text{CH}=\text{CH}_2 + \text{H}_2$	6.3	
P32	1,3-pentadien-4-yl + $\text{H}_2$	$\text{CH}_2=\text{CH}-\text{CH}=\dot{\text{C}}\text{H}-\text{CH}_2 + \text{H}_2$	5.2	
P33	1,3-pentadien-5-yl + $\text{H}_2$	$\text{CH}_2=\text{CH}-\text{CH}=\text{CH}-\dot{\text{C}}\text{H}_2 + \text{H}_2$	-21.3	

<sup>a</sup> Calculated values from Goldsmith et al.[11] at the G3 level of theory.

<sup>b</sup> Calculated values from Wang et al.[13, 14] at the CBS/QB3 level of theory at 298 K.

**Table 2.8** Barrier heights (0 K, ZPE corrected, kcal mol<sup>-1</sup>) of the transition states on the  $\dot{C}_5H_9$  PES.

Label	Reaction	This study	Literature
TS1	R→W1	2.3	
TS2	R→W2	5.8	2.7 <sup>b</sup>
TS3	R→W3	5.0	4.0 <sup>a</sup> , 1.9 <sup>b</sup> , 4.6 <sup>c</sup>
TS4	R→W4	3.4	2.5 <sup>a</sup> , 1.0 <sup>b</sup>
TS5	R→P29	17.2	
TS6	R→P30	14.4	
TS7	R→P31	15.1	
TS8	R→P32	14.3	
TS9	R→P33	7.7	
TS10	W1→W2	4.8	2.1 <sup>b</sup>
TS11	W1→W4	-5.8	-7.1 <sup>b</sup>
TS12	W1→W5	6.4	
TS13	W1→W7	17.6	
TS14	W1→W8	20.4	
TS15	W1→P4	17.2	
TS16	W2→W4	-10.5	-12.7 <sup>b</sup>
TS17	W2→W6	-16.2	-18.8 <sup>b</sup>
TS18	W2→W7	-2.0	-4.2 <sup>b</sup>
TS19	W2→W8	18.1	
TS20	W2→W16	9.1	
TS21	W2→P1	10.0	
TS22	W3→W4	5.5	5.5 <sup>a</sup> , 2.6 <sup>b</sup>
TS23	W3→W10	12.5	13.2 <sup>a</sup> , 12.1 <sup>b</sup>
TS24	W3→W11	19.5	22.8 <sup>a</sup>
TS25	W3→W12	0.6	1.6 <sup>a</sup> , -1.5 <sup>b</sup>
TS26	W3→W13	-16.3	-16.5 <sup>a</sup> , -19.1 <sup>b</sup>
TS27	W3→W17	5.0	
TS28	W3→P12	8.8	7.9 <sup>a</sup> , 6.4 <sup>b</sup> , 7.5 <sup>c</sup>
TS29	W3→P22	8.8	8.1 <sup>a</sup> , 8.5 <sup>c</sup>
TS30	W4→W7	22.2	
TS31	W4→W8	20.1	
TS32	W4→W9	9.8	
TS33	W4→W10	9.2	9.6 <sup>a</sup> , 6.3 <sup>b</sup>
TS34	W4→W11	22.5	20.6 <sup>a</sup>
TS35	W4→W12	22.6	22.9 <sup>a</sup>
TS36	W4→P11	19.0	
TS37	W4→P14	-2.9	-4.2 <sup>a</sup> , -6.2 <sup>b</sup> , -4.3 <sup>c</sup>
TS38	W5→W13	23.9	
TS39	W5→W20	29.3	
TS40	W5→P2	31.4	
TS41	W5→P3	34.6	
TS42	W6→W9	23.1	
TS43	W6→W16	22.9	
TS44	W6→W21	25.8	
TS45	W6→P8	13.3	
TS46	W6→P9	23.2	
TS47	W7→W8	26.4	
TS48	W7→P5	14.9	
TS49	W7→P6	11.7	9.9 <sup>b</sup>
TS50	W7→P11	17.9	
TS51	W8→P4	17.0	
TS52	W8→P5	15.3	

TS53	W8→P7	13.0	
TS54	W8→P10	11.7	
TS55	W9→W21	30.9	
TS56	W9→P17	36.5	
TS57	W9→P18	39.0	
TS58	W9→P19	30.9	
TS59	W10→W11	1.9	-0.6 <sup>b</sup>
TS60	W10→W12	-4.4	-3.7 <sup>a</sup> , -7.3 <sup>b</sup>
TS61	W10→W15	-8.2	-11.3 <sup>b</sup>
TS62	W10→W19	-8.6	
TS63	W10→P15	-3.2	-4.6 <sup>a</sup> , -6.6 <sup>b</sup> , -4.7 <sup>c</sup> , -7.7 <sup>d</sup>
TS64	W10→P22	11.2	9.5 <sup>a</sup> , 9.4 <sup>b</sup>
TS65	W11→W12	27.9	28.7 <sup>a</sup>
TS66	W11→P11	18.5	17.3 <sup>a</sup>
TS67	W11→P16	11.9	11.3 <sup>a</sup> , 9.8 <sup>b</sup>
TS68	W11→P20	18.9	17.3 <sup>a</sup>
TS69	W12→P20	20.5	18.8 <sup>a</sup>
TS70	W12→P21	16.7	16.0 <sup>a</sup> , 15.0 <sup>b</sup>
TS71	W13→W14	-17.1	-17.5 <sup>a</sup>
TS72	W13→W17	22.5	
TS73	W13→W20	24.7	
TS74	W13→P13	25.5	24.8 <sup>a</sup>
TS75	W14→W16	6.2	
TS76	W14→P12	10.2	9.4 <sup>a</sup>
TS77	W14→P14	1.6	0.6 <sup>a</sup> , 3.6 <sup>c</sup>
TS78	W14→P26	8.1	
TS79	W15→P23	-7.5	-10.3 <sup>b</sup>
TS80	W16→W19	18.9	
TS81	W16→P24	15.5	
TS82	W16→P25	13.7	
TS83	W16→P27	10.6	
TS84	W17→W19	9.2	
TS85	W17→P24	15.9	
TS86	W18→W19	16.9	
TS87	W19→P28	15.5	
TS88	P12→P15	11.7	10.8 <sup>a</sup>

<sup>a</sup> Calculated values from Goldsmith et al. [11] at the G3 level of theory.

<sup>b</sup> Calculated values from Wang et al. [13, 14] at the CBS/QB3 level of theory at 298 K.

<sup>c</sup> Estimated values from Tsang et al. [17].

<sup>d</sup> Calculated values from Awan et al. [59] at the G3MP2B3 level of theory.

For simplicity and clarity, the PES of each  $\dot{C}_5H_9$  radical and its subsequent reactions are presented separately. For each species, the related reactions are analysed in terms of the heat of reaction, barrier height, transition state structure and reaction class. The reactions are discussed in terms of their importance from the perspective of (1) 1,3-pentadiene +  $\dot{H}$ , (2) H-atom abstraction reactions from 1- and 2-pentene by  $\dot{H}$  atoms and (3) combustion modelling in general.

### 3.3.1 PES and kinetic study of $\dot{\text{H}}$ atom addition adducts

#### 3.3.1.1 2,4- $\dot{\text{C}}_5\text{H}_9$ (W1)

The 2,4- $\dot{\text{C}}_5\text{H}_9$  radical (2-pentene-4-yl, 2°a) is a resonantly stabilized radical that can be formed by  $\dot{\text{H}}$  atom addition to the first carbon atom ( $\text{C}=\text{CC}=\text{CC}$ , 1°v) in 1,3-pentadiene, or by  $\dot{\text{H}}$  atom addition to the third carbon atom ( $\text{CC}=\text{C}=\text{CC}$ ) in 2,3-pentadiene, and also by hydrogen atom abstraction reactions from the fourth carbon atom ( $\text{CC}=\text{CCC}$ , 2°) in 2-pentene. Depending on the temperature and/or pressure, the 2,4- $\dot{\text{C}}_5\text{H}_9$  radical is the dominant product produced from the addition of  $\dot{\text{H}}$  atoms to 1,3-pentadiene, and it is likely to be amongst the dominant products of abstraction reactions from 2-pentene by important radical species including  $\dot{\text{H}}$  and  $\ddot{\text{O}}$  atoms, and  $\dot{\text{O}}\text{H}$  and  $\text{H}\dot{\text{O}}_2$  radicals, etc. Its chemically activated and thermal unimolecular reactions are therefore of importance in numerous scenarios of relevance to alkene and diene high temperature combustion chemistry.

The PES for the reactions of the 2,4- $\dot{\text{C}}_5\text{H}_9$  radical is shown in Fig. 2.15(a), with the isomerization, ring-opening/closing, and  $\beta$ -scission reactions shown as blue, green and red lines, respectively. 2,4- $\dot{\text{C}}_5\text{H}_9$  has four potential intra-molecular H-shift reactions: (1) a 1,2-H shift forming 2,5- $\dot{\text{C}}_5\text{H}_9$ , (2) a 1,4-H shift forming 1,3- $\dot{\text{C}}_5\text{H}_9$ , (3) a 2,4-H shift forming 2,2- $\dot{\text{C}}_5\text{H}_9$ , (4) and a 3,4-H shift forming 2,3- $\dot{\text{C}}_5\text{H}_9$ . The barrier heights and heats of reaction for the isomerization reactions of  $\dot{\text{C}}_5\text{H}_9$  radicals in terms of different reaction types and ring sizes are listed in Table 2.12.

We find the reaction enthalpies and barrier heights follow some clear trends. In terms of reaction enthalpies, the endothermicity increases as the product radicals change from allylic, to primary, and then to vinylic, with the formation of the resonantly-stabilised 1,3- $\dot{\text{C}}_5\text{H}_9$  radical being close to thermo-neutral ( $\Delta_r H_{298\text{K}} = 2.8 \text{ kcal mol}^{-1}$ ) which is  $22.7 \text{ kcal mol}^{-1}$  less endothermic than the formation of the unstable vinylic 2,2- $\dot{\text{C}}_5\text{H}_9$  radical. The reaction barriers follow similar trends, with the thermo-neutral formation of 1,3- $\dot{\text{C}}_5\text{H}_9$  radical having the lowest barrier of  $38.7 \text{ kcal mol}^{-1}$ , and the formation of the 2,2- and 2,3- $\dot{\text{C}}_5\text{H}_9$  radicals having barriers of  $62.1 \text{ kcal mol}^{-1}$  and  $64.9 \text{ kcal mol}^{-1}$ , respectively. The formation of the latter is highly unlikely, as confirmed by the high-pressure limiting calculations shown in Fig. 2.15(b). In terms of barrier heights, the formation of the 2,5- $\dot{\text{C}}_5\text{H}_9$  radical, a primary alkenyl radical, requires  $9.0 \text{ kcal mol}^{-1}$  more energy than the 1,3- $\dot{\text{C}}_5\text{H}_9$  radical, and similar to the 2,2- and 2,3- $\dot{\text{C}}_5\text{H}_9$  radicals, its formation is also irrelevant in the context of 2,4- $\dot{\text{C}}_5\text{H}_9$  radical consumption.

Three further reaction pathways are possible, (i) dissociation to 2,3-pentadiene +  $\dot{\text{H}}$ , (ii)

dissociation to 1,3-pentadiene +  $\dot{\text{H}}$  via C–H  $\beta$ -scission reactions, and (iii) isomerisation to 1,2-dimethyl-3-cyclopropyl radical (W5) via an endo-cyclisation reaction. The C–H  $\beta$ -scission forming 2,3-pentadiene +  $\dot{\text{H}}$  can be neglected, due to its reaction enthalpy of 59.9 kcal mol<sup>-1</sup> and corresponding barrier of 61.7 kcal mol<sup>-1</sup>. Likewise, the endo-cyclisation reaction cannot compete with formation of 1,3- $\dot{\text{C}}_5\text{H}_9$ . Back-dissociation of 2,4- $\dot{\text{C}}_5\text{H}_9$  to 1,3-pentadiene +  $\dot{\text{H}}$  has a barrier of 46.8 kcal mol<sup>-1</sup>, which is 8.1 kcal mol<sup>-1</sup> greater than isomerization to 1,3- $\dot{\text{C}}_5\text{H}_9$ , with the formation of 1,3- $\dot{\text{C}}_5\text{H}_9$  radicals being dominant up to about 1300 K. However, at temperatures in excess of this, the back-dissociation to form 1,3-pentadiene +  $\dot{\text{H}}$  is dominant.

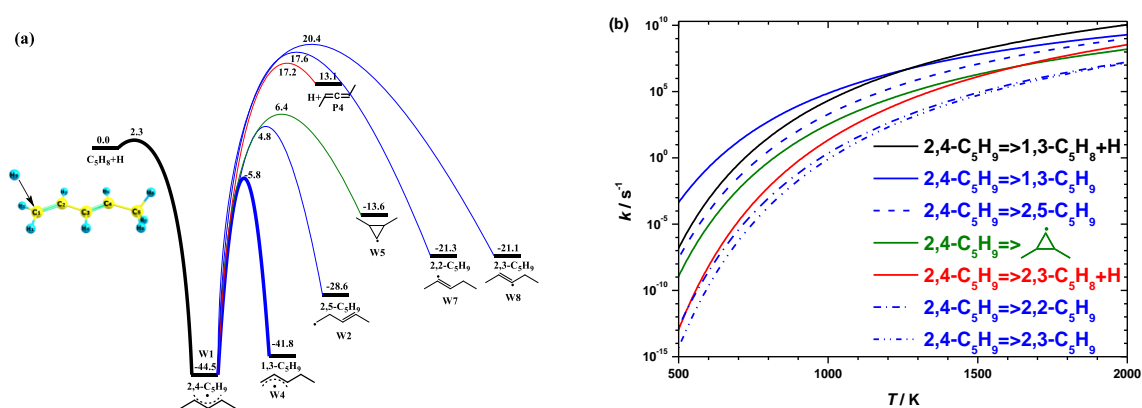


**Fig. 2.15** (a) Potential energy surface for the isomerization and decomposition reactions of 2,4- $\dot{\text{C}}_5\text{H}_9$  radicals (kcal mol<sup>-1</sup>), (b) Comparison of the high-pressure limiting rate constants for subsequent reactions of 2,4- $\dot{\text{C}}_5\text{H}_9$  (W1).

### 3.3.1.2 2,5- $\dot{\text{C}}_5\text{H}_9$ (W2)

The 2,5- $\dot{\text{C}}_5\text{H}_9$  radical (2-pentene-5-yl, 1<sup>o</sup>h) can be formed by  $\dot{\text{H}}$  atom addition to the second carbon atom (C=CC=CC, 2<sup>o</sup>v) on 1,3-pentadiene, and also by  $\dot{\text{H}}$  atom abstraction from the fifth carbon atom (CC=CCC, 1<sup>o</sup>) on 2-pentene. The PES depicting the related reactions of the 2,5- $\dot{\text{C}}_5\text{H}_9$  radical (W2) is shown in Fig. 2.16(a).

Four isomerization reactions can occur for 2,5- $\dot{\text{C}}_5\text{H}_9$  radicals including: (1) a 1,5-H shift forming 1,3- $\dot{\text{C}}_5\text{H}_9$ , (2) a 2,5-H shift forming 2,2- $\dot{\text{C}}_5\text{H}_9$ , (3) a 3,5-H shift forming 2,3- $\dot{\text{C}}_5\text{H}_9$ , (4) and a 4,5-H shift forming 2,4- $\dot{\text{C}}_5\text{H}_9$ . The formation of allylic radicals is exothermic due to their resonantly stabilised geometry, in contrast to the formation of vinylic radicals, which is at least 22 kcal mol<sup>-1</sup> more endothermic. The trend is a little different for energy barriers, with the 1,5-H shift to form the allylic 1,3- $\dot{\text{C}}_5\text{H}_9$  radical having the lowest energy barrier of

18.1 kcal mol<sup>-1</sup> followed by 2,5-H shift forming vinylic 2,2-Ċ<sub>5</sub>H<sub>9</sub> radical which has a barrier of 26.6 kcal mol<sup>-1</sup>, and is thus 8.5 kcal mol<sup>-1</sup> higher. The 4,5 H-shift to form the allylic 2,4-Ċ<sub>5</sub>H<sub>9</sub> radical through a 3-MR TS is third in importance, and has a barrier 6.8 kcal mol<sup>-1</sup> higher than the formation of vinylic 2,2-Ċ<sub>5</sub>H<sub>9</sub> radical via a 5-MR TS. Therefore, the 1,3-Ċ<sub>5</sub>H<sub>9</sub> radical is expected to be the dominant product via H-shift reactions and the other three product radicals are less important, which is consistent with the high-pressure limiting rate constant comparisons shown in Fig. 2.16(b).

2,5-Ċ<sub>5</sub>H<sub>9</sub> can undergo exo-cyclisation reaction to form sec-ethyl-cyclopropanyl (W6) or endo-cyclisation forming methyl-2-cyclobutyl (W16). The heat of reaction for the formation of W6 shown in Table 2.9 is slightly endothermic by 4.8 kcal mol<sup>-1</sup>, and the corresponding energy barrier is 12.4 kcal mol<sup>-1</sup>. Kinetically, this reaction is the most important channel followed by the formation of 1,3-Ċ<sub>5</sub>H<sub>9</sub> radicals. However, the ring-opening reaction of W6 back to 2,5-Ċ<sub>5</sub>H<sub>9</sub> radicals has the lowest barrier among its subsequent reactions shown in Fig. 2.26(b), this indicates that W6 does not contribute significantly to the consumption of 2,5-Ċ<sub>5</sub>H<sub>9</sub> radicals. Considering the endo-cyclisation reaction to form methyl-2-cyclobutyl (W16), as there are lower barrier pathways available (1,5-H shift isomerisation forming 1,3-Ċ<sub>5</sub>H<sub>9</sub>, β-scission forming 1,3-pentadiene + Ĥ), this pathway is unlikely to contribute to the consumption of 2,5-Ċ<sub>5</sub>H<sub>9</sub> radicals with energy barriers over 25.3 kcal mol<sup>-1</sup> higher than the exo-cyclisation.

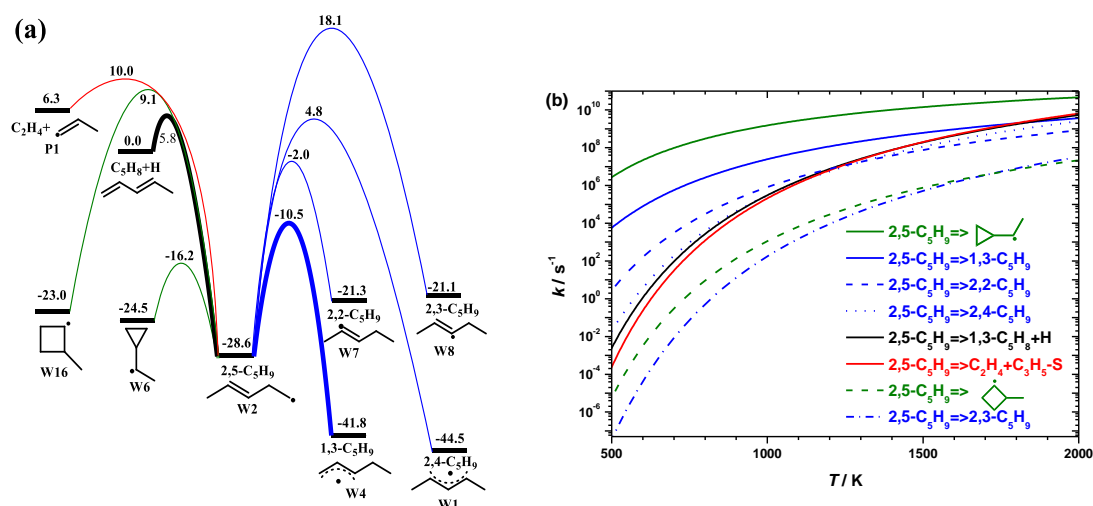


**Fig. 2.16** (a) Potential energy surface for the isomerization and decomposition reactions of 2,5-Ċ<sub>5</sub>H<sub>9</sub> radicals (kcal mol<sup>-1</sup>), (b) Comparison of the high-pressure limiting rate constants for subsequent reactions of 2,5-Ċ<sub>5</sub>H<sub>9</sub> (W2).

2,5- $\dot{C}_5H_9$  can also dissociate to  $C_2H_4 +$  allyl via C–C  $\beta$ -scission and/or 1,3-pentadiene +  $\dot{H}$  via C–H  $\beta$ -scission. The C–C  $\beta$ -scission reaction to form  $C_2H_4 +$  allyl has a reaction enthalpy of 35.1 kcal mol<sup>-1</sup> and its energy barrier of 38.6 kcal mol<sup>-1</sup> is 20.5 kcal mol<sup>-1</sup> higher than the formation of 1,3- $\dot{C}_5H_9$  radicals. Overall, the fate of 2,5- $\dot{C}_5H_9$  radicals is governed by isomerization via a 6-membered ring to form 1,3- $\dot{C}_5H_9$  radicals, and  $\beta$ -scission reactions forming  $C_2H_4 +$  allyl and 1,3-pentadiene +  $\dot{H}$  also play important role at temperature in excess of 1800 K.

### 3.3.1.3 1,3- $\dot{C}_5H_9$ (W4)

The 1,3- $\dot{C}_5H_9$  radical (1-pentene-3-yl, 1<sup>o</sup>a) can be formed by (i)  $\dot{H}$  atom addition to the fourth carbon atom (C=CC=CC, 2<sup>ov</sup>) in 1,3-pentadiene, (ii)  $\dot{H}$  atom addition to the second carbon atom (C=C=CCC) in 1,2-pentadiene, (iii) hydrogen atom abstraction from the third carbon atom (C=CCCC, 2<sup>o</sup>) in 1-pentene, and (iv) by hydrogen atom abstraction from the first carbon atom (CC=CCC, 1<sup>o</sup>) in 2-pentene. 1,3- $\dot{C}_5H_9$  radicals are resonantly stabilized and are the most important  $\dot{C}_5H_9$  radicals according to our previous discussions which shows that isomerization reactions are the most favoured ones leading from 2,4- $\dot{C}_5H_9$  and 2,5- $\dot{C}_5H_9$  radicals producing 1,3- $\dot{C}_5H_9$  radicals. 1,3- $\dot{C}_5H_9$  radicals are also likely to be the dominant intermediates of abstraction reactions from 1-pentene.

The PES for related reactions of 1,3- $\dot{C}_5H_9$  radical is shown in Fig. 2.17(a). 1,3- $\dot{C}_5H_9$  radicals have eight subsequent H-shift isomerization reactions: (1) a 1,2-H shift forming 2,2- $\dot{C}_5H_9$ , (2) 1,3-H shifts forming 1,1- $\dot{C}_5H_9$  or 2,3- $\dot{C}_5H_9$ , (3) a 1,4-H shift forming 2,4- $\dot{C}_5H_9$ , (4) a 1,5-H shift forming 2,5- $\dot{C}_5H_9$ , (5) 2,3-H shift forming 1,2- $\dot{C}_5H_9$ , (6) a 3,4-H shift forming 1,4- $\dot{C}_5H_9$ , (7) and a 3,5-H shift forming 1,5- $\dot{C}_5H_9$ . The isomerization reaction becomes more endothermic as the product radicals change from allylic to primary/secondary to vinylic radicals. The 1,4-H shift from the allylic 1,3- $\dot{C}_5H_9$  radical to the allylic 2,4- $\dot{C}_5H_9$  radical has the lowest reaction enthalpy of -2.8 kcal mol<sup>-1</sup> and is about 17 kcal mol<sup>-1</sup> less endothermic than the formation of primary/secondary radicals (e.g. 2,5- $\dot{C}_5H_9$ ) and over 25 kcal mol<sup>-1</sup> less endothermic than formation of the unstable vinylic radicals (e.g. 2,2- $\dot{C}_5H_9$ ).

The trend of energy barriers for these isomerization reactions is almost similar to that of the reaction enthalpies excluding the 1,5-H shift forming 2,5- $\dot{C}_5H_9$  radicals. For H-shifts via 3-MR (1,2-, 2,3-, 3,4-H shift), 4-MR (1,3-, 3,5-H shift) and 5-MR (1,4-H shift) TSs, the barrier heights increase as the reaction enthalpies increase. Excluding for the 6-MR reaction, the formation of allylic 2,4- $\dot{C}_5H_9$  radicals via a 5-MR TSs has the lowest barrier of 36.0 kcal mol<sup>-1</sup>, and the formation of vinylic 1,1- $\dot{C}_5H_9$  radicals via 4-MR TSs has the highest barrier of

64.4 kcal mol<sup>-1</sup>. Among all of the isomerisation reactions the formation of primary 2,5-Ċ<sub>5</sub>H<sub>9</sub> radicals via 6-MR TSs has the lowest energy barrier of 31.3 kcal mol<sup>-1</sup> which is 4.7 kcal mol<sup>-1</sup> lower than formation of allylic 2,4-Ċ<sub>5</sub>H<sub>9</sub> radicals. According to our reaction enthalpy and energy barrier analysis, the formation of 2,4-Ċ<sub>5</sub>H<sub>9</sub> radicals via 5-MR TSs, and 2,5-Ċ<sub>5</sub>H<sub>9</sub> radicals via 6-MR TSs are preferred over the other isomerisation reactions which is also proven by the rate constant comparisons shown in Fig. 2.17(b). The vinylic radicals are unlikely to be formed with their energy barriers being at least 30 kcal mol<sup>-1</sup> higher than those for the formation of 2,5-Ċ<sub>5</sub>H<sub>9</sub> radicals. Likewise, the formation of 1,4-Ċ<sub>5</sub>H<sub>9</sub> and 1,5-Ċ<sub>5</sub>H<sub>9</sub> radicals are expected to be negligible, as their energy barriers are over 16 kcal mol<sup>-1</sup> higher than the route leading to the formation of 2,5-Ċ<sub>5</sub>H<sub>9</sub> radicals.

1,3-Ċ<sub>5</sub>H<sub>9</sub> radicals can also undergo (i) C–C β-scission forming 1,3-butadiene + ĊH<sub>3</sub>, (ii) C–H β-scission forming 1,2-pentadiene + Ĥ and/or 1,3-pentadiene + Ĥ, and (iii) endo-cyclisation forming ethyl-2-cyclopropyl (W9). In contrast to C–C β-scission reactions, the C–H β-scission reactions, and the endo-cyclisation reaction can be neglected, with energy barriers being at least 6.3 kcal mol<sup>-1</sup> higher and rate constants being over an order of magnitude slower. From the above discussion of the fate of 2,4-Ċ<sub>5</sub>H<sub>9</sub> and 2,5-Ċ<sub>5</sub>H<sub>9</sub> radicals, we can see their most favoured subsequent reaction is isomerization to form 1,3-Ċ<sub>5</sub>H<sub>9</sub> radicals. The dominant product for 1,3-Ċ<sub>5</sub>H<sub>9</sub> radical is 1,3-butadiene + ĊH<sub>3</sub> via C–C β-scission, and therefore it is also the most important product for 2,4-Ċ<sub>5</sub>H<sub>9</sub> and 2,5-Ċ<sub>5</sub>H<sub>9</sub> radicals through the formation of 1,3-Ċ<sub>5</sub>H<sub>9</sub> radicals.

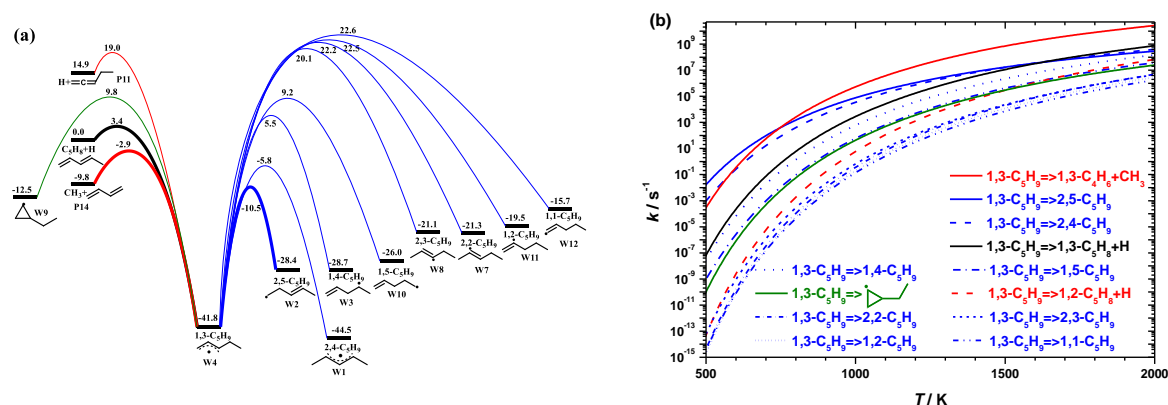


**Fig. 2.17** (a) Potential energy surface for the isomerization and decomposition reactions of 1,3-Ċ<sub>5</sub>H<sub>9</sub> radical (kcal mol<sup>-1</sup>). (b) Comparison of the high-pressure limiting rate constants for subsequent reactions of 1,3-Ċ<sub>5</sub>H<sub>9</sub> (W4).

### 3.3.1.4 1,4- $\dot{\text{C}}_5\text{H}_9$ (W3) and 3-methyl-1-buten-4-yl (W14)

The 1,4- $\dot{\text{C}}_5\text{H}_9$  radical (1-pentene-4-yl, 2°h) can be formed by (i)  $\dot{\text{H}}$  atom addition to the third carbon atom (C=CC=CC, 2°v) in 1,3-pentadiene, (ii)  $\dot{\text{H}}$  atom addition to the fifth carbon atom (C=CCC=C, 1°v) in 1,4-pentadiene, and (iii) by hydrogen atom abstraction from the fourth carbon atom (C=CCCC, 2°) in 1-pentene. The PES for the reactions of 1,4- $\dot{\text{C}}_5\text{H}_9$  radicals is shown in Fig. 2.18(a).

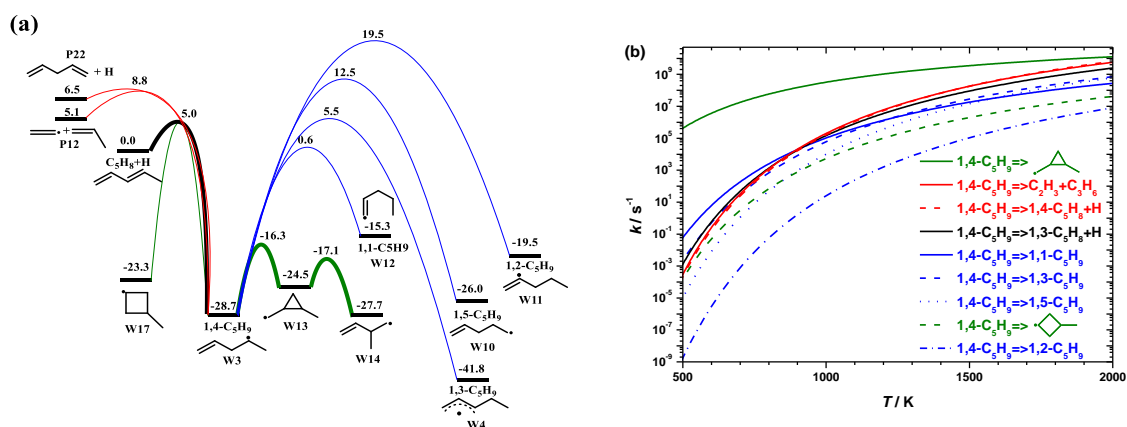


**Fig. 2.18** (a) Potential energy surface for the isomerization and decomposition reactions of 1,4- $\dot{\text{C}}_5\text{H}_9$  radical (kcal mol<sup>-1</sup>), (b) Comparison of the high-pressure limiting rate constants for subsequent reactions of 1,4- $\dot{\text{C}}_5\text{H}_9$  (W3).

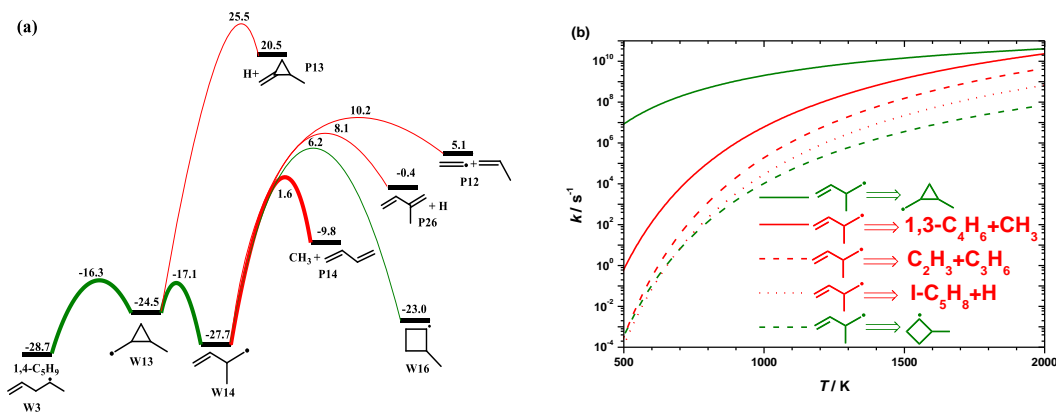
This radical can undergo (1) 1,4-H shift forming 1,1- $\dot{\text{C}}_5\text{H}_9$ , (2) 2,4-H shift forming 1,2- $\dot{\text{C}}_5\text{H}_9$ , (3) 3,4-H shift forming 1,3- $\dot{\text{C}}_5\text{H}_9$ , (4) and 4,5-H shift forming 1,5- $\dot{\text{C}}_5\text{H}_9$ . The reaction enthalpies of these four isomerization reactions show a clear dependence on the product radical type, while the ring size of the TS also needs to be considered in analysing the trend of the energy barriers. The reaction enthalpies to form different product radicals increase from allylic radicals (1,3- $\dot{\text{C}}_5\text{H}_9$ , -14.3 kcal mol<sup>-1</sup>) to primary radicals (1,5- $\dot{\text{C}}_5\text{H}_9$ , 2.4 kcal mol<sup>-1</sup>) to vinylic radicals (1,2- $\dot{\text{C}}_5\text{H}_9$ , 10.1 kcal mol<sup>-1</sup> and 1,1- $\dot{\text{C}}_5\text{H}_9$ , 12.9 kcal mol<sup>-1</sup>). For H-shifts via 3-MR or 4-MR TSSs, the energy barriers obey this trend to increase from 34.2 kcal mol<sup>-1</sup> forming the allylic 1,3- $\dot{\text{C}}_5\text{H}_9$  radical to 41.2 kcal mol<sup>-1</sup> forming the primary 1,5- $\dot{\text{C}}_5\text{H}_9$  radical to 48.2 kcal mol<sup>-1</sup> forming the vinylic 1,2- $\dot{\text{C}}_5\text{H}_9$  radical. What is interesting about these isomerisation reactions is that the formation of the vinylic 1,1- $\dot{\text{C}}_5\text{H}_9$  radical via a 5-MR TS has the lowest energy barrier of 29.3 kcal mol<sup>-1</sup> as 1,1- $\dot{\text{C}}_5\text{H}_9$  radicals are the least stable isomerisation products. Hence, the formation of 1,1- $\dot{\text{C}}_5\text{H}_9$  radicals is the most favoured H-shift reaction with the isomerization to form 1,3- $\dot{\text{C}}_5\text{H}_9$  radicals also becoming competitive at high temperatures.

There are two possible cyclisation pathways for 1,4- $\dot{\text{C}}_5\text{H}_9$  radicals with the

exo-cycloaddition through a 3-MR TS to form 1-methylidene-cyclopropylmethyl (W13) preferred compared to the endo-cycloaddition reaction to form methyl-3-cyclobutyl (W17) through a 4-MR TS. The energy barrier is 21.3 kcal mol<sup>-1</sup> lower for the former compared to the latter. The energy barrier of the exo-cycloaddition reaction forming 1-methylidene-cyclopropylmethyl (W13) is 16.9 kcal mol<sup>-1</sup> lower than the formation of 1,1-Ċ<sub>5</sub>H<sub>9</sub> which is the dominant isomerisation product. Moreover, the subsequent ring-opening reaction of 1-methylidene-cyclopropylmethyl (W13) has a low energy barrier (7.4 kcal mol<sup>-1</sup>) to form 3-methyl-1-buten-4-yl (W14). Thus 1,4-Ċ<sub>5</sub>H<sub>9</sub> radical prefers to undergo a fast homoallylic rearrangement reaction in a two-step sequence: (1) exo-cyclisation reaction to form a 3-MR radical (1-methylidene-cyclopropylmethyl, W13) and (2) a ring-opening reaction of the radical formed to yield 3-methyl-1-buten-4-yl (W14) radical.

The 1,4-Ċ<sub>5</sub>H<sub>9</sub> radical can also dissociate to propene + Ċ<sub>2</sub>H<sub>3</sub> and/or 1,4-pentadiene + Ĥ via β-scission reactions. The reaction enthalpy of 34.6 kcal mol<sup>-1</sup> for C–C β-scission is close to that for C–H β-scission with the difference being within 1.7 kcal mol<sup>-1</sup>, and these two β-scission reactions have the same energy barrier of 8.8 kcal mol<sup>-1</sup>. The β-scission reactions are about 32.6 kcal mol<sup>-1</sup> more endothermic than the exo-cycloaddition reaction forming 1-methylidene-cyclopropylmethyl (W13) and the corresponding energy barriers are also 25.1 kcal mol<sup>-1</sup> higher for the former. Obviously, the dominant channel for 1,4-Ċ<sub>5</sub>H<sub>9</sub> radical consumption is a fast homoallylic rearrangement reaction to form 3-methyl-1-buten-4-yl (W14) via 1-methylidene-cyclopropylmethyl (W13). This is also validated by the rate constant comparisons, which shows that this reaction is at least six orders of magnitude faster than the other reaction channels at low temperature and, at 2000 K, the differences decrease to over a factor of two times faster than β-scission reactions and over an order of magnitude faster than the other reactions.

The 3-methyl-1-buten-4-yl (W14) radical can also be formed via internal hydrogen atom addition to the third carbon atom (C=CC(C)=C) on isoprene, and via H-atom abstraction of the primary carbon atom (C=CC(C)C) of 3-methyl-butene by different radicals. The PES for the related reactions of 3-methyl-1-buten-4-yl (W14) is shown in Fig. 2.19(a).



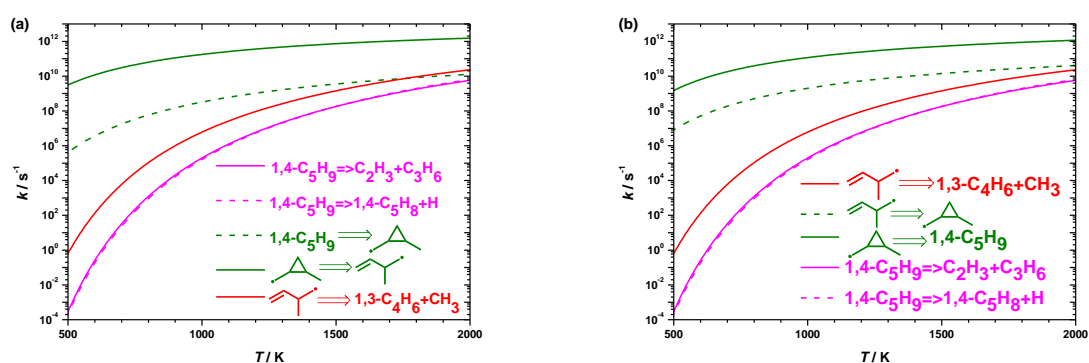
**Fig. 2.19** (a) PES for the formation and subsequent reactions of W14 ( $\text{kcal mol}^{-1}$ ), (b) Comparison of the high-pressure limiting rate constants for subsequent reactions of 3-methyl-1-buten-4-yl (W14).

Fig. 2.19(a) depicts the low energy barriers for the ring-opening reactions of 1-methylidene-cyclopropylmethyl (W13). These two ring-opening reactions have similar reaction enthalpies of about  $-3.0 \text{ kcal mol}^{-1}$  and energy barriers of  $\sim 7.8 \text{ kcal mol}^{-1}$ . In addition to the ring-opening reactions, 1-methylidene-cyclopropylmethyl (W13) can undergo C–H  $\beta$ -scission to produce 1-methylidene-2-methyl-cyclopropane and a hydrogen atom (P13). However, in contrast to the ring-opening reactions, C–H bond cleavage can be neglected, since it is about  $48.5 \text{ kcal mol}^{-1}$  more endothermic and its energy barrier is approximately  $42 \text{ kcal mol}^{-1}$  higher. Thus, 1-methylidene-cyclopropylmethyl (W13) radicals prefer to undergo ring-opening reactions to form  $1,4\text{-}\dot{\text{C}}_5\text{H}_9$  radicals and/or 3-methyl-1-buten-4-yl radicals.

Consistent with linear  $\dot{\text{C}}_5\text{H}_9$  radicals, the three-membered exo-cyclisation reaction of 3-methyl-1-buten-4-yl (W14) is more favoured than its four-membered endo-cyclisation reaction, with exo-cyclisation  $2.6 \text{ kcal mol}^{-1}$  less endothermic and its energy barrier  $23.3 \text{ kcal mol}^{-1}$  lower than endo-cyclisation. 3-methyl-1-buten-4-yl (W14) has three subsequent  $\beta$ -scission reactions: C–C bond breaking to form 1,3-butadiene + methyl and/or vinyl + propene, and C–H bond breaking to form isoprene +  $\dot{\text{H}}$ . The formation of 1,3-butadiene and methyl is the least endothermic reaction and has the lowest energy barrier of  $29.3 \text{ kcal mol}^{-1}$  among three  $\beta$ -scission reactions. Hence the exo-cyclisation and C–C  $\beta$ -scission to form 1,3-butadiene + methyl are expected to be the most important channels for 3-methyl-1-buten-4-yl (W14). This is proven by the high-pressure limiting rate constant comparisons in Fig. 2.19(b) that the formation of 1-methylidene-cyclopropylmethyl (W13) via exo-cyclisation is dominant over the entire temperature range of 500–2000 K, with C–C  $\beta$ -scission producing 1,3-butadiene +  $\dot{\text{C}}\text{H}_3$  beginning to play an important role at high

temperatures.

Aiming to find the dominant products of 1,4- $\dot{\text{C}}_5\text{H}_9$  and 3-methyl-1-buten-4-yl (W14) radical decomposition, high-pressure limiting rate constants for the subsequent reactions of 1,4- $\dot{\text{C}}_5\text{H}_9$  and 3-methyl-1-buten-4-yl radicals are shown in Fig. 2.20. The homoallylic rearrangement reactions between 1,4- $\dot{\text{C}}_5\text{H}_9$  and 3-methyl-1-buten-4-yl radicals are over two orders of magnitude faster than their C–C  $\beta$ -scission reactions. Hence, the C–C  $\beta$ -scission reactions are the rate-limiting steps for the consumption of 1,4- $\dot{\text{C}}_5\text{H}_9$  and 3-methyl-1-buten-4-yl radicals. The  $\beta$ -scission of 3-methyl-1-buten-4-yl forming 1,3-butadiene + methyl is over three orders of magnitude faster at 500 K, and four times faster at 2000 K, than the  $\beta$ -scission of 1,4- $\dot{\text{C}}_5\text{H}_9$  radicals. Since the inter-conversion of 1,4- $\dot{\text{C}}_5\text{H}_9$  and 3-methyl-1-buten-4-yl radicals is much faster than their  $\beta$ -scission reactions and  $k_\infty(3\text{-methyl-1-buten-4-yl} \rightarrow 1,3\text{-butadiene} + \text{methyl}) > k_\infty(1,4\text{-}\dot{\text{C}}_5\text{H}_9 \rightarrow \text{propene} + \dot{\text{C}}_2\text{H}_3 / 1,4\text{-pentadiene} + \dot{\text{H}})$ , the 1,3-butadiene + methyl product set is expected to be the dominant one for these two radicals.



**Fig. 2.20** (a) High-pressure limiting rate constants for the subsequent reactions of 1,4- $\dot{\text{C}}_5\text{H}_9$  ( $\text{kcal mol}^{-1}$ ), (b) High-pressure limiting rate constants for the subsequent reactions of 3-methyl-1-buten-4-yl (W14).

### 3.3.2 PES and kinetic study of vinylic $\dot{\text{C}}_5\text{H}_9$ radicals formed through isomerization reactions of the four main radicals

#### 3.3.2.1 2,2- $\dot{\text{C}}_5\text{H}_9$ (W7)

The four main radicals formed from  $\dot{\text{H}}$  atom addition entrance channels can isomerize to various radicals including 1,1- $\dot{\text{C}}_5\text{H}_9$  (W12), 1,2- $\dot{\text{C}}_5\text{H}_9$  (W11), 1,5- $\dot{\text{C}}_5\text{H}_9$  (W10), 2,2- $\dot{\text{C}}_5\text{H}_9$  (W7), 2,3- $\dot{\text{C}}_5\text{H}_9$  (W8) radicals. The 2,2- $\dot{\text{C}}_5\text{H}_9$  radical (1-pentene-3-yl,  $2^\circ\text{v}$ ) can also be formed by (i)  $\dot{\text{H}}$  atom addition to the first carbon atom ( $\text{C}=\text{C}=\text{CCC}$ ,  $1^\circ\text{v}$ ) in 1,2-pentadiene, (ii)  $\dot{\text{H}}$  atom addition to the third carbon atom ( $\text{CC}\equiv\text{CCC}$ ) in 2-pentyne, and (iii) by hydrogen atom

abstraction from the second carbon atom (CC=CCC, 2°v) in 2-pentene. The PES of 2,2-Ċ<sub>5</sub>H<sub>9</sub> radicals (W7) is shown in Fig. 2.21(a).

The 2,2-Ċ<sub>5</sub>H<sub>9</sub> radical has four possible H-shift reactions: (1) a 1,2-H shift forming 1,3-Ċ<sub>5</sub>H<sub>9</sub>, (2) a 2,3-H shift forming 2,3-Ċ<sub>5</sub>H<sub>9</sub>, (3) a 2,4-H shift forming 2,4-Ċ<sub>5</sub>H<sub>9</sub>, (4) and a 2,5-H shift forming 2,5-Ċ<sub>5</sub>H<sub>9</sub>. The formations of allylic and primary radicals are exothermic and the reaction enthalpies forming allylic radicals are about 15.9 kcal mol<sup>-1</sup> more exothermic than that of a primary radical. Moreover, the 2,3-H shift to form the vinylic 2,3-Ċ<sub>5</sub>H<sub>9</sub> radical is close to thermo-neutral and more endothermic than the formation of allylic and primary radicals. The energy barriers for these four isomerization reactions decrease from ~45.6 kcal mol<sup>-1</sup> (3-MR) to 38.9 kcal mol<sup>-1</sup> (4-MR) to 19.3 kcal mol<sup>-1</sup> (5-MR) as the ring size increases. Since the formation of 2,5-Ċ<sub>5</sub>H<sub>9</sub> radicals has an energy barrier at least 19.6 kcal mol<sup>-1</sup> lower than the other H-shift reactions, it is expected to be one of the most important channels for 2,2-Ċ<sub>5</sub>H<sub>9</sub> radical consumption. This conclusion is further confirmed by the high-pressure limiting rate constant comparisons shown in Fig. 2.21(b).

The 2,2-Ċ<sub>5</sub>H<sub>9</sub> radical can break a C–H bond to form 2-pentyne + Ĥ or 1,2-pentadiene + Ĥ and break a C–C bond to form propyne + Ċ<sub>2</sub>H<sub>5</sub> radical. The reaction enthalpies of C–H bond cleavages are about 12.0 kcal mol<sup>-1</sup> more endothermic than C–C bond breaking and energy barriers are about 3.2 kcal mol<sup>-1</sup> higher for the former. Considering that the energy barrier of C–C β-scission is 13.7 kcal mol<sup>-1</sup> higher than that for the formation of 2,5-Ċ<sub>5</sub>H<sub>9</sub> radicals, this the latter is expected to be the dominant product set which ultimately forms from 1,3-Ċ<sub>5</sub>H<sub>9</sub> radicals. The high-pressure limiting rate constants also suggest the importance of C–C β-scission forming propyne + Ċ<sub>2</sub>H<sub>5</sub> at temperatures above 1200 K.

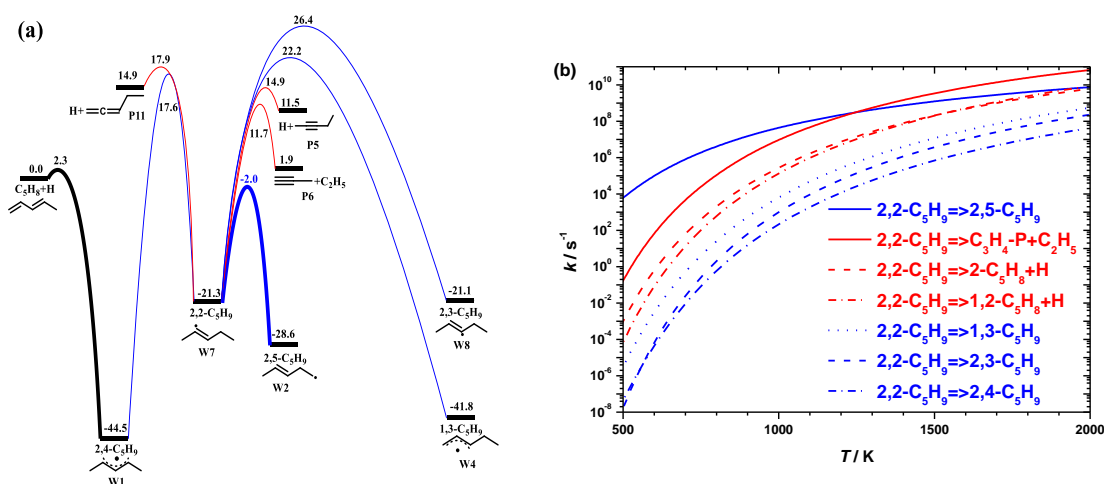


**Fig. 2.21** (a) PES for the isomerization and decomposition reactions of 2,2-Ċ<sub>5</sub>H<sub>9</sub> radical (kcal mol<sup>-1</sup>), (b) Comparison of the high-pressure limiting rate constants for subsequent reactions of 2,2-Ċ<sub>5</sub>H<sub>9</sub> (W7).

### 3.3.2.2 2,3-Ċ<sub>5</sub>H<sub>9</sub> (W8)

The 2,3-Ċ<sub>5</sub>H<sub>9</sub> (2°v) radical can be formed via (i) Ĥ atom addition to the second carbon atom (CC=C=CC, 2°v) in 2,3-pentadiene, (ii) Ĥ atom addition to the second carbon atom (CC≡CCC) in 2-pentyne, and (iii) by hydrogen atom abstraction from the third carbon atom (CC=CCC) in 2-pentene. The PES for 2,3-Ċ<sub>5</sub>H<sub>9</sub> radicals is shown in Fig. 2.22(a).

The 2,3-Ċ<sub>5</sub>H<sub>9</sub> radical can undergo four isomerization reactions, (1) a 1,3-H shift forming 1,3-Ċ<sub>5</sub>H<sub>9</sub>, (2) a 2,3-H shift forming 2,2-Ċ<sub>5</sub>H<sub>9</sub>, (3) a 3,4-H shift forming 2,4-Ċ<sub>5</sub>H<sub>9</sub>, (4) and a 3,5-H shift forming 2,5-Ċ<sub>5</sub>H<sub>9</sub>. Because the allylic and primary radicals are more stable than vinylic ones, the exothermicity for H-shift reactions of the 2,3-Ċ<sub>5</sub>H<sub>9</sub> radical increases as the product radicals change from vinylic (2,2-Ċ<sub>5</sub>H<sub>9</sub>) to primary (2,5-Ċ<sub>5</sub>H<sub>9</sub>) to allylic (1,3-Ċ<sub>5</sub>H<sub>9</sub> and 2,4-Ċ<sub>5</sub>H<sub>9</sub>) radicals. Consistent with the other Ċ<sub>5</sub>H<sub>9</sub> radicals, the H-shift reaction from a vinylic radical to another vinylic radical is found to be thermo-neutral, and the reaction enthalpy for 2,3-Ċ<sub>5</sub>H<sub>9</sub> → 2,2-Ċ<sub>5</sub>H<sub>9</sub> is -0.2 kcal mol<sup>-1</sup>. Formation of the primary 2,5-Ċ<sub>5</sub>H<sub>9</sub> radical via a 4-MR TS has an energy barrier that is 2.0 kcal mol<sup>-1</sup> lower than those for the allylic 2,4-Ċ<sub>5</sub>H<sub>9</sub> and 1,3-Ċ<sub>5</sub>H<sub>9</sub> radicals and 8.3 kcal mol<sup>-1</sup> lower than that of the vinylic 2,2-Ċ<sub>5</sub>H<sub>9</sub> radical. Hence 2,5-Ċ<sub>5</sub>H<sub>9</sub> radicals are expected to be the most important isomerisation products from 2,3-Ċ<sub>5</sub>H<sub>9</sub> radicals.

The 2,3-Ċ<sub>5</sub>H<sub>9</sub> radical can undergo C–C β-scission to produce 1,2-butadiene + methyl, 1-butyne + methyl, or C–H β-scission to produce 2,3-pentadiene + Ĥ or 2-pentyne + Ĥ. Because the C–H β-scission reactions are about 10 kcal mol<sup>-1</sup> more endothermic than the C–C β-scissions, C–C bond breaking to form 1,2-butadiene + methyl and 1-butyne + methyl dominate, Fig. 2.22(b).

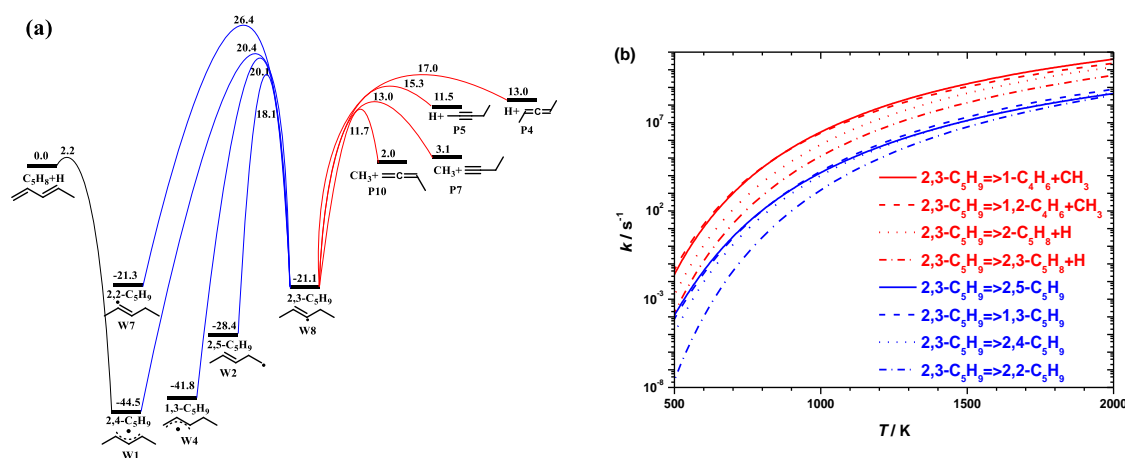


**Fig. 2.22** (a) PES for the isomerization and decomposition reactions of 2,3-Ċ<sub>5</sub>H<sub>9</sub> radical (kcal mol<sup>-1</sup>), (b) Comparison of the high-pressure limiting rate constants for subsequent reactions of 2,3-Ċ<sub>5</sub>H<sub>9</sub> (W8).

For the 1,3-pentadiene +  $\dot{\text{H}}$  system, there is no direct reaction pathway to form 2,3- $\dot{\text{C}}_5\text{H}_9$  radicals from the reactants and there is also no low energy barrier isomerisation reactions for its formation from other  $\dot{\text{C}}_5\text{H}_9$  radicals. For the 2-pentene +  $\dot{\text{H}}$  system, it can be formed directly via H-atom abstraction from the reactants, but the formation of allylic 1,3- $\dot{\text{C}}_5\text{H}_9$  and 2,4- $\dot{\text{C}}_5\text{H}_9$  radicals are expected to be more favoured based on our calculations. Thus, the 2,3- $\dot{\text{C}}_5\text{H}_9$  radical and its related reactions are unimportant for the reaction of  $\dot{\text{H}}$  atoms with 1,3-pentadiene and 2-pentene. However, for  $\dot{\text{H}}$  atom addition to 2,3-pentadiene and 2-pentyne, 2,3- $\dot{\text{C}}_5\text{H}_9$  radicals can be formed directly and their subsequent  $\beta$ -scission reactions can be important.

### 3.3.2.3 1,2- $\dot{\text{C}}_5\text{H}_9$ (W11)

The 1,2- $\dot{\text{C}}_5\text{H}_9$  ( $2^\circ\text{v}$ ) radical can be formed via (i)  $\dot{\text{H}}$  atom addition to the third carbon atom ( $\text{C}=\text{C}=\text{CCC}$ ,  $2^\circ\text{v}$ ) in 1,2-pentadiene, (ii) external  $\dot{\text{H}}$  atom addition to 1-pentyne ( $\text{C}\equiv\text{CCCC}$ ), and (iii) by hydrogen atom abstraction from the second carbon atom ( $\text{C}=\text{CCCC}$ ,  $2^\circ\text{v}$ ) in 1-pentene. The PES of 1,2- $\dot{\text{C}}_5\text{H}_9$  radicals (W11) is shown in Fig. 2.23(a).

Four H-shift reactions can happen for 1,2- $\dot{\text{C}}_5\text{H}_9$  radical forming (1) 1,1- $\dot{\text{C}}_5\text{H}_9$  via a 1,2-H shift, (2) 1,3- $\dot{\text{C}}_5\text{H}_9$  via a 2,3-H shift, (3) 1,4- $\dot{\text{C}}_5\text{H}_9$  via a 2,4-H shift, (4) and 1,5- $\dot{\text{C}}_5\text{H}_9$  via a 2,5-H shift. The reaction enthalpy for the formation of the allylic 1,3- $\dot{\text{C}}_5\text{H}_9$  radical is 14.3 kcal mol<sup>-1</sup> more exothermic than that for the formation of the secondary 1,4- $\dot{\text{C}}_5\text{H}_9$  radical, and is 16.8 kcal mol<sup>-1</sup> more than the primary 1,5- $\dot{\text{C}}_5\text{H}_9$  radical and 21.6 kcal mol<sup>-1</sup> more than the vinylic 1,1- $\dot{\text{C}}_5\text{H}_9$  radical. The energy barriers are more dependent on the ring size of the TSs with the 2,5-H shift via a 5-MR TS forming 1,5- $\dot{\text{C}}_5\text{H}_9$  having the lowest barrier of 21.4 kcal mol<sup>-1</sup>, followed by a 2,4-H shift via a 4-MR TS forming 1,4- $\dot{\text{C}}_5\text{H}_9$  radicals with an energy barrier of 38.0 kcal mol<sup>-1</sup>. For H-shifts via 3-MR TSs, the energy barrier for the formation of the allylic 1,3- $\dot{\text{C}}_5\text{H}_9$  radical is 5.4 kcal mol<sup>-1</sup> lower than that of the vinylic 1,1- $\dot{\text{C}}_5\text{H}_9$  radical. However, neither the 3-MR or 4-MR reactions compete with the 5-MR reaction forming 1,5- $\dot{\text{C}}_5\text{H}_9$  radicals.

Three  $\beta$ -scission reactions are possible for 1,2- $\dot{\text{C}}_5\text{H}_9$  radical, (i) C–C  $\beta$ -scission to form allene + ethyl radical, (ii) C–H  $\beta$ -scission to form 1,2-pentadiene +  $\dot{\text{H}}$  and (iii) 1-pentyne +  $\dot{\text{H}}$ . The reaction enthalpy for the C–C  $\beta$ -scission reaction is about 12.8 kcal mol<sup>-1</sup> lower than that for C–H  $\beta$ -scission reactions, and thus C–C  $\beta$ -scission dominates.

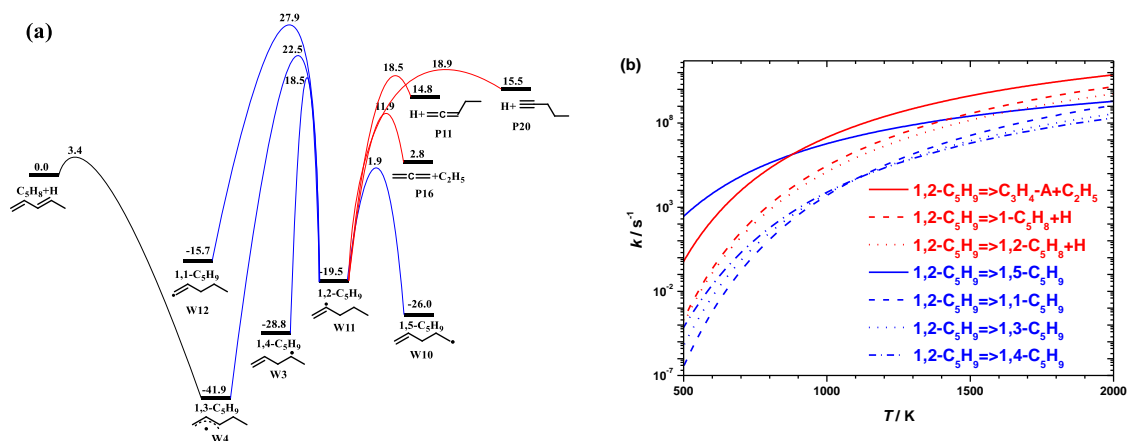


**Fig. 2.23** (a) PES for the isomerization and decomposition reactions of 1,2-Ċ<sub>5</sub>H<sub>9</sub> radical (kcal mol<sup>-1</sup>), (b) Comparison of the high-pressure limiting rate constants for subsequent reactions of 1,2-Ċ<sub>5</sub>H<sub>9</sub> (W11).

The high-pressure limiting rate constant comparison for the subsequent reactions of 1,2-Ċ<sub>5</sub>H<sub>9</sub> radicals is shown in Fig. 2.23(b). Consistent with our energy barrier analysis, the dominant channel for 1,2-Ċ<sub>5</sub>H<sub>9</sub> radical consumption is a 2,5-H shift reaction forming 1,5-Ċ<sub>5</sub>H<sub>9</sub> radicals at low temperatures (< 900 K). Thereafter, it is overtaken by C–C β-scission forming allene + ethyl, with its  $k_{\infty}$  becoming over an order of magnitude faster at 2000 K.

### 3.3.2.4 1,1-Ċ<sub>5</sub>H<sub>9</sub> (W12)

The 1,1-Ċ<sub>5</sub>H<sub>9</sub> radical (1°v) can be formed from (i) internal Ĥ atom addition to 1-pentyne (C≡CCCC), and (ii) by hydrogen atom abstraction from the first carbon atom (C=CCCC) on 1-pentene. 1,1-Ċ<sub>5</sub>H<sub>9</sub> radicals can undergo four isomerization reactions and two β-scission reactions, with its PES shown in Fig. 2.24(a).

Reaction enthalpies for H-shifts from 1,1-Ċ<sub>5</sub>H<sub>9</sub> to product radicals follow the same trend as for the other Ċ<sub>5</sub>H<sub>9</sub> radicals: 1,3-Ċ<sub>5</sub>H<sub>9</sub> (1°a, -27.2 kcal mol<sup>-1</sup>) < 1,4-Ċ<sub>5</sub>H<sub>9</sub> (2°, -12.9 kcal mol<sup>-1</sup>) < 1,5-Ċ<sub>5</sub>H<sub>9</sub> (1°, -10.5 kcal mol<sup>-1</sup>) < 1,2-Ċ<sub>5</sub>H<sub>9</sub> (2°v, -2.8 kcal mol<sup>-1</sup>). In addition, the energy barriers for these four isomerization reactions decrease with increasing ring size from 43.2 kcal mol<sup>-1</sup> (3-MR) to 10.9 kcal mol<sup>-1</sup> (6-MR). Thus, the formation of 1,5-Ċ<sub>5</sub>H<sub>9</sub> via a 6-MR TS and 1,4-Ċ<sub>5</sub>H<sub>9</sub> via a 5-MR TS are kinetically preferred for 1,1-Ċ<sub>5</sub>H<sub>9</sub> radicals.

1,1-Ċ<sub>5</sub>H<sub>9</sub> radicals can also undergo C–C β-scission to form 1-propyl + acetylene or C–H β-scissions to form 1-pentyne + Ĥ. The reaction enthalpy of C–C β-scission is 9.3 kcal mol<sup>-1</sup> lower than C–H β-scission. The energy barrier for C–C β-scission is 3.9 kcal mol<sup>-1</sup> lower than for C–H β-scission, so the favoured β-scission product is 1-propyl and acetylene.

The high-pressure limiting rate constant comparison for the subsequent reactions of 1,1- $\dot{\text{C}}_5\text{H}_9$  radicals is depicted in Fig. 2.24(b). At temperatures below 1100 K, the isomerisation reactions forming 1,4- $\dot{\text{C}}_5\text{H}_9$  and 1,5- $\dot{\text{C}}_5\text{H}_9$  radicals are faster than for the other channels, followed by C–C  $\beta$ -scission to form 1-propyl + acetylene. The difference between these two isomerisation reactions is over an order of magnitude at 500 K, but decreases with increasing temperature resulting in a difference of a factor of 2.5 in the temperature range of 900 to 2000 K. The C–C  $\beta$ -scission reaction surpasses the two isomerisation reactions at 1400 K and becomes over an order of magnitude faster than the other reactions at 2000 K. Taken together, 1,4- $\dot{\text{C}}_5\text{H}_9$  and 1,5- $\dot{\text{C}}_5\text{H}_9$  radicals are the most important products stemming from 1,1- $\dot{\text{C}}_5\text{H}_9$  at temperatures below 1400 K, with the formation of 1-propyl + acetylene dominating at higher temperatures.

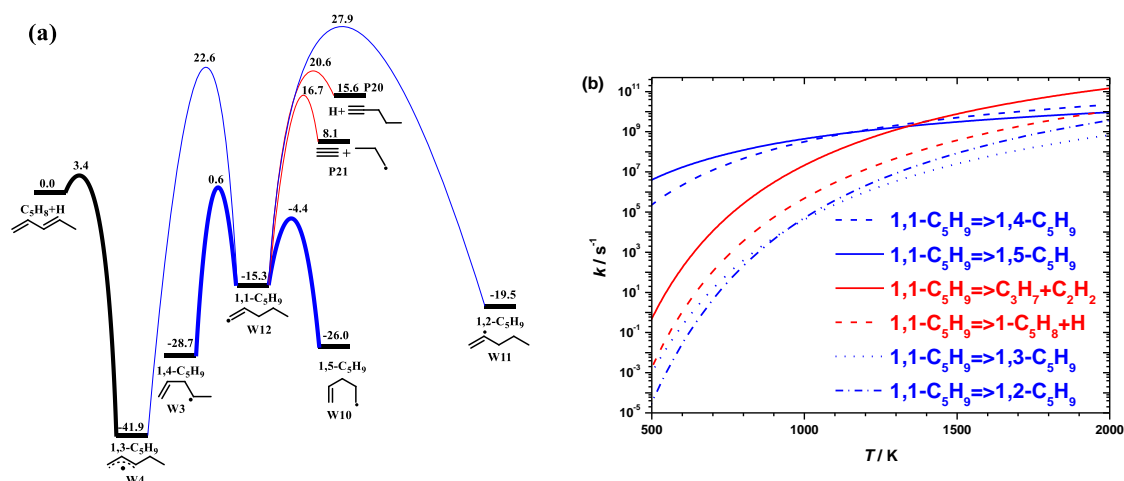


**Fig. 2.24** (a) PES for the isomerization and decomposition reactions of 1,1- $\dot{\text{C}}_5\text{H}_9$  radicals ( $\text{kcal mol}^{-1}$ ), (b) Comparison of the high-pressure limiting rate constants for subsequent reactions of 1,1- $\dot{\text{C}}_5\text{H}_9$ .

### 3.3.2.5 1,5- $\dot{\text{C}}_5\text{H}_9$ (W10)

The 1,5- $\dot{\text{C}}_5\text{H}_9$  radical ( $1^\circ$ ) can be formed through internal  $\dot{\text{H}}$  atom addition to 1,4-pentadiene ( $\text{C}=\text{CCC}=\text{C}$ ), and by hydrogen atom abstraction from the fifth carbon atom ( $\text{C}=\text{CCCC}$ ) in 1-pentene. Another important formation channel is through ring-opening of the cyclopentyl radical which can be generated from  $\dot{\text{H}}$  atom addition to cyclopentene or H-atom abstraction from cyclopentane. A study of the fate of 1,5- $\dot{\text{C}}_5\text{H}_9$  radicals is important in understanding the combustion of pentadiene isomers, pentene isomers and cyclopentane.

The PES for 1,5- $\dot{\text{C}}_5\text{H}_9$  radicals is shown in Fig. 2.25(a). There are four isomerization reactions, (1) a 1,5-H shift to form 1,1- $\dot{\text{C}}_5\text{H}_9$ , (2) a 2,5-H shift to form 1,2- $\dot{\text{C}}_5\text{H}_9$ , (3) a 3,5-H shift to form 1,3- $\dot{\text{C}}_5\text{H}_9$ , (4) and a 4,5-H shift to form 1,4- $\dot{\text{C}}_5\text{H}_9$ . The reaction enthalpies depend

on the product radical type, with exothermicities decreasing with the order of allylic (1,3- $\dot{C}_5H_9$ ), secondary (1,4- $\dot{C}_5H_9$ ), secondary vinylic (1,2- $\dot{C}_5H_9$ ) and primary vinylic (1,1- $\dot{C}_5H_9$ ) radicals. A 1,5-H shift to form 1,1- $\dot{C}_5H_9$  radicals via a 6-MR TS has the lowest energy barrier of 21.6 kcal mol<sup>-1</sup> compared to the formation of 1,4- $\dot{C}_5H_9$  radicals via a 3-MR TS whose barrier is 38.5 kcal mol<sup>-1</sup>. Comparisons of high-pressure limiting rate constants in Fig. 2.25(b) show that the production of 1,1- $\dot{C}_5H_9$  radicals is faster than for the other three H-shift reactions at temperatures below 1400 K, and then it is overtaken by the formation of 1,4- $\dot{C}_5H_9$  radicals at higher temperatures.

The 1,5- $\dot{C}_5H_9$  radical can undergo an endo-cycloaddition to form cyclopentyl (W15) or an exo-cycloaddition reaction to form methyldene-cyclobutyl (W19). The endo-cycloaddition reaction forming cyclopentyl is 20.9 kcal mol<sup>-1</sup> more exothermic than the exo-cycloaddition reaction forming methyldene-cyclobutyl radicals, and its energy barrier of 17.8 kcal mol<sup>-1</sup> is 0.4 kcal mol<sup>-1</sup> higher than that for the exo-cycloaddition reaction. Similar to the sec-ethyl-cyclopropanyl (W6) radical generated from the 2,5- $\dot{C}_5H_9$  radical via exo-cyclisation depicted in Fig. 2.15, the subsequent reactions of methyldene-cyclobutyl radicals have much higher energy barriers compared to the ring-opening reaction back to 1,5- $\dot{C}_5H_9$  radicals. Due to the lack of a low energy exit channel, the exo-cyclisation cannot contribute significantly to the consumption of 1,5- $\dot{C}_5H_9$  radicals and the endo-cyclisation forming cyclopentyl radicals is more important.

1,5- $\dot{C}_5H_9$  radicals can also undergo C–C  $\beta$ -scission reactions to form allyl + ethylene and C–H  $\beta$ -scissions to form 1,4-pentadiene +  $\dot{H}$ . Allyl and ethylene are more stable than 1,4-pentadiene +  $\dot{H}$  by 24 kcal mol<sup>-1</sup>, with C–C  $\beta$ -scission being 24.8 kcal mol<sup>-1</sup> lower in energy compared to C–H  $\beta$ -scission, and the energy barrier is also 14.4 kcal mol<sup>-1</sup> lower. Hence allyl + ethylene will be the dominant  $\beta$ -scission products from 1,5- $\dot{C}_5H_9$  radicals.

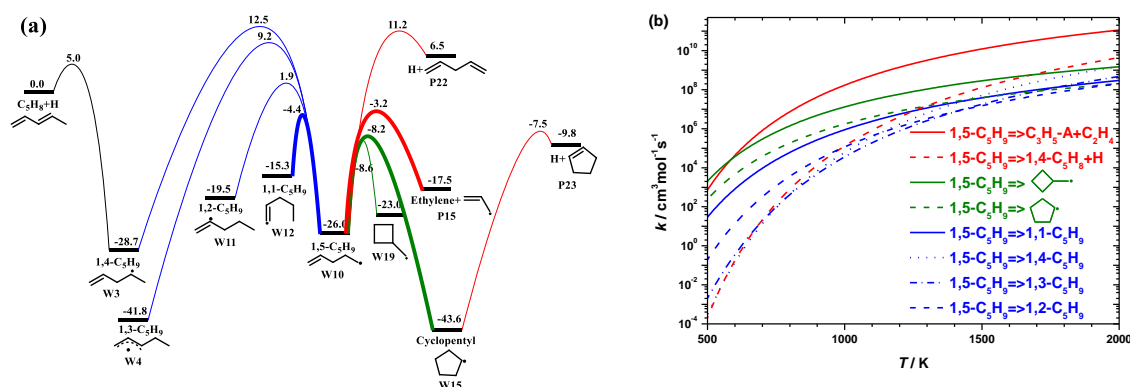


**Fig. 2.25** (a) PES for the isomerization and decomposition reactions of 1,5- $\dot{C}_5H_9$  radicals (kcal mol<sup>-1</sup>), (b) Comparison of the high-pressure limiting rate constants for subsequent

reactions of 1,5- $\dot{C}_5H_9$  radicals.

The high-pressure limiting rate constant comparisons for related reactions of the 1,5- $\dot{C}_5H_9$  radical is shown in Fig. 2.25(b). The importance of the C–C  $\beta$ -scission forming allyl + ethylene is confirmed, especially at high temperature with  $k_\infty$  over an order of magnitude faster than the other channels. The cyclopentyl radical can undergo a  $\beta$ -scission reaction to form cyclopentene and a hydrogen atom (P23) with an energy barrier of 36.1 kcal mol<sup>-1</sup>. The ring-opening reaction of a cyclopentyl radical to form 1,5- $\dot{C}_5H_9$  radical is about 17 kcal mol<sup>-1</sup> less endothermic than that for the C–H  $\beta$ -scission reaction, and the energy barrier is 0.7 kcal mol<sup>-1</sup> lower for the former. Since the branching ratio for cyclopentyl decomposition is very important in cyclopentene and cyclopentane reaction schemes, the high-pressure limiting and pressure-dependent rate constants of cyclopentyl decomposition is calculated and compared with literature data in greater detail in Chapter 3.

### 3.3.3 PES and kinetic study of $\dot{C}_5H_9$ radicals formed through ring-closing/opening reactions

#### 3.3.3.1 PES for ring-structured $\dot{C}_5H_9$ radicals

There are 12  $\dot{C}_5H_9$  radicals formed from ring-closing/opening reactions on the  $\dot{C}_5H_9$  PES in this study, 11 of which are ring-structured radicals. The 5-MR cyclopentyl radical has been discussed in the previous section. The six 3-MR  $\dot{C}_5H_9$  radicals can be divided into two groups, (i) methyl-substituted radicals including 1,2-dimethyl-3-cyclopropyl (W5), 1-methylidene-cyclopropylmethyl (W13), 1,2-dimethyl-1-cyclopropyl (W20) which have two substituents attached to a three-membered ring, (ii) ethyl-substituted radicals including sec-ethyl-cyclopropanyl (W6), ethyl-2-cyclopropyl (W9) and ethyl-1-cyclopropyl (W21). The PESs for 3-MR and 4-MR  $\dot{C}_5H_9$  radicals are shown in Figs. 2.26 and 2.27.

For the methyl-substituted radicals, the relative energies increase as the radical site changes from the substituent (W13, -24.5 kcal mol<sup>-1</sup>) to the tertiary carbon atom (W20, -16.8 kcal mol<sup>-1</sup>) to the secondary carbon atom on the ring (W5, -13.6 kcal mol<sup>-1</sup>). Consistent with the methyl-substituted radicals, the ethyl-substituted radicals follow the same trend. In contrast to the 3-MR radicals, the methyl-1-cyclobutyl radical (W18) with the radical site on the tertiary carbon atom is the most stable 4-MR radical with a relative energy approximately 2.3 kcal mol<sup>-1</sup> lower than the other three 4-MR radicals. Methyl-2-cyclobutyl (W16) and methyl-3-cyclobutyl (W17) radicals having radical sites on the ring have similar relative energies with methylidene-cyclobutyl (W19) whose radical site is on the substituent, the energy differences among these three radicals are within 0.3 kcal mol<sup>-1</sup>. It is also noticeable

that methyl-2-cyclobutyl and methyl-3-cyclobutyl radicals have similar energies of about  $-23.0 \text{ kcal mol}^{-1}$ , indicating the equivalence of the secondary carbon atoms on the ring in 4-MR  $\dot{\text{C}}_5\text{H}_9$  radicals. Hence, the relative energies for 3-MR and 4-MR radicals follow different trends, the trend in stability for 3-MR radicals is  $S(2^\circ \text{ on the ring}) < S(3^\circ) < S(1^\circ \text{ or } 2^\circ \text{ on the substituent})$ , while that for 4-MR radicals is  $S(1^\circ \text{ on the substituent}) \approx S(2^\circ \text{ on the ring}) < S(3^\circ)$ .

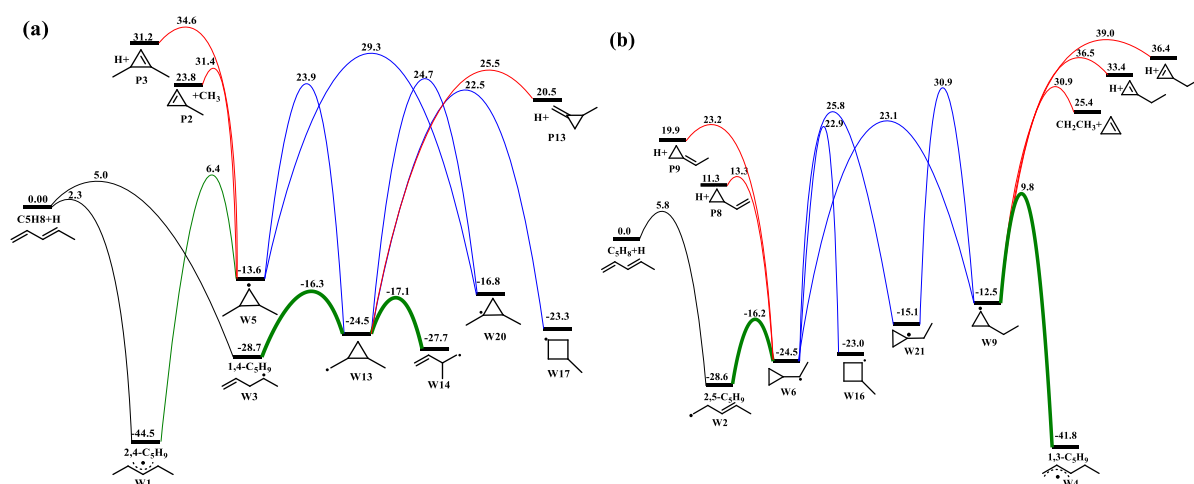


**Fig. 2.26** (a) PES for the formation and subsequent reactions of W5, W13 and W20 ( $\text{kcal mol}^{-1}$ ), (b) PES for the formation and subsequent reactions of W6, W9 and W21 ( $\text{kcal mol}^{-1}$ ).

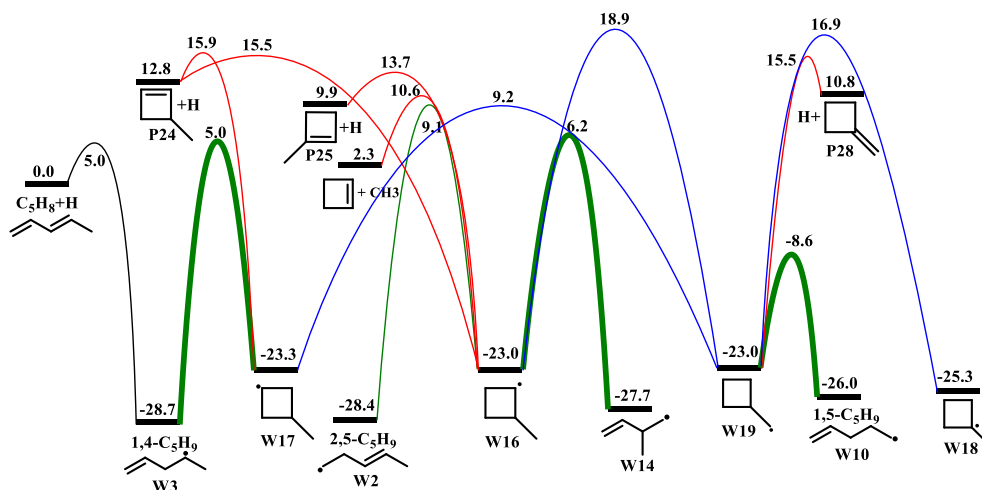


**Fig. 2.27** PES for the formation and subsequent reactions of four-membered ring  $\dot{\text{C}}_5\text{H}_9$  radicals ( $\text{kcal mol}^{-1}$ ).

### 3.3.3.2 Cyclisation reactions to form ring-structured $\dot{\text{C}}_5\text{H}_9$ radicals

As illustrated in Fig. 2.4, the cyclisation reactions can be divided into exo- and endo-cycloaddition, which can be further categorized based on the ring sizes of the TSs. Fig. 2.28(a) shows that the exo-cycloaddition reactions have barrier heights lower than

endo-cycloadditions for cyclisation via 3- and 4-MR TSs. The 5-MR endo-cycloaddition of 1,5- $\dot{C}_5H_9$  radicals forming cyclopentyl has a barrier height of 17.8 kcal mol<sup>-1</sup>, which is only 0.4 kcal mol<sup>-1</sup> higher than that of 4-MR exo-cycloaddition forming methyldene-cyclobutyl radical. The barrier heights of endo-cycloaddition reactions decrease with increasing ring size and a linear correlation is fitted to  $E_{0K} = 0.68 (\pm 0.04) \Delta_r H_{0K} + 30.53 (\pm 0.87 \text{ kcal mol}^{-1})$  with an  $R^2$  of 0.98. There is no clear Evans-Polanyi correlation found for the exo-cycloaddition reactions due to the limited number of samples.

The high-pressure limiting rate constants for these cyclisation reactions are compared in Fig. 2.28(b). We reach similar conclusions with the Evans-Polanyi plot in that (1) the  $k_\infty$  for exo-cycloaddition reactions are faster compared to those for endo-cycloaddition; (2) the 4-MR endo-cycloaddition reactions are faster than 3-MR endo-cycloaddition reactions at temperatures below 1200 K, with the trend of these two groups becoming ambiguous at higher temperatures. The findings suggest that the 3-MR and 4-MR  $\dot{C}_5H_9$  radicals formed via endo-cycloaddition reactions are unlikely to be formed and can be neglected; (3) the 5-MR endo-cycloaddition reaction forming cyclopentyl (W15) has a  $k_\infty$  similar to those for 4-MR exo-cycloaddition which suggests the importance of the 5-MR cycloaddition reaction. Hence, the most important cyclisation reactions of  $\dot{C}_5H_9$  radicals are exo-cyclisation and 5-MR endo-cyclisation reactions.

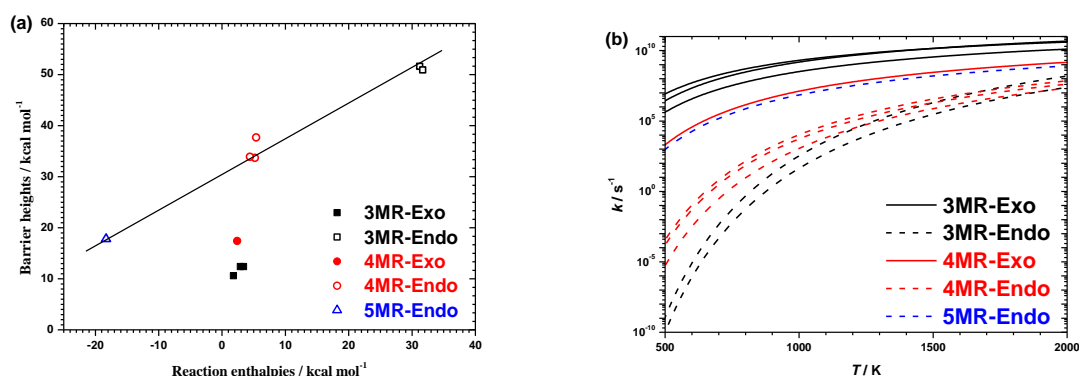


**Fig. 2.28** (a) Evans-Polanyi relationships for the exo- and endo-cycloaddition reactions. (b) High-pressure limiting rate constant comparisons for cyclisation reactions forming cyclic  $\dot{C}_5H_9$  radicals.

**Table 2.9** Calculated heats of reactions and energy heights (kcal mol<sup>-1</sup>) at 0 K for the cycloaddition reactions.

	Reactant		Product	Cycloaddition type		Ring size	$\Delta_r H_{0K}$	$E_{0K}$
1	3-methyl-1-buten-4-yl	W14	1-methylidene-cyclopropylmethyl	W13	Exo	3	2.3	10.6
2	1,4- $\dot{C}_5H_9$	W3	1-methylidene-cyclopropylmethyl	W13	Exo	3	3.4	12.4
3	2,5- $\dot{C}_5H_9$	W2	sec-ethyl-cyclopropanyl	W6	Exo	3	4.0	12.4
4	1,3- $\dot{C}_5H_9$	W4	ethyl-2-cyclopropyl	W9	Endo	3	30.5	51.6
5	2,4- $\dot{C}_5H_9$	W1	1,2-dimethyl-3-cyclopropyl	W5	Endo	3	32.1	50.9
6	1,5- $\dot{C}_5H_9$	W10	methylidene-cyclobutyl	W19	Exo	4	3.2	17.4
7	3-methyl-1-buten-4-yl	W14	methyl-2-cyclobutyl	W16	Endo	4	5.2	33.9
8	1,4- $\dot{C}_5H_9$	W3	methyl-3-cyclobutyl	W17	Endo	4	5.9	33.7
9	2,5- $\dot{C}_5H_9$	W2	methyl-2-cyclobutyl	W16	Endo	4	6.1	37.7
10	1,5- $\dot{C}_5H_9$	W10	Cyclopentyl	W15	Endo	5	-17.2	17.8

### 3.3.3.3 Isomerisation reactions of cyclic $\dot{C}_5H_9$ radicals

The reaction enthalpies and energy barriers for reactions relating to cyclic  $\dot{C}_5H_9$  radicals are calculated and divided into three groups based on reaction classes, namely isomerisation, ring-opening and  $\beta$ -scission reactions. For isomerisation reactions, the heats of reaction and corresponding energy barriers are listed in Table 2.10 according to the order of ring size and heat of reaction. The primary and secondary carbon atoms on the substituents are abbreviated as S1° and S2° to distinguish from the 2° carbon atoms on the ring. For simplicity and clarity, the isomerisation reaction via a 3-MR TS is defined as a 1,2-H shift reaction, and similar naming methods are applied for isomerisation reactions via 4- and 5-MR TSs. In addition, the transformation between 3-MR and 4-MR  $\dot{C}_5H_9$  radicals can occur through ring expansion and ring contraction reactions when the ring-opening and ring-closing happen at the same time. For example, the 3-MR sec-ethyl-cyclopropanyl (W6) radical can transform to the 4-MR methyl-2-cyclobutyl (W16) radical via ring expansion; and the 3-MR 1-methylidene-cyclopropylmethyl (W13) radical can transform to the 4-MR methyl-3-cyclobutyl (W17) radical.

Evans-Polanyi correlations for these isomerisation reactions are plotted in Fig. 2.29 which shows the obvious preference for 1,4-H shift reactions via 5-MR TSs. The barrier heights for 1,4-H shifts is at least 7.0 kcal mol<sup>-1</sup> lower than 1,2- and 1,3-H shifts with similar heats of reaction. The general trend for barrier heights of 1,2- and 1,3-H shifts is that they increase as the heats of reaction increases. What stands out in 1,2-H shifts are methylidene-cyclobutyl (W19, S1°)  $\rightleftharpoons$  methyl-1-cyclobutyl (W18, 3°) whose Evans-Polanyi

correlation seems to lie on the same trend with 1,3-H shifts and are marked as red open symbols. In comparison with other  $3^\circ \rightleftharpoons S1^\circ$  reaction (e.g. 1,2-dimethyl-1-cyclopropyl, W20  $\rightleftharpoons$  1-methylidene-cyclopropylmethyl, W13), the difference for barrier heights of the forward reaction is  $0.7 \text{ kcal mol}^{-1}$  while the difference for the reaction enthalpies is  $10.4 \text{ kcal mol}^{-1}$ . This is possibly due to the different stability trend for 3-MR and 4-MR radicals, when the stability trend for 3-MR radicals is  $S(3^\circ) < S(S1^\circ)$  and the trend is opposite for 4-MR radicals.

The correlation equation for 1,2-H shifts excluding W18  $\rightleftharpoons$  W19 is fitted to  $E_{0K} = 0.48 (\pm 0.03) * \Delta_r H_{0K} + 45.04 (\pm 0.19 \text{ kcal mol}^{-1})$  with an  $R^2$  of 0.98. The correlation equation for 1,3-H shifts (including W18  $\rightleftharpoons$  W19) is fitted to  $E_{0K} = 0.48 (\pm 0.04) * \Delta_r H_{0K} + 41.88 (\pm 0.29 \text{ kcal mol}^{-1})$  with an  $R^2$  of 0.97. These two equations have similar slopes, but the intercept for 1,2-H shifts is  $\sim 3.2 \text{ kcal mol}^{-1}$  larger which means that the barrier heights for 1,2-H shift reactions are expected to be  $\sim 3.2 \text{ kcal mol}^{-1}$  higher than for 1,3-H shift reactions with similar heats of reaction. The ring expansion and contraction reactions also have an Evans-Polanyi correlation of  $E_{0K} = 0.29 (\pm 0.06) * \Delta_r H_{0K} + 46.53 (\pm 0.13 \text{ kcal mol}^{-1})$  with an  $R^2$  of 0.90. Taken together, for isomerisation reactions with similar heats of reaction, the barrier heights follow the trend: 1,4-H shift < 1,3-H shift < 1,2-H shift < ring-expansion/contraction.

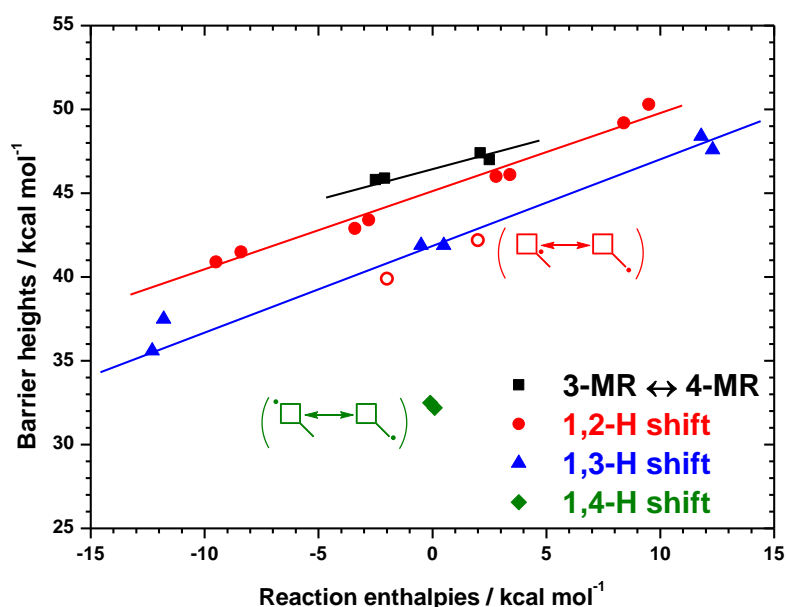


**Fig. 2.29** Evans-Polanyi relationships at 0 K for the isomerisation reactions of cyclic  $\dot{C}_5H_9$  radicals.

**Table 2.10** Calculated heats of reactions and barrier heights (kcal mol<sup>-1</sup>) at 0 K for the isomerisation reactions of cyclic  $\dot{C}_5H_9$  radicals.

	Reactant		Product		Radical site	Ring size	$\Delta_r H_{0K}$	$E_{0K}$
1	Ethyl-1-cyclopropyl	W21	Sec-ethyl-cycloprop anyl	W6	3°→S2°	3	-9.5	40.9
2	1,2-dimethyl-1-cycl opropyl	W20	1-methylidene-cyclo propylmethyl	W13	3°→S1°	3	-8.4	41.5
3	1,2-dimethyl-3-cycl opropyl	W5	1,2-dimethyl-1-cycl opropyl	W20	2°→3°	3	-3.4	42.9
4	Ethyl-2-cyclopropyl	W9	Ethyl-1-cyclopropyl	W21	2°→3°	3	-2.8	43.4
5	Methylidene-cyclob utyl	W19	Methyl-1-cyclobutyl	W18	S1°→3°	3	-2.0	39.9
6	Methyl-1-cyclobutyl	W18	Methylidene-cyclob utyl	W19	3°→S1°	3	2.0	42.2
7	Ethyl-1-cyclopropyl	W21	Ethyl-2-cyclopropyl	W9	3°→2°	3	2.8	46.0
8	1,2-dimethyl-1-cycl opropyl	W20	1,2-dimethyl-3-cycl opropyl	W5	3°→2°	3	3.4	46.1
9	1-methylidene-cyclo propylmethyl	W13	1,2-dimethyl-1-cycl opropyl	W20	S1°→3°	3	8.4	49.2
10	Sec-ethyl-cycloprop anyl	W6	Ethyl-1-cyclopropyl	W21	S2°→3°	3	9.5	50.3
11	Ethyl-2-cyclopropyl	W9	Sec-ethyl-cycloprop anyl	W6	2°→S2°	4	-12.3	35.6
12	1,2-dimethyl-3-cycl opropyl	W5	1-methylidene-Cycl opropylmethyl	W13	2°→S1°	4	-11.8	37.5
13	Methyl-2-cyclobutyl	W16	Methylidene-cyclob utyl	W19	2°→S1°	4	-0.5	41.9
14	Methylidene-cyclob utyl	W19	Methyl-2-cyclobutyl	W16	S1°→2°	4	0.5	41.9
15	1-methylidene-cyclo propylmethyl	W13	1,2-dimethyl-3-cycl opropyl	W5	S1°→2°	4	11.8	48.4
16	Sec-ethyl-cycloprop anyl	W6	Ethyl-2-cyclopropyl	W9	S2°→2°	4	12.3	47.6
17	Methyl-3-cyclobutyl	W17	Methylidene-cyclob utyl	W19	2°→S1°	5	-0.1	32.5
18	Methylidene-cyclob utyl	W19	Methyl-3-cyclobutyl	W17	S1°→2°	5	0.1	32.2
19	Methyl-3-cyclobutyl	W17	1-methylidene-cyclo propylmethyl	W13	2°→S1°	4→3	-2.5	45.8
20	Methyl-2-cyclobutyl	W16	Sec-ethyl-cycloprop anyl	W6	2°→S2°	4→3	-2.1	45.9
21	Sec-ethyl-cycloprop anyl	W6	Methyl-2-cyclobutyl	W16	S2°→2°	3→4	2.1	47.4
22	1-methylidene-cyclo propylmethyl	W13	Methyl-3-cyclobutyl	W17	S1°→2°	3→4	2.5	47.0

### 3.3.3.4 $\beta$ -scission reactions of ring-structured $\dot{C}_5H_9$ radicals

The cyclic  $\dot{C}_5H_9$  radicals can undergo C–H  $\beta$ -scission reactions to form cyclic  $C_5H_8$  and  $\dot{H}$  atoms, and C–C  $\beta$ -scission reactions to form cyclic  $C_4H_6$  isomers +  $\dot{C}H_3$  and/or cyclic  $C_3H_4$  isomers +  $\dot{C}_2H_5$ . The heats of reaction and barrier heights for these  $\beta$ -scission reactions are listed in Table 2.11 and are plotted in Fig. 2.30. The general trend for all of the  $\beta$ -scission

reactions is the increase in barrier heights with increasing heats of reaction. The Evans-Polanyi correlation for C–C  $\beta$ -scission reactions is fitted to  $E_{0K} = 0.82 (\pm 0.10) * \Delta_r H_{0K} + 12.78 (\pm 3.49 \text{ kcal mol}^{-1})$  with an  $R^2$  of 0.97, and the correlation is  $E_{0K} = 1.00 (\pm 0.05) * \Delta_r H_{0K} + 3.02 (\pm 2.03 \text{ kcal mol}^{-1})$  with an  $R^2$  of 0.98 for C–H  $\beta$ -scission reactions. The two correlations have a cross point at  $\Delta_r H_{0K} \approx 60 \text{ kcal mol}^{-1}$  which suggests that, for C–C and C–H  $\beta$ -scission with similar reaction enthalpies which are under  $60 \text{ kcal mol}^{-1}$ , C–C  $\beta$ -scission of cyclic  $\dot{C}_5H_9$  radicals is preferred over C–H  $\beta$ -scission reactions.

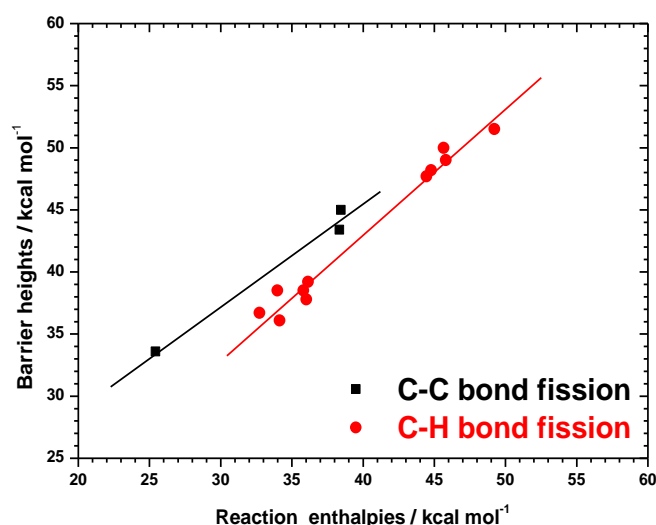


**Fig. 2.30** Evans-Polanyi relationships for C–C and C–H bond breaking reactions of cyclic  $\dot{C}_5H_9$  radicals.

**Table 2.11** Calculated heats of reactions and barrier heights ( $\text{kcal mol}^{-1}$ ) at 0 K for the  $\beta$ -scission reactions of cyclic  $\dot{C}_5H_9$  radicals.

	Reactant		Product		Bond fission	$\Delta_r H_0$ K	$E_{0K}$
1	Methyl-2-cyclobutyl	W16	Cyclobutene + methyl	P27	C–C	25.4	33.6
2	Ethyl-2-cyclopropyl	W9	Cyclopropene+ ethyl	P19	C–C	38.3	43.4
3	1,2-dimethyl-3-cyclopropyl	W5	3-methyl-cyclopropene+ methyl	P2	C–C	38.5	45.0
4	Methyl-2-cyclobutyl	W16	1-methylcyclobutene+ $\dot{H}$	P25	C–H	32.7	36.7
5	Methylidene-cyclobutyl	W19	Methylidenecyclobutane + $\dot{H}$	P28	C–H	34.0	38.5
6	Cyclopentyl	W15	Cyclopentene + $\dot{H}$	P23	C–H	34.1	36.1
7	Methyl-2-cyclobutyl	W16	3-methylcyclobutene+ $\dot{H}$	P24	C–H	35.8	38.5
8	Methyl-3-cyclobutyl	W17	3-methylcyclobutene+ $\dot{H}$	P24	C–H	36.1	39.2
9	Sec-ethyl-cyclopropanyl	W6	Ethenyl-cyclopropane+ $\dot{H}$	P8	C–H	36.0	37.8
10	Sec-ethyl-cyclopropanyl	W6	Ethylidene-cyclopropane+ $\dot{H}$	P9	C–H	44.5	47.7
11	1,2-dimethyl-3-cyclopropyl	W5	1,3-dimethyl-cyclopropene+ $\dot{H}$	P3	C–H	44.8	48.2
12	1-methylidene-cyclopropylmethyl	W13	1-methylidene-2-methyl-cyclopropane+ $\dot{H}$	P13	C–H	45.7	50.0
13	Ethyl-2-cyclopropyl	W9	1-ethyl-cyclopropene+ $\dot{H}$	P17	C–H	45.8	49.0
14	Ethyl-2-cyclopropyl	W9	3-ethyl-cyclopropene+ $\dot{H}$	P18	C–H	49.2	51.5

<sup>a</sup> The heats of formation at 0 K for C<sub>0</sub>–C<sub>4</sub> species are from the ATcT database [55], and Li and co-worker's calculations [8].

### 3.4 The energy barrier and rate constant trend analysis for different reaction classes

#### 3.4.1 Isomerisation reactions of linear alkenyl radicals

The forty isomerisation reactions of linear  $\dot{C}_5H_9$  radicals are classified into 1,2-, 1,3-, 1,4- and 1,5-H shift reactions and these four reaction classes are further divided into 18 reaction sub-classes which are listed in Table 2.12 depending on the types of the reactants and products. These can be classified into six types, 1°, 2°, 1°a, 2°a, 1°v and 2°v  $\dot{C}_5H_9$  radicals. For each type of  $\dot{C}_5H_9$  radical, the barrier heights of 1,5-H shifts via 6-MR TSs are consistently lower than those for 1,4-H shifts via 5-MR TSs, and the barrier heights of 1,4-H shift reactions are always lower than those for 1,3-H shifts via 4-MR TSs. However, there is no clear trend found for barrier heights involving 1,2- and 1,3-H shifts. Hence, for H-shift reactions of each  $\dot{C}_5H_9$  radical, the barrier height follows the trend of  $E_{0K}(1,5\text{-H shift}) < E_{0K}(1,4\text{-H shift}) < E_{0K}(1,3\text{-H shift})$  and/or  $E_{0K}(1,2\text{-H shift})$ . This conclusion is consistent with the general rule found for alkyl radicals in the literature [14, 82-87], in that 1,4- to 1,6-H shift reactions are favoured over the 1,2- and 1,3-H shift reactions.

The relationship between heats of reaction and barrier heights for H-shift reactions of C<sub>5</sub> alkenyl radicals are shown in Fig. 2.31. From the Evans-Polanyi plot, the 1,2- and 1,3-H shifts have the highest ring strain energies and there is no obvious difference between 1,2- and 1,3-H shift reactions excluding six reactions surrounded by the black-dotted circle in Fig. 2.31. The 1,2- and 1,3-H shift from a vinylic alkenyl radical to an allylic radical tends to have a higher ring strain energy compared to the other H-shift reactions. For instance, the 1,2- $\dot{C}_5H_9$  radical (2°v, W11) can isomerize to 1,3- $\dot{C}_5H_9$  (1°a, W4) and 1,1- $\dot{C}_5H_9$  radical (1°v, W12) via 1,2-H shift reactions. The heat of reaction for W2  $\rightleftharpoons$  W4 is 27.2 kcal mol<sup>-1</sup> smaller than for W2  $\rightleftharpoons$  W12, but the energy barrier difference is only 5.4 kcal mol<sup>-1</sup>. This is mainly due to the big difference in heats of reaction of the vinylic and allylic alkenyl radicals. Hence, the relationship between energy barriers and heats of reaction for vinylic  $\dot{C}_5H_9$  radical  $\rightleftharpoons$  allylic  $\dot{C}_5H_9$  radical is fitted to  $E_{0K} = 0.68 (\pm 0.08) * \Delta_r H_{0K} + 57.58 (\pm 1.78 \text{ kcal mol}^{-1})$  with an  $R^2$  of 0.97 for a 1,2-H shift and  $E_{0K} = 0.55 (\pm 0.17) * \Delta_r H_{0K} + 52.50 (\pm 3.97 \text{ kcal mol}^{-1})$  with an  $R^2$  of 0.83 for a 1,3-H shift. Thereafter, the 1,2- and 1,3-H shift reactions excluding the vinylic  $\rightleftharpoons$  allylic transformations are fitted to  $E_{0K} = 0.70 (\pm 0.06) * \Delta_r H_{0K} + 44.25 (\pm 0.82 \text{ kcal mol}^{-1})$  with an  $R^2$  of 0.88.

The 1,4-H shift reactions between allylic radicals marked in blue dot circle show different correlation with the other 1,4-H shift reactions, such as 2,4- $\dot{C}_5H_9$  ( $2^\circ a$ , W1)  $\rightleftharpoons$  1,3- $\dot{C}_5H_9$  ( $1^\circ a$ , W4). The 1,4-H shift reaction between 2,4- $\dot{C}_5H_9$  (W1) and 1,3- $\dot{C}_5H_9$  (W4) via a 5-MR TS is closer to 1,2- and 1,3-H shift on the plot. The Evans-Polanyi correlation for 1,4-H shift excluding the allylic  $\rightleftharpoons$  allylic transformation is fitted to  $E_{0K} = 0.53 (\pm 0.05) * \Delta_r H_{0K} + 23.40 (\pm 0.45 \text{ kcal mol}^{-1})$  with an  $R^2$  of 0.96.

The 1,5-H shift reactions consist of two reaction subclass,  $1^\circ \rightleftharpoons 1^\circ a$  and  $1^\circ \rightleftharpoons 1^\circ v$ . It can be clearly seen that the 1,5- $\dot{C}_5H_9$  ( $1^\circ$ , W10)  $\rightleftharpoons$  1,1- $\dot{C}_5H_9$  ( $1^\circ v$ , W12) reactions which are marked as green solid symbols have a smaller ring strain compared to 1,4-H shift reactions. However, the 2,5- $\dot{C}_5H_9$  ( $1^\circ$ , W2)  $\rightleftharpoons$  1,3- $\dot{C}_5H_9$  ( $1^\circ a$ , W4) reactions marked as green open symbols tend to show a different trend with the  $1^\circ \rightleftharpoons 1^\circ v$  reactions. More 1,5-H shift reactions of alkenyl radicals need to be studied in an attempt to explore the relationship between heats of reactions and energy barriers for those isomerization reactions.

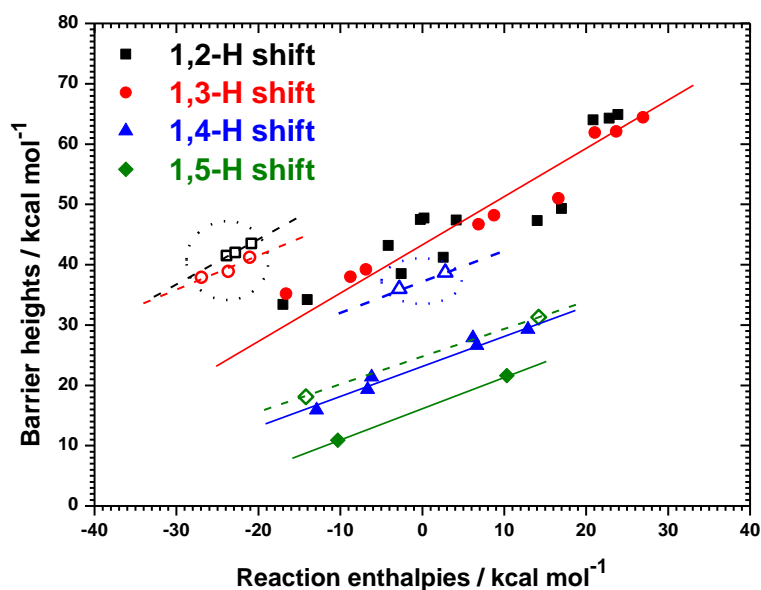


**Fig. 2.31** Evans-Polanyi relationships for the 1,2- to 1,5-H shift isomerization reactions of linear  $\dot{C}_5H_9$  radicals. Different symbols represent different subclasses,  $\blacksquare$  1,2-H shift reactions excluding vinylic radical  $\rightarrow$  allylic radical isomerisation reaction,  $\bullet$  1,3-H shift reactions excluding vinylic radical  $\rightarrow$  allylic radical isomerisation reaction,  $\blacktriangle$  1,4-H shift reactions excluding allylic radical  $\rightarrow$  allylic radical isomerisation reaction,  $\blacklozenge$  primary radical  $\rightarrow$  vinylic radical isomerisation reaction via 1,5-H shifts;  $\square$  vinylic radical  $\rightarrow$  allylic radical isomerisation reaction via 1,2-H shifts,  $\circ$  vinylic radical  $\rightarrow$  allylic radical isomerisation reaction via 1,3-H shifts,  $\triangle$  allylic radical  $\rightarrow$  allylic radical isomerisation reaction via 1,4-H shifts,  $\diamond$  primary radical  $\rightarrow$  allylic radical isomerisation reaction via 1,5-H shifts.

**Table 2.12** Calculated heats of reactions and activation energies for the H-shift reactions.

Label	Reactant		Product		Reaction type	TS Ring size	$\Delta_r H_{0K}$	$E_{0K}$
1	2,4- $\dot{C}_5H_9$	W1	2,3- $\dot{C}_5H_9$	W8	2°a→2°v	3	23.9	64.9
2	2,4- $\dot{C}_5H_9$	W1	2,5- $\dot{C}_5H_9$	W2	2°a→1°	3	17.0	49.3
3	2,4- $\dot{C}_5H_9$	W1	2,2- $\dot{C}_5H_9$	W7	2°a→2°v	4	23.7	62.1
4	2,4- $\dot{C}_5H_9$	W1	1,3- $\dot{C}_5H_9$	W4	2°a→1°a	5	2.8	38.7
5	2,5- $\dot{C}_5H_9$	W2	2,4- $\dot{C}_5H_9$	W1	1°→2°a	3	-17.0	33.4
6	2,5- $\dot{C}_5H_9$	W2	2,3- $\dot{C}_5H_9$	W8	1°→2°v	4	6.9	46.7
7	2,5- $\dot{C}_5H_9$	W2	2,2- $\dot{C}_5H_9$	W7	1°→2°v	5	6.7	26.6
8	2,5- $\dot{C}_5H_9$	W2	1,3- $\dot{C}_5H_9$	W4	1°→1°a	6	-14.2	18.1
9	1,4- $\dot{C}_5H_9$	W3	1,3- $\dot{C}_5H_9$	W4	2°→1°a	3	-14.1	34.2
10	1,4- $\dot{C}_5H_9$	W3	1,5- $\dot{C}_5H_9$	W10	2°→1°	3	2.6	41.2
11	1,4- $\dot{C}_5H_9$	W3	1,2- $\dot{C}_5H_9$	W11	2°→2°v	4	8.8	48.2
12	1,4- $\dot{C}_5H_9$	W3	1,1- $\dot{C}_5H_9$	W12	2°→1°v	5	12.9	29.3
13	1,3- $\dot{C}_5H_9$	W4	1,2- $\dot{C}_5H_9$	W11	1°a→2°v	3	22.8	64.3
14	1,3- $\dot{C}_5H_9$	W4	1,4- $\dot{C}_5H_9$	W3	1°a→2°	3	14.1	47.3
15	1,3- $\dot{C}_5H_9$	W4	2,2- $\dot{C}_5H_9$	W7	1°a→2°v	3	20.9	64.0
16	1,3- $\dot{C}_5H_9$	W4	2,3- $\dot{C}_5H_9$	W8	1°a→2°v	4	21.1	61.9
17	1,3- $\dot{C}_5H_9$	W4	1,1- $\dot{C}_5H_9$	W12	1°a→1°v	4	26.9	64.4
18	1,3- $\dot{C}_5H_9$	W4	1,5- $\dot{C}_5H_9$	W10	1°a→1°	4	16.6	51.0
19	1,3- $\dot{C}_5H_9$	W4	2,4- $\dot{C}_5H_9$	W1	1°a→2°a	5	-2.8	36.0
20	1,3- $\dot{C}_5H_9$	W4	2,5- $\dot{C}_5H_9$	W2	1°a→1°	6	14.2	31.3
21	2,2- $\dot{C}_5H_9$	W7	1,3- $\dot{C}_5H_9$	W4	2°v→1°a	3	-20.9	43.5
22	2,2- $\dot{C}_5H_9$	W7	2,3- $\dot{C}_5H_9$	W8	2°v→2°v	3	0.2	47.7
23	2,2- $\dot{C}_5H_9$	W7	2,4- $\dot{C}_5H_9$	W1	2°v→2°a	4	-23.7	38.9
24	2,2- $\dot{C}_5H_9$	W7	2,5- $\dot{C}_5H_9$	W2	2°v→1°	5	-6.7	19.3
25	2,3- $\dot{C}_5H_9$	W8	2,2- $\dot{C}_5H_9$	W7	2°v→2°v	3	-0.2	47.5
26	2,3- $\dot{C}_5H_9$	W8	2,4- $\dot{C}_5H_9$	W1	2°v→2°a	3	-23.9	41.5
27	2,3- $\dot{C}_5H_9$	W8	1,3- $\dot{C}_5H_9$	W4	2°v→1°a	4	-21.1	41.2
28	2,3- $\dot{C}_5H_9$	W8	2,5- $\dot{C}_5H_9$	W2	2°v→1°	4	-6.9	39.2
29	1,5- $\dot{C}_5H_9$	W10	1,4- $\dot{C}_5H_9$	W3	1°→2°	3	-2.6	38.5
30	1,5- $\dot{C}_5H_9$	W10	1,3- $\dot{C}_5H_9$	W4	1°→1°a	4	-16.6	35.2
31	1,5- $\dot{C}_5H_9$	W10	1,2- $\dot{C}_5H_9$	W11	1°→2°v	5	6.2	27.9
32	1,5- $\dot{C}_5H_9$	W10	1,1- $\dot{C}_5H_9$	W12	1°→1°v	6	10.3	21.6
33	1,2- $\dot{C}_5H_9$	W11	1,1- $\dot{C}_5H_9$	W12	2°v→1°v	3	4.1	47.4
34	1,2- $\dot{C}_5H_9$	W11	1,3- $\dot{C}_5H_9$	W4	2°v→1°a	3	-22.8	42.0
35	1,2- $\dot{C}_5H_9$	W11	1,4- $\dot{C}_5H_9$	W3	2°v→2°	4	-8.8	38.0
36	1,2- $\dot{C}_5H_9$	W11	1,5- $\dot{C}_5H_9$	W10	2°v→1°	5	-6.2	21.4
37	1,1- $\dot{C}_5H_9$	W12	1,2- $\dot{C}_5H_9$	W11	1°v→2°v	3	-4.1	43.2
38	1,1- $\dot{C}_5H_9$	W12	1,3- $\dot{C}_5H_9$	W4	1°v→1°a	4	-26.9	37.9
39	1,1- $\dot{C}_5H_9$	W12	1,4- $\dot{C}_5H_9$	W3	1°v→2°	5	-12.9	15.9
40	1,1- $\dot{C}_5H_9$	W12	1,5- $\dot{C}_5H_9$	W10	1°v→1°	6	-10.3	10.9

### 3.4.2 $\beta$ -scission reactions of alkenyl radicals

An Evans-Polanyi plot for  $\beta$ -scission reactions of linear  $\dot{C}_5H_9$  radicals is shown in Fig. 2.32(a). The barrier heights and heats of reactions for these reactions are listed in Table 2.13. The correlation equation is  $E_{0K} = 0.60 (\pm 0.03) * \Delta_r H_{0K} + 18.23 (\pm 0.85 \text{ kcal mol}^{-1})$  with an  $R^2$  of 0.98 for C–C bond cleavage,  $E_{0K} = 1.00 (\pm 0.03) * \Delta_r H_{0K} + 3.03 (\pm 1.00 \text{ kcal mol}^{-1})$  with an  $R^2$  of 0.99 for C–H bond cleavage. Interestingly, the energy barriers for C–H and C–C bond breaking have no clear trend for  $\beta$ -scission reactions with heats of formation (0 K) between 31 and 37 kcal mol<sup>-1</sup>, which results in the high-pressure limiting rate constants for these  $\beta$ -scission reactions become undistinguishable. Excluding these reactions C–C bond fission usually shows a lower energy barriers and heats of reaction than C–H bond fission. Hence, the high-pressure limiting rate constants have a trend of  $k_\infty(\text{C–H with } \Delta_r H_{0K} \text{ beyond } 31\text{--}37 \text{ kcal mol}^{-1}) < k_\infty(\text{C–H and C–C with } \Delta_r H_{0K} \text{ within } 31\text{--}37 \text{ kcal mol}^{-1}) < k_\infty(\text{C–C with } \Delta_r H_{0K} \text{ beyond } 31\text{--}37 \text{ kcal mol}^{-1})$ .

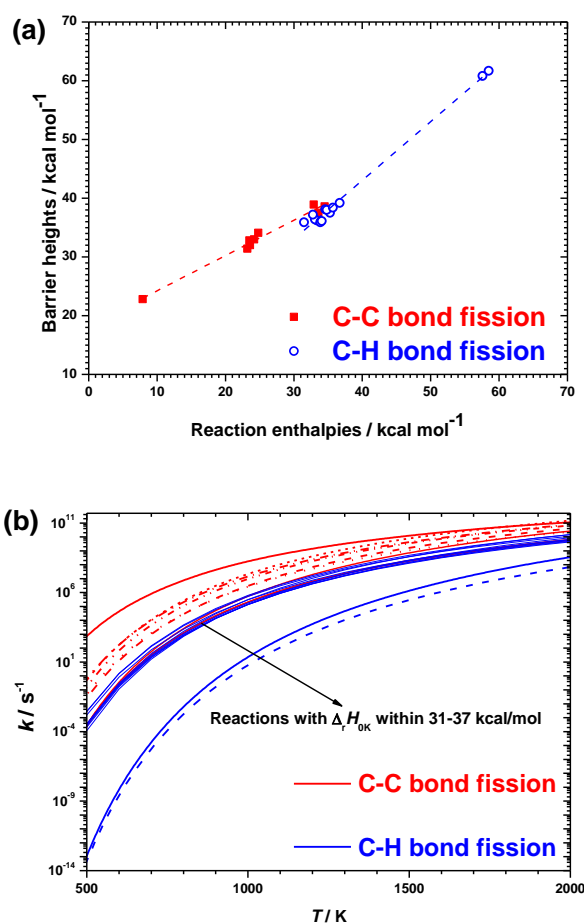


**Fig. 2.32** (a) Evans-Polanyi relationships for the C–H and C–C bond breaking reactions at 0 K, (b) High-pressure limiting rate constant comparisons for the C–H and C–C bond breaking reactions of  $\dot{C}_5H_9$  radicals.

**Table 2.13** Calculated heats of reaction and barrier heights for the  $\beta$ -scission reactions at 0 K.

Label	Reactant		Product		Bond fission	$\Delta_r H_{0K}$	$E_{0K}$
1	2,5- $\dot{C}_5H_9$	W2	$C_2H_4 + \dot{C}_3H_5$ -s	P1	C-C	34.5	38.6
2	1,4- $\dot{C}_5H_9$	W3	$\dot{C}_2H_3 + C_3H_6$	P12	C-C	33.6	37.5
3	1,3- $\dot{C}_5H_9$	W4	$1,3-C_4H_6 + \dot{C}H_3$	P14	C-C	32.9	38.9
4	2,2- $\dot{C}_5H_9$	W7	$C_3H_4-P + \dot{C}_2H_5$	P6	C-C	24.2	33.0
5	2,3- $\dot{C}_5H_9$	W8	$1-C_4H_6 + \dot{C}H_3$	P7	C-C	24.8	34.1
6	2,3- $\dot{C}_5H_9$	W8	$1,2-C_4H_6 + \dot{C}H_3$	P10	C-C	23.5	32.8
7	1,2- $\dot{C}_5H_9$	W11	$C_3H_4$ -a + $\dot{C}_2H_5$	P16	C-C	23.2	31.4
8	1,5- $\dot{C}_5H_9$	W10	$C_2H_4 + \dot{C}_3H_5$ -a	P15	C-C	7.9	22.8
9	1,1- $\dot{C}_5H_9$	W12	$C_2H_2 + \dot{C}_3H_7$	P21	C-C	23.6	32.0
10	2,4- $\dot{C}_5H_9$	W1	$2,3-C_5H_8 + \dot{H}$	P4	C-H	58.5	61.7
11	1,4- $\dot{C}_5H_9$	W3	$1,4-C_5H_8 + \dot{H}$	P22	C-H	35.3	37.5
12	1,3- $\dot{C}_5H_9$	W4	$1,2-C_5H_8 + \dot{H}$	P11	C-H	57.6	60.8
13	2,2- $\dot{C}_5H_9$	W7	$2-C_5H_8 + \dot{H}$	P5	C-H	33.4	36.2
14	2,2- $\dot{C}_5H_9$	W7	$1,2-C_5H_8 + \dot{H}$	P11	C-H	36.7	39.2
15	2,3- $\dot{C}_5H_9$	W8	$2,3-C_5H_8 + \dot{H}$	P4	C-H	34.6	38.1
16	2,3- $\dot{C}_5H_9$	W8	$2-C_5H_8 + \dot{H}$	P5	C-H	33.1	36.4
17	1,2- $\dot{C}_5H_9$	W11	$1,2-C_5H_8 + \dot{H}$	P11	C-H	34.8	38.0
18	1,2- $\dot{C}_5H_9$	W11	$1-C_5H_8 + \dot{H}$	P20	C-H	35.7	38.4
19	1,5- $\dot{C}_5H_9$	W10	$1,4-C_5H_8 + \dot{H}$	P22	C-H	32.8	37.2
20	1,1- $\dot{C}_5H_9$	W12	$1-C_5H_8 + \dot{H}$	P20	C-H	31.5	35.9

### 3.5 The important reaction channels for $\dot{H}$ atoms addition to linear 1,3-dienes

The most important products and dominant reaction pathways for  $\dot{H}$  atom addition to 1,3-pentadiene have been explored based on PES analyses and high-pressure limiting rate constant comparisons presented in the previous sections. To further understand the chemistry for  $\dot{H}$  atom addition to 1,3-dienes, the electronic energy barrier heights and high-pressure limiting rate constants of the dominant channels for  $\dot{H}$  atom addition to 1,3-butadiene [8] and 1,3-pentadiene have been compared in Figs. 2.33 and 2.34.

As shown in Fig. 2.33, it is clear that for 1,3-butadiene, the most important reaction pathway is  $\dot{H}$  atom addition to the terminal C=C bond forming the 1,3- $\dot{C}_4H_7$  resonantly-stabilized radical, followed by the isomerization reaction producing 1,4- $\dot{C}_4H_7$  which can ultimately lead to ethylene + vinyl radical which are the dominant products. Apart from the formation by isomerization reaction from 1,3- $\dot{C}_4H_7$ , the 1,4- $\dot{C}_4H_7$  radical can also be formed via  $\dot{H}$  atom addition to the central carbon atom on the double bond. It is interesting to note that similar reaction processes are also important for  $\dot{H}$  atom addition to 1,3-pentadiene, but with different barrier heights and with the dominant products being 1,3-butadiene +  $\dot{C}H_3$ .

For 1,3- $\dot{\text{C}}_4\text{H}_7$  radicals, there are no direct C–C  $\beta$ -scission reactions and the most dominant pathway is the isomerization reaction to form 1,4- $\dot{\text{C}}_4\text{H}_7$  radicals. Similarly, for  $\dot{\text{H}}$  atom addition to 1,3-pentadiene, the most favoured radical formed is 2,4- $\dot{\text{C}}_5\text{H}_9$  and it also prefers to undergo the lowest energy barrier pathway to form 1,3- $\dot{\text{C}}_5\text{H}_9$  which ultimately produces 1,3- $\text{C}_4\text{H}_6 + \dot{\text{C}}\text{H}_3$ .

A discussion of rate constant comparisons for the entrance channels of  $\dot{\text{H}}$  atom addition reactions to 1,3-butadiene and 1,3-pentadiene was presented in Section 3.2.4. The total rate constants for  $\dot{\text{H}}$  atom addition reactions to 1,3-butadiene and 1,3-pentadiene are within a factor of two at temperatures over 1000 K, where  $\dot{\text{H}}$  atom addition reactions are important for alkene oxidation. The barrier height for the isomerization reaction  $2,4\text{-}\dot{\text{C}}_5\text{H}_9 \rightarrow 1,3\text{-}\dot{\text{C}}_5\text{H}_9$  via a 5-MR TS is 9.7 kcal mol<sup>-1</sup> lower than that for  $1,3\text{-}\dot{\text{C}}_4\text{H}_7 \rightarrow 1,4\text{-}\dot{\text{C}}_4\text{H}_7$  via a 3-MR TS which results in large differences in rate constants at low temperatures (< 900 K). Due to the similarity in energy barriers from the wells to the products, the rate constants for these two  $\beta$ -scission reactions are similar at low temperatures and the difference increases to a factor of four at 2000 K. In general, the high-pressure limiting rate constants calculated in this study for the entrance channel for  $\dot{\text{H}}$  atom addition reactions and  $\beta$ -scission reactions can also act a good estimate for similar reactions associated with larger 1,3-dienes. The  $k_\infty$  for the isomerization reactions only show good convergence at temperatures above 1600 K. At low temperatures where the energy barriers play an important role, the Evans-Polanyi correlation (Section 3.4.1) for isomerization reactions among different types of alkenyl radicals can be used to estimate the energy barriers for similar reactions. This work provides 30 sub-classes (18 for isomerization reactions of linear  $\dot{\text{C}}_5\text{H}_9$  radicals, five for isomerization reactions of cyclic  $\dot{\text{C}}_5\text{H}_9$  radicals, five for cyclisation reactions and two for  $\beta$ -scission reactions) together with their barrier height comparisons, which give a good initial indication of the kinetic rate parameters for reactions involving  $\dot{\text{H}}$  atom addition to larger 1,3-dienes.

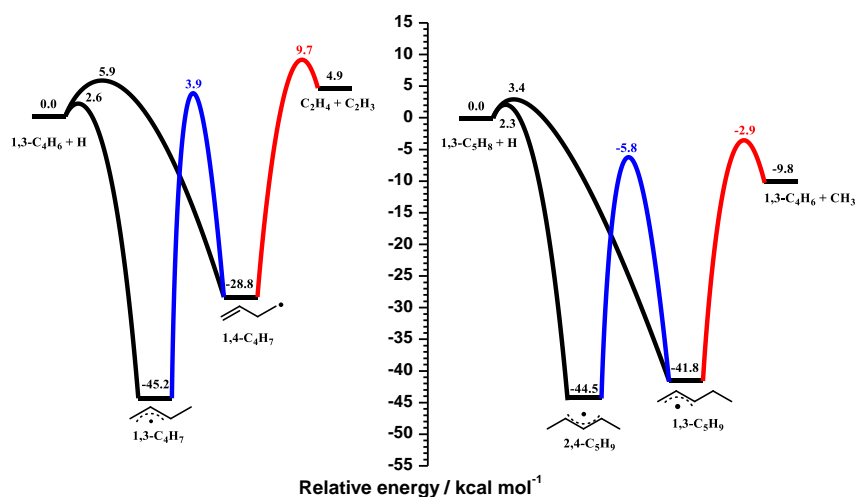


**Fig. 2.33** The important reaction channels for  $\dot{\text{H}}$  atom addition to 1,3-butadiene and 1,3-pentadiene with the energies for all species are relative to their corresponding reactants on two potential energy surfaces. The electronic energies for species on  $\dot{\text{C}}_4\text{H}_7$  PES are calculated at CCSD(T)/CBS//M06-2X/6-311++G(d,p) level of theory by Li et al. [8]. The electronic energies for species on  $\dot{\text{C}}_5\text{H}_9$  PES are calculated at CCSD(T)/CBS// $\omega$ B97X-D/aug-cc-pVTZ level of theory in this work.

Based on comparisons of the important reactions involving 1,3-butadiene +  $\dot{\text{H}}$  and 1,3-pentadiene +  $\dot{\text{H}}$ , some common conclusions can be drawn for  $\dot{\text{H}}$  atom addition to 1,3-dienes which will be helpful for the development of combustion mechanisms for larger 1,3-dienes. (1) the formation of resonantly stabilized allylic alkenyl radicals via  $\dot{\text{H}}$  atom addition to the terminal carbon atom on the C=C double bond dominates, these being  $1,3\text{-}\dot{\text{C}}_4\text{H}_7$  for 1,3-butadiene,  $2,4\text{-}\dot{\text{C}}_5\text{H}_9$  for 1,3-pentadiene,  $2,4\text{-}\dot{\text{C}}_6\text{H}_{11}$  for 1,3-hexadiene etc. (2) When the chain length is larger than  $\text{C}_5$ , the allylic alkenyl radicals so formed can produce smaller dienes and alkyl radicals through direct C-C  $\beta$ -scission reactions. (3) The important products for  $\dot{\text{H}}$  atoms addition to dienes larger than  $\text{C}_4$  are smaller dienes and alkyl radicals. For instance, the dominant products for  $1,3\text{-C}_5\text{H}_8 + \dot{\text{H}}$  and  $1,4\text{-C}_5\text{H}_8 + \dot{\text{H}}$  are  $1,3\text{-C}_4\text{H}_6 + \dot{\text{C}}\text{H}_3$  and the important products for  $1,3\text{-C}_7\text{H}_{12} + \dot{\text{H}}$  will probably be  $1,3\text{-C}_6\text{H}_{10} + \dot{\text{C}}\text{H}_3$ ,  $1,3\text{-C}_5\text{H}_8 + \dot{\text{C}}_2\text{H}_5$ , and  $1,3\text{-C}_4\text{H}_6 + \dot{\text{C}}_3\text{H}_7$ .

## 4. Conclusions

$\dot{\text{H}}$  atom addition to and H-atom abstraction reactions from 1,3-pentadiene by  $\dot{\text{H}}$  atoms have been theoretically studied. The geometry optimizations and vibrational frequency

calculations for all of the species are calculated at the  $\omega$ B97X-D/aug-cc-pVTZ level of theory, and the single point energy is calculated using the CCSD(T)/aug-cc-pVTZ level of theory with basis set corrections from MP2/aug-cc-pVXZ (where  $X = T$  and  $Q$ ). The thermochemical properties for  $C_5$  species on  $\dot{C}_5H_9$  PES are calculated using MESS and compared with available literature data resulting in good agreement. The high-pressure limiting rate constants are also calculated and can be used for any study aiming on species included on  $\dot{C}_5H_9$  PES, such as 1- and 2-pentene, and also cyclopentane and cyclopentene which relies strongly on the decomposition of cyclopentyl radicals.

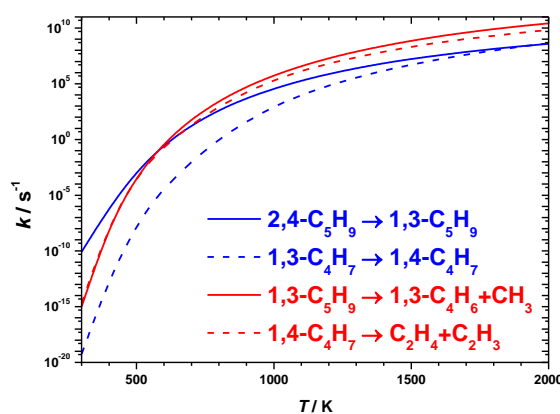


**Fig. 2.34** High-pressure limiting rate constant comparisons for important reaction pathways of 1,3-butadiene +  $\dot{H}$  [8] and 1,3-pentadiene +  $\dot{H}$ .

The entrance channels for  $\dot{H}$  atom addition reactions and H-atom abstraction reactions by  $\dot{H}$  atoms from 1,3-pentadiene are compared with  $C_2$ – $C_5$  alkynes and dienes. The  $k_\infty$  for H-atom abstraction reactions from 1,3-butadiene and 1,3-pentadiene shows a clear trend, hence the calculated results can be used to predict and validate the rate constants for H-atom abstraction reactions from larger 1,3-dienes. In addition, the Evans-Polanyi correlation for  $\dot{H}$  atom addition to  $C_3$ – $C_5$  dienes and  $C_2$ – $C_5$  alkynes are developed and can be used to predict the energy barriers for  $\dot{H}$  atom addition to larger dienes and alkynes. The  $k_\infty$  for  $\dot{H}$  atom addition to 1,3-pentadiene are also compared with the dominant channel for H-atom abstraction reactions, the result shows that at high temperatures, the rate constants for H-atom abstraction from the fifth (doubly-allylic) carbon atom on 1,3-pentadiene becomes competitive with  $\dot{H}$  atom addition.

A complex  $\dot{C}_5H_9$  PES including 63 stationary species and 88 transition states is explored. Due to the complexity of the entire PES, the  $\dot{C}_5H_9$  wells are illustrated separately from the perspective of both the  $C_5H_8$  and  $C_5H_{10}$  isomers. On the  $\dot{C}_5H_9$  PES, there are 21  $\dot{C}_5H_9$  isomers

included in this study, among which the 1,3- $\dot{C}_5H_9$  radical is the most important radical isomer which is initially formed, not only via  $\dot{H}$  atom addition reactions, but also from the isomerisation reactions of 2,4- $\dot{C}_5H_9$  and 2,5- $\dot{C}_5H_9$  radicals. Furthermore, it contributes significantly to the formation of the dominant products of 1,3-butadiene + methyl. The most favoured reaction pathway to form 1,3-butadiene + methyl is via the direct  $\beta$ -scission reaction of 1,3- $\dot{C}_5H_9$  radicals. In addition, the channel of 1,4- $\dot{C}_5H_9 \rightleftharpoons$  2-methyl-cyclopropylmethyl  $\rightleftharpoons$  3-methyl-1-buten-4-yl  $\rightleftharpoons$  methyl + 1,3-butadiene also plays a significant role in the formation of 1,3-butadiene + methyl at high temperatures.

For three reaction classes (H-shift isomerization, cyclo-addition and  $\beta$ -scission reactions) involved in this study, the influences of the TS structure and heat of reaction on the energy barrier for reaction has been studied. The Evans-Polanyi correlation for each reaction class or sub-class is developed and can be used to estimate the energy barrier where literature data is unavailable. The temperature and pressure-dependent rate constants for reactions on the  $\dot{C}_5H_9$  PES are also calculated and compared with both theoretical and experimental results in the literature which will be discussed in Chapter 3 of *this thesis*.

## Supporting Information

T1 diagnostic values; Evans-Polanyi correlation for  $\dot{H}$  atom addition to linear dienes and alkynes; high-pressure limiting rate constants in Arrhenius expression; thermochemistry data in NASA polynomial format; (PDF) input files for MESS calculations. (ZIP)

## Acknowledgements

This study is supported by Science Foundation Ireland and the China Scholarship Council (CSC). The authors want to acknowledge the financial support of Science Foundation Ireland under Grant No. 15/IA/3177, and the provision of computational resources from ICHEC under the NUI Galway shared condominium accounts. The Computational resources are provided by the Irish Centre for High-End Computing (ICHEC), under project number ngche063c, ngcom006c and ngche058c. The authors are grateful to Dr. Stephen Klippenstein for the help with MESS code study. Chong-Wen Zhou also acknowledges the support from National Science and Technology Major Project (2017-III-0004-0028) and Beihang University under the Fundamental Research Funds.

## References

- [1] S.M. Sarathy, G. Kukkadapu, M. Mehl, T. Javed, A. Ahmed, N. Naser, A. Tekawade, G. Kosiba, M. AlAbbad, E. Singh, Compositional effects on the ignition of FACE gasolines, *Combustion and Flame* 169 (2016) 171-193.
- [2] S. Davis, C. Law, Determination of and fuel structure effects on laminar flame speeds of C<sub>1</sub> to C<sub>8</sub> hydrocarbons, *Combustion Science and Technology* 140 (1998) 427-449.
- [3] M.E. Squillacote, F. Liang, Conformational thermodynamic and kinetic parameters of methyl-substituted 1, 3-butadienes, *The Journal of organic chemistry* 70 (2005) 6564-6573.
- [4] B. Atakan, A. Lamprecht, K. Kohse-Höinghaus, An experimental study of fuel-rich 1, 3-pentadiene and acetylene/propene flames, *Combustion and flame* 133 (2003) 431-440.
- [5] A. Chakir, M. Cathonnet, J. Boettner, F. Gaillard. Kinetic study of 1-butene oxidation in a jet-stirred flow reactor, *Symposium (International) on Combustion* 22 (1989), 873-881.
- [6] S. Touchard, R. Fournet, P.-A. Glaude, V. Warth, F. Battin-Leclerc, G. Vanhove, M. Ribaucour, R. Minetti, Modeling of the oxidation of large alkenes at low temperature, *Proceedings of the Combustion Institute* 30 (2005) 1073-1081.
- [7] C.-W. Zhou, Y. Li, U. Burke, C. Banyon, K.P. Somers, S. Ding, S. Khan, J.W. Hargis, T. Sikes, O. Mathieu, An experimental and chemical kinetic modeling study of 1, 3-butadiene combustion: Ignition delay time and laminar flame speed measurements, *Combustion and Flame* 197 (2018) 423-438.
- [8] Y. Li, S.J. Klippenstein, C.-W. Zhou, H.J. Curran, Theoretical Kinetics Analysis for H Atom Addition to 1,3-Butadiene and Related Reactions on the C<sub>4</sub>H<sub>7</sub> Potential Energy Surface, *The Journal of Physical Chemistry A* 121 (2017) 7433-7445.
- [9] F. Battin-Leclerc, Detailed chemical kinetic models for the low-temperature combustion of hydrocarbons with application to gasoline and diesel fuel surrogates, *Progress in Energy and Combustion Science* 34 (2008) 440-498.
- [10] F. Khaled, B.R. Giri, D. Liu, E. Assaf, C. Fittschen, A. Farooq, Insights into the Reactions of Hydroxyl Radical with Diolefins from Atmospheric to Combustion Environments, *The Journal of Physical Chemistry A*, 123 (2019), 2261-2271.
- [11] C.F. Goldsmith, H. Ismail, P.R. Abel, W.H. Green, Pressure and temperature dependence of the reaction of vinyl radical with alkenes II: Measured rates and predicted product distributions for vinyl+propene, *Proceedings of the Combustion Institute* 32 (2009) 139-148.
- [12] B. Sirjean, P.-A. Glaude, M. Ruiz-Lopez, R. Fournet, Theoretical kinetic study of thermal unimolecular decomposition of cyclic alkyl radicals, *The Journal of Physical Chemistry A* 112 (2008) 11598-11610.
- [13] K. Wang, S.M. Villano, A.M. Dean, Reactions of allylic radicals that impact molecular weight growth kinetics, *Physical Chemistry Chemical Physics* 17 (2015) 6255-6273.
- [14] K. Wang, S.M. Villano, A.M. Dean, Reactivity–structure-based rate estimation rules for alkyl radical H atom shift and alkenyl radical cycloaddition reactions, *The Journal of Physical Chemistry A* 119 (2015) 7205-7221.
- [15] L.A. Curtiss, K. Raghavachari, P.C. Redfern, V. Rassolov, J.A. Pople, Gaussian-3 (G3) theory for molecules containing first and second-row atoms, *The Journal of chemical physics* 109 (1998) 7764-7776.
- [16] J.A. Montgomery Jr, M.J. Frisch, J.W. Ochterski, G.A. Petersson, A complete basis set model chemistry. VI. Use of density functional geometries and frequencies, *The Journal of chemical physics* 110 (1999) 2822-2827.
- [17] W. Tsang, Mechanism and rate constants for the decomposition of 1-pentenyl radicals, *The Journal of Physical Chemistry A* 110 (2006) 8501-8509.
- [18] W. Tsang, J.A. Walker, Pyrolysis of 1, 7-octadiene and the kinetic and thermodynamic stability of allyl and 4-pentenyl radicals, *The Journal of Physical Chemistry* 96 (1992)

8378-8384.

- [19] J.P. Perdew, J.A. Chevary, S.H. Vosko, K.A. Jackson, M.R. Pederson, D.J. Singh, C. Fiolhais, Atoms, molecules, solids, and surfaces: Applications of the generalized gradient approximation for exchange and correlation, *Physical Review B* 46 (1992) 6671.
- [20] W.J. Hehre, R. Ditchfield, J.A. Pople, Self-consistent molecular orbital methods. XII. Further extensions of Gaussian-type basis sets for use in molecular orbital studies of organic molecules, *The Journal of Chemical Physics* 56 (1972) 2257-2261.
- [21] J.A. Kerr, M.J. Parsonage, Evaluated kinetic data on gas phase addition reactions: reactions of atoms and radicals with alkenes, alkynes and aromatic compounds, Butterworths London, 1972.
- [22] S.J. Klippenstein, R.C. Dunbar, D.M. Wardlaw, S. H. Robertson, J.A. Miller, *Variflex 2.02m*, 2010.
- [23] A.D. McNaught, A.D. McNaught, *Compendium of chemical terminology*, Blackwell Science Oxford, 1997.
- [24] D.M. Matheu, W.H. Green, J.M. Grenda, Capturing pressure-dependence in automated mechanism generation: Reactions through cycloalkyl intermediates, *International Journal of Chemical Kinetics* 35 (2003) 95-119.
- [25] W. Carter, D. Tardy, Homoallylic isomerization of 1-penten-4-yl and the critical energy for methyl+ 1,3-butadiene, *The Journal of Physical Chemistry* 78 (1974) 1245-1248.
- [26] M. Mehl, W.J. Pitz, C.K. Westbrook, H.J. Curran, Kinetic modeling of gasoline surrogate components and mixtures under engine conditions, *Proceedings of the Combustion Institute* 33 (2011) 193-200.
- [27] M.J. Al Rashidi, J.C. Mármol, C. Banyon, M.B. Sajid, M. Mehl, W.J. Pitz, S. Mohamed, A. Alfazazi, T. Lu, H.J. Curran, Cyclopentane combustion. Part II. Ignition delay measurements and mechanism validation, *Combustion and Flame* 183 (2017) 372-385.
- [28] M.J. Al Rashidi, S. Thion, C. Togbé, G. Dayma, M. Mehl, P. Dagaut, W.J. Pitz, J. Zádor, S.M. Sarathy, Elucidating reactivity regimes in cyclopentane oxidation: Jet stirred reactor experiments, computational chemistry, and kinetic modeling, *Proceedings of the Combustion Institute* 36 (2017) 469-477.
- [29] T. Gierczak, J. Gawłowski, J. Niedzielski, Mutual isomerization of cyclopentyl and 1-Penten-5-yl radicals, *International journal of chemical kinetics* 18 (1986) 623-637.
- [30] Y. Georgievskii, J.A. Miller, M.P. Burke, S.J. Klippenstein, Reformulation and solution of the master equation for multiple-well chemical reactions, *The Journal of Physical Chemistry A* 117 (2013) 12146-12154.
- [31] Y. Georgievskii, MESS, S. J. Klippenstein, MESS. 2016.3.23.
- [32] J.-D. Chai, M. Head-Gordon, Long-range corrected hybrid density functionals with damped atom-atom dispersion corrections, *Physical Chemistry Chemical Physics* 10 (2008) 6615-6620.
- [33] T.H. Dunning Jr, Gaussian basis sets for use in correlated molecular calculations. I. The atoms boron through neon and hydrogen, *The Journal of chemical physics* 90 (1989) 1007-1023.
- [34] G.W.T. M. J. Frisch, H. B. Schlegel, G. E. Scuseria, M. A. Robb, J. R. Cheeseman, G. Scalmani, V. Barone, G. A. Petersson, H. Nakatsuji, X. Li, M. Caricato, A. Marenich, J. Bloino, B. G. Janesko, R. Gomperts, B. Mennucci, H. P. Hratchian, J. V. Ortiz, A. F. Izmaylov, J. L. Sonnenberg, D. Williams-Young, F. Ding, F. Lipparini, F. Egidi, J. Goings, B. Peng, A. Petrone, T. Henderson, D. Ranasinghe, V. G. Zakrzewski, J. Gao, N. Rega, G. Zheng, W. Liang, M. Hada, M. Ehara, K. Toyota, R. Fukuda, J. Hasegawa, M. Ishida, T. Nakajima, Y. Honda, O. Kitao, H. Nakai, T. Vreven, K. Throssell, J. A. Montgomery, Jr., J. E. Peralta, F. Ogliaro, M. Bearpark, J. J. Heyd, E. Brothers, K. N. Kudin, V. N. Staroverov, T. Keith, R. Kobayashi, J. Normand, K. Raghavachari, A. Rendell, J. C. Burant, S. S. Iyengar, J. Tomasi,

- M. Cossi, J. M. Millam, M. Klene, C. Adamo, R. Cammi, J. W. Ochterski, R. L. Martin, K. Morokuma, O. Farkas, J. B. Foresman, D. J. Fox, Gaussian 09, Revision A.02, Gaussian, Inc., Wallingford CT, 2016.
- [35] M.J. Frisch, G.W. Trucks, H.B. Schlegel, G.E. Scuseria, M.A. Robb, J.R. Cheeseman, G. Scalmani, V. Barone, G.A. Petersson, H. Nakatsuji, X. Li, M. Caricato, A.V. Marenich, J. Bloino, B.G. Janesko, R. Gomperts, B. Mennucci, H.P. Hratchian, J.V. Ortiz, A.F. Izmaylov, J.L. Sonnenberg, Williams, F. Ding, F. Lipparini, F. Egidi, J. Goings, B. Peng, A. Petrone, T. Henderson, D. Ranasinghe, V.G. Zakrzewski, J. Gao, N. Rega, G. Zheng, W. Liang, M. Hada, M. Ehara, K. Toyota, R. Fukuda, J. Hasegawa, M. Ishida, T. Nakajima, Y. Honda, O. Kitao, H. Nakai, T. Vreven, K. Throssell, J.A. Montgomery Jr., J.E. Peralta, F. Ogliaro, M.J. Bearpark, J.J. Heyd, E.N. Brothers, K.N. Kudin, V.N. Staroverov, T.A. Keith, R. Kobayashi, J. Normand, K. Raghavachari, A.P. Rendell, J.C. Burant, S.S. Iyengar, J. Tomasi, M. Cossi, J.M. Millam, M. Klene, C. Adamo, R. Cammi, J.W. Ochterski, R.L. Martin, K. Morokuma, O. Farkas, J.B. Foresman, D.J. Fox, Gaussian 16 Rev. B.01, Wallingford, CT, 2016.
- [36] Y. Zhao, D.G. Truhlar, The M06 suite of density functionals for main group thermochemistry, thermochemical kinetics, noncovalent interactions, excited states, and transition elements: two new functionals and systematic testing of four M06-class functionals and 12 other functionals, *Theoretical Chemistry Accounts: Theory, Computation, and Modeling, Theoretica Chimica Acta* 120 (2008) 215-241.
- [37] R. Gerber, G. Chaban, B. Brauer, Y. Miller, *Theory and applications of computational chemistry: the first 40 years*, Elsevier: Amsterdam, (2005) 165-193.
- [38] J.A. Pople, M. Head-Gordon, K. Raghavachari, Quadratic configuration interaction. A general technique for determining electron correlation energies, *The Journal of chemical physics* 87 (1987) 5968-5975.
- [39] J.M. Martin, Ab initio total atomization energies of small molecules—towards the basis set limit, *Chemical physics letters* 259 (1996) 669-678.
- [40] S. Cagnina, A. Nicolle, T. de Bruin, Y. Georgievskii, S.J. Klippenstein, First-Principles Chemical Kinetic Modeling of Methyl trans-3-Hexenoate Epoxidation by HO<sub>2</sub>, *The Journal of Physical Chemistry A* 121 (2017) 1909-1915.
- [41] T. Lee, P.A. Taylor, Diagnostic for Determining the Quality of Single-Reference Electron Correlation Methods, *International Journal of Quantum Chemistry* 36 (1989), 199.
- [42] I. Alecu, D.G. Truhlar, Computational study of the reactions of methanol with the hydroperoxyl and methyl radicals. 1. Accurate thermochemistry and barrier heights, *The Journal of Physical Chemistry A* 115 (2011) 2811-2829.
- [43] D. Jayatilaka, T.J. Lee, Open-shell coupled-cluster theory, *The Journal of chemical physics* 98 (1993) 9734-9747.
- [44] C.F. Goldsmith, G.R. Magoon, W.H. Green, Database of small molecule thermochemistry for combustion, *The Journal of Physical Chemistry A* 116 (2012) 9033-9057.
- [45] S.R. Miller, N.E. Schultz, D.G. Truhlar, D.G. Leopold, A study of the ground and excited states of Al<sup>3</sup> and Al<sup>3-</sup>. II. Computational analysis of the 488 nm anion photoelectron spectrum and a reconsideration of the Al<sup>3</sup> bond dissociation energy, *The Journal of chemical physics* 130 (2009) 024304.
- [46] N. Lambert, N. Kaltsoyannis, S.D. Price, J. Žabka, Z. Herman, Bond-Forming Reactions of Dications with Molecules: A Computational and Experimental Study of the Mechanisms for the Formation of HCF<sup>2+</sup> from CF<sub>3</sub><sup>2+</sup> and H<sub>2</sub>, *The Journal of Physical Chemistry A* 110 (2006) 2898-2905.
- [47] J.M. Simmie, K.P. Somers, Benchmarking compound methods (CBS-QB3, CBS-APNO, G3, G4, W1BD) against the active thermochemical tables: A litmus test for cost-effective molecular formation enthalpies, *The Journal of Physical Chemistry A* 119 (2015) 7235-7246.

- [48] K.P. Somers, J.M. Simmie, Benchmarking compound methods (CBS-QB3, CBS-APNO, G3, G4, W1BD) against the active thermochemical tables: formation enthalpies of radicals, *The Journal of Physical Chemistry A* 119 (2015) 8922-8933.
- [49] M. Keçeli, S.N. Elliott, Y.-P. Li, M.S. Johnson, C. Cavallotti, Y. Georgievskii, W.H. Green, M. Pelucchi, J.M. Wozniak, A.W. Jasper, S.J. Klippenstein, Automated computational thermochemistry for butane oxidation: A prelude to predictive automated combustion kinetics, *Proceedings of the Combustion Institute* 37 (2019) 363-371.
- [50] S.J.K. Murat Keçeli, Bonnie J. McBride, Sanford Gordon Quantum Thermochemistry Calculator (QTC), 2018.
- [51] B.J. McBride, S. Gordon, Computer program for calculating and fitting thermodynamic functions, 1992.
- [52] V.V. Speybroeck, P. Vansteenkiste, D.V. Neck, M. Waroquier, Why does the uncoupled hindered rotor model work well for the thermodynamics of n-alkanes?, *Chemical Physics Letters* 402 (2005) 479-484.
- [53] C. Eckart, The penetration of a potential barrier by electrons, *Physical Review* 35 (1930) 1303.
- [54] J.M. Bland, D.G. Altman, Measuring agreement in method comparison studies, *Statistical methods in medical research* 8 (1999) 135-160.
- [55] B. Ruscic, D. Bross, Active Thermochemical Tables (ATcT) values based on ver. 1.122d of the Thermochemical Network, available at ATcT. anl. gov, 2018.
- [56] B. Ruscic, Active thermochemical tables: Sequential bond dissociation enthalpies of methane, ethane, and methanol and the related thermochemistry, *The Journal of Physical Chemistry A* 119 (2015) 7810-7837.
- [57] A. Burcat, B. Ruscic, Third millenium ideal gas and condensed phase thermochemical database for combustion (with update from active thermochemical tables), Argonne National Lab.(ANL), Argonne, IL (United States), 2005.
- [58] E. Lemmon, M. McLinden, D. Friend, P. Linstrom, W. Mallard, NIST chemistry WebBook, Nist standard reference database number 69, National Institute of Standards and Technology, Gaithersburg, (2011).
- [59] I.A. Awan, D.R. Burgess, W. Tsang, J.A. Manion, Shock tube study of the decomposition of cyclopentyl radicals, *Proceedings of the Combustion Institute* 33 (2011) 341-349.
- [60] J. Simmie, J. Sheahan, Validation of a database of formation enthalpies and of mid-level model chemistries, *The Journal of Physical Chemistry A* 120 (2016) 7370-7384.
- [61] B. Ruscic, R.E. Pinzon, M.L. Morton, G. von Laszewski, S.J. Bittner, S.G. Nijssure, K.A. Amin, M. Minkoff, A.F. Wagner, Introduction to active thermochemical tables: Several “key” enthalpies of formation revisited, *The Journal of Physical Chemistry A* 108 (2004) 9979-9997.
- [62] A.G. Baboul, L.A. Curtiss, P.C. Redfern, K. Raghavachari, Gaussian-3 theory using density functional geometries and zero-point energies, *The Journal of chemical physics* 110 (1999) 7650-7657.
- [63] A.D. Becke, Density-functional thermochemistry. III. The role of exact exchange, *The Journal of Chemical Physics* 98 (1993) 5648-5652.
- [64] B. Ruscic, Uncertainty quantification in thermochemistry, benchmarking electronic structure computations, and Active Thermochemical Tables, *International Journal of Quantum Chemistry* 114 (2014) 1097-1101.
- [65] G.L. Humphrey, R. Spitzer, Bond Hybridization in the Non-Tetrahedral Carbon Atom. The Heats of Combustion of Spiropentane and Methylcyclobutane, *The Journal of Chemical Physics* 18 (1950) 902-902.
- [66] N. Sebbar, H. Bockhorn, J.W. Bozzelli, Structures, thermochemical properties (enthalpy, entropy and heat capacity), rotation barriers, and peroxide bond energies of vinyl, allyl,

- ethynyl and phenyl hydroperoxides, *Physical Chemistry Chemical Physics* 4 (2002) 3691-3703.
- [67] F. Agapito, P.M. Nunes, B.J. Costa Cabral, R.M. Borges dos Santos, J.A. Martinho Simões, Energetics of the allyl group, *The Journal of organic chemistry* 72 (2007) 8770-8779.
- [68] J.A. Miller, S.J. Klippenstein, Dissociation of propyl radicals and other reactions on a C<sub>3</sub>H<sub>7</sub> potential, *The Journal of Physical Chemistry A* 117 (2013) 2718-2727.
- [69] M.J. Kurylo, N.C. Peterson, W. Braun, Temperature and pressure effects in the addition of H atoms to propylene, *The Journal of Chemical Physics* 54 (1971) 4662-4666.
- [70] G. Harris, J. Pitts Jr, Absolute rate constants and temperature dependencies for the gas phase reactions of H atoms with propene and the butenes in the temperature range 298 to 445 K, *The Journal of Chemical Physics* 77 (1982) 3994-3997.
- [71] T. Watanabe, T. Kyogoku, S. Tsunashima, S. Sato, S. Nagase, Kinetic Isotope Effects in the H+ C<sub>3</sub>H<sub>6</sub> → C<sub>3</sub>H<sub>7</sub> Reaction, *Bulletin of the Chemical Society of Japan* 55 (1982) 3720-3723.
- [72] J.S. Clarke, N.M. Donahue, J.H. Kroll, H.A. Rypkema, J.G. Anderson, An Experimental Method for Testing Reactivity Models: A High-Pressure Discharge- Flow Study of H+ Alkene and Haloalkene Reactions, *The Journal of Physical Chemistry A* 104 (2000) 5254-5264.
- [73] K. Oka, R. Cvetanović, Determination of rates of hydrogen atom reactions with alkenes at 298 K by a double modulation technique, *Canadian Journal of Chemistry* 57 (1979) 777-784.
- [74] Y.-i. Ishikawa, M. Yamabe, A. Noda, S. Sato, The Absolute Rate Constants of Reaction of Hydrogen Atoms with Several Olefins, *Bulletin of the Chemical Society of Japan* 51 (1978) 2488-2492.
- [75] J.A. Manion, I.A. Awan, Evaluated Kinetics of Terminal and Non-Terminal Addition of Hydrogen Atoms to 1-Alkenes: A Shock Tube Study of H+ 1-Butene, *The Journal of Physical Chemistry A* 119 (2015) 429-441.
- [76] H. Niki, E. Daby, B. Weinstock, Mass-spectrometric studies of rate constants for addition reactions of hydrogen and of deuterium atoms with olefins in a discharge-flow system at 300. deg. K, *The Journal of Physical Chemistry* 75 (1971) 1601-1610.
- [77] N.S.S.k. Nametkin, L. V.; Kalinenko, R. A. , Rate Constants of the Reactions of Hydrogen Atoms with Ethylene and Butadiene at High Temperatures, *Dokl. Chem.* 221 (1975) 851.
- [78] Y.-i. Ishikawa, K.-i. Sugawara, S. Sato, The Rate Constants for H and D-Atom Additions to O<sub>2</sub>, NO, Acetylene, and 1, 3-Butadiene, *Bulletin of the Chemical Society of Japan* 52 (1979) 3503-3506.
- [79] J.A. Miller, S.J. Klippenstein, The H+ C<sub>2</sub>H<sub>2</sub> (+ M) ⇌ C<sub>2</sub>H<sub>3</sub> (+ M) and H+ C<sub>2</sub>H<sub>2</sub> (+ M) ⇌ C<sub>2</sub>H<sub>5</sub> (+ M) reactions: Electronic structure, variational transition-state theory, and solutions to a two-dimensional master equation, *Physical Chemistry Chemical Physics* 6 (2004) 1192-1202.
- [80] J.A. Miller, J.P. Senosiain, S.J. Klippenstein, Y. Georgievskii, Reactions over multiple, interconnected potential wells: Unimolecular and bimolecular reactions on a C<sub>3</sub>H<sub>5</sub> potential, *The Journal of Physical Chemistry A* 112 (2008) 9429-9438.
- [81] J.A. Miller, S.J. Klippenstein, From the Multiple-Well Master Equation to Phenomenological Rate Coefficients: Reactions on a C<sub>3</sub>H<sub>4</sub> Potential Energy Surface, *The Journal of Physical Chemistry A* 107 (2003) 2680-2692.
- [82] A.C. Davis, J.S. Francisco, Ab initio study of hydrogen migration across n-alkyl radicals, *The Journal of Physical Chemistry A* 115 (2011) 2966-2977.
- [83] I.A. Awan, D.R. Burgess Jr, J.A. Manion, Pressure dependence and branching ratios in the decomposition of 1-pentyl radicals: shock tube experiments and master equation

modeling, *The Journal of Physical Chemistry A* 116 (2012) 2895-2910.

[84] L. Chen, W. Wang, C. Li, J. Lü, W. Wang, Thermal decomposition and isomerization of 1-heptyl radical: a computational investigation, *Theoretical Chemistry Accounts* 133 (2014) 1509.

[85] S. Dobe, T. Berces, F. Reti, F. Marta, Isomerization of n-hexyl and s-octyl radicals by 1, 5 and 1, 4 intramolecular hydrogen atom transfer reactions, *International journal of chemical kinetics* 19 (1987) 895-921.

[86] A. Miyoshi, J. Widjaja, N. Yamauchi, M. Koshi, H. Matsui, Direct investigations on the thermal unimolecular isomerization reaction of 1-pentyl radicals, *Proceedings of the Combustion Institute* 29 (2002) 1285-1293.

[87] N. Yamauchi, A. Miyoshi, K. Kosaka, M. Koshi, H. Matsui, Thermal decomposition and isomerization processes of alkyl radicals, *The Journal of Physical Chemistry A* 103 (1999) 2723-2733.

## Chapter 3

# An Ab Initio/Transition State Theory Study of the Reactions of $\dot{C}_5H_9$ Species of Relevance to 1,3-Pentadiene, Part II: Pressure Dependent Rate Constants and Implications for Combustion Modelling

Published in Journal of Physical Chemistry A 124(23) (2020) 4605–4631.

DOI: <https://doi.org/10.1021/acs.jpca.0c02244>

### Authors and Contributions

(1) Yanjin Sun

National University of Ireland, Galway

Contribution: Ab initio calculations, modelling simulations and manuscript preparation.

(2) Chong-Wen Zhou

School of Energy and Power Engineering, Beihang University

Contribution: Supervised ab initio calculations/modelling simulations and reviewed the manuscript.

(3) Kieran P. Somers

National University of Ireland, Galway

Contribution: Supervised ab initio calculations/modelling simulations and reviewed the manuscript.

(4) Henry J. Curran

National University of Ireland, Galway

Contribution: Project Management and manuscript review.

## Abstract

The temperature- and pressure-dependence of rate constants for several radical and unsaturated hydrocarbon reactions ( $1,3\text{-C}_5\text{H}_8/1,4\text{-C}_5\text{H}_8/\text{cyC}_5\text{H}_8 + \dot{\text{H}}$ ,  $\text{C}_2\text{H}_4 + \dot{\text{C}}_3\text{H}_5\text{-a}$ ,  $\text{C}_3\text{H}_6 + \dot{\text{C}}_2\text{H}_3$ ) are analysed in this paper. The abstraction reactions of these systems are also calculated and compared with available literature data.  $\dot{\text{C}}_5\text{H}_9$  radicals can be produced via  $\dot{\text{H}}$  atom addition reactions to the pentadiene isomers and cyclopentene, and also by H-atom abstraction reactions from 1- and 2-pentene and cyclopentane. Comprehensive  $\dot{\text{C}}_5\text{H}_9$  potential energy surface (PES) analyses and high-pressure limiting rate constants for related reactions have been explored in Part I of this work (*J. Phys. Chem. A* 2019, 123(22), 9019–9052). In this work, a chemical kinetic model is constructed based on the computed thermochemistry and high-pressure limiting rate constants from Part I, to further understand the chemistry of different  $\text{C}_5\text{H}_8$  molecules. The most important channels for these addition reactions are discussed in the present work based on reaction pathway analyses. The dominant reaction pathways for these five systems are combined together to generate a simplified  $\dot{\text{C}}_5\text{H}_9$  PES including nine reactants, 25 transition states (TSs) and nine products. Spin-restricted single point energies are calculated for radicals and TSs on the simplified PES at the ROCCSD(T)/aug-cc-pVTZ level of theory with basis set corrections from MP2/aug-cc-pVXZ (where  $X = \text{T}$  and  $\text{Q}$ ). Temperature- and pressure-dependent rate constants are calculated using RRKM theory with a Master Equation analysis, with restricted energies used for minima and transition states on the simplified  $\dot{\text{C}}_5\text{H}_9$  PES and unrestricted energies for other species, over a temperature range of 300–2000 K and in the pressure range 0.01–100 atm. The rate constants calculated are in good agreement with those in the literature. The chemical kinetic model is updated with pressure-dependent rate constants and is used to simulate the species concentration profiles for  $\dot{\text{H}}$  atom addition to cyclopentane and cyclopentene. Through detailed analyses and comparisons, this model can reproduce the experimental measurements of species qualitatively and quantitatively with reasonably good agreement.

## 1. Introduction

As highlighted in Part I of this study [1] (Chapter 2 of *this thesis*), olefins and dienes are important intermediates generated via heavy petroleum cracking. The reactions of  $\dot{\text{C}}_5\text{H}_9$  radicals have an important effect on the performance of a  $\text{C}_5$  combustion mechanism and may also influence the combustion chemistry of larger dienes and alkenes.  $\dot{\text{H}}$  atom addition to the pentadiene isomers and cyclopentene, allyl radical addition to ethylene, vinyl radical addition

to propene, and H-atom abstraction reactions are all studied in this work. In Part I, high-level ab initio calculations were carried out to investigate the comprehensive  $\dot{C}_5H_9$  PES upon  $\dot{H}$  atom addition to, and H-atom abstraction by  $\dot{H}$  atoms from 1,3-pentadiene. Thermochemistry for  $C_5$  species involved in the  $\dot{C}_5H_9$  PES have also been calculated using the MESS [2, 3] (Master Equation System Solver) code and compared with literature data resulting in very good agreement.

Here we present an investigation of temperature- and pressure-dependent rate constants using RRKM theory with Master Equation analysis. The aim of this work is to develop comprehensive kinetics for the title reaction for use in a detailed chemical kinetic model describing  $C_5$  species oxidation.  $\dot{H}$  atom addition reactions to the pentadiene isomers and cyclopentene have been extensively studied theoretically and literature papers describing the  $\dot{C}_5H_9$  PES have been documented in Part I of this study [1]. Moreover, the thermochemistry of the  $C_5$  species used in this study has been comprehensively validated against literature data in Part I. Here the important literature papers with kinetic calculations/estimations, and/or experimental measurements are discussed and synopsised in Table 3.1.

Based on our literature review, several features of these studies are summarized. (1) Most of the previous theoretical studies focused on reactions of radical addition to alkenes and/or the related reactions of cyclopentyl radicals; a systematic study of reactions on the  $\dot{C}_5H_9$  PES only began with Goldsmith's work [11] in 2009. In previous studies, there have been, at most, 20 minima and 48 TSs explored on the  $\dot{C}_5H_9$  PES. In addition, the electronic energies of species on the  $\dot{C}_5H_9$  PES were studied at the CBS-QB3, G3 or similar levels of theory except for the work of Al Rashidi [15] which only included high-level theory calculations for one reaction on the  $\dot{C}_5H_9$  PES. (2) With the exception of four experimental studies ( $740 < T < 1250$  K), all others were performed at temperatures below 1000 K. Seven of the fifteen experimental studies were carried out at pressures below 1 atm with the lowest pressure being 7.6 Torr (0.01 atm). As shown in Table 3.1, there are no direct measurements of 1,3-pentadiene +  $\dot{H}$  and the existing experimental studies have mainly focused on the  $C_2/C_3$ , 1-pentene, 2-pentene, cyclopentene and cyclopentane systems. Even though some of the important reactions on the  $\dot{C}_5H_9$  PES have been studied both theoretically and experimentally, a more systematic study is needed at a high-level of theory, providing thermochemistry and kinetic properties over a wide-range of temperatures and pressures, especially from the perspective of  $\dot{H}$  atom addition to dienes (1,3-pentadiene, 1,4-pentadiene, etc.).

**Table 3.1** Summary of the theoretical and experimental literature studies relevant to  $\dot{C}_5H_9$  species.

Year	Author	Reactions	$T / K$	$p$	Method	Result
<b>Theoretical studies</b>						
1991	W. Tsang[4]	$\dot{C}_2H_3 + C_3H_6 \rightarrow C_2H_4 + \dot{C}_3H_5\text{-a}$ (1) $\dot{C}_2H_3 + C_3H_6 \rightarrow 1,3\text{-}C_4H_6 + \dot{C}H_3$ (2) $\dot{C}_2H_3 + C_3H_6 \rightarrow 1,3\text{-}C_5H_8 + \dot{H}$ (3)	–	–	$k(R1)$ analogy to abstraction of $C_3H_6$ by $\dot{C}H_3$ . $k(R2)$ & $k(R3)$ estimated from Fahr and Stein's low-pressure pyrolysis reactor experiment [5] for $\dot{C}_2H_3$ addition to $C_2H_4$ and $C_2H_2$ .	$k_\infty$
2003	Matheu et al.[6]	$C_2H_4 + \dot{C}_3H_5\text{-a} \rightarrow 1,5\text{-}\dot{C}_5H_9$ $cyC_5H_8 + \dot{H} \rightarrow cy\dot{C}_5H_9$	–	High-pressure limiting (HPL)	CBS-Q	$k_\infty$
2004	Saeyns et al.[7]	$C_2H_4 + \dot{C}_3H_5\text{-a} \leftrightarrow 1,5\text{-}\dot{C}_5H_9$ $1,3\text{-}C_4H_6 + \dot{C}H_3 \leftrightarrow 1,3\text{-}\dot{C}_5H_9$ $1,3\text{-}C_4H_6 + \dot{C}H_3 \leftrightarrow 3Me\text{-}1,4\text{-}\dot{C}_4H_6^a$	0, 298, 1000	–	CBS-QB3	$E_a$
2006	W. Tsang[8]	Decomposition of 1,3- $\dot{C}_5H_9$ , 1,4- $\dot{C}_5H_9$ , 1,5- $\dot{C}_5H_9$	–	0.1, 1, 10 atm and HPL	Literature review and estimations	$E_a$ , $k_\infty$ and $k(T, p)$
2008	Sabbe et al.[9]	$1,3\text{-}\dot{C}_5H_9 \leftrightarrow 1,3\text{-}C_4H_6 + \dot{C}H_3$ $C_2H_4 + \dot{C}_3H_5\text{-a} \leftrightarrow 1,5\text{-}\dot{C}_5H_9$	300–1300	HPL	CBS-QB3//B3LYP/6-311G(d,p)	$E_a$ , $k_\infty$
2008	Sirjean et al.[10]	$cyC_5H_9 \leftrightarrow 1,5\text{-}\dot{C}_5H_9$ $cy\dot{C}_5H_9 \rightarrow cyC_5H_8 + \dot{H}$	500–2000	HPL	CBS-QB3//B3LYP/cbsb7	$E_a$ , $k_\infty$
2009	Goldsmith et	$\dot{C}_2H_3 + C_3H_6$	300–2000	1, 15, 100 and	G3 (B3PW91/6-31+G(d,p) for	• $\dot{C}_5H_9$ PES with 15 species and 48

	al.[11]			1000 Torr (0.001–1.3 atm)	hindered-rotor treatment); Variflex with RRKM/ME theory	TSs • $k(T, p)$
2011	Awan et al.[12]	$\text{cyC}_5\text{H}_8 + \dot{\text{H}} \leftrightarrow \text{cy}\dot{\text{C}}_5\text{H}_9$ $\text{cyC}_5\text{H}_9 \leftrightarrow 1,5\text{-}\dot{\text{C}}_5\text{H}_9$	700–1900	HPL	G3MP2B2	$k_\infty$
2015	Wang et al.[13, 14]	$\text{C}_2\text{H}_4 + \dot{\text{C}}_3\text{H}_5\text{-a}$	500–1800	1 atm, HPL	$\Delta H_{\text{rxn}}$ from CBS-QB3 and/or rate rules; $k(T, p)$ calculated by QRRK theory.	• $\dot{\text{C}}_5\text{H}_9$ PES with 20 species and 24 TSs • $k_\infty$ for 12 reactions and $k(T, p)$
2017	Al Rashidi et al.[15]	$\text{cy}\dot{\text{C}}_5\text{H}_9 \rightarrow \text{cyC}_5\text{H}_8 + \dot{\text{H}}$ $\text{cyC}_5\text{H}_9 \rightarrow 1,5\text{-}\dot{\text{C}}_5\text{H}_9$	300–1200	HPL	UCCSD(T)-F12b/cc-pVTZ– F12 //M06-2X/6-311++G(d,p)	$k_\infty$ calculated and $k(T, p)$ estimated based on the falloff parameters in Wang’s study[13]
2018	Manion and Awan[16]	$\text{cyC}_5\text{H}_8 + \dot{\text{H}} \leftrightarrow \text{cy}\dot{\text{C}}_5\text{H}_9$ $\text{cyC}_5\text{H}_9 \leftrightarrow 1,5\text{-}\dot{\text{C}}_5\text{H}_9$ $\text{C}_2\text{H}_4 + \dot{\text{C}}_3\text{H}_5\text{-a} \leftrightarrow 1,5\text{-}\dot{\text{C}}_5\text{H}_9$	300–2000	HPL	G3MP2B2	$k_\infty$

#### Experimental studies

1965	Gordon et al.[17]	$\text{cyC}_5\text{H}_9 \rightarrow \text{C}_2\text{H}_4 + \dot{\text{C}}_3\text{H}_5\text{-a}$	573–748	0.05–0.06 atm	Cylindrical quartz reaction cell set	$k(\text{cy}\dot{\text{C}}_5\text{H}_9 \rightarrow 1,5\text{-}\dot{\text{C}}_5\text{H}_9)$
1967	Getty et al.[18]	$\dot{\text{C}}_2\text{H}_5 + \text{C}_3\text{H}_4\text{-a}$	374–471	–	Cylindrical quartz vessel, medium-pressure mercury arc (photolysis of aldehydes to generate $\dot{\text{R}}$ )	$k(\dot{\text{C}}_2\text{H}_5 + \text{C}_3\text{H}_4\text{-a})$
1972	Watkins and Olsen[19]	$\text{C}_2\text{H}_2 + \dot{\text{C}}_3\text{H}_7$	319–405	90–480 Torr (0.1–0.6 atm)	Photolysis of the n-C <sub>3</sub> H <sub>8</sub> /C <sub>2</sub> H <sub>2</sub> mixture and measured by gas chromatography	$k(\text{C}_2\text{H}_2 + \dot{\text{C}}_3\text{H}_7)$

1975	Stein and Rabinovitch[20]	Decomposition of $\text{cy}\dot{\text{C}}_5\text{H}_9$ (generated by $\text{cyC}_5\text{H}_8 + \dot{\text{H}}$ )	300	1 atm	Conventional high vacuum Pyrex system	$E_a$
1981	Baldwin and Walker[21]	Oxidation of $\text{C}_2\text{-C}_5$ alkenes in $\text{H}_2/\text{O}_2$ mixtures	753–773	0.66 atm	Adding $\text{C}_2\text{-C}_5$ alkenes to $\text{H}_2/\text{O}_2$ mixtures in aged boric-acid-coated vessels	$k_{753\text{K}}(\text{1,3-}\dot{\text{C}}_5\text{H}_9 \leftrightarrow \text{1,3-C}_4\text{H}_6 + \dot{\text{C}}\text{H}_3)$ estimated
1986	Gierczak et al.[22]	$\text{cy}\dot{\text{C}}_5\text{H}_9 \leftrightarrow \text{1,5-}\dot{\text{C}}_5\text{H}_9$	298.15	7.6–383.2 Torr (0.01–0.5 atm)	Photolysis of $\text{H}_2\text{S-cyC}_5\text{H}_8$ and $\text{H}_2\text{S-1,4-C}_5\text{H}_8$ mixtures	$E_a$
1986	Kopinke et al.[23]	Pyrolysis of 1-pentene (isotope labelled $\text{C=CCCC}$ [14])	873	1.5–2 atm	Stainless steel reactor	The production ratio for 1,3-butadiene with/without labelled C-atoms (78 : 22 labelled)
1988	Perrin et al.[24]	Isomerization of 1- and 2-pentene	743–772	10–100 Torr (0.01–0.13 atm)	Conventional static reaction vessel with $\text{H}_2\text{S}$ -promoted	$k_{753\text{K}}(\text{1,3-}\dot{\text{C}}_5\text{H}_9 \leftrightarrow \text{1,3-C}_4\text{H}_6 + \dot{\text{C}}\text{H}_3)$
1992	W. Tsang[25]	Pyrolysis of $\text{1,7-C}_8\text{H}_{14}$ in Ar	1040–1200	2–7 atm	Single-pulse shock tube (ST)	<ul style="list-style-type: none"> <li>Product distributions relative to the initial reactant concentration</li> <li><math>k(\text{1,5-}\dot{\text{C}}_5\text{H}_9 \rightarrow \text{cyC}_5\text{H}_8 + \dot{\text{H}})/k(\text{1,5-}\dot{\text{C}}_5\text{H}_9 \rightarrow \text{C}_2\text{H}_4 + \dot{\text{C}}_3\text{H}_5\text{-a})</math> ratio derived based on the measured <math>[\text{cyC}_5\text{H}_8]/[\text{C}_2\text{H}_4]</math> ratio</li> </ul>
1995	Handford-Styring and Walker[26]	Oxidation of $\text{cyC}_5\text{H}_8$ by adding $\text{cyC}_5\text{H}_8$ to $\text{H}_2\text{-O}_2$ mixtures	580–783	0.66 atm	Cylindrical Pyrex vessel with gas chromatography/mass spectrometry	$k(\text{cy}\dot{\text{C}}_5\text{H}_9 \rightarrow \text{1,5-}\dot{\text{C}}_5\text{H}_9)$
2000	Clarke et al.[27]	$\dot{\text{H}}$ + alkenes and haloalkenes	298–370	0.067 atm	High-pressure flow system	$k(\text{cyC}_5\text{H}_8 + \dot{\text{H}} \rightarrow \text{cy}\dot{\text{C}}_5\text{H}_9)$

2009	Goldsmith et al.[11]	$\dot{C}_2H_3 + C_3H_6$	300–700	15, 25 and 100 Torr (0.02–0.13 atm)	Flow reactor + time-resolved absorption spectroscopy	The decay rate of $\dot{C}_2H_3$ was derived based on the measured [C3H6].
2011	Awan et al.[12]	Decomposition of $cy\dot{C}_5H_9$ (generated by $cyC_5H_{10} + \dot{H}$ )	950–1116	2.3–3.4 atm	ST	<ul style="list-style-type: none"> <li>Product concentrations</li> <li><math>k(1,5-\dot{C}_5H_9 \rightarrow C_2H_4 + C_3H_5-a)</math> derived from <math>[C_2H_4]/[cyC_5H_8]</math> ratio at 0.1–1000 bar and 700–1900 K</li> </ul>
2017	Al Rashidi et al.[15]	Decomposition of $cyC_5H_{10}$ ( $cyC_5H_{10}/O_2/N_2$ mixture, $\phi = 0.5-3.0$ )	740–1250	10 atm	Jet stirred reactor (JSR)	<ul style="list-style-type: none"> <li>Reactants and products concentrations</li> </ul>
2018	Manion and Awan[16]	Decomposition of $cy\dot{C}_5H_9$ (generated by $cyC_5H_8 + \dot{H}$ )	863–1167	1.6–3.7 atm	ST	<ul style="list-style-type: none"> <li>Reactant and product concentrations</li> <li><math>k(1,5-\dot{C}_5H_9 \rightarrow C_2H_4 + C_3H_5-a)</math> and <math>k_\infty(cyC_5H_8 + \dot{H} \leftrightarrow cy\dot{C}_5H_9)</math> derived from <math>[C_2H_4]/[cyC_5H_8]</math> ratio at experimental condition</li> </ul>

<sup>a</sup> 3Me-1,4- $\dot{C}_4H_6$  represents 3-methyl-1-buten-4-yl radical (W14 in this study).

In Part I we illustrated the  $\dot{C}_5H_9$  PES by discussing the reaction mechanism and kinetics of each  $\dot{C}_5H_9$  radical. For any species on the  $\dot{C}_5H_9$  PES, we are able to determine the detailed chemistry by tracing the first well ( $\dot{C}_5H_9$  isomers) which is connected to the species. In addition, the high-pressure limiting rate constants which are calculated at the UCCSD(T)/aug-cc-pVXZ level of theory ( $X = T$  and  $Q$ ) for 88 reactions on this PES are provided. For the 88 reactions studied (the forward and the reverse direction of a specific reaction is considered as one reaction), to the authors' knowledge, (1) high-pressure limiting rate constants for  $\sim 12$  reactions are available in the literature over a wide range of temperature and pressure; (2) pressure-dependent rate constants are available for  $\sim 11$  reactions; (3) enthalpy and entropy data are available for 8 of the 22  $C_5$  species while only 5 of them have existing heat capacities at temperatures in the range 300–1500 K. (4)  $\sim 12$  reactions have been implemented in combustion models (e.g. AramcoMech3.0 [28-35] and Awan and Manion's work [12, 16]).

In the current work, a chemical kinetic model describing the  $\dot{C}_5H_9$  PES is firstly developed using the high-pressure limiting rate constants for  $\dot{H}$  atom addition reactions, H-atom abstraction reactions by  $\dot{H}$  atoms and other radicals, and unimolecular decomposition reactions of related species. Thereafter, rate of production (ROP) analyses were performed using ANSYS Chemkin-Pro [36] to determine the important chemical pathways associated with 1,3-, 1,4-pentadiene, cyclopentene +  $\dot{H}$ , and vinyl + propene oxidation kinetics and a simplified  $\dot{C}_5H_9$  PES was generated, containing the important reaction channels. The SPEs for minima and TSs on the simplified PES are re-calculated at the higher, ROCCSD(T)/aug-cc-pVXZ (where  $X = T$  and  $Q$ ), level of theory. Thereafter temperature- and pressure-dependent rate constants of reactions on the complete PES are calculated using MESS, with restricted energies used for species on the simplified  $\dot{C}_5H_9$  PES and unrestricted energies for other species. Finally, a comprehensive model containing pressure-dependent rate constants with additional secondary chemistry (e.g. 1-, 2-pentene, cyclopentane, cyclopentene) was developed. This model has been used to simulate available literature data, with deviations of absolute species concentrations and product ratios of major products being within a factor of two of experimental measurements.

## 2. Computational methods

### 2.1 Theoretical methods

#### 2.1.1 Primary reactions

The theoretical methods used for quantum and thermochemistry calculations for reactions on the  $\dot{C}_5H_9$  PES are described in detail in Part I [1], and only the methods used to determine the minima on the simplified PES are described here. For free radicals with a single unpaired electron, the spin-unrestricted functions treat the variation of two sets of spatial molecular orbitals ( $\psi_i^\alpha$  and  $\psi_i^\beta$ ) as being completely independent in order to minimize the expectation value of the total energy [37]. However, the unrestricted wave functions are not Eigen functions of the spin-squared operators  $S^2$ , and thus an unrestricted wave function for a radical with one unpaired electron contains significant contamination by components of higher multiplicity such as quartets [38]. To address this problem, a spin-restricted coupled-cluster (ROCCSD(T)) method [39] is used in the SPE calculations to reduce spin contamination in the correlated wave function. With the Gaussian software used for all of the SPE calculations, the computational cost for the spin-restricted CCSD(T) calculation is found to be about 1.5 – 3.0 times more expensive than that for the spin-unrestricted CCSD(T) calculation.

In this work, the important species and TSs for the 1,3-pentadiene +  $\dot{H}$  system are identified using ROP simulations. Then, the spin-restricted SPEs for minima and TSs on the simplified  $\dot{C}_5H_9$  PES are calculated using the same equation (Eq.1) [40, 41] with spin-unrestricted SPE calculations used for the other species which is described in Part I. The relative energies of spin-unrestricted and spin-restricted calculations are compared, resulting in a difference of less than 0.6 kcal mol<sup>-1</sup> for wells and varies from 0.2 to 1.4 kcal mol<sup>-1</sup> for TSs.

$$E_{SPE} = E_{CCSD(T)/aug-cc-pVTZ} + (E_{MP2/aug-cc-pVQZ} - E_{MP2/aug-cc-pVTZ}) \quad (1)$$

The pressure-dependent rate constants are calculated using MESS which implements the one-dimensional Master Equation calculation for an arbitrary number of wells and products [2]. The single-exponential-down model  $\langle \Delta E_d \rangle = 234(T/300)^{0.88} \text{ cm}^{-1}$  used to model energy transfer is selected based on previous ab initio studies concerning C<sub>4</sub> and C<sub>5</sub> hydrocarbons [42, 43]. Rashidi and co-workers [42] used  $\langle \Delta E_d \rangle = 200(T/300)^{0.80} \text{ cm}^{-1}$  for cyclopentyl + O<sub>2</sub>, and Li and co-workers used  $\langle \Delta E_d \rangle = 200(T/300)^{0.75} \text{ cm}^{-1}$  for C<sub>4</sub>H<sub>6</sub> +  $\dot{H}$ . [43] For the parameters in this model, it is commonly suggested that the power  $n$  be approximately 0.8; the  $\Delta E_{down}^{(300)}$  ranges from 50–500 cm<sup>-1</sup> with larger species generally having higher values

[44]. Thus the parameters in this paper are close to those used in the literature for C<sub>4</sub> and C<sub>5</sub> hydrocarbons with a slightly larger  $\Delta E_{\text{down}}$ <sup>(300)</sup>.

The collision frequency used in the master equation simulation is estimated using the Lennard-Jones (L-J) parameters where  $\varepsilon$  is the well depth and  $\sigma$  is the characteristic distance [45]. In this study, the L-J parameters for  $\dot{\text{C}}_5\text{H}_9$  radicals are analogous to the parameters for C<sub>5</sub>H<sub>12</sub> calculated by Jasper and Miller [46] from full-dimensional intermolecular potentials using several methods,  $\sigma = 4.23 \text{ \AA}$ ,  $\varepsilon = 192.0 \text{ cm}^{-1}$  for  $\dot{\text{C}}_5\text{H}_9$  radicals and  $\sigma = 3.68 \text{ \AA}$ ,  $\varepsilon = 67.89 \text{ cm}^{-1}$  for N<sub>2</sub> [46] as the bath gas;  $\sigma = 4.04 \text{ \AA}$ ,  $\varepsilon = 235.0 \text{ cm}^{-1}$  for  $\dot{\text{C}}_5\text{H}_9$  radicals and  $\sigma = 3.33 \text{ \AA}$ ,  $\varepsilon = 94.87 \text{ cm}^{-1}$  for Ar [46] as the bath gas. To our knowledge, there are no high-level L-J parameters calculated for C<sub>5</sub>H<sub>10</sub> and  $\dot{\text{C}}_5\text{H}_9$  in the literature. We have carried out MESS calculations of L-J parameters for  $\dot{\text{C}}_5\text{H}_9$  based on analogy with C<sub>5</sub>H<sub>10</sub> ( $\sigma = 5.49 \text{ \AA}$ ,  $\varepsilon = 268.32 \text{ cm}^{-1}$  from AramcoMech 3.0). The maximum differences in the pressure-dependent rate constants observed were 20% at 1000 K, with no obvious differences at 2000 K. It should be noted that the L-J parameters for C<sub>5</sub>H<sub>12</sub> calculated by Jasper and Miller are  $\sigma = 4.23 \text{ \AA}$ ,  $\varepsilon = 192.0 \text{ cm}^{-1}$  in comparison with  $\sigma = 5.59 \text{ \AA}$ ,  $\varepsilon = 272.14 \text{ cm}^{-1}$  employed in AramcoMech 3.0. Hence, more studies of transport parameters need to be performed to accurately predict pressure-dependent rate constants, especially for larger alkenes and dienes.

The low-frequency torsional modes are treated as one-dimensional hindered rotors ignoring the coupling between adjacent torsional modes, and the hindrance potentials as a function of dihedral angle are calculated at the M06-2X/6-311++G(d,p) level of theory. The hindrance potentials are fitted to Fourier series, and the molecular geometries of each species are used to estimate rotational constants. Once the potential is obtained, the energy levels for the rotation are determined by solving a 1-D Schrödinger equation [47]. The energy levels from this calculation are used to calculate the partition functions as a function of temperature by direct counting for each internal rotation. Quantum mechanical tunneling corrections are included for all TSs using an asymmetrical Eckart barrier model [48]. The temperature- and pressure-dependent rate constants calculated in this study are fitted to the modified Arrhenius expression as a function of temperature and provided as Supporting Information. Moreover, there are some global keywords in the MESS input file which can influence the calculation of rate constants (e.g. Method Parameters, Energy Grid Parameters). In this work, we have selected rational levels of theory for quantum calculations and carried out tests to carefully confirm the global keywords used in our rate constant calculations.

### 2.1.2 Secondary reactions

To understand the importance of  $\dot{\text{H}}$  atom addition reactions at intermediate and high temperatures, the unimolecular decomposition reactions of 1,3-pentadiene and H-atom abstraction reactions of different reactants are calculated at lower levels of theory compared with  $\dot{\text{H}}$  atom addition reactions. The geometries and frequencies for the unimolecular decomposition products are calculated at the  $\omega\text{B97X-D/aug-cc-pVTZ}$  level of theory, and the SPEs are calculated at the  $\text{CCSD(T)/aug-cc-pVTZ}$  level of theory. The high-pressure limiting rate constants for the unimolecular decomposition reactions of 1,3-pentadiene are calculated based on the principle of microscopic reversibility (thermodynamic reversibility). This principle is widely used in kinetic modeling when the high-pressure limiting rate constants for a reaction of interest is unknown, and sensible rate constants for the reverse reaction can be inferred based on an analogy with a similar well-known chemical reaction [49]. Thereafter, pressure-dependent rate constants are calculated using Quantum-Rice-Ramsperger-Kassel (QRRK) theory with a Modified Strong Collision (MSC) approximation which is implemented in the ChemDis code [50, 51]. For H-atom abstraction reactions from 1,3-, 1,4-pentadiene, cyclopentane and cyclopentene by  $\dot{\text{H}}$  atoms, and H-atom abstraction reactions from propene by vinyl radicals, the quantum calculations are carried out at the  $\text{CCSD(T)/aug-cc-pVTZ//}\omega\text{B97X-D/aug-cc-pVTZ}$  level of theory with the basis set for SPE calculations corrected using the  $\text{MP2/aug-cc-pVQZ}$  method, with the rate constants calculated using MESS.

### 2.2 Detailed kinetic modelling

In this work, two chemical kinetic models were built. The first only consists of high-pressure limiting rate constants for  $\dot{\text{H}}$  atom addition to 1,3-pentadiene reactions, H-atom abstraction reactions by  $\dot{\text{H}}$  atoms from 1,3-, 1,4-pentadiene and cyclopentene, and unimolecular decomposition reaction of 1,3-pentadiene. The purpose of this is to identify the important reactions on the  $\dot{\text{C}}_5\text{H}_9$  PES for the 1,3-pentadiene +  $\dot{\text{H}}$  system. Thereafter, higher-level of theory SPE calculations can be applied to the important species and reactions. ANSYS Chemkin-Pro [36] is used to run ROP analyses which can provide complementary information on the direct contributions of individual reactions to species net production rates. The dilute mixture used for the ROP simulation is 0.0001% 1,3- $\text{C}_5\text{H}_8$  with 0.01% hydrogen atom in nitrogen at 1 atm and at different temperatures.

A more comprehensive model (the second model) was built by implementing our thermochemistry and kinetic results into AramcoMech 3.0 [28-35], including higher-level

RO-aug-cc-pVXZ ( $X = T$  and  $Q$ ) SPE calculations for 18 minima and 25 reactions on a simplified  $\dot{C}_5H_9$  PES. These 25 reactions are also proposed to be important for the combustion of 1- and 2-pentene, cyclopentene and cyclopentane as presented in Table 3.1 for previous experimental studies. Aiming to accurately simulate these experiments, rate constants for a series of secondary reactions have also been added to the mechanism, based on theoretical calculations, analogies to similar chemistry in AramcoMech 3.0, or from the literature. For experiments involving radical initiators and scavengers, the thermochemistry and kinetic parameters for these species have also been added to the mechanism to appropriately simulate the literature experiments. In previous experimental studies of cyclopentene +  $\dot{H}$  [16] and cyclopentane +  $\dot{H}$  [12], 1,3,5-trimethylbenzene (135TMB) was used as both a rate reference for  $\dot{H}$  atom reactions and as a radical scavenger. Hexamethylethane (HME) was used as a  $\dot{H}$  atom source for different mixtures at temperatures above 1000 K.

On the basis of the  $C_0$ – $C_4$  combustion chemistry in AramcoMech 3.0, the major updates of the  $\dot{C}_5H_9$  mechanism can be classified into five categories: (1) The calculated results from this work are updated, including thermochemistry data for  $C_5$  species, pressure-dependent rate constants for reactions on the  $\dot{C}_5H_9$  PES, H-atom abstraction reaction from 1,3-, 1,4-pentadiene, cyclopentene and cyclopentane by  $\dot{H}$  atoms, H-atom abstraction reaction from propene by vinyl radicals, and also the unimolecular decomposition of 1,3-pentadiene. (2) The related reactions for 1- and 2-pentene with hydrogen atoms and their kinetics and thermodynamics are taken from Power et al. [52]; (3) The reactions related to the  $\dot{C}_4H_7$  PES from the perspective of 1,3-butadiene +  $\dot{H}$  are updated from Li et al. [43]; (4) The thermochemistry and kinetic parameters for 135TMB, HME and their subsequent reactions are mainly from Power et al. [52], as 135TMB and HME have also been used in 1-, and 2-pentene +  $\dot{H}$  experiments by Awan et al. [53] as radical scavenger and as a  $\dot{H}$  atom source. (5) The related reactions of cyclopentene/cyclopentane decomposition from Al Rashidi et al. [15, 54] are also added. Thermochemical properties for these additional species are obtained from the literature [15, 54, 55] and/or calculated using the group additivity method incorporated in the THERM code [56].

### 3. Results and discussion

#### 3.1 Reaction pathway analysis exploring the dominant channels

The first chemical kinetic model for the  $\dot{C}_5H_9$  PES was built using high-pressure limiting rate constants for 88 reactions; including  $\dot{H}$  atom addition reactions, 14 reactions from

H-atom abstraction by  $\dot{\text{H}}$  atoms and 7 unimolecular decomposition reactions. The PES for unimolecular decomposition reactions from 1,3-pentadiene and rate constant comparisons are described in detail in Fig. B.1. The thermochemical properties for  $\text{C}_5$  species are calculated using MESS, while those for  $\text{C}_0\text{--}\text{C}_4$  species are adopted from AramcoMech 3.0. Since the unimolecular decomposition, H-atom abstraction by  $\dot{\text{H}}$  atoms and  $\dot{\text{H}}$  atom addition reactions to hydrocarbon fuels are important reaction classes at high temperatures, reaction pathway analyses are performed at 1400 K and 1800 K and 1 atm when 20% 1,3-pentadiene is consumed, as shown in Figs. 3.1 and 3.2. The important channels are marked in red.

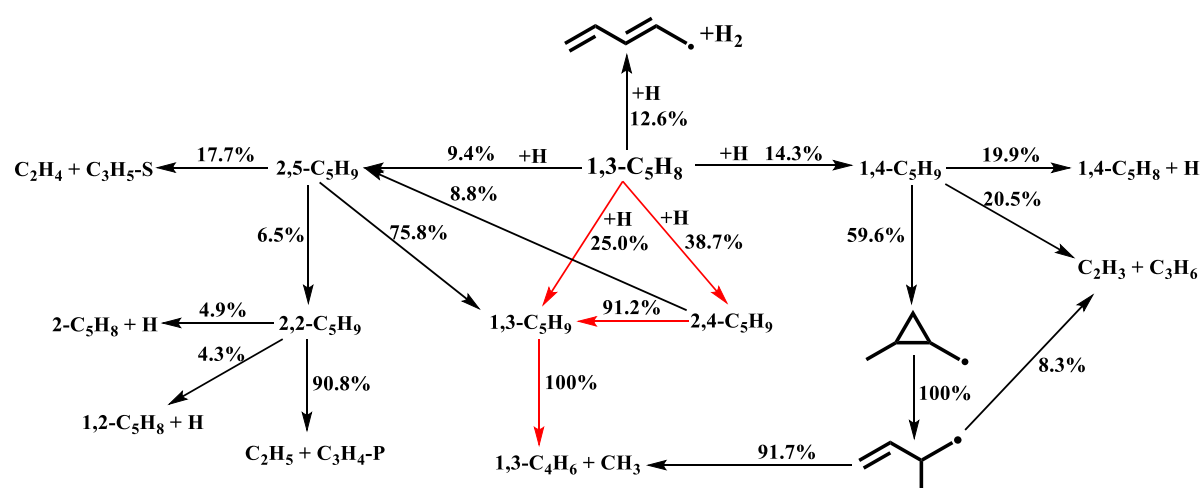


**Fig. 3.1** Flux analysis at 20% fuel consumption for 0.0001% 1,3-C<sub>5</sub>H<sub>8</sub>, 0.01%  $\dot{\text{H}}$  in N<sub>2</sub>,  $p = 1$  atm,  $T = 1400$  K.

At 1400 K, the dominant consumption pathways are the formation of 2,4- $\dot{\text{C}}_5\text{H}_9$  (38.7%) and 1,3- $\dot{\text{C}}_5\text{H}_9$  (25.0%) radicals via  $\dot{\text{H}}$  atom addition reactions. Moreover, 91.2% of 2,4- $\dot{\text{C}}_5\text{H}_9$  radicals isomerize to 1,3- $\dot{\text{C}}_5\text{H}_9$  radicals. Thus, these two isomerisation reaction channels combined with the  $\dot{\text{H}}$  atom addition entrance channel result in 60.3% of the 1,3-pentadiene reactant producing 1,3- $\dot{\text{C}}_5\text{H}_9$  radicals, which undergo  $\beta$ -scission producing 1,3-butadiene +  $\dot{\text{C}}\text{H}_3$  radicals. 14.3% of 1,3-C<sub>5</sub>H<sub>8</sub> +  $\dot{\text{H}}$  forms 1,4- $\dot{\text{C}}_5\text{H}_9$  radicals which can undergo subsequent exo-cyclisation, ring-opening and finally  $\beta$ -scission reactions to form 1,3-butadiene +  $\dot{\text{C}}\text{H}_3$  radicals. In addition, 1,4- $\dot{\text{C}}_5\text{H}_9$  radicals can also undergo C–H  $\beta$ -scission to form 1,4-pentadiene +  $\dot{\text{H}}$ , or C–C  $\beta$ -scission to form vinyl + propene which can also be formed via  $\beta$ -scission of 3-methyl-1-buten-4-yl radicals (W14). 9.4% of the reaction flux produces 2,5- $\dot{\text{C}}_5\text{H}_9$  radicals. In addition, 8.8% of 2,4- $\dot{\text{C}}_5\text{H}_9$  radicals undergo isomerization reaction to also form 2,5- $\dot{\text{C}}_5\text{H}_9$  radicals. Subsequently, 75.8% of 2,5- $\dot{\text{C}}_5\text{H}_9$  radicals isomerize to 1,3- $\dot{\text{C}}_5\text{H}_9$  radicals, 6.5% isomerize to 2,2- $\dot{\text{C}}_5\text{H}_9$  radicals and 17.7% produce ethylene + 1-propenyl radical via  $\beta$ -scission reactions. 2,2- $\dot{\text{C}}_5\text{H}_9$  radicals mainly undergo  $\beta$ -scission reactions to

form propyne + ethyl radical, and very small amount of 2-pentyne +  $\dot{\text{H}}$  atom and 1,2-pentadiene +  $\dot{\text{H}}$  atom. In addition, 12.6% of the reactant undergoes H-atom abstraction reactions by  $\dot{\text{H}}$  atom to form 1,3-pentadien-5-yl radical +  $\text{H}_2$ .

Fig. 3.1 shows that at 1400 K the dominant products for the reaction between 1,3-pentadiene and  $\dot{\text{H}}$  atoms are 1,3-butadiene +  $\dot{\text{C}}\text{H}_3$  radical (75.2%), of which about 90% is produced from the  $\beta$ -scission reaction of 1,3- $\dot{\text{C}}_5\text{H}_9$  radicals. The other important products generated are 1,3-pentadien-5-yl radical +  $\text{H}_2$  (12.6%), vinyl radical + propene (3.6%), 1,4-pentadiene +  $\dot{\text{H}}$  atom (2.8%), ethylene + 1-propenyl radical (2.3%), propyne + ethyl radical (0.8%).

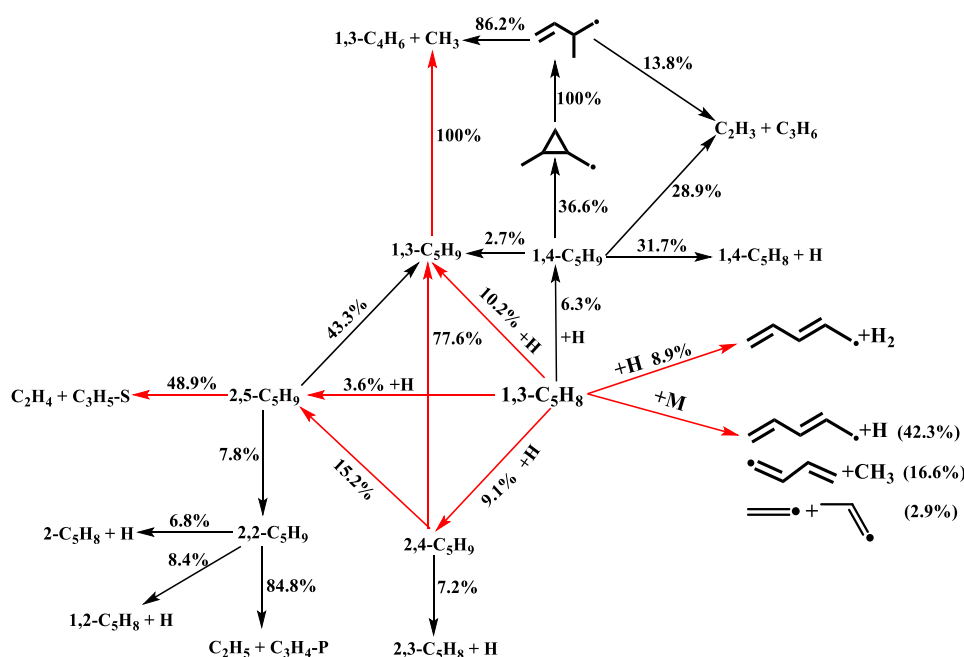


**Fig. 3.2** Flux analysis at 20% fuel consumption for 0.0001% 1,3- $\text{C}_5\text{H}_8$ , 0.01%  $\dot{\text{H}}$  in  $\text{N}_2$ ,  $p = 1$  atm,  $T = 1800$  K.

At 1800 K, unimolecular decomposition reactions consume 61.8% of 1,3-pentadiene in total, of which 42.3% undergo C-H  $\beta$ -scission to produce 1,3-pentadien-5-yl radicals +  $\dot{\text{H}}$  atoms and 16.6% produce 1,3-butadien-1-yl +  $\dot{\text{C}}\text{H}_3$  radicals via C-C  $\beta$ -scission. A small amount of vinyl + 1-propenyl (2.9%) radical can also be formed via C-C  $\beta$ -scission reactions. Another 8.9% of 1,3-pentadiene is consumed by H-atom abstraction reactions by  $\dot{\text{H}}$  atoms to produce 1,3-pentadien-5-yl radical +  $\text{H}_2$ . The amount of reactant consumed via  $\dot{\text{H}}$  atom addition reactions decreases from 87.4% at 1400 K to 29.3% at 1800 K. Among the four  $\dot{\text{C}}_5\text{H}_9$  radicals formed via  $\dot{\text{H}}$  atom addition reactions to 1,3-pentadiene, the most important is 1,3- $\dot{\text{C}}_5\text{H}_9$  which consumes 19.6% of the reactant with the contribution of direct  $\dot{\text{H}}$  atom addition reaction (10.2%), isomerisation reaction from 2,4- $\dot{\text{C}}_5\text{H}_9$  (7.1%), and isomerisation

reaction from 2,5- $\dot{\text{C}}_5\text{H}_9$  (2.2%). Thereafter 1,3- $\dot{\text{C}}_5\text{H}_9$  radicals undergo  $\beta$ -scission to form 1,3-butadiene +  $\dot{\text{C}}\text{H}_3$  radicals which can also be formed in small amounts through  $\beta$ -scission of 3-methyl-1-buten-4-yl radicals (W14). Both 3-methyl-1-buten-4-yl and 1,4- $\dot{\text{C}}_5\text{H}_9$  radicals can produce vinyl radicals + propene via C–C  $\beta$ -scission, while 1,4- $\dot{\text{C}}_5\text{H}_9$  radicals can also undergo C–H  $\beta$ -scission to produce 1,4-pentadiene +  $\dot{\text{H}}$  atoms.  $\dot{\text{H}}$  atoms also consume 9.1% of 1,3-pentadiene forming 2,4- $\dot{\text{C}}_5\text{H}_9$  which mainly undergo isomerization reactions to form 1,3- $\dot{\text{C}}_5\text{H}_9$  and 2,5- $\dot{\text{C}}_5\text{H}_9$  radicals, the remaining 7.2% of 2,4- $\dot{\text{C}}_5\text{H}_9$  radicals produce 2,3-pentadiene +  $\dot{\text{H}}$  atoms through a  $\beta$ -scission reaction. In addition, a small amount of 2,5- $\dot{\text{C}}_5\text{H}_9$  radicals can be formed through a  $\dot{\text{H}}$  atom addition reaction and isomerization reaction of 2,4- $\dot{\text{C}}_5\text{H}_9$  radicals, then almost half of the radicals undergo  $\beta$ -scission to form ethylene + 1-propenyl radical, 43.3% isomerize to 1,3- $\dot{\text{C}}_5\text{H}_9$  radicals, and 7.8% isomerize to 2,2- $\dot{\text{C}}_5\text{H}_9$  radicals which mainly form propyne + ethyl radicals.

In general, the important products for 1,3-pentadiene +  $\dot{\text{H}}$  at 1800 K are different from those at 1400 K. Although the unimolecular decomposition reactions start to play a major role and H-atom abstraction reactions become competitive with  $\dot{\text{H}}$  atom additions, the reader should keep in mind that the current simulations are in an excess of  $\dot{\text{H}}$  atom, and the relative ratios of unimolecular and bimolecular reaction will vary at different conditions. At 1800 K, 1,3-pentadiene reacts with  $\dot{\text{H}}$  atoms to produce various products: 1,3-pentadien-5-yl radical +  $\dot{\text{H}}$  (42.3%), 1,3-butadiene +  $\dot{\text{C}}\text{H}_3$  radical (21.6%), 1,3-butadien-1-yl +  $\dot{\text{C}}\text{H}_3$  radical (16.6%), 1,3-pentadien-5-yl radical +  $\text{H}_2$  (8.9%), vinyl radical + 1-propenyl radical (2.9%), ethylene + 1-propenyl radical (2.4%), vinyl radical + propene (2.1%), 1,4-pentadiene +  $\dot{\text{H}}$  atom (2.0%), 2,3-pentadiene +  $\dot{\text{H}}$  atom (0.7%), propyne + ethyl radical (0.3%).

### 3.2 Simplified $\dot{\text{C}}_5\text{H}_9$ PES

As outlined above, the important reaction channels for  $\dot{\text{H}}$  atom addition to 1,3-pentadiene were determined based on reaction pathway analyses. Similarly, the important reaction channels for 1,4- $\text{C}_5\text{H}_8$  +  $\dot{\text{H}}$ ,  $\text{cyC}_5\text{H}_8$  +  $\dot{\text{H}}$  and  $\dot{\text{C}}_2\text{H}_3$  +  $\text{C}_3\text{H}_6$  have also been explored. These important reactions usually have lower barrier heights compared with the other channels starting from the same reactants or intermediates, which are consistent with our barrier height analyses presented in Part I. A simplified PES is generated containing the most important reaction channels for these systems and is shown in Fig. 3.3, including nine wells, nine products and 25 TSs. The spin-restricted energies are calculated for radicals and TSs involved in these important reactions, the ZPVE corrected spin-restricted electronic energies for species on the simplified PES are shown in Table 3.2 and compared with ZPVE corrected

spin-unrestricted energies. From the comparison, we can see that the spin-restricted energies are less than  $0.6 \text{ kcal mol}^{-1}$  lower than spin-unrestricted energies for wells and radical products, but the differences for TSs can be up to  $1.5 \text{ kcal mol}^{-1}$ . In particular, the energy differences for TSs of the four entrance channels and the formation of 1,3-butadiene +  $\dot{\text{C}}\text{H}_3$  are within  $1.0\text{--}1.5 \text{ kcal mol}^{-1}$ . Considering the trade-off between accuracy and computational cost, the spin-unrestricted SPE calculations are used for the full  $\dot{\text{C}}_5\text{H}_9$  PES and the spin-restricted SPE calculations are only used for the species and TSs involved in important reactions.

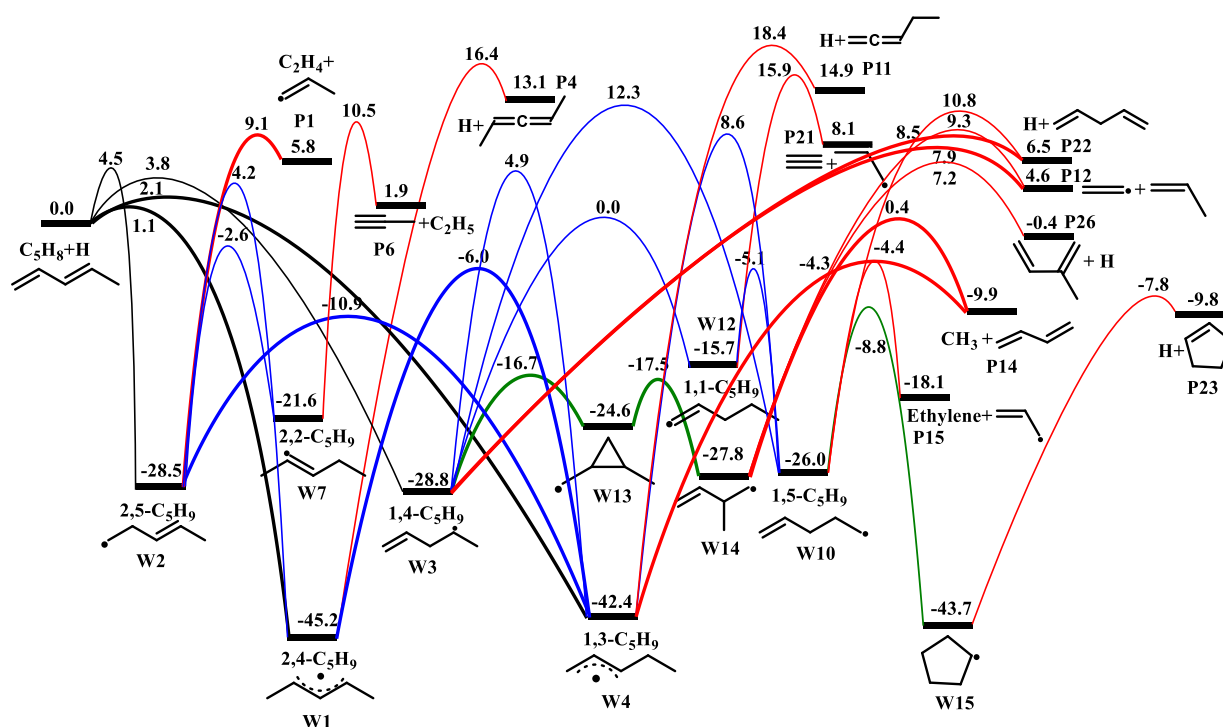


**Fig. 3.3** Simplified  $\dot{\text{C}}_5\text{H}_9$  PES with ZPVE corrected restricted energies (in  $\text{kcal mol}^{-1}$ ) relative to 1,3-pentadiene +  $\dot{\text{H}}$ .

### 3.3 Pressure dependency of important reaction channels

At infinite pressures, thermal equilibration is maintained and the reacting mixture has a Boltzmann distribution [57]. However, at lower pressures, collisions are not sufficiently rapid to maintain a Boltzmann distribution, and the competition between thermal equilibration via collisional energy transfer and the dissociation process results in the pressure-dependence of the reaction rates. The temperature- and pressure-dependent rate constants for reactions on the  $\dot{\text{C}}_5\text{H}_9$  PES are calculated in the temperature range 300–2000 K at pressures of 0.01 to 100 atm, with the electronic structure energies for species on the simplified  $\dot{\text{C}}_5\text{H}_9$  PES calculated at the higher, RO-aug-cc-VXZ (where  $X = \text{T and Q}$ ), level of theory. The modified-Arrhenius rate constant equation is used to fit the rate constants at 0.01, 0.1, 1, 10, 100 atm over the

available temperature range, with the fitted Arrhenius parameters provided in Chemkin format as Supporting Information.

**Table 3.2** Zero-point vibrational energy corrected electronic energies (kcal mol<sup>-1</sup>) relative to 1,3-pentadiene +  $\dot{\text{H}}$ , with spin-unrestricted and spin-restricted energies extrapolated using the same equation (Eq. 1).

Label	Species	Energies		
		Spin-unrestricted	Spin-restricted	$\Delta E_{0\text{K}}$
W1	2,4- $\dot{\text{C}}_5\text{H}_9$	-44.5	-45.2	0.7
W2	2,5- $\dot{\text{C}}_5\text{H}_9$	-28.4	-28.5	0.1
W3	1,4- $\dot{\text{C}}_5\text{H}_9$	-28.7	-28.8	0.1
W4	1,3- $\dot{\text{C}}_5\text{H}_9$	-41.8	-42.4	0.6
W7	2,2- $\dot{\text{C}}_5\text{H}_9$	-21.3	-21.6	0.3
W10	1,5- $\dot{\text{C}}_5\text{H}_9$	-26.0	-26.0	0.0
W13	1-methylene-cyclopropylmethyl	-24.5	-24.6	0.1
W14	3-methyl-1-buten-4-yl	-27.7	-27.8	0.1
W15	Cyclopentyl	-43.6	-43.7	0.1
R	1,3-pentadiene+ $\dot{\text{H}}$	0.0	---	---
P1	Ethylene + 1-propenyl	6.3	5.8	0.5
P6	Propyne + ethyl	1.9	1.9	0.0
P12	Vinyl + propene	5.1	4.6	0.5
P14	1,3-butadiene+methyl	-9.8	-9.9	0.1
P15	Ethylene + allyl	-17.5	-18.1	0.6
P22	1,4-pentadiene+ $\dot{\text{H}}$	6.5	---	---
P23	Cyclopentene+ $\dot{\text{H}}$	-9.8	---	---
P26	Isoprene + $\dot{\text{H}}$	-0.4	---	---

Label	Reactant	Product	Energy		
			Spin-unrestricted	Spin-restricted	$\Delta E_{0\text{K}}$
TS1	R	W1	2.3	1.1	1.2
TS2	R	W2	5.8	4.5	1.3
TS3	R	W3	5.0	3.8	1.2
TS4	R	W4	3.4	2.1	1.3
TS10	W1	W2	4.8	4.2	0.6
TS11	W1	W4	-5.8	-6.0	0.2
TS16	W2	W4	-10.5	-10.9	0.4
TS18	W2	W7	-2.0	-2.6	0.6
TS21	W2	P1	10.0	9.1	0.9
TS22	W3	W4	5.5	4.9	0.6
TS23	W3	W10	12.5	12.3	0.2
TS26	W3	W13	-16.3	-16.7	0.4
TS28	W3	P12	8.8	7.9	0.9
TS29	W3	P22	8.8	8.5	0.3
TS33	W4	W10	9.2	8.6	0.6
TS37	W4	P14	-2.9	-4.3	1.4
TS49	W7	P6	11.7	10.5	1.2
TS61	W10	W15	-8.2	-8.8	0.6
TS63	W10	P15	-3.2	-4.4	0.8
TS64	W10	P22	11.2	10.8	0.4
TS71	W13	W14	-17.1	-17.5	0.4
TS76	W14	P12	10.2	9.3	0.9
TS77	W14	P14	1.6	0.4	1.2
TS78	W14	P26	8.1	7.2	0.9
TS79	W15	P23	-7.5	-7.8	0.3

In the following Section, the pressure dependencies of important reactions on the  $\dot{C}_5H_9$  PES are discussed and compared to literature data where it exists. The important reactions can be divided into two types, namely unimolecular and bimolecular reactions. The total rate constants and the product branching ratios are also discussed for important unimolecular reactions. For important bimolecular reactions, the high-pressure limiting, and the temperature- and pressure-dependent total rate constants, product branching ratios, and the competition between addition and abstraction reactions are discussed.

The rate constants for some reactions become undefined at high temperatures when their rates of chemical equilibration exceed the rates of collisional relaxation [58], thus pressure-dependent rate constants are not always available over the entire temperature range. Based on Miller and Klippenstein's work [58], such phenomena occur when species equilibrate with each other as rapidly as their internal energy relaxes and the two species become chemically indistinguishable [59]. Consequently, we cannot discuss the branching ratios of important  $\dot{C}_5H_9$  radicals and bimolecular reactants over a wide range of temperature and pressure. For important reaction pathways which do not have definable rate constants at intermediate and high temperatures in following discussion, we have extrapolated their pressure-dependent rate constants by fitting Arrhenius parameters based on rate constant points at low and/or intermediate temperatures. Since the rate constants for these reactions become undefinable at lower temperatures as pressure decreases, the branching ratios are discussed only at  $p > 1$  atm. The detailed description of extrapolated rate constants and their resulting branching ratios are provided in the Figure captions where extrapolations are applied.

### 3.3.1 Bimolecular reactions

#### 3.3.1.1 1,3- $C_5H_8 + \dot{H}$

The total pressure-dependent rate constants for  $1,3-C_5H_8 + \dot{H} \rightarrow$  products are compared with the corresponding high-pressure limiting rate constants and are shown in Fig. 3.4(a). The pressure fall-off in rate constants increase as temperature increases with the  $k(T, p)/k_\infty$  ratio decreasing from 0.7 at 1000 K to 0.5 at 2000 K at a pressure of 0.01 atm. This finding is consistent with the general conclusion that deviations from the high-pressure limiting are particularly severe for small molecules at higher temperatures and lower pressures [57]. The fall off at 1200 K and 1 atm is about 56%, with similar conditions widely used for laminar flame and shock tube experiments. It is also noticeable that, even at 100 atm, the fall-off in rate constant is a factor of two at 2000 K. Hence, the  $k_{total}(1,3-C_5H_8 + \dot{H} \rightarrow$  products) have

shown an obvious pressure-dependency and the pressure-dependent rate constants should be used for accurate model predictions, especially at low pressures and high temperatures.

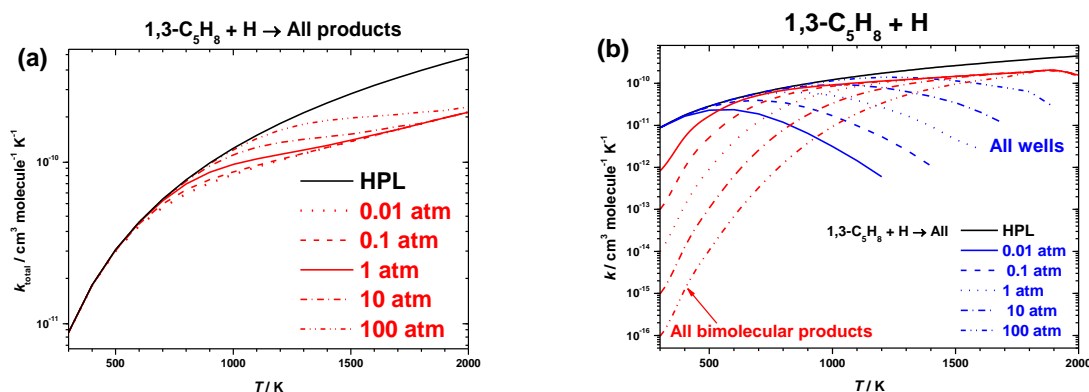


**Fig. 3.4** (a) The pressure-dependent rate constants and high-pressure limiting rate constants for 1,3-pentadiene +  $\dot{\text{H}} \rightarrow$  all products as a function of temperature. (b) The pressure-dependent and high-pressure limiting rate constants for 1,3-pentadiene +  $\dot{\text{H}} \rightarrow$  thermodynamically stabilized wells and bimolecular products at 0.01, 0.1, 1, 10, and 100 atm.

As the temperature and pressure dependence of a chemical rate constant arises from a complex interplay between chemical and collisional processes averaged over thermal distributions of reactant and collisional energies [57], the pressure-dependent  $k(1,3\text{-C}_5\text{H}_8 + \dot{\text{H}} \rightarrow \text{all bimolecular products})$  and  $k(1,3\text{-C}_5\text{H}_8 + \dot{\text{H}} \rightarrow \text{all wells})$  are compared as a function of temperature and plotted in Fig. 3.4(b). The  $k(1,3\text{-C}_5\text{H}_8 + \dot{\text{H}} \rightarrow \text{all wells})$  are not available at high temperatures as their rates of chemical equilibration exceed the rates of collisional relaxation [58]. The  $k_{\text{Wells}}$  is shown to have a positive pressure dependence with the collision stabilization getting stronger as pressure increases. For a specific pressure,  $k_{\text{Wells}}$  decreases as temperature increases, while  $k_{\text{Prods}}$  shows the opposite trend, which indicates that the production of the thermodynamically stabilized wells are preferred at low temperatures and high pressures, and the production of the bimolecular products are preferred at high temperatures and low pressures.

The branching ratios (BRs) for important products generated from  $\dot{\text{H}}$  addition to 1,3-pentadiene at 1 atm are plotted in Fig. 3.5(a). The formation of  $2,4\text{-}\dot{\text{C}}_5\text{H}_9$  radicals is mostly favoured at low temperatures with a branching ratio of 86.6% at 300 K, with  $\sim 12.0\%$   $1,3\text{-}\dot{\text{C}}_5\text{H}_9$  radical also formed. Hence, the formation of allylic  $\dot{\text{C}}_5\text{H}_9$  radicals is dominant at low temperatures. Allylic radical production is overtaken by the production of  $1,3\text{-C}_4\text{H}_6 + \dot{\text{C}}\text{H}_3$  radicals at 1000 K, which has the largest branching ratio of 76.9% at 1400 K, decreasing to 64.3% at 2000 K. At high temperatures, there are also other bimolecular products formed,

and their branching ratios are 11.4% for  $C_2H_4 + 1\text{-propenyl}$  radicals, 9.6% for  $1,4\text{-}C_5H_8 + \dot{H}$  atoms, 8.9% for  $\dot{C}_2H_3$  radicals +  $C_3H_6$  and 2.4% for  $2,3\text{-}C_5H_8 + \dot{H}$  atoms at 2000 K.

To analyse the pressure dependence of product branching ratios, those for the formation of  $2,4\text{-}\dot{C}_5H_9$  radicals and the  $1,3\text{-}C_4H_6 + \dot{C}H_3$  radical pathway at 0.01, 0.1, 1, 10 and 100 atm are compared and plotted in Fig. 3.5(b). The branching ratios of these two important channels show significant temperature and pressure dependencies. The branching ratios at different pressures show similar trends with various cross-over points for  $BR(2,4\text{-}\dot{C}_5H_9)$  and  $BR(1,3\text{-}C_4H_6 + \dot{C}H_3)$ . At 1000 K, the  $BR(2,4\text{-}\dot{C}_5H_9)$  increases from 2.6% to 62.9% as the pressure increases from 0.01 to 100 atm, while the  $BR(1,3\text{-}C_4H_6 + \dot{C}H_3)$  decreases from a value of 91.2% at 0.01 atm to 2.9% at 100 atm. Notably, the temperatures of the cross-over points vary from 580 K at 0.01 atm to 1560 K at 100 atm, while their corresponding branching ratios show small differences, they being  $32.3\% < BR(2,4\text{-}\dot{C}_5H_9) \approx BR(1,3\text{-}C_4H_6 + \dot{C}H_3) < 39.8\%$ . In general, the temperature and pressure dependencies of the rate constants should be considered when discussing important products and/or exploring their branching ratios.

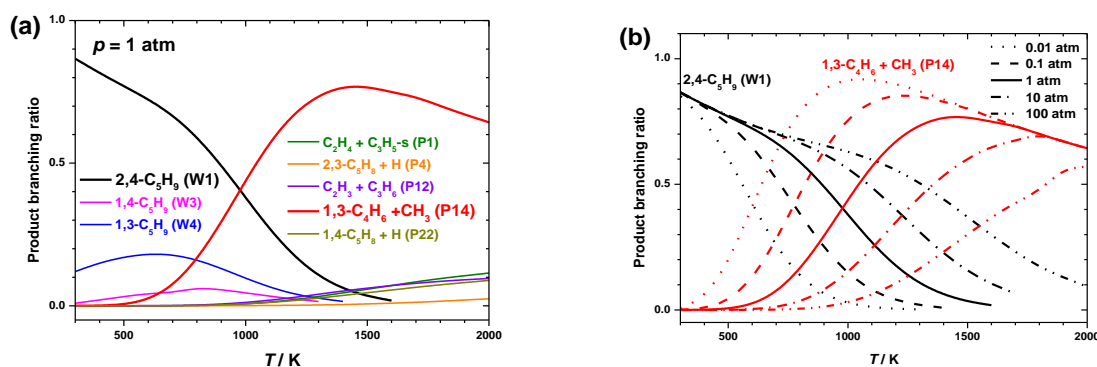


**Fig. 3.5** (a) The branching ratios for important products from  $\dot{H}$  addition to 1,3-pentadiene at 1 atm, (b) The branching ratios for  $2,4\text{-}\dot{C}_5H_9$  radical (W1) and  $1,3\text{-butadiene} + \dot{C}H_3$  (P14) produced from  $\dot{H}$  addition to 1,3-pentadiene at 0.01, 0.1, 1, 10, and 100 atm.

The PES and high-pressure limiting rate constants for H-atom abstraction reactions from 1,3-pentadiene by  $\dot{H}$  atoms was illustrated in Part I, and the total rate constants for H-atom abstraction reactions are compared with the pressure-dependent total rate constants for  $\dot{H}$  atom addition reactions of 1,3-pentadiene herein. Fig. 3.6 shows that H-atom abstraction reactions are negligible at low temperatures compared with  $\dot{H}$  atom addition reactions. However, the increased importance of H-atom abstraction reactions is observed at higher temperatures, with the  $k_{0.01\text{atm}}(\text{addition})/k_{\text{total}}(\text{abstraction})$  ratios being within an order of

magnitude at temperatures above 1200 K and are close to a factor of two at 2000 K.

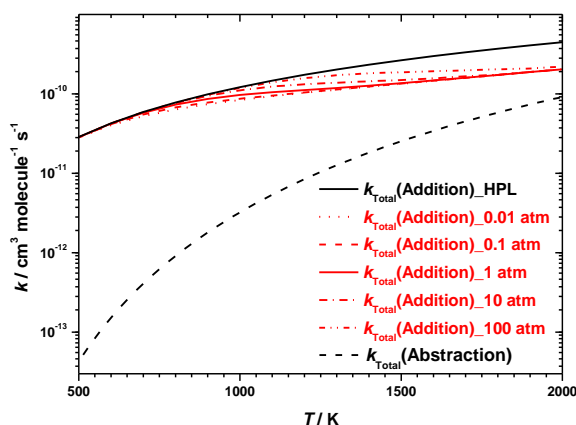


**Fig. 3.6** The total rate constant comparisons between the H-atom abstraction reactions by  $\dot{\text{H}}$  atoms and  $\dot{\text{H}}$  atom addition reactions from/to 1,3-pentadiene.

### 3.3.1.2 1,4-C<sub>5</sub>H<sub>8</sub> + $\dot{\text{H}}$

The branching ratios for important products generated from  $\dot{\text{H}}$  atom addition to 1,4-pentadiene at 1 atm are plotted in Fig. 3.7(a). At 1 atm and low temperatures (< 900 K), the production of 1,4- $\dot{\text{C}}_5\text{H}_9$  radicals dominates, followed by 3-methyl-1,4-butadienyl radical (3Me-1,4-C<sub>4</sub>H<sub>6</sub>). The formation of 1,3-C<sub>4</sub>H<sub>6</sub> +  $\dot{\text{C}}\text{H}_3$  radicals dominates in the temperature range 1000–1600 K, but is then overtaken by the production of  $\dot{\text{C}}_2\text{H}_3$  radical + C<sub>3</sub>H<sub>6</sub> at ~1600 K and C<sub>2</sub>H<sub>4</sub> +  $\dot{\text{C}}_3\text{H}_5\text{-a}$  at ~1700 K. It can be seen that the dominance of the formation of 1,3-butadiene, which is a lower hierarchy diene compared to 1,3- and 1,4-pentadiene, is weaker for  $\dot{\text{H}}$  addition to 1,4-pentadiene and the formation of C<sub>2</sub> + C<sub>3</sub> ( $\dot{\text{C}}_2\text{H}_3$  + C<sub>3</sub>H<sub>6</sub>, C<sub>2</sub>H<sub>4</sub> +  $\dot{\text{C}}_3\text{H}_5\text{-a}$ ) bimolecular products are more favoured at high temperatures.

Due to the absence of  $k(1,4\text{-C}_5\text{H}_8 + \text{H} \rightarrow 3\text{Me-1,4-C}_4\text{H}_6)$  at temperatures above 700 K, the branching ratios of the other products, which are relied on total rate constants, can't be accurately predicted. Hence,  $k(1,4\text{-C}_5\text{H}_8 + \text{H} \rightarrow 3\text{Me-1,4-C}_4\text{H}_6)$  are extrapolated from 800 K to 2000 K and included in total rate constant calculations. The branching ratios at 1, 10 and 100 atm for the formation of 1,4- $\dot{\text{C}}_5\text{H}_9$  radical and three major bimolecular products (1,3-C<sub>4</sub>H<sub>6</sub> +  $\dot{\text{C}}\text{H}_3$ ,  $\dot{\text{C}}_2\text{H}_3$  + C<sub>3</sub>H<sub>6</sub>, C<sub>2</sub>H<sub>4</sub> +  $\dot{\text{C}}_3\text{H}_5\text{-a}$ ) are compared. As shown in Fig. 3.7(b), the production of 1,4- $\dot{\text{C}}_5\text{H}_9$  radicals has a strong positive pressure-dependence and negative temperature-dependence. The branching ratios of 1,3-C<sub>4</sub>H<sub>6</sub> +  $\dot{\text{C}}\text{H}_3$  increases with temperature initially, then decreases to about 14% at 2000 K due to the competition of the other bimolecular products. The formation of these three bimolecular products all show negative pressure-dependencies and their branching ratios tend to converge at high temperatures. At

2000 K and different pressures, the most important product for  $\dot{\text{H}}$  atom addition to 1,4-pentadiene is  $\dot{\text{C}}_2\text{H}_3 + \text{C}_3\text{H}_6$ , followed by  $\text{C}_2\text{H}_4 + \dot{\text{C}}_3\text{H}_5\text{-a}$ ,  $1,3\text{-C}_4\text{H}_6 + \dot{\text{C}}\text{H}_3$ , and  $1,3\text{-C}_5\text{H}_8 + \dot{\text{H}}$ .

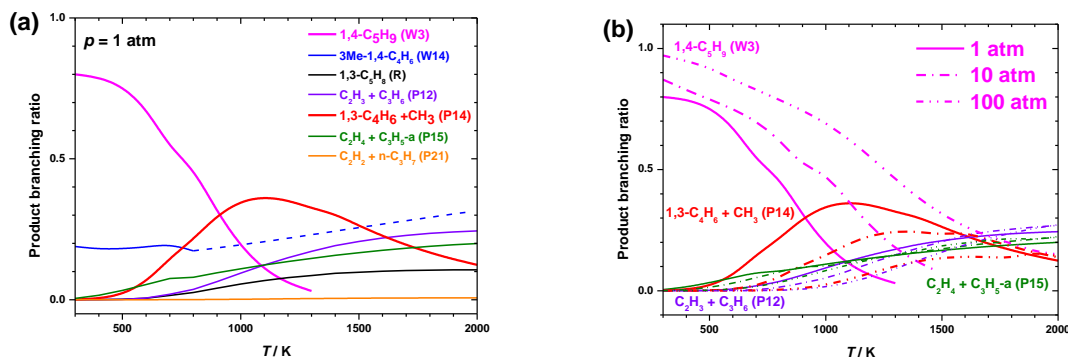


**Fig. 3.7** (a) The branching ratios for important products generated by  $\dot{\text{H}}$  atom addition to 1,4-pentadiene at 1 atm, with  $k(1,4\text{-C}_5\text{H}_8 + \text{H} \rightarrow 3\text{Me-1,4-C}_4\text{H}_6)$  extrapolated from 800 K to 2000 K. (b) The branching ratios for  $1,4\text{-}\dot{\text{C}}_5\text{H}_9$  radical (W3),  $1,3\text{-butadiene} + \dot{\text{C}}\text{H}_3$  (P14),  $\dot{\text{C}}_2\text{H}_3 + \text{C}_3\text{H}_6$  (P12), and  $\text{C}_2\text{H}_4 + \dot{\text{C}}_3\text{H}_5\text{-a}$  (P15) produced from  $\dot{\text{H}}$  atom addition to 1,4-pentadiene at 1, 10, and 100 atm. The BRs are calculated with extrapolated  $k(1,4\text{-C}_5\text{H}_8 + \text{H} \rightarrow 3\text{Me-1,4-C}_4\text{H}_6)$  including in total rate constants.

The PES for H-atom abstraction reactions of 1,4-pentadiene by  $\dot{\text{H}}$  atoms is described in detail in Fig. B.2. The high-pressure limiting rate constants for H-atom abstraction reactions of 1,4-pentadiene by  $\dot{\text{H}}$  atoms are shown in Fig. 3.8(a) and compared with those for H-atom abstraction reactions from 1,3-butadiene [43] and 1,3-pentadiene. It can be clearly seen that abstraction of an allylic hydrogen atom from 1,4-pentadiene and/or 1,3-pentadiene to form a doubly allylic 1,4-pentadien-3-yl (or 1,3-pentadien-5-yl) radical is favoured over the abstraction of vinylic hydrogen atoms. It is noticeable that the barrier height for H-atom abstraction from the allylic site on 1,4-pentadiene is  $2.8 \text{ kcal mol}^{-1}$  lower than that for H-atom abstraction from the allylic site on 1,3-pentadiene. As a result, rate constants for abstraction from 1,4-pentadiene are about an order of magnitude faster than from 1,3-pentadiene at 300 K and become similar to those for H-atom abstraction from the allylic site on 1,3-pentadiene at 2000 K. At temperatures below 700 K, the rate constants for H-atom abstraction from the secondary vinylic sites are faster than those from the primary vinylic sites, thereafter there is no appreciable difference between these two reaction classes at higher temperatures. For H-atom abstraction from the secondary vinylic and primary vinylic sites by  $\dot{\text{H}}$  atoms, the trend for rate constants is  $k_\infty(1,3\text{-pentadiene}) < k_\infty(1,3\text{-butadiene}) <$

$k_{\infty}(1,4\text{-pentadiene})$ ; and for H-atom abstraction from the allylic sites, the trend for rate constants is  $k_{\infty}(1,3\text{-pentadiene}) < k_{\infty}(1,4\text{-pentadiene})$ .

The total rate constants for H-atom abstraction reactions of 1,4-pentadiene are compared with the  $\dot{\text{H}}$  atom addition pressure-dependent total rate constants in Fig. 3.8(b). Similar to H-atom abstraction reactions from 1,3-pentadiene, H-atom abstraction from 1,4-pentadiene is negligible at low temperatures with the  $k_{0.01\text{atm}}(\text{addition})/k_{\text{total}}(\text{abstraction})$  ratio decreasing to within an order of magnitude at temperatures above 1000 K and 2.5 times at 2000 K. What stands out is that  $k_{\text{total}}(\text{addition})$  of  $1,4\text{-C}_5\text{H}_8 + \dot{\text{H}}$  shows a weaker pressure-dependence with the fall-off of the rate constants compared with the high-pressure limiting rate constants being within 26%. Considering the strong pressure-dependence of the product branching ratios, pressure-dependent rate constants for  $1,4\text{-C}_5\text{H}_8 + \dot{\text{H}}$  should still be used to accurately predict product yields.

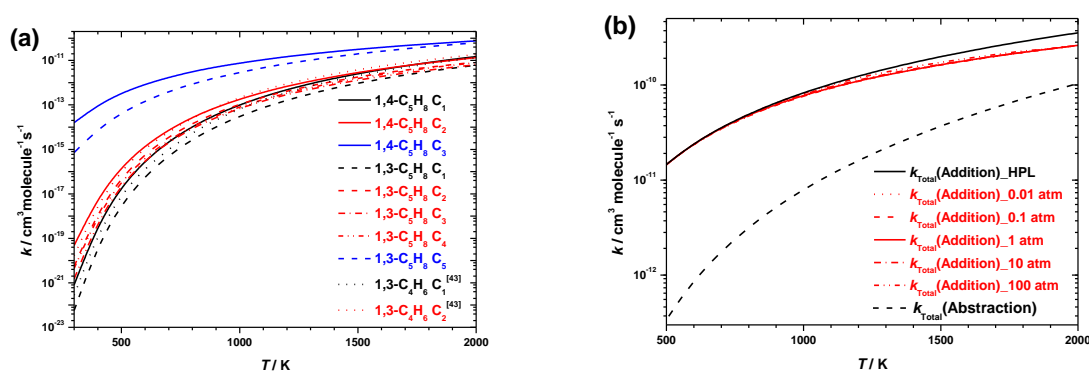


**Fig. 3.8** (a) Rate constant comparisons for H-atom abstraction reactions of 1,4-pentadiene by  $\dot{\text{H}}$  atoms. The solid lines represent H-atom abstraction reactions from 1,4-pentadiene, while the dash and dot lines represent H-atom abstraction reactions from 1,3-pentadiene and 1,3-butadiene[43] by  $\dot{\text{H}}$  atoms, respectively. The black lines represent H-atom abstraction from the primary vinylic sites of these three dienes, the red lines represent H-atom abstraction from the secondary vinylic sites, and the blue lines represent H-atom abstraction from the allylic sites. (b) The total rate constant comparisons between the H-atom abstraction reactions by  $\dot{\text{H}}$  atoms and  $\dot{\text{H}}$  atom addition reactions from/to 1,4-pentadiene.

### 3.3.1.3 Cyclopentene + $\dot{\text{H}}$

The branching ratios for important products at 1 atm generated from  $\dot{\text{H}}$  atom addition to cyclopentene ( $\text{cyC}_5\text{H}_8$ ) are plotted in Fig. 3.9(a). The direct formation of cyclopentyl radical ( $\text{cy}\dot{\text{C}}_5\text{H}_9$ ) via  $\dot{\text{H}}$  atom addition to cyclopentene dominates at low temperatures ( $< 1100$  K) and is then overtaken by the formation of  $\text{C}_2\text{H}_4 + \dot{\text{C}}_3\text{H}_5\text{-a}$ , with a largest branching ratio of 96.0%.

A small amount of 1,5- $\dot{C}_5H_9$  radical ( $\sim 4\%$ ) is formed at low temperatures and less than 3% of the flux proceeds through 1,4- $C_5H_8 + \dot{H}$  at high temperatures. The branching ratios of cy $\dot{C}_5H_9$  radical and  $C_2H_4 + \dot{C}_3H_5$ -a radical at different pressures are shown in Fig. 3.9(b) with BR(cy $\dot{C}_5H_9$ ) increasing as pressure increases and BR( $C_2H_4 + \dot{C}_3H_5$ -a) showing the opposite trend. Although BR( $C_2H_4 + \dot{C}_3H_5$ -a) at different pressures converge at high temperatures, the pressure-dependent rate constants for cy $C_5H_8 + \dot{H}$  still need to be considered at temperatures below 1900 K in order to simulate the product branching ratios.

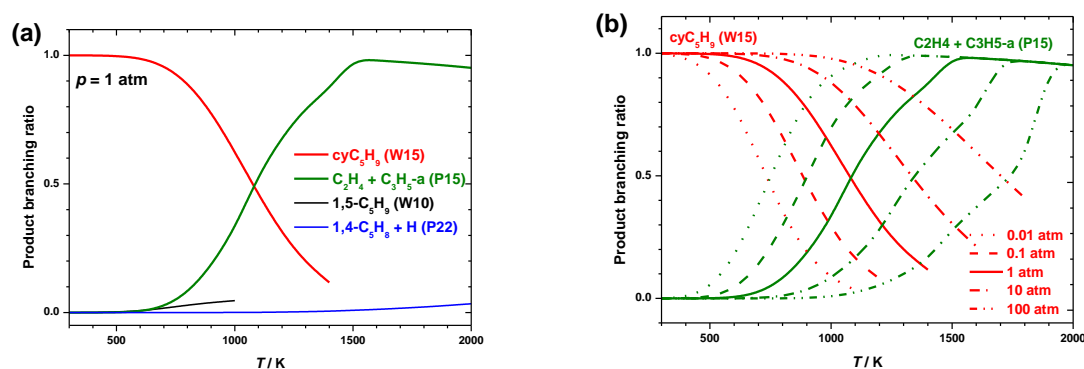


**Fig. 3.9** (a) The branching ratios for important products from  $\dot{H}$  atom addition to cy $C_5H_8$  at 1 atm, (b) the branching ratios for cy $\dot{C}_5H_9$  radical (W15) and  $C_2H_4 + \dot{C}_3H_5$ -a (P15) produced from  $\dot{H}$  atom addition to cy $C_5H_8$  at 0.01, 0.1, 1, 10, and 100 atm.

The PES for H-atom abstraction reactions of cy $C_5H_8$  by  $\dot{H}$  atoms are described in detail in Fig. B.3. The formation of 1,3- and 1,4-cyclopentenyl radicals via H-atom abstraction from cyclopentene has been included in Al Rashidi's cyclopentane mechanism, of which the rate constants for the former reaction are obtained by analogy to H-atom abstraction reaction from 1-hexene, while the rate constants for the formation of 1,4-cyclopentenyl radical is estimated by applying a rate rule for secondary allylic H-atom abstraction from alkenes [60]. Fig. 3.10(a) shows that the  $k(1,3\text{-cyclopentenyl})$  estimated by Al Rashidi agrees with this work with differences within a factor of two at temperatures above 600 K. Meanwhile, the  $k(1,4\text{-cyclopentenyl})$  obtained by analogy to H-atom abstraction from 1-hexene is 2–3 times faster than that calculated here. The comparisons indicate that H-atom abstraction from cyclopentene can be estimated using a rate rule by analogy for abstraction from alkenes with uncertainties within a factor of three.

The total rate constants for cy $C_5H_8 + \dot{H}$  via addition and abstraction reactions are compared in Fig. 3.10(b). The fall-off of  $k_{\text{total}}(\text{addition})$  at different pressures compared to the high-pressure limiting rate constants can reach up to a factor of 2.4 at 2000 K. In contrast to

the total rate constant comparisons for 1,3- and 1,4- $\text{C}_5\text{H}_8 + \dot{\text{H}}$ , H-atom abstraction of cyclopentene is competitive with  $\dot{\text{H}}$  atom addition, even at low temperatures, with the deviation between  $k_{\text{total}}(\text{addition})$  and  $k_{\text{total}}(\text{abstraction})$  within an order of magnitude at 500 K. In addition,  $k_{\text{total}}(\text{abstraction})$  overtakes  $k_{\text{total}}(\text{addition})$  at 0.01 atm and  $\sim 1100$  K and  $k_{\infty}(\text{addition})$  at 1800 K. Hence, H-atom abstraction reactions are relatively more important for cyclopentene than for 1,3- and 1,4-pentadiene at the temperatures studied. Based on the branching ratio study presented in Fig. 3.9, the product formed at temperatures below 400 K is mainly  $\text{cy}\dot{\text{C}}_5\text{H}_9$  radical. Hence, the  $k(\text{cyC}_5\text{H}_8 + \dot{\text{H}} \rightarrow \text{cy}\dot{\text{C}}_5\text{H}_9)$  from Clarke's work, which is measured in a flow tube over temperature range 298–370 K and 50 Torr (0.07 atm), is compared with our calculated results and shows good agreement with values being within 50% of one another.

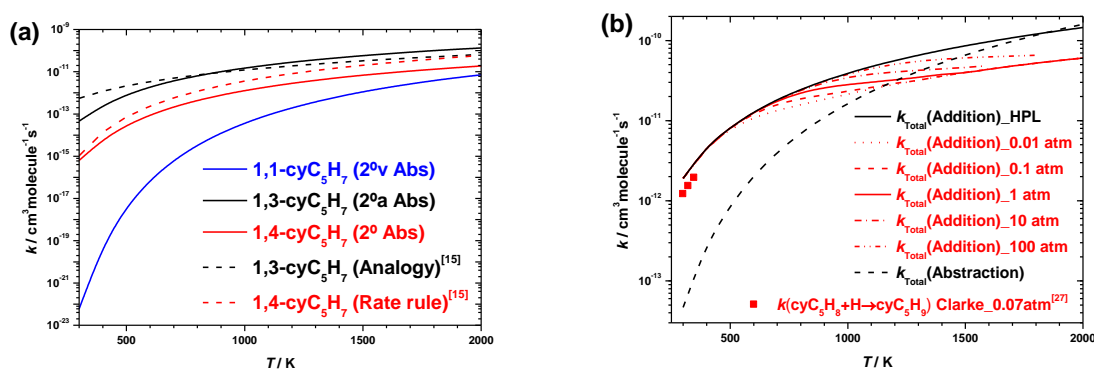


**Fig. 3.10** (a) Rate constant comparisons for H-atom abstraction reactions of  $\text{cyC}_5\text{H}_8$  by  $\dot{\text{H}}$  atoms from this work and literature [15]. (b) The total rate constant comparisons between the H-atom abstraction reactions by  $\dot{\text{H}}$  atoms and  $\dot{\text{H}}$  atom addition reactions from/to  $\text{cyC}_5\text{H}_8$ . The red symbol represents experimental results by Clarke et al. [27] at 0.07 atm for  $\text{cyC}_5\text{H}_8 + \dot{\text{H}} \rightarrow \text{cy}\dot{\text{C}}_5\text{H}_9$ .

### 3.3.1.4 Ethylene + allyl radical

The branching ratios for important products at 1 atm generated by allyl radical addition to ethylene are plotted in Fig. 3.11(a), with  $k(\text{C}_2\text{H}_4 + \dot{\text{C}}_3\text{H}_5\text{-a} \rightarrow 1,5\text{-}\dot{\text{C}}_5\text{H}_9)$  extrapolated from 1400 K to 2000 K. The dominant product at 1 atm is  $1,5\text{-}\dot{\text{C}}_5\text{H}_9$  radical at temperatures below 1700 K and  $1,4\text{-}\text{C}_5\text{H}_8 + \dot{\text{H}}$  at higher temperatures. There are also small amounts of  $\text{cy}\dot{\text{C}}_5\text{H}_9$  radicals (W15) and  $\text{cyC}_5\text{H}_8 + \dot{\text{H}}$  atoms (P23) formed, with a maximum  $\text{BR}(\text{cy}\dot{\text{C}}_5\text{H}_9)$  of 6.8% at 900 K and  $\text{BR}(\text{cyC}_5\text{H}_8 + \dot{\text{H}})$  of 11.8% at 1500 K. The pressure-dependence of dominant product branching ratios for allyl radical addition to ethylene are shown in Fig. 3.11(b). The branching ratios of important products show strong temperature- and pressure-dependencies.

The BR(1,5- $\dot{C}_5H_9$ ) increases rapidly as pressure increases from 1 atm to 100 atm at a specific temperature. While the BR(1,4- $C_5H_8 + \dot{H}$ ) has an opposite behavior with larger decreases being found as the pressure increases from 1–100 atm at temperatures above 1500 K. Due to the dominant product branching ratios for  $C_2H_4 + \dot{C}_3H_5$ -a being very sensitive to pressure, the pressure-dependent rate constants should be used for simulations related to this system.

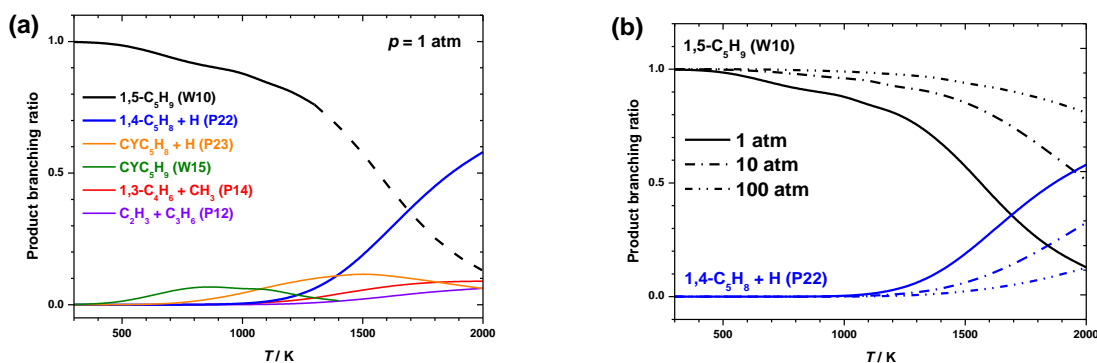


**Fig. 3.11** (a) The branching ratios for important products from allyl addition to ethylene at 1 atm, with  $k(C_2H_4 + \dot{C}_3H_5$ -a  $\rightarrow$  1,5- $\dot{C}_5H_9$ ) extrapolated from 1400 K to 2000 K. (b) the branching ratios for 1,5- $\dot{C}_5H_9$  (W10) and 1,4- $C_5H_8 + \dot{H}$  (P22) produced from allyl addition to ethylene at 0.01, 1.0 and 100 atm. The BRs are calculated with  $k(C_2H_4 + \dot{C}_3H_5$ -a  $\rightarrow$  1,5- $\dot{C}_5H_9$ ), which are included in the total rate constants, extrapolated over a temperature range of 1400–2000 K at 1 atm, 1600–2000 K at 10 atm, and 1900–2000 K at 100 atm.

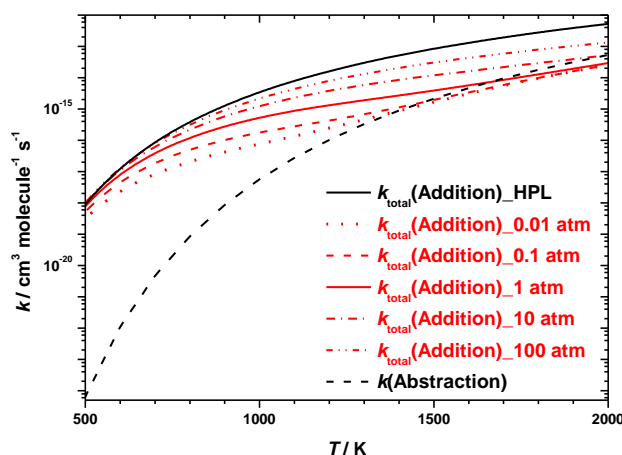


**Fig. 3.12** The total rate constant comparisons between the H-atom abstraction reactions and addition reactions of allyl radical with ethylene. The total rate constants for addition reactions include  $k(C_2H_4 + \dot{C}_3H_5$ -a  $\rightarrow$  1,5- $\dot{C}_5H_9$ ) extrapolated over a temperature range of 1100–2000 K at 0.01 atm, 1200–2000 K at 0.1 atm, 1400–2000 K at 1 atm, 1600–2000 K at 10 atm, and

1900 – 2000 K at 100 atm.

The rate constants for the H-atom abstraction reaction by allyl radicals from ethylene (reverse reaction of H-atom abstraction reaction of propene by vinyl radicals) are compared to its addition reactions at different pressures and high-pressure limiting values in Fig. 3.12. The pressure-dependent total rate constants have a fall-off in the intermediate temperature range, mainly due to the decrease of  $k(\text{C}_2\text{H}_4 + \text{C}_3\text{H}_5\text{-a} \rightarrow 1,5\text{-C}_5\text{H}_9)$ . As shown in the comparison,  $k(\text{abstraction})$  overtakes the  $k_{\text{total}}(0.01 \text{ atm})$  at 1500 K and is close to  $k_{\text{total}}(10 \text{ atm})$  at 2000 K. Hence, the abstraction reaction of  $\text{C}_2\text{H}_4 + \text{C}_3\text{H}_5\text{-a}$ , is important at high temperatures and needs to be included in the mechanism development.

### 3.3.1.5 Propene + vinyl radical

The branching ratios for important products generated from vinyl radical addition to propene at different pressures are plotted in Fig. 3.13(a) and (b), respectively. At 1.0 atm, the production of 1,4- $\dot{\text{C}}_5\text{H}_9$  radical (W3) is dominant at temperatures below 900 K, and 3-methyl-1-buten-4-yl radical (W14) also plays an important role with BRs close to 20% over the temperature range of 300 – 2000 K. At temperatures above 1200 K, the important products are 1,3- $\text{C}_4\text{H}_6 + \dot{\text{C}}\text{H}_3$  followed by 1,4- $\text{C}_5\text{H}_8 + \dot{\text{H}}$  and 1,3- $\text{C}_5\text{H}_8 + \dot{\text{H}}$  with BRs of 33.3%, 27.7% and 13.0% at 2000 K, respectively.

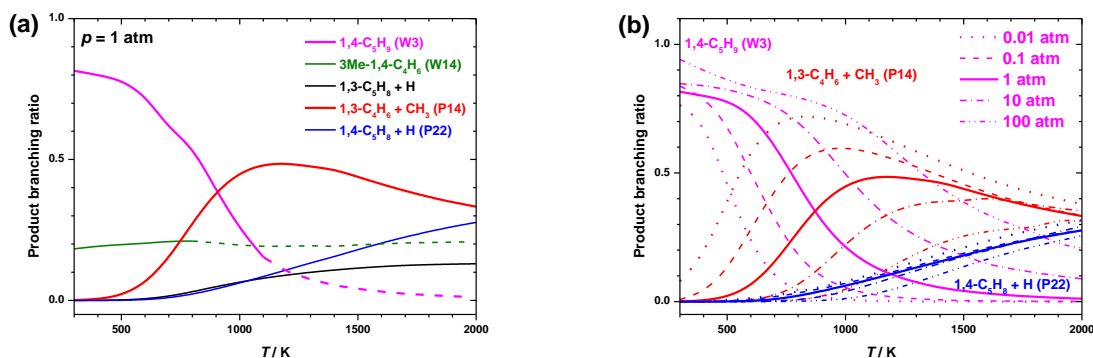


**Fig. 3.13** (a) The branching ratios for important products from vinyl addition to propene at 1 atm, with  $k(\dot{\text{C}}_2\text{H}_3 + \text{C}_3\text{H}_6 \rightarrow 1,4\text{-}\dot{\text{C}}_5\text{H}_9)$  extrapolated from 1200 K to 2000 K and  $k(\dot{\text{C}}_2\text{H}_3 + \text{C}_3\text{H}_6 \rightarrow 3\text{Me-1,4-}\dot{\text{C}}_4\text{H}_6)$  extrapolated from 800 K to 2000 K. (b) The branching ratios for 1,4- $\dot{\text{C}}_5\text{H}_9$  (W3), 1,3- $\text{C}_5\text{H}_8 + \dot{\text{H}}$ , 1,3- $\text{C}_4\text{H}_6 + \dot{\text{C}}\text{H}_3$  (P14) and 1,4- $\text{C}_5\text{H}_8 + \dot{\text{H}}$  (P22) produced from vinyl addition to propene at 0.01, 0.1, 1, 10 and 100 atm. The total rate constants are calculated with extrapolated  $k(\dot{\text{C}}_2\text{H}_3 + \text{C}_3\text{H}_6 \rightarrow 1,4\text{-}\dot{\text{C}}_5\text{H}_9)$  and  $k(\dot{\text{C}}_2\text{H}_3 + \text{C}_3\text{H}_6 \rightarrow 3\text{Me-1,4-}\dot{\text{C}}_4\text{H}_6)$ , where no available rate constants exist.

As shown in Fig. 3.13(b), at 0.01 atm and temperatures above 500 K, the production of 1,3-C<sub>4</sub>H<sub>6</sub> + ĊH<sub>3</sub> is the most favoured and its cross-over point with BR(1,4- Ċ<sub>5</sub>H<sub>9</sub>) changes from 500 K to 1700 K as the pressure increases from 0.01 atm to 100 atm. The production of 1,4-C<sub>5</sub>H<sub>8</sub> + Ĥ is also important at high temperatures which doesn't show a strong pressure-dependence. Hence, the dominant product branching ratios of vinyl radical addition to propene show strong temperature- and pressure-dependencies, and  $k(T, p)$  need to be used to quantitatively predict product formation.

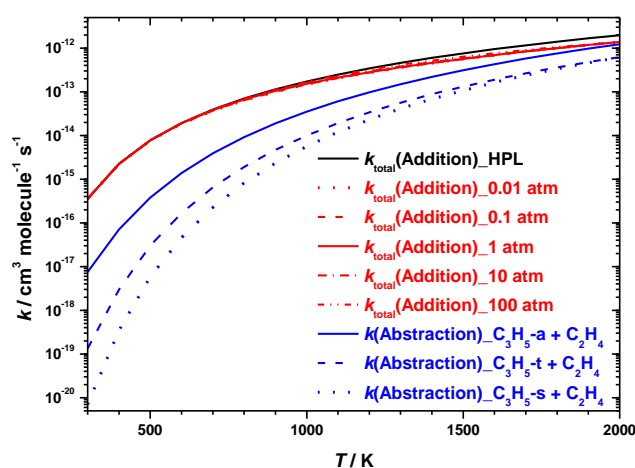


**Fig. 3.14** The total rate constant comparisons between the H-atom abstraction reactions and addition reactions of vinyl radical and propene.

The rate constants for H-atom abstraction reaction of propene by vinyl radicals are compared with its addition reactions at different pressures and high-pressure limiting rate constants in Fig. 3.14. The total addition rate constants are shown to have weak pressure dependence with a largest fall-off of 43% at 2000 K at pressures in the range 0.01–100 atm. The PES for H-atom abstraction reactions of C<sub>3</sub>H<sub>6</sub> by Ċ<sub>2</sub>H<sub>3</sub> radicals are described in detail in Fig. B.4. Vinyl radicals can abstract the allylic hydrogen atom from propene forming allyl radicals and ethylene, followed by forming 1-propen-2-yl radical and ethylene via abstraction of the secondary vinylic hydrogen atom on the central carbon, and finally abstraction of the two primary vinylic hydrogen atoms on the terminal carbon. As one might anticipate, the barrier heights for these three channels are 6.2, 10.0 and 12.1 kcal mol<sup>-1</sup>, respectively. The terminal abstractions can form cis- and trans-1-propen-1-yl radicals which have very similar barriers and the averaged rate constants are plotted in Fig. 3.14. The abstraction reactions for Ċ<sub>2</sub>H<sub>3</sub> + C<sub>3</sub>H<sub>6</sub> are non-negligible at high temperatures with the difference between  $k(\dot{C}_2H_3 + C_3H_6 \rightarrow C_2H_4 + \dot{C}_3H_5\text{-a})$  and  $k_{\text{total}}^{\text{HPL}}(\dot{C}_2H_3 + C_3H_6 \rightarrow \text{All products})$  being within a factor of

two at temperatures above 1700 K. For the pressure-dependent rate constants for addition reactions, the difference decreases to within a factor of two at temperatures above 1400 K. Therefore, H-atom abstraction from propene by vinyl radicals is important and needs to be considered at high temperatures.

Goldsmith et al. [11, 61, 62] carried out flow reactor experiments on vinyl + alkenes in the temperature range 300–700 K and at pressures of 15–100 Torr (0.02–0.13 atm), where the alkenes include ethylene, propene and butene isomers. They also studied vinyl + propene and its subsequent reactions at the G3 level of theory [11]. Li et al. [43] studied 1,3-butadiene +  $\dot{\text{H}}$  and related reactions on the  $\dot{\text{C}}_4\text{H}_7$  PES at the CCSD(T)/CBS//M06-2X/6-311++G(d,p) level of theory which includes vinyl addition to ethylene. The experimental and calculated rate constants for vinyl addition to different alkenes (ethylene, propene and butene isomers) at 0.13 atm are shown in Fig. 3.15. For the experiments at 0.13 atm, the fastest reaction is vinyl radical addition to propene, followed by isobutene, 1-butene, ethylene, and 2-butene [61]. The theoretical calculations also show that the rate constants for vinyl + propene are faster than vinyl + ethylene, and the averaged rate constant ratio ( $k_{\text{propene} + \text{vinyl}} / k_{\text{ethylene} + \text{vinyl}}$ ) for experiments and theoretical calculations is 1.8 and 1.7, respectively. Thus, the trends in our theoretical calculations for vinyl + propene and vinyl + ethylene are consistent with the experimental results.

In comparison with the experimental data at 0.13 atm, the rate constants for vinyl radical addition to propene producing all products calculated in this work are about two to three times slower in the temperature range 300–700 K. Goldsmith et al. [11, 61, 62] also carried out theoretical calculations for  $\text{C}_3\text{H}_6 + \dot{\text{C}}_2\text{H}_3$  which were in very good agreement with their experiments in the temperature range 350–700 K. Since we are using different levels of theory for theoretical calculations, detailed studies need to be carried out to analyse the possible reasons for the differences between the two theoretical studies. As shown in Fig. 3.13, 1,3-butadiene +  $\dot{\text{C}}\text{H}_3$  and 1,4- $\dot{\text{C}}_5\text{H}_9$  radicals are the dominant products for vinyl radical addition to propene at the experimental conditions. Furthermore, the  $k_\infty$  for vinyl + propene  $\rightarrow$  1,4- $\dot{\text{C}}_5\text{H}_9$  (R1) are over an order of magnitude faster than those for vinyl + propene  $\rightarrow$  3-methyl-1-buten-4-yl and/or vinyl + propene  $\rightarrow$  ethylene + allyl at temperature range 300–700 K. Hence, R1 is selected as a representative reaction to analyse the influence of different levels of theory on rate constant calculations.

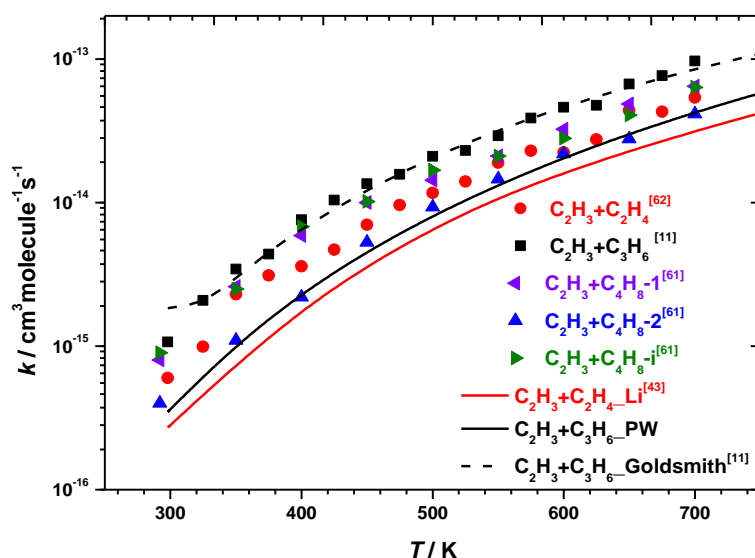


**Fig. 3.15** Comparison of the experimental and calculated rate constants for vinyl + alkenes (ethylene, propene and butene isomers) at 0.13 atm. Different symbols represent experimental results for different reactants: ● vinyl + ethylene [62], ■ vinyl + propene [11], ◀ vinyl + 1-butene [61], ▲ vinyl + 2-butene [61], ► vinyl + isobutene [61]. The red solid line represent calculated results from Li et al. [43] for vinyl + ethylene and the black dash line represent calculated results from Goldsmith et al. [11] for vinyl + propene.

The  $k_{\infty}$  for R1 are recalculated using Thermo and Densum code of MultiWell [63-65] at the level of theories used in this work and Goldsmith's study. The  $k_{\infty}$  of Goldsmith's calculations are 3.8 times larger at 300 K than this work and the difference decreases to 2.5 times at 700 K. The partition function contains all of the thermodynamic information associated with the system, including internal energy, entropy, heat capacity, etc.[66]. The partition function ratios for the TS of R1 taken from Goldsmith's work and this work are listed in Table 3.3. The comparison shows that: (i) at room temperature, the difference in energy barrier ( $0.6 \text{ kcal mol}^{-1}$  in R1) has the largest influence on the total ratio followed by the hindered-rotor treatment; (ii) the influence of vibrational partition functions ( $Q_{\text{vib}}$ ) increases as temperature increases, these becoming dominant at temperatures above 700 K; (iii) the rotational partition functions ( $Q_{\text{rot}}$ ) show smaller difference compared with other partition functions. These four partition function ratios are multiplied together to generate a total ratio to compare with the high-pressure limiting rate constant ratios of R1. The difference between these two ratios is within 20%, therefore, we can infer the difference between this work and Goldsmith's calculation is from the different theoretical methods used

for: (i) geometry optimization and vibrational frequency calculations, leading to differences in the prediction of vibrational partition functions  $Q_{\text{vib}}$  and rotational partition functions  $Q_{\text{rot}}$ ; (ii) single point energy calculation leading to 1.9 times difference at room temperature; (iii) hindered-rotor treatment which contribute to the 1.4 times difference of hindered-rotor partition function  $Q_{\text{hindro}}$ .

**Table 3.3** Comparison of the partition function ratios between this work and literature for vinyl + propene  $\rightarrow$  1,4- $\dot{\text{C}}_5\text{H}_9$ .

$T$	$R(Q_{\text{vib}})$	$R(Q_{\text{rot}})$	$R(Q_{\text{hindro}})$	$R(\text{Barrier})$	$R(Q_{\text{Total}})$	$R(k_{\infty})$
300	1.17	1.07	1.40	1.86	3.26	3.84
400	1.23	1.07	1.29	1.59	2.70	3.22
500	1.28	1.07	1.22	1.44	2.41	2.88
600	1.32	1.07	1.18	1.35	2.25	2.66
700	1.35	1.07	1.15	1.29	2.14	2.52

In this work, SPE calculations are carried out using ROCCSD(T) with augmented cc-pVTZ basis set extrapolated to cc-pVQZ and the uncertainty for CCSD(T) method is within 1 kcal mol<sup>-1</sup>. Goldsmith et al. [11] proposed that the tunneling correction and hindered rotor approximation are less accurate at lower temperature. Bugler et al. [67] studied reactions leading to cyclic ether formation and proposed that a factor of two may be assumed for uncertainties in harmonic vibrational frequencies and the anharmonicities of the 1-D hindered rotor mode. Jasper and Klippenstein [45, 68] proposed that neglecting vibrational anharmonicity can be the dominant source of uncertainty in *a priori* predictions of thermochemistry and kinetics. At room temperature an error of just 150 cm<sup>-1</sup> in the threshold or reaction energy leads to an uncertainty of a factor of two in the computed rate coefficient or equilibrium constant [69]. Thus, in this work, two to three times uncertainty is expected in our theoretical calculations and hence the deviation between our calculation and experimental results are within the uncertainty.

### 3.3.2 Unimolecular reactions

#### 3.3.2.1 1,3- $\dot{\text{C}}_5\text{H}_9$

The total pressure-dependent rate constants of 1,3- $\dot{\text{C}}_5\text{H}_9 \rightarrow$  all products are compared with the corresponding high-pressure limiting rate constants in Fig. 3.16(a). At 1000 K, the fall-off of  $k(1,3-\dot{\text{C}}_5\text{H}_9 \rightarrow \text{all})$  from the high-pressure limit to 0.01 atm is less than a factor of

two at temperatures below 800 K and increases to over two orders of magnitude at 1200 K. At 10 atm, which is a frequently used condition in shock tube experiments, the fall-off compared with  $k_\infty$  can be more than an order of magnitude at temperatures above 1600 K. Hence, the total rate constants of the decomposition of  $1,3-\dot{\text{C}}_5\text{H}_9$  show an obvious temperature- and pressure-dependence.

The branching ratios for the main products of  $1,3-\dot{\text{C}}_5\text{H}_9$  radical decomposition are plotted in Fig. 3.16(b). There is no significant pressure-dependence found for the branching ratios of these two dominant products, which is different with the phenomenon found for bimolecular reactions in our previous discussions. At low temperatures and at different pressures, the formation of  $2,5-\dot{\text{C}}_5\text{H}_9$  radicals are the most favoured having the largest BR of  $\sim 96\%$  at 400 K. The BRs for the formation of  $2,5-\dot{\text{C}}_5\text{H}_9$  radicals decrease rapidly with increasing temperature and are overtaken by the formation of  $1,3-\text{C}_4\text{H}_6 + \dot{\text{C}}\text{H}_3$  at temperatures around 650 K. At temperatures above 1000 K, over 87% of the products formed from  $1,3-\dot{\text{C}}_5\text{H}_9$  radicals are  $1,3-\text{C}_4\text{H}_6 + \dot{\text{C}}\text{H}_3$  radicals with the largest BR of 96.8%.

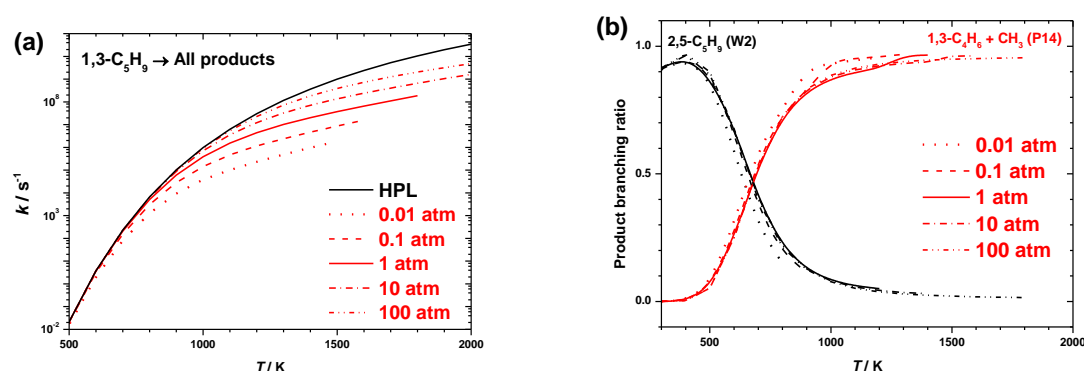


**Fig. 3.16** (a) The comparisons of pressure-dependent rate constants and high-pressure limiting rate constants for  $1,3-\dot{\text{C}}_5\text{H}_9 \rightarrow$  all products as a function of temperature. (b) The branching ratios for main products from decomposition of  $1,3-\dot{\text{C}}_5\text{H}_9$  radical at 0.01, 0.1, 1, 10 and 100 atm.

To validate our calculated rate constants,  $k(1,3-\dot{\text{C}}_5\text{H}_9 \rightarrow 1,3-\text{C}_4\text{H}_6 + \dot{\text{C}}\text{H}_3)$  the high-pressure limiting rate constants and those at different pressures are compared with available literature studies in Fig. 3.17. Wang et al. [13, 14] calculated the high-pressure limiting rate constants for this reaction using Quantum-Rice-Ramsperger-Kassel (QRRK) theory with species and TSs on the  $\dot{\text{C}}_5\text{H}_9$  PES calculated at the CBS-QB3 level of theory. Baldwin and Walker [21] estimated the rate constants at 500 Torr (0.66 atm) based on their alkenes/ $\text{H}_2/\text{O}_2$  experimental results, and Perrin et al. [24] carried out measurement on the

isomerisation reaction of 1- and 2-pentene and derived the rate constant for  $1,3\text{-}\dot{\text{C}}_5\text{H}_9 \rightarrow 1,3\text{-C}_4\text{H}_6 + \dot{\text{C}}\text{H}_3$  in the pressure range 10–100 Torr (0.01–0.13 atm). As shown in Fig. 3.17, the  $k_\infty$  from Wang are 3.6 times faster than that calculated here at 1000 K and decrease to within 1.3 times difference at 2000 K. The difference at low temperatures possibly arises from the initial guess of  $A$  and  $E_a$  for the reverse reaction used in the QRRK calculation. Meanwhile, the rate constants at 0.01 atm from this work agree reasonably well with Perrin’s experimentally derived results at pressures in the range 0.01–0.13 atm with the differences being within 2.3–2.7 times. It is worth noting that the rate constant at 0.7 atm from Baldwin et al. tends to be too fast in comparison with this work and close to Wang’s high-pressure limiting rate constant.

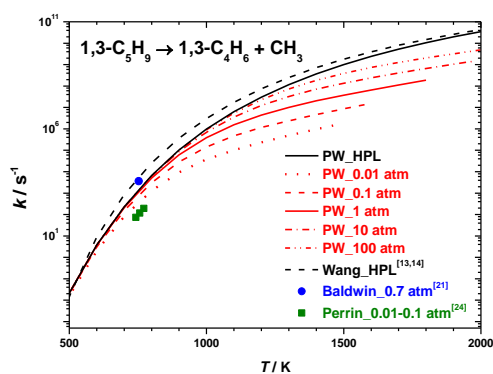


**Fig. 3.17** Rate constant comparisons for the  $\beta$ -scission reaction of  $1,3\text{-}\dot{\text{C}}_5\text{H}_9$  radical forming  $1,3\text{-C}_4\text{H}_6 + \dot{\text{C}}\text{H}_3$ . The dashed lines represent the calculated results from Wang et al. [13, 14] at CBS-QB3 level of theory, the blue symbol represents Baldwin and Walker’s [21] estimated result based on their alkenes/ $\text{H}_2/\text{O}_2$  experimental results, and the green symbols represent experimental results from Perrin et al. [24] over pressure range 10–100 Torr (0.01–0.13 atm).

Wang et al. [13, 14] also have studied rate constants for  $1,3\text{-}\dot{\text{C}}_5\text{H}_9 \rightarrow 1,3\text{-C}_5\text{H}_8 + \dot{\text{H}}$  and  $1,4\text{-}\dot{\text{C}}_5\text{H}_9 \rightarrow \text{C}_3\text{H}_6 + \dot{\text{C}}_2\text{H}_3$ ; the rate constant comparisons of these two reactions are shown in Fig. B.5. The rate constants calculated in the present work agrees relatively well with Wang’s calculation for these two reactions with the values being within 1.3 – 3.5 times in the temperature range 300–2000 K.

### 3.3.2.2 1,4- $\dot{\text{C}}_5\text{H}_9$

The total pressure-dependent rate constants of  $1,4\text{-}\dot{\text{C}}_5\text{H}_9 \rightarrow$  all products are compared with the corresponding high-pressure limiting rate constants in Fig. 3.18(a). The dominant products at low temperatures are methylenecyclopropylmethyl (W13,  $\dot{\text{C}}\text{H}_2\text{-cyC}_3\text{H}_4\text{CH}_3$ )

and 3-methyl-1-buten-4-yl (W14, 3Me-1,4- $\dot{C}_4H_6$ ) formed via a low-energy barrier ring-opening reaction from W13. Due to  $k(1,4-\dot{C}_5H_9 \rightarrow 3Me-1,4-\dot{C}_4H_6)$  and  $k(1,4-\dot{C}_5H_9 \rightarrow \dot{C}H_2-cyC_3H_4CH_3)$  are not available over the entire temperature range, rate constants for these two channels are extrapolated to intermediate and/or high temperatures. It is shown that the fall-off of the total rate constants at 1700 K and 1 atm is over an order of magnitude, which indicates the significant pressure-dependence of the decomposition of 1,4- $\dot{C}_5H_9$  radical.

Based on calculated and extrapolated pressure-dependent rate constants, the branching ratios for important products produced from the decomposition of 1,4- $\dot{C}_5H_9$  radical are shown in Fig. 3.18(b). At 1 atm, the formation of W14 is dominant with a BR over 80% at temperatures below 1100 K. Meanwhile, there is about 10 – 20% W13 formed over the temperature range of 300 – 1400 K. As pressure increases, the formation of W14 at a specific temperature decreases until overtaken by the formation of W13 at 100 atm. There are also reasonable amounts (<10%) of bimolecular products (1,3- $C_4H_6 + \dot{C}H_3$ ) formed via the direct  $\beta$ -scission reaction of W14 and/or the chemically activated reaction at high temperatures. The total rate constant and branching ratio comparisons show the total rate constants have strong pressure-dependence and the product branching ratios are also sensitive to pressure and temperature.

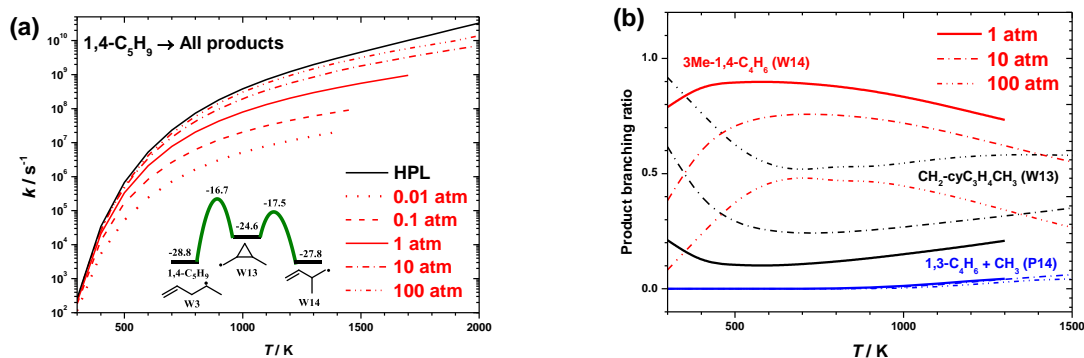


**Fig. 3.18** (a) The comparisons of pressure-dependent rate constants and high-pressure limiting rate constants for 1,4- $\dot{C}_5H_9 \rightarrow$  all products as a function of temperature.  $k(1,4-\dot{C}_5H_9 \rightarrow 3Me-1,4-\dot{C}_4H_6)$  are extrapolated over a temperature range of 800 – 1400 K at 0.01 atm, 900 – 1500 K at 0.1 atm, 1100 – 1700 K at 1 atm, 1400 – 2000 K at 10 atm.  $k(1,4-\dot{C}_5H_9 \rightarrow \dot{C}H_2-cyC_3H_4CH_3)$  are extrapolated over a temperature range of 600 – 1700 K at 1 atm, 700 – 2000 K at 10 atm and 900 – 2000 K at 10 atm. (b) The branching ratios for main products from decomposition of 1,4- $\dot{C}_5H_9$  radical at 0.01, 0.1, 1, 10 and 100 atm. The total rate constants are calculated with extrapolated  $k(1,4-\dot{C}_5H_9 \rightarrow 3Me-1,4-\dot{C}_4H_6)$  and  $k(1,4-\dot{C}_5H_9 \rightarrow \dot{C}H_2-cyC_3H_4CH_3)$ , where no available rate constants exist.

### 3.3.2.3 1,5- $\dot{\text{C}}_5\text{H}_9$

The total pressure-dependent rate constants of  $1,5\text{-}\dot{\text{C}}_5\text{H}_9 \rightarrow$  all products are compared with the corresponding high-pressure limiting rate constants in Fig. 3.19(a). The fall-off in pressure-dependent rate constants compared with  $k_\infty$  can be up to two orders of magnitude at 1000 K and 0.01 atm, and  $\sim 7.6$  times at 1500 K and 10 atm. Therefore, the total rate constants for the decomposition of  $1,5\text{-}\dot{\text{C}}_5\text{H}_9$  radicals show an obvious pressure-dependence. The branching ratios for the dominant products generated from the decomposition of  $1,5\text{-}\dot{\text{C}}_5\text{H}_9$  radical are shown in Fig. 3.19(b). At 0.01 atm, the formation of cyclopentyl radical dominates at temperatures below 600 K until it is overtaken by the production of ethylene and allyl radicals. At 100 atm and low temperatures ( $< 500$  K), about half of the reaction flux proceeds to form cyclopentyl radical with the other half forming methyldene-cyclobutyl radicals. The branching ratios of cyclopentyl and methyldene-cyclobutyl radicals have an obvious pressure-dependence at low temperatures, and their pressure-dependence diminishes gradually until it disappears at 1200 K. Meanwhile, the branching ratios of ethylene and allyl radical only show a pressure-dependence in the temperature range 500–1100 K. Hence, the pressure-dependent rate constants for the formation of ethylene and allyl radical should be considered in combustion mechanism development, and the pressure-dependent rate constants for the formation of cyclopentyl and methyldene-cyclobutyl radicals should also be included for simulations at temperatures below 1100 K.

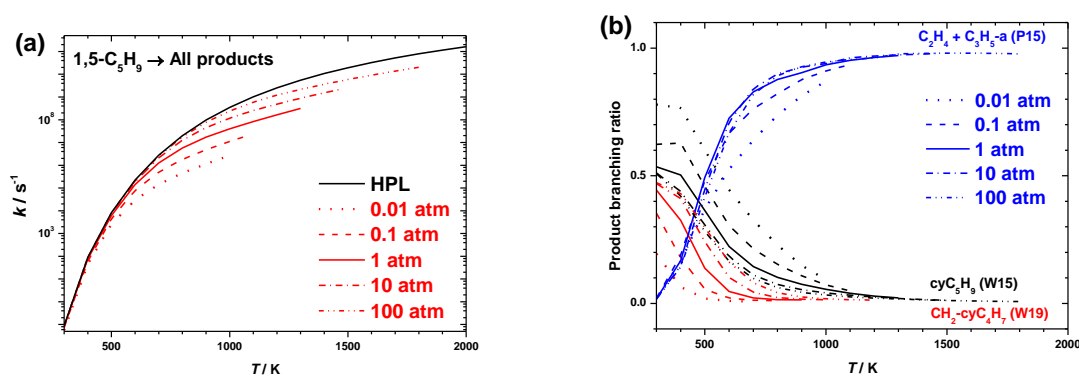


**Fig. 3.19** (a) The comparisons of pressure-dependent rate constants and high-pressure limiting rate constants for  $1,5\text{-}\dot{\text{C}}_5\text{H}_9 \rightarrow$  all products as a function of temperature. (b) The branching ratios for main products from decomposition of  $1,5\text{-}\dot{\text{C}}_5\text{H}_9$  radical at 0.01, 0.1, 1, 10 and 100 atm.

The  $\beta$ -scission reaction of  $1,5\text{-}\dot{\text{C}}_5\text{H}_9$  to form ethylene + allyl radical has been studied by Tsang et al. [8] and Awan et al. [12]; the comparison of the high-pressure limiting rate

constants is shown in Fig. 3.20. Awan and co-workers [12] calculated the structural properties of radicals and stable species at the G3MP2B3 level of theory with a frequency scale factor of 0.96. Slight adjustments were made to the low frequency vibrations and reaction barriers to create a model that fitted their experimental data. They proposed that the standard uncertainties in the absolute rate constants are about a factor of 1.5 near 1000 K, increasing to a factor of two at 700 K and a factor of three at 1900 K. Tsang [8] studied the decomposition and isomerization reactions of 1,5- $\dot{\text{C}}_5\text{H}_9$  radicals, estimating the energy barriers from available literature data. Rate constants were obtained by solving the Rice-Ramsperger-Kassel-Marcus (RRKM) and time-dependent Master Equation (ME). They proposed that breaking the allylic C–C bond to form allyl radicals and ethylene was the main reaction channel [8].

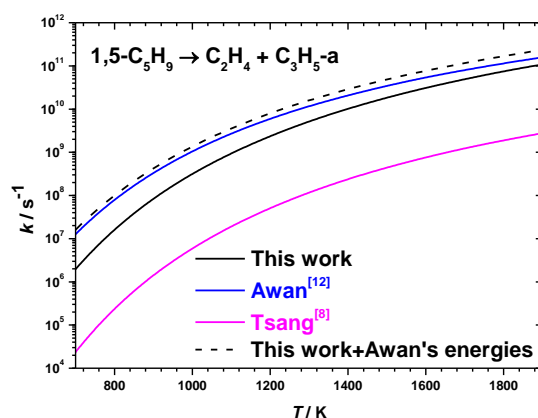


**Fig. 3.20** High-pressure limiting rate constants for  $\beta$ -scission reaction of 1,5- $\dot{\text{C}}_5\text{H}_9$  radical to allyl + ethylene. The blue line represents results calculated by Awan et al. [12] and the magenta line represents results calculated by Tsang et al. [8].

The energy barriers for  $\beta$ -scission of the 1,5- $\dot{\text{C}}_5\text{H}_9$  radical are 21.6 kcal mol<sup>-1</sup> in this work, 19.9 kcal mol<sup>-1</sup> in Awan's work and 24.7 kcal mol<sup>-1</sup> in Tsang's work. The rate constants calculated in this work also lie between those proposed by Awan and Tsang corresponding to the trend in the energy barriers. The rate constants from Awan's work are 4.9 times higher than this work at 800 K and are 1.4 times higher at 1900 K. To test the influence of the different energy barriers, a calculation was carried out by replacing only the energy barrier in the current work to Awan's value. The rate constants calculated from this test are within 1.5 times of Awan's values in the temperature range 700 – 1900 K. Thus, the rate constant difference between this work and Awan's are mainly derived from the difference in energy barriers calculated at the different levels of theory and/or their adjustments in reaction barrier

heights. Since the energies in this work are calculated at the ROCCSD(T) level of theory with the basis set extrapolated to aug-cc-pVQZ compared to the G3MP2B3 level used in Awan's work, we believe our calculations to be more reliable. Similarly, the rate constant difference between the present work and Tsang's study possibly arises from uncertainties in their A-factor estimations.

### 3.3.2.4 Cyclopentyl radical reactions

The total pressure-dependent rate constants of  $\text{cy}\dot{\text{C}}_5\text{H}_9 \rightarrow \text{all products}$  are compared with the corresponding high-pressure limiting rate constants in Fig. 3.21(a). Similar to the other  $\dot{\text{C}}_5\text{H}_9$  radicals, the total rate constants for the decomposition of  $\text{cy}\dot{\text{C}}_5\text{H}_9$  radicals show an obvious temperature- and pressure-dependence. The fall-off can be up to two orders of magnitude at 0.01 atm and over an order of magnitude at 10 atm. The branching ratios for the dominant products generated from the decomposition of  $\text{cy}\dot{\text{C}}_5\text{H}_9$  radical are shown in Fig. 3.21(b). At 300 K, approximately 86.4% of  $\text{cy}\dot{\text{C}}_5\text{H}_9$  radicals lead to 1,5- $\dot{\text{C}}_5\text{H}_9$  radicals, with 13.6% decomposing to  $\text{cyC}_5\text{H}_8 + \dot{\text{H}}$  atoms. As temperature increases, the BR leading to 1,5- $\dot{\text{C}}_5\text{H}_9$  radicals decreases rapidly and becomes undefinable, when well-skipping occurs and the chemically activated reactions forming bimolecular products start to dominant. The importance of  $\text{C}_2\text{H}_4 + \dot{\text{C}}_3\text{H}_5\text{-a}$  formation decreases with increasing pressure while the formation of  $\text{cyC}_5\text{H}_8 + \dot{\text{H}}$  only shows a slight positive pressure-dependence. The  $\text{BR}(\text{C}_2\text{H}_4 + \dot{\text{C}}_3\text{H}_5\text{-a})/\text{BR}(\text{cyC}_5\text{H}_8 + \dot{\text{H}})$  ratios are shown to be temperature- and pressure-dependent and are very important in the simulation of  $\text{cyC}_5\text{H}_8$  and  $\text{cyC}_5\text{H}_{10}$  profiles.

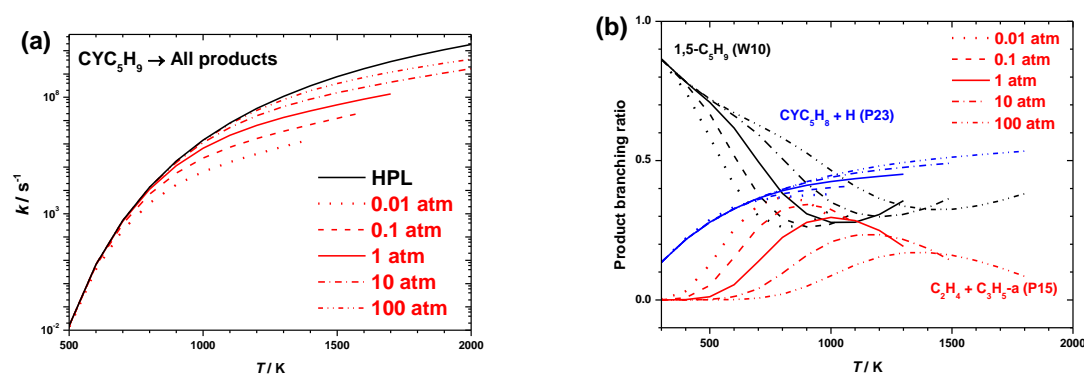


**Fig. 3.21** (a) The comparisons of pressure-dependent rate constants and high-pressure limiting rate constants for  $\text{cy}\dot{\text{C}}_5\text{H}_9 \rightarrow \text{all products}$  as a function of temperature. (b) The branching ratios for main products from decomposition of  $\text{cy}\dot{\text{C}}_5\text{H}_9$  radical at 0.01, 0.1, 1, 10 and 100 atm.

As described previously, Tsang [8] calculated the high-pressure limiting rate constants for the decomposition reactions of 1,5- $\dot{C}_5H_9$  using energy barriers estimated from available literature data at that time. Sirjean et al. [10] calculated the high-pressure limiting rate constants for cyclization reaction of 1,5- $\dot{C}_5H_9$  at the CBS-QB3 level of theory using classical TST in the temperature range 500–2000 K. Wang et al. [13, 14] studied reactions related to 1,5- $\dot{C}_5H_9$  on the  $\dot{C}_5H_9$  PES using the CBS-QB3 composite method. Pressure-dependent rate constants were calculated using Quantum-Rice-Ramsperger-Kassel (QRRK) theory and  $k_\infty$  were calculated from CBS-QB3 calculations or were estimated based on reaction rate rules. Al Rashidi et al. [15] calculated high-pressure limiting rate constants for C–C and C–H  $\beta$ -scission reactions at the UCCSD(T)-F12b/cc-pVTZ-F12//M06-2X/6-311++G(d,p) level of theory. Awan and co-workers [12, 16] calculated the rate constants for cy $\dot{C}_5H_9$  decomposition reactions using a combination of RRKM/ME calculations and the derived product ratio from their shock tube experiments for cy $\dot{C}_5H_9$  decomposition.

Gordon [17] measured the  $k(\dot{C}D_3 + cyC_5H_{10} \rightarrow CD_3H + cy\dot{C}_5H_9) \cdot k(cy\dot{C}_5H_9 \rightarrow C_2H_4 + \dot{C}_3H_5-a) / k(\dot{C}D_3 + cy\dot{C}_5H_9 \rightarrow CH_3-cyC_5H_9)$  ratios by studying the photolysis of cyclopentane–acetone mixtures between 580–680 K at pressures in the range 0.05–0.06 bar. The ratios were derived from product yields and the pre-exponential factor ( $A$ ) and the activation energy ( $E_a$ ) for  $cy\dot{C}_5H_9 \rightarrow C_3H_5-a + C_2H_4$  were derived with reasonable  $A$  and  $E_a$  values for the other two reactions obtained from the literature. Handford-Styring and Walker [26] studied cyclopentane oxidation by adding cyclopentane to  $H_2$ – $O_2$  mixtures in the temperature range 673–783 K at 500 Torr (0.66 atm). The  $k(cy\dot{C}_5H_9 \rightarrow 1,5-\dot{C}_5H_9)$  was considered as the rate determining step for the production of  $C_2H_4 + \dot{C}_3H_5-a$  and was determined by the yields of ethylene. They also reinterpreted Gordon’s data with new rate constants for  $CD_3 + cyC_5H_{10} \rightarrow CD_3H + cy\dot{C}_5H_9$  and  $CD_3 + cy\dot{C}_5H_9 \rightarrow CH_3-cy\dot{C}_5H_9$  which are plotted as revised data in Fig. 3.22(a).

The  $k_\infty$  comparisons between this work and the literature data for cy $\dot{C}_5H_9$  decomposition reactions are shown in Fig. 3.22. For  $cy\dot{C}_5H_9 \rightarrow cyC_5H_8 + \dot{H}$ , large discrepancies are observed among the different literature values (e.g. the difference between the rate constants of Sirjean and Tsang is about a factor of 50 at 2000 K). These large discrepancies are mainly due to three reasons: (1) different level of theories used in the quantum calculations; (2) different software employed in rate constant calculations; (3) empirical adjustments for the frequencies and energy barriers. At temperatures above 1200 K, the trend of  $k_\infty$  for this channel is:  $k_\infty(\text{Tsang}) < k_\infty(\text{This work}) < k_\infty(\text{Al Rashidi}) < k_\infty(\text{Awan}) < k_\infty(\text{Sirjean})$ . The  $k_\infty$  calculated here agrees well with Al Rashidi’s high-level calculation, with both values being

within 40% of one another in the temperature range 700–2000 K. For pressure-dependent rate constants, the values calculated here are compared with available experimental data as presented in Fig. 3.22(a). Handford-Styring and Walker [26] carried out measurements at 0.67 atm and our results, calculated at 1.0 atm agrees very well with theirs. The revised Gordon’s results also show good agreement with Handford-Styring and this work at low temperatures where the rate constants show no obvious fall-off.

For  $\text{cy}\dot{\text{C}}_5\text{H}_9 \rightarrow 1,5\text{-}\dot{\text{C}}_5\text{H}_9 + \text{H}$  shown in Fig. 3.22(b), the largest discrepancy in the literature data is a factor of 15 over the entire temperature range. The trend of  $k_\infty$  at 1000–2000 K is:  $k_\infty$  (Tsang) <  $k_\infty$  (This work)  $\approx$   $k_\infty$  (Al Rashidi) <  $k_\infty$  (Wang) <  $k_\infty$  (Awan) <  $k_\infty$  (Sirjean). The  $k_\infty$  of Sirjean are similar to those of Awan and are consistently over eight times faster than our calculations. Wang and Sirjean both used the CBS-QB3 level of theory for optimizations and energy calculations, the difference for  $k_\infty$  calculated from these two studies is less than a factor of two over the entire temperature range. Similar to  $\text{cy}\dot{\text{C}}_5\text{H}_9 \rightarrow \text{cyC}_5\text{H}_8 + \dot{\text{H}}$ , the  $k_\infty$  for the ring-opening reaction in the present work agree very well with those presented by Al Rashidi et al. [15], being within 20% of one another in the temperature range 700–2000 K. Al Rashidi et al. [15] simulated the combustion of  $\text{cyC}_5\text{H}_{10}$  in a JSR and found that the better fits to the concentration profiles of  $\text{cyC}_5\text{H}_{10}$  in the experiments were obtained using their rate constants compared with the literature data. In addition,  $k(\text{cy}\dot{\text{C}}_5\text{H}_9 \rightarrow 1,5\text{-}\dot{\text{C}}_5\text{H}_9)$  measured in Handford-Styring’s experiment agree very well with our results at 1 atm. Hence, we believe that the high-pressure limiting rate constants for  $\text{cy}\dot{\text{C}}_5\text{H}_9$  radical decomposition calculated in this work should be reliable.

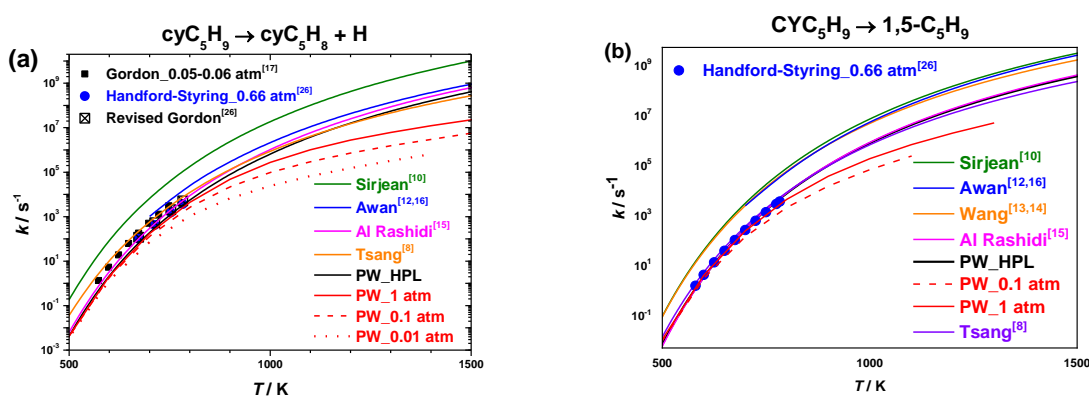


**Fig. 3.22** Rate constants for (a) C–H  $\beta$ -scission reaction of  $\text{cy}\dot{\text{C}}_5\text{H}_9$  radicals forming  $\text{cyC}_5\text{H}_8 + \dot{\text{H}}$ , (b) C–C  $\beta$ -scission reaction of  $\text{cy}\dot{\text{C}}_5\text{H}_9$  radicals forming  $1,5\text{-}\dot{\text{C}}_5\text{H}_9$ . The green, blue, orange, red and magenta lines represent results calculated by Sirjean et al. [10], Awan et al. [12, 16], Wang et al. [13, 14], Al Rashidi et al. [15], and Tsang et al. [8], respectively. The symbols stand for different results derived from experiments: ■ Gordon [17], ● Handford-Styring [26], ☒ revised values of Gordon’s work by Handford-Styring [26].

Al Rashidi and co-workers [15] carried out the identification and quantification of species generated during the oxidation of  $\text{cyC}_5\text{H}_{10}$  in a JSR. They conducted sensitivity and reaction path analyses and found that the reactivity of  $\text{cyC}_5\text{H}_8$  was highly sensitive to the C–C/C–H scission branching ratio of  $\text{cy}\dot{\text{C}}_5\text{H}_9$  radical decomposition. The high-pressure limiting branching ratio for  $\text{cy}\dot{\text{C}}_5\text{H}_9$  decompositions was compared with theoretical results from the literature in the temperature range 900–1200 K. The branching ratios from Awan [12], this work, Al Rashidi [15], Tsang [8] and Sirjean [10] at 1000 K are 3.46, 1.22, 0.84, 0.78 and 0.39, respectively. What stands out is that these high-pressure limiting branching ratios indicate the  $k_\infty$  for the ring-opening reaction (C–C  $\beta$ -scission) is similar or even slower than that for the C–H  $\beta$ -scission reaction excluding Awan’s result, which is 8.8 times larger than that of Sirjean. It is noticeable that the deviations in branching ratios between this work and those of Al Rashidi and Tsang are within 50% (Fig. 3.23). The C–C/C–H high-pressure limiting branching ratio in Awan’s work were derived from the experimental yields of  $\text{C}_2\text{H}_4$  and  $\text{cyC}_5\text{H}_8$  [12], with slight adjustments for low frequency vibrations in the TSs and small empirical changes in reaction barriers to fit their experimental data. As suggested by Manion and Awan [12, 16], the discrepancies in branching ratios between the experiments and theoretical calculations for  $\text{cy}\dot{\text{C}}_5\text{H}_9$  radical decomposition show the difficulties in precisely predicting branching ratios when two competitive channels have similar rate constants. In addition, it is also possible that the additives (species used as  $\dot{\text{H}}$  source, radical scavenger), which are used in large amounts in the experiment, and their decomposition products may react with  $\text{cyC}_5\text{H}_{10}$  or with the intermediates to influence the formation/consumption of  $\text{cyC}_5\text{H}_8$ . Hence, to obtain accurate branching ratios for  $\text{cy}\dot{\text{C}}_5\text{H}_9$  radical decomposition, more high-level theoretical calculations and benchmarking experimental measurements are needed. The species profiles for Manion’s  $\text{cyC}_5\text{H}_{10} + \dot{\text{H}}$  experiments are simulated with our model and the chemistry is discussed in detail in Section 3.4.2.

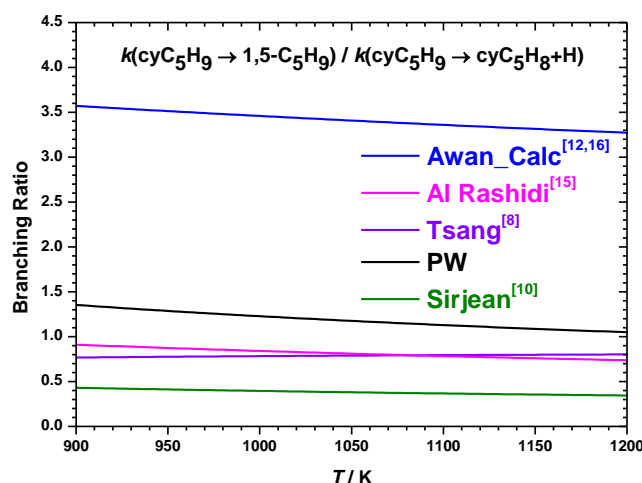


**Fig. 3.23** The branching ratios of  $\text{cy}\dot{\text{C}}_5\text{H}_9$  radicals comparing with high-pressure limiting rate constants in the literature. The blue, red, magenta and green lines represent results calculated by Awan et al. [12, 16], Al Rashidi et al. [15], Tsang et al. [8], and Sirjean et al. [10], respectively.

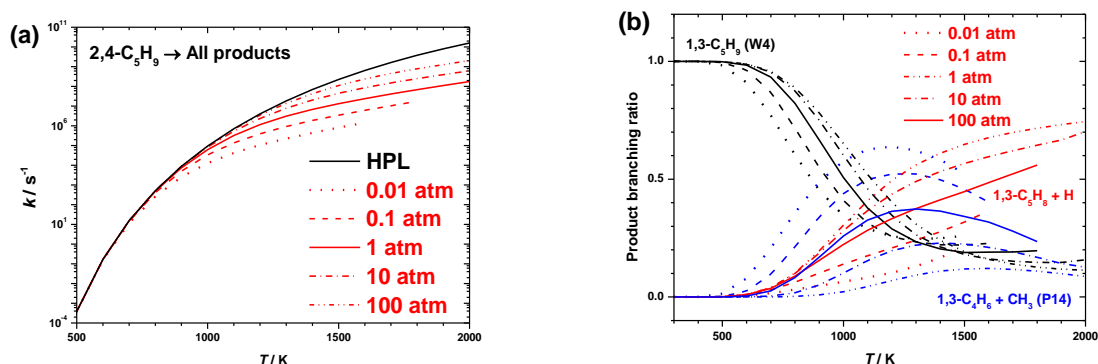


**Fig. 3.24** (a) The comparisons of pressure-dependent rate constants and high-pressure limiting rate constants for  $2,4\text{-}\dot{\text{C}}_5\text{H}_9 \rightarrow$  all products as a function of temperature. (b) The branching ratios for main products from decomposition of  $2,4\text{-}\dot{\text{C}}_5\text{H}_9$  radical at 0.01, 0.1, 1, 10 and 100 atm.

### 3.3.2.5 $2,4\text{-}\dot{\text{C}}_5\text{H}_9$

As shown in Fig. 3.24(a), the total pressure-dependent rate constants of  $2,4\text{-}\dot{\text{C}}_5\text{H}_9 \rightarrow$  all products show significant fall-off with a largest fall-off of over two orders of magnitude at 0.01 atm and 1500 K. At low temperatures ( $< 700$  K) shown in Fig. 3.24(b), over 90% of  $2,4\text{-}\dot{\text{C}}_5\text{H}_9$  radicals undergo isomerisation to form  $1,3\text{-}\dot{\text{C}}_5\text{H}_9$  radicals, and as temperature increases, the production of  $1,3\text{-}\text{C}_4\text{H}_6 + \dot{\text{C}}\text{H}_3$  is preferred at low pressures and the production of  $1,3\text{-}\text{C}_5\text{H}_8 + \dot{\text{H}}$  is preferred at high pressures. The branching ratios of bimolecular products

generated from the decomposition of 2,4- $\dot{C}_5H_9$  radicals are temperature- and pressure-dependent which should be considered in simulating species profiles.

### 3.3.2.6 2,5- $\dot{C}_5H_9$

The total pressure-dependent rate constants of 2,5- $\dot{C}_5H_9 \rightarrow$  all products are compared with the corresponding high-pressure limiting rate constants in Fig. 3.25(a). The rate constants for the dominant channel 2,5- $\dot{C}_5H_9 \rightarrow$  sec-ethyl-cyclopropane (W6,  $CH_3\dot{C}H-cyC_3H_5$ ) become undefinable at relatively low temperatures compared with other  $\dot{C}_5H_9$  radicals, which suggests the rate constant calculations for reactions related to 2,5- $\dot{C}_5H_9$  radical are more difficult. The rate constants for this channel are extrapolated to intermediate and/or high temperatures, and then the total rate constants and branching ratios are calculated. Similar to the other  $\dot{C}_5H_9$  radicals, the total rate constants for the decomposition of the 2,5- $\dot{C}_5H_9$  radical show obvious fall-off at high temperatures, and the fall-off at 10 atm can reach up to an order of magnitude.

The BRs of dominant products generated from the decomposition of 2,5- $\dot{C}_5H_9$  radical are shown in Fig. 3.25(b). At low temperatures and high pressures, the ring-formation channel forming sec-ethyl-cyclopropane ( $CH_3\dot{C}H-cyC_3H_5$ ) radical with a low-energy barrier is dominant. However, as illustrated in Part I, there are no subsequent reactions of sec-ethyl-cyclopropane radicals which have energy barriers lower than the reverse reaction of its formation. Meanwhile, at low pressures, the formation of 1,3- $\dot{C}_5H_9$  radical is also significant with a maximum BR over 40% at 0.01 atm. 1,3- $\dot{C}_5H_9$  radical is formed via a chemically activated reaction, which contributes to the formation of 1,3- $C_4H_6 + \dot{C}H_3$  via direct  $\beta$ -scission reaction. As one might anticipate, the BRs of  $CH_3\dot{C}H-cyC_3H_5$  radical increases as pressure increases and the BR(1,3- $\dot{C}_5H_9$ ) decreases as pressure increases due to their competition. The BRs of 1,3- $C_4H_6 + \dot{C}H_3$  increases as temperature increases and decreases with increasing pressure, and there are certain amounts of the other bimolecular products formed at high temperatures and high pressures. The obvious pressure-dependence of the BRs indicates the importance of pressure-dependent rate constants on product predictions.

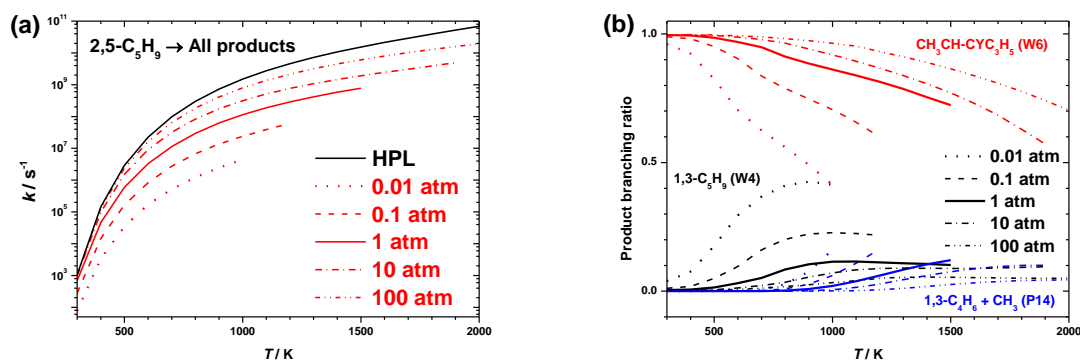


**Fig. 3.25** (a) The comparisons of pressure-dependent rate constants and high-pressure limiting rate constants for  $2,5\text{-}\dot{\text{C}}_5\text{H}_9 \rightarrow \text{all products}$  as a function of temperature.  $k(2,5\text{-}\dot{\text{C}}_5\text{H}_9 \rightarrow \text{CH}_3\dot{\text{C}}\text{H-cyC}_3\text{H}_5)$  are extrapolated over a temperature range of 600–1000 K at 0.01 atm, 700–1200 K at 0.1 atm, 800–1500 K at 1 atm, 900–1900 K at 10 atm. (b) The branching ratios for main products from decomposition of  $2,5\text{-}\dot{\text{C}}_5\text{H}_9$  radical at 0.01, 0.1, 1, 10 and 100 atm, with  $k(2,5\text{-}\dot{\text{C}}_5\text{H}_9 \rightarrow \text{CH}_3\dot{\text{C}}\text{H-cyC}_3\text{H}_5)$  extrapolated where no available rate constants exist.

### 3.4 Chemical kinetic modelling

The chemical kinetic model with pressure-dependent rate constants have been used for homogenous batch reactor simulations and the species profiles for different wells and products are compared with available experimental results to analyse and validate the chemistry of  $\dot{\text{C}}_5\text{H}_9$  radicals at different temperatures and pressures.

Awan et al. [12] performed single-pulse shock tube experiments to study the thermal decomposition of cyclopentyl radical in the temperature range 950–1116 K at pressures of 2.3–3.4 bar. Cyclopentyl radicals were generated by H-atom abstraction from cyclopentane by  $\dot{\text{H}}$  atoms, which were produced by the decomposition of hexamethylethane (HME). 1,3,5-trimethylbenzene (T135MB) was used as both a rate reference for  $\dot{\text{H}}$  atom reactions and as a radical scavenger. The reverse Diels-Alder reaction of 4-vinylcyclohexene (VCH) which produces 1,3-butadiene was used as a standard reaction, and the shock temperatures were determined by following the progression of this reaction which had a known rate constant. In 2018, Manion and Awan studied  $\dot{\text{H}}$  atom addition to cyclopentene in a single pulse shock tube at 863–1167 K and 160–370 kPa [16]. HME was used as a  $\dot{\text{H}}$  atom source and T135MB as a radical scavenger for three mixtures at temperatures above 1000 K.

To simulate their experiments, the rate constants for reactions related to these additives and the thermochemistry for them and their related species are included in our model which

is described in detail in detail below. The closed homogeneous batch reactor model in Chemkin-Pro is used to predict the mole fractions of different products generated from cyclopentane +  $\dot{\text{H}}$  and cyclopentene +  $\dot{\text{H}}$ . Five mixtures in total (two for  $\text{cyC}_5\text{H}_{10}$  +  $\dot{\text{H}}$  and three for  $\text{cyC}_5\text{H}_8$  +  $\dot{\text{H}}$ ) containing HME and 135TMB fuels are simulated at experimental conditions and the comparison results are shown in Figs. 3.26–3.28. For each experiment, Mixture A has been measured over a wide temperature range, while there are only a few data points measured for Mixtures B and C. To simplify the plots, the experimental data points for Mixtures B and C are plotted as open/crossed symbols, and their corresponding simulated concentrations are plotted together with Mixture A as outstanding points.

### 3.4.1 Cyclopentane + $\dot{\text{H}}$ $\rightarrow$ different products

For the cyclopentane +  $\dot{\text{H}}$  experiments, no concentration profiles of the reactants are provided in Manion’s paper [16]. Hence, only the concentration profiles for different products generated from the reactions of  $\text{cyC}_5\text{H}_{10}$ , HME, T135MB and VCH are simulated and analysed. For mixtures A and B used in the experiments, the main difference is the use of T135MB as a radical scavenger in Mixture A and not in Mixture B.

As shown in Fig. 3.26, the concentration profiles of isobutene, which is generated via  $\text{HME} \rightarrow 2\dot{\text{C}}_4\text{H}_9\text{-I} \rightarrow 2\text{C}_4\text{H}_8\text{-I} + 2\dot{\text{H}}$ , is very well predicted by our model, indicating the accurate prediction of the generation of  $\dot{\text{H}}$  atoms. Meanwhile, the prediction of  $[\text{C}_2\text{H}_4]$  agrees very well with the experiment, which are mostly produced together with allyl radicals via the decomposition of 1,5- $\dot{\text{C}}_5\text{H}_9$  radicals and also via chemically activated reactions from  $\text{cy}\dot{\text{C}}_5\text{H}_9$  radicals.  $\text{cy}\dot{\text{C}}_5\text{H}_9$  radicals are generated by H-atom abstraction reactions from  $\text{cyC}_5\text{H}_{10}$  by  $\dot{\text{H}}$  atoms produced from HME decomposition, and also by other radicals such as  $\dot{\text{C}}\text{H}_3$ ,  $\dot{\text{C}}_2\text{H}_3$ ,  $\dot{\text{C}}_3\text{H}_5\text{-a}$ , etc. The predicted concentrations of  $\text{cyC}_5\text{H}_8$  for Mixture A are about 3.2–2.1 times larger than the experimental results in the temperature range 950–1012 K and are 2.0–1.7 times larger at temperatures above 1012 K. However, the predicted concentrations of  $\text{cyC}_5\text{H}_8$  for Mixture B, which doesn’t contain T135MB as a radical scavenger, are within 50% of the experimental results. Therefore, we suggest the T135MB chemistry sub-mechanism can influence the prediction of  $\text{cyC}_5\text{H}_8$  in the  $\text{cyC}_5\text{H}_{10}$ /HME/VCH experiments. Due to the complexity of the decomposition mechanism of T135MB, the detailed chemistry of the influence of T135MB on the production of  $\text{cyC}_5\text{H}_8$  is still unclear.

Using the current model, we are able to predict [1,3-dimethylbenzene (D13MB)], [1-ethyl-3,5-dimethylbenzene (D35MBC<sub>2</sub>H<sub>5</sub>)] very well, and within a factor of two when [1-butenyl-3,5-dimethylbenzene (D35MBC<sub>4</sub>H<sub>7</sub>)] are larger than 1  $\mu\text{L/L}$ . D35MBC<sub>2</sub>H<sub>5</sub> and

D35MBC<sub>4</sub>H<sub>7</sub> are the recombination products of 1-methylene-3,5-dimethylbenzene (D35MBC<sub>2</sub>H<sub>2</sub>) radicals with methyl and allyl radicals, respectively. In addition, the other important products in order of decreasing concentration are 1,5-hexadiene, methane and propene, and there are also small amounts (< 5 μL/L) of ethane, allene, cyclopropane, cyclopentadiene (C<sub>5</sub>H<sub>6</sub>) and 1-pentene formed, for which the current model can provide good predictions.

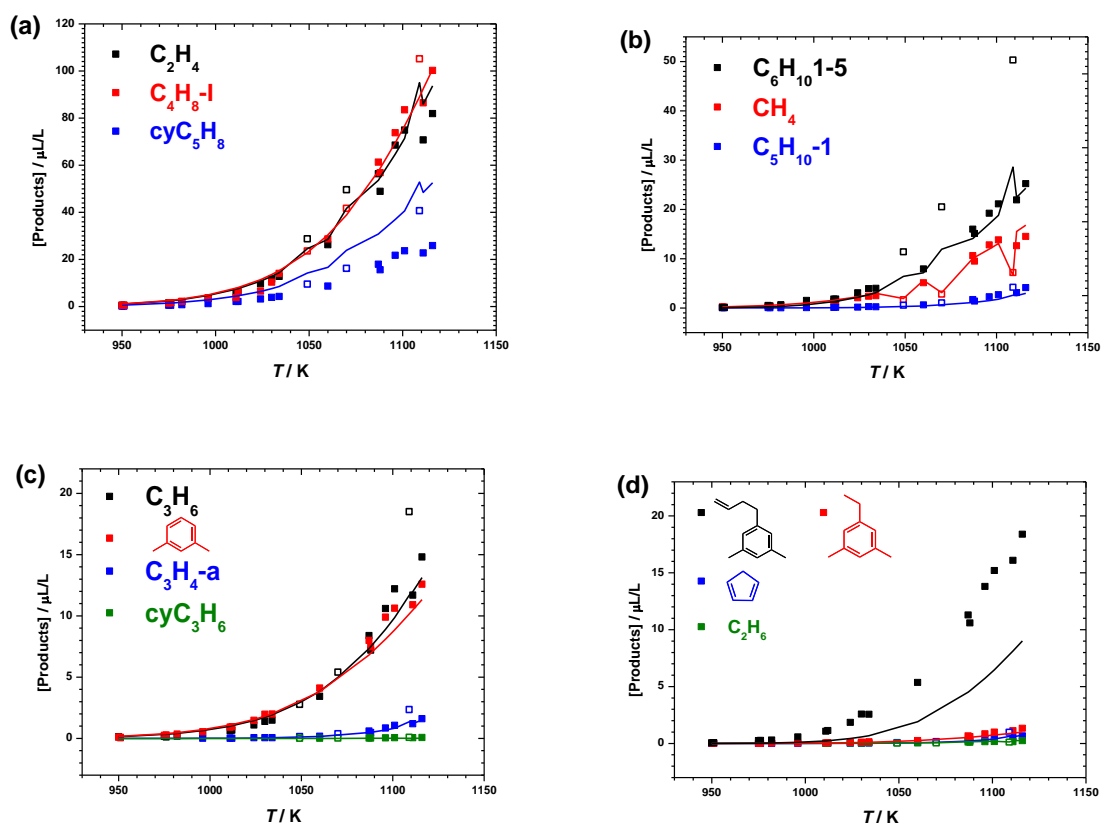


**Fig. 3.26** Experimental (symbols) [12] and modelled (lines) concentration profiles for products generated from  $\dot{\text{H}}$  atoms addition to cyclopentane at temperatures over 950 – 1116 K and pressures of 2.3 – 3.4 atm. The solid symbols represent product concentration profiles for Mixture A which contains 110 μL/L HME, 20700 μL/L cyC<sub>5</sub>H<sub>10</sub>, 100 μL/L VCH and 6500 μL/L T135MB in Argon. The results shown as open symbols are for Mixture B which contains 110 μL/L HME, 23000 μL/L cyC<sub>5</sub>H<sub>10</sub> and 100 μL/L VCH in Argon. Experiments were configured to have reaction times of  $500 \pm 50$  μs and the concentration profiles are simulated with same reaction times.

### 3.4.2 Cyclopentene + $\dot{\text{H}}$ → different products

To validate the reliability of our calculations, the same chemical kinetic model has been used to simulate the species profiles of the cyC<sub>5</sub>H<sub>8</sub> +  $\dot{\text{H}}$  experiments. For the single-pulse

shock tube experiments the product concentrations were based on FID analyses, with MS used to identify the products. Including possible systematic errors, the analytical uncertainty ( $1\sigma$ ) for the main products was estimated to be about 3%. Since large amounts of  $\text{cyC}_5\text{H}_8$  and T135MB are used in this experiment and small amounts of HME used as the  $\dot{\text{H}}$  atom source, the consumptions of  $\text{cyC}_5\text{H}_8$  and T135MB are relatively small compared with their initial concentrations. Hence, the absolute analytical uncertainties for the measurements of  $[\text{cyC}_5\text{H}_8]$  and  $[\text{T135MB}]$  can be up to  $\sim 500 \mu\text{L/L}$  based on their large concentrations. As a result, the measured concentrations of  $\text{cyC}_5\text{H}_8$  and T135MB can sometimes be larger than their initial concentrations, as shown in Fig. 3.27. We also see that our model is able to reproduce the consumption of the three reactants used in the experiments, especially the [HME] which has a smaller absolute analytical uncertainty.

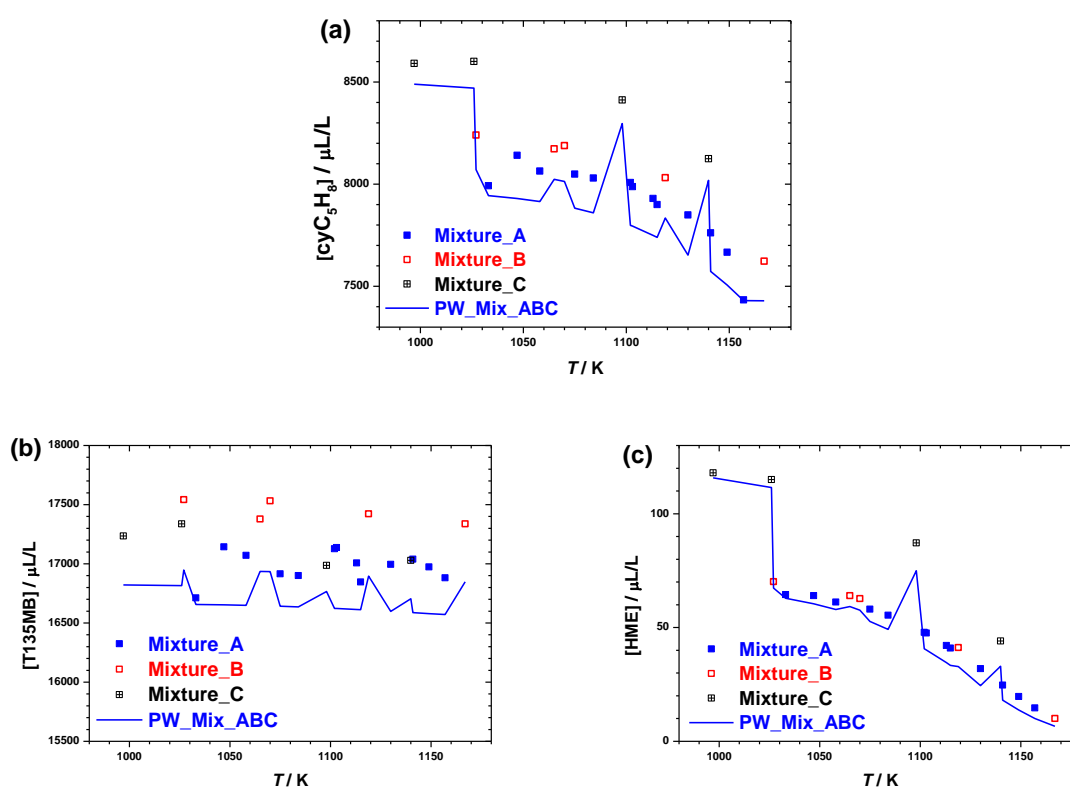


**Fig. 3.27** Experimental (symbols) [16] and simulated (lines) concentration profiles for reactants used in experimental studies for  $\dot{\text{H}}$  atom addition to cyclopentene at temperatures over 997–1167 K and pressures at 2.6–3.7 bar. The solid lines represent the predictions by our model for three mixtures. The initial compositions for three mixtures are: (A) 68  $\mu\text{L/L}$  HME, 7972  $\mu\text{L/L}$   $\text{cyC}_5\text{H}_8$ , 16659  $\mu\text{L/L}$  T135MB; (B) 72  $\mu\text{L/L}$  HME, 8098  $\mu\text{L/L}$   $\text{cyC}_5\text{H}_8$ , 16957  $\mu\text{L/L}$  T135MB; (C) 119  $\mu\text{L/L}$  HME, 8507  $\mu\text{L/L}$   $\text{cyC}_5\text{H}_8$ , 16834  $\mu\text{L/L}$  T135MB, in Argon. The concentration profiles in experiments and simulations are configured to have reaction times of  $500 \pm 50 \mu\text{s}$ .

The concentration profiles for the products generated in the  $\text{cyC}_5\text{H}_8 + \dot{\text{H}}$  experiments are shown in Fig. 3.28. What stands out in this Figure is the existence of outlier data points for several species. For instance, the initial concentration of HME of Mixture C is higher than that of Mixture A and there is enough  $\text{cyC}_5\text{H}_8$  in both systems, resulting in more  $\dot{\text{H}}$  atoms generated which should increase the reaction reactivity and intermediates formation, such as allyl radicals. The concentrations of 1,5- $\text{C}_6\text{H}_{10}$  predicted for Mixture C (which can be formed by allyl radical recombination) are shown to be higher than concentrations measured for Mixture A at similar temperatures, excluding one point at 1140 K which is ~a factor of two smaller than that for Mixture A at 1141 K. A similar phenomenon is found for [1- $\text{C}_4\text{H}_8$ ] of Mixture C at 1098 K and 1140 K. These outliers are neglected in deviation discussion below to reasonably validate the performance of the model.

Similar to the  $\text{cyC}_5\text{H}_{10} + \dot{\text{H}}$  experiment, HME decomposition and the formation of isobutene indicate the production of  $\dot{\text{H}}$  atoms in the system, which can be quantitatively predicted by our model. In addition, the quantity of ethylene, as the most important product produced from  $\text{cyC}_5\text{H}_8 + \dot{\text{H}}$ , is well predicted with the deviations being within 50%. The accurate prediction of [ $\text{C}_2\text{H}_4$ ] in Fig. 3.28(a) suggests the chemistry in our model including  $\text{cyC}_5\text{H}_8 + \dot{\text{H}} \rightarrow \text{cy}\dot{\text{C}}_5\text{H}_9 \rightarrow 1,5\text{-}\dot{\text{C}}_5\text{H}_9$ , the following  $\beta$ -scission reactions of 1,5- $\dot{\text{C}}_5\text{H}_9$  radicals, and also the chemically activated reactions from the intermediates on  $\dot{\text{C}}_5\text{H}_9$  PES to produce  $\text{C}_2\text{H}_4 + \dot{\text{C}}_3\text{H}_5\text{-a}$  are reasonable. The current model can also predict the formation and consumption of different intermediates: (1)  $\dot{\text{C}}\text{H}_3$  radicals, which are mainly formed through  $\text{T135MB} + \dot{\text{H}} \rightarrow \text{D13MB} + \dot{\text{C}}\text{H}_3$ , and about 10% are formed via decomposition reactions of iso-butyl/tert-butyl radicals to produce  $\text{C}_3\text{H}_6 + \dot{\text{C}}\text{H}_3$ . The dominant product from  $\dot{\text{C}}\text{H}_3$  radicals is  $\text{CH}_4$  produced via H-atom abstraction reactions from T135MB by  $\dot{\text{C}}\text{H}_3$ , whose concentrations are predicted with deviations within 50%. There is also a small amount of  $\text{C}_2\text{H}_6$  ( $< 0.4 \mu\text{L/L}$ ) formed through the self-recombination of  $\dot{\text{C}}\text{H}_3$  radicals, and the predicted concentrations agree with the measurements within a factor of two. (2) iso-butyl/tert-butyl radicals; the consumption of butyl radicals can be validated based on the good predictions of [ $\text{C}_4\text{H}_8\text{-I}$ ], [ $\text{C}_3\text{H}_6$ ] and [ $\text{CH}_4$ ]. (3) 1,3-pentadien-5-yl radicals (the dominant products of H-atom abstraction reactions of 1,3- and 1,4-pentadiene); [ $\text{C}_2\text{H}_2$ ] can be predicted with deviations within a factor of two indicating the formation of 1,3-pentadien-5-yl radicals and the decomposition pathway to form  $\dot{\text{C}}_3\text{H}_5\text{-a} + \text{C}_2\text{H}_2$  are well described in our model. (4) allyl radicals are the key intermediates for the formations of allene, 1-butene, 1,5-hexadiene and  $\text{D35MBC}_4\text{H}_7$  (recombination products of allyl and  $\text{D35MB}\dot{\text{C}}\text{H}_2$  radicals). [ $\text{C}_3\text{H}_4\text{-a}$ ] formed via the decomposition of allyl radicals are predicted within 50% when [ $\text{C}_3\text{H}_4\text{-a}$ ]  $> 0.5 \mu\text{L/L}$ .

[C<sub>4</sub>H<sub>8</sub>-1] formed via the recombination of allyl and methyl radicals can be relatively well predicted at temperatures below 1130 K and is less than 87% under-predicted at higher temperatures. 1,5-C<sub>6</sub>H<sub>10</sub>, which is mainly formed through the recombination of allyl radicals, can be predicted by the current model, with a largest deviation of a factor of two.

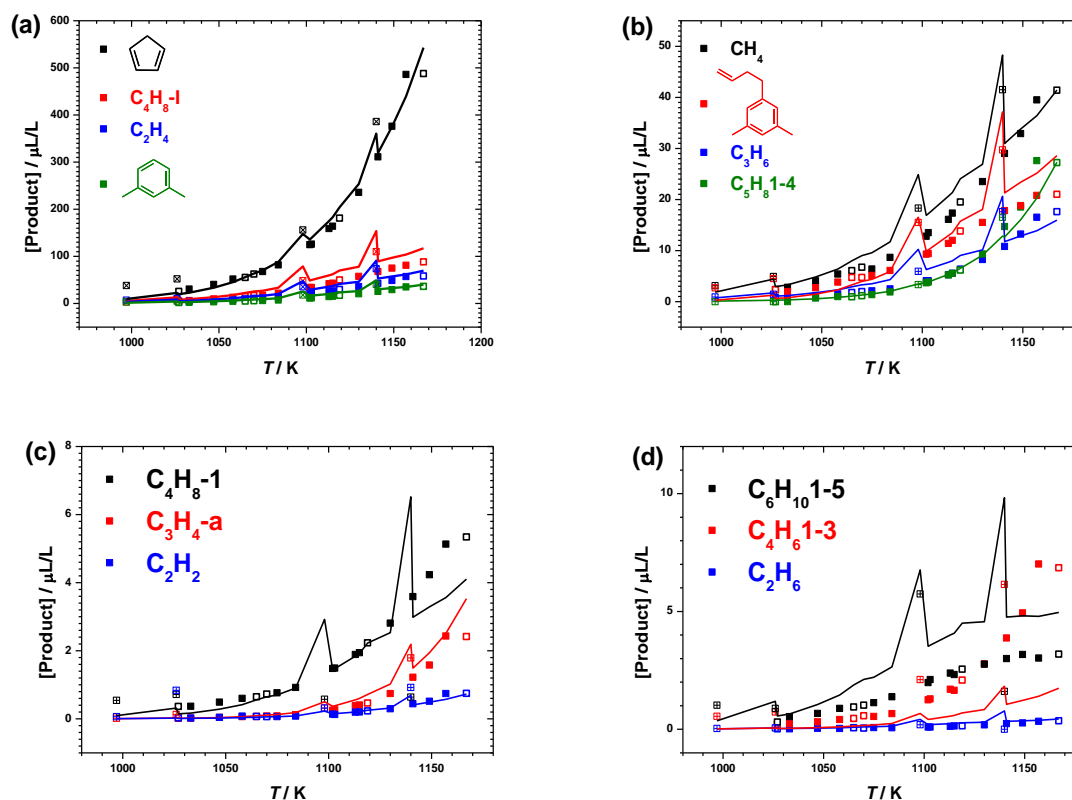


**Fig. 3.28** Experimental (symbols) [16] and simulated (lines) concentration profiles for products generated from  $\dot{\text{H}}$  atom addition to cyclopentene at temperatures over 997–1167 K and pressures at 2.6–3.7 bar. The solid symbols represent results for Mixture A, with open symbols and crossed symbols representing those for Mixture B and Mixture C, respectively.

In addition, the concentration profiles of C<sub>5</sub>H<sub>6</sub> (formed via H-atom abstraction reactions of cyC<sub>5</sub>H<sub>8</sub> by  $\dot{\text{H}}$  atoms), D13MB (formed via T135MB +  $\dot{\text{H}}$  → D13MB +  $\dot{\text{C}}\text{H}_3$ ), 1,4-C<sub>5</sub>H<sub>8</sub> (formed via isomerization of cyC<sub>5</sub>H<sub>8</sub>) are also accurately predicted by our model. The largest deviation between the model and experimental data are observed for 1,3-C<sub>4</sub>H<sub>6</sub> (up to a factor of five). The known pathways in our model relating to the formation and consumption of 1,3-C<sub>4</sub>H<sub>6</sub> tend to under-predict [1,3-C<sub>4</sub>H<sub>6</sub>] and this was also noted in Manion and Awan's studies. Although 1,3-C<sub>4</sub>H<sub>6</sub> isn't the main product for cyclopentene +  $\dot{\text{H}}$ , the chemistry related to its formation and consumption may be important for the other fuels and more studies about its chemistry will be useful for model development. In general, the chemical kinetic model

developed in this work can qualitatively and quantitatively predict the concentration profiles of the reactants and important products involved in  $\text{cyC}_5\text{H}_{10}/\text{cyC}_5\text{H}_8 + \dot{\text{H}}$  systems, which indicates the reliability of our thermochemistry and kinetic calculation results for species and reactions on  $\dot{\text{C}}_5\text{H}_9$  PES.

#### 4. Conclusions

Based on the comprehensive study of the  $\dot{\text{C}}_5\text{H}_9$  PES in Part I of this study, the calculated high-pressure limiting rate constants, together with the unimolecular decomposition reactions of 1,3-pentadiene, H-atom abstraction reactions of 1,3-, 1,4- $\text{C}_5\text{H}_8$ ,  $\text{cyC}_5\text{H}_8$  by  $\dot{\text{H}}$  atoms, and H-atom abstraction reactions of propene by vinyl radicals, are used to identify the dominant reaction pathways for four systems: 1,3-pentadiene +  $\dot{\text{H}}$ , 1,4-pentadiene +  $\dot{\text{H}}$ , cyclopentene +  $\dot{\text{H}}$ , and vinyl + propene. Based on the important pathways identified from the reaction pathway analysis, a simplified  $\dot{\text{C}}_5\text{H}_9$  PES is generated including 18 species and 25 TSs. The SPEs for radicals and TSs on the simplified PES are recalculated at the ROCCSD(T)/aug-cc-pVTZ level of theory with basis set corrections using MP2/aug-cc-pVXZ (where  $X = \text{T}$  and  $\text{Q}$ ).

Pressure-dependent rate constants are calculated in the temperature range 300–2000 K and at pressures in the range 0.01–100 atm using MESS, with spin-restricted energies used for important species on the simplified  $\dot{\text{C}}_5\text{H}_9$  PES and spin-unrestricted energies used for the other species. The reactions on the  $\dot{\text{C}}_5\text{H}_9$  PES are classified into unimolecular and bimolecular reactions. For bimolecular reactions (1,3-/1,4- $\text{cyC}_5\text{H}_8 + \dot{\text{H}}$ ,  $\dot{\text{C}}_3\text{H}_5\text{-a} + \text{C}_2\text{H}_4$ ,  $\text{C}_3\text{H}_6 + \dot{\text{C}}_2\text{H}_3$ ), the pressure-dependency of the total addition rate constants and product branching ratios are discussed. The rate constants for H-atom abstraction of these bimolecular reactions are compared with the total addition rate constants. Similarly, the pressure-dependency of the total addition rate constants and product branching ratios are also discussed for important unimolecular reactions. The high-pressure limiting and pressure-dependent rate constants are compared with available literature data with good agreement observed.

A chemical kinetic model is developed based on AramcoMech3.0 with pressure-dependent rate constants for reactions on the  $\dot{\text{C}}_5\text{H}_9$  PES and thermochemistry for  $\text{C}_5$  species calculated in the present study. Secondary chemistry for radical initiators and scavengers used in the experiment and thermochemistry and kinetic parameters for these species are added to the mechanism to appropriately simulate the literature experiments. This model is used to predict the mole fractions of different products generated for  $\dot{\text{H}}$  atom addition to cyclopentane and cyclopentene. The comparisons show that our model is able to

reproduce the consumption of the reactants and formation of the main products and can qualitatively and quantitatively predict the concentration profiles measured in the experiments.

Considering the limited literature data for thermochemistry (especially entropy and heat capacities) of C<sub>5</sub>H<sub>8</sub> and C<sub>5</sub>H<sub>9</sub> species, and the pressure-dependent rate constants for reactions on the  $\dot{C}_5H_9$  PES, this work is complementary for the development of a comprehensive pyrolysis and oxidation mechanism for C<sub>1</sub> – C<sub>5</sub> hydrocarbons and oxygenated fuels, and higher order alkanes and alkenes for which dienes and aromatics are important intermediates.

### Supporting Information

Unimolecular decomposition reactions of 1,3-pentadiene; H-atom abstraction reactions of 1,4-pentadiene/cyclopentene by  $\dot{H}$  atoms; H-atom abstraction reactions of propene by vinyl radicals;  $\beta$ -scission reactions of 1,3- $\dot{C}_5H_9$  and 1,4- $\dot{C}_5H_9$  (PDF); Simplified  $\dot{C}_5H_9$  PES; Species list for  $\dot{C}_5H_9$  PES;  $\dot{C}_5H_9$  mechanism including calculated rate constants and thermochemistry; Mechanism and input files used for cyC<sub>5</sub>H<sub>8</sub>/cyC<sub>5</sub>H<sub>10</sub> +  $\dot{H}$  experimental simulation; Output file of MESS calculation.

### Acknowledgements

This study is supported by Science Foundation Ireland and the China Scholarship Council (CSC). The authors want to acknowledge the financial support of Science Foundation Ireland under Grant No. 15/IA/3177 and 16/SP/3829, and the provision of computational resources from ICHEC under the NUI Galway shared condominium accounts. The Computational resources are provided by the Irish Centre for High-End Computing (ICHEC), under project number ngche063c, ngcom006c and ngche058c. The authors are grateful to Stephen Klippenstein for the help with MESS code study. Chong-Wen Zhou acknowledges the support from National Science and Technology Major Project (2017-III-0004-0028) and Beihang University under the Fundamental Research Funds.

## References

- [1] Y. Sun, C.-W. Zhou, K.P. Somers, H.J. Curran, Ab Initio/Transition-State Theory Study of the Reactions of  $\dot{C}_5H_9$  Species of Relevance to 1,3-Pentadiene, Part I: Potential Energy Surfaces, Thermochemistry, and High-Pressure Limiting Rate Constants, *J. Phys. Chem. A* 123 (2019) 9019-9052.
- [2] Y. Georgievskii, J.A. Miller, M.P. Burke, S.J. Klippenstein, Reformulation and solution of the master equation for multiple-well chemical reactions, *J. Phys. Chem. A* 117 (2013) 12146-12154.
- [3] Y. Georgievskii, MESS, S. J. Klippenstein, MESS. 2016.3.23.
- [4] W. Tsang, Chemical kinetic data base for combustion chemistry part V. Propene, *Journal of Physical and Chemical Reference Data* 20 (1991) 221-273.
- [5] A. Fahr, S. Stein. Reactions of vinyl and phenyl radicals with ethyne, ethene and benzene, 22nd Symposium (International) on Combustion (1988), 1023-1029.
- [6] D.M. Matheu, W.H. Green, J.M. Grenda, Capturing pressure-dependence in automated mechanism generation: Reactions through cycloalkyl intermediates, *International Journal of Chemical Kinetics* 35 (2003) 95-119.
- [7] M. Saeys, M.F. Reyniers, G.B. Marin, V. Van Speybroeck, M. Waroquier, Ab initio group contribution method for activation energies for radical additions, *AIChE J.* 50 (2004) 426-444.
- [8] W. Tsang, Mechanism and rate constants for the decomposition of 1-pentenyl radicals, *J. Phys. Chem. A* 110 (2006) 8501-8509.
- [9] M.K. Sabbe, M.F. Reyniers, V. Van Speybroeck, M. Waroquier, G.B. Marin, Carbon-centered radical addition and  $\beta$ -scission reactions: modeling of activation energies and pre-exponential factors, *ChemPhysChem* 9 (2008) 124-140.
- [10] B. Sirjean, P.-A. Glaude, M. Ruiz-Lopez, R. Fournet, Theoretical kinetic study of thermal unimolecular decomposition of cyclic alkyl radicals, *J. Phys. Chem. A* 112 (2008) 11598-11610.
- [11] C.F. Goldsmith, H. Ismail, P.R. Abel, W.H. Green, Pressure and temperature dependence of the reaction of vinyl radical with alkenes II: Measured rates and predicted product distributions for vinyl+propene, *Proceedings of the Combustion Institute* 32 (2009) 139-148.
- [12] I.A. Awan, D.R. Burgess, W. Tsang, J.A. Manion, Shock tube study of the decomposition of cyclopentyl radicals, *Proceedings of the Combustion Institute* 33 (2011) 341-349.
- [13] K. Wang, S.M. Villano, A.M. Dean, Reactions of allylic radicals that impact molecular weight growth kinetics, *Physical Chemistry Chemical Physics* 17 (2015) 6255-6273.
- [14] K. Wang, S.M. Villano, A.M. Dean, Reactivity–structure-based rate estimation rules for alkyl radical H atom shift and alkenyl radical cycloaddition reactions, *The Journal of Physical Chemistry A* 119 (2015) 7205-7221.
- [15] M.J. Al Rashidi, S. Thion, C. Togbé, G. Dayma, M. Mehl, P. Dagaut, W.J. Pitz, J. Zádor, S.M. Sarathy, Elucidating reactivity regimes in cyclopentane oxidation: Jet stirred reactor experiments, computational chemistry, and kinetic modeling, *Proceedings of the Combustion Institute* 36 (2017) 469-477.
- [16] J.A. Manion, I.A. Awan, A Shock Tube Study of H Atom Addition to Cyclopentene, *International Journal of Chemical Kinetics* 50 (2018) 225-242.
- [17] A.S. Gordon, A Study of Some Reactions of the Cyclopentyl Radical, *Canadian Journal of Chemistry* 43 (1965) 570-581.
- [18] R.R. Getty, J. A. Kerr, and A. F. Trotman-Dickenson, The reactions of alkyl radicals. Part XII. The additions of methyl, ethyl, and isopropyl radicals to allene, *Journal of the Chemical Society A*, (1967) 979-982.
- [19] K. Watkins, D. Olsen, Cyclization and decomposition of 4-penten-1-yl radicals in the gas

phase, *The Journal of Physical Chemistry* 76 (1972) 1089-1092.

[20] S. Stein, B. Rabinovitch, Ring opening and isomerization of a series of chemically activated cycloalkyl radicals, *The Journal of Physical Chemistry* 79 (1975) 191-198.

[21] R. Baldwin, R. Walker. Elementary reactions in the oxidation of alkenes, Symposium (International) on Combustion (1981), 819-829.

[22] T. Gierczak, J. Gawłowski, J. Niedzielski, Mutual isomerization of cyclopentyl and 1-Penten-5-yl radicals, *International journal of chemical kinetics* 18 (1986) 623-637.

[23] F.D. Kopinke, G. Zimmermann, G. Bach, B. Ondruschka., Pyrolysis of [5-<sup>14</sup>C]-1-pentene—evidence for homoallylic rearrangements at 873 K, *International journal of chemical kinetics* 18 (1986) 159-163.

[24] D. Perrin, C. Richard, R. Martin, H<sub>2</sub>S-promoted thermal isomerization of cis-2-pentene to 1-pentene and trans-2-pentene around 800 K, *International journal of chemical kinetics* 20 (1988) 621-632.

[25] W. Tsang, J.A. Walker, Pyrolysis of 1, 7-octadiene and the kinetic and thermodynamic stability of allyl and 4-pentenyl radicals, *The Journal of Physical Chemistry* 96 (1992) 8378-8384.

[26] S.M. Handford-Styring, R.W. Walker, Addition of cyclopentane to slowly reacting mixtures of H<sub>2</sub> + O<sub>2</sub> between 673 and 783 K: reactions of H and OH with cyclopentane and of cyclopentyl radicals, *Journal of the Chemical Society, Faraday Transactions* 91 (1995) 1431-1438.

[27] J.S. Clarke, N.M. Donahue, J.H. Kroll, H.A. Rypkema, J.G. Anderson, An Experimental Method for Testing Reactivity Models: A High-Pressure Discharge– Flow Study of H+ Alkene and Haloalkene Reactions, *J. Phys. Chem. A* 104 (2000) 5254-5264.

[28] Y. Li, C.-W. Zhou, K.P. Somers, K. Zhang, H.J. Curran, The oxidation of 2-butene: A high pressure ignition delay, kinetic modeling study and reactivity comparison with isobutene and 1-butene, *Proceedings of the Combustion Institute* 36 (2017) 403-411.

[29] C.-W. Zhou, Y. Li, E. O'Connor, K.P. Somers, S. Thion, C. Keesee, O. Mathieu, E.L. Petersen, T.A. DeVerter, M.A. Oehlschlaeger, G. Kukkadapu, C.-J. Sung, M. Alrefae, F. Khaled, A. Farooq, P. Dirrenberger, P.-A. Glaude, F. Battin-Leclerc, J. Santner, Y. Ju, T. Held, F.M. Haas, F.L. Dryer, H.J. Curran, A comprehensive experimental and modeling study of isobutene oxidation, *Combustion and Flame* 167 (2016) 353-379.

[30] U. Burke, W.K. Metcalfe, S.M. Burke, K.A. Heufer, P. Dagaut, H.J. Curran, A detailed chemical kinetic modeling, ignition delay time and jet-stirred reactor study of methanol oxidation, *Combust. Flame* 165 (2016) 125-136.

[31] S.M. Burke, U. Burke, R. Mc Donagh, O. Mathieu, I. Osorio, C. Keesee, A. Morones, E.L. Petersen, W. Wang, T.A. DeVerter, M.A. Oehlschlaeger, B. Rhodes, R.K. Hanson, D.F. Davidson, B.W. Weber, C.-J. Sung, J. Santner, Y. Ju, F.M. Haas, F.L. Dryer, E.N. Volkov, E.J.K. Nilsson, A.A. Konnov, M. Alrefae, F. Khaled, A. Farooq, P. Dirrenberger, P.-A. Glaude, F. Battin-Leclerc, H.J. Curran, An experimental and modeling study of propene oxidation. Part 2: Ignition delay time and flame speed measurements, *Combustion and Flame* 162 (2015) 296-314.

[32] S.M. Burke, W. Metcalfe, O. Herbinet, F. Battin-Leclerc, F.M. Haas, J. Santner, F.L. Dryer, H.J. Curran, An experimental and modeling study of propene oxidation. Part 1: Speciation measurements in jet-stirred and flow reactors, *Combust. Flame* 161 (2014) 2765-2784.

[33] W.K. Metcalfe, S.M. Burke, S.S. Ahmed, H.J. Curran, A hierarchical and comparative kinetic modeling study of C<sub>1</sub>–C<sub>2</sub> hydrocarbon and oxygenated fuels, *International Journal of Chemical Kinetics* 45 (2013) 638-675.

[34] A. Kéromnès, W.K. Metcalfe, K.A. Heufer, N. Donohoe, A.K. Das, C.-J. Sung, J. Herzler, C. Naumann, P. Griebel, O. Mathieu, M.C. Krejci, E.L. Petersen, W.J. Pitz, H.J. Curran, An

- experimental and detailed chemical kinetic modeling study of hydrogen and syngas mixture oxidation at elevated pressures, *Combust. Flame* 160 (2013) 995-1011.
- [35] C.-W. Zhou, Y. Li, U. Burke, C. Banyon, K.P. Somers, S. Ding, S. Khan, J.W. Hargis, T. Sikes, O. Mathieu, An experimental and chemical kinetic modeling study of 1, 3-butadiene combustion: Ignition delay time and laminar flame speed measurements, *Combust. Flame* 197 (2018) 423-438.
- [36] ANSYS CHEMKIN-PRO 15131, Reaction Design: San Diego, ANSYS CHEMKIN-PRO 15131, Reaction Design: San Diego, 2013.
- [37] J. Binkley, J. Pople, P. Dobosh, The calculation of spin-restricted single-determinant wavefunctions, *Molecular Physics* 28 (1974) 1423-1429.
- [38] T.D. Crawford, T.J. Lee, H.F. Schaefer III, A new spin-restricted triple excitation correction for coupled cluster theory, *The Journal of chemical physics* 107 (1997) 7943-7950.
- [39] J.A. Pople, M. Head-Gordon, K. Raghavachari, Quadratic configuration interaction. A general technique for determining electron correlation energies, *The Journal of chemical physics* 87 (1987) 5968-5975.
- [40] J.M. Martin, Ab initio total atomization energies of small molecules—towards the basis set limit, *Chemical physics letters* 259 (1996) 669-678.
- [41] S. Cagnina, A. Nicolle, T. de Bruin, Y. Georgievskii, S.J. Klippenstein, First-Principles Chemical Kinetic Modeling of Methyl trans-3-Hexenoate Epoxidation by HO<sub>2</sub>, *J. Phys. Chem. A* 121 (2017) 1909-1915.
- [42] M.J. Al Rashidi, M. Mehl, W.J. Pitz, S. Mohamed, S.M. Sarathy, Cyclopentane combustion chemistry. Part I: Mechanism development and computational kinetics, *Combustion and Flame* 183 (2017) 358-371.
- [43] Y. Li, S.J. Klippenstein, C.-W. Zhou, H.J. Curran, Theoretical Kinetics Analysis for H Atom Addition to 1, 3-Butadiene and Related Reactions on the C<sub>4</sub>H<sub>7</sub> Potential Energy Surface, *J. Phys. Chem. A* 121 (2017) 7433-7445.
- [44] S.J. Klippenstein, From theoretical reaction dynamics to chemical modeling of combustion, *Proceedings of the Combustion Institute* 36 (2017) 77-111.
- [45] N.J. Brown, L.A. Bastien, P.N. Price, Transport properties for combustion modeling, *Progress in Energy and Combustion Science* 37 (2011) 565-582.
- [46] A.W. Jasper, J.A. Miller, Lennard–Jones parameters for combustion and chemical kinetics modeling from full-dimensional intermolecular potentials, *Combust. Flame* 161 (2014) 101-110.
- [47] J. Pfaendtner, X. Yu, L.J. Broadbelt, The 1-D hindered rotor approximation, *Theoretical Chemistry Accounts* 118 (2007) 881.
- [48] C. Eckart, The penetration of a potential barrier by electrons, *Physical Review* 35 (1930) 1303.
- [49] K.P. Somers, On the pyrolysis and combustion of furans: quantum chemical, statistical rate theory, and chemical kinetic modelling studies, in: H.J. Curran, I. Science Foundation (Eds.), 2014.
- [50] A. Dean, Predictions of pressure and temperature effects upon radical addition and recombination reactions, *The Journal of Physical Chemistry* 89 (1985) 4600-4608.
- [51] A. Chang, J. Bozzelli, A. Dean, Kinetic analysis of complex chemical activation and unimolecular dissociation reactions using QRRK theory and the modified strong collision approximation, *Zeitschrift für Physikalische Chemie* 214 (2000) 1533.
- [52] J. Power, K.P. Somers, C.-W. Zhou, S. Peukert, H.J. Curran, Theoretical, Experimental, and Modeling Study of the Reaction of Hydrogen Atoms with 1-and 2-Pentene, *J. Phys. Chem. A* 123 (2019) 8506-8526.
- [53] I.A. Awan, D.R. Burgess Jr, J.A. Manion, Pressure dependence and branching ratios in the decomposition of 1-pentyl radicals: shock tube experiments and master equation

- modeling, *J. Phys. Chem. A* 116 (2012) 2895-2910.
- [54] M.J. Al Rashidi, J.C. Marmol, C. Banyon, M.B. Sajid, M. Mehl, W.J. Pitz, S. Mohamed, A. Alfazazi, T. Lu, H.J. Curran, Cyclopentane combustion. Part II. Ignition delay measurements and mechanism validation, *Combust. Flame* 183 (2017) 372-385.
- [55] Y.-X. Liu, Z.-Y. Tian, Oxidation chemistry of four C<sub>9</sub>H<sub>12</sub> isomeric transportation fuels: Experimental and modeling studies, *Combust. Flame* 205 (2019) 165-179.
- [56] E.R. Ritter, J.W. Bozzelli, THERM: Thermodynamic property estimation for gas phase radicals and molecules, *International Journal of Chemical Kinetics* 23 (1991) 767-778.
- [57] S.J. Klippenstein, C. Cavallotti, Ab initio kinetics for pyrolysis and combustion systems, *Computer Aided Chemical Engineering* (2019), 115-167.
- [58] J.A. Miller, S.J. Klippenstein, Determining phenomenological rate coefficients from a time-dependent, multiple-well master equation: "species reduction" at high temperatures, *Physical Chemistry Chemical Physics* 15 (2013) 4744-4753.
- [59] P. Zhang, S.J. Klippenstein, C.K. Law, Ab initio kinetics for the decomposition of hydroxybutyl and butoxy radicals of n-butanol, *J. Phys. Chem. A* 117 (2013) 1890-1906.
- [60] S.M. Sarathy, C.K. Westbrook, M. Mehl, W.J. Pitz, C. Togbe, P. Dagaut, H. Wang, M.A. Oehlschlaeger, U. Niemann, K. Seshadri, Comprehensive chemical kinetic modeling of the oxidation of 2-methylalkanes from C<sub>7</sub> to C<sub>20</sub>, *Combust. Flame* 158 (2011) 2338-2357.
- [61] C.F. Goldsmith, H. Ismail, W.H. Green, Pressure and Temperature Dependence of the Reaction of Vinyl Radical with Alkenes III: Measured Rates and Predicted Product Distributions for Vinyl + Butene, *J. Phys. Chem. A* 113 (2009) 13357-13371.
- [62] H. Ismail, C.F. Goldsmith, P.R. Abel, P.-T. Howe, A. Fahr, J.B. Halpern, L.E. Jusinski, Y. Georgievskii, C.A. Taatjes, W.H. Green, Pressure and Temperature Dependence of the Reaction of Vinyl Radical with Ethylene, *J. Phys. Chem. A* 111 (2007) 6843-6851.
- [63] J.R. Barker, Multiple-Well, multiple-path unimolecular reaction systems. I. MultiWell computer program suite, *International Journal of Chemical Kinetics* 33 (2001) 232-245.
- [64] J. R. Barker, T. L. Nguyen, J. F. Stanton, C. Aieta, M. Ceotto, F. Gabas, T. J. D. Kumar, C. G. L. Li, L. L. Lohr, A. Maranzana, N. F. Ortiz, J. M. Preses, J. M. Simmie, J. A. Sonk, and P. J. Stimac, MultiWell-2017 Software Suite, University of Michigan: Ann Arbor, Michigan, USA, 2017.
- [65] J.R. Barker, Energy transfer in master equation simulations: A new approach, *International Journal of Chemical Kinetics* 41 (2009) 748-763.
- [66] P. Atkins, J. De Paula, *Elements of physical chemistry*, Oxford University Press, USA 2013.
- [67] J. Bugler, J. Power, H.J. Curran, A theoretical study of cyclic ether formation reactions, *Proceedings of the Combustion Institute* 36 (2017) 161-167.
- [68] A.W. Jasper, N. Hansen, Hydrogen-assisted isomerizations of fulvene to benzene and of larger cyclic aromatic hydrocarbons, *Proceedings of the Combustion Institute* 34 (2013) 279-287.
- [69] A.W. Jasper, Z.B. Gruey, L.B. Harding, Y. Georgievskii, S.J. Klippenstein, A.F. Wagner, Anharmonic Rovibrational Partition Functions for Fluxional Species at High Temperatures via Monte Carlo Phase Space Integrals, *J. Phys. Chem. A*, (2018).

## Chapter 4

# Hindered Rotor Benchmarks for the Transition States of Free Radical Additions to Unsaturated Hydrocarbons

Published in Physical Chemistry Chemical Physics in 2020.

DOI: <https://doi.org/10.1039/D0CP04194G>

### Authors and Contributions

(1) Yanjin Sun

National University of Ireland, Galway

Contribution: Ab initio calculations and manuscript preparation.

(2) Kieran P. Somers

National University of Ireland, Galway

Contribution: Supervised ab initio calculations and reviewed the manuscript.

(3) Quan-De Wang

China University of Mining and Technology

Contribution: Carried out the DLPNO-CCSD(T) calculations and reviewed the manuscript.

(4) Caoimhe Farrell

National University of Ireland, Galway

Contribution: Reaction pathway discussion and ab initio calculation preparations.

(5) Henry J. Curran

National University of Ireland, Galway

Contribution: Project Management and manuscript review.

## Abstract

The hindered internal rotors of 32 transition states (TSs) formed through four free radicals, namely methyl, vinyl, ethyl, methoxy ( $\dot{\text{C}}\text{H}_3$ ,  $\dot{\text{C}}_2\text{H}_3$ ,  $\dot{\text{C}}_2\text{H}_5$ ,  $\text{CH}_3\dot{\text{O}}$ ) additions to acetylene, ethylene, allene, propyne, and propene ( $\text{C}_2\text{H}_2/\text{C}_2\text{H}_4/\text{C}_3\text{H}_4\text{-a}/\text{C}_3\text{H}_4\text{-p}/\text{C}_3\text{H}_6$ ) are studied. To validate the uncertainties of rate constants that stem from the use of different electronic structure methods to treat hindered rotors, the rotations of the newly formed C – C and/or C – O rotors in the transition states are calculated using commonly used DFT methods (B3LYP, M06-2X,  $\omega$ B97X-D and B2PLYP-D3 with two Pople basis sets (6-31+G(d,p), 6-311++G(d,p)) and cc-pVTZ). The hindrance potential energies  $V(\chi)$  calculated using the M06-2X/6-311++G(d,p) method are benchmarked at the CCSD(T), CCSD(T)-F12, DLPNO-CCSD(T) levels of theory with cc-pVTZ-F12 and cc-pVXZ ( $X=\text{T}, \text{Q}$ ) basis sets and are extrapolated to the complete basis set (CBS) limit. The DLPNO-CCSD(T)/CBS method is proven to reproduce the CCSD(T)/CBS energies within  $0.5 \text{ kJ mol}^{-1}$  and this method is selected as the benchmark for all of the rotors in this study. Rotational constants  $B(\chi)$  are computed for each method based on the optimized geometries for the hindrance potential via the  $I(2,3)$  approximation. Thereafter, the  $V(\chi)$  and  $B(\chi)$  values are used to compute hindered internal rotation partition functions,  $Q_{\text{HR}}$ , as a function of temperature. The uncertainties in the  $V(\chi)$ ,  $B(\chi)$  and  $Q_{\text{HR}}$  calculations stemming from the use of different DFT methods for the internal rotor treatment are discussed for these newly formed rotors. For rotors formed by  $\dot{\text{R}} + \text{C}_2$  alkenes/alkynes, the  $V(\chi)$  and  $Q_{\text{HR}}$  values calculated using DFT methods are compared with the DLPNO-CCSD(T)/CBS results and analysed according to reaction types. Based on comparisons of the DFT methods with the benchmarking method, reliable DFT methods are recommended for the treatment of internal rotors for different reaction types considering both accuracy and computational cost. This work, to the authors' knowledge, is the first to systematically benchmark hindrance potentials which can be used to estimate uncertainties in theoretically derived rate constants arising from the choice of different electronic structure methods.

## 1. Introduction

The bimolecular reactions of unstable free radicals with unsaturated hydrocarbons are important in the combustion of fuels, as well as in atmospheric, astrochemical, and chemical reaction engineering/refinery systems. To obtain accurate kinetic parameters for bimolecular reactions, the geometries, vibrational frequencies and electronic energies of the species involved in the reactions and in the transition states should be calculated at a reasonably high

level of theory, although for the most part DFT methods are employed for systems of any reasonable size. Thereafter, the molecular partition function, which is composed of the electronic, translational, rotational, and vibrational partition functions, can be calculated based on electronic structure information. As opposed to the electronic, translational and rotational partition functions, the vibrational partition function needs more careful treatment. Generally, the rigid-rotor harmonic-oscillator (RRHO) approximation performs well for high-frequency modes, but its inapplicability for low-frequency torsional modes can be an important source of error in calculating total partition functions [1]. Therefore, the output from quantum chemical calculations is usually used in conjunction with the RRHO approximation with corrections for hindered rotors to calculate the heats of formation, entropies, and heat capacities for all molecules, and by extension transition state properties and chemical kinetic properties [2]. Among the various hindered rotor treatments, the one-dimensional (1-D) hindered-rotor approximation is most widely used in the quantum mechanical treatment of low frequency vibrational modes.

There have been many studies in the literature that focus on radical addition reactions, especially for small systems (e.g.  $\dot{\text{C}}\text{H}_3 + \text{C}_2\text{H}_2$ ,  $\dot{\text{C}}\text{H}_3 + \text{C}_2\text{H}_4$ ) [3-9]. For simplicity and clarity, only the most widely used literature studies in prevalent combustion mechanisms relevant to the addition reactions are summarized in Table 4.1. It is observed that the electronic energies for most systems are calculated at a high level of theory (RCCSD(T)/CBS or RQCISD(T)/CBS), and the geometries and frequencies are often calculated using reliable DFT methods [8-11]. In addition, to obtain accurate kinetic and thermochemical properties for radical additions to unsaturated hydrocarbons, quantum chemistry calculations of geometry and high-frequency modes have also been applied with high accuracy for small systems [4]. However, the treatment for low-frequency modes are usually performed with lower-level methods including MP2 and/or DFT and the uncertainty arising from the application of different electronic structure methods has not been extensively discussed in the literature.

In this work, four free radical additions to  $\text{C}_2 - \text{C}_3$  alkenes, alkynes and dienes are selected as target reactions to compare the influence of different electronic structure methods applied in the hindered-rotor treatment of partition function calculations. Considering that the transition states of radical addition reactions to unsaturated species have one more internal rotor compared to the reactants, the proper treatment of this rotor can be crucial to the subsequent rate constant calculations. This work mainly focuses on the internal rotations of the newly formed C-C and/or C-O rotors in the TSs for radical addition reactions, which are

expected to have stronger influences on partition function calculations compared to the methyl group rotation presented both in the reactants and in the TSs.

The bimolecular reactions of 32 reactions including the internal (central carbon atom) and terminal radical addition reactions to C<sub>2</sub> and C<sub>3</sub> species are studied using twelve DFT methods. The geometries of the TSs formed through  $\dot{\text{C}}\text{H}_3/\dot{\text{C}}_2\text{H}_3/\dot{\text{C}}_2\text{H}_5/\text{CH}_3\dot{\text{O}}$  radical additions to C<sub>2</sub>H<sub>2</sub>/C<sub>2</sub>H<sub>4</sub>/C<sub>3</sub>H<sub>4-a</sub>/C<sub>3</sub>H<sub>4-p</sub>/C<sub>3</sub>H<sub>6</sub> are collated in Table 4.2, with the axis of the target hindered rotors connected with dashed lines. The Chemcraft program [12] is used to visualize and save geometries of all TSs, with bond widths, font sizes of atom labels and sizes of atoms across different TSs plotted as default. Detailed structures of each TS (optimized at B2PLYP-D3/cc-pVTZ level of theory as representatives) are also provided in the Supporting Information. The hindrance potentials of these hindered rotors calculated using different DFT functionals and basis sets are compared to benchmark results calculated at the DLPNO-CCSD(T)/CBS level of theory, and the influences of the hindrance potentials on the partition function calculations at different levels of theory are discussed. The final goal of this work is to determine which DFT methods can be reliably used to determine the hindered-rotor treatment for radical additions to larger unsaturated species with reasonable accuracy.

**Table 4.1** Summary of the most widely used literature studies relevant to different radical ( $\dot{\text{C}}\text{H}_3$ ,  $\dot{\text{C}}_2\text{H}_3$ ,  $\dot{\text{C}}_2\text{H}_5$ ,  $\text{CH}_3\dot{\text{O}}$ ) additions to  $\text{C}_2$ – $\text{C}_3$  alkenes, alkynes and dienes.

	Reactants		Products	Year	Author	Method	Results
1	$\text{C}_2\text{H}_2$	$\dot{\text{C}}\text{H}_3$	$\dot{\text{C}}=\text{CC}$	2008	Miller et al.[3]	RQCISD(T)/CBS//B3LYP/6-311++G(d,p)	$E_{0\text{K}}$ , PES, $k(T,p)$
2	$\text{C}_2\text{H}_4$		$\dot{\text{C}}\text{CC}$	2013	Miller and Klippenstein [4]	RQCISD(T)/CBS//CCSD(T)/cc-pVTZ	$E_{0\text{K}}$ , PES, $k(T,p)$
3	$\text{C}_3\text{H}_4\text{-a (E)}^a$		$\text{C}=\dot{\text{C}}\text{CC}$	2017	Li et al.[5]	RCCSD(T)/CBS//M06-2X/6-311++G(d,p)	$E_{0\text{K}}$ , PES, Thermo, $k(T,p)$
4	$\text{C}_3\text{H}_4\text{-a (I)}^a$		$\text{C}=\text{C}(\text{C})\dot{\text{C}}$				
5	$\text{C}_3\text{H}_4\text{-p (E)}$		$\text{CC}=\dot{\text{C}}\text{C}$	2017	Li et al.[5]	RCCSD(T)/CBS//M06-2X/6-311++G(d,p)	$E_{0\text{K}}$ , PES, Thermo, $k(T,p)$
6	$\text{C}_3\text{H}_4\text{-p (I)}$		$\dot{\text{C}}=\text{C}(\text{C})\text{C}$				
7	$\text{C}_3\text{H}_6 \text{ (E)}$		$\text{CC}\dot{\text{C}}\text{C}$	2017	Li et al.[13]	CCSD(T)/CBS//M06-2X/6-311++G(d,p)	$k(T,p)$
8	$\text{C}_3\text{H}_6 \text{ (I)}$		$\dot{\text{C}}\text{C}(\text{C})\text{C}$	2019	Power et al.[8]	CCSD(T)/CBS// $\omega$ B97X-D/aug-cc-pVTZ	$k(T,p)$ , Thermo
9	$\text{C}_2\text{H}_2$	$\dot{\text{C}}_2\text{H}_3$	$\dot{\text{C}}=\text{CC}=\text{C}$	1994	Wang and Frenklach[6]	HF/6-31G**	PES, $k(T)$ , Thermo
10	$\text{C}_2\text{H}_4$		$\dot{\text{C}}\text{CC}=\text{C}$	2017	Li et al.[5]	RCCSD(T)/CBS//M06-2X/6-311++G(d,p)	$E_{0\text{K}}$ , PES, Thermo, $k(T,p)$
11	$\text{C}_3\text{H}_4\text{-a (E)}$		$\text{C}=\dot{\text{C}}\text{CC}=\text{C}$	2006	Orme et al.[7]	Estimated by rate rule for internal addition	$k(T)$
12	$\text{C}_3\text{H}_4\text{-a (I)}$		$\text{C}=\text{C}(\dot{\text{C}})\text{C}=\text{C}$				
13	$\text{C}_3\text{H}_4\text{-p (E)}$		$\text{CC}\dot{\text{C}}=\text{CC}=\text{C}$	---			
14	$\text{C}_3\text{H}_4\text{-p (I)}$		$\dot{\text{C}}=\text{C}(\text{C})\text{C}=\text{C}$	---			
15	$\text{C}_3\text{H}_6 \text{ (E)}$		$\text{CC}\dot{\text{C}}\text{CC}=\text{C}$	2019	Sun et al.[9]	CCSD(T)/CBS// $\omega$ B97X-D/aug-cc-pVTZ	$E_{0\text{K}}$ , PES, Thermo, $k(T,p)$

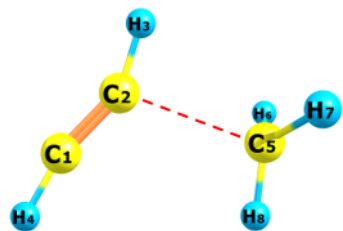
16	<b>C<sub>3</sub>H<sub>6</sub> (I)</b>		<b>CC(Ċ)C=C</b>	2019	Sun et al.[9]	CCSD(T)/CBS//ωB97X-D/aug-cc-pVTZ	<i>E</i> <sub>0K</sub> , PES, <i>k</i> ( <i>T</i> , <i>p</i> ), Thermo
17	<b>C<sub>2</sub>H<sub>2</sub></b>	<b>Ċ<sub>2</sub>H<sub>5</sub></b>	<b>Ċ=CCC</b>	2017	Li et al.[5]	RCCSD(T)/CBS//M06-2X/6-311++G(d,p)	<i>E</i> <sub>0K</sub> , PES, <i>k</i> ( <i>T</i> , <i>p</i> ), Thermo
18	<b>C<sub>2</sub>H<sub>4</sub></b>		<b>ĊCCC</b>	2017	Li et al.[13]	CCSD(T)/CBS//M06-2X/6-311++G(d,p)	<i>k</i> ( <i>T</i> , <i>p</i> )
19	<b>C<sub>3</sub>H<sub>4</sub>-a (E)</b>		<b>C=ĊCCC</b>	2019	Sun et al.[9]	CCSD(T)/CBS//ωB97X-D/aug-cc-pVTZ	<i>E</i> <sub>0K</sub> , PES, <i>k</i> ( <i>T</i> , <i>p</i> ), Thermo
20	<b>C<sub>3</sub>H<sub>4</sub>-a (I)</b>		<b>C=C(Ċ)CC</b>				
21	<b>C<sub>3</sub>H<sub>4</sub>-p (E)</b>		<b>CCĊ=CCC</b>	2019	Sun et al.[9]	CCSD(T)/CBS//ωB97X-D/aug-cc-pVTZ	<i>E</i> <sub>0K</sub> , PES, <i>k</i> ( <i>T</i> , <i>p</i> ), Thermo
22	<b>C<sub>3</sub>H<sub>4</sub>-p (I)</b>		<b>Ċ=C(C)CC</b>				
23	<b>C<sub>3</sub>H<sub>6</sub> (E)</b>		<b>CĊCCC</b>	2019	Power et al.[8]	CCSD(T)/CBS//ωB97X-D/aug-cc-pVTZ	<i>E</i> <sub>0K</sub> , PES, <i>k</i> ( <i>T</i> , <i>p</i> ), Thermo
24	<b>C<sub>3</sub>H<sub>6</sub> (I)</b>		<b>CC(Ċ)CC</b>	2020	Power et al.[14]	CCSD(T)/CBS//ωB97X-D/aug-cc-pVTZ	<i>E</i> <sub>0K</sub> , PES, <i>k</i> ( <i>T</i> , <i>p</i> ), Thermo
25	<b>C<sub>2</sub>H<sub>2</sub></b>		<b>CH<sub>3</sub>Ċ</b>	<b>Ċ=COC</b>	---		
26	<b>C<sub>2</sub>H<sub>4</sub></b>	<b>ĊCOC</b>		---			
27	<b>C<sub>3</sub>H<sub>4</sub>-a (E)</b>	<b>C=ĊCOC</b>		---			
28	<b>C<sub>3</sub>H<sub>4</sub>-a (I)</b>	<b>C=C(Ċ)OC</b>		---			
29	<b>C<sub>3</sub>H<sub>4</sub>-p (E)</b>	<b>CCĊ=COC</b>		---			
30	<b>C<sub>3</sub>H<sub>4</sub>-p (I)</b>	<b>Ċ=C(C)OC</b>		---			
31	<b>C<sub>3</sub>H<sub>6</sub> (E)</b>	<b>CĊCOC</b>		---			
32	<b>C<sub>3</sub>H<sub>6</sub> (I)</b>	<b>CC(Ċ)OC</b>		---			

<sup>a</sup> (E) representing radical additions to the external carbon atoms, and (I) representing radical additions to the internal (central) carbon atoms.

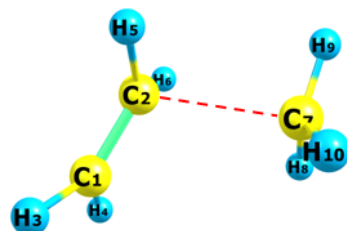
<sup>b</sup> PES representing potential energy surface for a specific system.

**Table 4.2** The geometries of the TSs formed by 32 radical additions to different unsaturated hydrocarbons with the axis of the target hindered rotors marked with dashed lines. C–C bonds with yellow, green and orange colors stand for single, double and triple bonds, respectively.

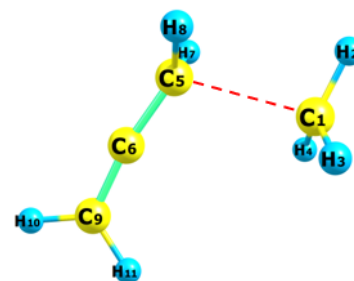
$\dot{\text{C}}\text{H}_3$  radical additions



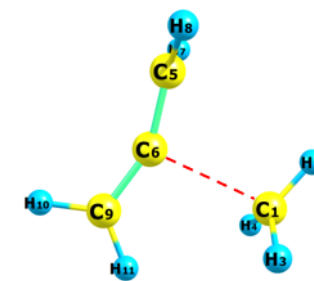
$\text{C}_2\text{H}_2$



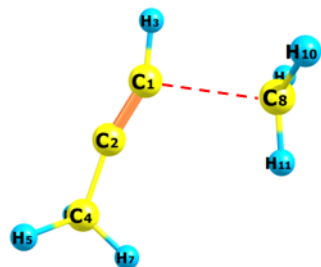
$\text{C}_2\text{H}_4$



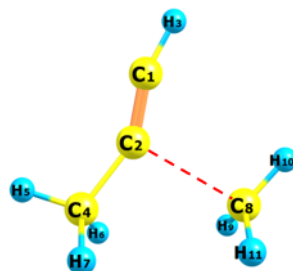
$\text{C}_3\text{H}_4\text{-a (E)}$



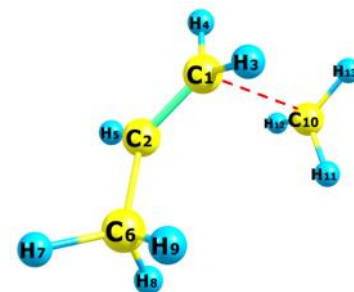
$\text{C}_3\text{H}_4\text{-a (I)}$



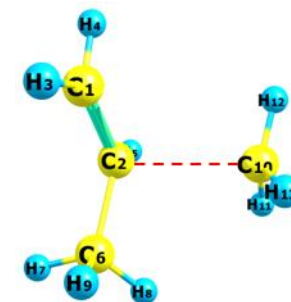
$\text{C}_3\text{H}_4\text{-p (E)}$



$\text{C}_3\text{H}_4\text{-p (I)}$



$\text{C}_3\text{H}_6 \text{ (E)}$

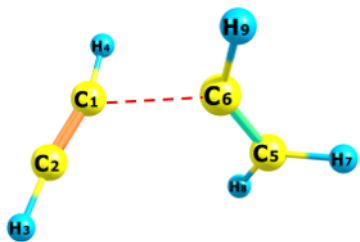


$\text{C}_3\text{H}_6 \text{ (I)}$

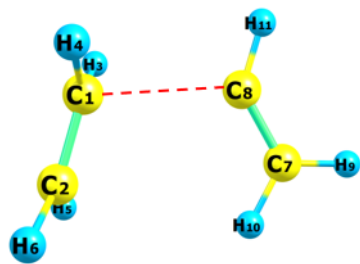
---

$\dot{\text{C}}_2\text{H}_3$  radical additions

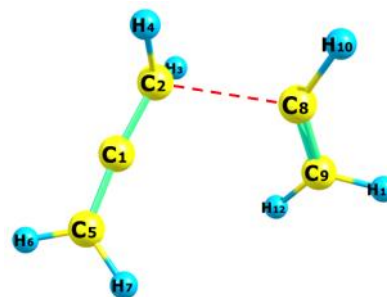
---



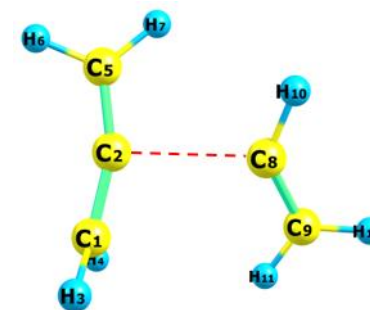
$\text{C}_2\text{H}_2$



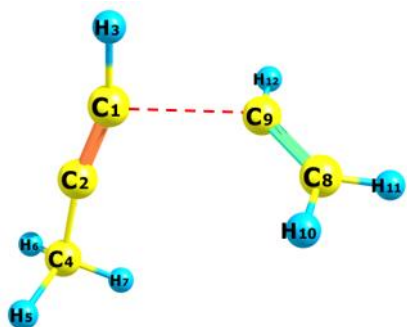
$\text{C}_2\text{H}_4$



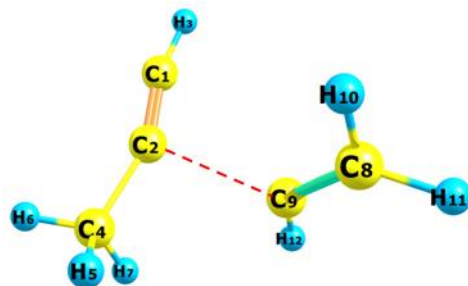
$\text{C}_3\text{H}_4\text{-a (E)}$



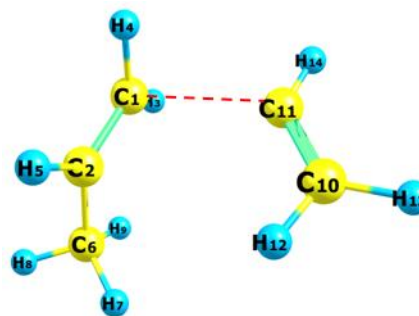
$\text{C}_3\text{H}_4\text{-a (I)}$



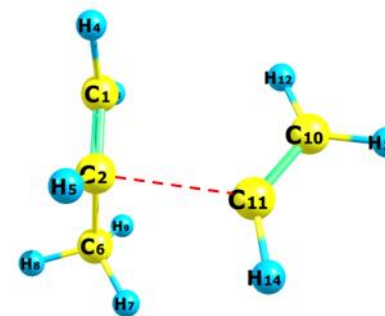
$\text{C}_3\text{H}_4\text{-p (E)}$



$\text{C}_3\text{H}_4\text{-p (I)}$



$\text{C}_3\text{H}_6 \text{ (E)}$

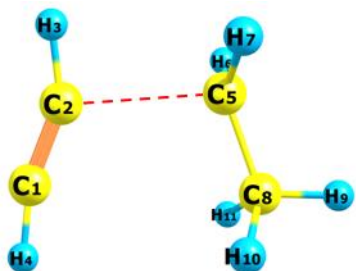


$\text{C}_3\text{H}_6 \text{ (I)}$

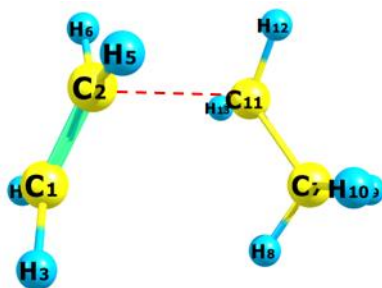
---

$\dot{C}_2H_5$  radical additions

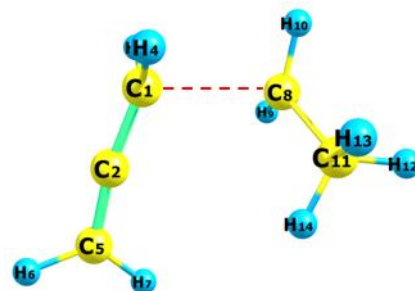
---



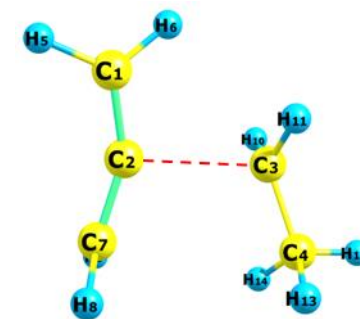
$C_2H_6$



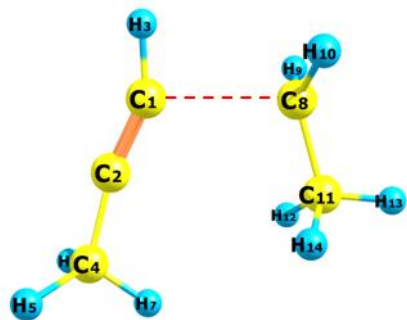
$C_2H_6$



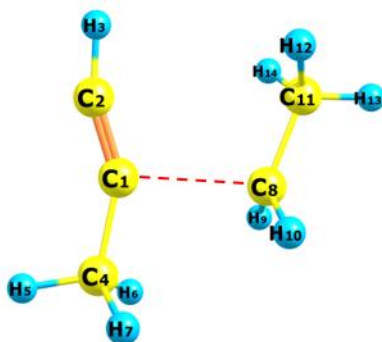
$C_3H_6$ -a (E)



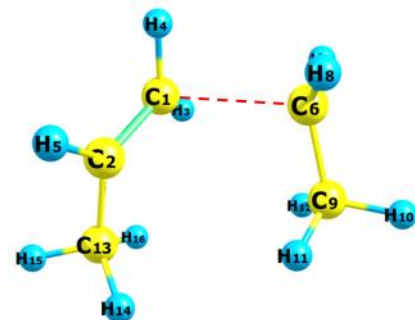
$C_3H_6$ -a (I)



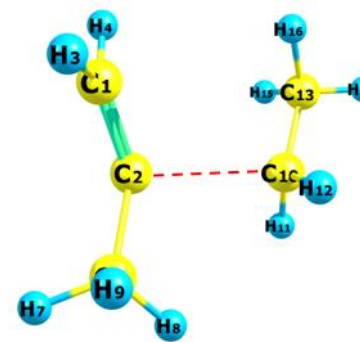
$C_3H_6$ -p (E)



$C_3H_6$ -p (I)



$C_3H_8$  (E)



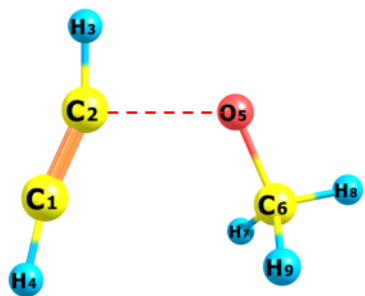
$C_3H_8$  (I)

---

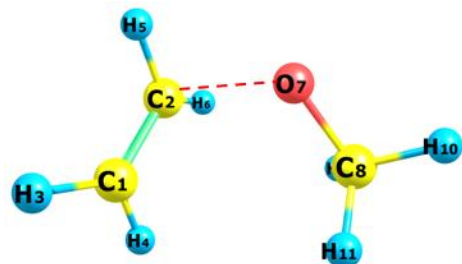
---

CH<sub>3</sub>Ö radical additions

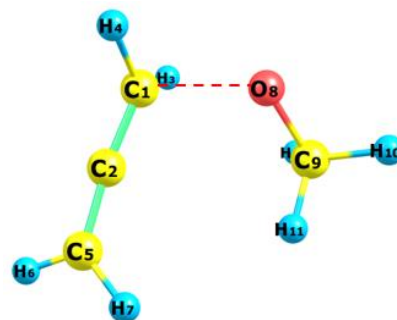
---



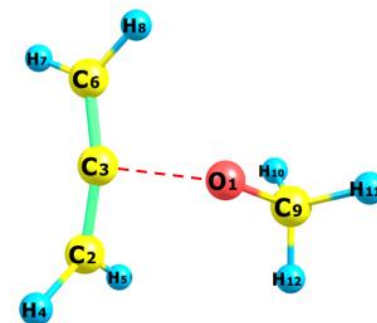
C<sub>2</sub>H<sub>2</sub>



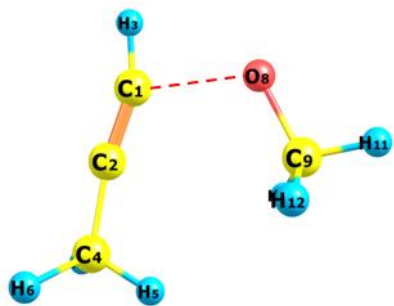
C<sub>2</sub>H<sub>4</sub>



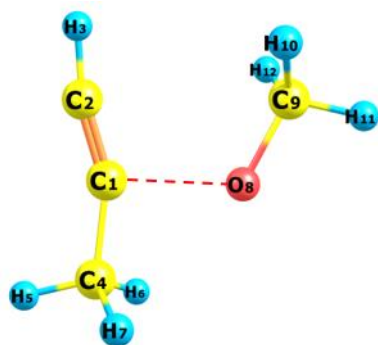
C<sub>3</sub>H<sub>4</sub>-a (E)



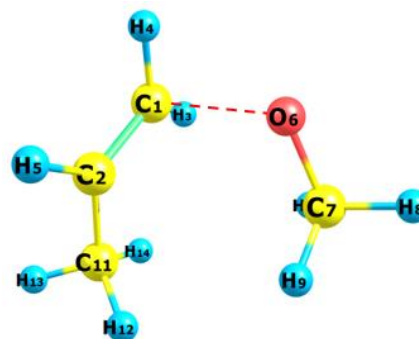
C<sub>3</sub>H<sub>4</sub>-a (I)



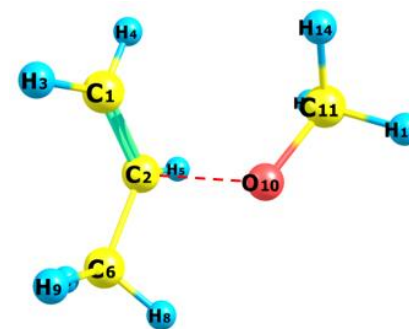
C<sub>3</sub>H<sub>4</sub>-p (E)



C<sub>3</sub>H<sub>4</sub>-p (I)



C<sub>3</sub>H<sub>6</sub> (E)



C<sub>3</sub>H<sub>6</sub> (I)

---

## 2. Theoretical methods

### 2.1 Quantum and kinetic calculation methods

In this work, a total of 32 bimolecular addition reactions of five stable species ( $C_2H_2$ ,  $C_2H_4$ ,  $C_3H_4$ -a,  $C_3H_4$ -p,  $C_3H_6$ ) with four radicals ( $\dot{C}H_3$ ,  $\dot{C}_2H_3$ ,  $\dot{C}_2H_5$ ,  $CH_3\dot{O}$ ) are studied. Four prevalent DFT functionals including B3LYP [15], M06-2X [16],  $\omega$ B97X-D [17] and B2PLYP-D3 [18] with three basis sets (6-31+G(d,p), 6-311++G(d,p) [19, 20] and cc-pVTZ [21]) are used to calculate the electronic structure information and obtain the hindrance potential which is needed to solve the one-dimensional Schrödinger equation. For internal rotors of each species and TS, relaxed PES scans involving TS optimization for each torsional angle are carried out at increments of ten degrees using the twelve DFT methods.

An in-house version of the method [22] implemented in the Thermo module of MultiWell [23, 24] is employed for the computation of the hindered rotor energy levels by solving a 1-D Schrödinger equation (Eq. 1) [22], whereby  $V(\chi)$  and  $B(\chi)$  are fitted to truncated Fourier series [25], with the fitted potentials used to construct the Hamiltonian matrix. The Hamiltonian is diagonalized to obtain energy levels, with the latter used to compute partition functions as a function of temperature (Eq. 2) [26].  $B(\chi)$  is computed based on the optimized geometries of each stationary point along the scanned potential for each method via the  $I(2,3)$  approximation [27],

$$\left[ -\frac{\partial}{\partial \chi} B_{HR}(\chi) \frac{\partial}{\partial \chi} + V(\chi) \right] \psi(\chi) = E\psi(\chi) \quad (1)$$

where  $\chi$  is the torsional dihedral,  $B_{HR}(\chi)$  is the rotational constant as a function of the torsional dihedral,  $V(\chi)$  is the torsional potential energy function,  $\psi$  and  $E$  are the eigenvectors and energy eigenvalues, respectively and  $\sigma_{HR}$  is the symmetry number for the hindered rotor and  $E_i$  is the  $i^{\text{th}}$  energy eigenvalue.

$$Q_{HR} = \frac{1}{\sigma_{HR}} \sum_{i=1}^{\infty} \exp\left(\frac{-E_i}{k_B T}\right) \quad (2)$$

One should note that differences in computed partition functions are not solely due to differences in  $V(\chi)$  but are also due to the approximation used for the computation of  $B(\chi)$ . Any absolute partition functions reported herein are symmetry uncorrected, but this does not influence the partition function ratios reported throughout.

For a true benchmark method to be defined against which all DFT methods can be benchmarked, it is correct to calculate the partition function for the transition state by optimising the geometry of the stationary point at each point along a relaxed potential energy scan to obtain the “real” hindrance potential and reduced moments of inertia constants. The additional computational demands imposed by this approach are significant and hence we introduced an approximate approach to save computational cost. For each relaxed potential energy scan performed using a given DFT method and

basis set, we carry out fixed SPE computations using high-level coupled cluster methods (the DLPNO-CCSD(T)/CBS method is selected as the benchmark throughout these discussions) to obtain an estimate of the true hindrance potential. A similar approach has been shown to provide acceptable approximations to the more rigorous hindrance potentials [28]. The DFT energies are compared with the corresponding DLPNO-CCSD(T)/CBS energies, of which the DFT optimized geometries are used for SPE calculations.

To verify the reliability of the geometries of the TSs calculated using the DFT methods, the TS geometries for  $\dot{\text{C}}\text{H}_3$ ,  $\dot{\text{C}}_2\text{H}_3$ ,  $\dot{\text{C}}_2\text{H}_5$ ,  $\text{CH}_3\dot{\text{O}}$  radical additions to  $\text{C}_2\text{H}_2$  are re-optimized at the CCSD(T)-F12/cc-pVDZ-F12 level of theory, which is recommended when highly accurate reference geometries are needed [2]. The bond lengths and dihedrals of the newly formed rotors in these TSs are collated in Tables C.1 and C.2. The deviations of bond lengths  $r_{\text{AB}}$  calculated using DFT and CCSD(T)-F12/cc-pVDZ-F12 are determined using Eq. 3. The dihedral angle deviations between the DFT and CCSD(T)-F12/cc-pVDZ-F12 results are within  $2.0^\circ$  excluding those for  $\dot{\text{C}}_2\text{H}_3 + \text{C}_2\text{H}_2$ , which will be discussed in Fig. 4.2b.

$$\Delta r_{\text{AB}}(\text{DFT} - \text{CCSD(T)-F12/DZ}) = r_{\text{AB}}(\text{DFT}) - r_{\text{AB}}(\text{CCSD(T)-F12/DZ}) \quad (3)$$

In order to identify an accurate and relatively cheap high-level of theory for benchmark calculations, the SPEs of the stationary points on different hindrance potentials, which are obtained at the M06-2X/6-311++G(d,p) level as a representative method, are calculated for rotors formed by  $\dot{\text{C}}\text{H}_3/\dot{\text{C}}_2\text{H}_3/\dot{\text{C}}_2\text{H}_5/\text{CH}_3\dot{\text{O}}$  radical additions to  $\text{C}_2\text{H}_2/\text{C}_2\text{H}_4$  at the following levels of theory: (1) CCSD(T)-F12/cc-pVTZ-F12, (2) the CCSD(T) functional with cc-pVTZ, cc-pVQZ basis sets, and (3) the DLPNO-CCSD(T) functional with cc-pVTZ, cc-pVQZ, def2-TZVPP, def2-QZVPP basis sets. Furthermore, the CCSD(T)/cc-pVXZ ( $X = \text{T}, \text{Q}$ ) and the DLPNO-CCSD(T)/cc-pVXZ ( $X = \text{T}, \text{Q}$ ) energies are extrapolated to the complete basis set limit using Eq. (4).

$$E_{\text{DLPNO-CCSD(T)/CBS}} = E_{\text{DLPNO-CCSD(T)/QZ}} + (E_{\text{DLPNO-CCSD(T)/QZ}} - E_{\text{DLPNO-CCSD(T)/TZ}}) \times \frac{4^4}{5^4 - 4^4} \quad (4)$$

The  $T_1$  diagnostic values for these open-shell coupled cluster calculations are within 0.027 – 0.045, and are listed in Table C.3. Since a  $T_1$  value of  $\leq 0.045$  was suggested in unrestricted CCSD(T) calculations as a threshold for the suitability of this single-reference method [29-31], the results calculated by single-reference coupled cluster methods in this work are acceptable for energy calculations.

The coupled cluster CCSD(T) method is considered as the gold-standard [32] for quantum chemistry calculations. In addition, the explicitly correlated coupled cluster CCSD(T)-F12 method in conjunction with the cc-pVTZ-F12 basis set can give reliable energies that are generally of equivalent accuracy to results at the CCSD(T)/cc-pVQZ level of theory but with a lower computational cost [33-36]. However, both the CCSD(T)/CBS and CCSD(T)-F12/cc-pVTZ-F12

methods are still computationally expensive for large molecules involving a number of internal rotors. The recently developed domain-based local pair natural orbital (DLPNO) coupled cluster [37] method has been shown to be an effective procedure for accurate energy calculations. Thus, the DLPNO-CCSD(T) method combined with the following four large basis sets, cc-pVTZ, cc-pVQZ, def2-TZVPP and def2-QZVPP, are also explored to check their performances in calculating hindrance potential energies.

The DLPNO-CCSD(T)/CBS method is proven in this study to be able to reproduce the hindrance potential energies calculated using the CCSD(T)/CBS method with differences being within  $0.5 \text{ kJ mol}^{-1}$  but at a fraction of the computational cost. In order to obtain accurate hindrance potential energies with reasonable computational cost, the DLPNO-CCSD(T) method with complete basis set limit extrapolated from the cc-pVTZ and cc-pVQZ basis sets (Eq. (4)) [11] is employed as the benchmark method. The energy calculations using the DLPNO-CCSD(T)/CBS method are based on the relax-scanned geometries at twelve DFT levels of theory. All of the DFT and CCSD(T) calculations were carried out using Gaussian 16 [38], while the CCSD(T)-F12 and DLPNO-CCSD(T) calculations were performed with the ORCA 4.2 software [39]. For the DLPNO-CCSD(T) calculations, the preferred way to control the accuracy of the method is by using specific keywords. These keywords select pre-defined sensible sets of thresholds to control the accuracy of the DLPNO calculations. In this work, the “TightPNO” and “TightSCF” keywords were used in the input files to select tight DLPNO thresholds and tight SCF convergences in the calculations. The default “TightPNO” settings ( $T_{\text{CutPairs}} = 10^{-5}$ ,  $T_{\text{CutPNO}} = 10^{-7}$ , and  $T_{\text{CutMKN}} = 10^{-3}$ ) were used, and many benchmark data sets indicate that this setting can provide essentially the same accuracy and reliability of the parent canonical method [39-41]. Further tightening the  $T_{\text{CutPNO}}$  threshold could, in principle, result in more accurate results, but the computational cost often approaches that of the canonical CCSD(T) method.

## 2.2 Data analysis methods

To cope with large amounts of data in this study, many statistical entities are adopted and/or created for data analysis in this study, with their definitions and equations described in detail here. The statistical entities for  $V(\chi)$ ,  $B(\chi)$  and  $Q_{\text{HR}}$  will be introduced in turn.

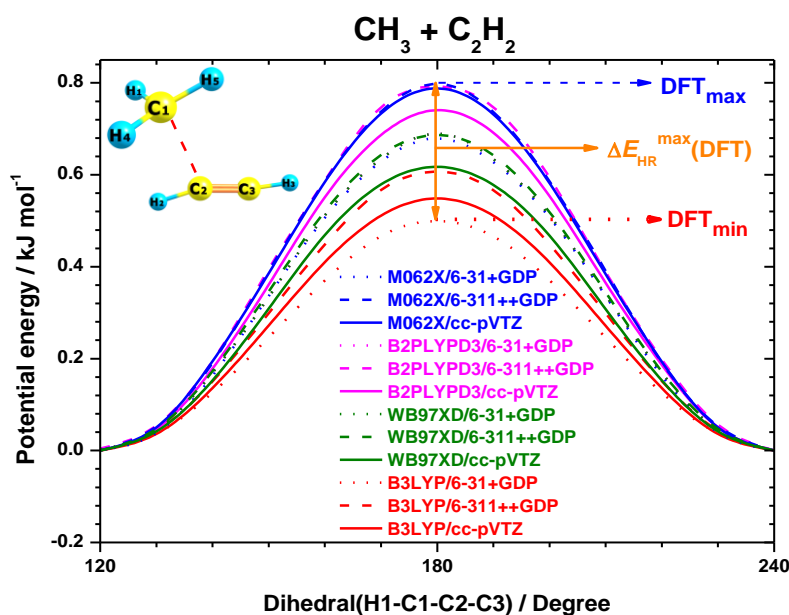


**Fig. 4.1** Hindrance potentials for the rotor formed by  $\dot{\text{C}}\text{H}_3$  radical addition to  $\text{C}_2\text{H}_2$  calculated using twelve DFT methods.

$V(\chi)$

(a) For each hindrance potential, the point with the highest energy is defined as the hindered barrier. The DFT method that gives the lowest hindered barrier is defined as  $\text{DFT}_{\min}$  for each rotor, with the hindrance potentials for the rotor formed by  $\dot{\text{C}}\text{H}_3 + \text{C}_2\text{H}_2$ , shown in Fig. 4.1 as an example. Similarly, the DFT method that gives the highest hindered barrier is defined as  $\text{DFT}_{\max}$ . For the  $i^{\text{th}}$  rotor out of the 32 target hindered rotors (numbers listed in Table 4.1), the hindered barrier deviation  $E_{\text{HR}}(\text{DFT}_{\max})_i - E_{\text{HR}}(\text{DFT}_{\min})_i$  is calculated and defined as  $\Delta E_{\text{HR}}^{\max}(\text{DFT})_i$ , which are collated in Table C.4.

(b) For the  $i^{\text{th}}$  rotor, the barrier height calculated at the  $j^{\text{th}}$  DFT method is defined as  $E_{\text{HR}}(\text{DFT}_{i,j})$ . Thereafter, an average barrier height is calculated for each rotor and defined as  $E_{\text{HR}}(\text{DFT}_i^{\text{mean}})$ . To illustrate the relative energy deviation of each DFT result from the mean value, with the consideration of the absolute barrier height, a plot of  $[E_{\text{HR}}(\text{DFT}_{i,j}) - E_{\text{HR}}(\text{DFT}_i^{\text{mean}})]$  on the  $y$ -axis and  $[(E_{\text{HR}}(\text{DFT}_{i,j}) - E_{\text{HR}}(\text{DFT}_i^{\text{mean}})) * 0.5]$  on the  $x$ -axis is generated and discussed below. In order to quantify differences in  $V(\chi)$ ,  $\Delta E_{\text{HR}}^{\max}(\text{DFT})$  described previously gives an estimate of maximum differences in computed energies. On the other hand,  $[E_{\text{HR}}(\text{DFT}_{i,j}) - E_{\text{HR}}(\text{DFT}_i^{\text{mean}})]$  provides an estimate of the variance or spread in hindrance potential energies calculated using DFT methods and whether methods tend to under-predict or over-predict energies relative to one other.

(c) Among the twelve target DFT methods, the hindrance potential obtained using the  $j^{\text{th}}$  DFT method is defined as  $E_{\text{HR}}^{\text{DFT}_{ij}}$  for the  $i^{\text{th}}$  rotor. Thereafter, the energies are re-calculated at the DLPNO-CCSD(T)/CBS level of theory with geometries optimized using the  $j^{\text{th}}$  DFT method and defined as  $E_{\text{HR}}^{\text{DLPNO}_{ij}}$ . To validate the deviations of DFT energies from the benchmark, the energy deviations are defined as  $\Delta E_{\text{HR}}(\text{DLPNO} - \text{DFT})_{ij} = E_{\text{HR}}^{\text{DLPNO}_{ij}} - E_{\text{HR}}^{\text{DFT}_{ij}}$  and the maximum deviations for each rotor are defined as  $\Delta E_{\text{HR}}^{\text{max}}(\text{DLPNO} - \text{DFT})_i$ . The relative energy deviations  $\Delta E_{\text{HR}}^{\text{relative}}(\text{DLPNO} - \text{DFT})_{ij}$  which are relative to the minimum of  $\Delta E_{\text{HR}}(\text{DLPNO} - \text{DFT})_{ij}$  for each rotor are plotted in Fig. C.9 to compare the performances of different DFT methods for energy predictions.

### **$B(\chi)$**

To compare the rotational constants calculated using different DFT methods, the DFT method that gives the smallest rotational constant is defined as  $\text{DFT}_{\text{min}}$  for each rotor with the method that gives the largest rotational constant being defined as  $\text{DFT}_{\text{max}}$ . For the  $i^{\text{th}}$  rotor and the  $k^{\text{th}}$  point on the scanned hindrance potential, the rotational constant deviation  $B(\chi)(\text{DFT}_{\text{max}})_{i,k} - B(\chi)(\text{DFT}_{\text{min}})_{i,k}$  is calculated. The maximum deviations of the rotational constants along the hindrance potentials are defined as  $\Delta B(\chi)_{\text{max}}$ , which are collated in Table C.5.  $\Delta B(\chi)_{\text{max}}$  provides a measure of the maximum variations in computed rotational constants, and therefore provides an estimate of the maximum differences that can be expected in  $B(\chi)$  arising from different DFT methods. Generally, uncertainties in  $B(\chi)$  were found to be much lower than those for  $V(\chi)$ , and most of the statistical comparisons are therefore made on  $V(\chi)$ .

### **$Q_{\text{HR}}$**

(a) The hindered internal rotation partition functions  $Q_{\text{HR}}$  are calculated over the temperature range 300–2000 K with increments of 100 K in this study. The ratios of  $Q_{\text{HR}}(\text{DFT}_j)$  and  $Q_{\text{HR}}(\text{DFT}_{\text{mean}})$  are calculated to explore the variation in  $Q_{\text{HR}}$  calculated using DFT methods.  $Q_{\text{HR}}(\text{DFT}_{\text{mean}})$  represent the mean values of  $Q_{\text{HR}}$  calculated using the twelve DFT methods at a specific temperature. The percentage difference of  $Q_{\text{HR}}(\text{DFT}_j)$  and  $Q_{\text{HR}}(\text{DFT}_{\text{mean}})$  is calculated for each DFT method using Eq. (5).

$$(Q_{\text{HR}}^{\text{DFT}} - Q_{\text{HR}}^{\text{mean}}) / Q_{\text{HR}}^{\text{mean}} = \frac{Q_{\text{HR}}(\text{DFT}_j) - Q_{\text{HR}}(\text{DFT}_{\text{mean}})}{Q_{\text{HR}}(\text{DFT}_{\text{mean}})} \times 100 \quad (5)$$

(b) To compare the maximum deviations of  $Q_{\text{HR}}$  calculated using different DFT methods, the DFT method that gives the smallest  $Q_{\text{HR}}$  is defined as  $\text{DFT}_{\text{min}}$  for each rotor with the method giving the largest  $Q_{\text{HR}}$  being defined as  $\text{DFT}_{\text{max}}$ . For the  $l^{\text{th}}$  temperature over the temperature range 300–2000 K with a step of 100 K, the percentage difference of  $Q_{\text{HR}}$  is calculated using Eq. (6). The maximum

percentage difference of  $Q_{\text{HR}}$  at different temperatures are defined as  $[(Q_{\text{HR}}^{\text{max}} - Q_{\text{HR}}^{\text{min}})/Q_{\text{HR}}^{\text{min}}]_{\text{max}}$ , which are collated in Table C.6.

$$(Q_{\text{HR}}^{\text{max}} - Q_{\text{HR}}^{\text{min}})/Q_{\text{HR}}^{\text{min}} = \frac{Q_{\text{HR}}^{\text{DFT}_{\text{max}}} - Q_{\text{HR}}^{\text{DFT}_{\text{min}}}}{Q_{\text{HR}}^{\text{DFT}_{\text{min}}}} \times 100 \quad (6)$$

(c) The hindrance potential energies and rotational constants for the  $i^{\text{th}}$  rotor calculated using the  $j^{\text{th}}$  DFT method are defined as  $E_{\text{HR}}^{\text{DFT}_{ij}}$  and  $B(\chi)^{\text{DFT}_{ij}}$ , respectively. The  $Q_{\text{HR}}^{\text{DLPNO}_{ij}}$  are calculated with  $E_{\text{HR}}^{\text{DLPNO}_{ij}}$  and  $B(\chi)^{\text{DFT}_{ij}}$ . The  $[(Q_{\text{HR}}^{\text{DFT}_{ij}} - Q_{\text{HR}}^{\text{DLPNO}_{ij}})/Q_{\text{HR}}^{\text{DLPNO}_{ij}} \times 100]$  percentage differences are calculated for each DFT method to validate the deviations between the DFT and the DLPNO-CCSD(T)/CBS results. These percentage differences provide an estimate of the uncertainty arising from a given DFT method as a result of uncertainties in  $E_{\text{HR}}^{\text{DFT}_{ij}}$ .

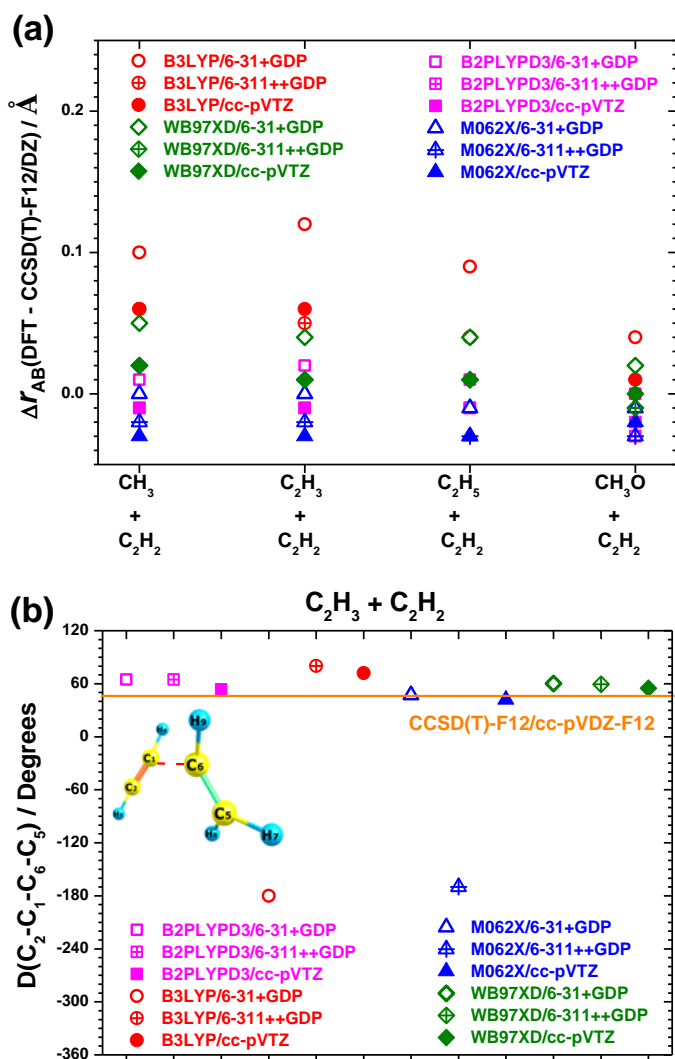
### 3. Results and discussions

#### 3.1 Optimized geometry validations

The TS geometries for  $\dot{\text{C}}\text{H}_3/\dot{\text{C}}_2\text{H}_3/\dot{\text{C}}_2\text{H}_5/\text{CH}_3\dot{\text{O}} + \text{C}_2\text{H}_2$  are optimized at the CCSD(T)-F12/cc-pVDZ-F12 level of theory and the twelve DFT methods, with the optimized geometry at the M06-2X/6-311++G(d,p) level used as an initial guess for the CCSD(T)-F12/cc-pVDZ-F12 optimization. The deviations of bond lengths  $r_{\text{AB}}$  calculated using DFT and the CCSD(T)-F12/cc-pVDZ-F12 method are plotted in Fig. 4.2(a). The absolute mean difference in bond lengths for the TSs in comparison to the geometries obtained from the CCSD(T)-F12/cc-pVDZ-F12 method is 0.03 Å with a standard deviation  $\sigma$  of 0.02 Å, and the B3LYP/6-31+G(d,p) method predicts a maximum difference of 0.12 Å.

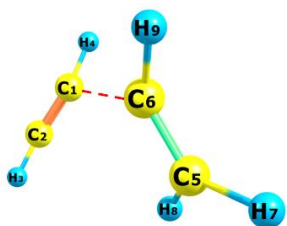
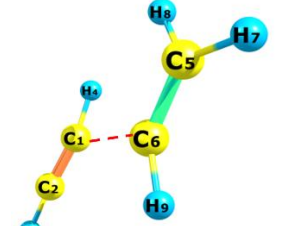
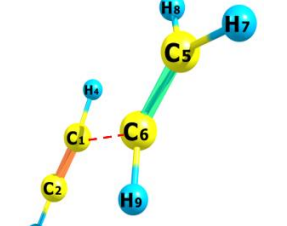
The dihedral deviations between the DFT and the CCSD(T)-F12/cc-pVDZ-F12 results are within 2.0° excluding the TS for  $\dot{\text{C}}_2\text{H}_3 + \text{C}_2\text{H}_2$ , for which the dihedrals of the newly formed rotor are plotted in Fig. 4.2(b). For optimizations starting with  $\text{D}(\text{C}_2-\text{C}_1-\text{C}_6-\text{C}_5) = 60^\circ$  as an initial guess, the dihedrals  $\text{D}(\text{C}_2-\text{C}_1-\text{C}_6-\text{C}_5)$  optimized by most of the DFT methods agree within 33.0° with the CCSD(T)-F12/cc-pVDZ-F12 result, excluding the B3LYP/6-31+G(d,p) and M06-2X/6-311++G(d,p) results. The optimized geometries and dihedral angles calculated using these two DFT methods are compared with the CCSD(T)-F12/cc-pVDZ-F12 result in Table 4.3. The optimized  $\text{D}(\text{C}_2-\text{C}_1-\text{C}_6-\text{C}_5)$  angle varies from  $-180.0^\circ$  using B3LYP/6-31+G(d,p) to  $-169.8^\circ$  using M06-2X/6-311++G(d,p), in comparison to  $47.1^\circ$  using CCSD(T)-F12/cc-pVDZ-F12. It should be noted that there are multiple different minima on the hindrance potentials for this rotor, and the absolute minimum of each hindrance potential is different using different DFT methods. Hence, the CCSD(T)-F12/cc-pVDZ-F12 results here only show the various performances of these DFT methods on optimization calculations and cannot be used as a benchmark for this rotor on hindrance potential

predictions. The large variations in optimized geometries from different DFT methods are also observed for the other TSs formed by  $\dot{\text{C}}_2\text{H}_3/\dot{\text{C}}_2\text{H}_5/\text{CH}_3\dot{\text{O}} + \text{C}_3\text{H}_4\text{-a}$  (internal additions) in this study. For rotors formed in the  $\dot{\text{C}}_2\text{H}_3 + \text{C}_2\text{H}_2$  and  $\dot{\text{C}}_2\text{H}_3/\dot{\text{C}}_2\text{H}_5/\text{CH}_3\dot{\text{O}} + \text{C}_3\text{H}_4\text{-a}$  (I) systems, qualitative and quantitative differences are observed in their DFT hindrance potentials (e.g. the number of the peaks and wells in Figs. C.6–C.8), and these differences will be discussed into detail in Section 3.3.3.



**Fig. 4.2** (a) The deviations of bond lengths for the newly formed rotors in the TSs of  $\dot{\text{C}}\text{H}_3$ ,  $\dot{\text{C}}_2\text{H}_3$ ,  $\dot{\text{C}}_2\text{H}_5$ ,  $\text{CH}_3\dot{\text{O}}$  radical additions to  $\text{C}_2\text{H}_2$ , calculated at DFT and CCSD(T)-F12/cc-pVDZ-F12 levels of theory. (b) The dihedrals of the newly formed rotors in the TS of  $\dot{\text{C}}_2\text{H}_3$  radical addition to  $\text{C}_2\text{H}_2$ , calculated at DFT and CCSD(T)-F12/cc-pVDZ-F12 levels of theory. Different DFT methods are plotted as  $x$  axis in this plot.

**Table 4.3** The optimized geometries and dihedral angles of  $D(C_2-C_1-C_6-C_5)$  for the TSs of  $\dot{C}_2H_3$  radical addition to  $C_2H_2$ , calculated at two DFT and CCSD(T)-F12/cc-pVDZ-F12 levels of theory.

CCSD(T)-F12/cc-pVDZ-F12	M06-2X/6-311++G(d,p)	B3LYP/6-31+G(d,p)
 <p><math>D(C_2-C_1-C_6-C_5) = 47.1^\circ</math></p>	 <p><math>D(C_2-C_1-C_6-C_5) = -169.8^\circ</math></p>	 <p><math>D(C_2-C_1-C_6-C_5) = -180.0^\circ</math></p>

### 3.2 Rotational constant comparisons

The rotational constants for rotors formed by  $\dot{C}H_3/\dot{C}_2H_3/\dot{C}_2H_5/CH_3\dot{O} + C_2H_2/C_2H_4/C_3H_4\text{-a}/C_3H_4\text{-p}/C_3H_6$  calculated using the twelve DFT methods are compared and plotted in Figs. C.1–C.4. The maximum deviations  $\Delta B(\chi)_{\max}$  along the hindrance potentials are collated in Table C.5. The maximum  $\Delta B(\chi)_{\max}$  for rotors formed by  $\dot{C}H_3$ ,  $\dot{C}_2H_3$ ,  $\dot{C}_2H_5$  and  $CH_3\dot{O}$  radical additions are 0.14, 0.20, 0.14 and 0.30  $\text{cm}^{-1}$ , respectively. For rotors formed by  $\dot{C}_2H_3 + C_2H_2$  and  $\dot{C}_2H_3/\dot{C}_2H_5/CH_3\dot{O} + C_3H_4\text{-a}$  (I), there is no significantly larger deviation of  $B(\chi)$  observed in comparison with the other rotors with smaller variations in optimized geometries.

In order to explore the sensitivity of the  $Q_{HR}$  calculations to the variations of  $B(\chi)$ , the  $B(\chi)$  values calculated using different DFT methods are varied with the addition/subtraction of  $\Delta B(\chi)_{\max}$  and used for the  $Q_{HR}$  calculation. For instance, the internal rotation formed by  $CH_3\dot{O} + C_3H_4\text{-a}$  (internal addition), which have the largest  $\Delta B(\chi)_{\max}$  of 0.30  $\text{cm}^{-1}$  among rotors formed by  $CH_3\dot{O}$  radical additions, is expected to represent the largest influence of  $\Delta B(\chi)_{\max}$  on the  $Q_{HR}$  calculation. For this internal rotation, the  $Q_{HR}(B(\chi) \pm \Delta B(\chi)_{\max})$  are calculated using the twelve DFT methods and compared with the original  $Q_{HR}$  value. It is shown that the largest deviation between  $Q_{HR}$  and  $Q_{HR}(B(\chi) \pm \Delta B(\chi)_{\max})$  for internal rotations formed by  $\dot{C}H_3$ ,  $\dot{C}_2H_3$ ,  $\dot{C}_2H_5$  and  $CH_3\dot{O}$  radical additions are 1.2%, 5.2%, 2.7% and 9.1% over the temperature range 300–2000 K, respectively. Hence, the variations in  $B(\chi)$  calculated using different DFT methods are small, but they also appear to be system-dependent for the rotors formed by different radical addition reactions.

### 3.3 Hindrance potential energy comparisons

#### 3.3.1 Overall analysis of DFT $E_{HR}$

The hindrance potentials for rotors formed by  $\dot{C}H_3/\dot{C}_2H_3/\dot{C}_2H_5/CH_3\dot{O}$  +  $C_2H_2/C_2H_4/C_3H_4\text{-a}/C_3H_4\text{-p}/C_3H_6$  calculated using the twelve DFT methods are compared and plotted in Figs. C.5–C.8 of Appendix C. The hindrance potential energy deviations between  $E_{HR}(DFT)$  and  $E_{HR}(DFT^{mean})$  are plotted in Fig. 4.3(a) for all target rotors with their mean values on the  $x$ -axis.  $E_{HR}(DFT^{mean})$  herein is an average hindered barrier for each rotor and for each DFT method. Similarly, we take the average hindered barrier over 12 DFT methods for each rotor and  $[E_{HR}(DFT) - E_{HR}(DFT^{mean})_r]$  versus  $[E_{HR}(DFT) + E_{HR}(DFT^{mean})_r]*0.5$  is also plotted in Fig. 4.3(b).

In comparison with the mean energies of the twelve DFT methods as shown in Fig. 4.3(a), in most cases the B3LYP functional tends to under-predict energies, the M06-2X functional tends to over-predict energies, and the energies predicted by the other two functionals seem to lie in between. This may be explained by the finding of DFT geometry validations that the B3LYP functional tends to over-predict bond lengths, the M06-2X functional tends to under-predict bond lengths, while the other two functionals seem to predict similar bond lengths and dihedrals compared to the CCSD(T)-F12/cc-pVDZ-F12 results. The hindered barriers for rotors formed by target radical additions shown in Fig. 4.3(b) have a clear trend that  $E_{HR}(CH_3\dot{O} \text{ additions}) > E_{HR}(\dot{C}_2H_5 \text{ additions}) \geq E_{HR}(\dot{C}_2H_3 \text{ additions}) \approx E_{HR}(\dot{C}H_3 \text{ additions})$ . When the radical size increases from  $\dot{C}H_3$  to  $\dot{C}_2H_5$  the absolute hindered barrier increases for additions to the same alkenes/dienes/alkynes. The variations of hindered barriers calculated using different DFT methods for rotors formed by  $\dot{C}H_3$  radical additions are much smaller than those formed by the other three radical additions, with  $[E_{HR}(DFT) - E_{HR}(DFT^{mean})_r]$  being within  $0.5 \text{ kJ mol}^{-1}$ . Hence, these twelve DFT methods all prove to be reliable for the hindered rotor treatment of the methyl group rotation. For the other rotors formed by  $\dot{C}_2H_3/\dot{C}_2H_5/CH_3\dot{O}$  radical additions, the  $[E_{HR}(DFT) - E_{HR}(DFT^{mean})_r]$  calculated using different DFT methods are within  $4.0 \text{ kJ mol}^{-1}$ .

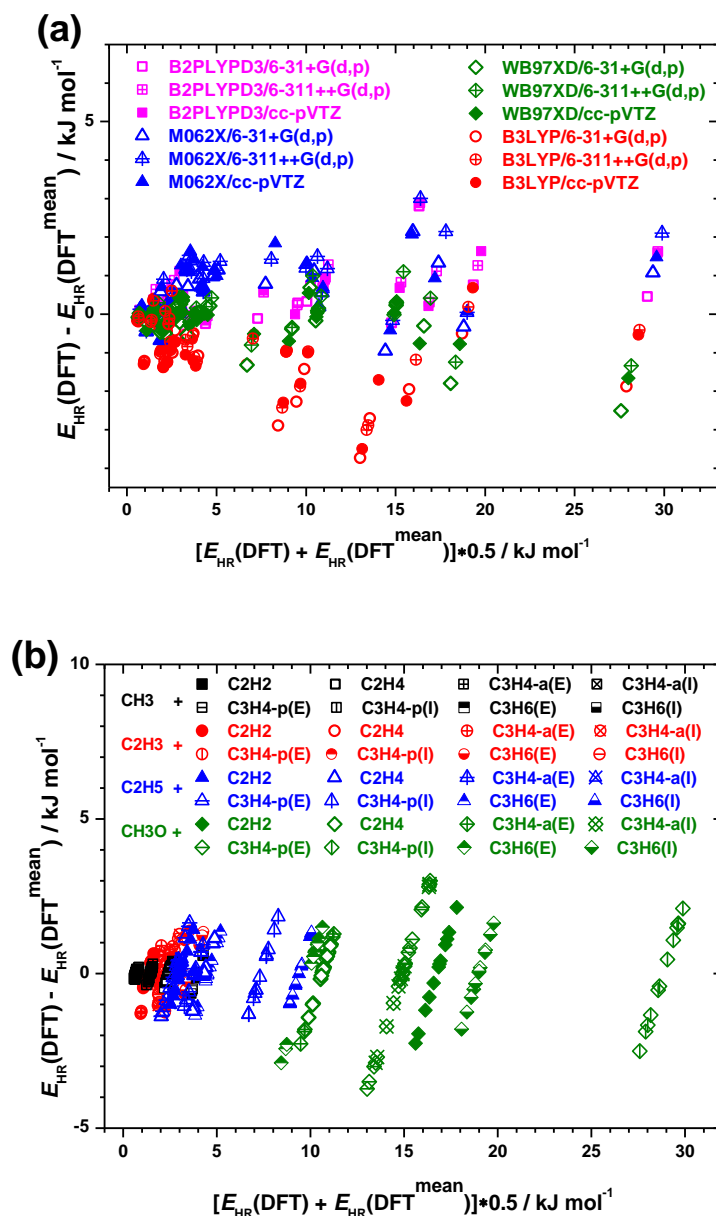


**Fig. 4.3** (a) The hindrance potential energy deviations plot with  $[E_{\text{HR}}(\text{DFT}) - E_{\text{HR}}(\text{DFT}^{\text{mean}})]$  on the y-axis and  $[E_{\text{HR}}(\text{DFT}) + E_{\text{HR}}(\text{DFT}^{\text{mean}})] \times 0.5$  on the x-axis, of which  $E_{\text{HR}}(\text{DFT}^{\text{mean}})$  is averaging over 32 rotors for each DFT method. (b) The hindrance potential energy deviations plot with  $[E_{\text{HR}}(\text{DFT}) - E_{\text{HR}}(\text{DFT}^{\text{mean}})_r]$  on the y-axis and  $[E_{\text{HR}}(\text{DFT}) + E_{\text{HR}}(\text{DFT}^{\text{mean}})_r] \times 0.5$  on the x-axis, of which  $E_{\text{HR}}(\text{DFT}^{\text{mean}})_r$  is averaging over 12 DFT methods for each rotor.

The maximum hindered barrier deviation  $\Delta E_{\text{HR}}^{\text{max}}(\text{DFT})_i$  which equals  $E_{\text{HR}}(\text{DFT}_{\text{max}})_i - E_{\text{HR}}(\text{DFT}_{\text{min}})_i$  is plotted versus the mean hindered barrier for the twelve DFT methods for each rotor in Fig. 4.4. A linear correlation is fitted to  $\Delta E_{\text{HR}}^{\text{max}}(\text{DFT})_i = (0.28 \pm 0.03) \times E_{\text{HR}}(\text{DFT}^{\text{mean}})_i$  for the  $i^{\text{th}}$  rotor, with an  $R^2$  of 0.77. This correlation indicates that as a general trend, the variation in hindered barriers calculated by different DFT methods increases as the absolute hindered barrier increases. Another trend observed is that the difference in hindered barrier calculated using different DFT methods increases when the same radical adding to the same site of a larger alkenes/alkynes. For

instance, the maximum hindered barrier deviations for rotors formed by  $\dot{\text{C}}_2\text{H}_3/\dot{\text{C}}_2\text{H}_5/\text{CH}_3\dot{\text{O}} + \text{C}_2\text{H}_2$  are consistently smaller than those of  $\dot{\text{C}}_2\text{H}_3/\dot{\text{C}}_2\text{H}_5/\text{CH}_3\dot{\text{O}} + \text{C}_3\text{H}_4\text{-p(E)}$ . A similar phenomenon is found for  $\dot{\text{C}}_2\text{H}_3/\dot{\text{C}}_2\text{H}_5/\text{CH}_3\dot{\text{O}} + \text{C}_2\text{H}_4$  in comparison to  $\dot{\text{C}}_2\text{H}_3/\dot{\text{C}}_2\text{H}_5/\text{CH}_3\dot{\text{O}} + \text{C}_3\text{H}_6\text{(E)}$ . Hence, we assume that the variations of hindered barriers (representing the variation of  $V(\chi)$ ) for rotors formed by  $\dot{\text{R}} +$  alkenes/alkynes increase with the size of both the radical and alkenes/alkynes.

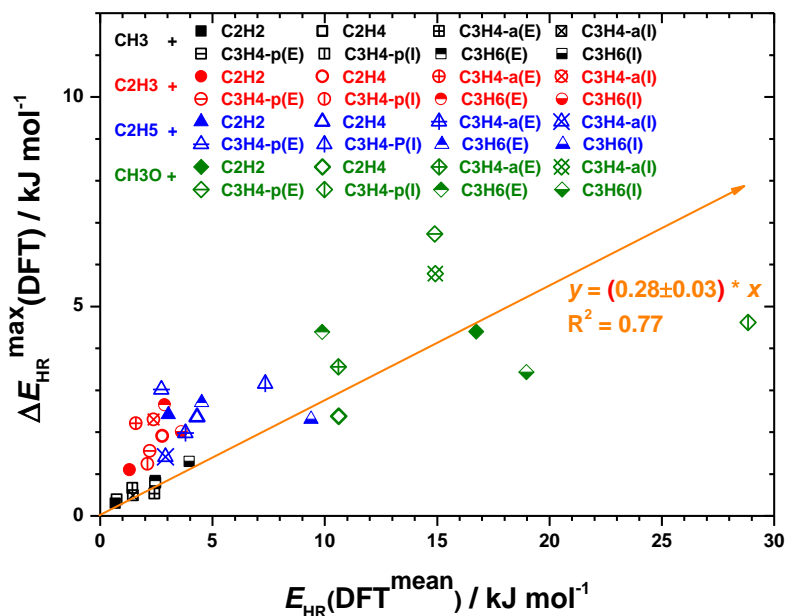


**Fig. 4.4** The linear correlation of mean hindered barriers and the maximum energy deviations of twelve DFT methods for rotors formed by  $\dot{\text{C}}\text{H}_3/\dot{\text{C}}_2\text{H}_3/\dot{\text{C}}_2\text{H}_5/\text{CH}_3\dot{\text{O}} + \text{C}_2\text{H}_2/\text{C}_2\text{H}_4/\text{C}_3\text{H}_4\text{-a}/\text{C}_3\text{H}_4\text{-p}/\text{C}_3\text{H}_6$ .

### 3.3.2 Hindrance potential energy benchmarking

To identify a reliable benchmark method in an efficient way, the SPEs of the geometries optimized along the hindrance potential at the M06-2X/6-311++G(d,p) level are recalculated at nine high-levels of theory (CCSD(T)-F12/cc-pVTZ-F12, CCSD(T)/cc-pVTZ, CCSD(T)/cc-pVQZ, CCSD(T)/CBS, DLPNO-CCSD(T)/def2-TZVPP, DLPNO-CCSD(T)/def2-QZVPP, DLPNO-CCSD(T)/cc-pVTZ, DLPNO-CCSD(T)/cc-pVQZ, and DLPNO-CCSD(T)/CBS) as a representative test, for rotors formed by  $\dot{\text{C}}\text{H}_3/\dot{\text{C}}_2\text{H}_3/\dot{\text{C}}_2\text{H}_5/\text{CH}_3\dot{\text{O}}$  radical additions to  $\text{C}_2\text{H}_2/\text{C}_2\text{H}_4$ .

The hindrance potentials calculated using coupled cluster methods for  $\dot{\text{R}} + \text{C}_2\text{H}_2$  are plotted in Fig. 4.5 and the hindrance potentials for  $\dot{\text{R}} + \text{C}_2\text{H}_4$  are plotted in Fig. 4.6. For  $\dot{\text{R}} + \text{C}_2\text{H}_2/\text{C}_2\text{H}_4$ , the maximum differences in hindered barriers obtained from these coupled cluster methods are within 0.2 – 1.7  $\text{kJ mol}^{-1}$ . The hindered barriers obtained from CCSD(T)-F12/cc-pVTZ-F12 and CCSD(T)/CBS have a largest difference of 0.2  $\text{kJ mol}^{-1}$ . It is also noticeable that the DLPNO-CCSD(T)/CBS method can produce a similar result compared to CCSD(T)/CBS method with a largest difference of 0.5  $\text{kJ mol}^{-1}$  but at a fraction of the computational cost. Liakos and Neese [42] proposed that the DLPNO-CCSD(T) method could generate coupled cluster energies at near

DFT cost.

Among these nine methods, the DLPNO-CCSD(T)/CBS energies are selected as the benchmark method to validate the uncertainties in hindrance potential energy calculations of different DFT methods. Due to the significant computational cost needed for an optimization calculation at the DLPNO-CCSD(T)/CBS level of theory, the SPEs of the minima on different hindrance potentials are re-calculated based on geometries optimized using the twelve DFT methods for rotors formed by  $\dot{\text{C}}\text{H}_3/\dot{\text{C}}_2\text{H}_3/\dot{\text{C}}_2\text{H}_5/\text{CH}_3\dot{\text{O}}$  radical additions to  $\text{C}_2\text{H}_2/\text{C}_2\text{H}_4$ . The SPEs of the geometries optimized along the hindrance potential using each DFT method are compared with their corresponding DLPNO-CCSD(T)/CBS SPEs in the following discussions. The  $B(\chi)$  values calculated using different DFT methods are used together with the DLPNO-CCSD(T)/CBS energies for further  $Q_{\text{HR}}(\text{DLPNO-CCSD(T)/CBS})$  calculations.

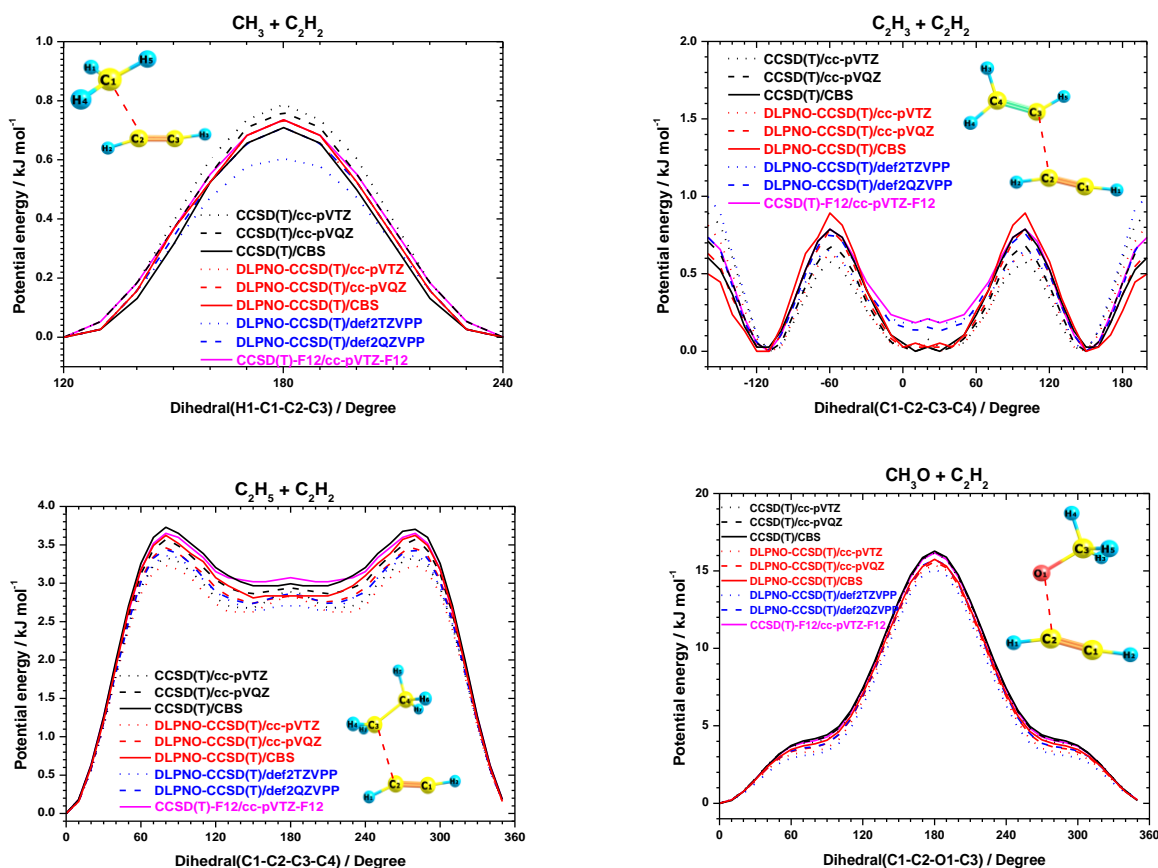


**Fig. 4.5** Hindrance potentials for internal rotors formed by  $\dot{\text{C}}\text{H}_3$ ,  $\dot{\text{C}}_2\text{H}_3$ ,  $\dot{\text{C}}_2\text{H}_5$ ,  $\text{CH}_3\dot{\text{O}}$  radical additions to  $\text{C}_2\text{H}_2$  calculated at CCSD(T) and DLPNO-CCSD(T) level of theories with the use of different basis sets, based on the geometries optimized along the hindrance potential at the M06-2X/6-311++G(d,p) level.

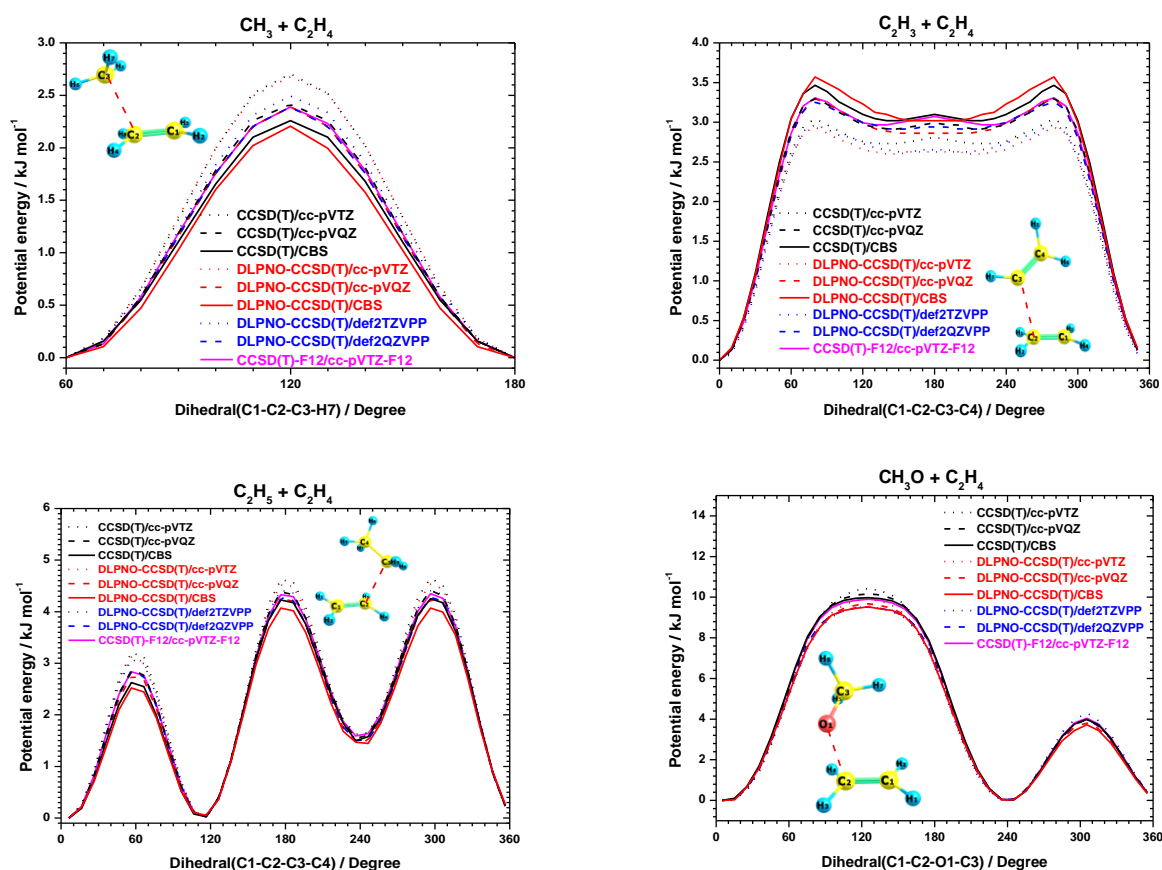


**Fig. 4.6** Hindrance potentials for internal rotors formed by  $\dot{\text{C}}\text{H}_3$ ,  $\dot{\text{C}}_2\text{H}_3$ ,  $\dot{\text{C}}_2\text{H}_5$ ,  $\text{CH}_3\dot{\text{O}}$  additions to  $\text{C}_2\text{H}_4$  calculated at CCSD(T) and DLPNO-CCSD(T) level of theories with the use of different basis sets, based on the geometries optimized along the hindrance potential at the M06-2X/6-311++G(d,p) level.

### 3.3.3 Rotors with large variations in optimized geometries

As discussed previously, for rotors formed in the  $\dot{\text{C}}_2\text{H}_3 + \text{C}_2\text{H}_2$  and  $\dot{\text{C}}_2\text{H}_3/\dot{\text{C}}_2\text{H}_5/\text{CH}_3\dot{\text{O}} + \text{C}_3\text{H}_4$ -a (I) systems, there are qualitative and quantitative differences in their DFT hindrance potentials (Figs. C.6–C.8). The hindrance potentials for rotors formed by  $\dot{\text{C}}_2\text{H}_3 + \text{C}_2\text{H}_2$  calculated at the DFT and DLPNO-CCSD(T)/CBS levels are plotted to explore the influences of the larger variations in optimized geometries on  $V(\chi)$  and the further  $Q_{\text{HR}}$  predictions, Figs. 4.7(a) and 4.7(b). These DLPNO-CCSD(T)/CBS energies show small deviations, being within  $0.3 \text{ kJ mol}^{-1}$  with similar shapes, in comparison with a  $\Delta E_{\text{HR}}^{\text{max}}$  (DFT) of  $1.1 \text{ kJ mol}^{-1}$  for the DFT energies. An important finding is that the qualitative and quantitative differences in  $V(\chi)$  values predicted by different DFT methods can be reduced if the DLPNO-CCSD(T), or similar benchmark methods, are carried out for energy calculations using the DFT-derived geometries.

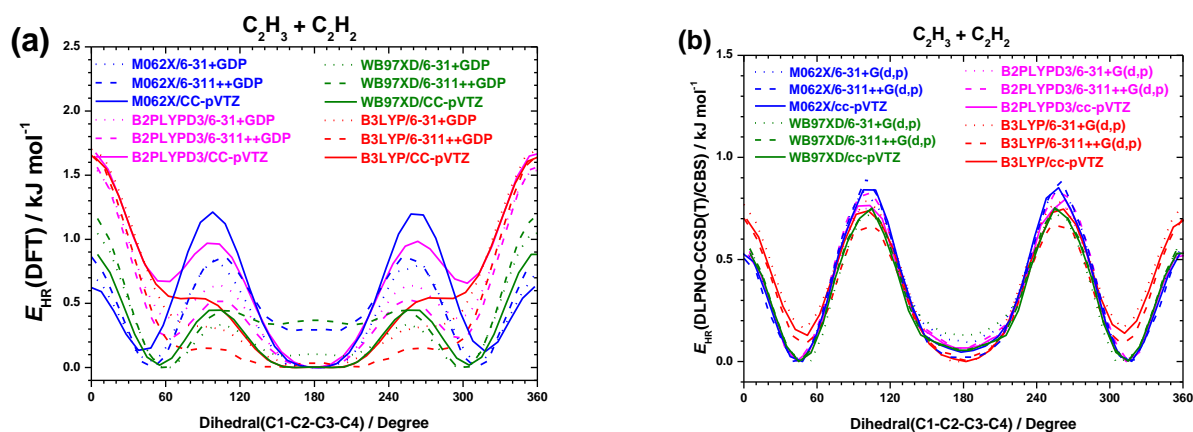


**Fig. 4.7** (a) The hindrance potential energies calculated using twelve DFT methods for the rotor formed by  $\dot{C}_2H_3$  radical addition to  $C_2H_2$ . (b) The hindrance potential energies calculated at DLPNO-CCSD(T)/CBS level of theory based on optimized geometries calculated using twelve DFT methods for the rotor formed by  $\dot{C}_2H_3$  radical addition to  $C_2H_2$ .

The relative energy deviations between the DLPNO-CCSD(T)/CBS and DFT results  $\Delta E_{HR}^{relative}(\text{DLPNO} - \text{DFT})$  for each DFT method are plotted in Fig. 4.8 for the rotor formed by  $\dot{C}_2H_3$  radical addition to  $C_2H_2$ . It is shown that the energy deviations predicted by the B2PLYP-D3 functional from the DLPNO-CCSD(T)/CBS energies are somewhat sensitive to the use of basis set, with the maximum deviation being within  $0.6 \text{ kJ mol}^{-1}$  using the cc-pVTZ basis set and close to  $1.8 \text{ kJ mol}^{-1}$  using the 6-311++G(d,p) basis set. Similarly, the cc-pVTZ basis set, in combination with B3LYP and  $\omega$ B97X-D functionals, show better energy predictions compared to those predicted using Pople basis sets. However, the use of the cc-pVTZ basis set with the M06-2X functional predicts larger deviations from the benchmark energies compared to those using Pople basis sets. The increase of basis set from 6-31+G(d,p) to 6-311++G(d,p) working together with these four functionals does not show any obvious positive influence on energy predictions, and hence the smaller basis sets can be employed where necessary in place of 6-311++G(d,p). However, it is important to note that the differences between the DFT and the DLPNO-CCSD(T)/CBS energies computed based on geometries derived via Pople type basis sets are generally larger than those using Dunning-type basis sets.

In general, the maximum energy deviations between DFT and DLPNO-CCSD(T)/CBS energies follow the trend (three basis sets were indicated where the basis sets were omitted): B2PLYP-D3 with Pople basis sets > B3LYP >  $\omega$ B97X-D with Pople basis sets > B2PLYP-D3/cc-pVTZ  $\approx$   $\omega$ B97X-D/cc-pVTZ > M06-2X.

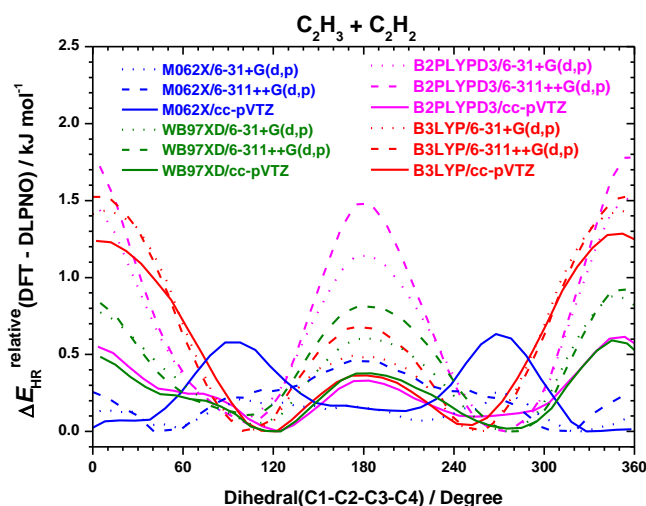


**Fig. 4.8** The relative potential energy deviations  $\Delta E_{\text{HR}}^{\text{relative}}$  (DLPNO – DFT) for each DFT method in comparison with the benchmarking DLPNO-CCSD(T)/CBS energies for rotors formed by  $\dot{\text{C}}_2\text{H}_3$  radical additions to  $\text{C}_2\text{H}_2$ .

### 3.3.4 $E_{\text{HR}}$ comparisons between DFT and DLPNO-CCSD(T)/CBS

For rotors formed through  $\dot{\text{C}}\text{H}_3/\dot{\text{C}}_2\text{H}_3/\dot{\text{C}}_2\text{H}_5/\text{CH}_3\dot{\text{O}}$  radical additions to  $\text{C}_2\text{H}_2/\text{C}_2\text{H}_4$ , the relative energy deviations between the DLPNO-CCSD(T)/CBS and DFT results  $\Delta E_{\text{HR}}^{\text{relative}}$  (DLPNO – DFT) for each DFT method are plotted in Fig. C.9. The maximum deviations in energy between the DFT and DLPNO-CCSD(T)/CBS methods  $\Delta E_{\text{HR}}^{\text{max}}$  (DLPNO – DFT) for rotors formed through  $\dot{\text{C}}\text{H}_3/\dot{\text{C}}_2\text{H}_3/\dot{\text{C}}_2\text{H}_5/\text{CH}_3\dot{\text{O}}$  radical additions to  $\text{C}_2\text{H}_2/\text{C}_2\text{H}_4$  are collated in Table C.7 and plotted in Fig. 4.9.

For rotors formed by  $\dot{\text{C}}\text{H}_3$  radical addition to  $\text{C}_2\text{H}_2/\text{C}_2\text{H}_4$ , the maximum deviation in  $V(\chi)$  values calculated using the twelve DFT methods from the DLPNO-CCSD(T)/CBS energies is  $0.4 \text{ kJ mol}^{-1}$ . The variations of hindered barriers calculated using different DFT methods for methyl group rotations are previously found to be within  $0.5 \text{ kJ mol}^{-1}$  in Section 3.3.1. Therefore, the cheapest method, namely the B3LYP functional in this study, should be good enough to predict hindrance potential energies for methyl group rotations.

For rotors formed by  $\dot{\text{C}}_2\text{H}_3$  radical additions to  $\text{C}_2\text{H}_2$  and  $\text{C}_2\text{H}_4$ , the B2PLYP-D3 functional with Pople basis sets [43] and the B3LYP functional with three basis sets show relatively poor performances in predicting  $V(\chi)$  values, with the maximum deviation being  $2.0 \text{ kJ mol}^{-1}$  compared to the DLPNO-CCSD(T)/CBS energies. The B2PLYP-D3/cc-pVTZ method shows a similar performance to the  $\omega\text{B97X-D}$  methods in predicting  $V(\chi)$  values for these two rotors. M06-2X functional performs best in predicting  $V(\chi)$  values which agree with the DLPNO-CCSD(T)/CBS energies within  $0.52 \text{ kJ mol}^{-1}$ . The 6-31+G(d,p) basis set with M06-2X functional shows the best performance for  $\dot{\text{C}}_2\text{H}_3 + \text{C}_2\text{H}_2$ , while the cc-pVTZ basis set with M06-2X functional works better for



For rotors formed by  $\dot{\text{C}}_2\text{H}_5$  radical additions to  $\text{C}_2\text{H}_2$  and  $\text{C}_2\text{H}_4$ , the B3LYP functional shows the worst performance in predicting  $V(\chi)$  values especially with the 6-31+G(d,p) basis set, followed by the M06-2X method. The performance of the B2PLYP-D3 functional in predicting  $V(\chi)$  values is somewhat sensitive to the use of the basis set, with maximum deviations using the 6-31+G(d,p) basis set being within  $1.3 \text{ kJ mol}^{-1}$ , while those for the cc-pVTZ basis set are within  $0.7 \text{ kJ mol}^{-1}$ . The  $V(\chi)$  values predicted using the  $\omega\text{B97X-D/cc-pVTZ}$  and B2PLYP-D3/cc-pVTZ methods are within  $0.7 \text{ kJ mol}^{-1}$  from the DLPNO-CCSD(T)/CBS energies over the dihedral  $0-360^\circ$ . In consideration of the more expensive computational cost of B2PLYP-D3 calculations, the  $\omega\text{B97X-D/cc-pVTZ}$  method is more recommended for rotors formed via  $\dot{\text{C}}_2\text{H}_5$  radical additions in calculating  $V(\chi)$  values.

For rotors formed by  $\text{CH}_3\dot{\text{O}}$  radical additions to  $\text{C}_2\text{H}_2$  and  $\text{C}_2\text{H}_4$ , the maximum deviation can be up to  $3.1 \text{ kJ mol}^{-1}$ . The 6-311++G(d,p) basis set with the B3LYP functional shows the best performance in predicting  $V(\chi)$  values. Those calculated using the  $\omega\text{B97X-D/cc-pVTZ}$  method agree reasonably well with the DLPNO-CCSD(T)/CBS energies, with a maximum deviation being  $1.7 \text{ kJ mol}^{-1}$  but at a higher computational cost. Hence, the  $\omega\text{B97X-D}$  functional with an appropriate basis set is the recommended method for calculating  $V(\chi)$  values for rotors formed by  $\text{CH}_3\dot{\text{O}}$  radical additions. Moreover, the B3LYP functional with Pople basis sets can also be used to save computational cost with reasonably reliable  $V(\chi)$  values calculated.

In general, the  $\omega\text{B97X-D}$  functional shows a good performance for  $V(\chi)$  predictions among the twelve DFT methods, especially using the cc-pVTZ basis set for most rotors. The maximum deviations of  $\omega\text{B97X-D/cc-pVTZ}$  energies from DLPNO-CCSD(T)/CBS energies are  $0.8 \text{ kJ mol}^{-1}$ , excluding the rotor formed by  $\text{CH}_3\dot{\text{O}} + \text{C}_2\text{H}_4$ . The B2PLYP-D3/cc-pVTZ method also shows reliable  $V(\chi)$  value predictions for these eight rotors at a higher computational cost. Considering the reliability of these functionals for geometry optimizations with the use of different basis sets (Section 3.1) and their computational costs, the  $\omega\text{B97X-D}$  functional with the cc-pVTZ basis set is the recommended method for scan calculations for rotors formed by  $\dot{\text{C}}_2\text{H}_3$  and  $\dot{\text{C}}_2\text{H}_5$  radical additions, while the B3LYP-cc-pVTZ method is a reliable and practical method for scan calculations for rotors formed by  $\dot{\text{C}}\text{H}_3$  and  $\text{CH}_3\dot{\text{O}}$  radical additions.

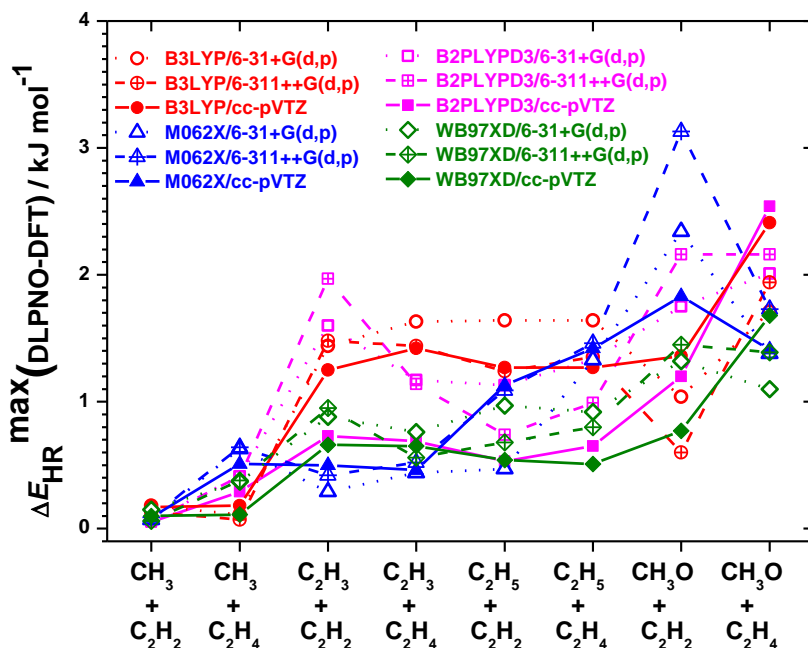


**Fig. 4.9** The maximum deviations between DFT and DLPNO-CCSD(T)/CBS potential energies for rotors formed by  $\dot{\text{C}}\text{H}_3/\dot{\text{C}}_2\text{H}_3/\dot{\text{C}}_2\text{H}_5/\text{CH}_3\dot{\text{O}}$  radical additions to  $\text{C}_2\text{H}_2/\text{C}_2\text{H}_4$ , with geometries optimized at DFT methods used for DLPNO-CCSD(T)/CBS potential energy calculations.

### 3.4 Partition function comparisons

#### 3.4.1 Overall analysis of DFT $Q_{\text{HR}}$

The percentage differences  $[(Q_{\text{HR}}^{\text{DFT}} - Q_{\text{HR}}^{\text{mean}})/Q_{\text{HR}}^{\text{mean}}]$  between the DFT methods and their corresponding mean energies at 300 K are plotted in Fig. 4.10, with the TS number on the  $x$ -axis as shown in Table 4.1, and the percentage differences at 500 K, 1000 K and 2000 K are plotted in Fig. C.10. Consistent with our previous finding for hindered barriers, the B3LYP functional tends to over-predict  $Q_{\text{HR}}$ , the M06-2X functional tends to under-predict  $Q_{\text{HR}}$ , and the  $Q_{\text{HR}}$  values predicted by the other two functionals lie in-between. In general, the  $\omega\text{B97X-D}$  and B2PLYP-D3 functionals with three basis sets have smaller variations for these eight rotors, which are within 20% from the  $Q_{\text{HR}}^{\text{mean}}$ . The maximum percentage differences of the DFT results  $[(Q_{\text{HR}}^{\text{max}} - Q_{\text{HR}}^{\text{min}})/Q_{\text{HR}}^{\text{min}}]_{\text{max}}$  are collated in Table C.6, which shows the maximum variation of  $Q_{\text{HR}}(\text{DFT})$  is 12.6%, 87.1%, 123.5% and 77.3% for rotors formed by  $\dot{\text{C}}\text{H}_3$ ,  $\dot{\text{C}}_2\text{H}_3$ ,  $\dot{\text{C}}_2\text{H}_5$  and  $\text{CH}_3\dot{\text{O}}$  radical additions to  $\text{C}_2\text{H}_2/\text{C}_2\text{H}_4$ , respectively. This finding suggests that, for rotors formed by  $\dot{\text{C}}_2\text{H}_3/\dot{\text{C}}_2\text{H}_5/\text{CH}_3\dot{\text{O}}$  radical additions, the  $Q_{\text{HR}}$  calculated using the methods studied herein can vary from each other by up to a factor of two per rotor.

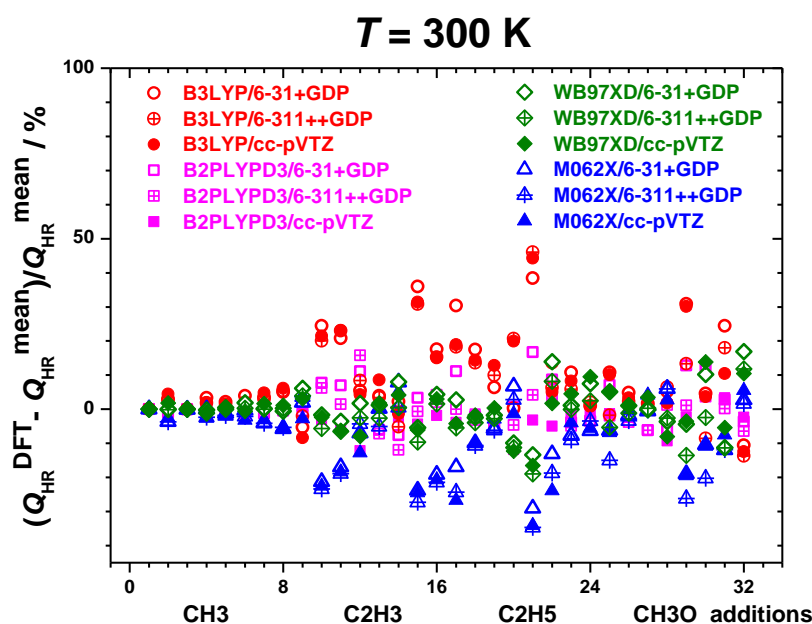


**Fig. 4.10** The percentage deviations between DFT and the corresponding mean energies for rotors formed by  $\dot{\text{C}}\text{H}_3/\dot{\text{C}}_2\text{H}_3/\dot{\text{C}}_2\text{H}_5/\text{CH}_3\dot{\text{O}}$  radical additions to  $\text{C}_2\text{H}_2/\text{C}_2\text{H}_4$  at 300 K.

### 3.4.2 $Q_{\text{HR}}$ comparisons between DFT and DLPNO-CCSD(T)/CBS

To validate the influences of different DFT methods used for  $V(\gamma)$  predictions, the percentage differences  $[(Q_{\text{HR}}^{\text{DFT}} - Q_{\text{HR}}^{\text{DLPNO}})/Q_{\text{HR}}^{\text{DLPNO}}]$  are calculated for rotors formed by  $\dot{\text{C}}\text{H}_3/\dot{\text{C}}_2\text{H}_3/\dot{\text{C}}_2\text{H}_5/\text{CH}_3\dot{\text{O}}$  radical additions to  $\text{C}_2\text{H}_2/\text{C}_2\text{H}_4$  and are plotted in Fig. 4.11 (Table C.8). The  $Q_{\text{HR}}$  predicted using the twelve DFT methods in comparison to  $Q_{\text{HR}}(\text{DLPNO-CCSD(T)/CBS})$  follow a similar trend to that shown for  $\Delta E_{\text{HR}}^{\text{max}}(\text{DLPNO} - \text{DFT})$ . In general, the  $Q_{\text{HR}}$  values calculated using the  $\omega\text{B97X-D/cc-pVTZ}$  method show the best agreement with the DLPNO-CCSD(T)/CBS results, which over-predicts  $Q_{\text{HR}}$  within a percentage difference of 12.6% over the temperature range 300–2000 K. The M06-2X/cc-pVTZ method under-predicts  $Q_{\text{HR}}$  within 13.2% of  $Q_{\text{HR}}(\text{DLPNO-CCSD(T)/CBS})$ . In addition, the  $\omega\text{B97X-D/6-31+G(d,p)}$ ,  $\omega\text{B97X-D/6-311++G(d,p)}$ , and B2PLYP-D3/cc-pVTZ methods all predict  $Q_{\text{HR}}$  values within 20% of  $Q_{\text{HR}}(\text{DLPNO-CCSD(T)/CBS})$ . It is worth noting that the largest ratio of 40.6% between DFT and DLPNO-CCSD(T)/CBS results is observed for  $\dot{\text{R}} + \text{C}_2$  alkenes/alkynes, which is expected to increase with an increase in the size of  $\dot{\text{R}}$  and alkenes/alkynes.

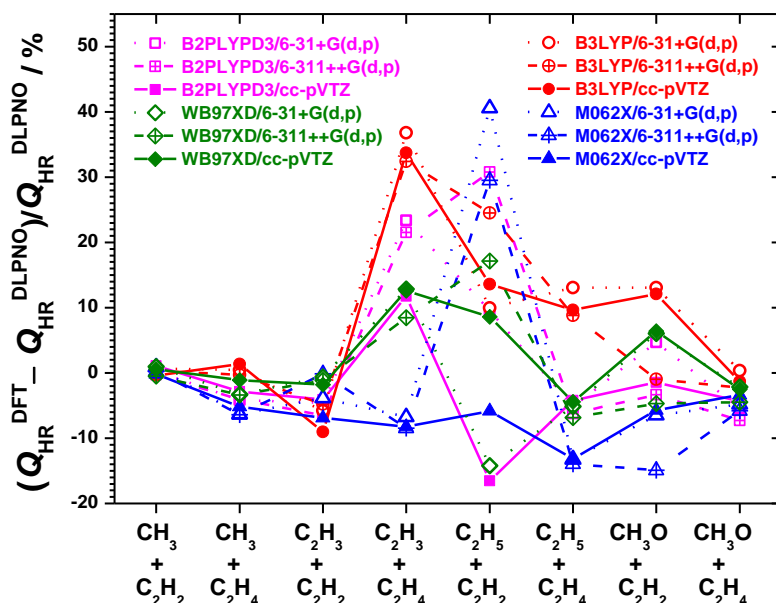


**Fig. 4.11** The maximum percentage differences of  $Q_{\text{HR}}$  ( $T = 300$  K) between DFT and DLPNO-CCSD(T)/CBS results, with the same  $B(\chi)$  used together with the  $V(\chi)$  calculated at DFT and DLPNO-CCSD(T)/CBS levels of theory separately, for rotors formed by  $\dot{\text{C}}\text{H}_3/\dot{\text{C}}_2\text{H}_3/\dot{\text{C}}_2\text{H}_5/\text{CH}_3\dot{\text{O}}$  radical additions to  $\text{C}_2\text{H}_2/\text{C}_2\text{H}_4$ .

#### 4. Conclusions

Four prevalent methods (B2PLYP-D3, B3LYP, M06-2X,  $\omega$ B97X-D) with three basis sets (6-31+G(d,p), 6-311++G(d,p), cc-pVTZ) are used for geometry optimizations, frequency calculations and relaxed scans for the newly formed internal rotors of the TSs. 32 addition reactions are studied, namely four free radical ( $\dot{\text{C}}\text{H}_3$ ,  $\dot{\text{C}}_2\text{H}_3$ ,  $\dot{\text{C}}_2\text{H}_5$ ,  $\text{CH}_3\dot{\text{O}}$ ) additions to  $\text{C}_2-\text{C}_3$  alkenes, alkynes and dienes. The influences of different electronic structure methods applied for hindered-rotor treatments on hindrance potential energy and partition function calculations are discussed. The DLPNO-CCSD(T)/CBS method is employed as the benchmark for hindrance potential energy calculations, for which the calculated energies agree within  $0.5 \text{ kJ mol}^{-1}$  of the gold-standard CCSD(T)/CBS results.

The DFT optimized geometries of the TSs, for rotors formed by  $\dot{\text{C}}\text{H}_3$ ,  $\dot{\text{C}}_2\text{H}_3$ ,  $\dot{\text{C}}_2\text{H}_5$ ,  $\text{CH}_3\dot{\text{O}}$  radical additions to  $\text{C}_2\text{H}_2$ , are compared with the CCSD(T)-F12/cc-pVDZ-F12 geometries. The maximum difference in bond lengths for the TSs is  $0.12 \text{ \AA}$ , and the dihedral deviations are within  $2.0^\circ$  excluding  $\dot{\text{C}}_2\text{H}_3 + \text{C}_2\text{H}_2$ . The  $\omega$ B97X-D and B2PLYP-D3 functionals are found to be more reliable and stable for geometry optimizations among the four DFT functionals.

The maximum deviations of the rotational constants  $\Delta B(\chi)_{\text{max}}$  calculated using twelve DFT methods for each rotor are calculated and the  $(B(\chi) \pm \Delta B(\chi)_{\text{max}})$  are used for  $Q_{\text{HR}}$  calculations. It is shown that the differences in  $B(\chi)$  calculations contribute approximately no more than 1.2%, 5.2%,

2.7% and 9.1% to the differences in  $Q_{\text{HR}}(\text{DFT})$ , for internal rotations formed by  $\dot{\text{C}}\text{H}_3$ ,  $\dot{\text{C}}_2\text{H}_3$ ,  $\dot{\text{C}}_2\text{H}_5$  and  $\text{CH}_3\dot{\text{O}}$  radical additions over the temperature range 300–2000 K.

Through a broad analysis of  $E_{\text{HR}}(\text{DFT})$  and  $Q_{\text{HR}}(\text{DFT})$ , in most cases, the B3LYP functional under-predicts energies, the M06-2X functional over-predicts energies, and the energies predicted by the other two functionals lie between the other two compared to the mean DFT values. The B3LYP functional consistently over-predicts  $Q_{\text{HR}}$  values, the M06-2X functional under-predicts  $Q_{\text{HR}}$  values, and the  $Q_{\text{HR}}$  values predicted by the other two functionals lie in-between the other two.

The  $V(\chi)$  values calculated using the DFT and the DLPNO-CCSD(T)/CBS methods are compared for rotors formed in the reactions  $\dot{\text{C}}\text{H}_3/\dot{\text{C}}_2\text{H}_3/\dot{\text{C}}_2\text{H}_5/\text{CH}_3\dot{\text{O}} + \text{C}_2\text{H}_2/\text{C}_2\text{H}_4$ . The  $\omega\text{B97X-D/cc-pVTZ}$  and the B2PLYP-D3/cc-pVTZ methods show good performances in predicting  $V(\chi)$  values among the twelve DFT methods, with the former having a lower computational cost. The maximum deviations in calculated  $\omega\text{B97X-D/cc-pVTZ}$  energies compared to DLPNO-CCSD(T)/CBS energies are  $1.7 \text{ kJ mol}^{-1}$ . The  $Q_{\text{HR}}$  calculated using DFT and DLPNO-CCSD(T)/CBS methods are also compared for these eight rotors, the  $\omega\text{B97X-D/cc-pVTZ}$  method shows the best performance in general with a maximum difference of 12.6% over the temperature range 300–2000 K.

Considering both the performances of the twelve DFT methods on geometry optimizations and the  $V(\chi)$  predictions, the  $\omega\text{B97X-D}$  and the B2PLYP-D3 functionals using the cc-pVTZ basis set are recommended for hindered rotor treatments of rotors formed by  $\dot{\text{C}}\text{H}_3/\dot{\text{C}}_2\text{H}_3/\dot{\text{C}}_2\text{H}_5/\text{CH}_3\dot{\text{O}}$  radical additions to alkenes/alkynes/dienes. Maximum deviations of  $3.1 \text{ kJ mol}^{-1}$  for  $V(\chi)$  and 40.6% for  $Q_{\text{HR}}$  between DFT and DLPNO-CCSD(T)/CBS results are discovered for rotors formed by  $\dot{\text{R}} + \text{C}_2$ . For rotors formed by  $\dot{\text{R}} + \text{alkenes/alkynes}$ , the variations of  $V(\chi)$  values calculated using different DFT methods are found to increase with the size of both the radical and alkenes/alkynes. Hence the deviations between DFT and DLPNO-CCSD(T)/CBS results for rotors formed by larger addition systems should be larger than the values presented herein.

Finally, the uncertainties in  $V(\chi)$  and  $Q_{\text{HR}}$  values presented in this study are on a per rotor basis. For molecules with more rotors, errors in  $V(\chi)$  and  $Q_{\text{HR}}$  values may grow as a function of the rotor number or in a more complex way, perhaps with error-cancellation involved. For example, the loss of internal rotors in TSs for cyclization reactions of alkenyl radicals (e.g. 1-hexen-1-yl), sets higher demands for the accuracy of hindered rotor treatments aiming for more accurate rate constants. The study is limited by the lack of a benchmark hindrance potential based on optimized geometries using a coupled cluster method due to the significantly high computational cost involved. A “real” benchmarking hindrance potential can be extremely useful to validate the performances of the DFT methods on optimization calculations, especially for rotors with qualitative and quantitative differences in their DFT hindrance potentials. For rotors formed through  $\dot{\text{C}}_2\text{H}_5/\text{CH}_3\dot{\text{O}}$  radical additions to alkenes which have coupled rotations, the  $V(\chi)$  and  $Q_{\text{HR}}$  value comparisons between a

multi-dimensional and 1-D hindered rotor treatment would be helpful for us to evaluate the accuracy of the DFT methods for systems with higher dimensionality.

### Supporting Information

Detailed structures of each TS (optimized at B2PLYP-D3/cc-pVTZ level of theory; Bond lengths and dihedrals of the rotors formed by  $\dot{\text{C}}\text{H}_3/\dot{\text{C}}_2\text{H}_3/\dot{\text{C}}_2\text{H}_5/\text{CH}_3\dot{\text{O}} + \text{C}_2\text{H}_2$  calculated using CCSD(T)-F12/cc-pVDZ-F12 method;  $T_1$  diagnostic values of the CCSD(T)/cc-pVQZ calculations for  $\dot{\text{C}}\text{H}_3/\dot{\text{C}}_2\text{H}_3/\dot{\text{C}}_2\text{H}_5/\text{CH}_3\dot{\text{O}} + \text{C}_2\text{H}_2/\text{C}_2\text{H}_4$ ; Maximum differences of  $E_{\text{HR}}$ , maximum differences of  $B(\chi)$ , and maximum percentage errors of  $Q_{\text{HR}}$  calculated using twelve DFT methods;  $E_{\text{HR}}$  and  $B(\chi)$  for newly formed rotors; Relative energy deviations between DFT and DLPNO-CCSD(T)/CBS, and percentage deviations between DFT and the corresponding mean energies for rotors formed by  $\dot{\text{C}}\text{H}_3/\dot{\text{C}}_2\text{H}_3/\dot{\text{C}}_2\text{H}_5/\text{CH}_3\dot{\text{O}} + \text{C}_2\text{H}_2/\text{C}_2\text{H}_4$ ; Maximum  $E_{\text{HR}}$ (DLPNO-CCSD(T)/CBS – DFT) deviations; Maximum deviations of  $Q_{\text{HR}}$ .

### Acknowledgements

Y. Sun and Q.-D. Wang would like to acknowledge financial funding by the China Scholarship Council (CSC). The authors want to acknowledge the financial support of Science Foundation Ireland under Grant No. 15/IA/3177. The Computational resources are provided by the Irish Centre for High-End Computing (ICHEC), under project number ngche063c, ngcom006c and ngche076c.

## References

- [1] A. Fernández-Ramos, J.A. Miller, S.J. Klippenstein, D.G. Truhlar, Modeling the kinetics of bimolecular reactions, *Chem. Rev.* 106 (2006) 4518-4584.
- [2] S. Sharma, S. Raman, W.H. Green, Intramolecular hydrogen migration in alkylperoxy and hydroperoxyalkylperoxy radicals: accurate treatment of hindered rotors, *The Journal of Physical Chemistry A* 114 (2010) 5689-5701.
- [3] J.A. Miller, J.P. Senosiain, S.J. Klippenstein, Y. Georgievskii, Reactions over multiple, interconnected potential wells: Unimolecular and bimolecular reactions on a C<sub>3</sub>H<sub>5</sub> potential, *J. Phys. Chem. A* 112 (2008) 9429-9438.
- [4] J.A. Miller, S.J. Klippenstein, Dissociation of propyl radicals and other reactions on a C<sub>3</sub>H<sub>7</sub> potential, *J. Phys. Chem. A* 117 (2013) 2718-2727.
- [5] Y. Li, S.J. Klippenstein, C.-W. Zhou, H.J. Curran, Theoretical Kinetics Analysis for H Atom Addition to 1, 3-Butadiene and Related Reactions on the C<sub>4</sub>H<sub>7</sub> Potential Energy Surface, *The Journal of Physical Chemistry A* 121 (2017) 7433-7445.
- [6] H. Wang, M. Frenklach, Calculations of rate coefficients for the chemically activated reactions of acetylene with vinylic and aromatic radicals, *The Journal of Physical Chemistry* 98 (1994) 11465-11489.
- [7] J. Orme, H. Curran, J. Simmie, Experimental and modeling study of methyl cyclohexane pyrolysis and oxidation, *J. Phys. Chem. A* 110 (2006) 114-131.
- [8] J. Power, K.P. Somers, C.-W. Zhou, S. Peukert, H.J. Curran, Theoretical, Experimental, and Modeling Study of the Reaction of Hydrogen Atoms with 1-and 2-Pentene, *J. Phys. Chem. A* 123 (2019) 8506-8526.
- [9] Y. Sun, C.-W. Zhou, K.P. Somers, H.J. Curran, An Ab Initio/Transition State Theory Study of the Reactions of C<sub>5</sub>H<sub>9</sub> Species of Relevance to 1, 3-Pentadiene, Part I: Potential Energy Surfaces, Thermochemistry and High-Pressure Limiting Rate Constants, *The Journal of Physical Chemistry A* 123 (2019), 9019-9052.
- [10] E.E. Greenwald, S.W. North, Y. Georgievskii, S.J. Klippenstein, A two transition state model for radical- molecule reactions: A case study of the addition of OH to C<sub>2</sub>H<sub>4</sub>, *J. Phys. Chem. A* 109 (2005) 6031-6044.
- [11] C.F. Goldsmith, W.H. Green, S.J. Klippenstein, Role of O<sub>2</sub>+ QOOH in low-temperature ignition of propane. 1. Temperature and pressure dependent rate coefficients, *J. Phys. Chem. A* 116 (2012) 3325-3346.
- [12] Chemcraft - graphical software for visualization of quantum chemistry computations. <https://www.chemcraftprog.com>.
- [13] Y. Li, C.-W. Zhou, K.P. Somers, K. Zhang, H.J. Curran, The oxidation of 2-butene: A high pressure ignition delay, kinetic modeling study and reactivity comparison with isobutene and 1-butene, *Proceedings of the Combustion Institute* 36 (2017) 403-411.
- [14] J. Power, K.P. Somers, S.S. Nagaraja, W. Wyreback, H.J. Curran, A Theoretical Study of the Reaction of Hydrogen atoms with three pentene isomers; 2-methyl-1-butene, 2-methyl-2-butene, and 3-methyl-1-butene., *The Journal of Physical Chemistry A* (2021), Submitted.
- [15] A.D. Becke, Density-functional thermochemistry. III. The role of exact exchange, *The Journal of Chemical Physics* 98 (1993) 5648-5652.
- [16] Y. Zhao, D.G. Truhlar, The M06 suite of density functionals for main group thermochemistry, thermochemical kinetics, noncovalent interactions, excited states, and transition elements: two new functionals and systematic testing of four M06-class functionals and 12 other functionals, *Theoretical Chemistry Accounts: Theory, Computation, and Modeling, Theoretica Chimica Acta* 120 (2008) 215-241.
- [17] J.-D. Chai, M. Head-Gordon, Long-range corrected hybrid density functionals with damped atom-atom dispersion corrections, *Physical Chemistry Chemical Physics* 10 (2008) 6615-6620.
- [18] S. Grimme, J. Antony, S. Ehrlich, H. Krieg, A consistent and accurate ab initio parametrization of density functional dispersion correction (DFT-D) for the 94 elements H-Pu, *The Journal of chemical physics* 132 (2010) 154104.

- [19] W.J. Hehre, W.A. Lathan, Self-Consistent Molecular Orbital Methods. XIV. An Extended Gaussian-Type Basis for Molecular Orbital Studies of Organic Molecules. Inclusion of Second Row Elements, *The Journal of Chemical Physics* 56 (1972) 5255-5257.
- [20] J.A. Kerr, M.J. Parsonage, Evaluated kinetic data on gas phase addition reactions: reactions of atoms and radicals with alkenes, alkynes and aromatic compounds, Butterworths London, 1972.
- [21] T.H. Dunning Jr, Gaussian basis sets for use in correlated molecular calculations. I. The atoms boron through neon and hydrogen, *The Journal of chemical physics* 90 (1989) 1007-1023.
- [22] R. Meyer, Trigonometric interpolation method for one-dimensional quantum-mechanical problems, *The Journal of Chemical Physics* 52 (1970) 2053-2059.
- [23] J.R. Barker, Multiple-Well, multiple-path unimolecular reaction systems. I. MultiWell computer program suite, *International Journal of Chemical Kinetics* 33 (2001) 232-245.
- [24] J. R. Barker, T. L. Nguyen, J. F. Stanton, C. Aieta, M. Ceotto, F. Gabas, T. J. D. Kumar, C. G. L. Li, L. L. Lohr, A. Maranzana, N. F. Ortiz, J. M. Preses, J. M. Simmie, J. A. Sonk, and P. J. Stimac, MultiWell-2017 Software Suite, University of Michigan: Ann Arbor, Michigan, USA, 2017.
- [25] K.P. Somers, On the pyrolysis and combustion of furans: quantum chemical, statistical rate theory, and chemical kinetic modelling studies, PhD, National University of Ireland, Galway, 2014.
- [26] B.A. Ellingson, V.A. Lynch, S.L. Mielke, D.G. Truhlar, Statistical thermodynamics of bond torsional modes: Tests of separable, almost-separable, and improved Pitzer–Gwinn approximations, *The Journal of chemical physics* 125 (2006) 084305.
- [27] A.L. East, L. Radom, Ab initio statistical thermodynamical models for the computation of third-law entropies, *The Journal of chemical physics* 106 (1997) 6655-6674.
- [28] J. Pfaendtner, X. Yu, L.J. Broadbelt, The 1-D hindered rotor approximation, *Theoretical Chemistry Accounts* 118 (2007) 881.
- [29] I. Alecu, D.G. Truhlar, Computational study of the reactions of methanol with the hydroperoxyl and methyl radicals. 1. Accurate thermochemistry and barrier heights, *J. Phys. Chem. A* 115 (2011) 2811-2829.
- [30] S.R. Miller, N.E. Schultz, D.G. Truhlar, D.G. Leopold, A study of the ground and excited states of Al 3 and Al 3<sup>-</sup>. II. Computational analysis of the 488 nm anion photoelectron spectrum and a reconsideration of the Al 3 bond dissociation energy, *The Journal of chemical physics* 130 (2009) 024304.
- [31] N. Lambert, N. Kaltsoyannis, S.D. Price, J. Žabka, Z. Herman, Bond-Forming Reactions of Dications with Molecules: A Computational and Experimental Study of the Mechanisms for the Formation of HCF<sup>2+</sup> from CF<sub>3</sub><sup>2+</sup> and H<sub>2</sub>, *J. Phys. Chem. A* 110 (2006) 2898-2905.
- [32] P. Jurečka, J. Šponer, J. Černý, P. Hobza, Benchmark database of accurate (MP2 and CCSD (T) complete basis set limit) interaction energies of small model complexes, DNA base pairs, and amino acid pairs, *Physical Chemistry Chemical Physics* 8 (2006) 1985-1993.
- [33] P.R. Spackman, D. Jayatilaka, A. Karton, Basis set convergence of CCSD (T) equilibrium geometries using a large and diverse set of molecular structures, *The Journal of chemical physics* 145 (2016) 104101.
- [34] T.B. Adler, G. Knizia, H.-J. Werner, A simple and efficient CCSD (T)-F12 approximation, *AIP*, 2007.
- [35] K.A. Peterson, T.B. Adler, H.-J. Werner, Systematically convergent basis sets for explicitly correlated wavefunctions: The atoms H, He, B–Ne, and Al–Ar, *The Journal of chemical physics* 128 (2008) 084102.
- [36] F.A. Bischoff, S. Wolfsegger, D.P. Tew, W. Klopper, Assessment of basis sets for F12 explicitly-correlated molecular electronic-structure methods, *Molecular Physics* 107 (2009) 963-975.
- [37] C. Riplinger, F. Neese, An efficient and near linear scaling pair natural orbital based local coupled cluster method, *The Journal of chemical physics* 138 (2013) 034106.
- [38] M.J. Frisch, G.W. Trucks, H.B. Schlegel, G.E. Scuseria, M.A. Robb, J.R. Cheeseman, G. Scalmani, V. Barone, G.A. Petersson, H. Nakatsuji, X. Li, M. Caricato, A.V. Marenich, J. Bloino, B.G. Janesko, R. Gomperts, B. Mennucci, H.P. Hratchian, J.V. Ortiz, A.F. Izmaylov, J.L. Sonnenberg, Williams, F. Ding, F. Lipparini, F. Egidi, J. Goings, B. Peng, A. Petrone, T. Henderson, D.

Ranasinghe, V.G. Zakrzewski, J. Gao, N. Rega, G. Zheng, W. Liang, M. Hada, M. Ehara, K. Toyota, R. Fukuda, J. Hasegawa, M. Ishida, T. Nakajima, Y. Honda, O. Kitao, H. Nakai, T. Vreven, K. Throssell, J.A. Montgomery Jr., J.E. Peralta, F. Ogliaro, M.J. Bearpark, J.J. Heyd, E.N. Brothers, K.N. Kudin, V.N. Staroverov, T.A. Keith, R. Kobayashi, J. Normand, K. Raghavachari, A.P. Rendell, J.C. Burant, S.S. Iyengar, J. Tomasi, M. Cossi, J.M. Millam, M. Klene, C. Adamo, R. Cammi, J.W. Ochterski, R.L. Martin, K. Morokuma, O. Farkas, J.B. Foresman, D.J. Fox, Gaussian 16 Rev. C.01, Wallingford, CT, 2016.

[39] F. Neese, Software update: the ORCA program system, version 4.0, Wiley Interdisciplinary Reviews: Computational Molecular Science 8 (2018) e1327.

[40] M. Koerstz, J. Elm, K.V. Mikkelsen, Benchmark Study of the Structural and Thermochemical Properties of a Dihydroazulene/Vinylheptafulvene Photoswitch, The Journal of Physical Chemistry A 121 (2017) 3148-3154.

[41] D.G. Liakos, Y. Guo, F. Neese, Comprehensive Benchmark Results for the Domain Based Local Pair Natural Orbital Coupled Cluster Method (DLPNO-CCSD (T)) for Closed-and Open-Shell Systems, The Journal of Physical Chemistry A 124 (2019) 90-100.

[42] D.G. Liakos, F. Neese, Is it possible to obtain coupled cluster quality energies at near density functional theory cost? Domain-based local pair natural orbital coupled cluster vs modern density functional theory, Journal of chemical theory and computation 11 (2015) 4054-4063.

[43] R.H. Ditchfield, W.J. Hehre, J.A. Pople, Self-consistent molecular-orbital methods. IX. An extended Gaussian-type basis for molecular-orbital studies of organic molecules, The Journal of Chemical Physics 54 (1971) 724-728.

## Chapter 5

# Comparative chemical kinetic analysis and skeletal mechanism generation for syngas combustion with NO<sub>x</sub> chemistry

Published in: Energy and Fuels 34(1) (2020) 949–964.

DOI: <https://doi.org/10.1021/acs.energyfuels.9b03440>

### Authors and Contributions

(1) Quan-De Wang

China University of Mining and Technology

Contribution: Most of the ab initio calculations and modelling simulations, and manuscript preparation.

(2) Yanjin Sun

National University of Ireland, Galway

Contribution: Part of the ab initio calculations and modelling simulations, and manuscript review.

(3) Henry J. Curran

National University of Ireland, Galway

Contribution: Project Management and manuscript review.

## Abstract

Emission of nitrogen oxides ( $\text{NO}_x$ ) is one of the major environmental concerns arising from the combustion of syngas. Strategies to reduce emission and improve the efficiency of syngas combustion can be developed using computational fluid dynamic simulations to design cleaner and more efficient combustors. Toward this end, an accurate and efficient chemical kinetic mechanism that can describe the combustion chemistry of syngas with  $\text{NO}_x$  under engine-relevant conditions is critical. In this work, a comprehensive survey of detailed mechanisms available in the literature for syngas/ $\text{NO}_x$  combustion reaction system is first conducted. A systematic and comparative chemical kinetic analysis of five detailed mechanisms is performed based on reaction pathway and sensitivity analyses to identify the key reactions of the nitrogen species for a wide range of mixtures including the formation of  $\text{NO}_x$  during syngas combustion, ignition of  $\text{NH}_3$ ,  $\text{H}_2/\text{N}_2\text{O}$ , and  $\text{H}_2/\text{NO}_2$  mixtures. Comparisons of the reaction pathways from different detailed mechanisms indicate that the detailed chemistry is controlled by a small set of reactions and species. Recent high-level theoretical studies on HONO and  $\text{HNO}_2$  chemistry including previously neglected important reactions are updated. The rate constants for  $\text{HNO} + \text{O}_2 = \text{NO} + \text{HO}_2$  are calculated using *ab initio* calculations in this work. An efficient high-fidelity skeletal mechanism consisting of 27 species and 130 reactions is developed based on a combination of the directed relation graph with error propagation (DRGEP) method and the simplified iterative screening and structure analysis (ISSA) method. Compared to the detailed mechanisms, the skeletal mechanism retains the major species and reactions for the syngas/ $\text{NO}_x$  system and is validated against typical experimental data resulting in a very good performance.

## 1. Introduction

Combustion has been the major process of power generation and will continue to dominate into the future. As the world's energy demands and environmental concerns continue to increase, novel ideas and innovations in the areas of fuels and combustors to reduce emission and improve efficiency are needed to achieve cleaner and more efficient combustion. Syngas, composed of varying amounts of hydrogen ( $\text{H}_2$ ) and carbon monoxide ( $\text{CO}$ ), is expected to be a potential alternative fuel for energy generation because it can be

largely derived from biomass/coal gasification and can significantly improve combustion efficiency in stationary gas turbines via Integrated Gasification Combined Cycle (IGCC) systems [1-3]. Compared to conventional fuels such as coal for power generation, one of the major advantages for syngas is the lack of particle matter (PM) emissions and corrosive ash elements. However, due to increasingly stringent emission regulations, the emission of nitrogen oxides ( $\text{NO}_x$ ) as the major drawback has become a major challenge for syngas combustion. As available computational power continues to grow, computational fluid dynamic (CFD) simulations have become an important tool in the design of advanced combustion systems with low- $\text{NO}_x$  emissions and improved efficiency. It is now generally recognized that these CFD simulations must necessarily incorporate realistic descriptions of the chemical kinetics of fuel combustion and  $\text{NO}_x$  formation [4, 5]. Hence, a large body of work has been dedicated to improve the chemistry of syngas and nitrogen chemistry in combustion.

The development of detailed chemical kinetic mechanisms for syngas is essential to understand not only the combustion properties of  $\text{H}_2$  and  $\text{CO}$  themselves, but also the larger hierarchical hydrocarbon systems which rely on this core chemistry. A large number of detailed reaction mechanisms for syngas combustion with a focus on hydrogen combustion have been developed and continue to be updated, see e.g., Ó Conaire et al. [6], Konnov [7, 8], Hong et al. [9], and Kéromnès et al. [10] These detailed reaction mechanisms were mainly validated through selected experimental targets and were not extensively validated at high pressures and temperatures relevant to practical combustor conditions. The detailed mechanism developed by Kéromnès et al. [10] for syngas combustion was validated against the most extensive experimental targets for  $\text{H}_2$  and syngas. According to a systematic comparison of error function values in the prediction of  $\text{H}_2$  combustion by Varga et al. [11], the Kéromnès mechanism exhibits the best performance covering a wide range of experimental targets compared with 13 published mechanisms, and thus is selected as the base mechanism for syngas in this work.

The nitrogen chemistry in combustion has been extensively studied after Miller and Bowman [12] published their review thirty years ago. Detailed chemical kinetic mechanisms to describe the  $\text{NO}_x$  formation process during combustion of hydrocarbon and oxygenated

fuels with focus on small  $H_2/C_1-C_2$  hydrocarbons have been proposed by different research groups [13-18]. A most recent study by Glarborg et al. [19] comprehensively revisited this topic and they also proposed a detailed reaction mechanism with updated thermochemistry and reaction rate constants from recent advances in experiments and high-level theoretical calculations. Generally, reaction mechanisms for syngas combustion with  $NO_x$  chemistry are usually defined as sub-mechanisms in these detailed chemical kinetic models except some proposed mechanisms specifically for  $NO_x$  formation during syngas combustion. For example, Zhang et al. [20] recently developed a detailed mechanism to describe the pyrolysis and oxidation of the  $H_2/NO_x$  and syngas/ $NO_x$  systems by using the K romn s mechanism [10] for syngas. These detailed kinetic mechanisms developed by different research groups exhibit different performances in predicting combustion properties.

The underlying reason for the different predictabilities of combustion properties using different detailed mechanisms is caused by the different species and reaction paths embodied in them, including their corresponding thermochemistry and reaction rates. Hence, not only evaluating the comparative mechanism performances, but also carrying out detailed comparisons of the reaction lists, reaction rates and thermochemistry of different mechanisms is helpful in refining them. Sirumalla et al. [21] performed comparisons of detailed kinetic mechanisms using butanol isomers as an example and revealed significant discrepancies in the thermochemistry of many species and rates of many reactions. However, such comparisons require large computational resources since detailed combustion mechanisms of complicated fuels can contain thousands of species and reactions. Furthermore, the large size of a detailed mechanism may also limit its application in CFD simulations for engine design due to the tremendous computational resources needed. Therefore, decreasing the size of a detailed mechanism is necessary to incorporate realistic combustion chemistry with CFD simulations. Thus, mechanism reduction has been extensively studied in the past three decades. Although a series of reduced mechanisms for  $H_2$  and syngas were developed [22-24], very few reduced mechanisms have been developed for syngas combustion including  $NO_x$  chemistry. In addition, the discrepancies among detailed mechanisms developed by different authors need to be clarified.

Based on the above considerations, this work aims to develop an efficient high-fidelity

skeletal mechanism that is able to describe the combustion chemistry of syngas with NO<sub>x</sub> chemistry under practical combustor conditions. To achieve this, a systematic and comparative chemical kinetic analysis of five detailed mechanisms for the syngas/NO<sub>x</sub> system has been performed by comparing reaction pathway analyses and the associated rate constants of key reactions. An updated detailed mechanism is proposed with updated kinetics from recent high-level theoretical studies [25-27]. Finally, a skeletal mechanism consisting of 27 species and 130 reactions has been developed based on a combination of the DRGEP and ISSA methods.

This paper is organized as follows. The methodology used in this work is outlined in Section 2, including an overview of detailed mechanism for syngas combustion with NO<sub>x</sub> chemistry and a concise explanation of the mechanism reduction and analysis methods. Section 3 describes the comprehensive comparisons of different detailed mechanisms and the skeletal mechanism reduction results. The performance and applicability of the skeletal mechanisms are further investigated for a broad range of conditions relevant to engine simulations. Section 4 lists our conclusions.

## **2. Methods**

### **2.1 Mechanism overview and development**

A series of detailed mechanisms describing syngas/NO<sub>x</sub> oxidation have been developed. However, most of them have been developed based on loose combinations of different parts from a small number of systematically developed mechanisms and validated for their target experiments. Thus, in the present work, we do not intend to provide a comprehensive model performance of all of these mechanisms. Instead, this work aims to clarify the chemical kinetics of NO<sub>x</sub> chemistry during syngas combustion and develop an efficient skeletal mechanism describing syngas/NO<sub>x</sub> combustion. The detailed mechanism developed by Zhang et al. [20] has been selected as the initial mechanism because this sub-mechanism provides the best performance and the detailed mechanism was validated against a large number of experimental data over a wide range of combustion conditions. Major reaction pathways, species and reactions related to NO<sub>x</sub> sub-mechanism are compared with GRI-Mech 3.0 [28] and three other detailed mechanisms developed by Konnov [13], Glarborg et al. [19], and

Mathieu et al. [14] These selected mechanisms represent state-of-the-art kinetic mechanisms for NO<sub>x</sub> chemistry in combustion, based on a systematic evaluation of the knowledge of thermochemistry and reaction rates from theoretical/experimental works.

## 2.2 Mechanism analysis method

To perform comparative chemical kinetic analyses and determine the reaction paths of the skeletal mechanism for the studied syngas/NO<sub>x</sub> system, an elemental flux analysis for N is performed. Details of the analytical method can be found in references [29, 30]. In addition, brute-force sensitivity analysis is employed to identify the dominant ignition chemistry. Based on these systematic analyses, key reactions and species affecting model performances are identified and discussed in detail.

## 2.3 Skeletal mechanism generation

Mechanism reduction methods have been extensively studied and applied to a wide range of combustion reaction systems [5]. Skeletal reduction, aiming to remove unimportant species and reactions for the target system, is the basis for further mechanism optimization or time-scale reduction. To obtain a minimal skeletal mechanism, skeletal reduction methods are combined together, starting by removing unimportant species, followed by removing unimportant reactions because one species generally corresponds to five reactions and the computational cost of simulations typically scales quadratically with the number of species and linearly with the number of reactions [5]. A variety of methodologies have been developed for this purpose. In this work, an integrated method that combines the DRGEP [31] and ISSA methods [32-34] has been employed. The DRGEP method is selected as the first step as this method has proven to be more efficient compared to other DRG-based methods [35]. The ISSA method is then used to remove unimportant species and reactions simultaneously as it is efficient in capturing the major reaction pathways in the mechanism reduction process compared to other pure mathematical methods.

To achieve a comprehensive high-fidelity skeletal mechanism for the syngas/NO<sub>x</sub> combustion system, skeletal reduction is performed over a wide range of conditions. Specifically, the DRGEP and ISSA methods are successively applied to reaction state points

densely sampled from constant volume ignition simulations over a wide range of simulation conditions within the parameter range of pressures from 1 to 30 atm and equivalence ratios from 0.5 – 2.0 at initial temperatures in the range 800–1700 K for H<sub>2</sub>/CO/O<sub>2</sub>/N<sub>2</sub>, H<sub>2</sub>/NO<sub>2</sub>/O<sub>2</sub>/Ar, H<sub>2</sub>/N<sub>2</sub>O/O<sub>2</sub>/Ar, H<sub>2</sub>/NO/O<sub>2</sub>/Ar and NH<sub>3</sub>/O<sub>2</sub>/N<sub>2</sub> mixtures. Reaction states solely sampled from ignition simulations for mechanism reduction have been confirmed to be efficient in generating skeletal mechanisms, which can also exhibit good performance in predicting other combustion properties including laminar flame speed, species concentration profiles, etc.[5, 34, 35]. The species H<sub>2</sub>, CO, N<sub>2</sub>O, NO<sub>2</sub>, NO, NH<sub>3</sub> together with H atom are selected as targeted species during the reduction processes.

### 3. Results and discussions

#### 3.1 Preliminary mechanism analysis

Table 5.1 lists the species related to the syngas/NO<sub>x</sub> combustion reaction system considered in the six selected detailed mechanisms and the species retained in the derived final skeletal mechanism. In fact, in developing detailed mechanisms, species and reactions are interdependent and mutual. The sub-mechanism for syngas in the detailed mechanism developed by Mathieu et al. [14] were based on Metcalfe et al. [36] and Kéromnès et al. [10], and the NO<sub>x</sub> section was largely based on the work of Dagaut et al. [18], which mainly focused on the formation and oxidation of hydrogen cyanide (HCN). This sub-mechanism was also updated in the Glarborg mechanism [19]. Hence, the detailed mechanism of Dagaut et al. [18] is not discussed in detail. GRI-Mech 3.0 [28] was published about twenty years ago representing the advanced level at that time and has been the industrial standard for the last two decades. The mechanism developed by Konnov was mainly focused on NCN pathway of prompt-NO formation. From Table 5.1, the Zhang mechanism contains the most comprehensive nitrogen related species for syngas combustion except for the HNNO species, which only exists in Konnov mechanism. The HNNO species is an energetic adduct for the reaction of  $\dot{H}$  atom with N<sub>2</sub>O. At low temperatures, the addition reaction to the formation of cis- and trans-HNNO isomers can be dominant due to addition-stabilization process [37, 38]. However, the bimolecular channels of the reaction for  $\dot{H} + N_2O$  leading to the formation of N<sub>2</sub> +  $\dot{O}H$ , NH +  $\dot{N}O$ , NNH +  $\ddot{O}$  become dominant at high temperatures, with N<sub>2</sub> +  $\dot{O}H$  being

the most important [39]. The HNNO species and its related reactions were added to Zhang mechanism to test its importance in syngas/NO<sub>x</sub> reaction system at combustion relevant conditions and nearly no influence is observed in the comparison. Table 5.2 compares the thermodynamic properties of selected important N-containing species, and it can be seen that the differences of the thermodynamic properties in the selected detailed mechanisms are very small. The transport properties of the nitrogen related species in Table 5.1, mostly based on GRI-Mech 3.0, agree well with each other among the mechanisms, and thus model performances should be mainly controlled by the chemical kinetics.

**Table 5.1** Species related to the syngas/NO<sub>x</sub> combustion reaction system in the selected detailed mechanisms and the derived skeletal mechanism.

	Zhang et al.[20]	Skeletal mechanism (this work)	Glarborg et al.[19]	Konnov[13]	GRI-Mech 3.0[28]	Dagaut et al.[18]	Mathieu et al.[14]
Shared species			N NH NH <sub>2</sub> NH <sub>3</sub> NNH	NO	NO <sub>2</sub> N <sub>2</sub> O HNO		
	N <sub>2</sub> H <sub>2</sub>	N <sub>2</sub> H <sub>2</sub>	N <sub>2</sub> H <sub>2</sub>	N <sub>2</sub> H <sub>2</sub>			
	N <sub>2</sub> H <sub>3</sub>		N <sub>2</sub> H <sub>3</sub>	N <sub>2</sub> H <sub>3</sub>			
	N <sub>2</sub> H <sub>4</sub>		N <sub>2</sub> H <sub>4</sub>	N <sub>2</sub> H <sub>4</sub>			
	HONO	HONO	HONO	HONO		HONO	HONO
	HNOH		HNOH	HNOH		HNOH	HNOH
	H <sub>2</sub> NO	H <sub>2</sub> NO	H <sub>2</sub> NO	H <sub>2</sub> NO		H <sub>2</sub> NO	H <sub>2</sub> NO
	NO <sub>3</sub>		NO <sub>3</sub>	NO <sub>3</sub>		NO <sub>3</sub>	NO <sub>3</sub>
Individual species	HNO <sub>2</sub>	HNO <sub>2</sub>	HNO <sub>2</sub>			HNO <sub>2</sub>	HNO <sub>2</sub>
	HONO <sub>2</sub>		HONO <sub>2</sub>			HONO <sub>2</sub>	HONO <sub>2</sub>
	HNO <sub>3</sub>			HNO <sub>3</sub>			
	H <sub>2</sub> NN		H <sub>2</sub> NN				
	HON	HON	HON			HON	HON
	NH <sub>2</sub> OH		NH <sub>2</sub> OH	NH <sub>2</sub> OH			
	N <sub>2</sub> O <sub>4</sub>			N <sub>2</sub> O <sub>4</sub>			N <sub>2</sub> O <sub>4</sub>
	N <sub>2</sub> O <sub>3</sub>			N <sub>2</sub> O <sub>3</sub>			N <sub>2</sub> O <sub>3</sub>
				HNNO			

**Table 5.2** Thermodynamic properties of selected important N-containing species in the reaction mechanisms. Units are kcal mol<sup>-1</sup> for  $\Delta_f H_{298}^0$ , and cal mol<sup>-1</sup> K<sup>-1</sup> for S and  $C_p$ . Temperatures are in K.

Species	Mechanism	$\Delta_f H_{298}^0$	$S_{298}^0$	$C_{p, 300\text{ K}}$	$C_{p, 400}$	$C_{p, 500}$	$C_{p, 600}$	$C_{p, 800}$	$C_{p, 1000}$	$C_{p, 1500}$
<b>NH<sub>3</sub></b>	GRI 3.0	-10.97	46.07	8.58	9.30	10.10	10.90	12.32	13.60	15.98
	Konnov	-10.98	46.07	8.58	9.28	10.10	10.90	12.30	13.54	15.84
	Glarborg	-10.89	46.07	8.53	9.24	10.04	10.81	12.22	13.44	15.76
	Zhang	-10.43	45.99	8.52	9.24	10.00	10.80	12.40	13.90	16.46
<b>NH<sub>2</sub></b>	GRI 3.0	45.90	46.60	8.14	8.36	8.66	9.00	9.74	10.48	11.94
	Konnov	45.20	46.60	8.14	8.36	8.66	8.98	9.70	10.44	11.88
	Glarborg	44.46	46.57	8.05	8.24	8.51	8.81	9.50	10.19	11.64
	Zhang	44.58	46.51	8.08	8.28	8.54	8.86	9.56	10.26	11.68
<b>NH</b>	GRI 3.0	85.30	43.31	7.02	7.02	7.04	7.10	7.28	7.52	8.12
	Konnov	85.33	43.31	7.02	7.02	7.04	7.10	7.28	7.52	8.12
	Glarborg	85.75	43.32	6.97	6.97	6.99	7.04	7.22	7.47	8.07
	Zhang	85.11	43.26	7.00	7.00	7.02	7.06	7.24	7.48	8.02
<b><math>\dot{\text{N}}\text{O}</math></b>	GRI 3.0	21.81	50.37	7.18	7.20	7.34	7.52	7.84	8.18	8.60
	Konnov	21.81	50.37	7.18	7.20	7.34	7.52	7.84	8.18	8.60
	Glarborg	21.78	50.37	7.14	7.16	7.29	7.47	7.83	8.12	8.55
	Zhang	21.65	50.32	7.16	7.18	7.30	7.46	7.82	8.10	8.54
<b>N<sub>2</sub>O</b>	GRI 3.0	19.50	52.58	9.32	10.28	11.04	11.66	12.62	13.28	14.20
	Konnov	19.50	52.58	9.32	10.28	11.04	11.66	12.62	13.28	14.20
	Glarborg	19.73	52.58	9.25	10.21	10.96	11.59	12.54	13.20	14.15
	Zhang	19.74	52.45	9.20	10.12	10.88	11.50	12.42	13.04	13.90
<b>NO<sub>2</sub></b>	GRI 3.0	8.17	57.40	8.96	9.74	10.50	11.16	12.12	12.76	13.52
	Konnov	8.17	57.40	8.96	9.74	10.50	11.16	12.12	12.76	13.52
	Glarborg	8.14	57.40	8.90	9.68	10.44	11.09	12.05	12.67	13.49
	Zhang	7.14	57.31	8.90	9.68	10.40	11.04	12.00	12.58	13.36
<b>HNO</b>	GRI 3.0	25.40	52.80	8.16	8.54	9.04	9.60	10.64	11.50	13.30
	Konnov	25.60	52.80	8.16	8.54	9.04	9.60	10.64	11.48	13.36
	Glarborg	25.56	52.79	8.09	8.45	8.96	9.51	10.52	11.36	13.17
	Zhang	25.82	52.71	8.12	8.48	8.96	9.52	10.56	11.40	12.82
<b>NNH</b>	GRI 3.0	59.63	53.65	8.34	8.86	9.44	9.98	10.86	11.56	12.56
	Konnov	59.63	53.65	8.34	8.86	9.44	9.98	10.86	11.56	12.56
	Glarborg	59.70	53.65	8.22	8.62	9.11	9.61	10.52	11.26	12.36
	Zhang	60.28	53.59	8.32	8.78	9.32	9.88	10.92	11.72	13.08

### 3.2 Comparative reaction path analysis

To achieve a comprehensive understanding of the chemical kinetics of the syngas/ $\text{NO}_x$  reaction system, a systematic reaction path analysis is performed for a wide range of mixtures including the formation of  $\text{NO}_x$  during syngas combustion,  $\text{NH}_3/\text{O}_2/\text{N}_2$ ,  $\text{H}_2/\text{N}_2\text{O}/\text{O}_2/\text{Ar}$ , and  $\text{H}_2/\text{NO}_2/\text{O}_2/\text{Ar}$  mixtures. The reaction pathways of the formation of  $\text{NO}$  species for ignition delay time (IDT) simulations of a 50/50  $\text{H}_2/\text{CO}$  syngas mixture in air is analyzed using the five detailed mechanisms.

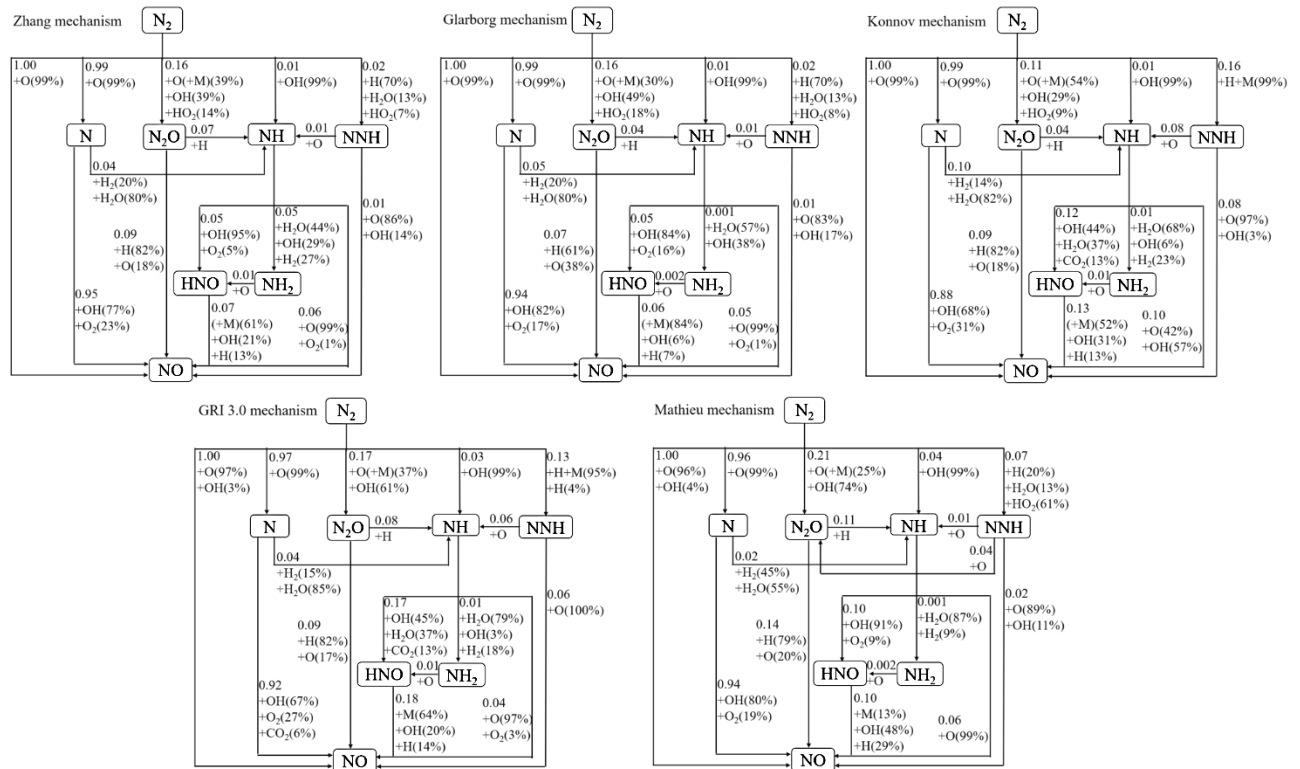


**Fig. 5.1** Element flux analysis of N during ignition delay time simulation of syngas/air mixture at initial temperature of 1200 K with equivalence ratio ( $\phi$ ) of 1.0 and pressure of 20 atm.

Fig. 5.1 shows the N element flux analysis at 20%  $\text{H}_2$  consumption. The reaction pathways demonstrate the thermal formation of  $\dot{\text{N}}\text{O}$  during syngas combustion. All five mechanisms reveal that the thermal formation of  $\dot{\text{N}}\text{O}$  is mainly initiated by the reaction of  $\text{N}_2$  with oxygen atom:  $\text{N}_2 + \ddot{\text{O}} = \dot{\text{N}}\text{O} + \text{N}$ , and the N radical subsequently reacts with  $\text{O}_2$  and  $\dot{\text{O}}\text{H}$  to form  $\dot{\text{N}}\text{O}$ . However, the other reaction pathways leading to the formation of  $\dot{\text{N}}\text{O}$  from  $\text{N}_2$  exhibit large deviations in different mechanisms. The results based on the Zhang and

Glarborg mechanisms show very similar reaction pathways because they mainly use the same reaction rate constants for the key reactions. The Konnov mechanism and GRI-Mech 3.0 predict that the NNH pathway is competitive with the N<sub>2</sub>O pathway. At low temperature conditions, the pathway through NNH and N<sub>2</sub>O become important.

The ignition delay time of H<sub>2</sub>/O<sub>2</sub>/Ar and H<sub>2</sub>/O<sub>2</sub>/Ar mixtures with NO<sub>2</sub> and N<sub>2</sub>O as additives [40, 41] are used to benchmark these detailed mechanisms. The major reaction path for N<sub>2</sub>O during the ignition of the H<sub>2</sub>/N<sub>2</sub>O/O<sub>2</sub>/Ar mixture is simple and N<sub>2</sub>O mainly converts into N<sub>2</sub>. The reaction of N<sub>2</sub>O +  $\dot{\text{H}}$  producing N<sub>2</sub> +  $\dot{\text{O}}\text{H}$  completely controls the transformation with the exception of N<sub>2</sub>O + H<sub>2</sub> = N<sub>2</sub> + H<sub>2</sub>O which only presents in Zhang's mechanism and also contributes to the transformation of N<sub>2</sub>O into N<sub>2</sub>, especially at low temperatures (< 1200 K). Fig. 5.1 shows that at 20% H<sub>2</sub> consumption with an initial temperature of 1200 K, the contributions of these two reactions of N<sub>2</sub>O with  $\dot{\text{H}}$  and H<sub>2</sub> are 1% and 99%, respectively, while the contributions of the reaction of N<sub>2</sub>O with H<sub>2</sub> decreases to 6% at 1200 K. The rate constant for this reaction has a large uncertainty. Mulvihill et al. [42] recently recommended a new rate constant for this reaction based on shock tube studies of IDTs and H<sub>2</sub>O time histories, which is three times lower than the rate constant used in Zhang's mechanism. For H<sub>2</sub>/NO<sub>2</sub>/O<sub>2</sub>/Ar mixtures, the reaction NO<sub>2</sub> +  $\dot{\text{H}}$  =  $\dot{\text{N}}\text{O}$  +  $\dot{\text{O}}\text{H}$  is completely dominant. Other species including HONO, HNO<sub>2</sub>, and HNO also participate in the flux, but their relative percentages are minor.

Syngas from gasification or de-volatilization of solid fuels may also include ammonia (NH<sub>3</sub>), which is the key volatile-N species in combustion. Although a number of modeling and experimental studies on NH<sub>3</sub> oxidation chemistry have been reported [19, 43], the development of reliable detailed mechanisms for NH<sub>3</sub> oxidation remains challenging. Fig. 5.2 shows the element flux analysis results for IDT simulations of NH<sub>3</sub>/air mixture at an initial temperature of 1500 K for an equivalence ratio of 1.0 at a pressure of 20 atm. No ignition is predicted at temperatures below 1500 K using GRI-Mech 3.0. The Zhang mechanism and Glarborg mechanism exhibit very similar reaction pathways, while the Konnov and Mathieu mechanisms show very different analysis results. All of the mechanisms reveal that the initial reaction pathway for NH<sub>3</sub> oxidation is the formation of NH<sub>2</sub> through H-atom abstraction reactions by  $\dot{\text{O}}\text{H}$  radicals, and  $\dot{\text{H}}$  and  $\ddot{\text{O}}$  atoms, but the relative

contributions from these reactions are different due to differing reaction rate constants. It is shown that the most important reaction path of  $\text{NH}_2$  is through the reactions with  $\text{NH}_2$  and  $\text{NH}$  forming  $\text{N}_2\text{H}_2$ , which are not considered in the Mathieu mechanism and in GRI-Mech 3.0.

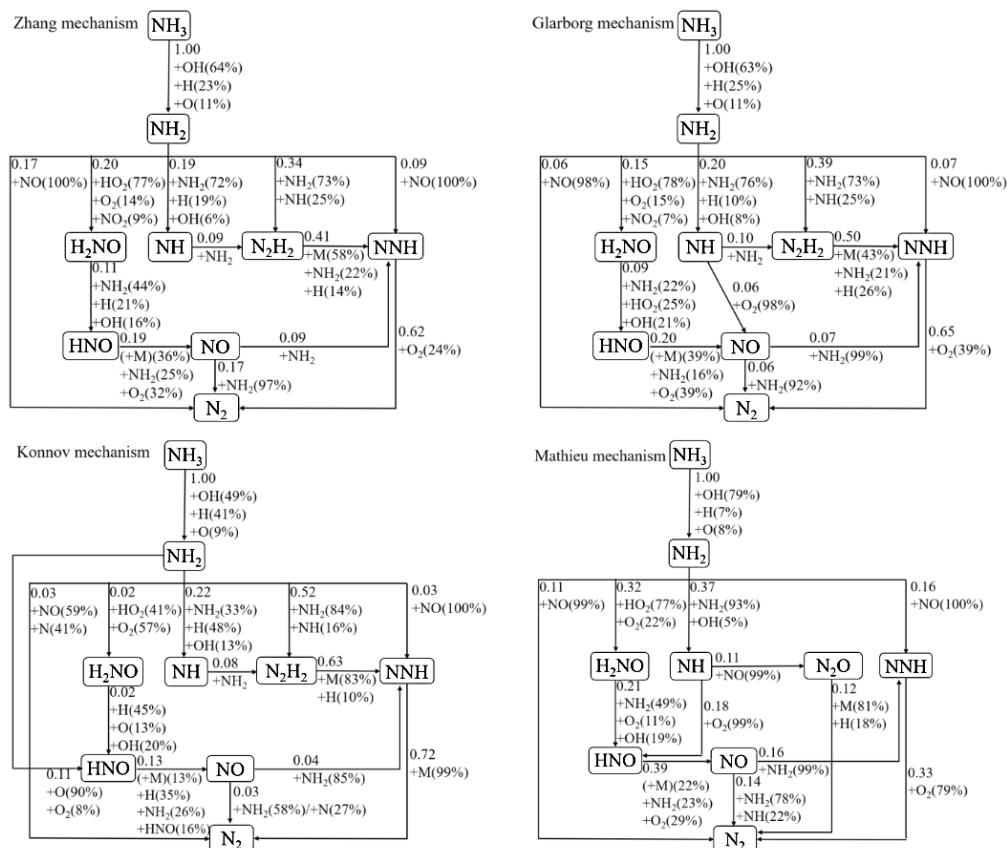


**Fig. 5.2** Element flux analysis of N during ignition delay time simulation of  $\text{NH}_3$ /air mixture at initial temperature of 1500 K with equivalence ratio ( $\phi$ ) of 1.0 and pressure of 20 atm.

A major difference of the Konnov mechanism compared to the Zhang and Glarborg mechanisms is the direct formation of  $\text{HNO}$  through  $\text{NH}_2$  via reactions with  $\ddot{\text{O}}$  and  $\text{O}_2$ . Another difference is that the reactions contribute to the formation of  $\text{NNH}$  and finally to  $\text{N}_2$ . At the conditions studied, the decomposition reaction totally controls the transformation from  $\text{NNH}$  to  $\text{N}_2$  in Konnov mechanism, and the reaction of  $\text{NNH}$  with  $\text{O}_2$  also plays an important role. Besides these differences, it can be concluded that although the relative transformations among major species and the contributions from dominant reactions are different for the considered reactive mixtures, the key reactions and species retained in different detailed mechanisms are mostly identical and the different performances of these detailed mechanisms

are essentially affected by the use of different reaction rate constants for a small number of key reactions. Besides element flux analyses of the mixtures, we also employ sensitivity analyses to identify and compare key reactions in the detailed mechanisms.

### 3.3 Sensitivity analysis and mechanism updates

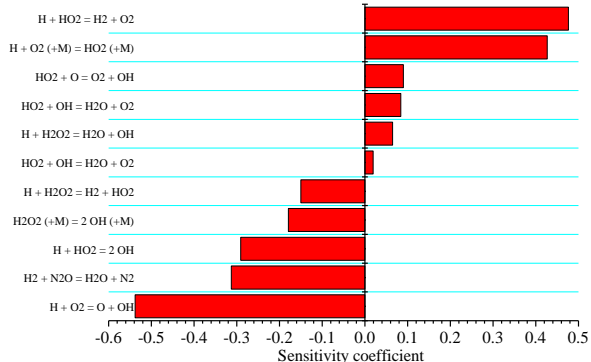
In an attempt to elucidate the selection of accurate rate constants for important reactions, a brute-force sensitivity analysis is employed for IDT simulations to identify important reactions and their differences in the various detailed mechanisms and to provide further help in the selection of accurate reaction rate constants. The sensitivity coefficient of the rate constants of reaction  $i$  on IDT is defined by the following formulation:

$$\text{Sensitivity}(i) = \frac{\tau_{ign}(2k_i) - \tau_{ign}(k_i)}{\tau_{ign}(k_i)} \quad (1)$$

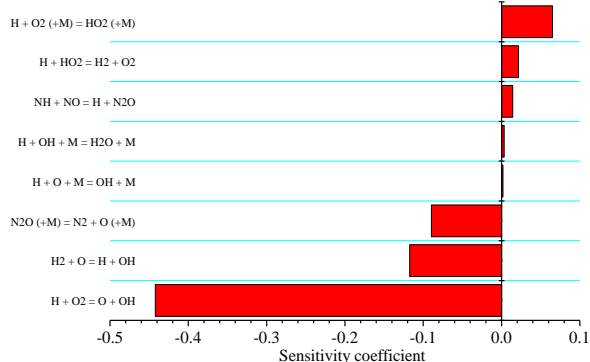
where  $k_i$  is the rate constants of reaction  $i$ ,  $\tau_{ign}(2k_i)$  is the IDT when the rate of reaction  $i$  is doubled, and  $\tau_{ign}(k_i)$  is the nominal value of the IDT. Therefore, a negative sensitivity coefficient value means that the IDT becomes shorter when the rate of reaction  $i$  is doubled and the overall reaction rate increases. Brute-force sensitivity analyses to IDT for H<sub>2</sub>/N<sub>2</sub>O/Ar and H<sub>2</sub>/NO<sub>2</sub>/Ar mixtures are conducted using the five detailed mechanisms at a pressure of 20 atm and at temperatures of 950 and 1500 K, Fig. 5.3.

According to Fig. 5.3, only four reactions, namely, N<sub>2</sub>O (+M) = N<sub>2</sub> +  $\ddot{O}$  (+M),  $\dot{H} + N_2O = NH + \dot{N}O$ ,  $\dot{H} + N_2O = N_2 + \dot{O}H$  and H<sub>2</sub> + N<sub>2</sub>O = N<sub>2</sub> + H<sub>2</sub>O have a large effect on the IDT predictions of the H<sub>2</sub>/N<sub>2</sub>O/Ar mixture excluding the H<sub>2</sub> chemistry. The sensitivity coefficients of the two reaction channels of  $\dot{H} + N_2O$  are smaller compared with the other two reactions. The sensitivity coefficient for the decomposition of N<sub>2</sub>O increases as temperature increases, while the sensitivity coefficient for the reaction H<sub>2</sub> + N<sub>2</sub>O = N<sub>2</sub> + H<sub>2</sub>O decreases as temperature increases. The rate constants of these two reactions both show a positive influence on the reactivity of the H<sub>2</sub>/N<sub>2</sub>O/Ar mixture. It is noticeable that the reaction H<sub>2</sub> + N<sub>2</sub>O = N<sub>2</sub> + H<sub>2</sub>O is only included in the Zhang mechanism which is the second most sensitive reaction, having a positive influence in increasing reactivity.

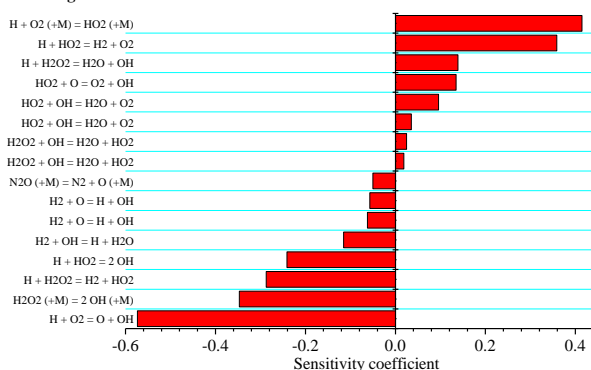
**Zhang mechanism**



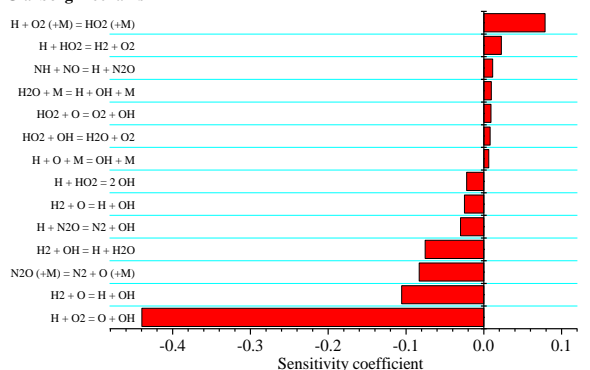
**Zhang mechanism**



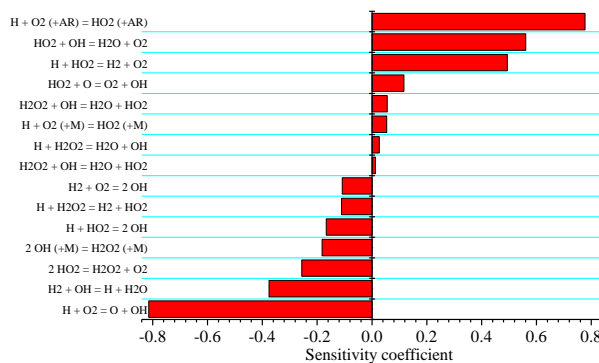
**Glarborg mechanism**



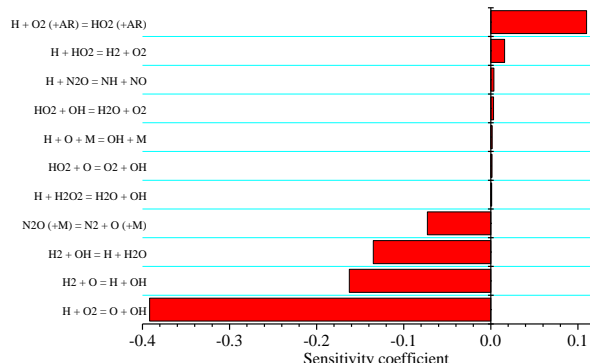
**Glarborg mechanism**



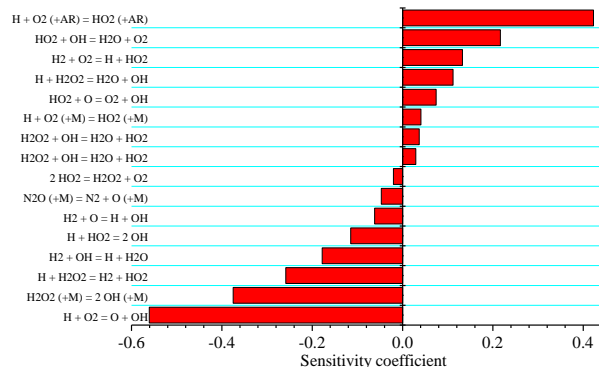
**Konnov mechanism**



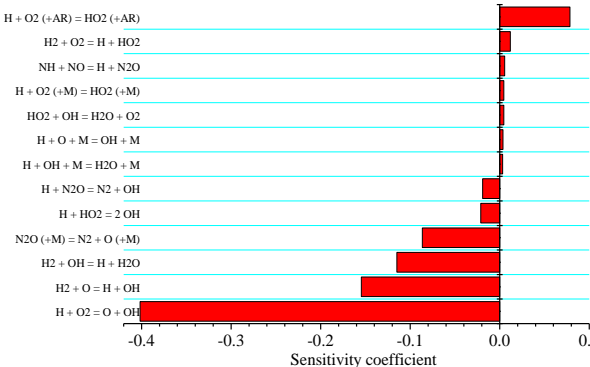
**Konnov mechanism**



**Mathieu mechanism**



**Mathieu mechanism**



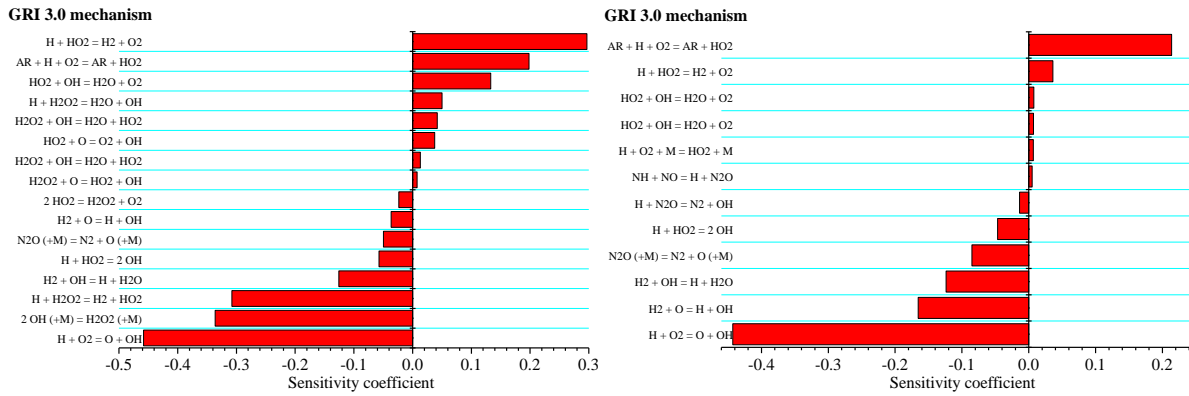
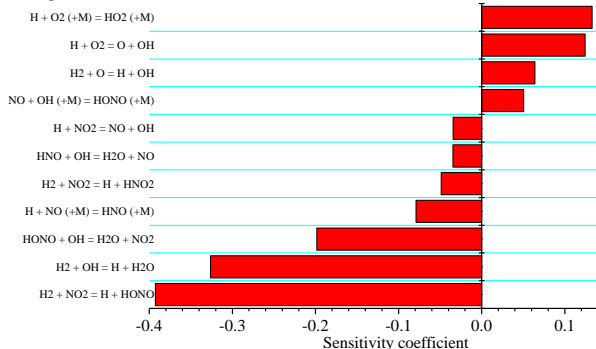


**Fig. 5.3** Sensitivity analysis of auto-ignition for  $\text{H}_2/\text{N}_2\text{O}/\text{Ar}$  mixture (0.01/0.0016/0.9784) by using the five detailed mechanisms at pressure of 20 atm and temperatures of 950 K (left) and 1500 K (right).

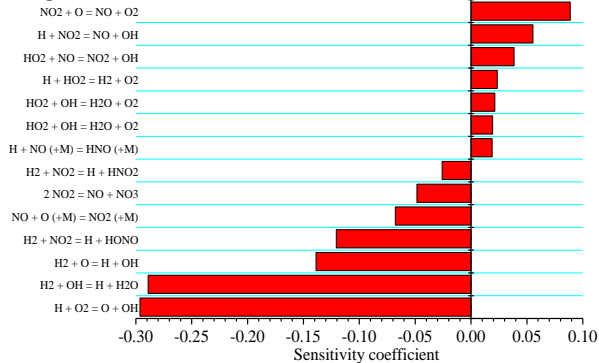
Considering the sensitivity analysis results shown in Fig. 5.4 for the  $\text{H}_2/\text{NO}_2/\text{Ar}$  mixture, the five mechanisms exhibit very different characteristics. (1) At 950 K, the most sensitive reactions in the Zhang and Glarborg mechanisms are identical, although the sensitivity coefficients are slightly different. The recombination reaction of  $\dot{\text{O}}\text{H}$  and  $\dot{\text{N}}\text{O}$  leading to the formation of HONO decreases the reactivity, while the reactions of  $\text{NO}_2$  with  $\text{H}_2$  /  $\text{H}_2\text{O}$  increase the reactivity on doubling their rate constants. (2) The sensitive reactions related to nitrogen species in the Konnov and Mathieu mechanisms are different. The recombination reactions of HONO show large sensitivity coefficients in the Konnov mechanism, which results from the significantly larger rate constants employed in the Konnov mechanism than those used in other mechanisms. However, this reaction exhibits very small contribution to reaction activity based on our flux analysis. (3) The reaction  $\text{HONO} + \dot{\text{O}}\text{H} = \text{NO}_2 + \text{H}_2\text{O}$  demonstrates opposite effects on IDT predictions in the Mathieu mechanism compared with the Zhang and Glarborg mechanisms. The major reason for this may be due to the use of different reaction rate coefficients. (4) GRI-Mech 3.0 does not include the HONO species, thus, the sensitivity analysis results demonstrate different characteristics at low temperatures. However, at 1500 K, all mechanisms show very similar sensitivity analysis results. Increasing the reaction rate constants of the  $\text{H}_2 + \text{NO}_2$  reaction and the decomposition reaction  $\text{NO}_2 = \dot{\text{N}}\text{O} + \ddot{\text{O}}$  significantly increases reactivity, while the three reactions of  $\dot{\text{N}}\text{O}$  with  $\text{O}_2$ ,  $\dot{\text{O}}\text{H}$  and  $\text{H}\dot{\text{O}}_2$  leading to the formation of  $\text{NO}_2$  and  $\ddot{\text{O}}$ ,  $\dot{\text{H}}$ , and  $\dot{\text{O}}\text{H}$  decrease the reactivity when the rate

constants are doubled. To summarize, the HONO species and related reactions have a large effect at low temperatures (< 1200 K), while the transformation reaction between NO and NO<sub>2</sub> become important at high temperatures.

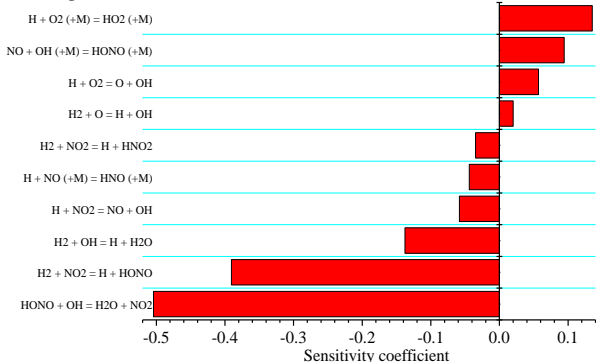
#### Zhang mechanism



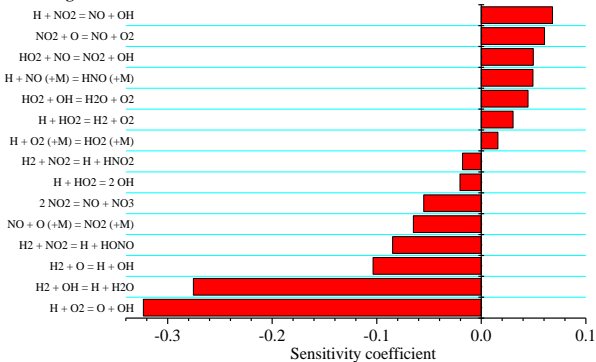
#### Zhang mechanism



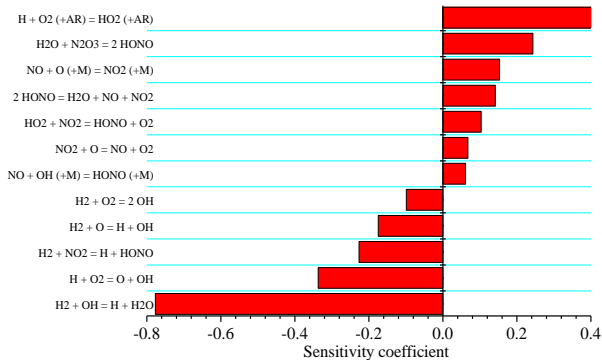
#### Glarborg mechanism



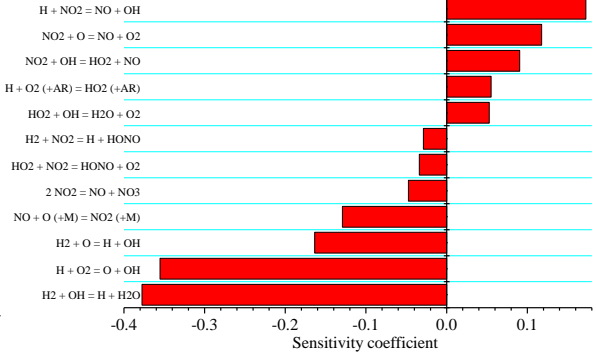
#### Glarborg mechanism



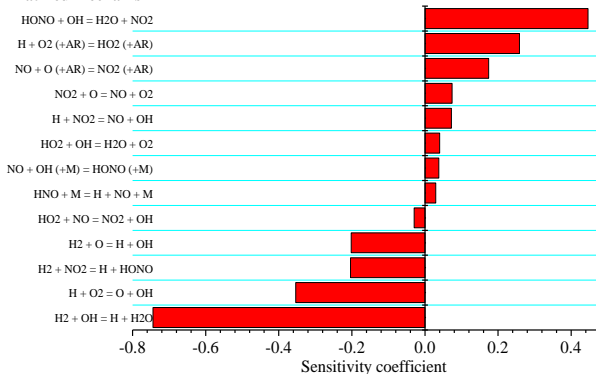
#### Konnov mechanism



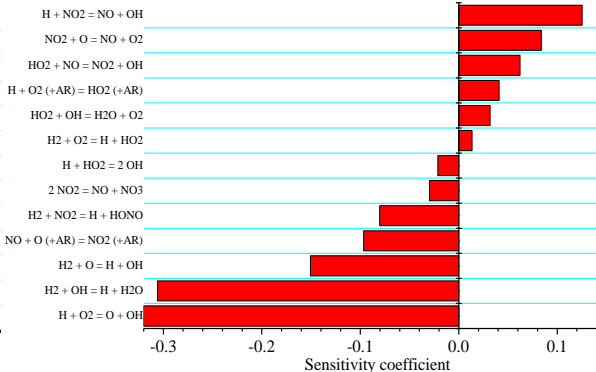
#### Konnov mechanism



#### Mathieu mechanism



#### Mathieu mechanism



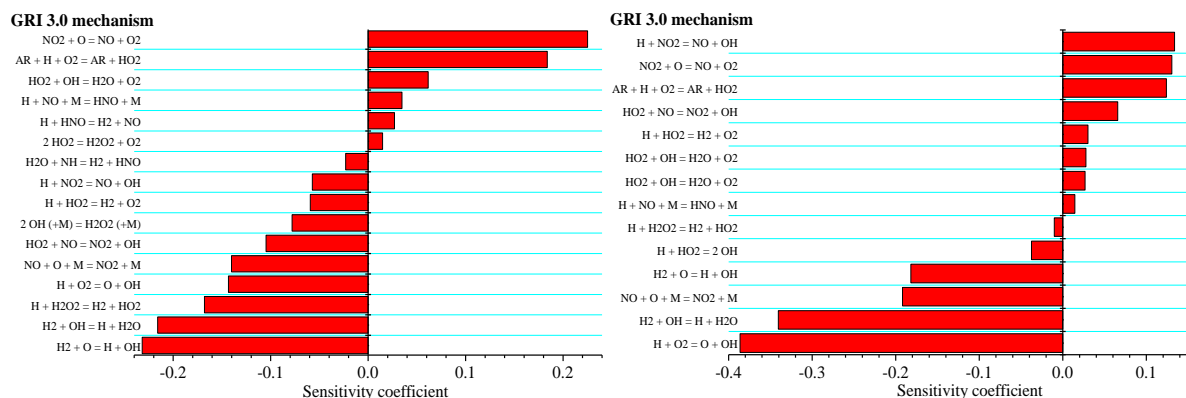


**Fig. 5.4** Sensitivity analysis of auto-ignition for  $\text{H}_2/\text{NO}_2/\text{Ar}$  mixture (0.01/0.0016/0.9784) by using the five detailed mechanisms at pressure of 20 atm and temperatures of 950 K (left) and 1500 K (right).

Based on systematic flux and sensitivity analyses, the high-temperature chemistry in these detailed mechanisms exhibits small differences, and major differences among these detailed mechanisms lie in the low temperature sub-mechanisms, especially in the HONO and  $\text{HNO}_2$  related reactions. Recent interest in advanced combustion engines promotes intense research in low-temperature combustion chemistry involving the  $\text{NO}_x$  sub-mechanism. To obtain better and more accurate prediction of  $\text{NO}_x$  chemistry in combustion, high-level theoretical chemistry calculations together with uncertainty minimization methods are employed to obtain more accurate rate constants and uncover unknown reactions using detailed potential energy surface analyses. In an attempt to continuously update detailed mechanisms, key reactions with large uncertainties and new reaction pathways have been updated based on Zhang's mechanism. Table 5.3 lists the updated reactions together with their related rate coefficients.

The decomposition reaction of HONO to form  $\dot{\text{N}}\text{O}$  and  $\dot{\text{O}}\text{H}$  is firstly updated with new rate constants, which plays an important role in the formation of  $\dot{\text{N}}\text{O}$  together with the isomerization reaction between HONO and  $\text{HNO}_2$ . Generally, all of the detailed mechanisms employ this reaction as  $\dot{\text{N}}\text{O} + \dot{\text{O}}\text{H} = \text{HONO}$ . Two sets of reaction rate coefficients from Tsang et al. [44] and Fulle et al. [45] were employed in the Konnov/Mathieu mechanisms and in the Glarborg mechanism, respectively. The Zhang mechanism adopted the rate coefficients recommended by Atkinson et al. [46] with a slight modification of the Troe broadening factor.

However, a major drawback of these rate constants was that they were derived at temperatures below 500 K, which were not very relevant to typical combustion conditions. Recently, Chen et al. [26] revisited the decomposition reaction kinetics of HONO and HNO<sub>2</sub> using high-level electronic structure calculations coupled with micro-canonical rate theory and the master equation method (RRKM/ME). They computed temperature- and pressure-dependent rate coefficients at temperatures in the range 200–2500 K and at pressures in the range 0.01–100 bar. They compared their computed rate constants with those used in the detailed mechanisms. It was shown that the rate constants used in the Glarborg mechanism exhibited the best agreement within a factor of two compared with their computed results, while the others showed large deviations but were generally within an order of magnitude.

For HNO<sub>2</sub>, the Dagaut, Konnov and GRI-Mech 3.0 mechanisms do not include it as a distinct species, while the other mechanisms mainly consider the isomerization reaction between HNO<sub>2</sub> and HONO. Based on high-level theoretical calculations, Chen et al. [26] indicated that the decomposition reaction of HNO<sub>2</sub> to  $\dot{\text{N}}\text{O} + \dot{\text{O}}\text{H}$  was the dominant product channel, which was not considered in all previous detailed mechanisms. Thus, to show the impact of this new reaction and its rate constants on model performance, the isomerization and decomposition reactions of HNO<sub>2</sub> and HONO are updated and the rate constants are listed in Table 5.3.

As demonstrated from flux analysis and sensitivity analysis, the reaction  $\dot{\text{H}} + \text{NO}_2 = \dot{\text{N}}\text{O} + \dot{\text{O}}\text{H}$  is critical. The rate expression  $k(T) = 1.3 \times 10^{14} \exp(-182 \text{ K}/T) \text{ cm}^3 \text{ mol}^{-1} \text{ s}^{-1}$  derived by Ko and Fontijn [47] based on high-temperature photochemistry technique at temperatures in the range 296–760 K was employed in all of the detailed mechanisms but was multiplied by a factor of 1.2 in the Zhang mechanism. Su et al. [48] extended the temperature range for this reaction to 1100 – 2000 K by using a shock tube facility and recommended a temperature-independent rate constant as  $8.85 \times 10^{13} \text{ cm}^3 \text{ mol}^{-1} \text{ s}^{-1}$  for  $195 \leq T \leq 2000 \text{ K}$ . In 2015, Hass et al. [49] replenished experimental results for this reaction for temperatures of 737–882 K in the pressure range 10–20 atm using laminar and turbulent flow reactors, and found a representative rate constant for this reaction of  $1.05 \times 10^{14} \text{ cm}^3 \text{ mol}^{-1} \text{ s}^{-1}$ . To minimize the uncertainty in the rate of this reaction, Chen et al. [26] proposed a novel

strategy to incorporate uncertainty in the minimum energy pathway into an optimization process and obtained a final rate expression, which was in excellent agreement with all of the experimental data.

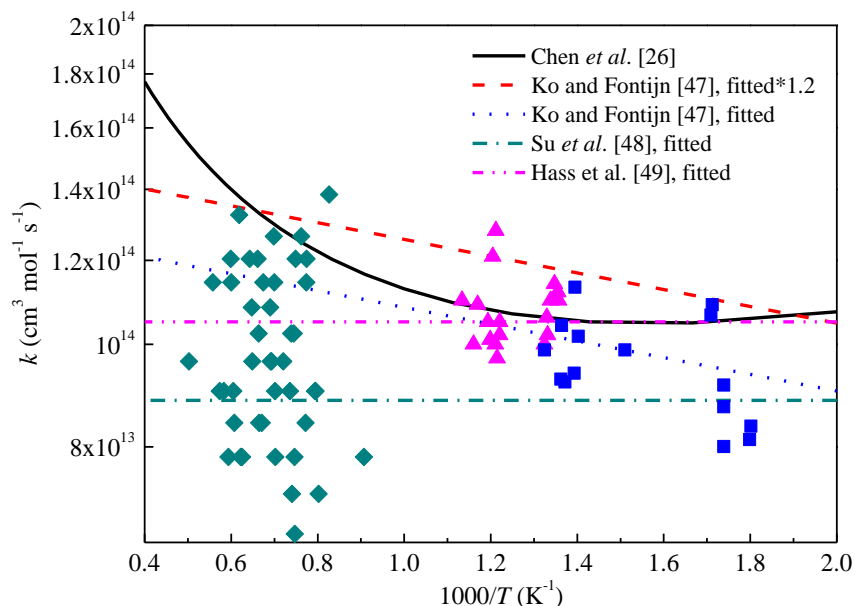


**Fig. 5.5** Reaction rate constants for reaction  $\dot{\text{H}} + \text{NO}_2 = \dot{\text{O}}\text{H} + \dot{\text{N}}\text{O}$  as a function of temperature. Symbols represent the corresponding experimental measured rate constants.

Fig. 5.5 demonstrates the rate constants for this reaction as a function of temperature. Although the deviations among these suggested rate constants are not large, the final rate constants optimized by Chen et al. [26] exhibits a strong temperature dependence.

Besides the reaction  $\dot{\text{H}} + \text{NO}_2 = \dot{\text{N}}\text{O} + \dot{\text{O}}\text{H}$ , the abstraction reaction of  $\text{H}_2$  and  $\text{NO}_2$  to form  $\dot{\text{N}}\text{O}$  and  $\text{H}_2\text{O}$  also shows large sensitivity coefficients. The recent high-level theoretical calculations by Chai et al. [25] for this abstraction reaction were employed in the Zhang and Glarborg mechanisms and adopted in this work. The reaction  $\text{HONO} + \dot{\text{O}}\text{H} = \text{H}_2\text{O} + \text{NO}_2$  represents a major consumption pathway for HONO and also shows a large sensitivity coefficient at low temperature conditions, but this reaction exhibits an opposite sensitivity coefficient in the Mathieu mechanism compared with the other three mechanisms as shown in Fig. 5.6. The rate constant employed in the Mathieu mechanism increases with increasing temperature, while the rate constants used in the other three mechanisms [50] exhibit a slight negative temperature dependence. Theoretical calculations for this reaction [51] also indicated a negative temperature dependence at temperatures below 1000 K, which correlates

with the experimental results [50]. In this work the reactions between  $\dot{\text{H}}$  and HONO are also updated using the theoretical calculations of Chai et al. [25]

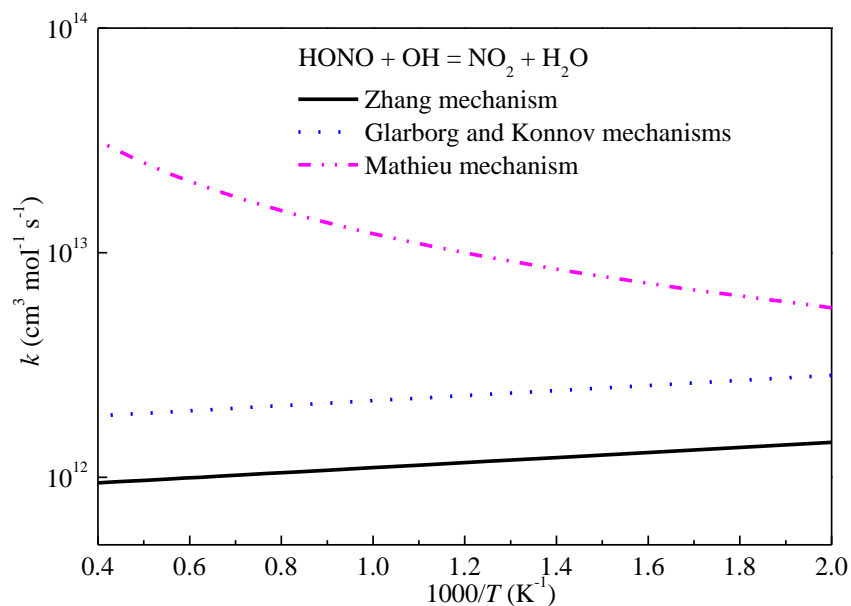


**Fig. 5.6** Reaction rate constants used for reaction  $\text{HONO} + \dot{\text{O}}\text{H} = \text{H}_2\text{O} + \text{NO}_2$  as a function of temperature.

Although the reaction reactivity of  $\text{H}_2/\text{NO}_2/\text{Ar}$  mixture is not sensitive to the reactions relevant to HNO according to our sensitivity analysis, nevertheless the HNO species plays a critical role in the formation of  $\text{NO}_x$  and in the oxidation of ammonia. The reactions between HNO and  $\dot{\text{O}}\text{H}$  have been updated with theoretical calculated rate coefficients [27]. In addition, the reaction  $\text{HNO} + \text{NO}_2 = \dot{\text{N}}\text{O} + \text{HONO}$  involving the inter-conversion of  $\dot{\text{N}}\text{O}$  and  $\text{NO}_2$  was found to be important in the oxidation of nitromethane  $\text{CH}_3\text{NO}_2$ , and was theoretically studied at the G4 level of theory by Shang et al. [52] Their calculated rate expression has been used in our updated mechanism.

The reactions  $\text{H}_2\text{NO} + \text{O}_2 = \text{HNO} + \text{H}\dot{\text{O}}_2$  and  $\text{HNO} + \text{O}_2 = \dot{\text{N}}\text{O} + \text{H}\dot{\text{O}}_2$  are major consumption steps for  $\text{H}_2\text{NO}$  and HNO. The first reaction was studied theoretically by Song et al. [19, 53], and the activation energy was slightly decreased within the estimated uncertainty to facilitate modeling predictions of ammonia oxidation and thermal  $\text{DeNO}_x$  at high oxygen concentrations [19]. The rate expression calculated by Song has been adopted here. However, for the reaction  $\text{HNO} + \text{O}_2 = \dot{\text{N}}\text{O} + \text{H}\dot{\text{O}}_2$ , no experimental or theoretical results were found, and the estimated rate constants from QRRK theory [37] were adopted in

previous mechanisms. To minimize the uncertainty of this reaction, its rate constants have been calculated here using high-level quantum chemistry calculations together with transition state theory. Specifically, geometry optimization and hindered rotor scan analyses are performed at the B2PLYP-D3/aug-cc-pVTZ level of theory [54]. Geometry optimization at this level can approach the accuracy of CCSD(T)/cc-pVTZ level [55]. Single-point energies are refined at the CCSD(T) level with aug-cc-pVTZ and aug-cc-pVQZ basis sets and then extrapolated to the complete basis set (CBS) limit [56, 57]. For all the species calculated with open-shell CCSD(T) method, all  $T1$  diagnostics values [58] are within 0.035, indicating that single-reference CCSD(T) method is adequate for this reaction [55, 59]. The energy barrier at the CCSD(T)/CBS level is  $14.68 \text{ kcal mol}^{-1}$  and Eckart tunneling corrections [60] are included in the calculation. The rate constants are calculated in the temperature range 500–2500 K with 100 K increments using MultiWell software [61] and fitted to the modified Arrhenius expression. The rate constants for this reaction as a function of temperature are plotted in Fig. 5.7. It can be seen that the rate constants used by Konnov and Mathieu are different from those used in the Zhang and Glarborg mechanisms. The computed rate constants in this work are lower than those used in the Zhang and Glarborg mechanisms at temperatures below 1000 K. Moreover, as the initial major consumption reactions of  $\text{NH}_3$ , the abstraction reactions by  $\dot{\text{H}}$  atoms and  $\dot{\text{O}}\text{H}$  radicals were theoretically investigated by Nguyen and Stanton [62, 63] by combining the high-accuracy extrapolated ab initio thermochemistry (HEAT) protocol with semi-classical transition state theory (SCTST). The computed results for  $\text{NH}_3 + \dot{\text{H}}$  were found to be in good correlation with the experimental results of Michael et al. [64], which were employed in detailed mechanisms. The calculated and fitted rate constants for  $\text{NH}_3 + \dot{\text{O}}\text{H}$  by Nguyen et al. [62] slightly deviate from the previous results, but the overall deviations are within 30%. The computed and fitted rate coefficients by Nguyen et al. [62, 63] extend the temperature ranges and are employed in the updated mechanism.

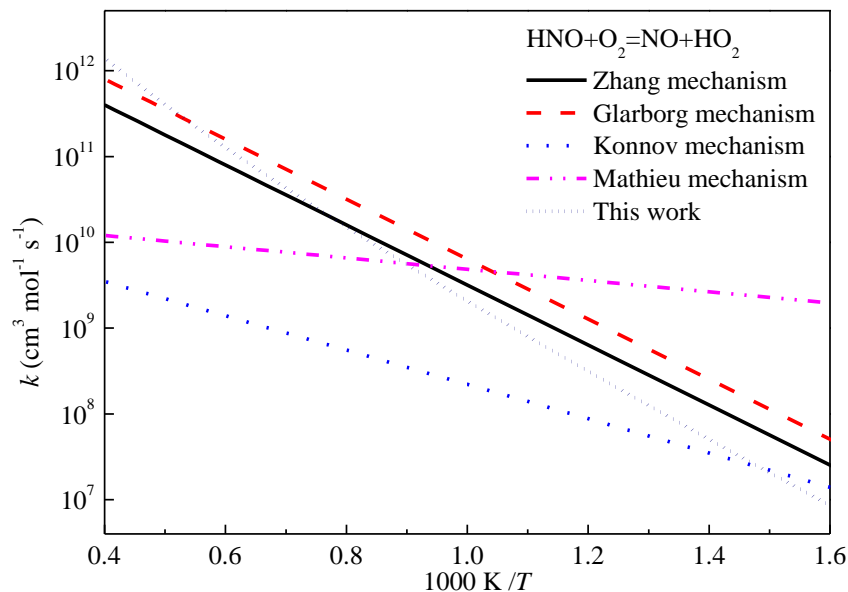


**Fig. 5.7** Reaction rate constants for reaction  $\text{HNO} + \text{O}_2 = \text{NO} + \text{HO}_2$  as a function of temperature.

**Table 5.3** Updated reactions and the corresponding reaction rate coefficients.

	Reaction	Rate coefficient (cm, mol, s, cal)				Source
		$p / \text{atm}$	$A$	$n$	$E$	
<b>1</b>	$\text{HNO}_2 = \text{HONO}$	0.01	$3.26 \times 10^{34}$	-7.97	45490.	[26]
		0.10	$2.77 \times 10^{33}$	-7.58	45250.	
		0.316	$1.93 \times 10^{32}$	-7.18	44940.	
		1.00	$1.56 \times 10^{30}$	-6.47	44360.	
		3.16	$2.17 \times 10^{27}$	-5.49	43670.	
		10.0	$4.68 \times 10^{24}$	-4.52	43320.	
		31.6	$1.14 \times 10^{23}$	-3.81	43640.	
		100.0	$2.03 \times 10^{22}$	-3.35	44430.	
<b>2</b>	$\dot{\text{O}}\text{H} + \dot{\text{N}}\text{O} = \text{HONO}$	0.01	$5.02 \times 10^{21}$	-4.24	899.	[26]
		0.10	$5.31 \times 10^{22}$	-4.24	1184.	
		0.316	$1.38 \times 10^{23}$	-4.22	1376.	
		1.00	$3.09 \times 10^{23}$	-4.17	1621.	
		3.16	$5.45 \times 10^{23}$	-4.09	1911.	
		10.0	$6.35 \times 10^{23}$	-3.97	2222.	
		31.6	$3.68 \times 10^{23}$	-3.75	2501.	
		100.0	$7.29 \times 10^{22}$	-3.41	2660.	
<b>3</b>	$\dot{\text{O}}\text{H} + \dot{\text{N}}\text{O} = \text{HNO}_2$	0.01	$3.16 \times 10^{18}$	-3.74	1405.	[26]
		0.10	$3.03 \times 10^{18}$	-3.43	2618.	
		0.316	$2.23 \times 10^{18}$	-3.24	3248.	
		1.00	$1.43 \times 10^{18}$	-3.03	3899.	
		3.16	$6.91 \times 10^{17}$	-2.79	4535.	

		10.0	$2.04 \times 10^{17}$	-2.49	5125.	
		31.6	$3.07 \times 10^{16}$	-2.12	5648.	
		100.0	$1.95 \times 10^{15}$	-1.64	6099.	
<b>4</b>	$\dot{\text{H}} + \text{NO}_2 = \dot{\text{O}}\text{H} + \dot{\text{N}}\text{O}$		$2.01 \times 10^{11}$	0.84	-1058.	[26]
<b>5</b>	$\dot{\text{H}} + \text{HONO} = \dot{\text{N}}\text{O} + \text{H}_2\text{O}$	0.01	$3.91 \times 10^{09}$	0.99	4049.	[27]
		0.10	$3.93 \times 10^{09}$	0.99	4049.	
		0.316	$3.97 \times 10^{09}$	0.99	4051.	
		1.00	$4.30 \times 10^{09}$	0.98	4070.	
		3.16	$7.04 \times 10^{09}$	0.92	4225.	
		10.0	$2.60 \times 10^{10}$	0.76	4736.	
		31.6	$7.91 \times 10^{10}$	0.64	5519.	
		100.0	$2.79 \times 10^{10}$	0.80	6146.	
<b>6</b>	$\dot{\text{H}} + \text{HONO} = \text{H}_2 + \text{NO}_2$		$1.89 \times 10^{03}$	2.83	1423.	[27]
<b>7</b>	$\dot{\text{H}} + \text{HNO}_2 = \text{H}_2 + \text{NO}_2$		$2.33 \times 10^{04}$	2.77	-2022.	[27]
<b>8</b>	$\dot{\text{H}} + \text{HNO}_2 = \dot{\text{N}}\text{O} + \text{H}_2\text{O}$	0.01	$3.39 \times 10^{09}$	1.07	5568.	[27]
		0.10	$3.39 \times 10^{09}$	1.07	5567.	
		0.316	$3.39 \times 10^{09}$	1.07	5567.	
		1.00	$3.38 \times 10^{09}$	1.07	5565.	
		3.16	$3.38 \times 10^{09}$	1.07	5560.	
		10.0	$3.40 \times 10^{09}$	1.07	5546.	
		31.6	$4.32 \times 10^{09}$	1.04	5591.	
		100.0	$1.27 \times 10^{10}$	0.91	5968.	
<b>9</b>	$\dot{\text{H}} + \text{HNO}_2 = \text{HNO} + \dot{\text{O}}\text{H}$	0.01	$3.61 \times 10^{07}$	1.78	5565.	[27]
		0.10	$3.61 \times 10^{07}$	1.78	5566.	
		0.316	$3.62 \times 10^{07}$	1.78	5567.	
		1.00	$3.65 \times 10^{07}$	1.78	5570.	
		3.16	$3.74 \times 10^{07}$	1.77	5580.	
		10.0	$4.14 \times 10^{07}$	1.76	5617.	
		31.6	$6.23 \times 10^{07}$	1.71	5770.	
		100.0	$1.81 \times 10^{08}$	1.59	6233.	
<b>10</b>	$\text{HNO} + \dot{\text{O}}\text{H} = \dot{\text{H}} + \text{HONO}$	0.01	$1.06 \times 10^{03}$	2.76	4439.	[27]
		0.10	$1.09 \times 10^{03}$	2.75	4450.	
		0.316	$1.18 \times 10^{03}$	2.74	4476.	
		1.00	$1.48 \times 10^{03}$	2.72	4554.	
		3.16	$2.71 \times 10^{03}$	2.64	4768.	
		10.0	$9.67 \times 10^{03}$	2.49	5253.	
		31.6	$5.31 \times 10^{04}$	2.29	6063.	
		100.0	$1.03 \times 10^{05}$	2.24	6951.	
<b>11</b>	$\text{HNO} + \dot{\text{O}}\text{H} = \dot{\text{N}}\text{O} + \text{H}_2\text{O}$	0.01	$5.82 \times 10^{10}$	0.40	3762.	[27]
		0.10	$5.85 \times 10^{10}$	0.40	3763.	
		0.316	$5.92 \times 10^{10}$	0.40	3764.	
		1.00	$6.30 \times 10^{10}$	0.39	3782.	
		3.16	$9.53 \times 10^{10}$	0.34	3931.	
		10.0	$2.60 \times 10^{11}$	0.23	4413.	

		31.6	$3.83 \times 10^{11}$	0.20	5099.	
		100.0	$4.18 \times 10^{10}$	0.51	5532.	
<b>12</b>	$\text{HNO} + \text{NO}_2 = \dot{\text{N}}\text{O} + \text{HONO}$		$7.85 \times 10^{02}$	3.06	3882.	[52]
<b>13</b>	$\text{HNO} + \text{O}_2 = \dot{\text{N}}\text{O} + \text{H}\dot{\text{O}}_2$		$3.99 \times 10^{05}$	2.30	14605.	this work
<b>14</b>	$\text{N}_2\text{O} + \text{H}_2 = \text{N}_2 + \text{H}_2\text{O}$		$7.00 \times 10^{12}$	0.00	32500.	[42]
<b>15</b>	$\text{NH}_3 + \dot{\text{O}}\text{H} = \text{NH}_2 + \text{H}_2\text{O}$		$4.30 \times 10^{03}$	2.83	-431.	[62]
<b>16</b>	$\text{NH}_3 + \dot{\text{H}} = \text{NH}_2 + \text{H}_2$		$2.89 \times 10^{06}$	2.23	10406.	[63]
<b>17</b>	$\text{H}_2\text{NO} + \text{O}_2 = \text{HNO} + \text{H}\dot{\text{O}}_2$		$2.30 \times 10^{02}$	2.99	16500.	[19, 53]

### 3.4 Skeletal reduction results

During the skeletal reduction process, the size of the skeletal mechanism is controlled by a threshold value, and the resulting skeletal mechanisms at different threshold values can be validated by comparing their model performance with the detailed mechanism. Starting from the updated detailed mechanism consisting of 44 species and 252 reactions, a skeletal mechanism with 28 species and 163 reactions is obtained using the DRGEP method at a threshold value of 0.4 and the predicted relative errors of ignition under sampling conditions are within 10%. To further reduce the number of species, we also perform a second-stage skeletal reduction via the DRGEP method, but it is hard to remove any species within the same error range. The resulting 28 species mechanism is further reduced via the ISSA method, and a final skeletal mechanism with 27 species and 130 reactions is obtained. The species  $\text{H}_2\text{NN}$  and its related reactions are deleted at this stage, also indicating that a single skeletal reduction is usually not enough to derive a minimal skeletal mechanism [35]. Table 5.1 lists the retained species in the final skeletal mechanism relevant to the  $\text{NO}_x$  sub-mechanism, and the  $\text{HO}\dot{\text{C}}\text{O}$  species has been removed compared with the syngas sub-mechanism in the detailed mechanism. It was shown by Nilsson and Konnov [65] that this species and its related chemistry were in fact not important to any significant extent under a wide range of combustion conditions for syngas with different compositions of  $\text{H}_2$  and  $\text{CO}$ .

Based on reaction pathway and sensitivity analyses, it can be concluded that, although the species and reactions in different detailed mechanisms show large differences, most of the species and reactions have little effect on mechanism performance. When considering the retained species and reactions in the skeletal mechanism compared to the detailed one, it is found that the small set of reactions controlling the major reaction pathways and affecting the predictive capability of the detailed mechanism are the same, and the different performance

relies in the selection of rate constants for this small set of reactions. The reduction in computational cost of the skeletal mechanism was measured for both the homogeneous ignition and diffusive flame systems. It is found that there is approximately a 60% CPU-time reduction for ignition and JSR species profile simulations and a 40% reduction for laminar simulations using the skeletal mechanism.

### 3.5 Performance of the developed mechanism

The updated detailed mechanism and the reduced skeletal mechanism for syngas/NO<sub>x</sub> have been validated against typical experimental data including IDTs and species profiles. A series of experimental investigations on nitrogen chemistry relevant to the syngas oxidation process have been reported in the last few decades as summarized by Glarborg et al. [19] and Zhang et al. [20] IDTs for H<sub>2</sub>/NO<sub>2</sub>/O<sub>2</sub>/Ar, H<sub>2</sub>/N<sub>2</sub>O/O<sub>2</sub>/Ar, and NH<sub>3</sub>/O<sub>2</sub>/Ar mixtures are selected as the primary major targets for validation since they can cover a wide range of pressures and temperatures.

To improve the predictability of NO<sub>x</sub> mechanism, the effect of NO<sub>x</sub> addition on the combustion properties of fuel oxidation system have been widely studied. Mathieu et al. [41] measured ignition delay times of H<sub>2</sub>/O<sub>2</sub>/NO<sub>2</sub> mixtures in a shock tube behind reflected shock waves. Fig. 5.8 illustrates the experimental data with simulations using the updated detailed and skeletal mechanisms as well as the other five detailed mechanisms. One can see that all of the mechanisms considered, except GRI-Mech 3.0, exhibit similar and good performance. The reduced skeletal mechanism reproduces the simulation results in good agreement with the detailed one. The major reason for the poor performance of GRI-Mech 3.0 is the omission of the HONO species because NO<sub>2</sub> is mostly converted to  $\dot{N}O$  by the reaction  $\dot{H} + NO_2 = \dot{N}O + \dot{O}H$ , which is included in all mechanisms and the adopted rate constants also show small differences. GRI-Mech 3.0 can still predict some reasonable ignition delay time since the HONO related reactions mainly affect IDTs at low temperature conditions as illustrated by Fig. 5.4.

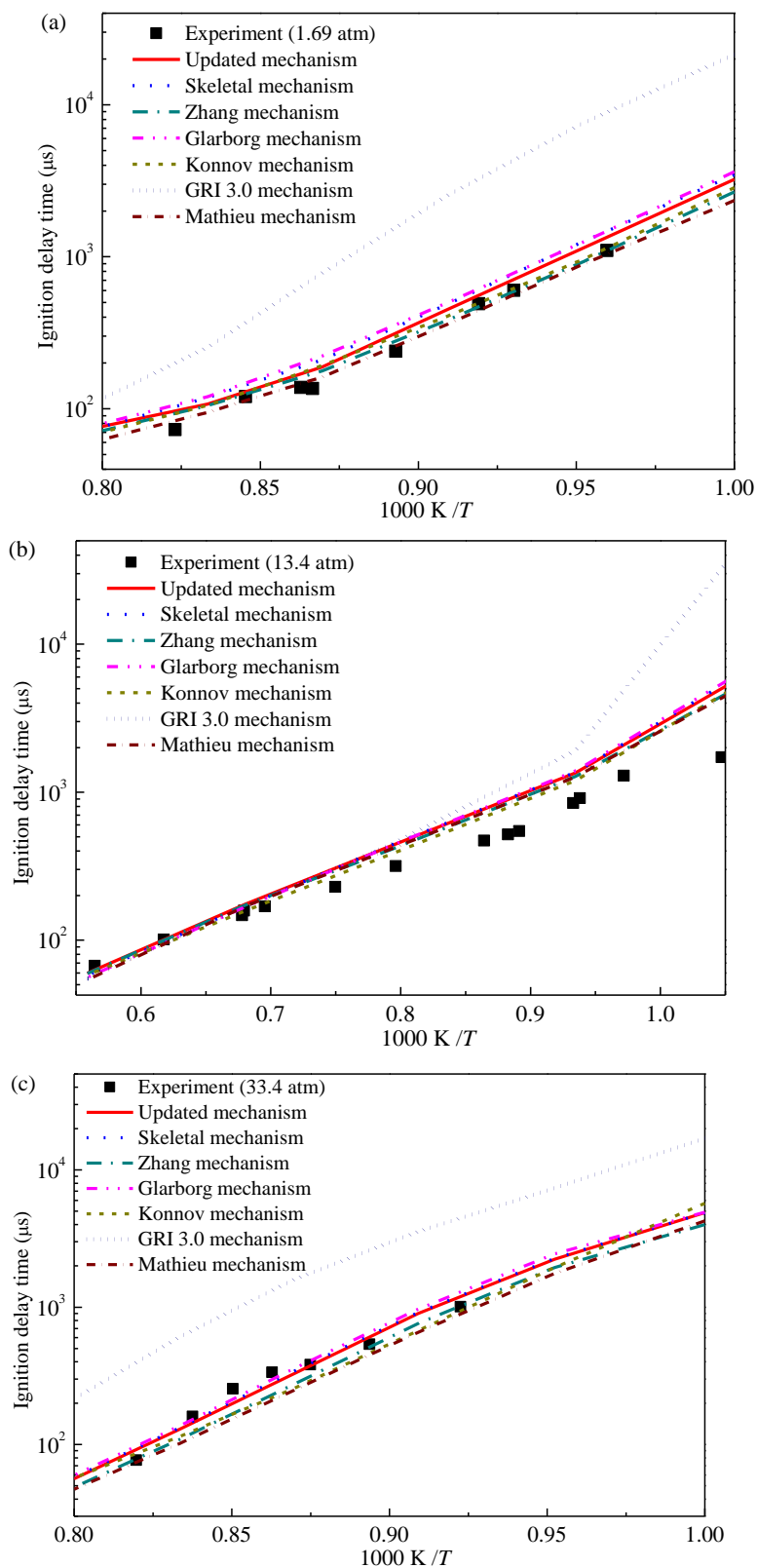


**Fig. 5.8** Ignition delay times from shock tube experiments [41] in comparison to model predictions for  $0.0133\text{H}_2/0.0067\text{O}_2/0.0001\text{NO}_2/0.9799\text{Ar}$  mixtures (mole fraction) at different pressures.

The  $\text{H}_2/\text{N}_2\text{O}/\text{O}_2$  reaction system is considered as another target to explore the interaction of hydrogen and  $\text{NO}_x$  and validate the performances of different mechanisms. Mathieu et al. [40] conducted shock tube studies on the effect of  $\text{N}_2\text{O}$  addition on the ignition of the  $\text{H}_2/\text{O}_2$  system over a wide range of temperatures (940–1675 K) and pressures (1.6, 13 and 32 atm), and recently Mulvihill et al. [42] performed a shock tube study on the less-dilute  $\text{H}_2/\text{N}_2\text{O}$  reaction system. They recommended new rate constants for the reaction  $\text{H}_2 + \text{N}_2\text{O} = \text{N}_2 + \text{H}_2\text{O}$ , which is used in the updated mechanism. Fig. 5.9 shows IDTs from shock tube experiments for the  $\text{H}_2/\text{N}_2\text{O}$  reaction systems together with modeling results. It can be seen that the updated and skeletal mechanisms exhibit better performance compared to the other mechanisms. For the less-dilute  $\text{H}_2/\text{N}_2\text{O}$  system shown in Fig. 5.9(d), the updated mechanism shows an improved performance using the rate constants recommended by Mulvihill et al. [42] for the reaction  $\text{H}_2 + \text{N}_2\text{O} = \text{N}_2 + \text{H}_2\text{O}$ .

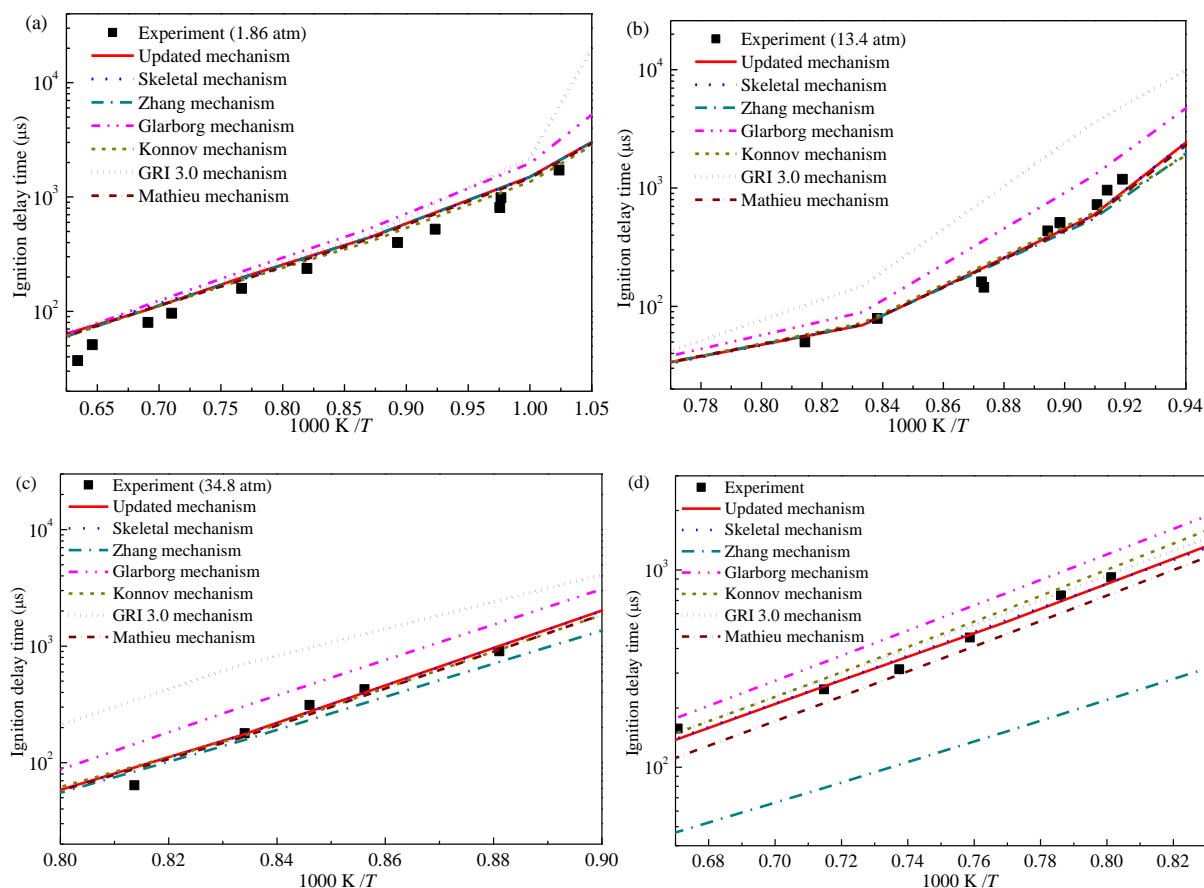


**Fig. 5.9** Ignition delay times from shock tube experiments in comparison to model predictions for  $0.01\text{H}_2/0.01\text{O}_2/0.0032\text{N}_2\text{O}/0.9768\text{Ar}$  mixtures (mole fraction) at different pressures [40] (a)–(c) and for  $0.10\text{H}_2/0.10\text{N}_2\text{O}/0.80\text{Ar}$  mixture at 0.68 atm [42] ((d)).

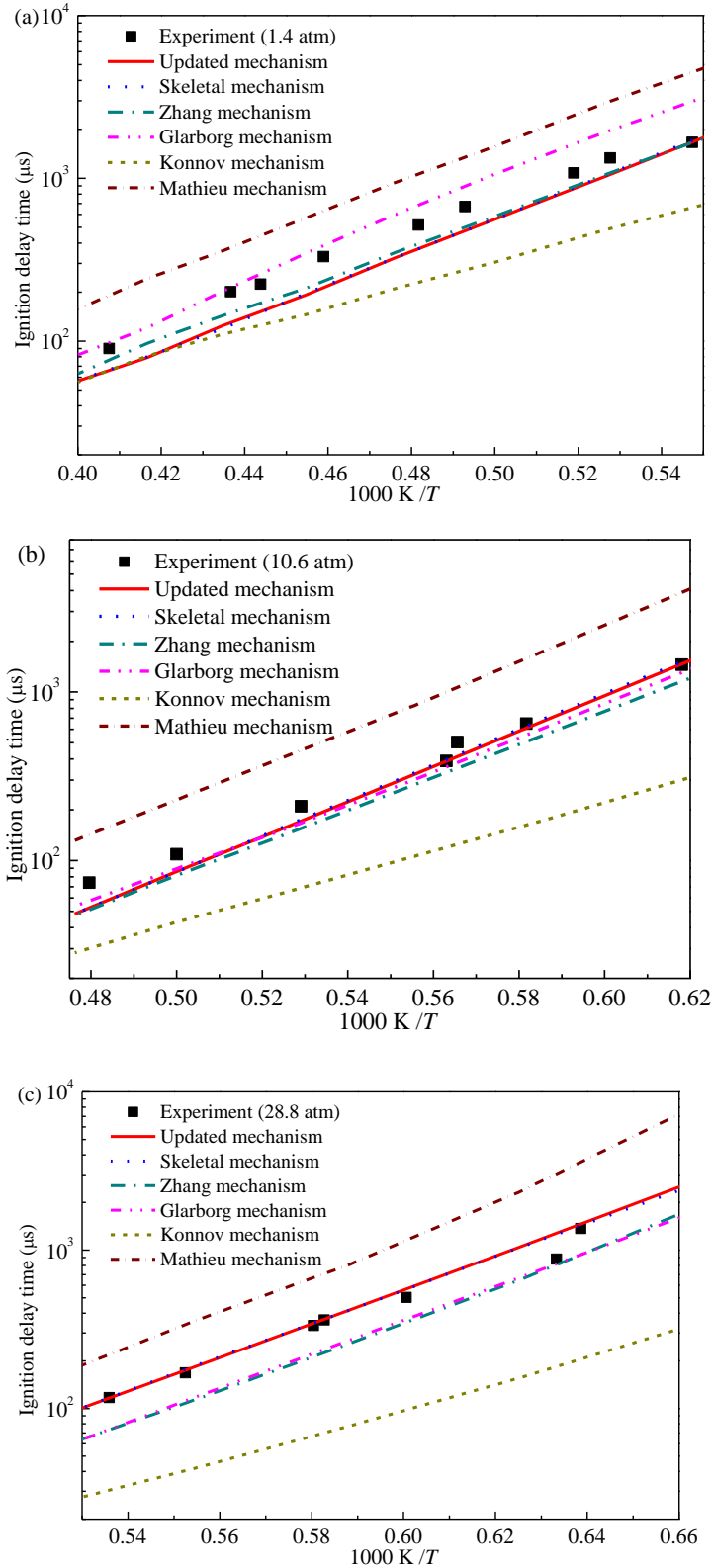


**Fig. 5.10** Ignition delay times from shock tube experiments [66] in comparison to model predictions for  $0.01143\text{NH}_3/0.00857\text{O}_2/0.98\text{Ar}$  mixtures (mole fraction) at different pressures.

Fig. 5.10 shows IDTs for  $\text{NH}_3/\text{O}_2/\text{Ar}$  mixtures at different pressures obtained from shock tube experiments [66] together with modeling results. The updated detailed and reduced skeletal mechanisms show improved predictions, especially at high pressure conditions. Fig. 5.11 shows sensitivity analysis results for  $\text{NH}_3/\text{O}_2/\text{Ar}$  mixture using the updated detailed mechanism at 20 atm pressure and 1500 K. It can be seen that the reactions related to  $\text{H}_2\text{NO}$  and  $\text{HNO}$  species are very important. The reactions of these two species with  $\text{O}_2$  exhibit large sensitivity coefficients. By employing high-level theoretical calculation results together with abstraction reactions of  $\text{NH}_3$  by  $\dot{\text{H}}$  atoms and  $\dot{\text{O}}\text{H}$  radicals as shown in Table 5.3, the updated detailed mechanism shows better performance in predicting IDTs for these  $\text{NH}_3/\text{O}_2/\text{Ar}$  mixtures.

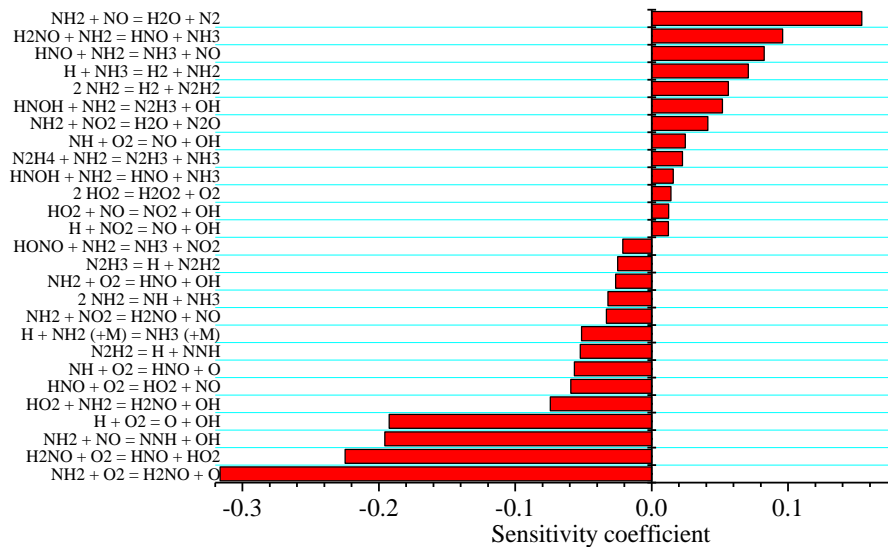


**Fig. 5.11** Sensitivity analysis for the auto-ignition of a  $\text{NH}_3/\text{O}_2/\text{Ar}$  mixture using the updated detailed mechanisms at a pressure of 20 atm and at a temperature of 1500 K.

Species concentration profiles from Jet-stirred reactors (JSR) and Flow reactor (FR) experiments are another important target to validate a detailed mechanism for nitrogen chemistry and  $\text{NO}_x$  emission prediction. The FR experiment designed by Abian et al. [67] provided a benchmark dataset for the prediction of thermal  $\dot{\text{N}}\text{O}$ . This mechanism is controlled by the reaction  $\text{N}_2 + \ddot{\text{O}} = \dot{\text{N}}\text{O} + \text{N}$ , and the rate constants employed in all of the mechanisms show small differences. Thus, the predicted  $\dot{\text{N}}\text{O}$  concentrations using the considered detailed mechanisms are very similar to one another. Fig. 5.12 demonstrates typical experimental JSR species profiles by Dayma and Dagaut [68] and the predicted

results. The updated and skeletal mechanism together with the Zhang and Glarborg mechanisms exhibit better performances compared with the other mechanisms. GRI-Mech 3.0 is outdated due to the lack of many key species relevant to low-temperature nitrogen chemistry. As shown in Table 5.3, major updates in the current mechanism and the differences among previous mechanisms lie in the low-temperature chemistry, especially for HONO and HNO<sub>2</sub> related reactions. To demonstrate the difference and analyze the impact of the new reaction pathway on model performance, a rate-of-production (ROP) analysis is performed for the H<sub>2</sub>/O<sub>2</sub>/N<sub>2</sub> mixture perturbed by  $\dot{N}O$  using the updated mechanism together with the Zhang and Glarborg mechanisms at 30 atm and 850 K, Fig. 5.13. The major reactions controlling the transformation of  $\dot{N}O$  and NO<sub>2</sub> are the same but with different rate constants. However, by incorporating the latest identified decomposition reaction of HNO<sub>2</sub> [26], it can be seen that the unimolecular decomposition reaction of HNO<sub>2</sub> to directly generate  $\dot{O}H$  and  $\dot{N}O$  is favored over the isomerization reaction.

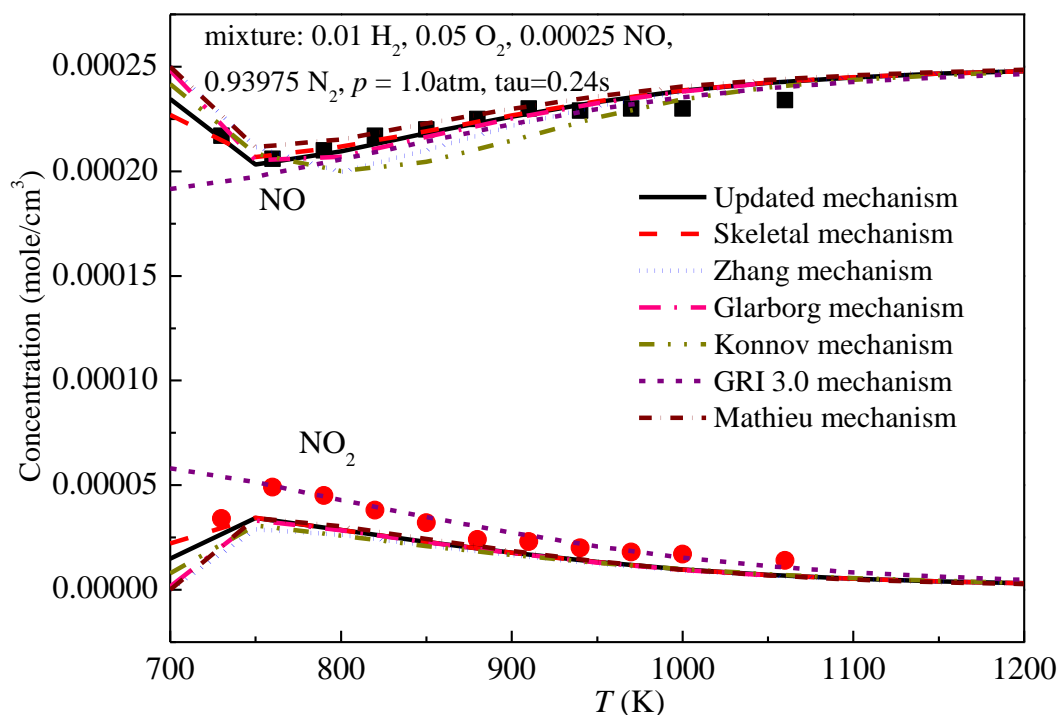


**Fig. 5.12**  $\dot{N}O$  and NO<sub>2</sub> species profiles as a function of temperature from experiment and modeling results. Symbols represent experimental measurements [68].

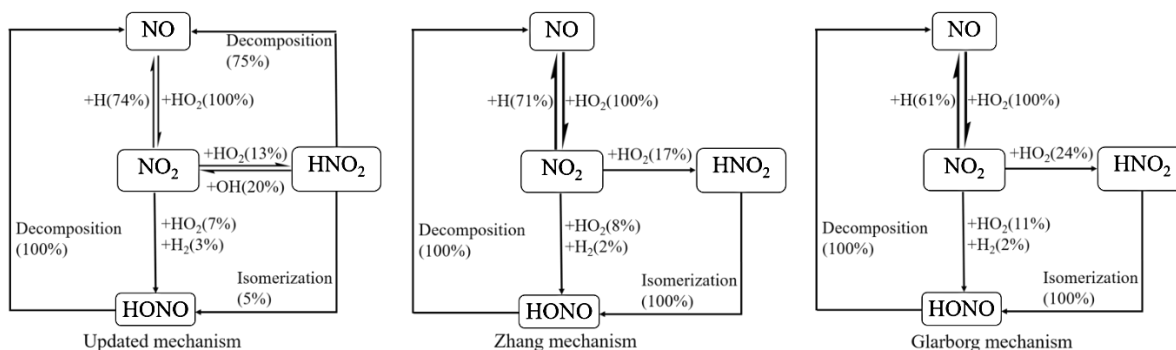


**Fig. 5.13** ROP analysis for NO species during JSR simulations for 0.01 H<sub>2</sub>/0.05 O<sub>2</sub>/0.93975 N<sub>2</sub>/0.00025 NO mixture with residence time of 0.24 s at 30 atm and 850 K.

Finally, to further validate the updated detailed and skeletal mechanisms, laminar flame speeds for H<sub>2</sub>/N<sub>2</sub>O mixture diluted by 60% Ar measured by Mével et al. [69] are used to test the mechanism performance. Fig. 5.14 shows the predicted laminar flame speeds as a function of equivalence ratio compared with experimental results at pressure of 1 atm and initial temperature of 300 K. It can be seen that the skeletal mechanism also exhibits high-fidelity in prediction of laminar flame speed compared with the detailed mechanism and experimental results.

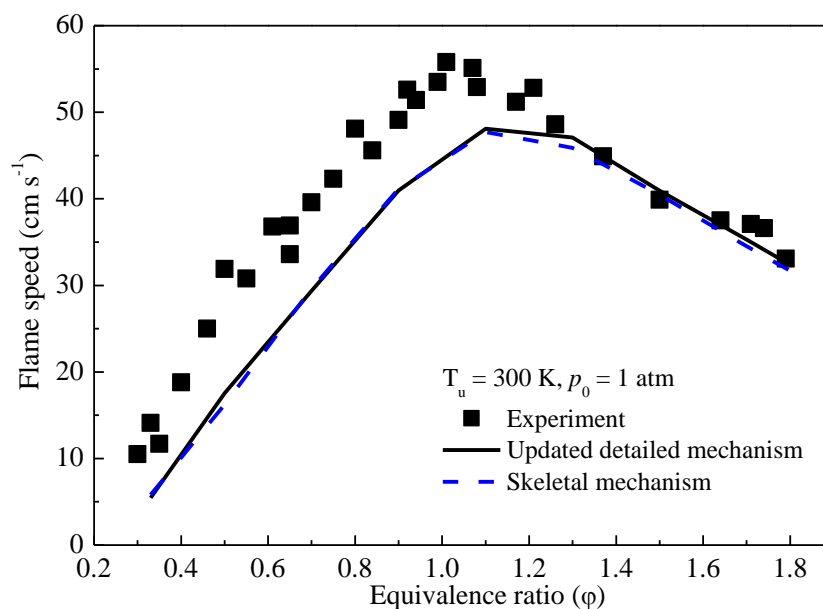


**Fig. 5.14** Laminar flame speed comparisons between experimental data and mechanism predictions for H<sub>2</sub>/N<sub>2</sub>O mixture diluted by 60% Ar at 1.0 atm and 300 K.

#### 4. Conclusions

In spite of the apparent simplicity of the syngas/NO<sub>x</sub> reaction system, available detailed mechanisms describing it still exhibit different performances in predicting combustion properties and NO<sub>x</sub> emissions. To clarify the differences among various detailed mechanisms, we have performed a comparative chemical kinetic analysis by using flux and sensitivity analyses for five available detailed mechanisms describing the syngas/NO<sub>x</sub> system. An updated detailed mechanism has been developed by incorporating recent theoretical advancements of several important elementary reactions. The main conclusions of the present study are summarized as follows.

- (1) The species relevant to nitrogen chemistry included in different detailed mechanisms for syngas combustion are different, and none of the selected detailed mechanisms are comprehensive enough to contain all of the species. Naturally, the recently developed detailed mechanisms such as the Zhang and Glarborg mechanisms are more comprehensive than the earlier ones.
- (2) Although the species and reactions included in various detailed mechanisms show large differences, the major reaction pathways and overall mechanism performances are affected by a small number of species and reactions based on flux and sensitivity analyses. The thermal  $\dot{\text{N}}\text{O}$  formation mechanism in contemporary detailed mechanisms is identical and only small deviations exist in rate constants. Major differences among the detailed mechanisms lie in the low-temperature sub-mechanism, especially for the reactions related to HONO and HNO<sub>2</sub>.
- (3) The rate constants for reaction  $\text{HNO} + \text{O}_2 = \dot{\text{N}}\text{O} + \text{HO}_2$  are calculated at the CCSD(T)/CBS level of theory together with TST and Eckart tunneling correction. With recent advancement in several important reactions, an updated detailed mechanism has been developed and validated. The updated mechanism incorporates new reaction pathways and exhibits a better performance for a series of conditions, especially at high-pressure conditions.
- (4) A reduced skeletal mechanism is obtained using a combination of the DRGEP and ISSA methods, and the skeletal mechanism, which can be coupled with CFD simulations, exhibits a high-fidelity performance compared to the detailed one.

## **Supporting Information**

The updated detailed and skeletal mechanisms; thermodynamic and transport properties.

## **Acknowledgments**

Q.-D. Wang and Y. Sun would like to acknowledge financial funding by the China Scholarship Council (CSC). The authors want to acknowledge financial support of Science Foundation Ireland under Grant Nos. 15/IA/3177 and 16/SP/3829 and also the National Natural Science Foundation of China (21403296). The Computational resources are provided by the Irish Centre for High-End Computing (ICHEC), under project number ngche064c and ngche073c.

## References

- [1] U. Ahmed, U. Zahid, Y. Lee, Process simulation and integration of IGCC systems for H<sub>2</sub>/syngas/electricity generation with control on CO<sub>2</sub> emissions, *Int. J. Hydrogen Energy* 44 (2019) 7137-7148.
- [2] H.J. Ge, H.F. Zhang, W.J. Guo, T. Song, L.H. Shen, System simulation and experimental verification: Biomass-based integrated gasification combined cycle (BIGCC) coupling with chemical looping gasification (CLG) for power generation, *Fuel* 241 (2019) 118-128.
- [3] A. Ryzhkov, T. Bogatova, S. Gordeev, Technological solutions for an advanced IGCC plant, *Fuel* 214 (2018) 63-72.
- [4] H.J. Curran, Developing detailed chemical kinetic mechanisms for fuel combustion, *Proc. Combust. Inst.* 37 (2019) 57-81.
- [5] T.F. Lu, C.K. Law, Toward accommodating realistic fuel chemistry in large-scale computations, *Prog. Energy Combust. Sci.* 35 (2009) 192-215.
- [6] M. O Conaire, H.J. Curran, J.M. Simmie, W.J. Pitz, C.K. Westbrook, A comprehensive modeling study of hydrogen oxidation, *Int. J. Chem. Kinet.* 36 (2004) 603-622.
- [7] A.A. Konnov, Yet another kinetic mechanism for hydrogen combustion, *Combust. Flame* 203 (2019) 14-22.
- [8] A.A. Konnov, Remaining uncertainties in the kinetic mechanism of hydrogen combustion, *Combust. Flame* 152 (2008) 507-528.
- [9] Z.K. Hong, D.F. Davidson, R.K. Hanson, An improved H<sub>2</sub>/O<sub>2</sub> mechanism based on recent shock tube/laser absorption measurements, *Combust. Flame* 158 (2011) 633-644.
- [10] A. Keromnes, W.K. Metcalfe, K.A. Heufer, N. Donohoe, A.K. Das, C.J. Sung, J. Herzler, C. Naumann, P. Griebel, O. Mathieu, M.C. Krejci, E.L. Petersen, W.J. Pitz, H.J. Curran, An experimental and detailed chemical kinetic modeling study of hydrogen and syngas mixture oxidation at elevated pressures, *Combust. Flame* 160 (2013) 995-1011.
- [11] T. Varga, T. Nagy, C. Olm, I.G. Zsely, R. Palvolgyi, E. Valko, G. Vincze, M. Cserhati, H.J. Curran, T. Turanyi, Optimization of a hydrogen combustion mechanism using both direct and indirect measurements, *Proc. Combust. Inst.* 35 (2015) 589-596.
- [12] J.A. Miller, C.T. Bowman, Mechanism and Modeling of Nitrogen Chemistry in Combustion, *Prog. Energy Combust. Sci.* 15 (1989) 287-338.
- [13] A.A. Konnov, Implementation of the NCN pathway of prompt-NO formation in the detailed reaction mechanism, *Combust. Flame* 156 (2009) 2093-2105.
- [14] O. Mathieu, B. Giri, A.R. Agard, T.N. Adams, J.D. Mertens, E.L. Petersen, Nitromethane ignition behind reflected shock waves: Experimental and numerical study, *Fuel* 182 (2016) 597-612.
- [15] S.F. Ahmed, J. Santner, F.L. Dryer, B. Padak, T.I. Farouk, Computational Study of NO<sub>x</sub> Formation at Conditions Relevant to Gas Turbine Operation, Part 2: NO<sub>x</sub> in High Hydrogen Content Fuel Combustion at Elevated Pressure, *Energy Fuels* 30 (2016) 7691-7703.
- [16] A. Frassoldati, T. Faravelli, E. Ranzi, The ignition, combustion and flame structure of carbon monoxide/hydrogen mixtures. Note 1: Detailed kinetic modeling of syngas combustion also in presence of nitrogen compounds, *Int. J. Hydrogen Energy* 32 (2007) 3471-3485.
- [17] J. Santner, S.F. Ahmed, T. Farouk, F.L. Dryer, Computational Study of NO<sub>x</sub> Formation

- at Conditions Relevant to Gas Turbine Operation: Part 1, *Energy Fuels* 30 (2016) 6745-6755.
- [18] P. Dagaut, P. Glarborg, M.U. Alzueta, The oxidation of hydrogen cyanide and related chemistry, *Prog. Energy Combust. Sci.* 34 (2008) 1-46.
- [19] P. Glarborg, J.A. Miller, B. Ruscic, S.J. Klippenstein, Modeling nitrogen chemistry in combustion, *Prog. Energy Combust. Sci.* 67 (2018) 31-68.
- [20] Y.J. Zhang, O. Mathieu, E.L. Petersen, G. Bourque, H.J. Curran, Assessing the predictions of a NO<sub>x</sub> kinetic mechanism on recent hydrogen and syngas experimental data, *Combust. Flame* 182 (2017) 122-141.
- [21] S.K. Sirumalla, M.A. Mayer, K.E. Niemeyer, R.H. West, Assessing impacts of discrepancies in model parameters on autoignition model performance: A case study using butanol, *Combust. Flame* 190 (2018) 284-292.
- [22] P. Boivin, A.L. Sanchez, F.A. Williams, Four-step and three-step systematically reduced chemistry for wide-range H<sub>2</sub>-air combustion problems, *Combust. Flame* 160 (2013) 76-82.
- [23] P. Boivin, F.A. Williams, Extension of a wide-range three-step hydrogen mechanism to syngas, *Combust. Flame* 196 (2018) 85-87.
- [24] R. Li, G.Q. He, F. Qin, C. Pichler, A.A. Konnov, Comparative analysis of detailed and reduced kinetic models for CH<sub>4</sub> + H<sub>2</sub> combustion, *Fuel* 246 (2019) 244-258.
- [25] J.J. Chai, C.F. Goldsmith, Rate coefficients for fuel + NO<sub>2</sub>: Predictive kinetics for HONO and HNO<sub>2</sub> formation, *Proc. Combust. Inst.* 36 (2017) 617-626.
- [26] X. Chen, M.E. Fuller, C.F. Goldsmith, Decomposition kinetics for HONO and HNO<sub>2</sub>, *Reaction Chemistry & Engineering* 4 (2019) 323-333.
- [27] M.E. Fuller, C.F. Goldsmith, On the relative importance of HONO versus HNO<sub>2</sub> in low-temperature combustion, *Proc. Combust. Inst.* 37 (2019) 695-702.
- [28] G.P. Smith, D.M. Golden, M. Frenklach, N.W. Moriarty, B. Eiteneer, M. Goldenberg, C.T. Bowman, R.K. Hanson, S. Song, W.C. Gardiner Jr, GRI 3.0 Mechanism, <http://combustion.berkeley.edu/gri-mech/releases.html>, 1999.
- [29] M. Cathonnet, J.-C. Boettner, H. James, Etude expérimentale et simulation de la pyrolyse du méthanol, *J. Chim. Phys.* 76 (1979) 183-189.
- [30] Q.D. Wang, Y.M. Fang, F. Wang, X.Y. Li, Systematic analysis and reduction of combustion mechanisms for ignition of multi-component kerosene surrogate, *Proc. Combust. Inst.* 34 (2013) 187-195.
- [31] P. Pepiot-Desjardins, H. Pitsch, An efficient error-propagation-based reduction method for large chemical kinetic mechanisms, *Combust. Flame* 154 (2008) 67-81.
- [32] G. Mauersberger, ISSA (iterative screening and structure analysis) - a new reduction method and its application to the tropospheric cloud chemical mechanism RACM/CAPRAM2.4, *Atmos. Environ.* 39 (2005) 4341-4350.
- [33] A.G. Xia, D.V. Michelangeli, P.A. Makar, Mechanism reduction for the formation of secondary organic aerosol for integration into a 3-dimensional regional air quality model: alpha-pinene oxidation system, *Atmos. Chem. Phys.* 9 (2009) 4341-4362.
- [34] Q.D. Wang, Y.M. Fang, F. Wang, X.Y. Li, Skeletal mechanism generation for high-temperature oxidation of kerosene surrogates, *Combust. Flame* 159 (2012) 91-102.
- [35] Q.D. Wang, Skeletal Mechanism Generation for Methyl Butanoate Combustion via Directed Relation Graph Based Methods, *Acta Physico-Chimica Sinica* 32 (2016) 595-604.
- [36] W.K. Metcalfe, S.M. Burke, S.S. Ahmed, H.J. Curran, A Hierarchical and Comparative

Kinetic Modeling Study of C<sub>1</sub>–C<sub>2</sub> Hydrocarbon and Oxygenated Fuels, *Int. J. Chem. Kinet.* 45 (2013) 638-675.

[37] A.M. Dean, J.W. Bozzelli, *Combustion chemistry of nitrogen*, Gas-phase combustion chemistry, Springer (2000), 125-341.

[38] E.W.G. Diau, M.C. Lin, Theoretical-Study of H(D)+N<sub>2</sub>O - Effects of Pressure, Temperature, and Quantum-Mechanical Tunneling on H(D)-Atom Decay and Oh(D)-Radical Production, *J. Phys. Chem.* 99 (1995) 6589-6594.

[39] S.J. Klippenstein, L.B. Harding, P. Glarborg, J.A. Miller, The role of NNH in NO formation and control, *Combust. Flame* 158 (2011) 774-789.

[40] O. Mathieu, A. Levacque, E.L. Petersen, Effects of N<sub>2</sub>O addition on the ignition of H<sub>2</sub>-O<sub>2</sub> mixtures: Experimental and detailed kinetic modeling study, *Int. J. Hydrogen Energy* 37 (2012) 15393-15405.

[41] O. Mathieu, A. Levacque, E.L. Petersen, Effects of NO<sub>2</sub> addition on hydrogen ignition behind reflected shock waves, *Proc. Combust. Inst.* 34 (2013) 633-640.

[42] C.R. Mulvihill, O. Mathieu, E.L. Petersen, The unimportance of the reaction H<sub>2</sub> + N<sub>2</sub>O reversible arrow H<sub>2</sub>O + N<sub>2</sub>: A shock-tube study using H<sub>2</sub>O time histories and ignition delay times, *Combust. Flame* 196 (2018) 478-486.

[43] H. Kobayashi, A. Hayakawa, K.D.Kunkuma A. Somarathne, Ekenechukwu C. Okafor, Science and technology of ammonia combustion, *Proc. Combust. Inst.* 37 (2019) 109-133.

[44] W. Tsang, J.T. Herron, *Chemical Kinetic Data-Base for Propellant Combustion .1. Reactions Involving NO, NO<sub>2</sub>, HNO, HNO<sub>2</sub>, HCN and N<sub>2</sub>O*, *J. Phys. Chem. Ref. Data* 20 (1991) 609-663.

[45] D. Fulle, H.F. Hamann, H. Hippler, J. Troe, Temperature and pressure dependence of the addition reactions of HO to NO and to NO<sub>2</sub>. IV. Saturated laser-induced fluorescence measurements up to 1400 bar, *J. Chem. Phys.* 108 (1998) 5391-5397.

[46] R. Atkinson, D.L. Baulch, R.A. Cox, J.N. Crowley, R.F. Hampson, R.G. Hynes, M.E. Jenkin, M.J. Rossi, J. Troe, *Evaluated kinetic and photochemical data for atmospheric chemistry: Volume I - gas phase reactions of Ox, HOx, NOx and SOx species*, *Atmos. Chem. Phys.* 4 (2004) 1461-1738.

[47] T. Ko, A. Fontijn, High-Temperature Photochemistry Kinetics Study of the Reaction H + NO<sub>2</sub> -> OH + NO from 296 K to 760 K, *J. Phys. Chem.* 95 (1991) 3984-3987.

[48] M.C. Su, S.S. Kumaran, K.P. Lim, J.V. Michael, A.F. Wagner, L.B. Harding, D.C. Fang, Rate constants, 1100 <= T <= 2000 K, for H+NO<sub>2</sub> -> OH+NO using two shock tube techniques: Comparison of theory to experiment, *J. Phys. Chem. A* 106 (2002) 8261-8270.

[49] F.M. Haas, F.L. Dryer, Rate Coefficient Determinations for H + NO<sub>2</sub> -> OH plus NO from High Pressure Flow Reactor Measurements, *J. Phys. Chem. A* 119 (2015) 7792-7801.

[50] J.B. Burkholder, A. Mellouki, R. Talukdar, A.R. Ravishankara, Rate Coefficients for the Reaction of OH with HONO between 298 K and 373 K, *Int. J. Chem. Kinet.* 24 (1992) 711-725.

[51] W.S. Xia, M.C. Lin, Ab initio MO/statistical theory prediction of the OH plus HONO reaction rate: evidence for the negative temperature dependence, *Physchemcomm* 3 (2000) 71-78.

[52] Y. Shang, J. Shi, H. Ning, R. Zhang, H. Wang, S. Luo, Ignition delay time measurements and kinetic modeling of CH<sub>4</sub> initiated by CH<sub>3</sub>NO<sub>2</sub>, *Fuel* 243 (2019) 288-297.

- [53] Y. Song, H. Hashemi, J.M. Christensen, C. Zou, P. Marshall, P. Glarborg, Ammonia oxidation at high pressure and intermediate temperatures, *Fuel* 181 (2016) 358-365.
- [54] S. Grimme, S. Ehrlich, L. Goerigk, Effect of the Damping Function in Dispersion Corrected Density Functional Theory, *J. Comput. Chem.* 32 (2011) 1456-1465.
- [55] S.J. Klippenstein, From theoretical reaction dynamics to chemical modeling of combustion, *Proc. Combust. Inst.* 36 (2017) 77-111.
- [56] Q.-D. Wang, M.-M. Sun, J.-H. Liang, Reaction Mechanisms and Kinetics of the Hydrogen Abstraction Reactions of C<sub>4</sub>-C<sub>6</sub> Alkenes with Hydroxyl Radical: A Theoretical Exploration, *International journal of molecular sciences* 20 (2019) 1275.
- [57] C.F. Goldsmith, W.H. Green, S.J. Klippenstein, Role of O-2 + QOOH in Low-Temperature Ignition of Propane. 1. Temperature and Pressure Dependent Rate Coefficients, *J. Phys. Chem. A* 116 (2012) 3325-3346.
- [58] T.J. Lee, P.R. Taylor, A Diagnostic for Determining the Quality of Single-Reference Electron Correlation Methods, *Int. J. Quantum Chem.* (1989) 199-207.
- [59] C.F. Goldsmith, G.R. Magoon, W.H. Green, Database of Small Molecule Thermochemistry for Combustion, *J. Phys. Chem. A* 116 (2012) 9033-9057.
- [60] H.S. Johnston, J. Heicklen, Tunnelling Corrections for Unsymmetrical Eckart Potential Energy Barriers, *J. Phys. Chem.* 66 (1962) 532-533.
- [61] J.R. Barker, Multiple-well, multiple-path unimolecular reaction systems. I. MultiWell computer program suite, *Int. J. Chem. Kinet.* 33 (2001) 232-245.
- [62] T.L. Nguyen, J.F. Stanton, High-level theoretical study of the reaction between hydroxyl and ammonia: Accurate rate constants from 200 to 2500 K, *J. Chem. Phys.* 147 (2017) 152704.
- [63] T.L. Nguyen, J.F. Stanton, Ab initio thermal rate coefficients for  $H + NH_3 = H_2 + NH_2$ , *Int. J. Chem. Kinet.* 51 (2019) 321-328.
- [64] J.V. Michael, J.W. Sutherland, R.B. Klemm, Rate-Constant for the Reaction  $H + NH_3$  over the Temperature-Range 750-1777 K, *J. Phys. Chem.* 90 (1986) 497-500.
- [65] E.J.K. Nilsson, A.A. Konnov, Role of HOCO Chemistry in Syngas Combustion, *Energy Fuels* 30 (2016) 2443-2457.
- [66] O. Mathieu, E.L. Petersen, Experimental and modeling study on the high-temperature oxidation of Ammonia and related NO<sub>x</sub> chemistry, *Combust. Flame* 162 (2015) 554-570.
- [67] M. Abian, M.U. Alzueta, P. Glarborg, Formation of NO from N<sub>2</sub>/O<sub>2</sub>Mixtures in a Flow Reactor: Toward an Accurate Prediction of Thermal NO, *Int. J. Chem. Kinet.* 47 (2015) 518-532.
- [68] G. Dayma, P. Dagaut, Effects of Air Contamination on the Combustion of Hydrogen—Effect of NO and NO<sub>2</sub> Addition on Hydrogen Ignition and Oxidation Kinetics, *Combust. Sci. Technol.* 178 (2006) 1999-2024.
- [69] R. Mevel, F. Lafosse, N. Chaumeix, G. Dupre, C.E. Paillard, Spherical expanding flames in H<sub>2</sub>-N<sub>2</sub>O-Ar mixtures: flame speed measurements and kinetic modeling, *Int. J. Hydrogen Energy* 34 (2009) 9007-9018.



## Chapter 6

# Chemical Kinetics of Hydrogen Atom Abstraction from Propargyl Sites by Hydrogen and Hydroxy Radicals

Published in: International Journal of Molecular Sciences 20 (13) (2019) 3227.

DOI: <https://doi.org/10.3390/ijms20133227>

### Authors and Contributions

(1) Quan-De Wang

China University of Mining and Technology

Contribution: Project design and management, chemical kinetic calculations and manuscript preparation.

(2) Yanjin Sun

National University of Ireland, Galway

Contribution: Project design, part of the ab initio and chemical kinetic calculations, and manuscript review.

(3) Mao-Mao Sun

China University of Mining and Technology

Contribution: Most of the ab initio calculations and manuscript review.

(4) Jin-Hu Liang

North University of China

Contribution: Project Management and manuscript review.

## Abstract

Hydrogen atom abstraction from propargyl C–H sites of alkynes plays a critical role in determining the reactivity of alkyne molecules and understanding the formation of soot precursors. This work reports a systematic theoretical study on the reaction mechanisms and rate constants for hydrogen abstraction reactions by hydrogen and hydroxy radicals from a series of alkyne molecules with different structural propargyl C–H atoms. Geometry optimizations and frequency calculations for all species are performed at M06-2X/cc-pVTZ level of theory and the hindered internal rotations are also treated at this level. The high-level W1BD and CCSD(T)/CBS theoretical calculations are used as a benchmark for a series of DFT calculations toward the selection of accurate DFT functionals for large reaction systems in this work. Based on the quantum chemistry calculations, rate constants are computed using the canonical transition state theory with tunneling correction and the treatment of internal rotations. The effects of the structure and reaction site on the energy barriers and rate constants are examined systematically. To the best of our knowledge, this work provides the first systematic study for one of the key initiation abstraction reactions for compounds containing propargyl hydrogen atoms.

## 1. Introduction

Alkynes are important intermediates during the oxidation of hydrocarbon fuels, and they are critical initiation species towards soot formation [1, 2]. The development of a detailed combustion mechanism to predict the combustion properties of alkynes and soot formation requires a better understanding of the reactivity of alkyne molecules, especially the alkyne molecules with phenyl group. In combustion reaction systems, hydrogen ( $\dot{\text{H}}$ ) and hydroxy ( $\dot{\text{O}}\text{H}$ ) radicals are usually the most abundant radicals [3, 4], and the hydrogen atom abstraction reactions of alkynes by  $\dot{\text{H}}$  and  $\dot{\text{O}}\text{H}$  radicals play a critical role in understanding the reactivity of alkyne molecules among various reaction pathways. In addition, the activation of alkyne molecules is also a challenging area in organic chemistry [5]. A better understanding of the reactivity of these molecules based on theoretical chemical calculations is also fundamental to organic chemistry.

For alkyne molecules, H-atom abstraction from the acetylenic sites can be ignored due to the large bond dissociation energies (BDEs) [6]. However, abstraction from the propargyl C–H sites forming resonance-stabilized propargyl radicals is believed to be an important step in the formation of large Polycyclic Aromatic Hydrocarbons (PAHs) and soot [2, 4, 7-10]. Hence, understanding the underlying chemistry and obtaining accurate rate constants for

these abstraction reactions are fundamental to understand the combustion properties of alkynes and soot formation and develop reliable detailed combustion mechanisms. However, limited research has been carried out for the abstraction reactions of alkynes and most studies for alkynes are still limited to propyne.

Miller et al. analyzed the reaction of  $\dot{\text{H}}$  with propyne based on a  $\text{C}_3\text{H}_5$  potential and found that the abstraction reaction channel at the propargyl C–H site is also important, especially at high temperatures [11]. They also compared the computed results with experiment by Bentz et al. [12] and good agreement was obtained. Rosado-Reyes et al. studied the thermal reaction of H atoms with propyne in a heated single pulse-shock tube and derived rate constants for H-atom attack on propyne [13]. Hansen et al. [14] incorporated the rate constants obtained by Miller et al. [11] to understand the isomer-specific combustion chemistry in allene and propyne flames and proposed that implementing the accurate theoretical results for important reactions is critical for an accurate prediction of combustion properties. Zádor and Miller used the KinBot software to explore the potential energy surfaces for  $\dot{\text{O}}\text{H} + \text{allene}$  and  $\dot{\text{O}}\text{H} + \text{propyne}$  reactions systematically [15]. It was demonstrated that the major channel of these bimolecular reactions at high temperatures is the abstraction reactions to the formation of propargyl and  $\text{H}_2\text{O}$ , also indicating the studied reaction systems are very important for soot formation at high temperatures. In addition, Senosiain et al. performed a theoretical study of diacetylene with  $\dot{\text{O}}\text{H}$  radicals and found that direct abstraction reaction channels for alkyne molecules are very important [16]. Besides these typical studies on allene/propyne and diacetylene, few studies have been performed on larger alkyne molecules. Systematic studies on structure and reaction site effect on energy barriers and rate constants for the H-atom abstraction reactions at the propargyl sites of alkynes are badly needed to develop accurate detailed combustion mechanisms.

Based on the above considerations, in this study, we employ high-level ab initio methods together with transition state theory to study the hydrogen abstraction reactions by  $\dot{\text{H}}$  and  $\dot{\text{O}}\text{H}$  radicals for a series of alkynes with different structural propargyl C–H sites. To obtain accurate reaction barriers and enthalpies for large reaction systems studied in this work, the high-level W1BD [17] and CCSD(T)/CBS [18] methods are used as benchmark methods for small systems to select a proper DFT method for large reactions. The rate constants are computed based on quantum chemistry calculations. The structure and reaction site effect on the energies and rate constants for the abstraction reactions at propargyl C–H sites are systematically investigated.

## 2. Results and Discussion

To investigate the structure and reaction site effect on the abstraction reactions from propargyl C–H sites, eight alkyne molecules with different propargyl C–H sites are considered. The studied alkyne molecules are propyne, 1-butyne, 1-pentyne, penta-1,4-diyne, 4-penten-1-yne, isopentyne, 3-phenyl-1-propyne, and but-3-yn-2-ylbenzene, which can represent the primary, secondary, tertiary, and doubly secondary propargyl H atoms of alkynes and the effect of phenyl substituents which is important for soot precursor formation is also considered.

### 2.1. Geometry Analysis

Figs. 6.1 and 6.2 depict the optimized transition state structures at M06-2X/cc-pVTZ level of theory. It should be noted that the lowest energy conformation for each species is obtained by scanning all the relevant internal rotational degrees of freedom and then the global minimum point is used for optimization. As shown in Fig. 6.1, the C–H bond breaking along the reaction coordinate are elongated from an averaged value of 1.09 Å to an averaged value of 1.24 Å and the angles of C–H–H between the breaking C–H bond and the forming H–H bond are near-linear.

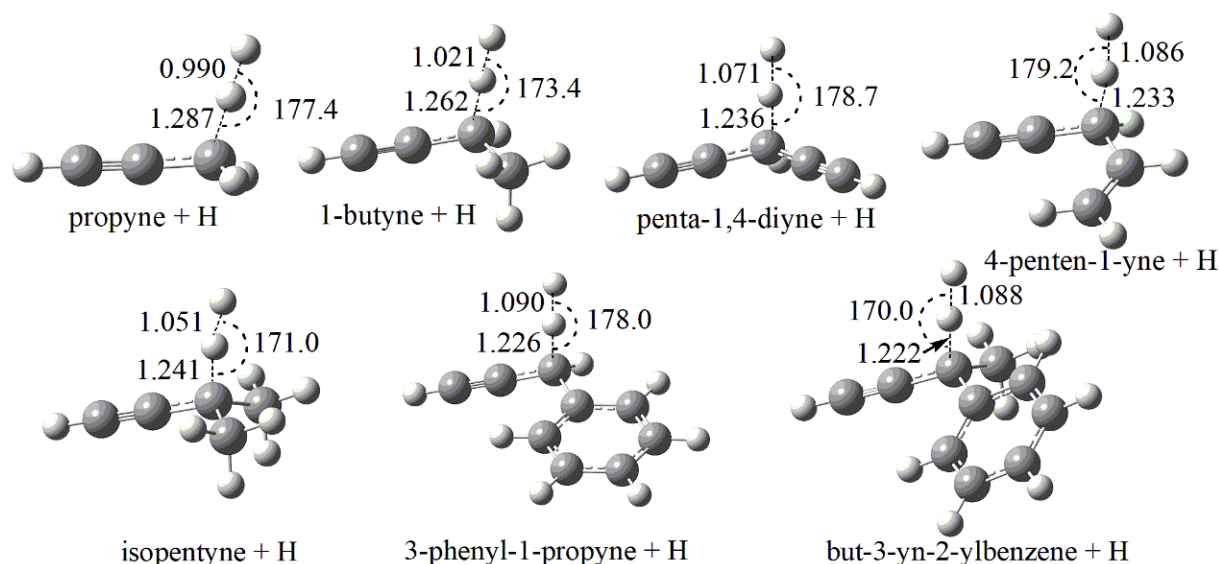


**Fig. 6.1** Optimized geometries (in Å and degrees) of TSs for the abstraction reactions by  $\dot{\text{H}}$  atom at M06-2X/cc-pVTZ level. The geometry centers of TS for 1-pentyne are identical to that of 1-butyne, and thus not explicitly shown.

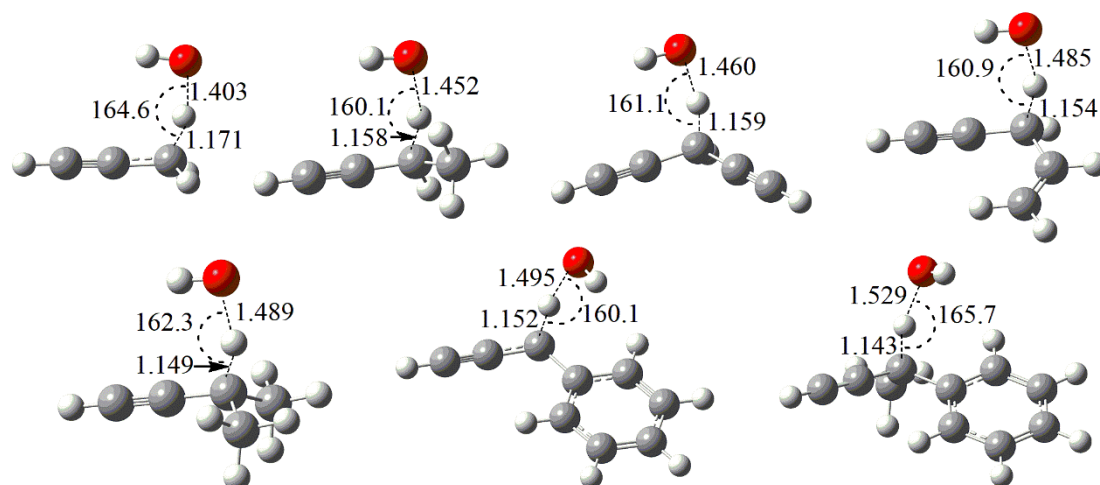


**Fig. 6.2** Optimized geometries (in Å and degrees) of TSs for the studied abstraction reactions by  $\dot{\text{O}}\text{H}$  radical at M06-2X/cc-pVTZ level. The geometry centers of TS for 1-pentyne are identical to that of 1-butyne, and thus not explicitly shown.

Unlike the simple TS structures for H-atom abstraction reactions of alkynes by  $\dot{\text{H}}$  atoms at the propargyl reaction sites, the TS structures of abstraction reactions by  $\dot{\text{O}}\text{H}$  radicals are more complex due to the interaction of oxygen atom with other functional groups in the reactant molecules. For the studied reactants of propyne, 1-butyne, 1-pentyne, penta-1,4-diyne, 4-penten-1-yne, and isopentyne, the  $\dot{\text{O}}\text{H}$  radical is nearly parallel along the  $\text{C}\equiv\text{C}$  triple bond of the reactants. However, for 3-phenyl-1-propyne and but-3-yn-2-ylbenzene, the  $\dot{\text{O}}\text{H}$  radical tends to locate above the benzene ring and the  $\dot{\text{O}}\text{H}$  radical is nearly parallel along the  $\text{C}-\text{C}$  bond connecting the phenyl group.

To further confirm the minimal structures corresponding to the global minima, Fig. 6.3 shows the hindrance potential of relaxed scans of the internal rotation of H atom in  $\dot{\text{O}}\text{H}$  radical for 1-butyne, 4-penten-1-yne, and 3-phenyl-1-propyne. Fig. 6.4 illustrates the Mulliken charge distributions [19] of the TSs for these three reactions. The relative energies between the highest and lowest structures are computed at the CCSD(T)/cc-pVTZ level of theory to validate the scanned results at the M06-2X/cc-pVTZ level of theory. It has been verified that the two theoretical methods can give similar energy curves and the deviations between CCSD(T)/cc-pVTZ and M06-2X/cc-pVTZ are within  $0.5 \text{ kcal mol}^{-1}$ .

As shown in Fig. 6.3, for the TS of H-atom abstraction reaction of 1-butyne by  $\dot{\text{O}}\text{H}$  radical, the energy difference between the lowest and highest energy conformations is  $1.23 \text{ kcal mol}^{-1}$ . The negative charge distributions of the two carbon atoms in the  $\text{C}\equiv\text{C}$  triple bond attract the H atom in  $\dot{\text{O}}\text{H}$  radical pointing to the  $\text{C}\equiv\text{C}$  triple bond resulting in the  $\text{O}-\text{H}$  bond parallel to the  $\text{C}\equiv\text{C}$  triple bond. The energy difference between the lowest and highest

energy conformations for 4-penten-1-yne and 3-phenyl-1-propyne are 1.48 and 1.46 kcal mol<sup>-1</sup>, respectively. The charge distribution of the C atom near the propargyl site in the C=C double bond (-0.062) is slightly larger than that in the C≡C triple bond (-0.086), which makes the  $\dot{\text{O}}\text{H}$  radical orient toward the C≡C triple bond. However, the strong negative charge distribution of the phenyl group in 3-phenyl-1-propyne attracts the  $\dot{\text{O}}\text{H}$  radical, shifting it towards the aromatic ring to form a more stable TS structure.

From Fig. 6.3, the most unstable TS structures of these three reactants are found when the H atom in  $\dot{\text{O}}\text{H}$  radical shifts toward the opposite sites along the C≡C triple bond. Similar trend is observed for the other reaction systems. Based on the above analysis, it can be concluded that the formation of the lowest energy conformations of the TSs for the studied reaction systems are mainly affected through the electron-withdrawing inductive effect by the surrounding groups around the reactivity center. Specifically, the lone pair of electrons of oxygen atom are attracted by the conjugated  $\pi$ -system of phenyl group which is similar to the mesomeric effect. Since the electron-withdrawing inductive effect (-I effect) of phenyl group is stronger than C=C double bond and C≡C triple bond, the  $\dot{\text{O}}\text{H}$  radical prefers to shift toward the aromatic ring to form a more stable TS structure. In addition, the delocalization effect of the C=C double bond of 4-penten-1-yne is less competitive compared with the C≡C triple bond, the TS structure of the former is expected to be less stable. Furthermore, due to the interaction between the reactants and  $\dot{\text{O}}\text{H}$  radical, reactant complexes (RCs) and product complexes (PCs) are formed via weakly hydrogen bond and IRC analysis results are adopted to determine the geometries of these complexes. The optimized geometries are provided as supplementary materials.

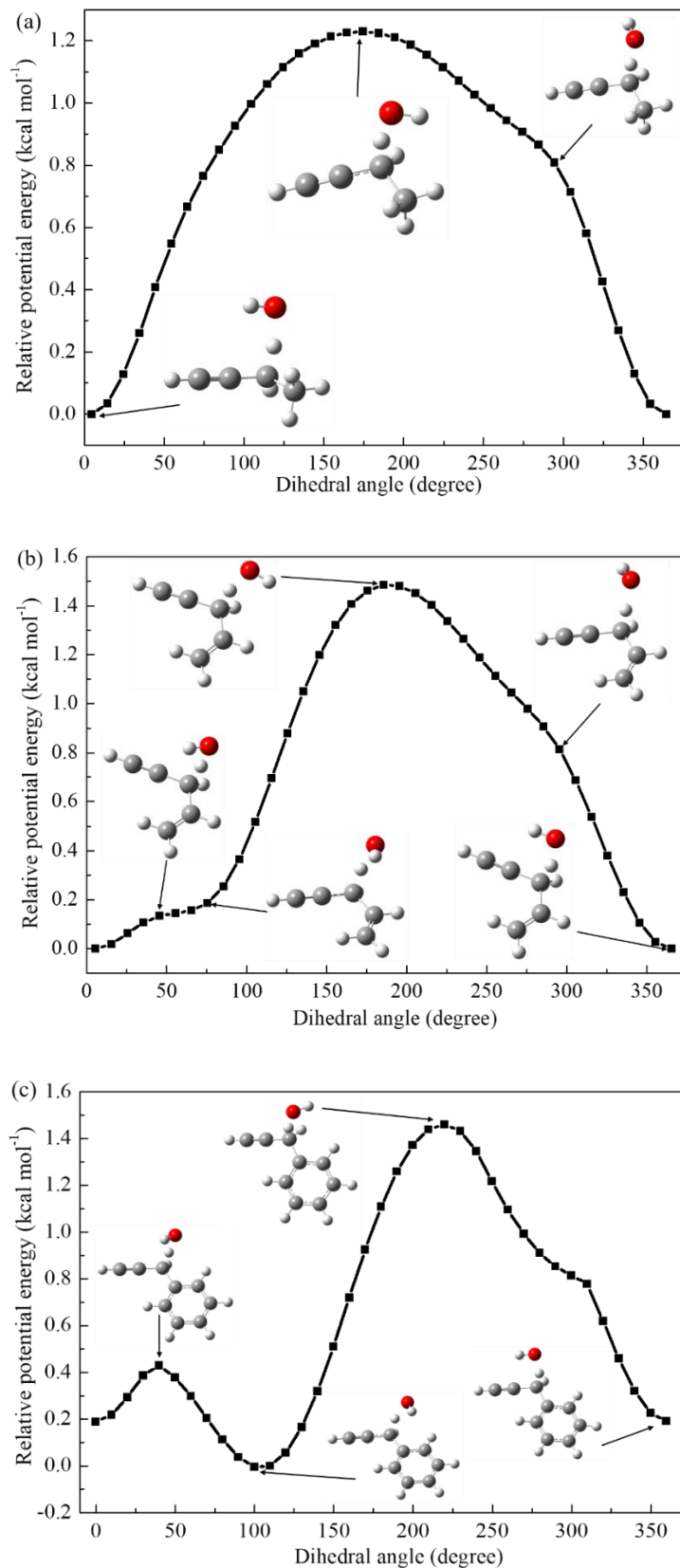


**Fig. 6.3** Relative potential energies of the internal rotation of H atom in  $\dot{\text{O}}\text{H}$  radical along the reaction center for 1-butyne (a), 4-penten-1-yne (b), and 3-phenyl-1-propyne (c), respectively.

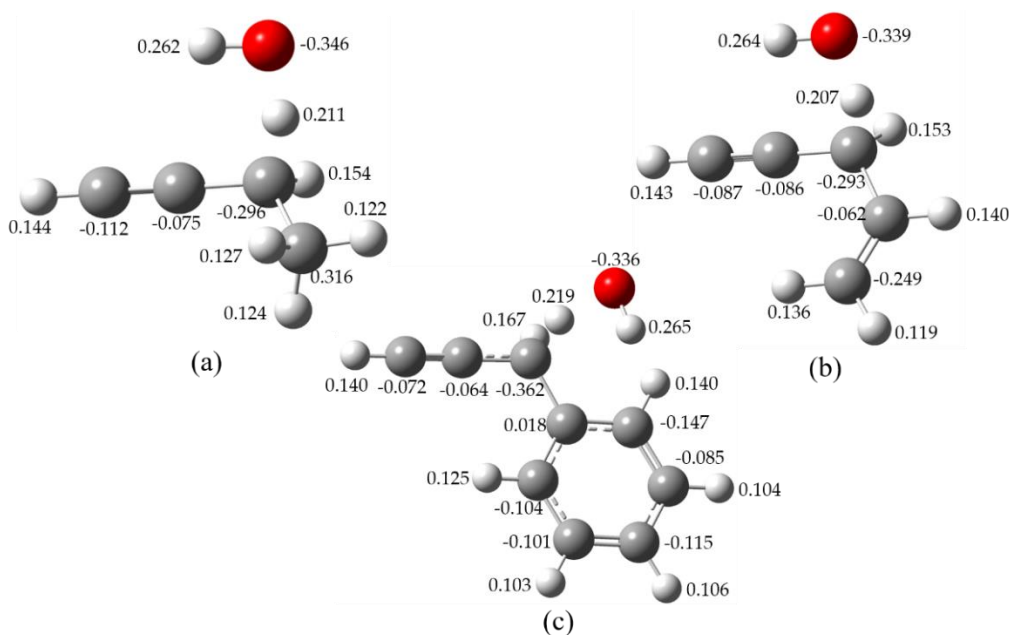


**Fig. 6.4** Mulliken charge distributions of the TSs for 1-butyne, 4-penten-1-yne, and 3-phenyl-1-propyne with OH, respectively.

## 2.2. Reaction Barriers and Enthalpies

The accuracy of the computed rate constants critically depends on the reliability of reaction barriers; thus, it is important to obtain reliable single-point energy results by employing high-level quantum chemistry methods. However, it is computationally prohibitive for the studied large reaction systems. Hence, we have adopted the accurate W1BD and CCSD(T)/CBS methods to benchmark a series of DFT functionals to select an appropriate DFT method, since different DFT functionals provide very different results for various chemical properties.

To verify the selected benchmark methods, the bond dissociation energies (BDEs) of acetylenic C–H bond and propargyl C–H bond for acetylene and propyne are computed first using W1BD and CCSD(T)/CBS methods as shown in Fig. 6.5. It can be seen that the computed BDEs for acetylenic C–H and propargyl C–H bonds by using the W1BD and CCSD(T) methods are in very good correlation with the recommended values by Luo et al. [6], indicating that the W1BD and CCSD(T)/CBS methods should be as accurate as benchmark methods. The BDE of propargyl C–H bond is lower than that of acetylenic C–H bond by 40 kcal mol<sup>-1</sup>, thus, abstraction reactions at the acetylenic site are very difficult. Hence, in this work, we just focus on the hydrogen abstraction channels at the propargyl C–H sites, and systematically investigate the reaction kinetics of structural variant effect on propargyl C–H reaction sites.

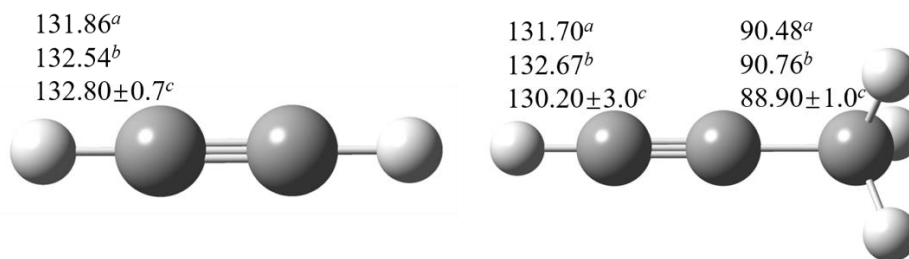


**Fig. 6.5** Computed BDEs (in kcal mol<sup>-1</sup>) for C–H bond in acetylene and propyne.

<sup>a</sup>W1BD method, <sup>b</sup>CCSD(T)/CBS method, <sup>c</sup>Recommended value from Luo [6].

Table 6.1 lists the computed reaction barriers by using high-level W1BD and CCSD(T)/CBS methods and different DFT methods with cc-pVTZ basis set for H-atom abstraction reactions of propyne and 1-butyne by  $\dot{\text{H}}$  and  $\dot{\text{O}}\text{H}$  radicals. The last column represents the absolute average errors compared with the benchmark results from W1BD method. From Table 6.1 it can be seen that the results via CCSD(T)/CBS method are in good correlation with those from accurate W1BD method. The absolute average error is 0.23 kcal mol<sup>-1</sup>, which is also in good accordance with the computed BDEs shown in Fig. 6.3, indicating that the two high-level methods can provide consistent reliable energy information for the studied reactions. Among the selected 13 DFT functionals, the M08-HX exhibits the best performance and the absolute average errors compared with W1BD and CCSD(T)/CBS methods are 0.36 and 0.24 kcal mol<sup>-1</sup>, respectively. The BMK functional shows good performance for abstraction reactions by  $\dot{\text{H}}$  atoms, but not for abstraction reactions by  $\dot{\text{O}}\text{H}$  radicals. Similarly, the MPW1K shows better performance only for H-atom abstraction reactions by  $\dot{\text{O}}\text{H}$  radical. Thus, one should be better to validate these DFT methods before directly apply them for these reaction systems to obtain energy information. In addition, to check the performance of M08-HX functional for 3-phenyl-1-propyne and but-3-yn-2-ylbenzene which contain phenyl group, the results calculated from M08-HX are compared with the results from CCSD(T)/cc-pVTZ level since CCSD(T)/cc-pVQZ level are still computationally prohibitive for a system with over 10 heavy atoms. For H-atom abstraction reactions of 3-phenyl-1-propyne by  $\dot{\text{H}}$  and  $\dot{\text{O}}\text{H}$  radicals, the computed reaction barriers are 5.14 and -0.22 kcal mol<sup>-1</sup> via CCSD(T)/cc-pVTZ method, while the results at M08-HX/cc-pVTZ level are 5.11 and -0.50 kcal mol<sup>-1</sup>, indicating that the M08-HX/cc-pVTZ level of theory is able to provide reasonable energy information for the studied reaction systems. In addition, from Table 6.1, the MUE of M08-HX functional relative to W1BD method is mainly affected by the H-atom abstraction from propyne by  $\dot{\text{H}}$  atoms. The uncertainty of rate constants calculated with reaction barriers at M08-HX level

are found to be within a factor of two compared with those at W1BD method over the studied temperature ranges. What is interesting to note is that a strong correlation of the reaction barriers at W1BD and M08-HX levels are fitted to  $\Delta E_{\text{W1BD}} = 1.0668 \times \Delta E_{\text{M08-HX}} + 0.0682$  with an adjusted R-squared value of 0.998. Such a correlation expression further reduces the MUE of the four reactions at M08-HX level to 0.075 kcal mol<sup>-1</sup> relative to the results via W1BD method. Based on this linear correlation, the M08-HX barrier heights for the studied systems are corrected to approach those calculated at W1BD level and listed in Table 6.2 and Table 6.3.

**Table 6.1** The computed reaction barriers using different methods for H-atom abstraction reactions of propyne and 1-butyne by  $\dot{\text{H}}$  and  $\dot{\text{O}}\text{H}$  radicals (units: kcal mol<sup>-1</sup>).

Methods		Propyne + $\dot{\text{H}}$	Propyne + $\dot{\text{O}}\text{H}$	1-Butyne + $\dot{\text{H}}$	1-Butyne + $\dot{\text{O}}\text{H}$	MUE <sup>b</sup>
Benchmark	W1BD	8.96	2.23	6.76	0.80	
	CCSD(T)/CBS	8.80	2.07	6.52	0.43	0.23
DFT <sup>a</sup>	M06-2X	9.27	1.17	7.19	-0.36	0.74
	B3LYP	2.58	-2.29	0.76	-3.83	5.38
	CAM-B3LYP	4.73	-1.18	2.71	-2.58	3.77
	BH&HLYP	6.47	4.38	4.54	2.74	2.20
	BMK	8.71	0.84	6.78	-0.57	0.76
	M05-2X	10.09	1.32	8.11	-0.18	1.09
	MN15	8.27	0.38	6.31	-1.16	1.24
	M08-HX	8.23	2.03	6.41	0.65	0.36
	MPW1K	6.98	2.54	4.96	1.13	1.11
	B2PLYP	6.30	0.37	4.20	-1.09	2.24
	$\omega$ B97X-D	7.41	-0.78	5.40	-2.35	2.27
	B2PLYPD3	5.93	-0.30	3.74	-1.90	2.82
	PBE0	4.78	-2.47	2.76	-3.69	4.34

<sup>a</sup> DFT calculations are performed with cc-pVTZ basis set.

<sup>b</sup> Mean unsigned error are relative to benchmark values from W1BD method.

Table 6.2 lists the computed reaction barriers and enthalpies at M08-HX/cc-pVTZ level for the studied H-atom abstraction reactions by  $\dot{\text{H}}$  atoms. With the use of this method, the computed potential energies for TSs, RCs and PCs of H-atom abstraction reactions by  $\dot{\text{O}}\text{H}$  radical are listed in Table 6.3 which are relative to their reactants, respectively. For the studied abstraction reaction of propyne with H atom, the predicted reaction barrier and enthalpies are compared with those by Bentz et al. [12] at the QCISD(T)/cc-pVTZ//B3LYP/6-31G(d) level of theory. The reaction barrier and enthalpy by M08-HX/cc-pVTZ in this work are 8.23 and -12.07 kcal mol<sup>-1</sup>, which are slightly lower than the results by Bentz et al. [12] by 0.92 and 0.65 kcal mol<sup>-1</sup>, respectively. While the computed barrier at M08-HX/cc-pVTZ level in this work is much closer to the results from Wang et al. by using the composite G3 method [20]. Compared with those obtained at W1BD and

CCSD(T)/CBS methods in this work, the predicted barrier with a value of 8.67 kcal mol<sup>-1</sup> by Miller et al. [11] at the QCISD(T)/inf//B3LYP/6-311++G(d,p) level of theory is quite close to the present estimation, while the reaction barrier by Bentz et al. [12] is higher by 0.19 and 0.35 kcal mol<sup>-1</sup>. The energy barrier and enthalpy for the H-atom abstraction reaction of propyne by  $\dot{\text{O}}\text{H}$  are 2.00 and -26.31 kcal mol<sup>-1</sup> at M08-HX/cc-pVTZ level, which are also in good agreement with the values of 2.00 and -25.16 kcal mol<sup>-1</sup> which are computed at the UCCSD(T)-F12b/cc-PVQZ-F12 level [15].

From Table 6.2 and 6.3, it can be seen that the average reaction barrier and enthalpy for H-atom abstraction reactions by  $\dot{\text{O}}\text{H}$  radicals are lower than those for abstraction by  $\dot{\text{H}}$  atoms by values of 5.62 and 14.24 kcal mol<sup>-1</sup>, respectively. Hence, the H-atom abstraction reactions of alkynes by  $\dot{\text{O}}\text{H}$  radicals are kinetically more favored than those by  $\dot{\text{H}}$  atoms. The structural nature of the alkynes tends to show similar effect on the reaction barriers and enthalpies of H-atom abstraction reactions by  $\dot{\text{H}}$  atoms and  $\dot{\text{O}}\text{H}$  radicals. For non-aromatic alkynes, the abstraction reaction at the tertiary (3°) propargyl C–H site in isopentyne is the easiest which has the lowest relative reaction barrier of -0.39 kcal mol<sup>-1</sup>, followed by the secondary (2°) propargyl C–H site in 1-butyne, then the primary (1°) propargyl C–H site in propyne is the most difficult. For the two propargyl C–H sites in 3-phenyl-1-propyne and but-3-yn-2-ylbenzene molecules involving phenyl group, the same trend is also observed that the abstraction reaction at tertiary propargyl C–H site in but-3-yn-2-ylbenzene is easier to occur than that at the secondary propargyl C–H site in 3-phenyl-1-propyne. Thus, the trend for reaction barriers of H-atom abstraction reactions by  $\dot{\text{H}}$  and  $\dot{\text{O}}\text{H}$  radicals is  $E_{0\text{K}}(3^\circ) < E_{0\text{K}}(2^\circ) < E_{0\text{K}}(1^\circ)$ . Compared with the results of 1-butyne and 1-pentyne, the length of alkyne chains has negligible effect on the H-atom abstraction reactions by  $\dot{\text{H}}$  atoms, but it shows moderate effect on the H-atom abstraction reactions by  $\dot{\text{O}}\text{H}$  radicals. The reaction barriers of H-atom abstraction reactions by  $\dot{\text{O}}\text{H}$  radicals decrease with the growth of the chain length. For the five secondary propargyl C–H sites in 1-butyne, 1-pentyne, penta-1,4-diyne, 4-penten-1-yne and 3-phenyl-1-propyne, the existences of vinyl group, phenyl group and acetylenic group all increase the reactivity compared with 1-butyne and 1-pentyne by the following order: vinyl group > phenyl group > acetylenic group. On the other hand, this also means that abstraction reaction at the allylic C–H site is easier than that at the benzyl site, which is easier than that at propargyl site considering the reaction sites connected the other same groups. Table 6.3 also shows that for the studied H-atom abstraction reactions by  $\dot{\text{O}}\text{H}$  radical, weak van der Waals RCs and PCs are formed at the entrance and exit channels. The

energies of RCs are lower than the reactants by 3.97–5.58 kcal mol<sup>-1</sup>, while the PCs are lower than the products by 3.22–4.30 kcal mol<sup>-1</sup> for the studied reactions.

**Table 6.2** Reaction barriers and enthalpies for different alkynes reacting with H atoms at M08-HX/cc-pVTZ level (kcal mol<sup>-1</sup>). All the energies are relative to the reactants.

Reactions	Barriers <sup>a</sup>	Enthalpies	BDE
	8.23 (8.85)	-12.07	
propyne + $\dot{\text{H}}$	9.15 <sup>b</sup>	-12.72 <sup>b</sup>	89.74
	8.40 <sup>c</sup>	-14.00 <sup>c</sup>	
	8.67 <sup>d</sup>	-12.73 <sup>d</sup>	
1-butyne + $\dot{\text{H}}$	6.41 (6.91)	-15.56	86.26
1-pentyne + $\dot{\text{H}}$	6.26 (6.75)	-14.59	87.23
penta-1,4-diyne + $\dot{\text{H}}$	5.69 (6.14)	-23.27	78.54
4-penten-1-yne + $\dot{\text{H}}$	4.56 (4.93)	-25.75	76.07
isopentyne + $\dot{\text{H}}$	5.05 (5.46)	-18.26	83.55
3-phenyl-1-propyne + $\dot{\text{H}}$	5.11 (5.52)	-23.64	78.17
but-3-yn-2-ylbenzene + $\dot{\text{H}}$	4.48 (4.85)	-25.87	75.94

<sup>a</sup> The values in parentheses represent the corrected barriers using linear correlation.

<sup>b</sup> Results were performed at QCISD(T)/cc-pVTZ//B3LYP/6-31G(d) level of theory by Bentz et al. [12].

<sup>c</sup> Results were performed at G3//UB3LYP/6-31G(d) level of theory by Wang et al. [20].

<sup>d</sup> Results were computed at QCISD(T)/inf//B3LYP/6-311++G(d,p) level by Miller et al. [11].

**Table 6.3** Potential energies for the studied alkynes with  $\dot{\text{O}}\text{H}$  at M08-HX/cc-pVTZ level (kcal mol<sup>-1</sup>). All the energies are relative to the reactants.

Reactions	Reactants	RC	Barriers <sup>a</sup>	PC	Products
propyne + $\dot{\text{O}}\text{H}$	0.00	-4.15	2.03 (2.23)	-29.53	-26.31
1-butyne + $\dot{\text{O}}\text{H}$	0.00	-4.40	0.65 (0.76)	-33.63	-29.80
1-pentyne + $\dot{\text{O}}\text{H}$	0.00	-5.11	-0.07 (-0.01)	-33.79	-28.83
penta-1,4-diyne + $\dot{\text{O}}\text{H}$	0.00	-3.97	0.42 (0.52)	-40.99	-37.52
4-penten-1-yne + $\dot{\text{O}}\text{H}$	0.00	-5.58	-0.96 (-0.96)	-43.75	-39.99
isopentyne + $\dot{\text{O}}\text{H}$	0.00	-4.51	-0.39 (-0.35)	-36.54	-32.50
3-phenyl-1-propyne + $\dot{\text{O}}\text{H}$	0.00	-4.62	-0.50 (-0.47)	-41.15	-37.88
but-3-yn-2-ylbenzene + $\dot{\text{O}}\text{H}$	0.00	-4.31	-1.03 (-1.03)	-44.41	-40.11

<sup>a</sup> The values in parentheses represent the corrected barriers using linear correlation.

### 2.3. Rate Constants

For the abstraction reactions by  $\dot{\text{O}}\text{H}$  radical, rate constants calculations need to consider the formed Van der Waals complexes (RCs and PCs), and two-TS models are usually employed [21, 22]. However, a series of previous studies indicated that this model only

showed significant effect at low temperatures below 200 K [21-26]. For the interested combustion relevant temperature range of 500–2500 K, the rate-limiting step is the inner TSs. Furthermore, the formed RCs are unstable at high temperatures. Hence, the abstraction reactions by  $\dot{\text{H}}$  and  $\dot{\text{O}}\text{H}$  radicals are all computed by using canonical TST with 1-D hindered rotor approximations for the treatment of internal rotations. The Fourier-series are used for fitting the scanned results of international rotations. To obtain rate constants with minimal uncertainty, the corrected M08-HX barrier height are adopted.

The high-pressure limiting rate constants ( $k_{\infty}$ ) of H-atom abstraction reaction of propyne by  $\dot{\text{H}}$  and  $\dot{\text{O}}\text{H}$  radicals in this work are compared with available literature data and shown in Figs. 6.6 and 6.7, respectively. From Fig. 6.6, the rate constants obtained in this work are in good correlation with the results by Miller et al. [11] at the QCISD(T)/inf//B3LYP/6-311++G(d,p) level of theory over the studied temperature ranges. The rate constants by Wang et al. [20] tended to underestimate the rate constants at low temperature. The predicted results show good agreement with the rate constants derived from a heated single pulse-shock tube at temperatures of 874-1196 K by Rosado-Reyes et al. [13]. For the H-atom abstraction reaction of propyne with  $\dot{\text{O}}\text{H}$ , Hansen et al. [14] estimated the rate constants for this reaction and used it in kinetic modeling. The deviations of the rate constants between present results and Zador's calculations [15] are within a factor of two and decrease with increasing temperature. The H-atom abstraction reaction of propyne by  $\dot{\text{O}}\text{H}$  radical is in fact important at temperatures over 1000 K and it can be seen that the three different sets of rate constants for this reaction at the interested temperature ranges are close to each other. Overall, the results computed at M08-HX level are in good agreement with literature data, but can significantly reduce the computational cost to obtain accurate reaction barriers compared with other expensive W1BD or CCSD(T) methods.

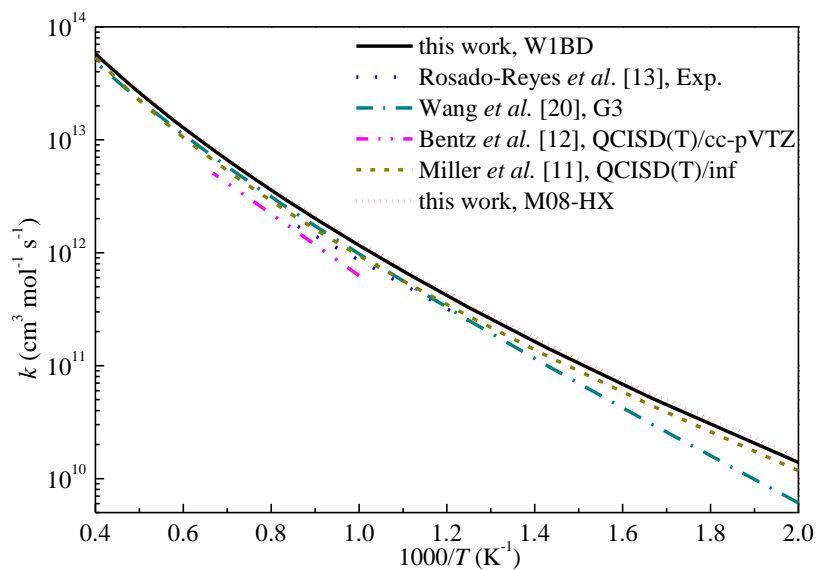


**Fig. 6.6** Computed rate constants for the H-atom abstraction reaction of propyne with  $\dot{\text{H}}$  at the propargyl site.

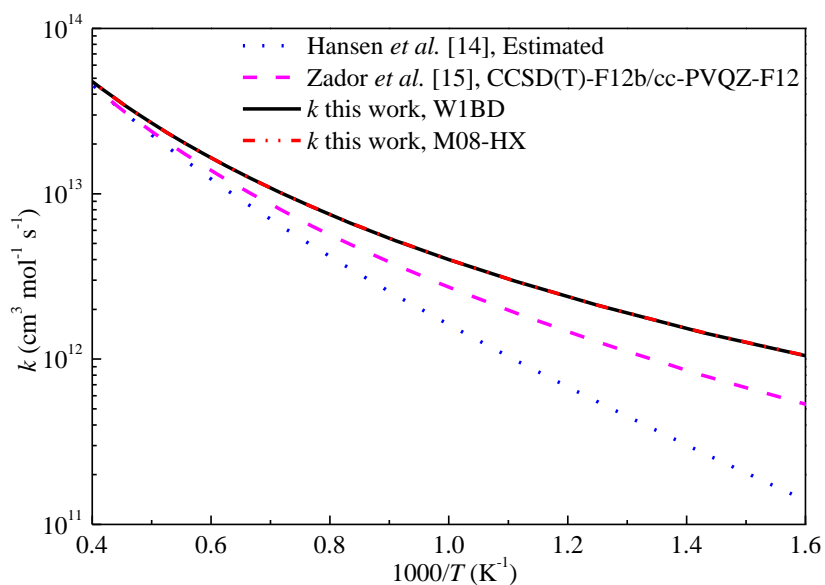


**Fig. 6.7** Computed rate constants for the H-atom abstraction reaction of propyne with  $\dot{\text{O}}\text{H}$  at the propargyl site.

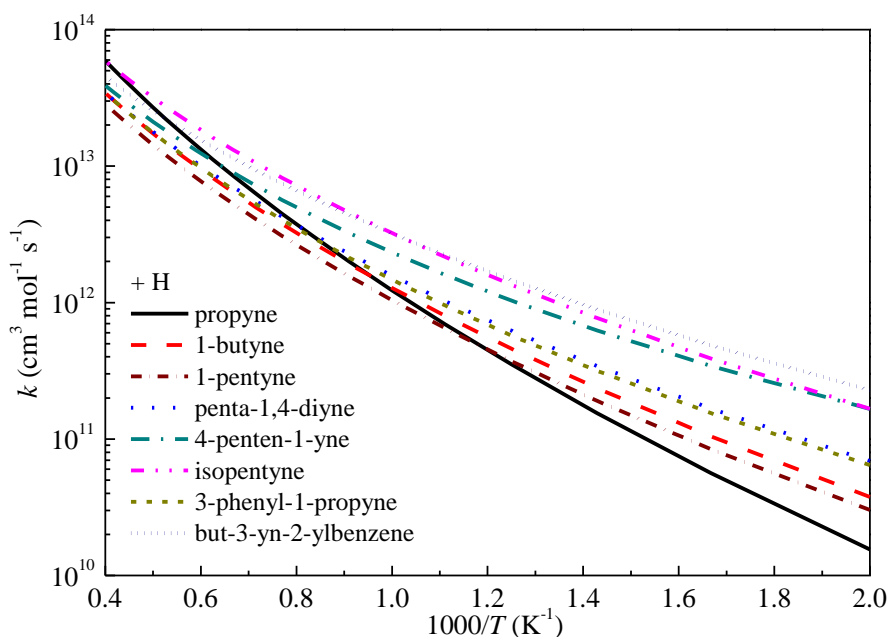


**Fig. 6.8** Computed rate constants for the abstraction reactions with  $\dot{\text{H}}$  at the propargyl site.

Fig. 6.8 compares the rate constants as a function of temperature for the studied H-atom abstraction reactions by  $\dot{\text{H}}$  atoms. The TSs for H-atom abstraction reactions from eight reactants by  $\dot{\text{H}}$  atoms and/or  $\dot{\text{O}}\text{H}$  radicals can be divided into three types: primary propargyl radical (propyne), secondary propargyl radicals (1-butyne, 1-pentyne, penta-1,4-diyne, 4-penten-1-yne and 3-phenyl-1-propyne) and tertiary propargyl radicals (isopentyne and but-3-yn-2-ylbenzene). As can be seen from the graph, the  $k_{\infty}$  of the tertiary propargyl radicals are higher than those of the secondary propargyl radicals. For the five secondary propargyl radicals, in comparison with 1-butyne, the trend is  $k_{\infty}(\text{1-pentyne}) < k_{\infty}(\text{1-butyne}) < k_{\infty}(\text{3-phenyl-1-propyne}) \approx k_{\infty}(\text{penta-1,4-diyne}) < k_{\infty}(\text{4-penten-1-yne})$  which suggests the positive (+) or negative (-) influence of different groups on the reaction activity is:  $-\text{C}_2\text{H}_5$  (-)  $< -\text{CH}_3$  (+)  $< -\text{C}_6\text{H}_5 \approx -\text{C}_2\text{H} < -\text{C}_2\text{H}_3$ . In addition, the  $-\text{C}_2\text{H}_3$  group tends to show stronger influence on the reaction activity especially at low temperature since the deviation between  $k_{\infty}(\text{penta-1,4-diyne})$  and  $k_{\infty}(\text{4-penten-1-yne})$  is larger than those between the other secondary propargyl radicals.

The  $k_{\infty}$  of the primary propargyl radical (propyne) tends to show different trend with that of the secondary propargyl radicals which is slower at low temperatures, but overtaking the  $k_{\infty}$  of secondary propargyl radicals at high temperatures. For the tertiary propargyl radicals,  $k_{\infty}(\text{isopentyne})$  is slower than that of but-3-yn-2-ylbenzene at temperatures lower than 1000 K which is consistent with the trend of the secondary propargyl radicals that phenyl group

has stronger positive influence on the reaction reactivity. However, as the temperature increases,  $k_{\infty}$ (but-3-yn-2-ylbenzene) is overtaken by  $k_{\infty}$ (isopentyne).

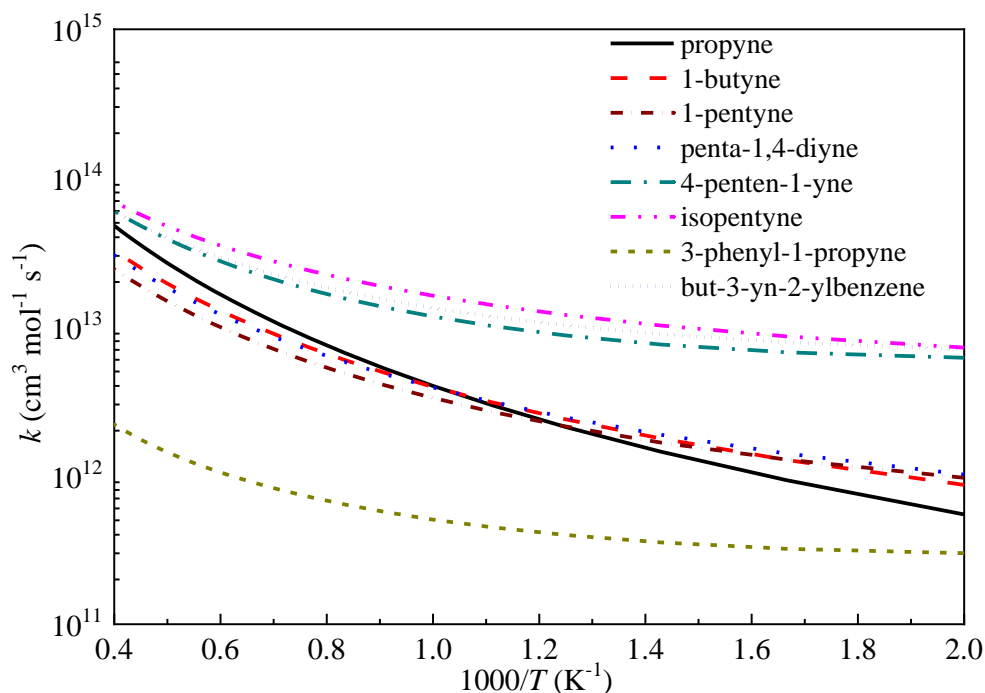


**Fig. 6.9** Computed rate constants for the abstraction reactions with  $\dot{\text{O}}\text{H}$  at the propargyl site.

Unlike the H-atom abstraction reactions of the studied alkyne molecules by  $\dot{\text{H}}$  atoms, the rate constants by  $\dot{\text{O}}\text{H}$  radicals exhibit large differences. Fig. 6.9 shows that the rate constant of a tertiary propargyl radical (isopentyne) is the largest over the whole temperature range, while the  $k_{\infty}$  of a secondary propargyl radical (3-phenyl-1-propyne) is the smallest. It can be clearly seen from this graph that the tertiary propargyl radicals (isopentyne and but-3-yn-2-ylbenzene) have higher  $k_{\infty}$  than secondary propargyl radicals which is consistent with H-atom abstraction by H atom. The deviations between the primary and secondary propargyl C–H sites with alkyl groups (propyne, 1-butyne and 1-pentyne) are small which are within 3 times over the whole temperature range. For secondary propargyl radicals, (1) the  $k_{\infty}$  of penta-1,4-diyne is similar to that of 1-butyne which may suggest the equivalent influence of methyl and acetylenic group on rate constant calculation for H-atom abstraction reactions of alkynes by  $\dot{\text{O}}\text{H}$  radicals; (2) the vinyl group in 4-penten-1-yne significantly increases the rate constants compared with  $k_{\infty}$  of 1-butyne. (3) the phenyl group in 3-phenyl-1-propyne significantly decreases the rate constants compared with  $k_{\infty}$  of 1-butyne. Hence, the methyl, vinyl and acetylenic groups in secondary propargyl radicals tend to increase the reactivity of H-atom abstraction reaction by  $\dot{\text{O}}\text{H}$  radical compared with the

primary propargyl radicals, the trends of influence for these three groups are  $-C_2H \approx -CH_3 < -C_2H_3$ . While phenyl group tends to decrease the reactivity of H-atom abstraction reaction by  $\dot{O}H$  radical. To facilitate kinetic modeling studies, the computed rate constants are fitted into the modified Arrhenius format as shown in Table 6.4.

**Table 6.4** Fitted Arrhenius coefficients of the studied reactions in  $k(T) = AT^n \exp(-E_a/RT)$ .

( $A$ :  $\text{cm}^3 \text{mol}^{-1} \text{s}^{-1}$ ;  $E_a$ :  $\text{cal mol}^{-1}$ ).

Alkyne Molecules	+ $\dot{H}$			+ $\dot{O}H$		
	$A$	$n$	$E_a$	$A$	$n$	$E_a$
propyne	$6.40 \times 10^7$	1.94	7042	$4.71 \times 10^5$	2.38	986
1-butyne	$1.83 \times 10^7$	1.97	4921	$4.52 \times 10^5$	2.31	-32
1-pentyne	$2.41 \times 10^7$	1.92	5191	$1.78 \times 10^5$	2.38	-639
penta-1,4-diyne	$1.70 \times 10^7$	1.97	4291	$2.51 \times 10^5$	2.37	-427
4-penten-1-yne	$9.31 \times 10^6$	2.03	3203	$2.45 \times 10^5$	2.42	-1959
isopentyne	$4.20 \times 10^7$	1.91	3856	$1.82 \times 10^7$	1.91	-1012
3-phenyl-1-propyne	$1.03 \times 10^7$	2.03	4331	$1.04 \times 10^4$	2.39	-2354
but-3-yn-2-ylbenzene	$3.75 \times 10^7$	1.87	3110	$1.38 \times 10^6$	2.20	-1745

### 3. Computational Methodology

The quantum chemistry calculations in this paper are carried out using Gaussian 09 software [27]. Geometry optimization and frequency analysis are performed at M06-2X/cc-pVTZ level [28]. The resulting frequencies and zero-point energies (ZPEs) are scaled by 0.96 and 0.97, respectively. For the treatment of internal rotations, relaxed potential energy scans are performed as a function of the corresponding dihedral angle with an interval of  $10^\circ$  at M06-2X/cc-pVTZ level. The scanned results are then fitted to a Fourier-series used for rate constant calculations. For the transition state structures, intrinsic reaction coordinate (IRC) calculations [29] are carried out to make sure the saddle points connect the desired reactants and products. Moreover, the IRC results for abstraction reactions by  $\dot{O}H$  radical are also used to determine the structures of the formed reactant complex (RC) and product complex (PC) at the entrance and exit channels.

To obtain reliable rate constants, single-point energy calculations should be performed with high-level quantum chemistry methods. For the studied reaction systems ( $C_3 - C_{10}$ ) in this work, high-level CCSD(T)/CBS or very accurate composite W1BD methods can only be used for small systems since the largest molecule (but-3-yn-2-ylbenzene) contains 10 carbon atoms. Considering the trade-off between accuracy and computational cost, W1BD and CCSD(T)/CBS methods are employed for the abstraction reactions of propyne and 1-butyne as benchmark results to choose an appropriate DFT method for larger reaction systems. The T1 diagnostics [30] are complemented to CCSD(T) calculations to check the multi-reference

nature of the studied reactions. Generally, a single-reference coupled cluster calculation for closed-shell species is considered to be reliable if the  $T1$  diagnostic value is within 0.020 [30, 31]. For open-shell systems, a higher threshold value for the  $T1$  diagnostic up to 0.044 can be acceptable [32]. For all the species during open-shell CCSD(T) calculations, it is found that all  $T1$  diagnostics values are within 0.025, which indicates that single-reference methods are adequate for the studied reactions in this work.

To select an appropriate DFT method, the computed reaction barriers using 13 typical DFT methods including B3LYP [33, 34], BH&HLYP [35], B2PLYP [36], B2PLYPD3 [37], CAM-B3LYP [38], BMK [39], M05-2X [40], MN15 [41], MPW1K [42], PBE0 [43],  $\omega$ B97X-D [44], M08HX [45] and M06-2X [28] with cc-pVTZ basis set are compared with the benchmark results via W1BD and CCSD(T)/CBS methods. In addition, basis set effect on the computed results are also examined by using M06-2X functional with cc-pVTZ, cc-pVQZ, aug-cc-pVTZ and aug-cc-pVQZ basis set [46]. It is found that the basis sets show small influence on reaction barriers for propyne and 1-butyne with  $\dot{\text{H}}$  and  $\dot{\text{O}}\text{H}$  radicals and the deviations are less than 0.40 kcal mol<sup>-1</sup>. Thus, all the DFT calculations are performed using cc-pVTZ basis set unless otherwise mentioned.

Based on quantum chemistry calculations, reaction rate constants of the hydrogen abstraction reactions are computed using the canonical transition state theory. The quantum mechanical tunneling corrections are included by using unsymmetrical Eckart barrier model [47] for reactions with positive barrier heights, while the Wigner method [48] is adopted for some H-atom abstraction reactions by  $\dot{\text{O}}\text{H}$  radicals with slight negative barrier heights. It has been shown that the two methods can provide very close tunneling coefficients under the studied temperature ranges [49, 50]. The rate constants are computed at temperatures from 500 to 2500 K in increments of 100 K and are fitted into the modified Arrhenius equation as  $k(T) = AT^n \exp(-E_a/RT)$ , in which  $A$  is the Arrhenius pre-exponential factor,  $E_a$  is the barrier height, and  $n$  is the temperature exponent representing the deviation from the standard Arrhenius equation. The fitted rate coefficients listed in Table 6.4 can be directly used for kinetic modeling studies. The rate constant calculations are performed using MultiWell software [51].

#### 4. Conclusions

This work reports a systematic ab initio and chemical kinetic study of H-atom abstraction reactions from a series of alkyne molecules by  $\dot{\text{H}}$  atoms and  $\dot{\text{O}}\text{H}$  radicals at the propargyl C–H site. Different types of propargyl C–H sites and the effect of methyl, ethyl,

vinyl, phenyl and acetylenic groups in the studied alkyne molecules on reaction reactivity are considered. Geometry optimizations for all species are performed at M06-2X/cc-pVTZ level of theory and each optimized geometry is confirmed to be the lowest energy conformation by scanning all the relevant internal rotational degrees of freedom. It is found that the TS structures of the H-atom abstraction reactions by  $\dot{\text{H}}$  atoms are similar, while the existence of vinyl, phenyl and acetylenic groups greatly affects the TS structures of the H-atom abstraction reactions by  $\dot{\text{O}}\text{H}$  radicals due to the electron-withdrawing inductive effect.

To obtain reliable energy information, accurate W1BD and CCSD(T)/CBS methods are used as benchmark for small reaction systems toward the selection of accurate DFT functionals for large reaction systems. The effect of the basis set used for the DFT calculations was considered and it was found that the M08-HX/cc-pVTZ method exhibits a better performance among the selected DFT functionals. General trends of the reaction barriers of the H-atom abstraction reactions from these alkyne molecules by  $\dot{\text{H}}$  and  $\dot{\text{O}}\text{H}$  radicals have been outlined. The computed results reveal that the reaction barriers decrease as the nature of the abstracted H atom at the propargyl C–H site from primary through secondary to tertiary. The existence of vinyl, phenyl and acetylenic groups also decreases the energy barriers with the following order: vinyl > phenyl > acetylenic.

Based on the quantum chemistry calculations, rate constants are computed using the canonical transition state theory with tunneling correction and the treatment of internal rotations. The computed rate constants for abstraction reactions of propyne by  $\dot{\text{H}}$  and  $\dot{\text{O}}\text{H}$  radicals are compared with literature data and show good agreement. The TSs for H-atom abstraction reactions from eight alkynes by  $\dot{\text{H}}$  and/or  $\dot{\text{O}}\text{H}$  radicals are further divided into three types: primary propargyl, secondary propargyl and tertiary propargyl radicals. The high-pressure limiting rate constants of the tertiary propargyl radicals are consistently faster than those of the secondary propargyl radicals for H-atom abstraction reactions by  $\dot{\text{H}}$  and  $\dot{\text{O}}\text{H}$  radicals. For the secondary propargyl radicals, the ability of different groups on increasing reaction activity of H-atom abstraction reactions by H atom is:  $-\text{C}_2\text{H}_5$  (negative) <  $-\text{CH}_3$  <  $-\text{C}_6\text{H}_5 \approx -\text{C}_2\text{H} < -\text{C}_2\text{H}_3$ , while the trend for H-atom abstraction reactions by OH atom is  $-\text{C}_6\text{H}_5$  (negative) <  $-\text{C}_2\text{H} \approx -\text{CH}_3 < -\text{C}_2\text{H}_3$ . Finally, the computed rate constants are fitted into the three-parameter Arrhenius expressions to facilitate kinetic modeling studies. Compared with literature studies on small reactions in this work, the employed ab initio calculations together with statistical transition state theory provide an accurate description of the chemical kinetics of the studied abstraction reactions. However, the subsequent reactions of the formed radicals of alkyne molecules can exhibit complex reaction pathways, which may need direct

dynamics to uncover [52]. Currently, direct dynamics is limited to small polyatomic systems because it still depends on accurate potential energy surfaces (PES) from ab initio calculations. The benchmark results of DFT methods in this work also provide fundamental information to select efficient method for PES constructions used in future direct dynamics studies on these reaction systems.

### **Supporting Information**

Optimized geometries for the studied abstraction reactions.

### **Acknowledgments**

This research was funded by National Natural Science Foundation of China, grant number 21403296 and International Scientific Cooperation Projects of Key R&D Programs in Shanxi Province, grant number 201803D421101. We thank Supercomputing Center in Shenzhen and The Irish Centre for High-End Computing (ICHEC) for providing the computational resources (ngche064c and ngche073c).

## References

- [1] J.M. Simmie, Detailed chemical kinetic models for the combustion of hydrocarbon fuels, *Progress in energy and combustion science* 29 (2003) 599-634.
- [2] H. Wang, Formation of nascent soot and other condensed-phase materials in flames, *Proceedings of the Combustion institute* 33 (2011) 41-67.
- [3] H.J. Curran, Developing detailed chemical kinetic mechanisms for fuel combustion, *Proceedings of the Combustion Institute* 37 (2019) 57-81.
- [4] S.J. Klippenstein, From theoretical reaction dynamics to chemical modeling of combustion, *Proceedings of the Combustion Institute* 36 (2017) 77-111.
- [5] R. Dorel, A.M. Echavarren, Gold (I)-catalyzed activation of alkynes for the construction of molecular complexity, *Chemical reviews* 115 (2015) 9028-9072.
- [6] Y.-R. Luo, *Handbook of bond dissociation energies in organic compounds*, CRC press 2002.
- [7] R.D. Kern, K. Xie, Shock tube studies of gas phase reactions preceding the soot formation process, *Progress in energy and combustion science* 17 (1991) 191-210.
- [8] K. Wang, S.M. Villano, A.M. Dean, Reactivity–structure-based rate estimation rules for alkyl radical H atom shift and alkenyl radical cycloaddition reactions, *The Journal of Physical Chemistry A* 119 (2015) 7205-7221.
- [9] K. Wang, S.M. Villano, A.M. Dean, Fundamentally-based kinetic model for propene pyrolysis, *Combustion and Flame* 162 (2015) 4456-4470.
- [10] K. Wang, S.M. Villano, A.M. Dean, Reactions of allylic radicals that impact molecular weight growth kinetics, *Physical Chemistry Chemical Physics* 17 (2015) 6255-6273.
- [11] J.A. Miller, J.P. Senosiain, S.J. Klippenstein, Y. Georgievskii, Reactions over multiple, interconnected potential wells: Unimolecular and bimolecular reactions on a C<sub>3</sub>H<sub>5</sub> potential, *The Journal of Physical Chemistry A* 112 (2008) 9429-9438.
- [12] T. Bentz, B.R. Giri, H. Hippler, M. Olzmann, F. Striebel, M. Szöri, Reaction of hydrogen atoms with propyne at high temperatures: An experimental and theoretical study, *The Journal of Physical Chemistry A* 111 (2007) 3812-3818.
- [13] C.M. Rosado-Reyes, J.A. Manion, W. Tsang, Kinetics of the thermal reaction of H atoms with propyne, *The Journal of Physical Chemistry A* 114 (2010) 5710-5717.
- [14] N. Hansen, J.A. Miller, P.R. Westmoreland, T. Kasper, K. Kohse-Höinghaus, J. Wang, T.A. Cool, Isomer-specific combustion chemistry in allene and propyne flames, *Combustion and flame* 156 (2009) 2153-2164.
- [15] J. Zádor, J.A. Miller, Adventures on the C<sub>3</sub>H<sub>5</sub>O potential energy surface: OH<sup>+</sup> propyne, OH<sup>+</sup> allene and related reactions, *Proceedings of the Combustion Institute* 35 (2015) 181-188.
- [16] J.P. Senosiain, S.J. Klippenstein, J.A. Miller, Oxidation pathways in the reaction of diacetylene with OH radicals, *Proceedings of the Combustion Institute* 31 (2007) 185-192.
- [17] E.C. Barnes, G.A. Petersson, J.A. Montgomery Jr, M.J. Frisch, J.M.L. Martin, Unrestricted coupled cluster and Brueckner doubles variations of W1 theory, *Journal of chemical theory and computation* 5 (2009) 2687-2693.
- [18] C.F. Goldsmith, W.H. Green, S.J. Klippenstein, Role of O<sub>2</sub><sup>+</sup> QOOH in

low-temperature ignition of propane. 1. Temperature and pressure dependent rate coefficients, *The Journal of Physical Chemistry A* 116 (2012) 3325-3346.

[19] R.S. Mulliken, Electronic Population Analysis on LCAO–MO Molecular Wave Functions. I, *The Journal of Chemical Physics* 23 (1955) 1833-1840.

[20] B. Wang, H. Hou, Y. Gu, Mechanism and rate constant of the reaction of atomic hydrogen with propyne, *The Journal of Chemical Physics* 112 (2000) 8458-8465.

[21] E.E. Greenwald, S.W. North, Y. Georgievskii, S.J. Klippenstein, A two transition state model for radical– molecule reactions: A case study of the addition of OH to C<sub>2</sub>H<sub>4</sub>, *The Journal of Physical Chemistry A* 109 (2005) 6031-6044.

[22] V.S. Bharadwaj, S. Vyas, S.M. Villano, C.M. Maupin, A.M. Dean, Unravelling the impact of hydrocarbon structure on the fumarate addition mechanism—a gas-phase ab initio study, *Physical Chemistry Chemical Physics* 17 (2015) 4054-4066.

[23] E.E. Greenwald, S.W. North, Y. Georgievskii, S.J. Klippenstein, A Two Transition State Model for Radical– Molecule Reactions: Applications to Isomeric Branching in the OH– Isoprene Reaction, *The Journal of Physical Chemistry A* 111 (2007) 5582-5592.

[24] H. Ning, D. Liu, J. Wu, L. Ma, W. Ren, A. Farooq, A theoretical and shock tube kinetic study on hydrogen abstraction from phenyl formate, *Physical Chemistry Chemical Physics* 20 (2018) 21280-21285.

[25] Q.-D. Wang, Z.-H. Ni, Theoretical and kinetic study of the hydrogen atom abstraction reactions of unsaturated C<sub>6</sub> methyl esters with hydroxyl radical, *Chemical Physics Letters* 650 (2016) 119-125.

[26] Q.-D. Wang, M.-M. Sun, J.-H. Liang, Reaction Mechanisms and Kinetics of the Hydrogen Abstraction Reactions of C<sub>4</sub>–C<sub>6</sub> Alkenes with Hydroxyl Radical: A Theoretical Exploration, *International journal of molecular sciences* 20 (2019) 1275.

[27] M.J. Frisch, G.W. Trucks, H.B. Schlegel, G.E. Scuseria, M.A. Robb, J.R. Cheeseman, G. Scalmani, V. Barone, G.A. Petersson, H. Nakatsuji, X. Li, M. Caricato, A.V. Marenich, J. Bloino, B.G. Janesko, R. Gomperts, B. Mennucci, H.P. Hratchian, J.V. Ortiz, A.F. Izmaylov, J.L. Sonnenberg, Williams, F. Ding, F. Lipparini, F. Egidi, J. Goings, B. Peng, A. Petrone, T. Henderson, D. Ranasinghe, V.G. Zakrzewski, J. Gao, N. Rega, G. Zheng, W. Liang, M. Hada, M. Ehara, K. Toyota, R. Fukuda, J. Hasegawa, M. Ishida, T. Nakajima, Y. Honda, O. Kitao, H. Nakai, T. Vreven, K. Throssell, J.A. Montgomery Jr., J.E. Peralta, F. Ogliaro, M.J. Bearpark, J.J. Heyd, E.N. Brothers, K.N. Kudin, V.N. Staroverov, T.A. Keith, R. Kobayashi, J. Normand, K. Raghavachari, A.P. Rendell, J.C. Burant, S.S. Iyengar, J. Tomasi, M. Cossi, J.M. Millam, M. Klene, C. Adamo, R. Cammi, J.W. Ochterski, R.L. Martin, K. Morokuma, O. Farkas, J.B. Foresman, D.J. Fox, Gaussian 09 Revision A.02, Wallingford, CT, 2016.

[28] Y. Zhao, D.G. Truhlar, The M06 suite of density functionals for main group thermochemistry, thermochemical kinetics, noncovalent interactions, excited states, and transition elements: two new functionals and systematic testing of four M06-class functionals and 12 other functionals, *Theoretical Chemistry Accounts* 120 (2008) 215-241.

[29] C. Gonzalez, H.B. Schlegel, Reaction path following in mass-weighted internal coordinates, *Journal of Physical Chemistry* 94 (1990) 5523-5527.

[30] T.J. Lee, P.R. Taylor, A diagnostic for determining the quality of single-reference electron correlation methods, *International Journal of Quantum Chemistry* 36 (1989)

199-207.

- [31] T.J. Lee, Comparison of the T1 and D1 diagnostics for electronic structure theory: a new definition for the open-shell D1 diagnostic, *Chemical physics letters* 372 (2003) 362-367.
- [32] J.C. Rienstra-Kiracofe, W.D. Allen, H.F. Schaefer, The  $C_2H_5^+ O_2$  reaction mechanism: high-level ab initio characterizations, *The Journal of Physical Chemistry A* 104 (2000) 9823-9840.
- [33] A.D. Becke, Density-functional thermochemistry. III. The role of exact exchange, *The Journal of Chemical Physics* 98 (1993) 5648-5652.
- [34] P.J. Stephens, F.J. Devlin, C.F. Chabalowski, M.J. Frisch, Ab initio calculation of vibrational absorption and circular dichroism spectra using density functional force fields, *The Journal of physical chemistry* 98 (1994) 11623-11627.
- [35] A.D. Becke, A new mixing of Hartree–Fock and local density-functional theories, *The Journal of chemical physics* 98 (1993) 1372-1377.
- [36] S. Grimme, Semiempirical hybrid density functional with perturbative second-order correlation, *The Journal of chemical physics* 124 (2006) 034108.
- [37] S. Grimme, S. Ehrlich, L. Goerigk, Effect of the damping function in dispersion corrected density functional theory, *Journal of computational chemistry* 32 (2011) 1456-1465.
- [38] T. Yanai, D.P. Tew, N.C. Handy, A new hybrid exchange–correlation functional using the Coulomb-attenuating method (CAM-B3LYP), *Chemical physics letters* 393 (2004) 51-57.
- [39] A.D. Boese, J.M.L. Martin, Development of density functionals for thermochemical kinetics, *The Journal of chemical physics* 121 (2004) 3405-3416.
- [40] Y. Zhao, N.E. Schultz, D.G. Truhlar, Design of density functionals by combining the method of constraint satisfaction with parametrization for thermochemistry, thermochemical kinetics, and noncovalent interactions, *Journal of Chemical Theory and Computation* 2 (2006) 364-382.
- [41] S.Y. Haoyu, X. He, S.L. Li, D.G. Truhlar, Correction: MN15: A Kohn–Sham global-hybrid exchange–correlation density functional with broad accuracy for multi-reference and single-reference systems and noncovalent interactions, *Chemical Science* 7 (2016) 6278-6279.
- [42] B.J. Lynch, P.L. Fast, M. Harris, D.G. Truhlar, Adiabatic connection for kinetics, *The Journal of Physical Chemistry A* 104 (2000) 4811-4815.
- [43] C. Adamo, V. Barone, Toward reliable density functional methods without adjustable parameters: The PBE0 model, *The Journal of chemical physics* 110 (1999) 6158-6170.
- [44] J.-D. Chai, M. Head-Gordon, Long-range corrected hybrid density functionals with damped atom–atom dispersion corrections, *Physical Chemistry Chemical Physics* 10 (2008) 6615-6620.
- [45] Y. Zhao, D.G. Truhlar, Exploring the limit of accuracy of the global hybrid meta density functional for main-group thermochemistry, kinetics, and noncovalent interactions, *Journal of Chemical Theory and Computation* 4 (2008) 1849-1868.
- [46] D.E. Woon, T.H. Dunning, Gaussian basis sets for use in correlated molecular

- calculations. III. The atoms aluminum through argon, *The Journal of Chemical Physics* 98 (1993) 1358-1371.
- [47] H.S. Johnston, J. Heicklen, Tunnelling corrections for unsymmetrical Eckart potential energy barriers, *The Journal of Physical Chemistry* 66 (1962) 532-533.
- [48] J.O. Hirschfelder, E. Wigner, Some Quantum-Mechanical Considerations in the Theory of Reactions Involving an Activation Energy, *The Journal of Chemical Physics* 7 (1939) 616-628.
- [49] Q.-D. Wang, Z.-W. Liu, Reaction Kinetics of Hydrogen Atom Abstraction from C<sub>4</sub>–C<sub>6</sub> Alkenes by the Hydrogen Atom and Methyl Radical, *The Journal of Physical Chemistry A* 122 (2018) 5202-5210.
- [50] Q.-D. Wang, W. Zhang, Influence of the double bond on the hydrogen abstraction reactions of methyl esters with hydrogen radical: An ab initio and chemical kinetic study, *RSC advances* 5 (2015) 68314-68325.
- [51] J.R. Barker, Multiple-Well, multiple-path unimolecular reaction systems. I. MultiWell computer program suite, *International Journal of Chemical Kinetics* 33 (2001) 232-245.
- [52] S. Pratihar, X. Ma, Z. Homayoon, G.L. Barnes, W.L. Hase, Direct Chemical Dynamics Simulations, *Journal of the American Chemical Society* 139 (2017) 3570-3590.

# Chapter 7

## Conclusions and future work

The work presented in *this thesis* focuses on ab initio studies of  $\dot{\text{H}}$  atom addition to and H-atom abstraction reactions by  $\dot{\text{H}}$  atoms from unsaturated  $\text{C}_2 - \text{C}_5$  hydrocarbons in Chapters 2, 3, 4 and 6. The unsaturated hydrocarbons of interest are acetylene, ethylene, allene, propyne, propene, 1-butyne, 1-pentyne and 1,3-pentadiene and its isomers. The H-atom abstraction reactions of highly unsaturated  $\text{C}_5 - \text{C}_{10}$  hydrocarbons by  $\dot{\text{H}}$  and  $\dot{\text{O}}\text{H}$  radicals were also studied in Chapter 6. Chapter 5 presented another project on the generation of a skeletal combustion mechanism for the syngas/ $\text{NO}_x$  system, the reliability of which is validated through IDT, flame simulations, ROP and sensitivity analyses in comparison to the detailed mechanism.

For most of the calculations, four prevalent DFT functionals including B3LYP, M06-2X,  $\omega$ B97X-D and B2PLYP-D3, with four widely used basis sets, namely 6-31+G(d,p), 6-311++G(d,p), cc-pVTZ and aug-cc-pVTZ, were used for geometry optimizations, vibrational frequency calculations and hindered-rotor treatment. High levels of theory including the CCSD(T)/CBS level, the DLPNO-CCSD(T) with Dunning's and Karlsruhe's basis sets, and the composite W1BD method were used for single-point energy calculations. In addition, BH&HLYP, B2PLYP, CAM-B3LYP, BMK, M05-2X, MN15, MPW1K, PBE0, and M08HX functionals were used for SPE calculations for the H-atom abstraction reactions of propyne and 1-butyne by  $\dot{\text{H}}$  and  $\dot{\text{O}}\text{H}$  radicals (Chapter 6).

Thermochemical properties for  $\text{C}_5$  species, high-pressure limiting and pressure-dependent rate constants for reactions on the  $\dot{\text{C}}_5\text{H}_9$  PES were calculated and fitted into NASA and Arrhenius format, respectively. The thermodynamic properties were validated against the ATcT database and other literature data, and the rate constants were compared with available theoretical and experimental results. A chemical kinetic model

with the newly calculated thermochemistry and kinetic results was developed, and used to simulate the species profiles of the reactants and products for  $\dot{\text{H}}$  atoms reacting with cyclopentene/cyclopentane.

For the  $\dot{\text{C}}_5\text{H}_9$  PES formed either via  $\dot{\text{H}}$  atom addition to the pentadiene isomers or via H-atom abstraction reactions from the pentene isomers, the 1,3- $\dot{\text{C}}_5\text{H}_9$  radical is the most important intermediate which contributes significantly to the formation of 1,3-butadiene and methyl radicals. Excluding the common decomposition channel of the 1,3- $\dot{\text{C}}_5\text{H}_9$  radical, another important channel for the production of 1,3-butadiene is through a two-step sequence—a cyclisation reaction followed by a ring-opening reaction of the radical formed. This channel is extremely important for branched alkenyl radicals and needs to be considered when the reactions of  $\dot{\text{H}}$  atoms with larger linear and/or branched dienes are studied in the future.

Based on our experience relating to  $\dot{\text{H}}$  atom addition to 1,3-butadiene and 1,3-pentadiene, the formation of allylic alkenyl radicals (e.g. the 1,3- $\dot{\text{C}}_4\text{H}_7$  radical on the  $\dot{\text{C}}_4\text{H}_7$  PES and the 2,4- $\dot{\text{C}}_5\text{H}_9$  radical on the  $\dot{\text{C}}_5\text{H}_9$  PES) are the most favoured. Hence, for larger 1,3-dienes, the formations of 1,3- and 2,4- allylic alkenyl radicals are expected to be the most important intermediates. As a result, the products formed through the direct  $\beta$ -scission reactions of these allylic alkenyl radicals are expected to be the dominant products. For instance, the most important intermediates formed through  $\dot{\text{H}}$  atom addition to 1,3-hexadiene are expected to be 1,3- $\dot{\text{C}}_6\text{H}_{11}$  and 2,4- $\dot{\text{C}}_6\text{H}_{11}$  radicals. The most favoured decomposition channel for 2,4- $\dot{\text{C}}_6\text{H}_{11}$  radical is proposed to be the C–C bond breaking forming 1,3-pentadiene and a methyl radical. Similarly, the most favoured product for 1,3- $\dot{\text{C}}_6\text{H}_{11}$  radical is expected to be 1,3-butadiene and an ethyl radical. Hence, for  $\dot{\text{H}}$  atom addition to larger 1,3-dienes, the dominant products are expected to be smaller 1,3-dienes and an alkyl radical. It is proven that studies exploring the chemistry of small 1,3-dienes (e.g. 1,3-butadiene, 1,3-pentadiene) are worth performing, which are also important for hierarchical mechanism development.

Twelve DFT methods were used for the hindered-rotor treatment of the rotors formed by  $\dot{\text{C}}\text{H}_3/\dot{\text{C}}_2\text{H}_3/\dot{\text{C}}_2\text{H}_5/\text{C}\dot{\text{H}}_3\dot{\text{O}} + \text{C}_2\text{H}_2/\text{C}_2\text{H}_4/\text{C}_3\text{H}_4\text{-a}/\text{C}_3\text{H}_4\text{-p}/\text{C}_3\text{H}_6$ . The SPE of the points on the

hindrance potentials calculated using DFT methods were compared to the DLPNO-CCSD(T)/CBS results. The maximum uncertainties for  $V(\chi)$ ,  $B(\chi)$  and  $Q_{\text{HR}}$  calculations stemming from the use of different DFT methods for internal rotor treatment are (1) 1.30 kJ mol<sup>-1</sup>, 0.14 cm<sup>-1</sup> and 12.64%, respectively, for  $\dot{\text{C}}\text{H}_3$  radical additions; (2) 2.65 kJ mol<sup>-1</sup>, 0.20 cm<sup>-1</sup> and 87.08%, respectively, for  $\dot{\text{C}}_2\text{H}_3$  radical additions; (3) 3.16 kJ mol<sup>-1</sup>, 0.14 cm<sup>-1</sup> and 123.54%, respectively, for  $\dot{\text{C}}_2\text{H}_5$  radical additions; (4) 6.73 kJ mol<sup>-1</sup>, 0.30 cm<sup>-1</sup> and 77.30%, respectively, for  $\text{CH}_3\dot{\text{O}}$  radical additions.

For H-atom abstraction reactions from a series of alkyne molecules by  $\dot{\text{H}}$  and  $\dot{\text{O}}\text{H}$  radicals at the propargyl C–H site, the TSs can be divided into three types: primary propargyl radical (propyne), secondary propargyl radicals (e.g. 1-butyne, 1-pentyne) and tertiary propargyl radicals (e.g. isopentyne). The energy barriers of these H-atom abstraction reactions were found to decrease with the existence of vinyl, phenyl and acetylenic groups following the order: vinyl > phenyl > acetylenic. The high-pressure limiting rate constants for H-atom abstraction from the tertiary propargyl C–H site are consistently faster than those from the secondary propargyl C–H site. For abstractions from the secondary propargyl C–H site, the ability of different groups on increasing reaction activity is:  $-\text{C}_2\text{H}_5$  (negative) <  $-\text{CH}_3$  <  $-\text{C}_6\text{H}_5 \approx -\text{C}_2\text{H} < -\text{C}_2\text{H}_3$  for H-atom abstraction reactions by  $\dot{\text{H}}$  atom, and  $-\text{C}_6\text{H}_5$  (negative) <  $-\text{C}_2\text{H} \approx -\text{CH}_3 < -\text{C}_2\text{H}_3$  for H-atom abstraction reactions by  $\dot{\text{O}}\text{H}$  radical.

The thermodynamic and kinetic properties calculated in this work can be implemented into a chemical kinetic mechanism to simulate the oxidation of C<sub>5</sub> hydrocarbons. In combination with the previous studies of dienes, some common findings drawn in Chapter 2 and 3 are useful for the development of combustion mechanisms for larger 1,3-dienes. This study estimates uncertainties in theoretically derived rate constants arising from the choice of different electronic structure methods used for hindered-rotor treatment. Through the analysis of these uncertainties, reliable DFT methods are recommended for the internal rotor treatment for different reaction types considering both accuracy and computational cost.

### **Future work and recommendations**

Whilst the ab initio and kinetic studies in the literature and in *this thesis* provide a basis for future studies on dienes and alkynes, further experimental and quantum chemical works are likely necessary. The following studies are recommended:

- (1) There is no direct study of the reactions of  $\dot{\text{H}}$  atoms with 1,3-pentadiene in the literature. Direct or indirect experiments on 1,3-pentadiene +  $\dot{\text{H}}$  would be helpful for the kinetic mechanism development of 1,3-dienes.
- (2) As 1,3-butadiene is the simplest 1,3-diene and is one of the most important products of  $\dot{\text{H}}$  atom reactions with larger 1,3-dienes, the fidelity of combustion simulations for larger dienes is dependent on the accuracy of the thermochemical properties and rate constants for 1,3-butadiene +  $\dot{\text{H}}$ . Hence, an ab initio study of 1,3-butadiene +  $\dot{\text{H}}$  at a higher-level of theory (e.g. ANL0 method) would be of interest to improve the reliability of its combustion mechanism.
- (3) Ab initio studies of the reactions between  $\dot{\text{H}}$  atoms and 1,3-pentadiene are illustrated in this Thesis, hence further studies about the reactions of  $\dot{\text{O}}\text{H}$  and  $\text{H}\dot{\text{O}}_2$  radicals with 1,3-pentadiene are recommended to explore the oxidation chemistry of 1,3-dienes.
- (4) The Evans-Polanyi correlation (barrier heights versus reaction enthalpies at 0 K) for  $\dot{\text{H}}$  atom addition to  $\text{C}_3 - \text{C}_5$  dienes and  $\text{C}_2 - \text{C}_5$  alkynes are explored in Chapter 2 of this thesis. These dienes are further divided into three groups which have different correlations of barrier heights and reaction enthalpies. Rate rule studies for  $\dot{\text{H}}$  atom addition reactions to these dienes and alkynes are recommended, which can be used to estimate rate constants for larger dienes and alkynes.
- (5) Based on the 1-D hindered rotor benchmarking study in *this thesis* (Chapter 4), studies considering a multi-dimensional hindered rotor treatment and a “real” benchmark hindrance potential based on optimized geometries using a coupled cluster method would be interesting.

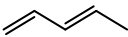
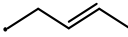
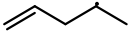
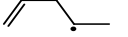
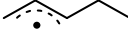
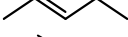
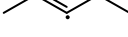
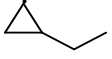
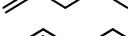
# Appendix A

## Supplemental Material for:

### An Ab Initio/Transition State Theory Study of the Reactions of $\dot{\text{C}}_5\text{H}_9$ species of Relevance to 1,3-Pentadiene, Part I: Potential Energy Surfaces, Thermochemistry and High-Pressure Limiting Rate Constants

#### A.1 $T_1$ diagnostic values for all the species on the $\dot{\text{C}}_5\text{H}_9$ PES.

Table A.1  $T_1$  diagnostic values for all the species excluding TSs on the  $\dot{\text{C}}_5\text{H}_9$  PES.

Label	Species	Structure	$T_1$ (Unrestricted)	$T_1$ (Restricted)
R	1,3-pentadiene		0.011	0.011
W1	2,4- $\dot{\text{C}}_5\text{H}_9$		0.022	0.019
W2	2,5- $\dot{\text{C}}_5\text{H}_9$		0.012	0.013
W3	1,4- $\dot{\text{C}}_5\text{H}_9$		0.013	0.013
W4	1,3- $\dot{\text{C}}_5\text{H}_9$		0.012	
W4	1,3- $\dot{\text{C}}_5\text{H}_9$		0.022	0.021
W5	1,3-dimethyl-2-cyclopropyl		0.012	
W6	Ethyl-cyclopropane		0.012	
W7	2,2- $\dot{\text{C}}_5\text{H}_9$		0.024	0.016
W8	2,3- $\dot{\text{C}}_5\text{H}_9$		0.024	
W9	2-ethyl-cyclopropyl		0.011	
W10	1,5- $\dot{\text{C}}_5\text{H}_9$		0.011	0.013
W11	1,2- $\dot{\text{C}}_5\text{H}_9$		0.025	
W12	1,1- $\dot{\text{C}}_5\text{H}_9$		0.026	
			0.026	0.016

W13	1-methylene-cyclopropylmethyl		0.010	0.015
W14	3-methyl-1-buten-4-yl		0.011	0.013
W15	Cyclopentyl		0.011	0.013
W16	Methyl-2-cyclobutyl		0.011	
W17	Methyl-3-cyclobutyl		0.011	
W18	Methyl-1-cyclobutyl		0.012	
W19	Methylene-cyclobutyl		0.011	
W20	1,3-dimethyl-1-cyclopropyl		0.012	
W21	ethyl-1-cyclopropyl		0.012	
P1	Ethylene		0.011	
	1-propenyl		0.033	0.019
P2	3-methyl-cyclopropene		0.009	
	methyl	CH <sub>3</sub>	0.009	0.014
P3	1,3-dimethyl-cyclopropene		0.009	
P4	2,3-pentadiene		0.011	
P5	2-pentyne		0.010	
P6	Propyne		0.011	
	ethyl		0.011	0.014
P7	Butyne		0.010	
P8	Ethenyl-cyclopropane		0.012	
P9	Ethylidene-cyclopropane		0.010	
P10	1,2-butadiene		0.011	
P11	1,2-pentadiene		0.011	
P12	Vinyl		0.041	0.022
	propene		0.010	
P13	2-methyl-1-methylenecyclopropane+H		0.010	

P14	1,3-butadiene		0.011	
P15	allyl		0.028	0.024
P16	Allene	$=C=C=$	0.012	
P17	1-ethyl-cyclopropene		0.009	
P18	3-ethyl-cyclopropene		0.009	
P19	Cyclopropene		0.010	
P20	1-pentyne		0.010	
P21	Acetylene	$\equiv\equiv\equiv$	0.013	
	1-propyl		0.011	0.013
P22	1,4-pentadiene		0.011	
P23	Cyclopentene		0.010	
P24	3-methylcyclobutene		0.010	
P25	1-methylcyclobutene		0.010	
P26	Isoprene		0.011	
P27	Cyclobutene		0.010	
P28	Methylenecyclobutane		0.010	
P29	1-pentadienyl		0.042	
	H <sub>2</sub>		0.005	
P30	2-pentadienyl+H <sub>2</sub>		0.043	
P31	3-pentadienyl+H <sub>2</sub>		0.044	
P32	4-pentadienyl+H <sub>2</sub>		0.041	
P33	5-pentadienyl+H <sub>2</sub>		0.033	

**Table A.2** Open-shell  $T_1$  diagnostic values for all TSs on the  $\dot{C}_5H_9$  PES.

Label	Reaction	Reactant	Product	$T_1$ (Unrestricted)	$T_1$ (Restricted)
TS1	R→W1		2,4- $\dot{C}_5H_9$	0.038	0.015
TS2	R→W2		2,5- $\dot{C}_5H_9$	0.037	0.020
TS3	R→W3		1,4- $\dot{C}_5H_9$	0.038	0.019
TS4	R→W4		1,3- $\dot{C}_5H_9$	0.038	0.016
TS5	R→P29		1-pentadienyl + H <sub>2</sub>	0.041	
TS6	R→P30		2-pentadienyl + H <sub>2</sub>	0.042	
TS7	R→P31		3-pentadienyl + H <sub>2</sub>	0.042	
TS8	R→P32		4-pentadienyl + H <sub>2</sub>	0.041	
TS9	R→P33		5-pentadienyl + H <sub>2</sub>	0.039	
TS10	W1→W2	2,4- $\dot{C}_5H_9$	2,5- $\dot{C}_5H_9$	0.026	0.019
TS11	W1→W4	2,4- $\dot{C}_5H_9$	1,3- $\dot{C}_5H_9$	0.014	0.015
TS12	W1→W5	2,4- $\dot{C}_5H_9$	1,3-dimethyl-2-cyclopropyl	0.033	
TS13	W1→W7	2,4- $\dot{C}_5H_9$	2,2- $\dot{C}_5H_9$	0.028	
TS14	W1→W8	2,4- $\dot{C}_5H_9$	2,3- $\dot{C}_5H_9$	0.021	
TS15	W1→P4	2,4- $\dot{C}_5H_9$	2,3-pentadiene + $\dot{H}$	0.031	0.017
TS16	W2→W4	2,5- $\dot{C}_5H_9$	1,3- $\dot{C}_5H_9$	0.018	0.015
TS17	W2→W6	2,5- $\dot{C}_5H_9$	Ethyl-cyclopropane	0.023	
TS18	W2→W7	2,5- $\dot{C}_5H_9$	2,2- $\dot{C}_5H_9$	0.024	0.015
TS19	W2→W8	2,5- $\dot{C}_5H_9$	2,3- $\dot{C}_5H_9$	0.027	
TS20	W2→W16	2,5- $\dot{C}_5H_9$	Methyl-2-cyclobutyl	0.033	0.032
TS21	W2→P1	2,5- $\dot{C}_5H_9$	Ethylene + 1-propenyl	0.035	0.024
TS22	W3→W4	1,4- $\dot{C}_5H_9$	1,3- $\dot{C}_5H_9$	0.026	0.020
TS23	W3→W10	1,4- $\dot{C}_5H_9$	1,5- $\dot{C}_5H_9$	0.014	0.013
TS24	W3→W11	1,4- $\dot{C}_5H_9$	1,2- $\dot{C}_5H_9$	0.027	
TS25	W3→W12	1,4- $\dot{C}_5H_9$	1,1- $\dot{C}_5H_9$	0.026	0.016
TS26	W3→W13	1,4- $\dot{C}_5H_9$	1-methylene-cyclopropyl methyl	0.023	0.027
TS27	W3→W17	1,4- $\dot{C}_5H_9$	Methyl-3-cyclobutyl	0.032	0.022
TS28	W3→P12	1,4- $\dot{C}_5H_9$	Vinyl + propene	0.035	0.024
TS29	W3→P22	1,4- $\dot{C}_5H_9$	1,4-pentadiene + $\dot{H}$	0.024	0.016
TS30	W4→W7	1,3- $\dot{C}_5H_9$	2,2- $\dot{C}_5H_9$	0.018	
TS31	W4→W8	1,3- $\dot{C}_5H_9$	2,3- $\dot{C}_5H_9$	0.028	
TS32	W4→W9	1,3- $\dot{C}_5H_9$	2-ethyl-cyclopropyl	0.035	
TS33	W4→W10	1,3- $\dot{C}_5H_9$	1,5- $\dot{C}_5H_9$	0.027	0.020
TS34	W4→W11	1,3- $\dot{C}_5H_9$	1,2- $\dot{C}_5H_9$	0.020	
TS35	W4→W12	1,3- $\dot{C}_5H_9$	1,1- $\dot{C}_5H_9$	0.029	0.015
TS36	W4→P11	1,3- $\dot{C}_5H_9$	1,2-pentadiene + $\dot{H}$	0.030	0.018

TS37	W4→ P14	1,3-Ċ <sub>5</sub> H <sub>9</sub>	1,3-butadiene + methyl	0.037	0.023
TS38	W5→W13	1,3-dimethyl-2-cyclopropyl	1-methylene-cyclopropyl methyl	0.015	
TS39	W5→W20	1,3-dimethyl-2-cyclopropyl	1,3-dimethyl-1-cyclopropyl	0.014	
TS40	W5→ P2	1,3-dimethyl-2-cyclopropyl	3-methyl-cyclopropene + methyl	0.027	
TS41	W5→ P3	1,3-dimethyl-2-cyclopropyl	1,3-dimethyl-cyclopropene + Ĥ	0.024	
TS42	W6→ W9	Ethyl-cyclopropane	2-ethyl-cyclopropyl	0.015	
TS43	W6→ W16	Ethyl-cyclopropane	Methyl-2-cyclobutyl	0.022	
TS44	W6→ W21	Ethyl-cyclopropane	ethyl-1-cyclopropyl	0.014	
TS45	W6→ P8	Ethyl-cyclopropane	Ethenyl-cyclopropane + Ĥ	0.023	
TS46	W6→ P9	Ethyl-cyclopropane	Ethylidene-cyclopropane + Ĥ	0.025	
TS47	W7→ W8	2,2-Ċ <sub>5</sub> H <sub>9</sub>	2,3-Ċ <sub>5</sub> H <sub>9</sub>	0.017	
TS48	W7→ P5	2,2-Ċ <sub>5</sub> H <sub>9</sub>	2-pentyne + Ĥ	0.020	
TS49	W7→ P6	2,2-Ċ <sub>5</sub> H <sub>9</sub>	Propyne + ethyl	0.028	0.021
TS50	W7→ P11	2,2-Ċ <sub>5</sub> H <sub>9</sub>	1,2-pentadiene + Ĥ	0.027	
TS51	W8→ P4	2,3-Ċ <sub>5</sub> H <sub>9</sub>	2,3-pentadiene + Ĥ	0.028	
TS52	W8→ P5	2,3-Ċ <sub>5</sub> H <sub>9</sub>	2-pentyne + Ĥ	0.021	
TS53	W8→ P7	2,3-Ċ <sub>5</sub> H <sub>9</sub>	Butyne + methyl	0.028	
TS54	W8→ P10	2,3-Ċ <sub>5</sub> H <sub>9</sub>	Methyl + 1,2-butadiene	0.031	
TS55	W9→W21	2-ethyl-cyclopropyl	Ethyl-1-cyclopropyl	0.014	
TS56	W9→ P17	2-ethyl-cyclopropyl	1-ethyl-cyclopropene + Ĥ	0.024	
TS57	W9→ P18	2-ethyl-cyclopropyl	3-ethyl-cyclopropene + Ĥ	0.025	
TS58	W9→ P19	2-ethyl-cyclopropyl	Cyclopropene + ethyl	0.027	
TS59	W10→W11	1,5-Ċ <sub>5</sub> H <sub>9</sub>	1,2-Ċ <sub>5</sub> H <sub>9</sub>	0.026	
TS60	W10→W12	1,5-Ċ <sub>5</sub> H <sub>9</sub>	1,1-Ċ <sub>5</sub> H <sub>9</sub>	0.026	0.016
TS61	W10→W15	1,5-Ċ <sub>5</sub> H <sub>9</sub>	Cyclopentyl	0.028	0.028
TS62	W10→W19	1,5-Ċ <sub>5</sub> H <sub>9</sub>	Methylene-cyclobutyl	0.024	
TS63	W10→ P15	1,5-Ċ <sub>5</sub> H <sub>9</sub>	Ethylene + allyl	0.034	0.028
TS64	W10→ P22	1,5-Ċ <sub>5</sub> H <sub>9</sub>	1,4-pentadiene + Ĥ	0.027	0.018
TS65	W11→ W12	1,2-Ċ <sub>5</sub> H <sub>9</sub>	1,1-Ċ <sub>5</sub> H <sub>9</sub>	0.014	
TS66	W11→ P11	1,2-Ċ <sub>5</sub> H <sub>9</sub>	1,2-pentadiene + Ĥ	0.030	
TS67	W11→ P16	1,2-Ċ <sub>5</sub> H <sub>9</sub>	Allene + ethyl	0.031	
TS68	W11→ P20	1,2-Ċ <sub>5</sub> H <sub>9</sub>	1-pentyne + Ĥ	0.021	
TS69	W12→ P20	1,1-Ċ <sub>5</sub> H <sub>9</sub>	1-pentyne + Ĥ	0.023	
TS70	W12→ P21	1,1-Ċ <sub>5</sub> H <sub>9</sub>	Acetylene + 1-propyl	0.030	0.021
TS71	W13→ W14	1-methylene-cyclopropylmethyl	3-methyl-1-buten-4-yl	0.023	0.028
TS72	W13→ W17	1-methylene-cyclopropylmethyl	Methyl-3-cyclobutyl	0.022	

TS73	W13→W20	1-methylene-cyclopropylmethyl	1,3-dimethyl-1-cyclopropyl	0.014	
TS74	W13→P13	1-methylene-cyclopropylmethyl	2-methyl-1-methylenecyclopropane + $\dot{H}$	0.026	
TS75	W14→W16	3-methyl-1-buten-4-yl	Methyl-2-cyclobutyl	0.032	
TS76	W14→P12	3-methyl-1-buten-4-yl	Vinyl+propene	0.035	0.025
TS77	W14→P14	3-methyl-1-buten-4-yl	1,3-butadiene+methyl	0.037	0.027
TS78	W14→P26	3-methyl-1-buten-4-yl	Isoprene + $\dot{H}$	0.035	0.019
TS79	W15→P23	Cyclopentyl	Cyclopentene + $\dot{H}$	0.024	0.016
TS80	W16→W19	Methyl-2-cyclobutyl	Methylene-cyclobutyl	0.015	
TS81	W16→P24	Methyl-2-cyclobutyl	3-methylcyclobutene + $\dot{H}$	0.025	0.016
TS82	W16→P25	Methyl-2-cyclobutyl	1-methylcyclobutene + $\dot{H}$	0.025	0.017
TS83	W16→P27	Methyl-2-cyclobutyl	Cyclobutene + methyl	0.026	
TS84	W17→W19	Methyl-3-cyclobutyl	Methylene-cyclobutyl	0.014	
TS85	W17→P24	Methyl-3-cyclobutyl	3-methylcyclobutene + $\dot{H}$	0.025	0.016
TS86	W18→W19	Methyl-1-cyclobutyl	Methylene-cyclobutyl	0.013	
TS87	W19→P28	Methylene-cyclobutyl	Methylenecyclobutane + $\dot{H}$	0.025	
TS88	P12→P15	Vinyl + propene	Ethylene + allyl	0.034	0.020

## A.2 Evans-Polanyi correlation for H atom addition to C<sub>3</sub>–C<sub>5</sub> dienes and C<sub>2</sub>–C<sub>5</sub> alkynes

The Evans-Polanyi correlation for  $\dot{H}$  atom addition to linear 1,3-dienes is fitted to:  $E(\text{kcal mol}^{-1}) = 0.18(\pm 0.02) \times \Delta_r H_{298\text{K}} + 10.92(\pm 0.75)$ , with  $R^2$  to be 0.94. The Evans-Polanyi correlation for  $\dot{H}$  atom addition to linear 1,2- and 2,3-dienes forming allylic alkenyl radical is fitted to:  $E(\text{kcal mol}^{-1}) = 0.27(\pm 0.07) \times \Delta_r H_{298\text{K}} + 20.17(\pm 3.96)$ , with  $R^2$  to be 0.83. The Evans-Polanyi correlation for the third group is weaker than 1,3-dienes, with  $E(\text{kcal mol}^{-1}) = 0.45(\pm 0.09) \times \Delta_r H_{298\text{K}} + 19.51(\pm 3.03)$  and  $R^2 = 0.60$ .

**Table A.3** The reaction enthalpies at 298 K and barrier heights for  $\dot{\text{H}}$  atom addition to different alkynes and dienes.

Label	Reactant	Addition position	Product	Product type	Reaction enthalpy	Barrier height
<b>1,2-dienes</b>						
1	1,2-C <sub>3</sub> H <sub>4</sub>	External	1,2- $\dot{\text{C}}_3\text{H}_5$	2 <sup>o</sup> v	-37.1	2.5[1]
2	1,2-C <sub>3</sub> H <sub>4</sub>	Internal	1,3- $\dot{\text{C}}_3\text{H}_5$	1 <sup>o</sup> a	-57.4	4.7[1]
3	1,2-C <sub>4</sub> H <sub>6</sub>	External	2,2- $\dot{\text{C}}_4\text{H}_7$	2 <sup>o</sup> v	-37.6	3.3[2]
4	1,2-C <sub>4</sub> H <sub>6</sub>	Internal	1,2- $\dot{\text{C}}_4\text{H}_7$	2 <sup>o</sup> v	-35.4	4.2[2]
5	1,2-C <sub>4</sub> H <sub>6</sub>	Internal	1,3- $\dot{\text{C}}_4\text{H}_7$	1 <sup>o</sup> a	-59.0	4.3[2]
6	1,2-C <sub>5</sub> H <sub>8</sub>	External	2,2- $\dot{\text{C}}_5\text{H}_9$	2 <sup>o</sup> v	-36.3	3.0
7	1,2-C <sub>5</sub> H <sub>8</sub>	Internal	1,2- $\dot{\text{C}}_5\text{H}_9$	2 <sup>o</sup> v	-34.6	3.6
8	1,2-C <sub>5</sub> H <sub>8</sub>	Internal	1,3- $\dot{\text{C}}_5\text{H}_9$	1 <sup>o</sup> a	-59.0	4.1
<b>2,3-dienes</b>						
9	2,3-C <sub>5</sub> H <sub>8</sub>	Internal	2,3- $\dot{\text{C}}_5\text{H}_9$	2 <sup>o</sup> v	-34.2	3.9
10	2,3-C <sub>5</sub> H <sub>8</sub>	Internal	2,4- $\dot{\text{C}}_5\text{H}_9$	2 <sup>o</sup> a	-59.9	4.1
<b>1,3-dienes</b>						
11	1,3-C <sub>4</sub> H <sub>6</sub>	External	1,3- $\dot{\text{C}}_4\text{H}_7$	1 <sup>o</sup> a	-46.8	2.6[2]
12	1,3-C <sub>4</sub> H <sub>6</sub>	Internal	1,4- $\dot{\text{C}}_4\text{H}_7$	1 <sup>o</sup>	-29.6	5.9[2]
13	1,3-C <sub>5</sub> H <sub>8</sub>	External	2,4- $\dot{\text{C}}_5\text{H}_9$	2 <sup>o</sup> a	-48.0	2.3
14	1,3-C <sub>5</sub> H <sub>8</sub>	Internal	1,3- $\dot{\text{C}}_5\text{H}_9$	1 <sup>o</sup> a	-45.2	3.4
15	1,3-C <sub>5</sub> H <sub>8</sub>	Internal	1,4- $\dot{\text{C}}_5\text{H}_9$	2 <sup>o</sup>	-30.9	5.0
16	1,3-C <sub>5</sub> H <sub>8</sub>	Internal	2,5- $\dot{\text{C}}_5\text{H}_9$	1 <sup>o</sup>	-30.8	5.8
<b>1,4-dienes</b>						
17	1,4-C <sub>5</sub> H <sub>8</sub>	External	1,4- $\dot{\text{C}}_5\text{H}_9$	2 <sup>o</sup>	-36.3	2.3
18	1,4-C <sub>5</sub> H <sub>8</sub>	Internal	1,5- $\dot{\text{C}}_5\text{H}_9$	1 <sup>o</sup>	-33.9	4.7
<b>Alkynes</b>						
19	C <sub>2</sub> H <sub>2</sub>	External	$\dot{\text{C}}_2\text{H}_3$	1 <sup>o</sup> v	-35.7	4.3[3]
20	1-C <sub>3</sub> H <sub>4</sub>	External	$\dot{\text{C}}_3\text{H}_5\text{-s}$	2 <sup>o</sup> v	-36.2	3.0[1]
21	1-C <sub>3</sub> H <sub>4</sub>	Internal	$\dot{\text{C}}_3\text{H}_5\text{-p}$	1 <sup>o</sup> v	-32.4	4.9[1]
22	1-C <sub>4</sub> H <sub>6</sub>	External	1,2- $\dot{\text{C}}_4\text{H}_7$	2 <sup>o</sup> v	-36.6	3.6[2]
23	1-C <sub>4</sub> H <sub>6</sub>	Internal	1,1- $\dot{\text{C}}_4\text{H}_7$	1 <sup>o</sup> v	-33.1	5.2[2]
24	2-C <sub>4</sub> H <sub>6</sub>	Internal	2,2- $\dot{\text{C}}_4\text{H}_7$	2 <sup>o</sup> v	-33.9	4.2[2]
25	1-C <sub>5</sub> H <sub>8</sub>	External	1,2- $\dot{\text{C}}_5\text{H}_9$	2 <sup>o</sup> v	-36.7	3.4
26	1-C <sub>5</sub> H <sub>8</sub>	Internal	1,1- $\dot{\text{C}}_5\text{H}_9$	1 <sup>o</sup> v	-33.9	5.0
27	2-C <sub>5</sub> H <sub>8</sub>	Internal	2,3- $\dot{\text{C}}_5\text{H}_9$	2 <sup>o</sup> v	-34.3	3.8
28	2-C <sub>5</sub> H <sub>8</sub>	Internal	2,2- $\dot{\text{C}}_5\text{H}_9$	2 <sup>o</sup> v	-34.5	3.4



# Appendix B

## Supplemental Material for

### An Ab Initio/Transition State Theory Study of the Reactions of $\dot{\text{C}}_5\text{H}_9$ Species of Relevance to 1,3-Pentadiene, Part II: Pressure Dependent Rate Constants and Implications for Combustion Modelling

#### B.1 Unimolecular decomposition reactions of 1,3-pentadiene

1,3-pentadiene can break C–C bond to produce vinyl + 1-propenyl and 1,3-butadien-1-yl +  $\dot{\text{C}}\text{H}_3$  or break C–H bond to produce five  $\dot{\text{C}}_5\text{H}_7$  isomers and hydrogen atoms. The zero-point vibrational energy (ZPVE) corrected energies of the products relative to the reactant are shown in Fig. B.1(a). The energy trend of the decomposition products is:  $E(1,3\text{-pentadien-5-yl} + \dot{\text{H}}) < E(1,3\text{-butadien-1-yl} + \dot{\text{C}}\text{H}_3) < E(1,3\text{-pentadien-4-yl} + \dot{\text{H}}) \approx E(1,3\text{-pentadien-2-yl} + \dot{\text{H}}) < E(1,3\text{-pentadien-3-yl} + \dot{\text{H}}) < E(1,3\text{-pentadien-1-yl} + \dot{\text{H}}) < E(\text{vinyl} + 1\text{-propenyl})$ .

The high-pressure limiting rate constant comparison of the dissociation reactions of 1,3-pentadiene is shown in Fig. B.1(b), the C–C bond cleavage reactions are marked as black colour and C–H bond cleavage reactions are marked as red. The comparison indicates that the dominant decomposition channel of 1,3-pentadiene is producing 1,3-pentadien-5-yl +  $\dot{\text{H}}$  followed by 1,3-butadien-1-yl +  $\dot{\text{C}}\text{H}_3$ . At low temperatures, the rate constants for the decomposition reactions are over 10 orders of magnitude smaller than those for the entrance channels of  $\dot{\text{H}}$  atom addition and H-atom abstraction reactions of 1,3-pentadiene, hence the unimolecular decomposition reactions can be neglected. At 2000 K, the difference between  $k_\infty(1,3\text{-pentadien-5-yl} + \dot{\text{H}})$  and those for reactions with hydrogen atoms decreases to within

four to six orders of magnitude which suggests the importance of this channel when the reaction rates of  $\dot{\text{H}}$  atom addition and H-atom abstraction reactions are limited by the concentration of hydrogen atoms.

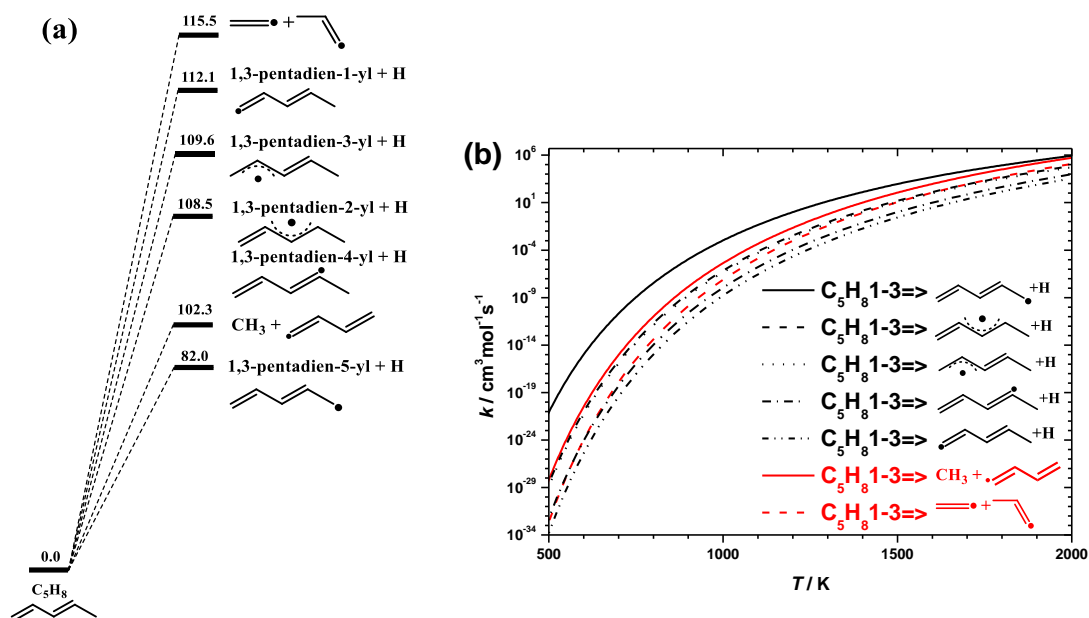


**Fig. B.1** (a) PES for unimolecular decomposition of 1,3-pentadiene (in kcal mol<sup>-1</sup>). (b) High-pressure limiting rate constant comparison for 1,3-pentadiene dissociation reactions.

## B.2 H-atom abstraction reactions of 1,4-pentadiene by $\dot{\text{H}}$ atoms

1,4-pentadiene is the smallest 1,4-diene and its  $\dot{\text{H}}$  atom addition reactions lie on the same PES with 1,3-pentadiene which has been illustrated in previous section. The studies about important reaction pathways and rate constants for  $\dot{\text{H}}$  atom addition reactions of 1,4-pentadiene can be a starting point to explore the combustion chemistry of larger 1,4-dienes. Meanwhile, the H-atom abstraction reactions of 1,4-pentadiene by  $\dot{\text{H}}$  atoms also need to be studied which can be competitive with its  $\dot{\text{H}}$  atom addition reactions at intermediate and high temperatures based on experience from similar study about 1,3-pentadiene. The PES for H-atom abstraction reactions of 1,4-pentadiene with the ZPVE corrected unrestricted energies relative to the reactant are shown in Fig. B.2(a).  $\dot{\text{H}}$  atoms can abstract the hydrogen atoms on primary vinylic (1°v), secondary vinylic (2°v) and secondary (2°) carbon atoms of 1,4-pentadiene, the 1,4-pentadien-3-yl radical is the most stable product whose relative energy is over 31.3 kcal mol<sup>-1</sup> lower than the other two

products. In addition, the 1,4-pentadien-3-yl radical ( $C=C\dot{C}C=C$ ) with a high electron delocalization is equivalent to 1,3-pentadien-5-yl ( $C=CC=CC\dot{C}$ ) which can be generated through  $\dot{H}$  atoms abstracting the hydrogen atom on the fifth carbon atom ( $1^\circ$ ) of 1,3-pentadiene. As expected, the abstraction of an allylic hydrogen from 1,4-pentadiene by  $\dot{H}$  is the most energetically favoured, followed by the abstraction of the  $2^\circ$  hydrogen atom, and finally the abstraction of the two hydrogen atoms on the  $1^\circ$  carbon atom. The H-atom abstraction from the  $1^\circ$  site can lead to two isomers depending on the  $HC=CH$  moiety is in the cis or trans configuration. These two reactions have similar energy barriers with  $15.8 \text{ kcal mol}^{-1}$  for the formation of cis-1,4-pentadien-1-yl and  $15.6 \text{ kcal mol}^{-1}$  for the formation of trans-1,4-pentadien-1-yl. The averaged barrier height of these two reactions is plotted on the PES for clarity. Interestingly, the cis-configuration of 1,4-pentadien-2-yl is found to be about  $2.0 \text{ kcal mol}^{-1}$  more stable than its trans-configuration from the hindrance potential analysis of internal rotation. The C2–C3 bond rotation ( $C=C\dot{C}C=C$ ) which connects the trans- and cis-configurations has been scanned, the two configurations are treated as a joint well and the cis-configuration of 1,4-pentadien-2-yl is used in the later rate constant calculation.

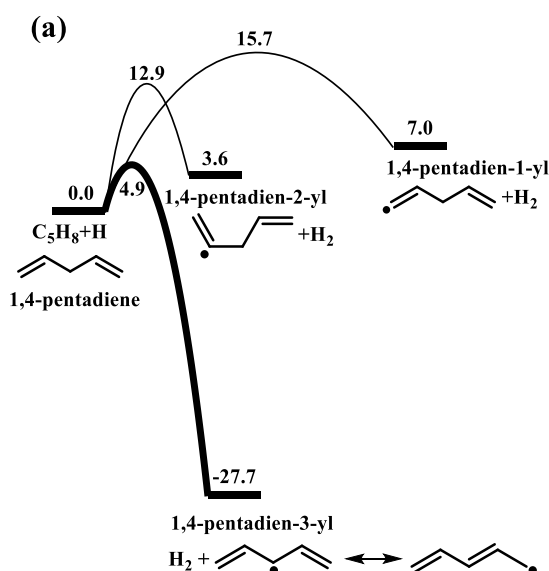


**Fig. B.2** PES for H-atom abstraction reactions from 1,4-pentadiene by  $\dot{H}$  atoms (in  $\text{kcal mol}^{-1}$ ).

### B.3 H-atom abstraction reactions of cyclopentene by $\dot{\text{H}}$ atoms

There are three kinds of hydrogen atoms on the ring of cyclopentene which are vinylic ( $2^\circ\text{v}$ ), allylic ( $2^\circ\text{a}$ ) and secondary ( $2^\circ$ ) hydrogen atoms. Fig. B.3(a) shows the most favoured channel is the abstraction of the allylic hydrogen atoms forming 3-cyclopentenyl +  $\text{H}_2$  as expected. The abstraction from the secondary sites forming 4-cyclopentenyl +  $\text{H}_2$  is 1.9 kcal  $\text{mol}^{-1}$  higher than the abstraction from the allylic sites. The abstraction from the vinylic sites forming 1-cyclopentenyl +  $\text{H}_2$  has the highest barrier height which is 10.2 kcal  $\text{mol}^{-1}$  higher than the abstraction from the secondary site. Hence, the abstraction from the vinylic sites is expected to be the least important channel. The high-pressure limiting rate constants for H-atom abstraction reactions of cyclopentene by  $\dot{\text{H}}$  atoms are shown in Fig. B.3(b). The dominant channel is the abstraction of the allylic hydrogen atoms to form 3-cyclopentenyl, followed by the abstraction of the secondary hydrogen atoms, and the abstraction from the vinylic sites is the slowest which is over an order of magnitude slower than the dominant channel over the entire temperature range.

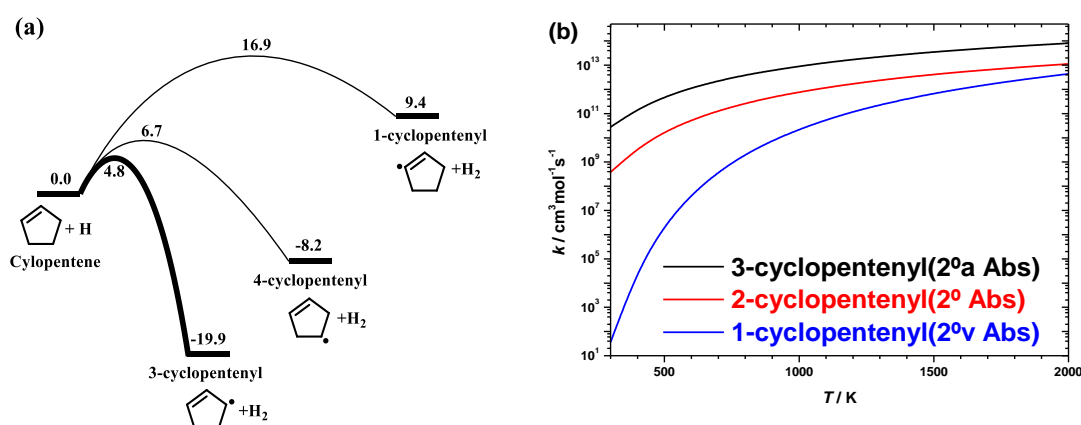


**Fig. B.3** (a) PES for H-atom abstraction reactions from cyclopentene by  $\dot{\text{H}}$  atoms (in kcal  $\text{mol}^{-1}$ ). (b) High-pressure limiting rate constant comparison for H-atom abstraction reactions from cyclopentene by  $\dot{\text{H}}$  atoms.

### B.4 H-atom abstraction reactions of propene by vinyl radicals

Vinyl addition to propene is an important reaction pathway on  $\dot{\text{C}}_3\text{H}_5$  PES and have been studied both theoretically and experimentally [4]. Besides the addition reaction, the

primary-, secondary-vinylic and allylic hydrogen atoms of propene can be abstracted by vinyl radicals and the barrier heights and relative energies are shown in Fig. B.4(a). Consistently with the rate rule for H-atom abstraction reactions of alkenes by different radicals, the abstraction from the allylic sites ( $1^\circ\text{a}$ ) to form ethylene and allyl is energetically favoured, followed by the abstraction from the secondary vinylic sites ( $2^\circ\text{v}$ ) with a barrier height  $3.8 \text{ kcal mol}^{-1}$  higher, and finally the abstraction from the primary vinylic sites ( $1^\circ\text{v}$ ). The abstraction from the  $1^\circ\text{v}$  sites can generate cis- and trans-1-propenyl radicals depending on the HC=CH moiety is in the cis- or trans-configuration. The barrier height different between these two reactions is  $0.1 \text{ kcal mol}^{-1}$  and their average value is plotted on the PES.

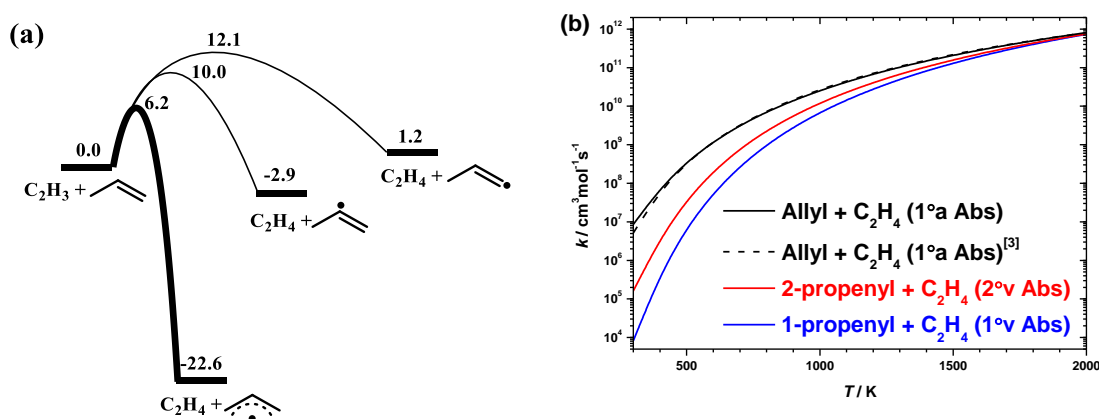


**Fig. B.4** (a) PES for H-atom abstraction reactions from propene by vinyl radicals (in  $\text{kcal mol}^{-1}$ ). (b) High-pressure limiting rate constant comparison for H-atom abstraction reactions from propene by vinyl radicals. The black dashed line represents the calculated results from Goldsmith et al. [4] at G3 level of theory.

The high-pressure limiting rate constants for H-atom abstraction reactions of propene by vinyl radicals are shown in Fig. B.4(b). At low and intermediate temperatures, the abstraction of the allylic hydrogen atoms has the largest rate constants, followed by the abstraction of the secondary vinylic hydrogen atoms, and the abstraction from the primary vinylic sites is the slowest. At temperatures above 1300 K, the rate constants for these three reactions become converged with the difference within two times. The  $k_\infty(\text{C}_3\text{H}_6 + \dot{\text{C}}_2\text{H}_3 \rightarrow 1,3\text{-}\dot{\text{C}}_3\text{H}_5 + \text{C}_2\text{H}_4)$  are compared with Goldsmith's work (black dash line) calculated at

G3//B3PW91/6-311++G(3df,pd) level of theory and reach a very good agreement with the largest deviation less than 70% over the temperature range 300–2000 K.

### B.5 $\beta$ -scission reactions of 1,3- $\dot{\text{C}}_5\text{H}_9$ and 1,4- $\dot{\text{C}}_5\text{H}_9$

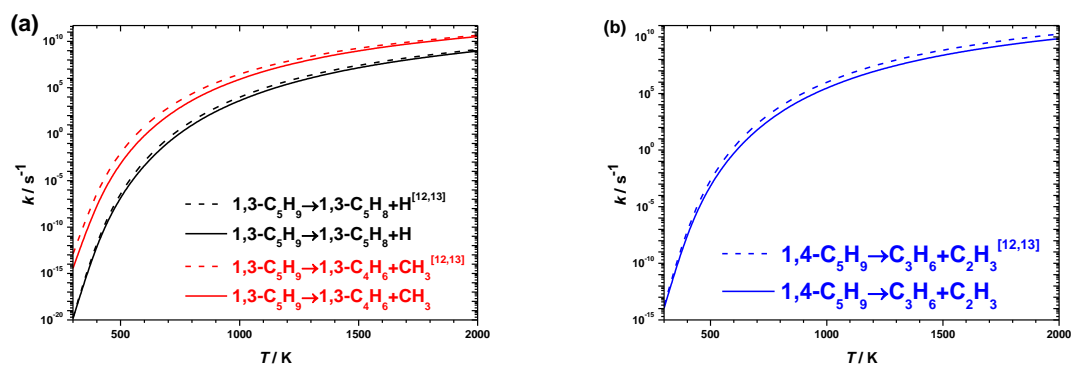


**Fig. B.5** (a) High-pressure limiting rate constant comparison for  $\beta$ -scission reactions of 1,3- $\dot{\text{C}}_5\text{H}_9$  radicals. (b) High-pressure limiting rate constant comparison for  $\beta$ -scission reactions of 1,4- $\dot{\text{C}}_5\text{H}_9$  radicals. The dashed lines represent the calculated results from Wang et al. [5, 6] at the CBS-QB3 level of theory.

# Appendix C

**Supplemental Material for**

**Hindered Rotor Benchmarks for the Transition States of Free**

**Radical Additions to Unsaturated Hydrocarbons**

**C.1 The bond lengths of the newly formed rotors for the TSs of  $\dot{\text{C}}\text{H}_3$ ,  $\dot{\text{C}}_2\text{H}_3$ ,  $\dot{\text{C}}_2\text{H}_5$ ,  $\text{CH}_3\dot{\text{O}}$  radical additions to  $\text{C}_2\text{H}_2$ , which are calculated at CCSD(T)-F12/cc-pVDZ-F12 and twelve DFT methods.**

**Table C.1** The bond lengths of the newly formed rotors for the TSs of  $\dot{\text{C}}\text{H}_3$ ,  $\dot{\text{C}}_2\text{H}_3$ ,  $\dot{\text{C}}_2\text{H}_5$ ,  $\text{CH}_3\dot{\text{O}}$  radical additions to  $\text{C}_2\text{H}_2$ .

Label	$\dot{\text{R}}$	CCSD(T)-F12	B2PLYP-D3			B3LYP			M06-2X			$\omega$ B97X-D		
		cc-pVDZ-F12	6-31+ G(d,p)	6-311++ G(d,p)	cc-pVTZ	6-31+ G(d,p)	6-311++ G(d,p)	cc-pVTZ	6-31+ G(d,p)	6-311++ G(d,p)	cc-pVTZ	6-31+G (d,p)	6-311++ G(d,p)	cc-pVTZ
TS1	$\dot{\text{C}}\text{H}_3$	2.24	2.26	2.23	2.23	2.34	2.30	2.30	2.24	2.22	2.22	2.29	2.26	2.26
TS9	$\dot{\text{C}}_2\text{H}_3$	2.28	2.30	2.27	2.27	2.40	2.33	2.34	2.28	2.26	2.25	2.32	2.29	2.29
TS17	$\dot{\text{C}}_2\text{H}_5$	2.24	2.25	2.23	2.23	2.33	2.29	2.29	2.23	2.21	2.21	2.28	2.25	2.25
TS25	$\text{CH}_3\dot{\text{O}}$	1.98	1.98	1.96	1.97	2.02	1.99	2.00	1.97	1.95	1.96	2.00	1.97	1.98

**C.2 The dihedrals of the newly formed rotors for the TSs of  $\dot{\text{C}}\text{H}_3$ ,  $\dot{\text{C}}_2\text{H}_3$ ,  $\dot{\text{C}}_2\text{H}_5$ ,  $\text{CH}_3\dot{\text{O}}$  radical additions to  $\text{C}_2\text{H}_2$ , which are calculated at CCSD(T)-F12/cc-pVDZ-F12 and twelve DFT methods.**

**Table C.2** The dihedrals of the newly formed rotors for the TSs of  $\dot{\text{C}}\text{H}_3$ ,  $\dot{\text{C}}_2\text{H}_3$ ,  $\dot{\text{C}}_2\text{H}_5$ ,  $\text{CH}_3\dot{\text{O}}$  radical additions to  $\text{C}_2\text{H}_2$ .

Label	$\dot{\text{R}}$	CCSD(T)- F12	B2PLYP-D3			B3LYP			M06-2X			$\omega$ B97X-D		
			cc-pVDZ- F12	6-31+ G(d,p)	6-311++ G(d,p)	cc-pVTZ	6-31+ G(d,p)	6-311++ G(d,p)	cc-pVTZ	6-31+ G(d,p)	6-311++ G(d,p)	cc-pVTZ	6-31+ G(d,p)	6-311++ G(d,p)
TS1	$\dot{\text{C}}\text{H}_3$	-0.96	0.00	0.00	0.00	0.00	0.00	0.00	0.00	0.00	0.00	0.00	0.00	0.00
TS9	$\dot{\text{C}}_2\text{H}_3$	47.07	64.60	64.68	53.44	-180.00	80.03	72.09	47.30	-169.83	-42.00	60.33	59.35	54.98
TS17	$\dot{\text{C}}_2\text{H}_5$	0.86	0.00	0.00	0.00	0.00	0.00	0.00	0.00	0.00	0.00	0.00	0.00	0.00
TS25	$\text{CH}_3\dot{\text{O}}$	1.94	0.00	0.00	0.00	0.00	0.00	0.00	0.00	0.00	0.00	0.00	0.00	0.0

**C.3 The  $T_1$  diagnostic values of the CCSD(T)/cc-pVQZ calculations for the TSs of  $\dot{\text{C}}\text{H}_3$ ,  $\dot{\text{C}}_2\text{H}_3$ ,  $\dot{\text{C}}_2\text{H}_5$ ,  $\text{CH}_3\dot{\text{O}}$  radical additions to  $\text{C}_2\text{H}_2$  and  $\text{C}_2\text{H}_4$ .**

**Table C.3**  $T_1$  diagnostic values of the CCSD(T)/cc-pVQZ calculations.

Reactant		$T_1$ diagnostic
A	B	CCSD(T)/cc-pVQZ
$\text{C}_2\text{H}_2$	$\dot{\text{C}}\text{H}_3$	0.0383
$\text{C}_2\text{H}_4$		0.0302
$\text{C}_2\text{H}_2$	$\dot{\text{C}}_2\text{H}_3$	0.0446
$\text{C}_2\text{H}_4$		0.0398
$\text{C}_2\text{H}_2$	$\dot{\text{C}}_2\text{H}_5$	0.0336
$\text{C}_2\text{H}_4$		0.0271
$\text{C}_2\text{H}_2$	$\text{CH}_3\dot{\text{O}}$	0.0344
$\text{C}_2\text{H}_4$		0.0311

## C.4 Maximum differences of the hindered barriers

**Table C.4** Maximum differences of the hindered barriers calculated using twelve DFT methods for the newly formed internal rotors in target reactions. (kJ mol<sup>-1</sup>)

Label	Reac. <i>B</i>	$\Delta E_{HR}^{\max}$	Label	Reac. <i>B</i>	$\Delta E_{HR}^{\max}$
<b><math>\dot{C}H_3</math> addition</b>					
TS1	C <sub>2</sub> H <sub>2</sub>	0.30	TS2	C <sub>2</sub> H <sub>4</sub>	0.79
TS3	C <sub>3</sub> H <sub>4</sub> -a(E)	0.53	TS4	C <sub>3</sub> H <sub>4</sub> -a(I)	0.49
TS5	C <sub>3</sub> H <sub>4</sub> -p(E)	0.39	TS6	C <sub>3</sub> H <sub>4</sub> -p(I)	0.67
TS7	C <sub>3</sub> H <sub>6</sub> (E)	0.84	TS8	C <sub>3</sub> H <sub>6</sub> (I)	1.30
<b><math>\dot{C}_2H_3</math> addition</b>					
TS9	C <sub>2</sub> H <sub>2</sub>	1.10	TS10	C <sub>2</sub> H <sub>4</sub>	1.91
TS11	C <sub>3</sub> H <sub>4</sub> -a(E)	2.21	TS12	C <sub>3</sub> H <sub>4</sub> -a(I)	2.30
TS13	C <sub>3</sub> H <sub>4</sub> -p(E)	1.55	TS14	C <sub>3</sub> H <sub>4</sub> -p(I)	1.24
TS15	C <sub>3</sub> H <sub>6</sub> (E)	2.65	TS16	C <sub>3</sub> H <sub>6</sub> (I)	2.01
<b><math>\dot{C}_2H_5</math> addition</b>					
TS17	C <sub>2</sub> H <sub>2</sub>	2.42	TS18	C <sub>2</sub> H <sub>4</sub>	2.36
TS19	C <sub>3</sub> H <sub>4</sub> -a(E)	1.98	TS20	C <sub>3</sub> H <sub>4</sub> -a(I)	1.41
TS21	C <sub>3</sub> H <sub>4</sub> -p(E)	3.02	TS22	C <sub>3</sub> H <sub>4</sub> -p(I)	3.16
TS23	C <sub>3</sub> H <sub>6</sub> (E)	2.71	TS24	C <sub>3</sub> H <sub>6</sub> (I)	2.31
<b>CH<sub>3</sub><math>\dot{O}</math> addition</b>					
TS25	C <sub>2</sub> H <sub>2</sub>	4.40	TS26	C <sub>2</sub> H <sub>4</sub>	2.38
TS27	C <sub>3</sub> H <sub>4</sub> -a(E)	3.56	TS28	C <sub>3</sub> H <sub>4</sub> -a(I)	5.78
TS29	C <sub>3</sub> H <sub>4</sub> -p(E)	6.73	TS30	C <sub>3</sub> H <sub>4</sub> -p(I)	4.62
TS31	C <sub>3</sub> H <sub>6</sub> (E)	4.39	TS32	C <sub>3</sub> H <sub>6</sub> (I)	3.43

## C.5 Maximum differences of rotational constants

**Table C.5** Maximum differences of rotational constants calculated using twelve DFT methods for the newly formed internal rotors in target reactions. ( $\text{cm}^{-1}$ )

Label	Reac. <i>B</i>	$\Delta B(\chi)_{\text{max}}$	Label	Reac. <i>B</i>	$\Delta B(\chi)_{\text{max}}$
<b><math>\dot{\text{C}}\text{H}_3</math> addition</b>					
TS1	C <sub>2</sub> H <sub>2</sub>	0.13	TS2	C <sub>2</sub> H <sub>4</sub>	0.09
TS3	C <sub>3</sub> H <sub>4</sub> -a(E)	0.12	TS4	C <sub>3</sub> H <sub>4</sub> -a(I)	0.07
TS5	C <sub>3</sub> H <sub>4</sub> -p(E)	0.14	TS6	C <sub>3</sub> H <sub>4</sub> -p(I)	0.08
TS7	C <sub>3</sub> H <sub>6</sub> (E)	0.13	TS8	C <sub>3</sub> H <sub>6</sub> (I)	0.08
<b><math>\dot{\text{C}}_2\text{H}_3</math> addition</b>					
TS9	C <sub>2</sub> H <sub>2</sub>	0.18	TS10	C <sub>2</sub> H <sub>4</sub>	0.09
TS11	C <sub>3</sub> H <sub>4</sub> -a(E)	0.12	TS12	C <sub>3</sub> H <sub>4</sub> -a(I)	0.13
TS13	C <sub>3</sub> H <sub>4</sub> -p(E)	0.14	TS14	C <sub>3</sub> H <sub>4</sub> -p(I)	0.10
TS15	C <sub>3</sub> H <sub>6</sub> (E)	0.20	TS16	C <sub>3</sub> H <sub>6</sub> (I)	0.11
<b><math>\dot{\text{C}}_2\text{H}_5</math> addition</b>					
TS17	C <sub>2</sub> H <sub>2</sub>	0.14	TS18	C <sub>2</sub> H <sub>4</sub>	0.06
TS19	C <sub>3</sub> H <sub>4</sub> -a(E)	0.09	TS20	C <sub>3</sub> H <sub>4</sub> -a(I)	0.05
TS21	C <sub>3</sub> H <sub>4</sub> -p(E)	0.04	TS22	C <sub>3</sub> H <sub>4</sub> -p(I)	0.04
TS23	C <sub>3</sub> H <sub>6</sub> (E)	0.13	TS24	C <sub>3</sub> H <sub>6</sub> (I)	0.04
<b>CH<sub>3</sub><math>\dot{\text{O}}</math> addition</b>					
TS25	C <sub>2</sub> H <sub>2</sub>	0.15	TS26	C <sub>2</sub> H <sub>4</sub>	0.19
TS27	C <sub>3</sub> H <sub>4</sub> -a(E)	0.17	TS28	C <sub>3</sub> H <sub>4</sub> -a(I)	0.30
TS29	C <sub>3</sub> H <sub>4</sub> -p(E)	0.08	TS30	C <sub>3</sub> H <sub>4</sub> -p(I)	0.07
TS31	C <sub>3</sub> H <sub>6</sub> (E)	0.25	TS32	C <sub>3</sub> H <sub>6</sub> (I)	0.11

## C.6 Maximum percentage errors of $Q_{HR}$

**Table C.6** Maximum percentage errors of  $Q_{HR}$  as a function of temperature calculated using twelve DFT methods for the newly formed internal rotors in target reactions. (in percentage)

Label	Reac. <i>B</i>	$\frac{Q_{HR}^{DFT_{max}} - Q_{HR}^{DFT_{min}}}{Q_{HR}^{DFT_{min}}}$	Label	Reac. <i>B</i>	$\frac{Q_{HR}^{DFT_{max}} - Q_{HR}^{DFT_{min}}}{Q_{HR}^{DFT_{min}}}$
<b><math>\dot{C}H_3</math> addition</b>					
TS1	C <sub>2</sub> H <sub>2</sub>	2.81	TS2	C <sub>2</sub> H <sub>4</sub>	8.43
TS3	C <sub>3</sub> H <sub>4</sub> -a(E)	5.49	TS4	C <sub>3</sub> H <sub>4</sub> -a(I)	6.05
TS5	C <sub>3</sub> H <sub>4</sub> -p(E)	4.11	TS6	C <sub>3</sub> H <sub>4</sub> -p(I)	7.32
TS7	C <sub>3</sub> H <sub>6</sub> (E)	9.31	TS8	C <sub>3</sub> H <sub>6</sub> (I)	12.64
<b><math>\dot{C}_2H_3</math> addition</b>					
TS9	C <sub>2</sub> H <sub>2</sub>	15.79	TS10	C <sub>2</sub> H <sub>4</sub>	62.43
TS11	C <sub>3</sub> H <sub>4</sub> -a(E)	51.75	TS12	C <sub>3</sub> H <sub>4</sub> -a(I)	32.78
TS13	C <sub>3</sub> H <sub>4</sub> -p(E)	17.04	TS14	C <sub>3</sub> H <sub>4</sub> -p(I)	22.68
TS15	C <sub>3</sub> H <sub>6</sub> (E)	87.08	TS16	C <sub>3</sub> H <sub>6</sub> (I)	49.61
<b><math>\dot{C}_2H_5</math> addition</b>					
TS17	C <sub>2</sub> H <sub>2</sub>	77.85	TS18	C <sub>2</sub> H <sub>4</sub>	31.44
TS19	C <sub>3</sub> H <sub>4</sub> -a(E)	20.27	TS20	C <sub>3</sub> H <sub>4</sub> -a(I)	37.56
TS21	C <sub>3</sub> H <sub>4</sub> -p(E)	123.54	TS22	C <sub>3</sub> H <sub>4</sub> -p(I)	49.74
TS23	C <sub>3</sub> H <sub>6</sub> (E)	21.81	TS24	C <sub>3</sub> H <sub>6</sub> (I)	16.84
<b>CH<sub>3</sub><math>\dot{O}</math> addition</b>					
TS25	C <sub>2</sub> H <sub>2</sub>	30.4	TS26	C <sub>2</sub> H <sub>4</sub>	9.16
TS27	C <sub>3</sub> H <sub>4</sub> -a(E)	11.06	TS28	C <sub>3</sub> H <sub>4</sub> -a(I)	17.55
TS29	C <sub>3</sub> H <sub>4</sub> -p(E)	77.30	TS30	C <sub>3</sub> H <sub>4</sub> -p(I)	42.83
TS31	C <sub>3</sub> H <sub>6</sub> (E)	41.33	TS32	C <sub>3</sub> H <sub>6</sub> (I)	35.47

**C.7 Rotational constants for the newly formed rotors of  $\dot{\text{C}}\text{H}_3/\dot{\text{C}}_2\text{H}_3/\dot{\text{C}}_2\text{H}_5/\text{CH}_3\dot{\text{O}}$  radical additions to  $\text{C}_2\text{H}_2/\text{C}_2\text{H}_4/\text{C}_3\text{H}_4\text{-a}/\text{C}_3\text{H}_4\text{-p}/\text{C}_3\text{H}_6$  calculated at twelve DFT methods.**

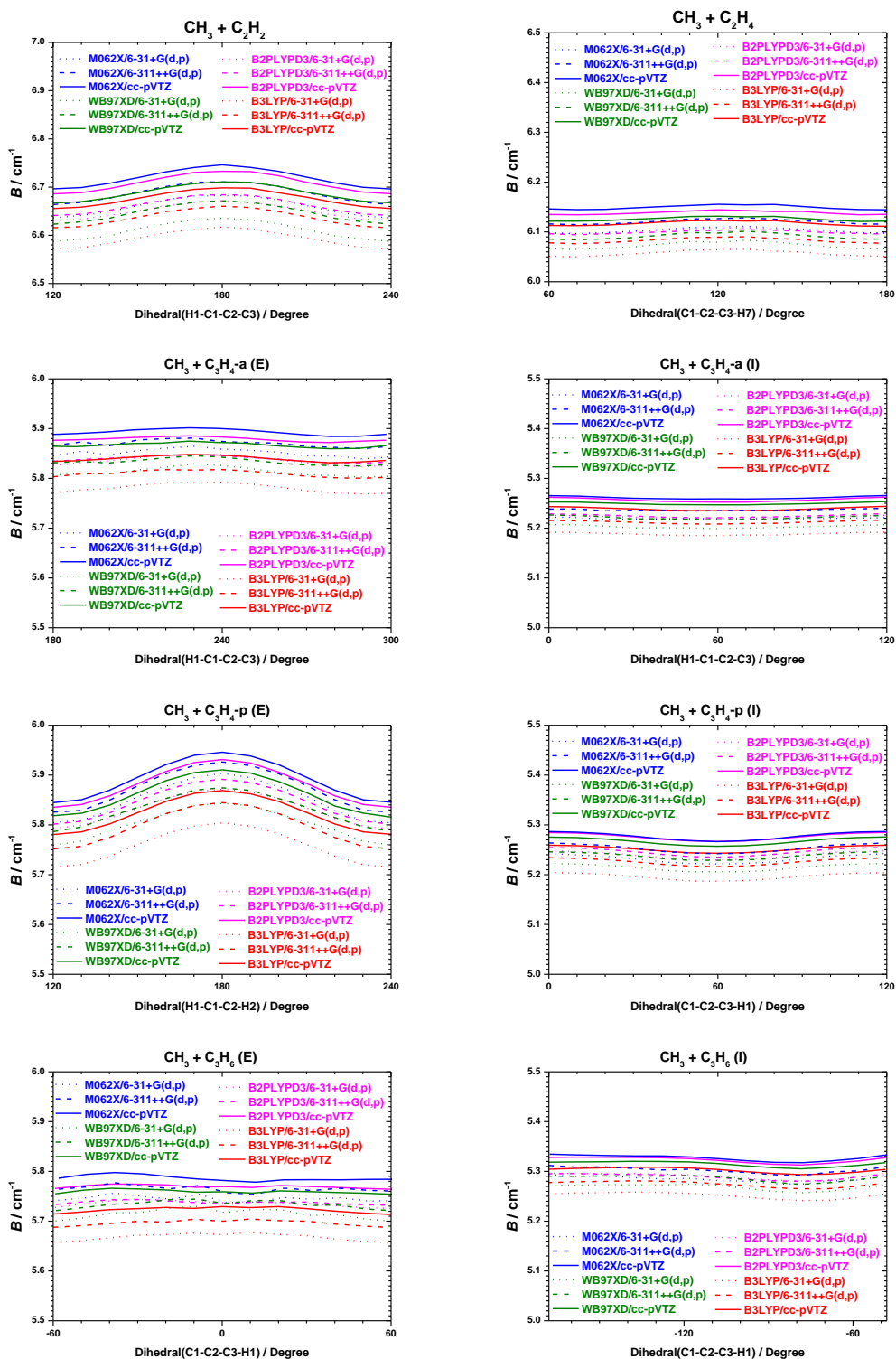


**Fig. C.1** Rotational constants for the newly formed methyl rotors of  $\dot{\text{C}}\text{H}_3$  radical additions to  $\text{C}_2\text{H}_2/\text{C}_2\text{H}_4/\text{C}_3\text{H}_4\text{-a}/\text{C}_3\text{H}_4\text{-p}/\text{C}_3\text{H}_6$  calculated using twelve DFT methods.

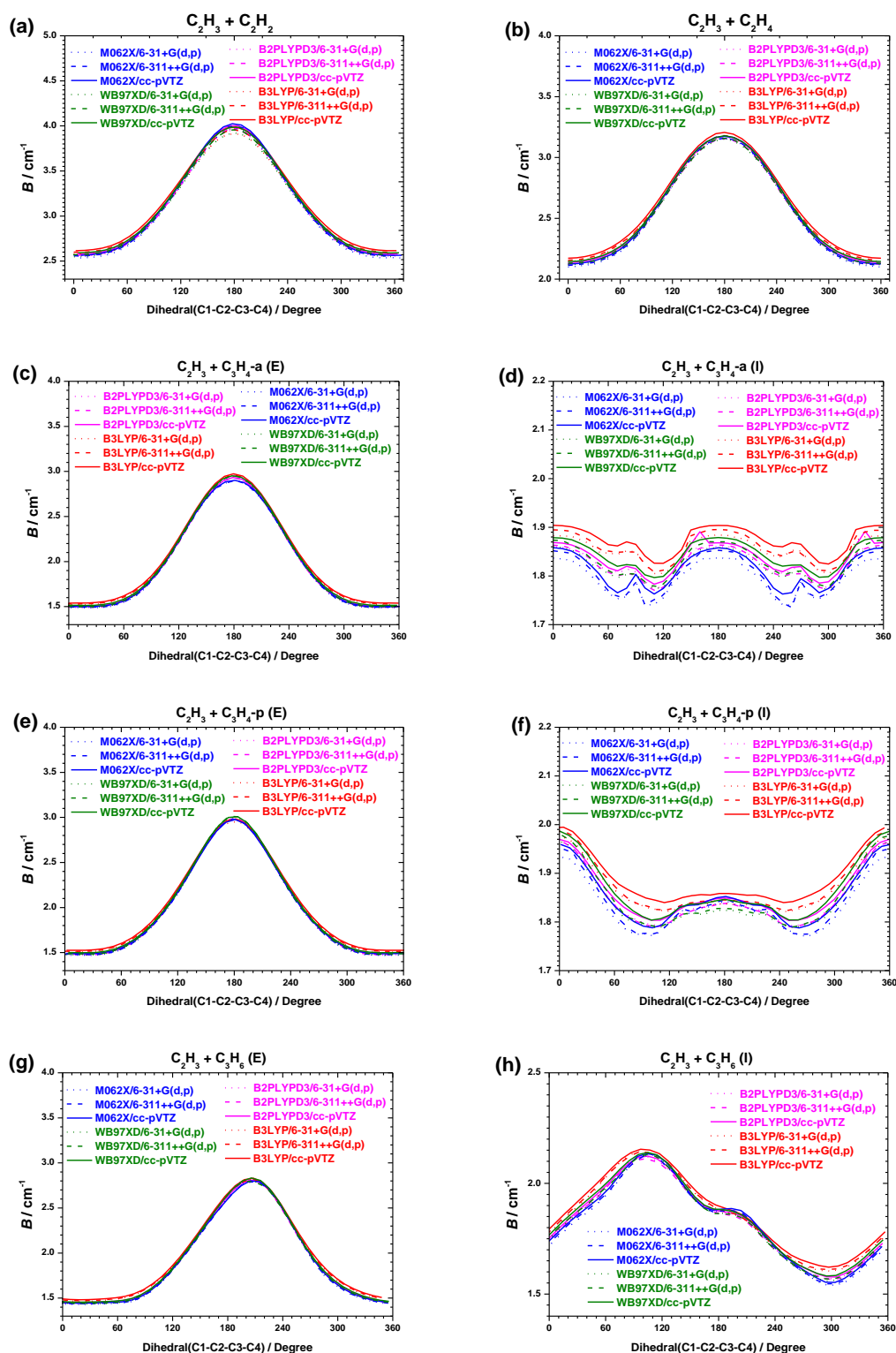


**Fig. C.2** Rotational constants for rotors formed by  $\dot{\text{C}}_2\text{H}_3$  radical additions to  $\text{C}_2\text{H}_2/\text{C}_2\text{H}_4/\text{C}_3\text{H}_4\text{-a}/\text{C}_3\text{H}_4\text{-p}/\text{C}_3\text{H}_6$  calculated using twelve DFT methods.

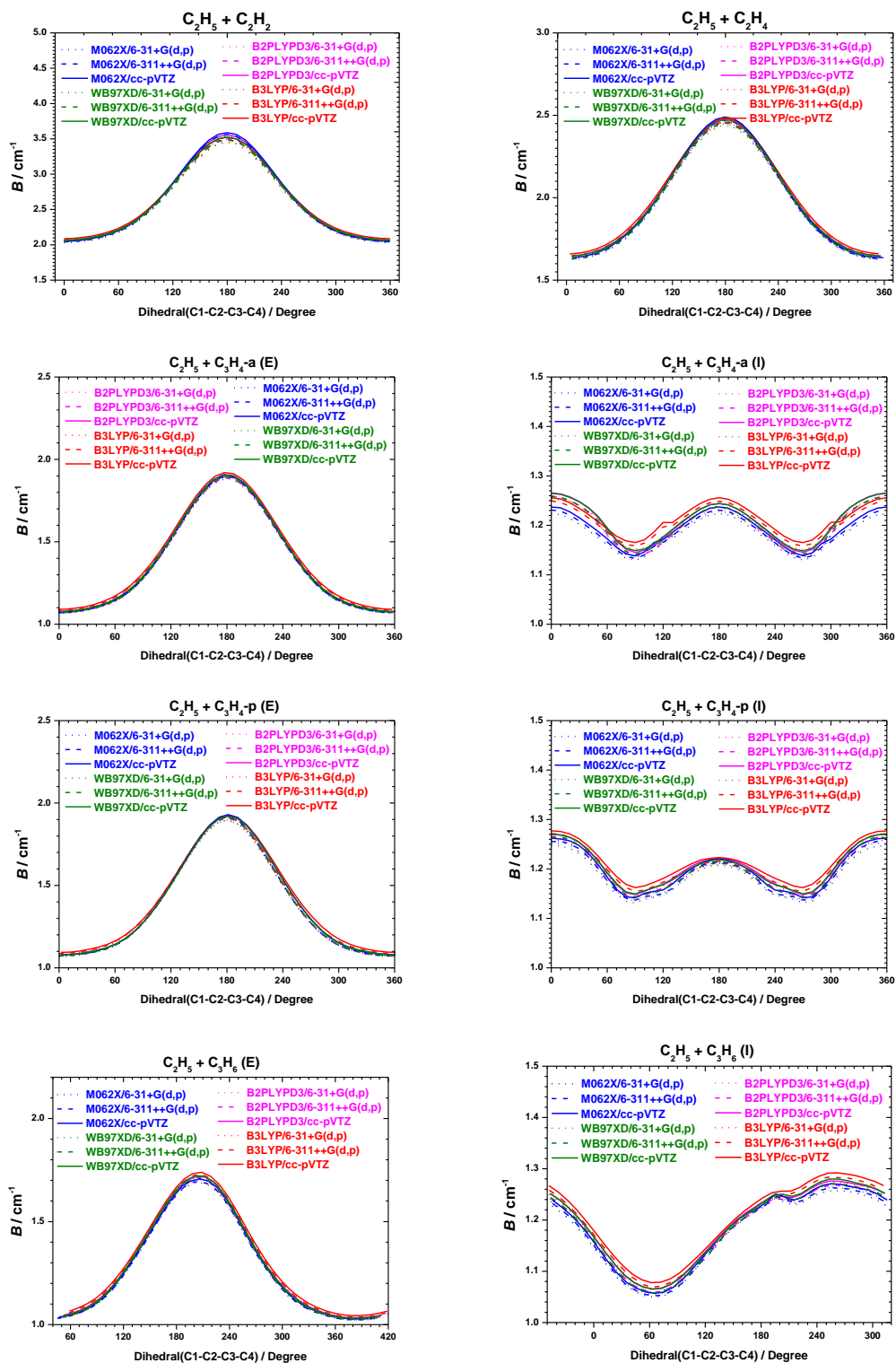


**Fig. C.3** Rotational constants for rotors formed by  $\dot{\text{C}}_2\text{H}_5$  radical additions to  $\text{C}_2\text{H}_2/\text{C}_2\text{H}_4/\text{C}_3\text{H}_4\text{-a}/\text{C}_3\text{H}_4\text{-p}/\text{C}_3\text{H}_6$  calculated using twelve DFT methods.

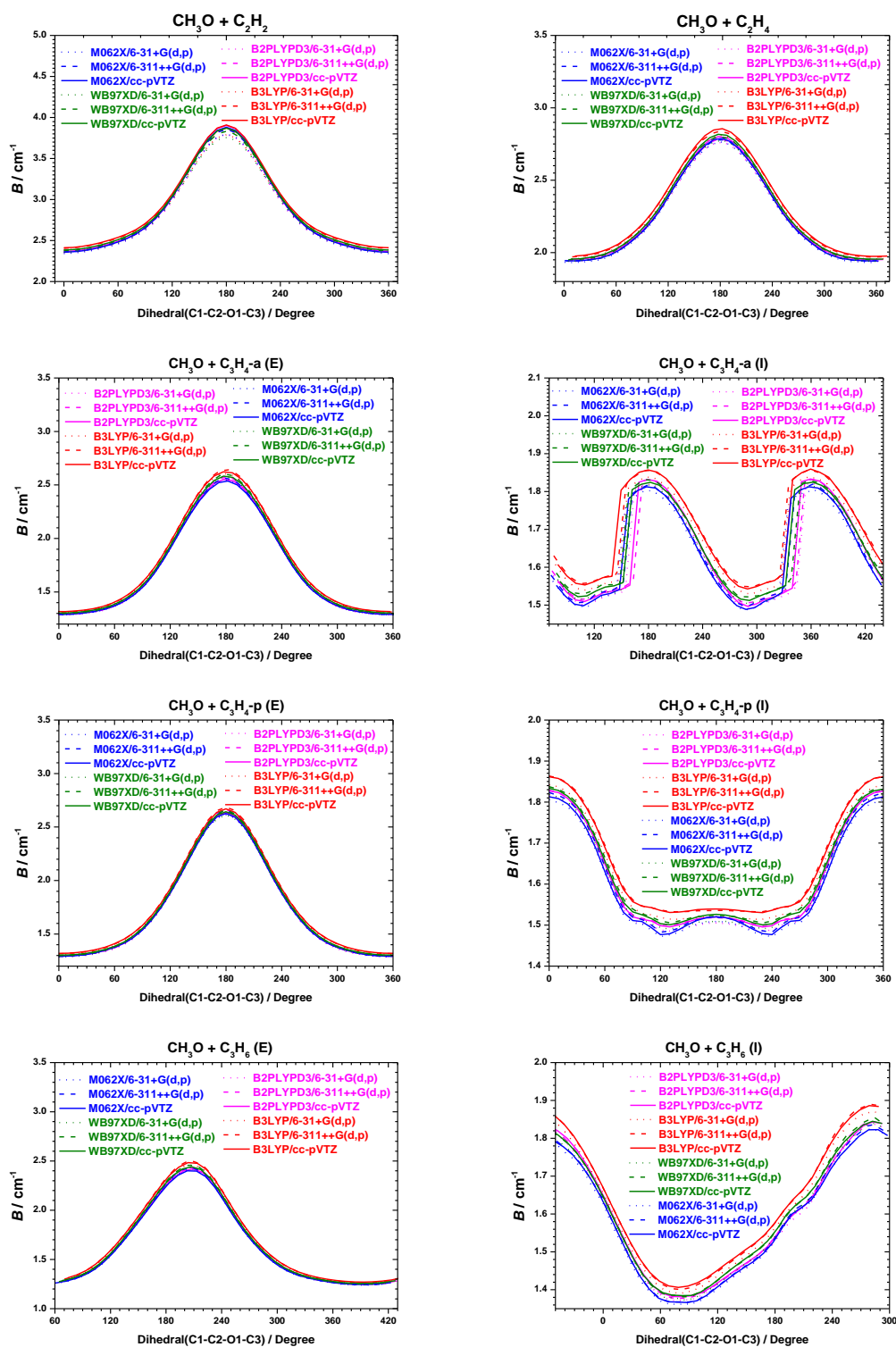


**Fig. C.4** Rotational constants for rotors formed by  $\text{CH}_3\dot{\text{O}}$  radical additions to  $\text{C}_2\text{H}_2/\text{C}_2\text{H}_4/\text{C}_3\text{H}_4\text{-a}/\text{C}_3\text{H}_4\text{-p}/\text{C}_3\text{H}_6$  calculated using twelve DFT methods.

**C.8 Hindrance potentials for the newly formed rotors of  $\dot{\text{C}}\text{H}_3/\dot{\text{C}}_2\text{H}_3/\dot{\text{C}}_2\text{H}_5/\text{CH}_3\dot{\text{O}}$  radical additions to  $\text{C}_2\text{H}_2/\text{C}_2\text{H}_4/\text{C}_3\text{H}_4\text{-a}/\text{C}_3\text{H}_4\text{-p}/\text{C}_3\text{H}_6$  calculated at twelve DFT methods.**

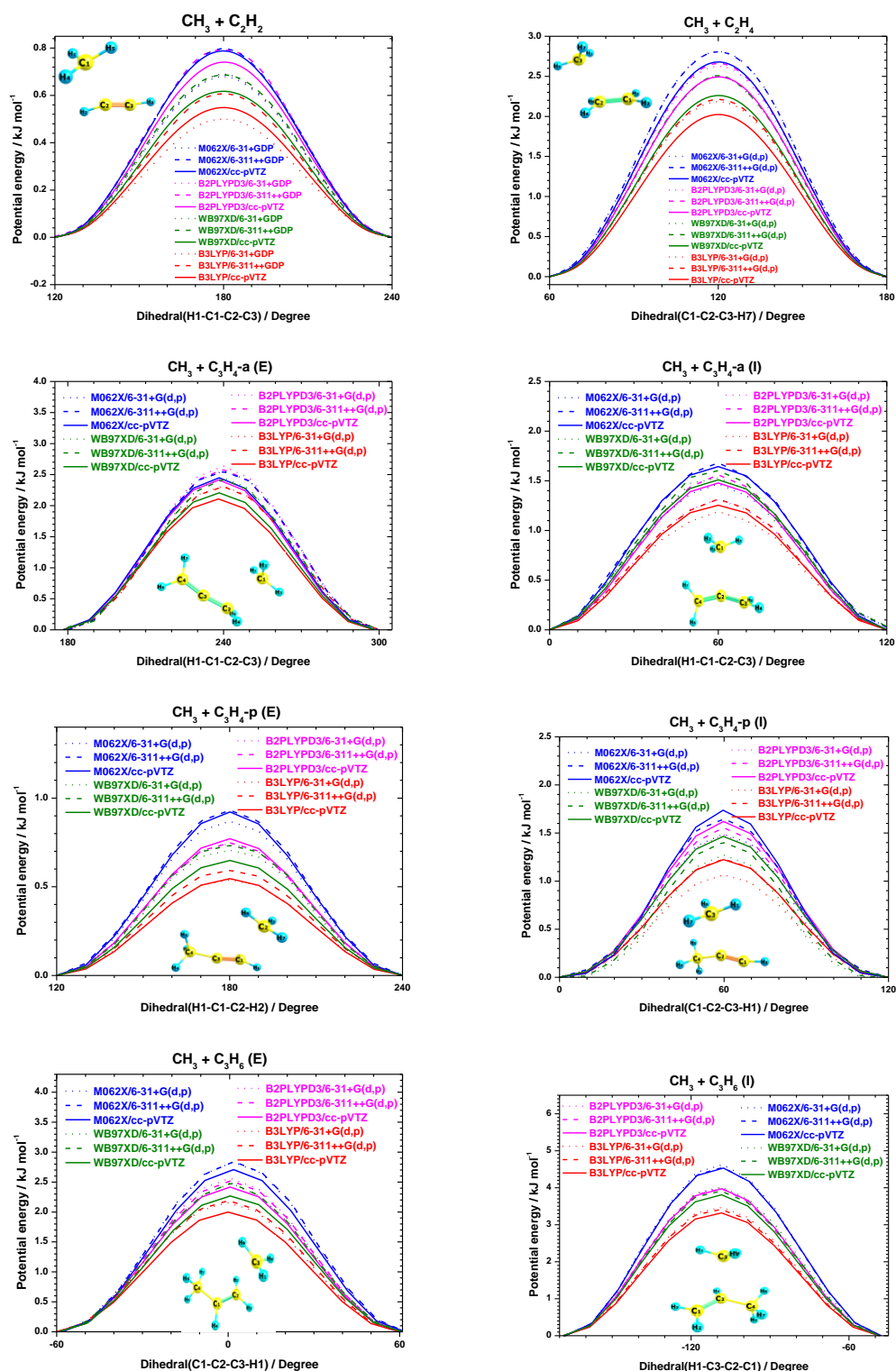


**Fig. C.5** Hindrance potentials for the newly formed methyl rotors of  $\dot{\text{C}}\text{H}_3$  radical additions to  $\text{C}_2\text{H}_2/\text{C}_2\text{H}_4/\text{C}_3\text{H}_4\text{-a}/\text{C}_3\text{H}_4\text{-p}/\text{C}_3\text{H}_6$  calculated using twelve DFT methods.

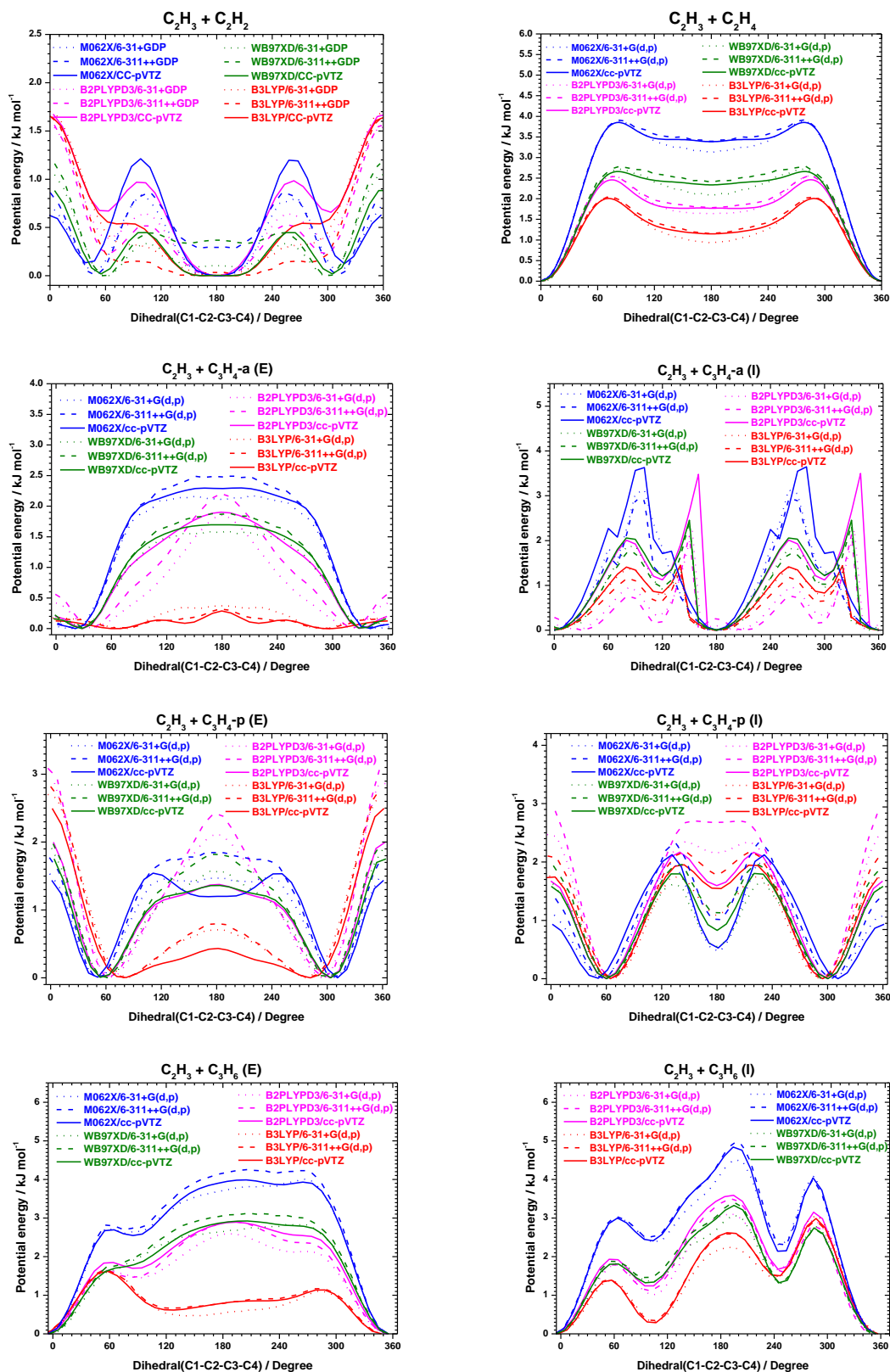


**Fig. C.6** Hindrance potentials for the newly formed methyl rotors of  $\dot{C}_2H_3$  radical additions to  $C_2H_2/C_2H_4/C_3H_4\text{-a}/C_3H_4\text{-p}/C_3H_6$  calculated using twelve DFT methods.

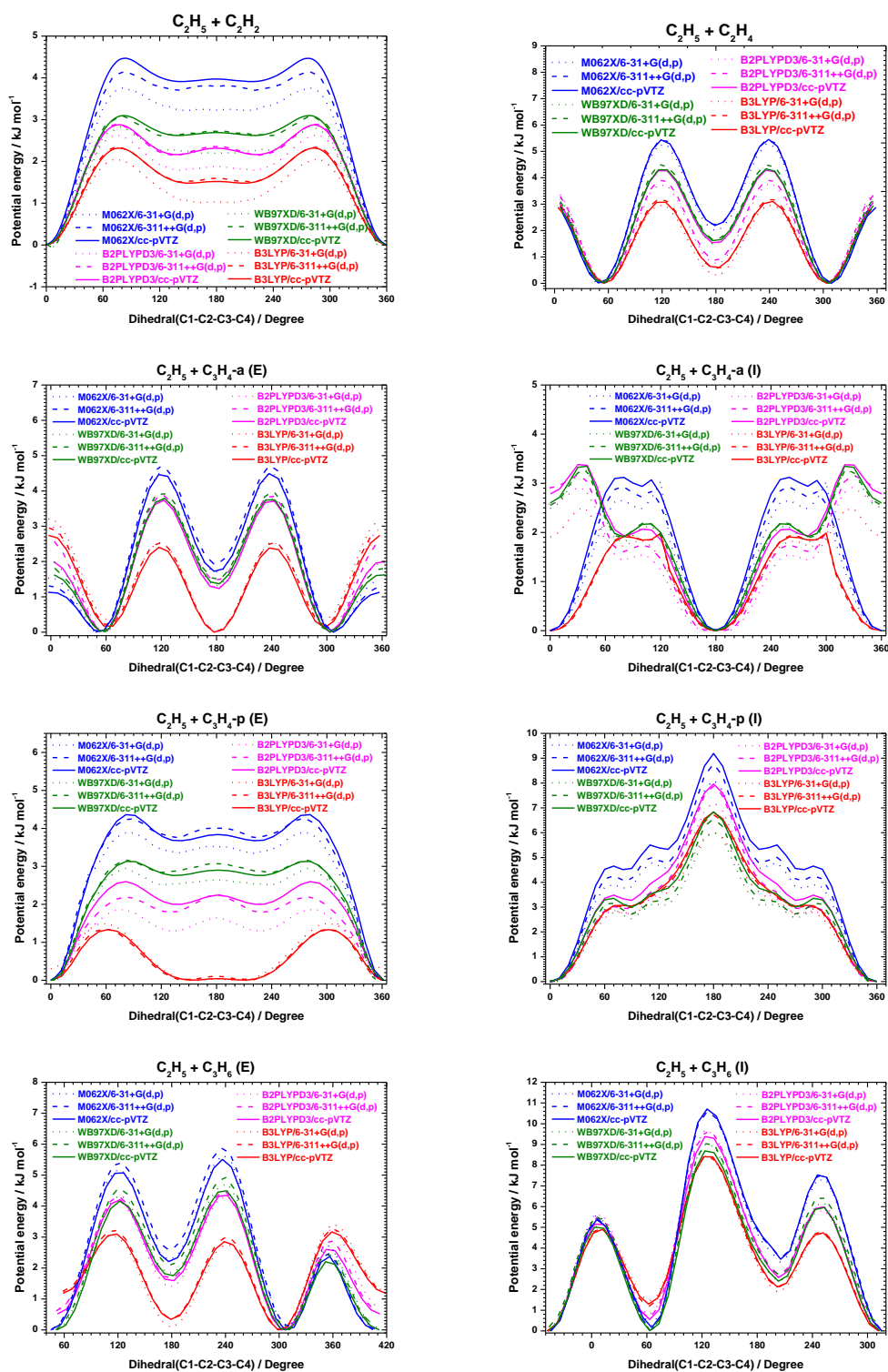


**Fig. C.7** Hindrance potentials for the newly formed methyl rotors of  $\dot{\text{C}}_2\text{H}_5$  radical additions to  $\text{C}_2\text{H}_2/\text{C}_2\text{H}_4/\text{C}_3\text{H}_4\text{-a}/\text{C}_3\text{H}_4\text{-p}/\text{C}_3\text{H}_6$  calculated using twelve DFT methods.

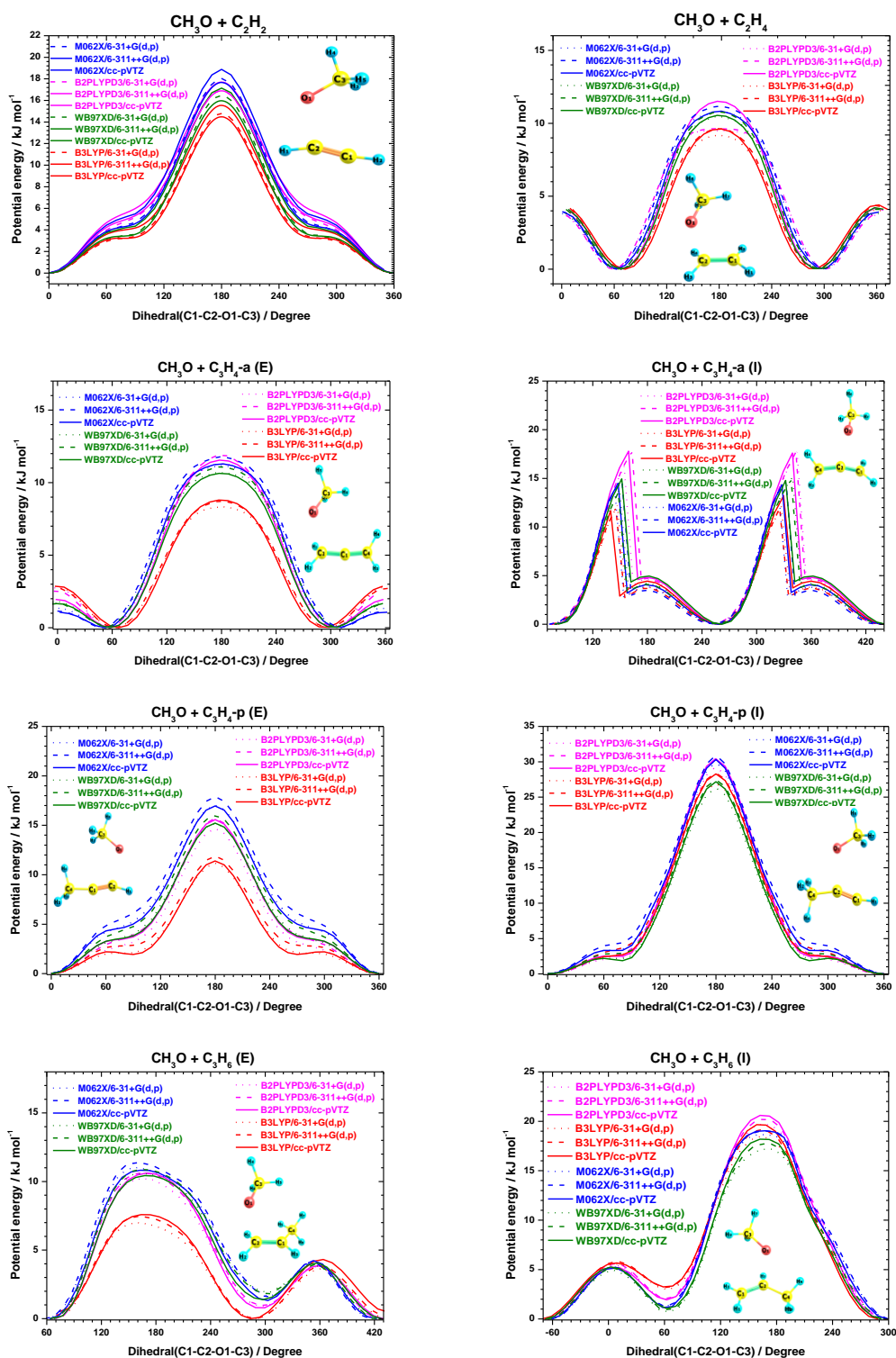


**Fig. C.8** Hindrance potentials for the newly formed methyl rotors of  $\text{CH}_3\dot{\text{O}}$  radical additions to  $\text{C}_2\text{H}_2/\text{C}_2\text{H}_4/\text{C}_3\text{H}_4\text{-a}/\text{C}_3\text{H}_4\text{-p}/\text{C}_3\text{H}_6$  calculated using twelve DFT methods.

**C.9 The relative energy deviations between DFT and DLPNO-CCSD(T)/CBS results for the newly formed rotors of  $\dot{\text{C}}\text{H}_3/\dot{\text{C}}_2\text{H}_3/\dot{\text{C}}_2\text{H}_5/\text{CH}_3\dot{\text{O}}$  radical additions to  $\text{C}_2\text{H}_2/\text{C}_2\text{H}_4$ .**

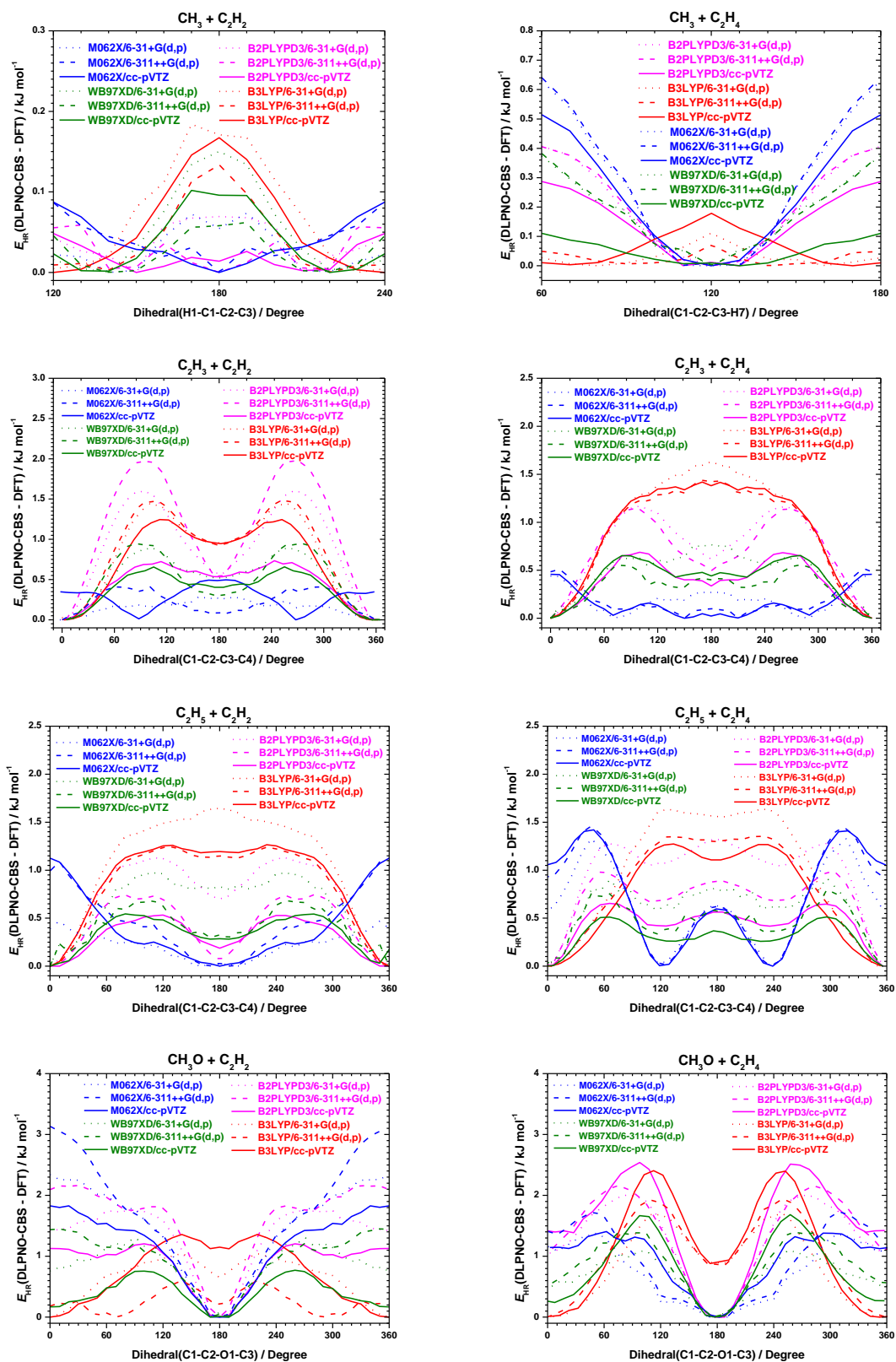


**Fig. C.9** The relative potential energy differences calculated using DFT and DLPNO-CCSD(T)/CBS methods for rotors formed by  $\dot{\text{C}}\text{H}_3/\dot{\text{C}}_2\text{H}_3/\dot{\text{C}}_2\text{H}_5/\text{CH}_3\dot{\text{O}}$  radical additions to  $\text{C}_2\text{H}_2$  and  $\text{C}_2\text{H}_4$ , and potential energy differences are relative to the lowest energy difference of each hindrance potential.

**C.10** The percentage deviations between DFT and the corresponding mean energies for rotors formed by  $\dot{\text{C}}\text{H}_3/\dot{\text{C}}_2\text{H}_3/\dot{\text{C}}_2\text{H}_5/\text{CH}_3\dot{\text{O}}$  radical additions to  $\text{C}_2\text{H}_2/\text{C}_2\text{H}_4$  at 500 K, 1000 K and 2000 K.

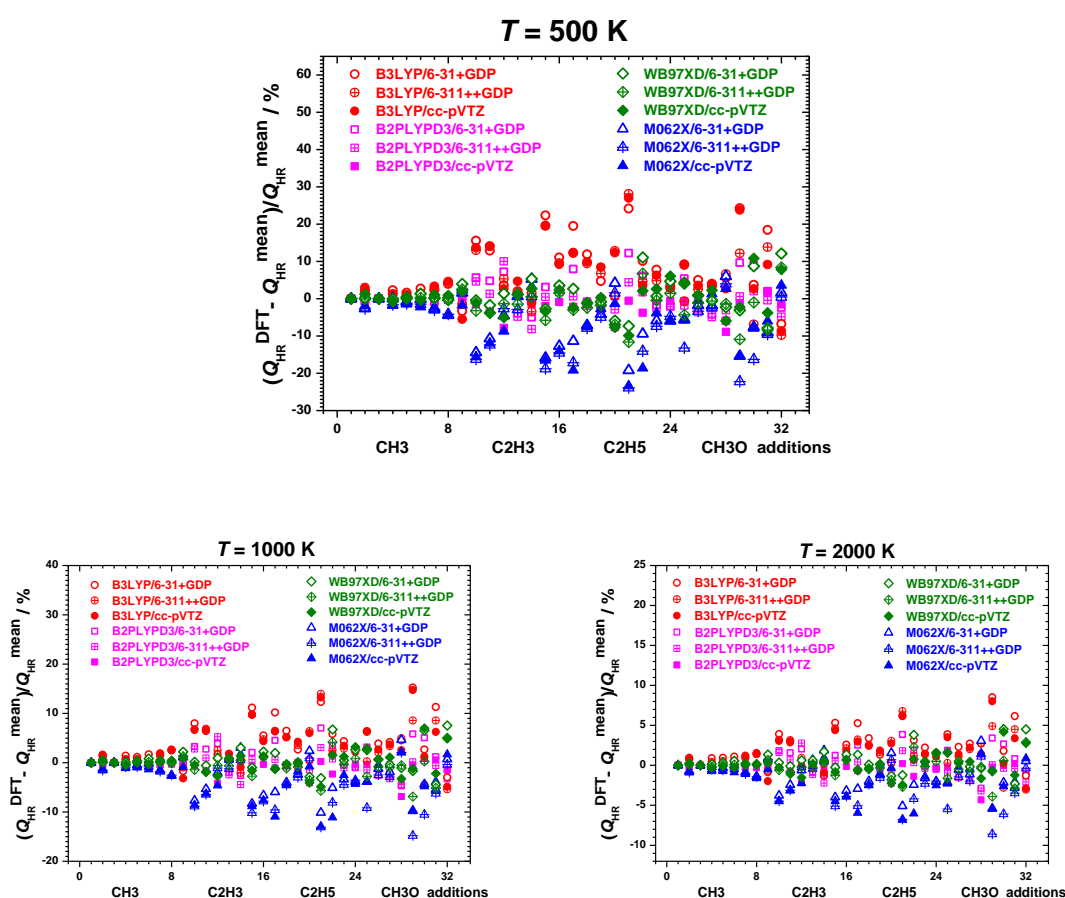


**Fig. C.10** The percentage deviations between DFT and the corresponding mean energies for rotors formed by  $\dot{\text{C}}\text{H}_3/\dot{\text{C}}_2\text{H}_3/\dot{\text{C}}_2\text{H}_5/\text{CH}_3\dot{\text{O}}$  radical additions to  $\text{C}_2\text{H}_2/\text{C}_2\text{H}_4$  at 500 K, 1000 K and 2000 K.

### C.11 Maximum $E_{HR}$ (DLPNO-CCSD(T)/CBS – DFT) deviations

**Table C.7** Maximum deviations of hindrance potential energies between DFT and DLPNO-CCSD(T) methods for rotors formed through  $\dot{C}H_3/\dot{C}_2H_3/\dot{C}_2H_5/CH_3\dot{O}$  radical additions to  $C_2H_2/C_2H_4$ .

$\Delta E_{HR}(MAX)$	B2PLYP-D3			B3LYP			M06-2X			$\omega$ B97X-D		
	6-31+ G(d,p)	6-311++ G(d,p)	cc-pVTZ									
TS1	0.07	0.06	0.05	0.18	0.13	0.17	0.07	0.09	0.09	0.15	0.06	0.10
TS2	0.41	0.41	0.29	0.11	0.07	0.18	0.63	0.64	0.51	0.37	0.38	0.11
TS9	1.60	1.97	0.73	1.44	1.48	1.25	0.29	0.42	0.50	0.88	0.95	0.66
TS10	1.17	1.14	0.69	1.63	1.44	1.42	0.44	0.52	0.46	0.76	0.56	0.65
TS17	1.13	0.74	0.53	1.64	1.24	1.27	0.47	1.09	1.13	0.97	0.68	0.54
TS18	1.33	0.99	0.65	1.64	1.35	1.27	1.33	1.46	1.42	0.92	0.80	0.51
TS25	1.75	2.16	1.20	1.04	0.60	1.36	2.34	3.13	1.83	1.32	1.45	0.77
TS26	2.01	2.16	2.54	1.71	1.94	2.41	1.38	1.73	1.41	1.10	1.39	1.68

## C.12 Maximum deviations of hindered internal rotation partition function

**Table C.8** Maximum deviations of  $Q_{\text{HR}}$  between DFT and DLPNO-CCSD(T) methods for rotors formed through  $\dot{\text{C}}\text{H}_3/\dot{\text{C}}_2\text{H}_3/\dot{\text{C}}_2\text{H}_5/\text{CH}_3\dot{\text{O}}$  radical additions to  $\text{C}_2\text{H}_2/\text{C}_2\text{H}_4$ .

$\Delta Q_{\text{HR}}(\text{MAX})$	B2PLYP-D3			B3LYP			M06-2X			$\omega$ B97X-D		
	6-31+ G(d,p)	6-311++ G(d,p)	cc-pVTZ									
TS1	0.25	-0.28	1.11	0.68	0.35	-0.40	0.89	0.28	-0.18	0.98	-0.50	0.59
TS2	-4.17	-4.10	-2.87	0.44	-0.31	1.38	-6.30	-6.42	-5.19	-3.29	-3.37	-1.08
TS9	-4.58	-6.47	-4.10	-5.80	-4.79	-9.05	-3.88	-0.13	-6.88	-0.61	-1.15	-1.79
TS10	23.38	21.55	11.74	36.79	32.43	33.71	-6.76	-8.48	-8.25	12.85	8.47	12.58
TS17	9.57	30.78	-16.55	9.94	24.52	13.61	40.57	29.52	-5.82	-14.23	17.16	8.60
TS18	-5.19	-6.22	-4.21	13.08	8.82	9.67	-13.18	-13.95	-13.15	-5.14	-6.83	-4.41
TS25	4.69	-3.34	-1.44	13.06	-0.97	12.12	-6.51	-14.90	-5.69	6.05	-4.71	6.39
TS26	-5.45	-7.26	-4.36	0.37	-2.25	-1.33	-4.82	-5.79	-3.36	-2.13	-4.47	-2.49

## References

- [1] J.A. Miller, J.P. Senosiain, S.J. Klippenstein, Y. Georgievskii, Reactions over multiple, interconnected potential wells: Unimolecular and bimolecular reactions on a C<sub>3</sub>H<sub>5</sub> potential, *The Journal of Physical Chemistry A* 112 (2008) 9429-9438.
- [2] Y. Li, S.J. Klippenstein, C.-W. Zhou, H.J. Curran, Theoretical Kinetics Analysis for H Atom Addition to 1, 3-Butadiene and Related Reactions on the C<sub>4</sub>H<sub>7</sub> Potential Energy Surface, *The Journal of Physical Chemistry A* 121 (2017) 7433-7445.
- [3] J.A. Miller, S.J. Klippenstein, The H+ C<sub>2</sub>H<sub>2</sub> (+ M) ⇌ C<sub>2</sub>H<sub>3</sub> (+ M) and H+ C<sub>2</sub>H<sub>2</sub> (+ M) ⇌ C<sub>2</sub>H<sub>5</sub> (+ M) reactions: Electronic structure, variational transition-state theory, and solutions to a two-dimensional master equation, *Physical Chemistry Chemical Physics* 6 (2004) 1192-1202.
- [4] C.F. Goldsmith, H. Ismail, P.R. Abel, W.H. Green, Pressure and temperature dependence of the reaction of vinyl radical with alkenes II: Measured rates and predicted product distributions for vinyl+propene, *Proceedings of the Combustion Institute* 32 (2009) 139-148.
- [5] K. Wang, S.M. Villano, A.M. Dean, Reactions of allylic radicals that impact molecular weight growth kinetics, *Physical Chemistry Chemical Physics* 17 (2015) 6255-6273.
- [6] K. Wang, S.M. Villano, A.M. Dean, Reactivity–structure-based rate estimation rules for alkyl radical H atom shift and alkenyl radical cycloaddition reactions, *The Journal of Physical Chemistry A* 119 (2015) 7205-7221.